NASA
Technical
Paper
2660
Part 1

July 1987

Study of Lee-Side Flows Over Conically Cambered Delta Wings at Supersonic Speeds

Richard M. Wood
and Carolyn B. Watson

NASA

NASA
Technical
Paper
2660
Part 1

1987

Study of Lee-Side Flows Over Conically Cambered Delta Wings at Supersonic Speeds

Richard M. Wood
and Carolyn B. Watson

Langley Research Center
Hampton, Virginia

National Aeronautics
and Space Administration

**Scientific and Technical
Information Office**

1987

CONTENTS

Part 1

Part 2*

*Pages 209 through 611 are published under separate cover.

SUMMARY

An experimental investigation was performed in which surface pressure data, flow visualization data, and force and moment data were obtained on four conical delta wing models which differed in leading-edge camber. Experimental flow visualization data were obtained over a range of flow conditions to determine the various flow mechanisms which occur on the lee side of cambered delta wings. Extensive surface pressure data were obtained to evaluate flow conicity, the effect of Reynolds number, and scale effects both at angle of sideslip and angle of attack. Force and moment data were obtained to evaluate the potential of separated flows to improve the performance of wings at supersonic speeds.

The series of four delta wing models varied in leading-edge camber only. Wing leading-edge camber was achieved through a deflection of the outboard 30 percent of the local wing semispan of a reference 75° swept flat delta wing. The four wing models had leading-edge deflection angles δ_F of 0°, 5°, 10°, and 15° measured streamwise.

Surface pressure data showed that the influence of Mach number on the lee-side pressure is directly related to the angle of attack and wing camber. Data for the wings with $\delta_F = 10°$ and 15° showed that hinge-line separation dominated the lee-side wing loading and prohibited the development of leading-edge separation on the deflected portion of wing leading edge. However, data for the wing with $\delta_F = 5°$ showed that at an angle of attack of 5° a vortex was positioned on the deflected leading edge with reattachment at the hinge line.

Flow visualization results have been presented which detail the influence of Mach number, angle of attack, and camber on the lee-side flow characteristics of conically cambered delta wings. Analysis of photographic data identified the existence of 12 distinctive lee-side flow types. These 12 flow types were then further categorized into two groups identified as having either one or two dominant features in the lee-side flow field. The first group of flow types were those which had a single dominant flow feature which emanated from either the leading edge or the hinge line. The second group of flow types were those which had features which emanated from both the wing leading edge and wing hinge line.

In general, the aerodynamic force and moment data correlated well with the pressure and flow visualization results. In particular the aerodynamic data showed that only the wing with $\delta_F = 5°$ consistently provided improved aerodynamic performance compared with that of the flat reference wing. It was also shown that despite the large variation in lee-side flow conditions with increasing angle of attack, the linearity of the pitching-moment curve for all wings was maintained.

INTRODUCTION

It is necessary to develop an understanding of all flows which may exist over a wing before any significant improvements in wing design may be made. One particular area of interest in which there exist little experimental data is that of wing leading-edge vortex flows at supersonic speeds. Experimental studies have concentrated on flat delta wings in which several unique flow phenomena have been

identified (refs. 1, 2, and 3). The flat wing data have compared well with computational results (refs. 4, 5, and 6). However, the continued development of Euler and Navier-Stokes solvers could be hindered by the lack of experimental data for separated flows. To address this important issue, several experimental studies have been made with the express purpose to develop an understanding of the fundamental characteristics of this class of flow and to define their dependence on various geometric and flow conditions. These studies are being directed from both the experimental and computational viewpoints (refs. 6 and 7).

This present experimental study is a direct extension of the work reported in references 3 and 6. The purpose of this paper is to determine the influence of wing camber on the lee-side flow characteristics of delta wings. An experimental investigation was performed in which surface pressure coefficient data, flow visualization data, and force and moment data were obtained on four conical delta wing models which differed in leading-edge camber. Experimental flow visualization data were obtained over a range of flow conditions to determine the various flow mechanisms which occur on the lee side of cambered delta wings. Extensive surface pressure coefficient data were obtained to evaluate flow conicity, the effect of Reynolds number, and scale effects both at angle of attack and angle of sideslip. Force and moment data were obtained to evaluate the potential of separated flows to improve the performance of wings at supersonic speeds. These results provide a comprehensive set of experimental data which may be used by the aerodynamic community to evaluate existing prediction techniques and to assess the separated flow wing design concept.

SYMBOLS

b span of undeflected wing model, 18.000 in.

C_A axial-force coefficient, $\frac{\text{Axial force}}{qS}$

C_D drag coefficient, $\frac{\text{Drag}}{qS}$

$C_{D,min}$ minimum drag coefficient

C_L lift coefficient, $\frac{\text{Lift}}{qS}$

C_{L_α} lift-curve slope at $C_L = 0.00$

C_l rolling-moment coefficient, $\frac{\text{Rolling moment}}{qSb}$

C_m pitching-moment coefficient, $\frac{\text{Pitching moment}}{qS\bar{c}}$

$C_{m,o}$ zero-lift pitching-moment coefficient

C_N normal-force coefficient, $\frac{\text{Normal force}}{qS}$

C_N^l normal-force coefficient on lower surface

C_N^u normal-force coefficient on upper surface

C_n yawing-moment coefficient, $\frac{\text{Yawing moment}}{qSb}$

C_p pressure coefficient, $\frac{p - p_\infty}{q}$

C_Y side-force coefficient, $\frac{\text{Side force}}{qS}$

$\bar{c}$ mean aerodynamic chord of undeflected wing model, 22.390 in.

L/D lift-drag ratio

$(L/D)_{max}$ maximum lift-drag ratio

l configuration length of undeflected wing model, 33.588 in.

M Mach number

M_N component of Mach number normal to wing leading edge, $M \cos \Lambda(1 + \sin^2\alpha \tan^2\Lambda)^{1/2}$

p local static pressure, lb/ft^2

p_∞ free-stream static pressure, lb/ft^2

q free-stream dynamic pressure, lb/ft^2

R Reynolds number per foot

S reference area of undeflected wing model, 302.292 in^2

WF wing-forebody

WOF wing without forebody

x longitudinal distance from model nose, in.

y spanwise distance from model centerline, in.

z vertical distance from model upper wing surface, in.

α angle of attack, deg

α_N angle of attack normal to wing leading edge, $\tan^{-1} \frac{\tan \alpha}{\cos \Lambda}$, deg

β angle of sideslip, deg

$\beta \cot \Lambda$ wing leading-edge sweep parameter, where $\beta = \sqrt{M^2 - 1}$

δ_F streamwise deflection angle of wing leading edge, deg

η fraction of local wing semispan referenced to undeflected wing model

Λ wing leading-edge sweep angle, deg

MODELS AND TESTS

Model Description

The test program included a series of four delta wing models which varied in leading-edge camber only. Wing leading-edge camber was achieved through a deflection of the outboard 30 percent of the local wing semispan of a reference 75° swept flat delta wing. The four wing models have leading-edge deflection angles of 0°, 5°, 10°, and 15° measured streamwise. This method of defining the parametric wing set resulted in a reduction in wing span and planform area and an increase in wing leading-edge sweep compared with that of the flat wing. However, this parametric study should provide a true representation of a simple vortex flap system. The geometric characteristics of the four wing models are listed in table I, and details of the wing models and supporting hardware are depicted in figures 1 through 4. Figure 1 is a sketch of the wing-body model assembly and figures 2, 3, and 4 contain the details of the wing, balance block, and fuselage, respectively. A photograph of the flat delta wing model is shown as figure 5 and a photograph of the $\delta_F = 10°$ cambered wing is shown as figure 6.

To minimize the effect of airfoil shape, the leading edge was made sharp and the wing upper surface was flat. The wing lower surface consisted of a bevel angle of 10° measured normal to the wing leading edge. This wedge surface extended inboard to a maximum thickness of 0.600 in., which then remained constant. Each wing was fitted with a minimum conical body which emanated from the wing apex and extended back to 48 percent of the model length. The conical body changed to a cylindrical balance housing which was common to all four delta wings. Both the conical body and balance block were symmetrically located about the wing upper surface. The resultant wind-tunnel models were conical on the upper surface to a value of x/ℓ of 0.48 and were nearly conical, except for the minimum balance housing, over the remainder of the model length. All wings were designed to accept a minimum fuselage forebody which extended beyond the wing apex, as shown in figures 1 and 4. A limited amount of testing was conducted on the delta wing with $\delta_F = 5°$ with and without the extended fuselage.

The upper surface of each wing was instrumented with six spanwise rows of evenly spaced pressure orifices located at 0.10, 0.20, 0.30, 0.60, 0.80, and 0.90 of the model length as indicated in figure 1. The pressure orifices were distributed spanwise between 0 and 90 percent of the local semispan in increments of 5 percent at x/ℓ stations of 0.20, 0.30, 0.60, 0.80, and 0.90. At the most forward station ($x/\ell = 0.10$), the pressure orifices were alternated between the left and right side of the wing and only extended to 70 percent of the wing semispan. Presented in table II is a listing of all pressure orifice locations for the flat wing. The pressure orifices for the cambered wings ($\delta_F = 5°$, 10°, and 15°) were at the same spanwise positions, measured along the wing surface, as those for the flat wing. The streamwise locations of each spanwise row of pressure orifices for the cambered wings were identical to those for the flat wing. All pressure tubing was routed internal to the model and terminated within the model at two locations on the lower surface of the wing. (See fig. 2.) For flow visualization and force and moment testing, the pressure tube model exit locations were covered with a flush-mounted plate. For pressure tests, two multiple pressure tube connector pads (figs. 2 and 7) were attached to the model to route the tubes to a scanning-valve, pressure-gauge system mounted external to the tunnel. Location and size of the two multiple pressure tube connector pads were designed to minimize their interference on the wing lee-side flow characteristics.

All wing models were mounted to a common balance housing (fig. 3) which was connected to the permanent model-actuating system through a balance and sting arrangement. All wing models also employed the same multiple pressure tube connectors and external tubing.

Test Conditions

A wind-tunnel test program was conducted in the low Mach number test section of the Langley Unitary Plan Wind Tunnel (ref. 8) to obtain surface pressure, flow visualization, and force and moment data.

The pressure and force data were obtained at angles of sideslip from -8° to 8° and angles of attack from -4° to 20° for the nominal test conditions listed in the following table:

Mach number	Stagnation pressure, lb/ft^2	Stagnation temperature, °F	Reynolds number per foot
1.50	1051	125	2×10^6
1.70	1114	125	2×10^6
1.70	557	125	1×10^6
2.00	1254	125	2×10^6
2.40	1521	125	2×10^6
2.80	1875	125	2×10^6
2.80	937	125	1×10^6

To ensure fully turbulent flow over the model surface for all testing, boundary-layer transition strips composed of No. 60 sand grit were applied 0.2 in. behind the wing leading edges (measured normal to the leading edge) and 1.2 in. aft of the model nose (ref. 9). The transition strips were 0.0625 in. wide.

Balance chamber pressure was measured during the force tests with a pressure transducer mounted external to the wind tunnel and connected by pressure tubing to a pressure probe mounted within the balance chamber. Force and moment data were corrected to free-stream static pressure at the model base. Angles of attack for force and moment data were adjusted for flow misalignment and sting and balance deflections. The force and moment data were reduced relative to the wing upper surface. Pressure data angles of attack were adjusted for flow misalignment only. The pressure data angles of attack were not adjusted for sting and balance deflections because of the unknown influence of the pressure tubing during testing. A discussion of the pressure test angle of attack is contained in appendix A.

Flow Visualization Techniques

In addition to the surface-pressure data and force and moment data three types of flow visualization data were obtained. Vapor-screen photographs were obtained to provide information on the flow field above the wing leeward surface, and both tuft and oil-flow photographs were used to examine the flow characteristics on the model surface. Model preparation for all flow visualization tests consisted of painting one coat of flat black paint over a coat of zinc chromate primer.

Vapor-screen photographs were obtained by adding water in the diffuser downstream from the tunnel test section until a uniform vapor was produced in the test section. The test conditions which provided the best vapor quality for $R = 2 \times 10^6$ are given in the following table:

Mach number	Stagnation pressure, lb/ft^2	Stagnation temperature, °F	Dew point, °F
1.50	1051	90	9
1.70	1114	100	13
2.00	1254	117	19
2.40	1521	125	25
2.80	1875	125	29

The dew point was measured in the tunnel settling chamber and corrected to standard atmospheric conditions. The nominal test conditions at which pressure and force data were obtained correspond to a dew point of -20°F.

A high-intensity tungsten light source mounted outside the tunnel on the sidewall was used to produce a thin light sheet across the tunnel test section. The light sheet was positioned normal to the flow and was positioned so that the model could be moved longitudinally to align the light sheet with the desired location. Photographs were taken by a camera mounted to the ceiling inside the tunnel and located approximately 3 ft downstream from the model.

Tuft photographs were obtained by affixing fluorescent minitufts to the model surface and illuminating the model with ultraviolet light. Chordwise rows of tufts were attached to the model with a thinned solution of radio cement. The tufts were 0.75-in. lengths of 0.003-in-diameter nylon monofilament. Each chordwise row of tufts began at the downstream edge of the leading-edge grit with a longitudinal spacing of 0.75 in. between tuft-model attachment points. The longitudinal rows were spaced 0.50 in. apart in the spanwise direction, with the first row located on the model centerline. Tufts were affixed only to the left wing panel so that the right wing panel could be used for oil-flow photographs. Tuft photographs were taken through the window by two cameras mounted outside the tunnel on the sidewall door. The model was rolled 90° (wings vertical) and was illuminated by four ultraviolet lamps also mounted on the sidewall door.

Oil-flow photographs required the same model-surface flat black painting as previously discussed. The model surface was then brushed with a mixture of 90W oil containing yellow fluorescent powder. The model was illuminated and cameras were positioned the same as for the tuft photographs. During the tunnel start-up period, the model was kept in a wings-horizontal position to prevent the oil from running; to obtain photographs, the model was rolled 90° (wings vertical) and angle of attack was set by yawing the model. After the model was positioned, approximately 3 to 4 min was required for the oil-flow pattern to stabilize. Normally, only 3 or 4 different angles of attack could be documented before the oil had to be replaced.

DISCUSSION

A review of the literature has shown that previous studies of wing leading-edge vortex flows at supersonic speeds failed to investigate sideslip conditions and Reynolds number effects and have not fully verified at which conditions conical flow exists. To address each of these areas of concern in addition to the effect of wing camber, a parametric set of four conically cambered delta wings have been tested. It should be noted that the primary purpose of the wings under investigation was to develop an extensive data base on the fundamental flow characteristics over cambered delta wings at supersonic speeds. The present wing geometries do not represent any particular design philosophy but were defined to provide a large variation in flow conditions based upon the data of references 3 and 6.

An extensive amount of lee-side surface pressure coefficient data, lee-side flow visualization data, and force and moment data have been obtained on a parametric set of conically cambered delta wings. This paper addresses the critical elements of the data collected; however, because of the uniqueness of this data set all the data are presented in four appendixes (B, C, D, and E). Appendixes C, D, and E are published under separate cover in part 2 of this report. Plots of surface pressure coefficient data are presented in appendix B, and tables of surface pressure coefficient data are presented in appendix C. Flow visualization data are contained in appendix D, and force and moment data are contained in appendix E.

This paper reviews the surface pressure distributions first, followed by a look at the flow visualization results and finally a summary of the force and moment data.

Lee-Side Surface Pressure Distributions

All models have been instrumented with six spanwise rows of pressure orifices to study conical flow effects and to investigate scale effects along the length of the wing. Pressure data were obtained on each wing at Mach numbers of 1.50 to 2.80, angles of attack of -4° to 20°, angles of sideslip of -8° to 8°, and Reynolds numbers per foot of 2×10^6 and 1×10^6. These pressure data are presented in the form of plots of spanwise surface pressure coefficient.

Unless noted otherwise, all pressure data presented in the paper are for the spanwise row of pressure orifices located at $x/l = 0.90$, for a free-stream Reynolds number per foot of 2×10^6. The spanwise location of the pressure orifices for all wings are at equal distances measured along the wing surface. The nondimensional spanwise position parameter η is defined with respect to the flat wing. The values specified for α, β, M, and R are approximate values; their absolute values may be found in the tabulated listing of appendix C.

Effect of M and α.- Previous experimental studies have shown that both Mach number and angle of attack have a strong influence on the lee-side pressures of flat wings with separated flows. To assess the influence of M and α on the lee-side flow for this cambered wing series, spanwise surface pressure distributions for each wing are presented in figures 8 through 12. The effect of Mach number on the surface pressure coefficient for each wing at angles of attack of 0°, 4°, and 12° is shown in figures 8, 9, and 10, respectively, and the effect of α at M = 1.70 and 2.80 is shown in figures 11 and 12, respectively.

Pressure data at $\alpha = 0°$ appear to vary about the line at $C_p = 0.00$ due to a change in Mach number. (See figs. 8(a), 8(b), 8(c), and 8(d).) The inability to achieve $C_p = 0.00$ may be attributed to the variation in flow angularity, total pressure, or temperature within the tunnel test section. An examination of the cambered wing data of figures 8(b), 8(c), and 8(d) shows an expansion occurring at the sharp break in the wing upper surface (hinge line). As wing camber is increased, the wing pressures outboard of the hinge line ($\eta > 0.7$) increase and the wing pressures at the hinge line decrease due to the increased expansion angle. It is interesting to note that for the wing with $\delta_F = 5°$, the expansion is centrally located about the hinge line ($\eta = 0.7$); however, as wing camber is increased the expansion peak moves inboard and the pressures decrease. This would indicate that flow separation has occurred at the hinge line. It is difficult to draw any conclusions about the effect of M at $\alpha = 0°$ because of the previously discussed shift in the data; however, at positive incidence angles significant effects of M are observed (figs. 9 and 10). The data clearly show that the relative influence of M on the lee-side pressures is directly related to the angle of attack and wing camber. At $\alpha = 4°$, the data show a small effect of M which decreases with increasing δ_F, and at $\alpha = 12°$, the data for all wings show a significant influence of M. The pressure data at $\alpha = 4°$ for the wings with $\delta_F = 5°$, 10°, and 15° indicate that the influence of hinge-line separation has increased for the wings with $\delta_F = 10°$ and 15° compared with the data at $\alpha = 0°$ despite the varying flow condition at the leading edges. The data show that at $\alpha = 4°$, the leading edge of the wing with $\delta_F = 5°$ is at a positive incidence due to an induced upwash field and the leading edges of the wings with $\delta_F = 10°$ and 15° are at a negative incidence. A comparison of the data at $\alpha = 12°$ for each wing (fig. 10) shows that the flow has separated for all wings; however, the data for the wing with $\delta_F = 15°$ (fig. 10(d)) still show a strong influence of the hinge line. For these thin, sharp-leading-edge, conical wing geometries, lee-side leading-edge separation would not be expected to occur until the angle of attack exceeds the wing streamwise deflection angle. These results suggest that the local flow conditions at the wing apex are producing a disturbance which has perturbed the total wing flow field and are producing a local upwash which then feeds down the wing. This conclusion is further supported by the variation in the flow separation angle of attack with changes in camber and Mach number.

To better understand the influence of angle of attack and Mach number on the lee-side wing loading, plots of variations in angle of attack at Mach numbers 1.70 and 2.80 are shown in figures 11 and 12, respectively. The data for the flat wing show that increasing angle of attack results in an increase in separation, an increase in the lee-side wing loading, and an inboard movement of the vortex. (See figs. 11(a) and 12(a).) The data for the three cambered wings also show results similar to those observed for the flat wing; however, there are several interesting characteristics unique to each of the cambered wings. For the wing with $\delta_F = 5°$ at $M = 1.70$ (fig. 11(b)), the data show that leading-edge separation occurs at $\alpha = 3°$ and remains confined to the deflected portion of the leading edge ($\eta > 0.7$) until $\alpha = 5°$. At $\alpha = 5°$, a vortex resides on the deflected leading edge only, with reattachment at the hinge line. The resultant pressure distribution for this condition would appear to be beneficial to achieving good aerodynamic performance. An increase in α to 6° produces a large change in the flow field, and the vortex migrates off the flap moving inboard and increases in size. Further increases in α result in spanwise pressure distributions similar to those observed for the flat wing.

The data for the wings with $\delta_F = 10°$ and 15° show that the hinge-line separation persists for all angles of attack and appears to dominate the leading-edge

separation and resultant lee-side wing loading. Another observation is the large influence of Mach number on the leading-edge flow condition. At $M = 1.70$, the data show that leading-edge separation has occurred (negative C_p) at $\alpha = 6°$ for $\delta_F = 10°$ (fig. 11(c)) and at $\alpha = 8°$ for $\delta_F = 15°$ (fig. 11(d)), but at $M = 2.80$ the data (figs. 12(c) and 12(d)) show that the leading edge is in compression at both of these angles of attack. The cambered wing data of figures 11 and 12 have consistently shown that wing lee-side leading-edge separation occurs at angles of attack less than the wing leading-edge deflection angle.

Effect of β.- To provide insight into the lee-side flow over delta wings at sideslip conditions, spanwise surface pressure distributions are presented for all wings at angles of sideslip from -8° to 8° for $\alpha = 12°$ at $M = 1.70$ and 2.80, in figures 13 and 14, respectively. A review of the data presented in figures 13 and 14 shows large effects of β, M, and δ_F. The data show an increased loading on the windward panel and a decreased loading on the leeward panel with increasing sideslip. This loading would result in a stable rolling moment.

The influence of camber is most readily seen in figure 13 where the data show significant changes in the leading-edge flow condition with increasing δ_F. Also evident in the data is the large change in the windward pressure distributions with increased camber. For the wing with $\delta_F = 10°$ at $\beta = 8°$, the data indicate that the flow separates at the leading edge followed by recompression and then a large expansion about the hinge line. Similar results are also evident for the wing with $\delta_F = 15°$ at $\beta = 2°$, 4°, and 8°, with the data at $\beta = 8°$ showing that the leading edge is in compression ($C_p > 0.00$).

The large influence of angle of sideslip on the lee-side pressure distributions could not be a leading-edge-sweep-dominated effect because these results contradict the findings of reference 3 for flat wings. The data of reference 3 showed no significant effect of leading-edge sweep on any of the wing upper surface loading characteristics. These present data suggest that a strong coupling is occurring between the leeward and windward wing panels for this asymmetric condition. At sideslip conditions, a strong cross-flow velocity component develops which flows from the windward to the leeward wing panel and which increases the windward vortex rotational velocity and retards the leeward vortex rotational velocity (ref. 7).

The influence of Mach number on the data obtained at sideslip is similar to that observed for the data of figures 11 and 12, that is, a reduced total lee-side wing loading and a change in the conditions at which initial lee-side leading-edge separation occurs. This observation is especially true for the cambered wings as seen by a comparison of figures 13(c) and 13(d) with figures 14(c) and 14(d).

Effect of R.- Tests were conducted at free-stream Reynolds numbers per foot of 1×10^6 and 2×10^6 in order to determine the effect of Reynolds number on the lee-side flow characteristics at both angles of attack and angle of sideslip. Spanwise pressure distributions detailing the effect of Reynolds number R at angle of attack for each wing are presented for $x/\ell = 0.20$ in figure 15 and for $x/\ell = 0.90$ in figure 16. The influence of Reynolds number at sideslip condition is shown in figures 17 and 18.

The data of figures 15 and 16 show that decreasing the free-stream Reynolds number per foot from 2×10^6 to 1×10^6 results in a nearly constant decrease in pressure coefficient across the span of the wing with no change in the character of the pressure distribution. The reduced lee-side wing loading with decreasing Reynolds

number was suggested in reference 6 based upon pressure data for thick, blunt leading-edge wings.

Additional Reynolds number effects are seen by comparing the data of figures 15 and 16. This analysis shows an additional decrease in the minimum pressure coefficient value (more negative C_p) for the most aft station ($x/\ell = 0.90$). The scale Reynolds numbers for these two stations, based upon their theoretical mean aerodynamic chord, are 0.37×10^6 and 0.74×10^6 at $x/\ell = 0.20$ and 1.66×10^6 and 3.33×10^6 at $x/\ell = 0.90$ for a free-stream Reynolds number per foot of 1×10^6 and 2×10^6, respectively. The result is an order of magnitude increase in the scale Reynolds number between the data obtained at a free-stream Reynolds number per foot of 1×10^6 at $x/\ell = 0.20$ and the data obtained at a free-stream Reynolds number per foot of 2×10^6 at $x/\ell = 0.90$. A comparison of these data shows a 16-percent increase in the minimum value of the lee-side pressure coefficient for the wing with $\delta_F = 0°$. (See figs. 15(a) and 16(a).) Similar results also are evident for the cambered wings. Additional scale Reynolds number effects are shown in figures 19 through 22.

The effect of Reynolds number at sideslip is shown for all wings in figures 17 and 18, respectively. Spanwise pressure distributions at $M = 1.70$, $\alpha = 12°$, and $\beta = 8°$ (fig. 17) and $\beta = -8°$ (fig. 18) show results similar to those observed in figures 15 and 16. The increased values of pressure coefficient caused by a reduction in Reynolds number are not limited to conditions which produce negative C_p values. The pressure data of figure 17(d) show that this increased pressure coefficient is observed at all flow conditions whether the flow is in a compression or expansion. Further review of the tabulated pressure coefficients of appendix C verified this effect. From a wing design point of view, a reduced Reynolds number would be detrimental to aerodynamic performance. Wing performance at supersonic speed has been shown to be a strong function of the distribution of the wing loading between the upper and lower wing surfaces such that any reduction in the lee-side contribution to the total wing loading would inhibit efficient aerodynamic performance.

Conicity and scale effects.- This section of the paper presents plots containing the pressure data from all spanwise rows of pressure orifices in order to establish flow conicity conditions for each wing. The data are also used to investigate scale Reynolds number effects. The scale Reynolds numbers based upon the theoretical mean aerodynamic chord for each wing station are 0.37×10^6 at $x/\ell = 0.10$, 0.74×10^6 at $x/\ell = 0.20$, 1.1×10^6 at $x/\ell = 0.30$, 2.2×10^6 at $x/\ell = 0.60$, 2.95×10^6 at $x/\ell = 0.80$, and 3.32×10^6 at $x/\ell = 0.90$ for a free-stream Reynolds number per foot of 2×10^6.

Presented in figures 19 and 20 are data for each wing at $\alpha = 12°$, $M = 1.70$ and 2.80, respectively. The oscillatory nature of the data for $x/\ell = 0.10$ is a result of the alternating left- and right-hand location of the surface pressure orifices on the wing, which would tend to magnify any flow or geometry asymmetries. The nonconical nature of the flow may be attributed to the nonconical balance housing. For x/ℓ values between 0.00 and 0.48, the balance housing is conical and extends to 22 percent of the semispan. The pressure values in this region of the wing ($x/\ell = 0.20$ and 0.30) are equivalent and the influence of the balance housing on the pressures is a rise in the local pressure at $\eta = 0.25$. For values of x/ℓ between 0.48 to 0.58, the balance housing changes to a cylinder which continues aft to $x/\ell = 1.00$. The spanwise extent of the balance housing is to $\eta = 0.2$ at $x/\ell = 0.60$, $\eta = 0.15$ at $x/\ell = 0.80$, and $\eta = 0.13$ at $x/\ell = 0.90$. The spanwise

location of the balance housing side of the body correlates quite well with the observed pressure rise at each location of spanwise pressure taps. These effects of the balance housing are evident in all the data presented.

The data for $\delta_F = 0°$ of figures 19(a) and 20(a) show that the flow is basically conical with slight deviations at $x/\ell = 0.10$ and at the inboard region of all stations. A comparison of the pressure data in figure 19(a) shows a 13-percent decrease in the minimum pressure coefficients between $x/\ell = 0.20$ and 0.90. There is not any noticeable change in the pressures for $M = 2.80$ probably because of the influence of the vacuum pressure limit. Further review of the data of figures 19 and 20 shows increasing deviations from flow conicity with increasing wing camber. A comparison of figures 19(b), 19(c), and 19(d) shows that the wing with $\delta_F = 5°$ is as conical as the wing with $\delta_F = 0°$ except for a slight change in the leading-edge conditions. An increase in wing camber to $\delta_F = 10°$ produced an increased scattering of the data, and at $\delta_F = 15°$ the flow appears to be nonconical. Similar characteristics were also evident in the $M = 2.80$ data of figure 20. The data presented in figures 19 and 20 are for $\alpha = 12°$ which is a condition of minimal leading-edge separation for the wing with $\delta_F = 15°$. A review of the tabulated data of appendix C shows that the lee-side flow over the cambered wings does approach conical flow at higher angles of attack once extensive leading-edge separation has occurred. The data suggest that flow conicity is not guaranteed by conical geometry but that model geometry limitations such as extreme camber must be addressed.

The data of figures 21 and 22 are used to evaluate flow conicity and scale effects at sideslip. Presented in figure 21 are the windward pressures at $M = 1.70$, $\alpha = 12°$, and $\beta = 8°$, and figure 22 contains the leeward pressures. The plots of surface pressure coefficients at sideslip conditions were created by combining the data for $x/\ell = 0.60$, 0.80, and 0.90 obtained at $\beta = 8°$ with the data for $x/\ell = 0.10$, 0.20, and 0.30 obtained at $\beta = -8°$. All the pressure data of figure 21 show a large effect of the balance housing in the spanwise pressure distributions, whereas the leeward pressures show only a minimal effect. The windward flow field would be dominated by large cross-flow velocities which would interact strongly with the balance housing as the flow moves across the wing centerline toward the leeward wing panel. The windward data show that the influence of wing camber is adverse to flow conicity for wings in sideslip. The leeward data (fig. 22) show increased conical flow compared with the windward data, and there appear to be no significant effects of wing camber. The data presented in figures 21 and 22 show large nonconical flow regions on all wings and that flow conicity was greatly influenced by the balance housing; as a result, conclusions could not be drawn concerning possible Reynolds number effects.

Effect of camber.- The previous sections presented the data as a function of various flow parameters for each wing geometry. This section presents cross plots of these data in order to emphasize the effect of wing camber. Presented in figures 23 and 24 are plots detailing the influence of δ_F, and shown in figures 25 and 26 are plots detailing the influence of β.

Spanwise surface pressure coefficient plots are presented in figure 23 for angles of attack of 0°, 4°, 8°, and 12° at $M = 1.70$. At $\alpha = 0°$ (fig. 23(a)), the data clearly show the influence of the hinge line ($\eta = 0.7$) and the intersection of the wing and balance housing ($\eta = 0.12$). An increase in leading-edge camber results in an increase in pressure coefficient outboard of the hinge line and a decrease in the pressure coefficient inboard of the hinge line. The only irregular behavior noticed in the pressures occurred at $\eta = 0.7$ where an increase in wing

camber first produced a reduction in pressure coefficient, which was then followed by an increase in pressure coefficient with further increases in camber. The data indicate that for $\delta_F = 5°$ the flow is attached at the wing upper surface leading edge and remains attached as it expands about the hinge line; this results in a pressure distribution which is centrally located about the hinge line. As camber is increased ($\delta_F = 10°$ and $15°$), the character of the pressure distribution near the hinge line changes dramatically for both $\delta_F = 10°$ and $15°$. The data show an attached flow condition at the leading edge which extends to the hinge line; this is followed by a large expansion region which lies inboard of the hinge line extending from $\eta = 0.7$ to 0.55. This type of pressure distribution would indicate that the flow has separated. A further review of the data of figure 23(a) shows a nearly equal increment in the leading-edge pressures ($\eta > 0.7$) between $\delta_F = 0°$ and $\delta_F = 5°$ and between $\delta_F = 5°$ and $\delta_F = 10°$; however, the increase in leading-edge pressure for $\delta_F = 15°$ compared with $\delta_F = 10°$ is considerably less. The data at $\alpha = 4°$, $8°$, and $12°$ of figures 23(b), 23(c), and 23(d), respectively, in addition to the data at $\alpha = 0°$ indicate that the four wings can be divided into two groups with each group having similar hinge-line flow characteristics. The first group consists of the wings with $\delta_F = 0°$ and $5°$, which are characterized by an attached flow condition at $\alpha = 0°$ and leading-edge flow separation at the higher angles of attack. The data show that the lee-side pressure distribution for these two wings is dominated by the leading-edge flow conditions. The second group consists of the wings with $\delta_F = 10°$ and $15°$, which appear to be dominated by the flow characteristics at the hinge line. The data at $\alpha = 0°$, $4°$, and $8°$ for both the wings with $\delta_F = 10°$ and $15°$ indicate that the lee-side flow is dominated by hinge-line separation. The data show that not until $\alpha = 12°$ (fig. 23(d)) do all four wings develop similar lee-side flow characteristics. Similar characteristics were also observed for all wings at $M = 2.80$, as shown in figure 24. These characteristics are discussed in more detail in the section "Lee-Side Flow Visualization."

The influence of camber on the lee-side pressures at sideslip conditions is presented in figures 25 and 26 for $M = 1.70$ and 2.80, respectively. Both the data at $M = 1.70$ and 2.80 show that camber has a greater influence on the windward pressures than the leeward pressures. The data of figures 25(a) and 26(a) show that the majority of the variation in the windward surface pressures with camber is confined to the deflected portion of the wing leading edge. The pressure data show that the average value of wing leading-edge pressure coefficient varies from -0.35 for $\delta_F = 0°$ to 0.00 for $\delta_F = 15°$ at $M = 1.70$ and from -0.15 for $\delta_F = 0°$ to 0.10 for $\delta_F = 15°$ at $M = 2.80$. This significant variation in wing loading on the windward wing panel combined with the nearly constant loading on the leeward wing panel would combine to produce a less stable configuration in rolling moment with increasing leading-edge camber.

Effect of forebody.- Experimental pressure data presented in previous sections of this paper for a series of conically cambered delta wings showed that the lee-side flow characteristics and the leading-edge flow characteristics are dependent upon the leading-edge camber. The data also showed that only for the cambered wing with $\delta_F = 5°$ did classical leading-edge separation (vortex) conditions exist. The pressure data for the wing with $\delta_F = 5°$ also indicated that for a limited set of conditions ($\alpha = 4°$ and $5°$), the flow over the wing was characterized by a leading-edge separation which was confined to the deflected portion of the wing leading edge. This flow condition is theorized as being optimum for aerodynamic performance of a wing with separated flow (ref. 6). To extend the analysis of the wing with $\delta_F = 5°$, the model was fitted with a fuselage forebody in order to assess forebody effects on the leading-edge separation characteristics. The resultant wing-forebody model was

nonconical along the entire length. Details of the fuselage forebody are contained in figures 1 and 4.

The effect of Mach number, angle of attack, and flow conicity is summarized in figures 27, 28, and 29, respectively. The effect of Mach number on the spanwise surface pressure distributions at $\alpha = 0°$, 4°, 6°, and 12° for the wing with $\delta_F = 5°$ with forebody is similar to the wing with $\delta_F = 5°$ alone results of figures 8, 9, and 10. The lee-side flow appears to be dominated by the leading-edge flow separation. An interesting characteristic of the data was observed for $\alpha = 6°$ (fig. 27(c)) where the leading-edge vortex reattachment line is observed to migrate inboard from $\eta = 0.7$ at $M = 1.50$ to $\eta = 0.5$ at $M = 2.00$. The extent of this migration could not be resolved because data were not obtained for Mach numbers above 2.00.

A comparison of the data at $\alpha = 6°$ and $M = 1.70$ (fig. 27(c)) with the data for the wing alone at $M = 1.70$ in figure 11(b) shows an increased loading on the deflected portion of the wing leading edge and a delay in the inboard migration of the vortex. These characteristics will be discussed further in the discussion of figures 28 and 30.

The effect of angle of attack on the spanwise surface pressure distribution at $M = 1.70$ is presented in figure 28. A comparison of the data of figure 28 with the data of figure 11(b) shows that the forebody appears to be increasing the strength and delaying the inboard migration of the leading-edge vortex, as evident in the data at $\alpha = 6°$ in both figures. The increased vortex strength, as indicated by the reduced pressure coefficient at a given angle of attack, can be attributed to the induced upwash field caused by the forebody which results in an effective increase in wing incidence angle. It should be noted that even though the effective increase in wing incidence is increasing the vortex strength it is not producing an equivalent inboard migration of the vortex as would be expected. The reduced inboard migration of the leading-edge vortex may be attributed to the outward shift in the initial wing leading-edge separation point with employment of the forebody. For the wing-alone geometry, initial separation occurs at the apex ($\eta = 0.0$, $x/\ell = 0.00$); however, once the forebody is added, initial separation occurs at the wing-forebody juncture ($\eta = 1.0$, $x/\ell = 0.12$); thus, more flap area is provided on which the vortex may act. This outboard shift in the initial separation point also produces nonconical flow as shown in figure 29. Spanwise surface pressure distributions are only presented for $x/\ell = 0.20$, 0.30, 0.60, 0.80, and 0.90 because the pressure orifices at $x/\ell = 0.10$ have been covered by the forebody. In addition, the fuselage extended spanwise to $\eta = 0.58$ at $x/\ell = 0.20$ and to $\eta = 0.39$ at $x/\ell = 0.3$. The data of figure 29 show a trend toward conical flow as you move aft on the wing. At $x/\ell = 0.20$, the data show a large expansion located on the leading edge only ($\eta > 7$) with recompression on the hinge line. At $x/\ell = 0.30$, the leading-edge expansion has been reduced and the recompression has migrated to $\eta = 0.45$. The final three spanwise rows of pressures show conical flow with reattachment at $\eta = 0.3$. These data were obtained at $\alpha = 12°$ where the leading-edge separation would be expected to dominate the lee-side flow field. The delay in the inboard migration at $x/\ell = 0.20$ and 0.30 suggests that the forebody itself is acting as a boundary to the flow and prohibits the inboard migration of the leading-edge vortex at the most forward stations.

A direct comparison of the wing with $\delta_F = 5°$ with and without forebody is presented in figure 30. Surface pressure coefficient data are shown for $M = 1.70$ at $\alpha = 4°$, 5°, 6°, 8°, and 12° in figures 30(a), 30(b), 30(c), 30(d), and 30(e), respectively. The data clearly show that addition of the forebody increases the

performance potential of the wing with $\delta_F = 5°$ by increasing the loading on the flap and delaying the inboard migration of the vortex. These results were consistent at angles of attack of 4°, 5°, 6°, and 8°. At $\alpha = 12°$, the data of figure 30(a) show that both geometries have a similar lee-side wing loading. However, as noted previously the flow field for the wing with forebody is nonconical in which the loading on the forward portion of the wing is concentrated on the deflected leading edge.

Lee-Side Flow Visualization

Extensive flow visualization data were obtained on all wings to aid in defining the lee-side flow phenomena. Three types of flow visualization data were obtained, with vapor screen photographs being the primary diagnostic tool.

Flow visualization methods.- Vapor screen flow visualization photographs provide information on the flow field above the wing in a plane perpendicular to the free-stream flow direction. Previous correlations with pressure data and other flow visualization techniques have shown that vapor screen flow visualization data can be used to investigate the formation of shocks, flow separation, wakes, or any viscous dominated effect. However, it should be noted that the physics which governs the formation of vapor screens is not completely understood, and therefore there is some question as to the interpretation of the data.

The other two types of flow visualization data were tuft and oil flow photographs which were used to investigate the flow characteristics on the wing upper surface. Tuft photographs provide information on the flow direction within the outer portion of the boundary layer. The tufts should only be directly influenced by the local velocities and not by pressure gradients or viscous shear forces. On the other hand, oil flow patterns are influenced by the local pressure gradients, viscous shear forces, and the flow velocities. The dominant mechanism which governs the development of an oil flow pattern is also subject to other effects such as flow conditions and oil viscosity. Each of the three flow visualization techniques employed in this study has particular deficiencies, yet these three methods are the only nonintrusive experimental techniques to obtain information on the local flow field about a wing at supersonic speeds.

Shown in figure 31 are representative photographic data of each of the three flow visualization techniques for the wing with $\delta_F = 5°$ with forebody at $M = 1.70$ and $\alpha = 6°$. Based upon the previously presented pressure data, these conditions correspond to a leading-edge separation which is located on the deflected portion of the wing leading edge. A review of the photographic data verifies the existence of these suggested flow conditions. The vapor screen photographs clearly show a separation bubble located on the deflected portion of the leading edge, and the tuft and oil flow patterns support this observation as indicated by the abrupt change in flow pattern for both at the hinge line. Outboard of the hinge line, both the tuft and oil flow photographs show an outboard flow direction, and inboard of the hinge line the photographs show a streamwise flow pattern. The oil flow photographs also show an accumulation of oil at the wing leading edge; this indicates a low pressure region associated with the initial expansion.

The remainder of this section only presents the vapor screen flow visualization results; however, periodic reference will be made to the tuft and oil flow photographs contained in appendix D. The wing with $\delta_F = 5°$ alone and wing with forebody vapor screen photographs were similar; however, the data obtained with the

forebody were of better quality. As a result, the data obtained with the forebody are presented.

Effect of α, M, and δ_F.- The experimentally obtained pressure data showed that increasing angle of attack produced increased separation and an inboard migration of the separation region or vortex. An example of these characteristics is presented in figure 32 for the wing with $\delta_F = 5°$ with forebody at $M = 1.70$. The photographic data show increasing amounts of leading-edge separation with increasing angle of attack. At $\alpha = 0°$ the lee-side flow field is free of separation and shocks as shown by the uniform density of the flow field. At $\alpha = 4°$ the data show both a small separation bubble at the leading edge and inboard of the hinge line. An increase in angle of attack to 5°, 6°, and 7° results in an increase in leading-edge separation and a reduction in the separation inboard of the hinge line. The photographs for $\alpha = 4°$, 5°, and 6° show that the leading-edge separation is confined to the deflected portion of the wing leading edge as suggested by the pressure data of figure 28. However, unlike the pressure data, the photographic data show that flow separation is also confined to the deflected portion of the wing at $\alpha = 7°$. Further increases in angle of attack to 8° show an inboard migration of the vortex off of the flap, and at $\alpha = 16°$ a classical wing leading-edge vortex exists which lies above the wing surface. Also evident in the photograph for $\alpha = 16°$ are a cross-flow shock under the main vortex and a secondary separation located outboard of the hinge line. The occurrence of both of these conditions appears to be interrelated and is discussed in more detail later along with other observed flow phenomena.

As previously noted in figures 9 and 10, the primary influence of increasing Mach number for all wings without forebody was a reduction in the lee-side wing loading with no apparent change in flow characteristics. However, a review of the flat wing data of reference 1 suggests that increasing the free-stream Mach number could result in the formation of shocks or the increased occurrence of attached flow. Presented in figure 33 is the effect of increasing Mach number on the lee-side flow characteristics of the wing with $\delta_F = 10°$ at $\alpha = 8°$ and 16°. The $\alpha = 8°$ photographs show that increasing Mach number from 1.70 to 2.80 changed the flow on the deflected leading edge from a leading-edge bubble at $M = 1.70$, 2.00, and 2.40 to a cross-flow shock at 2.80. Inboard on the hinge line the flow field is characterized by a vortex emanating from the hinge line. At an angle of attack of 16° the data show that an increase in the free-stream Mach number produced an extremely complex shock and vortex system which lay above the wing. The photograph for $M = 1.70$ shows a classical leading-edge vortex system which is quite similar to the conditions observed in figure 31. As the Mach number is increased to 2.00, a shock begins to develop on top of the vortex, the shock under the vortex appears to weaken, and the secondary separation is reduced. At $M = 2.40$ and 2.80, a second shock is developed which lies above the vortex feed sheet and emanates from a region near the hinge line. The data of figure 33 agree qualitatively with the findings of reference 1 which indicated the development of shocks above a leading-edge vortex with increases in angle of attack and/or Mach number.

The effect of leading-edge camber on the lee-side flow characteristics is the final parameter to be addressed. Presented in figure 34 are vapor screen flow visualization data for each wing at $\alpha = 12°$ and $M = 1.70$ and 2.80. The photographs at $M = 1.70$ show a wing leading-edge vortex for all wings. The data indicate that with increasing wing camber the vortex strength, as indicated by the size of the darkened region, is reduced and the vortex lies closer to the wing surface.

At $M = 2.80$, the flow field varies from a vortex with shock on top for the wings with $\delta_F = 0°$ and $5°$ to a shock-induced hinge-line vortex system for the wings with $\delta_F = 10°$ and $15°$.

Flow classification.- The vapor screen photographs of figures 32, 33, and 34 have shown that lee-side flow characteristics are dependent upon angle of attack, Mach number, or wing camber. The example flow visualization data presented in the previous figures have also revealed various complex flow phenomena which were not observed in previous flow visualization studies. In an attempt to document the various flow conditions observed in the present study, the flow conditions over the wings were described by the local flow at the wing leading edge and at the wing hinge line. A complete description of the flow type for all conditions is contained in appendix D. The result of this classification effort was the identification of 12 different flow types which could be divided into 2 groups. The first group of flow types were those which had a single dominant flow feature which enamated from either the leading edge or the hinge line (fig. 35). The second group of flow types are shown in figure 36. It includes those flows which had features which emanated from both the wing leading edge and wing hinge line. The flow visualization photographs presented in both figures 35 and 36 comprise a range of wing geometries and flow conditions. In general the wings with $\delta_F = 0°$ and $5°$ were dominated by leading-edge flows and the wings with $\delta_F = 10°$ and $15°$ were dominated by hinge-line flows. The six single-feature flow types consisted of an attached flow condition, three leading-edge-only separation conditions, and two hinge-line-only separation conditions. The six double-feature flow types consisted of leading-edge separations or leading-edge shock systems in combination with various hinge-line separation systems. To assist in describing each of these unique flow conditions, a sketch of the flow field as observed in the vapor screen photograph and the spanwise surface pressure distribution of each flow type is presented in figures 37 through 48.

Single-feature flows.- Attached flow over the wing upper surface was only observed on the wings with $\delta_F = 0°$ and $5°$ at $\alpha = 0°$. Shown in figure 37 are the spanwise pressure distribution and a sketch of the flow field for the wing with $\delta_F = 5°$ at $M = 1.70$.

The formation of a leading-edge bubble was limited to the wing with $\delta_F = 5°$ at moderate angles of attack. The results presented in figure 38 are for the wing with $\delta_F = 5°$ at $M = 1.70$ and $\alpha = 6°$. A bubble is defined as a rotational flow region which lies on the wing surface and does not induce a rotational flow external to its core (i.e., all rotational flow is constrained to the core). The bubble appears to act as an extension of the physical wing surface. For the conditions presented in figure 38, the leading-edge bubble lies solely on the deflected portion of the wing leading edge. This condition provides a smooth contour of the wing upper surface which the external flow field may traverse as it expands about the wing leading edge. The resultant pressure distribution is characterized by a large suction plateau located about the deflected portion of the wing followed by an abrupt recompression at the hinge line. This abrupt recompression occurs at the most inboard point of the dark region of the vapor screen; this indicates that the bubble is not inducing any rotationality to the external flow field such as that observed for a vortex system.

As angle of attack is increased, the bubble will lift from the surface and develop into a leading-edge vortex as shown in figure 39. These results are for the wing with $\delta_F = 5°$ at $M = 1.70$ and $\alpha = 12°$. A review of the flow

visualization data of appendix D shows that a wing leading-edge vortex did exist for all wings. In general a leading-edge vortex is characterized by a rotational viscous core which lies above the wing surface and inboard of the wing leading edge. The vortex core is connected to the leading edge by a viscous feed sheet. The flow field external to the vortex core is influenced by the rotational core and is usually termed "the induced flow field." The extent of the induced flow field can be determined by the spanwise location of the recompression in the pressure distribution. The data of figure 39 show that the vortex extends inboard to $\eta = 0.45$, yet recompression is occurring at $\eta = 0.30$ where flow reattachment is probably occurring. The region between $\eta = 0.45$ and 0.30 is termed "the induced flow region." Inboard of $\eta = 0.30$, the flow is streamwise, and outboard of $\eta = 0.30$, the flow will be directed outward toward the leading edge. As the induced flow field passes beneath the vortex, the flow may accelerate to Mach numbers greater than 1.00 and then recompress through a shock. Another character which may exist in these types of flows is a secondary vortex. The mechanism from which the secondary vortex develops is unknown; however, it does not appear to be induced by the shock which lies under the primary vortex. The induced pressure distribution correlates well to all the disturbances in the flow field.

The final leading-edge flow condition which was observed was that of a leading-edge vortex with a cross-flow shock located on top of the primary vortex. Typical conditions of this flow type are shown in figure 40 for the wing with $\delta_F = 5°$ at $M = 2.00$ and $\alpha = 16°$. As with the leading-edge vortex, this particular flow type was also observed for all wings. The characteristics of the flow field are the same as those observed for the leading-edge vortex except for the addition of the cross-flow shock. The pressure distribution presented at the top of figure 40 does not show any influence of the cross-flow shock. These findings are consistent with those of reference 3.

The final two single-feature flow types are the hinge-line bubble presented in figure 41 and the hinge-line vortex shown in figure 42. Hinge-line flow types were only observed for the wings with $\delta_F = 10°$ and 15°. Representative hinge-line bubble results are presented for the wing with $\delta_F = 10°$ at $M = 2.80$ and $\alpha = 0°$, and hinge-line vortex results are presented for the wing with $\delta_F = 10°$ at $M = 2.40$ and $\alpha = 6°$. The characteristics of a hinge-line bubble or hinge-line vortex are similar to their leading-edge counterparts as depicted in figures 38 and 39. An examination of the induced pressure distributions for the hinge-line separation condition also reveals a similar correlation between the pressures and the details observed in the vapor screen as that for the leading-edge flows. For all hinge-line flow phenomena, the flow on the outboard deflected portion of the wing leading edge was observed to have a large range of pressure coefficient values which varied between large positive values, as observed in figure 41, to slightly negative values, as shown in figure 42. The flow visualization data of appendix D also showed that the hinge-line separation was the single dominant characteristic of the flow field of the wings with $\delta_F = 10°$ and 15° at all conditions tested.

Double-feature flows.- Figures 43 through 48 detail the six double-feature flow types which were identified in this study. Double-feature flow types were those which had major flow characteristics which emanated from both the wing leading edge and the wing hinge line. All three cambered wings experienced double-feature flow types.

Presented in figure 43 is a sketch of the details observed in the vapor screen photograph (fig. 36, upper left) along with the associated spanwise pressure

distribution for the condition of a leading-edge bubble in combination with a hinge-line bubble. This particular flow pattern was only observed for the wing with $\delta_F = 5°$. The individual character of both the leading-edge and hinge-line bubbles is identical to the characteristics of an isolated bubble located at either the leading edge or hinge line. At $M = 1.70$ and $\alpha = 5°$ for the wing with $\delta_F = 5°$, the leading edge is at a positive incidence with respect to the free-stream flow which results in flow separation at the leading edge. This leading-edge separation takes the form of a bubble which extends from the leading edge inboard to approximately 80 percent of the semispan of the wing. The external flow field expands about the leading-edge bubble and recompresses on the flap between 80 and 70 percent of the semispan. The flow must then reexpand about the hinge line resulting in a separation of the boundary layer at the hinge line to produce the second bubble. These characteristics are supported by the pressure distribution shown at the top of figure 43. The existence of the two bubble system rather than vortices is due to the small expansion angles at the leading edge and hinge line. If the leading-edge angle was increased, the leading-edge separation would increase and produce results shown in figures 38 and 39.

The second double-feature flow type is a leading-edge bubble in combination with a hinge-line vortex. These characteristics were only observed for the wings with $\delta_F = 10°$ and 15°. The particular condition detailed in figure 44 is for the wing with $\delta_F = 10°$ at $M = 2.40$ and $\alpha = 8°$. This flow type results when the leading edge is at a small angle of incidence and the hinge-line angle is sufficiently large to create a strong separation as discussed previously. The supporting spanwise pressure distribution shows the expansion above the leading-edge bubble followed by a recompression at 75 percent semispan. The flow then expands about the hinge line and separates producing a vortex which provides a larger lee-side loading than that observed for the hinge-line bubble of figure 43.

As discussed previously the primary influence of increasing Mach number on the lee-side flow characteristics is the development of shocks. Presented in figures 45, 46, 47, and 48 are four double-feature flow types which are all characterized by strong cross-flow shocks on the deflected portion of the wing leading edge.

The leading-edge bubble with shock and hinge-line bubble flow type was only observed on the wing with $\delta_F = 5°$ at $M = 2.80$. (See fig. 45.) These flow types are identical to those shown in figure 43 with the exception of the cross-flow shock on top of the leading-edge bubble. A review of the spanwise pressure distribution shows a small recompression which correlates well with the location of the cross-flow shock. The pressure data also show an abrupt recompression of the flow at the most inboard location of the hinge-line bubble.

Shown in figure 46 is the leading-edge bubble with shock and hinge-line vortex flow type. This double-feature flow type was observed on both the wings with $\delta_F = 5°$ and 10°. The particular conditions documented in figure 46 are for the wing with $\delta_F = 10°$ at $M = 2.40$ and $\alpha = 10°$. A comparison of these results to those of figure 44 shows that the formation of the cross-flow shock results from the increased expansion of the flow about the leading edge. The spanwise pressure distribution again supports these characteristics observed in the vapor screen photograph.

At a Mach number of 2.80 both the wings with $\delta_F = 10°$ and 15° experienced conditions of attached flow with a shock on the deflected leading edge of the wing followed by a strong hinge-line vortex. Shown in figure 47 are the details of the

leading-edge shock and hinge-line vortex flow type. This particular condition is shown for the wing with $\delta_F = 10°$ at $M = 2.80$ and $\alpha = 12°$. For the wing with $\delta_F = 10°$ at $\alpha = 12°$, flow separation would be expected to occur at the leading edge; however, the vapor screen photograph shows a strong cross-flow shock emanating near the leading edge. The pressure data show that the flow is expanding about the wing leading edge with an immediate but gradual recompression occurring over the span of the flap. As the flow expands about the hinge line, the flow separates and forms a vortex. Similar characteristics were observed in figure 48 where the double-feature flow structure was that of a leading-edge shock and hinge-line vortex with shock. This particular flow type was only observed on the wing with $\delta_F = 15°$. The condition presented in figure 48 is $M = 2.80$ and $\alpha = 16°$. The spanwise surface pressure distribution is similar to that of figure 47. The cross-flow shock located on the deflected leading edge produces a dramatic change in the pressures. The flow appears to expand about the leading edge and undergoes a gradual recompression as it flows inboard to the hinge line. Inboard of the hinge line, the flow undergoes a reduction in pressure due to the high-line separation.

Correlation of flow types.- Flow visualization results have been presented which detail the influence of Mach number, angle of attack, and camber on the lee-side flow characteristics of conically cambered delta wings. Analysis of photographic data identified the existence of 12 distinctive lee-side flow types. These 12 flow types were then further categorized into two groups identified as having either one or two dominant features in the lee-side flow field. To compile all the flow classification data of appendix D into a single figure, the classification results are presented as a function of conditions normal to the wing leading edge. The symbols used to define the flows are given in table DI. The two correlation parameters are the angle of attack normal to the wing leading edge α_N minus the wing camber streamwise deflection angle δ_F and the Mach number normal to the wing leading edge M_N. In a previous study (ref. 3) of flat delta wings, data were obtained at M_N above and below 1.0 in which seven distinctly different flow types were categorized on a M_N-α_N chart. These flow classification boundaries are depicted as dashed lines in figure 49. For the present study, data were obtained primarily at conditions of $M_N < 1.00$ as shown in figure 49. The locations of the data points for all wings in figure 49 are referenced to the values of M_N and α_N derived for the delta wing with $\delta_F = 0°$. The location of the cambered wing data was determined by computing the value of α_N for the wing with $\delta_F = 0°$, at a given value of α and M, and subtracting the value of the free-stream deflection angle of each cambered wing. The value of M_N for the cambered wings was the same as those for the wing with $\delta_F = 0°$. This method of presenting the data resulted in the loss of several data points because their $(\alpha_N - \delta_F)$ values were less than 0.0.

To assist in identifying the various flow types and the associated wing geometry, the single-feature flows are designated by open or solid symbols, the double-feature flows are half-solid symbols, and the wing camber is denoted by a tick protruding from either the top, side, or bottom of each symbol. The leading-edge dominant single-feature flow types are indicated by open symbols and hinge-line dominant flows are indicated by a solid symbol. To reduce the number of data points to be plotted on the figure, results are only presented for $\alpha = 0°$, 4°, 8°, 12°, 16°, and 20°. One result of this limited method of presentation was the omission of the bubble with shock and hinge-line bubble double-feature flow type from the graph. This flow type was only observed for the wing with $\delta_F = 5°$ at $M = 2.80$ and $\alpha = 5°$ and 6°. The attached flow and hinge-line bubble single-feature flow types were also omitted because they occurred at values of $(\alpha_N - \delta_F)$ of 0.0 and below.

A review of the data shows a division of the cambered wing data based upon the existence of any hinge-line separation. The data show that a boundary can be drawn from a point located approximately at $M_N = 0.4$, $(\alpha_N - \delta_F) = 20$, to $M_N = 1.2$, $(\alpha_N - \delta_F) = 40$. Above this line, cambered wing data show leading-edge separation only, and below this line, the cambered wings experience various types of hinge-line separation. The only discrepancy observed is for the flat wing data (symbols with no tick) which show leading-edge separation at all angles of attack.

The pressure data indicate that hinge-line separation was an unfavorable condition which dominated the lee-side wing loading and prohibited the development of leading-edge separation on the deflected portion of the wing leading edge. The data of figure 49 provide information which may be useful in future designs by defining the limiting conditions for the development of hinge-line separation. The data also show that the angle-of-attack range at which hinge-line separation occurs increases with increasing Mach number and wing camber. As mentioned previously these results may be useful as a guide to future wing design studies; however, the data correlation parameters presented in figure 49 are not easily related to the more traditional geometric and flow parameters. To help clarify the trends of figure 49, the data at $M = 1.70$ have been evaluated and presented as a plot of wing camber δ_F against angle of attack (fig. 50). This method of presentation produced five distinct flow regions. The graph shows that only the wing with $\delta_F = 5°$ exhibits an optimum flow condition, that of a leading-edge separation located on the deflected leading edge. The data for the wing with $\delta_F = 10°$ show a double-feature flow condition and the wing with $\delta_F = 15°$ changes immediately from hinge-line-only separation to leading-edge-only separation with the dominant loading residing inboard of the wing hinge line. These flow visualization data are shown to correlate well with the pressure data.

Forces and Moments

The separated flow wing design philosophy has been extensively studied at subsonic and transonic speeds. These previous (refs. 10, 11, and 12) experimental studies have resulted in the development of several unique aerodynamic devices, such as vortex flaps, for the management of flow separation for improved aerodynamic performance. To assess the merits of the separated flow wing design philosophy at supersonic speeds, aerodynamic force and moment data were also obtained during testing.

The aerodynamic characteristics presented in this section of the paper are correlated to the pressure and flow visualization data to provide additional insight into the flow conditions. Representative results will be shown to document the effect of Mach number and wing camber on all aerodynamic properties. Longitudinal aerodynamic characteristics were obtained on all wings; however, lateral-directional characteristics were only obtained for the wing with $\delta_F = 5°$.

The aerodynamic characteristics of delta wings have been extensively documented. In reference 13 it was shown that the aerodynamic performance potential at supersonic speeds is directly related to the value of the leading-edge sweep parameter ($\beta \cot \Lambda$) and lift coefficient. These results were based upon the analysis of a limited amount of data consisting of both delta and nondelta wings. For the present study, the range of $\beta \cot \Lambda$ varied between 0.37 and 0.70 for a Mach number range of 1.70 to 2.80. The data of reference 10 show that for a 75° swept wing, significant improvements in aerodynamic performance would only occur for values of $\beta \cot \Lambda$ of 0.5 or

less. In addition, the pressure data and the flow visualization data discussed previously showed that large amounts of wing camber can have a detrimental effect on the lee-side loading and flow structure; this would suggest a loss in aerodynamic performance with increased wing camber.

The variation in minimum drag and lift-curve slope with Mach number is presented in figure 51. The data for each wing show that the minimum drag decreases with increasing Mach number and increases with increasing wing camber, except for the wing with $\delta_F = 5°$ at the lower Mach numbers. The increased minimum drag levels for the wings with $\delta_F = 10°$ and $15°$ are due to a combination of hinge-line separation on the leeward wing surface and leading-edge separation on the windward wing surface. The tabulated force data of appendix E show that minimum drag for the wings with $\delta_F = 5°$, $10°$, and $15°$ occurs at angles of attack of approximately $1.0°$, $2.0°$, and $3.0°$, respectively. At these angles of attack, the pressure data and the flow visualization data for the wings with $\delta_F = 10°$ and $15°$ show that the flow is separated at the hinge line on the wing leeward surface, and vapor screen photographs contained in appendix D show a leading-edge vortex on the windward surface. In comparison, the pressure and flow visualization data for the wing with $\delta_F = 5°$ show that the local flow angle is nearly aligned with the wing leading-edge deflection angle. This would result in attached flow on both the wing upper and lower surfaces; thus, low drag values are produced compared with those for the wings with $\delta_F = 10°$ and $15°$. The impact of minimum drag on the aerodynamic performance of each wing is discussed further in the discussion of figures 52 through 55.

The effect of Mach number on the lifting characteristics is shown in the right-hand side of figure 51. The data show a variation with increasing Mach number similar to that which would be predicted by linear theory. The reduced lift-curve slope with increasing wing camber and the nonlinear character of each of the cambered wing curves was unexpected. Linear theory indicates that the lift-curve slope is independent of wing camber and would decrease with increasing wing leading-edge sweep. Perhaps this variation in lift-curve slope with wing camber is due to either the reduced wing planform area or increased wing sweep for each of the cambered wings compared with the flat wing. The combination of these geometric characteristics with the various separated flow conditions which were observed for each wing could account for the erratic behavior with Mach number. In general it may be concluded that wing camber can have a negative influence on both the minimum drag value and lift-curve slope; however, both of these negative effects may be canceled by improvements in the drag due to lift. To attain high levels of aerodynamic performance (L/D), both the minimum drag and the drag due to lift must be optimized.

Presented in figure 52 are the maximum lift-drag ratios $(L/D)_{max}$ and the lift coefficients at which they occur for each wing. Maximum lift-drag ratios presented in the left-hand side of the figure show an increase in performance for the wings with $\delta_F = 0°$ and $5°$ and a decrease in performance for the wings with $\delta_F = 10°$ and $15°$ with increasing Mach number. The data show that only the wing with $\delta_F = 5°$ consistently provides improved aerodynamic performance at all Mach numbers when compared with the wing with $\delta_F = 0°$. However, the maximum L/D of the wing with $\delta_F = 10°$ does exceed that of the wing with $\delta_F = 0°$ at all Mach numbers except at $M = 2.80$, where the two values are identical. These data indicate that both the wings with $\delta_F = 5°$ and $10°$ are providing significant improvements in drag due to lift over the flat wing. The reduced effectiveness with Mach number of the wings with $\delta_F = 10°$ and $15°$ is partially due to the increased minimum drag of each wing compared with that of the wing with $\delta_F = 5°$. Shown on the right of figure 52 is the lift coefficient at which $(L/D)_{max}$ occurs for each wing plotted as a function

of Mach number. The flat wing data show that as Mach number is increased the C_L at which $(L/D)_{max}$ occurs is lowered by 40.0 percent from 0.15 at $M = 1.70$ to 0.09 at $M = 2.80$. This trend is typical of a flat wing. The data for the wings with $\delta_F = 5°$ and $10°$ show a nearly constant value of C_L across the Mach number range with an equivalent or lower value of C_L than the wing with $\delta_F = 0°$, except at $M = 2.80$. The wing with $\delta_F = 15°$ shows characteristics similar to the flat wing to indicate a lack of camber effectiveness for this geometry.

The evaluation of the performance of each wing is extended to higher lift coefficients to assess the camber effectiveness and the merits of the wing design space concept of reference 6. The wing design space concept suggests that wing camber effectiveness is dependent upon the design lift coefficient, the wing loading distribution between the leeward and windward surfaces, and the value of the leading-edge sweep parameter. The design space concept was developed based upon the aerodynamics of delta wings and was initially evaluated in reference 14 for a series of arrow wings. For the present study, the design space concept is evaluated for design lift coefficients of 0.2 and 0.4.

Presented in figure 53 are the lift-drag ratio of each wing at $C_L = 0.2$ and 0.4 plotted as a function of $\beta \cot \Lambda$. The values of $\beta \cot \Lambda$ were derived based upon the flat-wing geometry. The data for $C_L = 0.2$ and 0.4 show trends similar to those observed in figure 52 for $(L/D)_{max}$. The wing with $\delta_F = 5°$ shows a definite advantage over the other two cambered wings at all conditions.

To assess the merits of the wing design space concept, the percent change in wing performance of each cambered wing, compared with that of the flat wing, was determined and plotted on the two wing design space charts of figure 54. In computing the percent change, negative values were noted as 0 percent; for example, see $\delta_F = 15°$ at $\beta \cot \Lambda = 0.6$. The 0.2 and 0.4 design spaces are defined according to the Mach number and angle of attack normal to the wing leading edge. The shaded region is the design space. Within the design space, the wing lift force is distributed between the leeward and windward surfaces such that the leeward wing loading is equal to or exceeds the windward wing loading. Also presented on the figure are lines of constant wing leading-edge sweep (solid lines) and lines of constant $\beta \cot \Lambda$ (dashed lines). The performance data of figure 53 are plotted as solid circles with the associated percent change in lift-drag ratio noted to the right of each symbol. Notice that increasing wing camber, $\beta \cot \Lambda$, and design lift coefficient reduces the percent improvement in aerodynamic performance. The data support the design space concept in which wing camber effectiveness is reduced for conditions which lie outside the design space.

All data have consistently shown a reduced camber effectiveness with increasing Mach number and increasing wing camber. To further study the effect of increasing wing camber on the aerodynamics of delta wings, a detailed analysis of the $M = 1.70$ data has been conducted. Presented in figure 55 are the drag characteristics of each wing at $M = 1.70$. These results clearly support the data of figures 52 and 53. Also noted in the figure are the conditions at which each cambered wing drag polar crosses the flat wing polar. This crossover point is seen to occur at an increasing lift coefficient with increasing wing camber. The data show that the wing with $\delta_F = 5°$ maintains excellent performance at all lift coefficients, with the wing with $\delta_F = 10°$ providing slight improvements over the wing with $\delta_F = 5°$ at $C_L = 0.15$.

In its most elemental form, improved aerodynamic performance results from decreasing the axial force at a given angle of attack without losing a significant amount of normal force. A detailed examination of these normal and axial forces for each wing is presented in figures 56 and 57. The data of figure 56 show that an increase in wing camber results in a negative shift in the curve for C_N against α and a slight reduction in the slope of the curve for C_N against α at low angles of attack. It is interesting to note that the shift in the curve for C_N does not vary linearly with increasing wing camber. At $\alpha = 0°$, the flow has separated at the leading edge onto the lower surface for all cambered wings and at the hinge line on the upper surface for the wings with $\delta_F = 10°$ and 15°. For the wings with $\delta_F = 5°$ and 10°, the upper surface separation is not of sufficient strength to counteract the loading due to the lower surface separation; thus, a negative shift in C_N results. The data for the wing with $\delta_F = 15°$ show no change in C_N from the wing with $\delta_F = 10°$; this indicates an increased upper surface separation which is equal to the increased lower surface separation with respect to the wing with $\delta_F = 10°$. At higher angles of attack, all curves show a nonlinearly increasing trend. The angle of attack at which each curve becomes nonlinear is shown to be delayed to higher values of angle of attack. The angle of attack at which the break in the cambered wing normal-force curves occurs correlates well with the development of a lee-side wing leading-edge separation condition. (See fig. 50.)

A review of the data of figure 57 shows that at $\alpha = 0°$, there is an increase in axial force and a reduced camber efficiency (axial-force reduction) with increasing wing camber. Also noted for each curve is the normal-force break point. For the wing with $\delta_F = 5°$, both pressure and flow visualization data showed a migration of the leading-edge vortex off the deflected leading edge for angles of attack above 6°. This would produce an increase in the slope of the normal-force curve and a decrease in the axial-force curve. The data for the wings with $\delta_F = 10°$ and 15° also show a break in their curves at different angles of attack and for drastically different flow conditions. The flow visualization data for these wings showed the onset of leading-edge-only separation at $\alpha = 8°$ and 9° for the wings with $\delta_F = 10°$ and 15°, respectively. The longitudinal aerodynamic force data have been shown to correlate with and support the analysis of the pressure and flow visualization data.

Longitudinal stability characteristics for each wing are presented in figures 58 and 59. The data show that wing camber has a minimal effect on both the zero-lift pitching moment and the longitudinal stability level at all Mach numbers (fig. 58). Presented in figure 59 are typical pitching-moment characteristics for each wing at $M = 1.70$. The data show that despite the large variation in flow conditions with increasing angle of attack the linearity of the pitching-moment curve was maintained.

Lateral-directional data are presented in figure 60. Experimental results were obtained for the wing with $\delta_F = 5°$ at $M = 1.70$ and 2.80, $\alpha = 12°$, and $\beta = 0°$ to 8°. The data show that increasing Mach number reduces the rolling moment and has a varying effect on the side force and yawing moment. The rolling moment at sideslip results from the asymmetric lee-side loading on the leeward and windward wing panels. As Mach number increases, the asymmetric lee-side loading remains but its contribution to the total wing loading is reduced due to the limiting effect of the vacuum pressure limit on the lee-side loading. This effect is supported by a review of the design space chart of figure 54 which indicates that the wing loading at $M = 1.70$ would be equally distributed between the upper and lower surfaces; however, at $M = 2.80$, the lower surface loading would dominate.

CONCLUDING REMARKS

An experimental investigation was performed in which surface pressure data, flow visualization data, and force and moment data were obtained on four conical delta wing models which differed in leading-edge camber. Experimental flow visualization data were obtained over a range of flow conditions to determine the various flow mechanisms which occur on the lee-side of cambered delta wings. Extensive surface pressure data were obtained to evaluate flow conicity, the effect of Reynolds number, and scale effects both at angle of sideslip and angle of attack. Force and moment data were obtained to evaluate the potential of separated flows to improve the performance of wings at supersonic speeds.

The series of four delta wing models varied in leading-edge camber only. Wing leading-edge camber was achieved through a deflection of the outboard 30 percent of the local wing semispan of a reference 75° swept flat delta wing. The four wing models had leading-edge deflection angles δ_F of 0°, 5°, 10°, and 15°, measured streamwise.

Surface pressure data showed that the influence of Mach number on the lee-side pressure is directly related to the angle of attack and wing camber. Data for the wings with $\delta_F = 10°$ and 15° showed that hinge-line separation dominated the lee-side wing loading and prohibited the development of leading-edge separation on the deflected portion of wing leading edge. However, data for the wing with $\delta_F = 5°$ showed that at an angle of attack of 5°, a vortex was positioned on the deflected leading edge with reattachment at the hinge line. It was also shown that addition of a forebody increased the performance potential of the wing with $\delta_F = 5°$ by increasing the loading on the flap and delaying the inboard migration of the vortex at a given angle of attack. It was shown that flow conicity is not guaranteed by a conical geometry but model geometry limitations must be addressed.

Three types of flow visualization data were obtained on all wings to aid in defining the lee-side flow phenomena. Flow visualization results have been presented which detailed the influence of Mach number, angle of attack, and camber on the lee-side flow characteristics of conically cambered delta wings. Analysis of photographic data identified the existence of 12 distinctive lee-side flow types. These 12 flow types were then further categorized into two groups identified as having either one or two dominant features in the lee-side flow field. The first group of flow types were those which had a single dominant flow feature which emanated from either the leading edge or the hinge line. The second group of flow types were those which had features which emanated from both the wing leading edge and wing hinge line. In general the wings with $\delta_F = 10°$ and 5° were dominated by leading-edge flows, and the wings with $\delta_F = 10°$ and 15° were dominated by hinge-line flows. The six single-feature flow types consisted of an attached flow condition, three leading-edge-only separation conditions, and two hinge-line-only separation conditions. The six double-feature flow types consisted of leading-edge separations or leading-edge shock systems in combination with various hinge-line separation systems. Flow visualization data also show that the angle of attack at which hinge-line separation occurs increases with increasing Mach number and wing camber; these results may be useful as a guide to future wing design studies.

In general, the aerodynamic force and moment data correlated well with the pressure and flow visualization results. In particular the aerodynamic data showed that only the wing with $\delta_F = 5°$ consistently provided improved aerodynamic performance compared with the flat reference wing. It was also shown that despite the large variation in lee-side flow conditions with increasing angle of attack, the linearity of the pitching-moment curve for all wings was maintained.

NASA Langley Research Center
Hampton, VA 23665-5225
March 27, 1987

REFERENCES

1. Stanbrook, A.; and Squire, L. C.: Possible Types of Flow at Swept Leading Edges. Aeronaut. Q., vol. XV, pt. 1, Feb. 1964, pp. 72-82.

2. Ganzer, U.; Hoder, H.; and Szodruch, J.: On the Aerodynamics of Hypersonic Cruise Vehicles at Off-Design Conditions. ICAS Proceedings - 1978, Volume 1 - Fuel Conservation, Hypersonic Vehicles, Environmental Effects, Materials and Structures, Computational Aerodynamics, Wind Tunnels, Flight Testing, Stability and Control. J. Singer and R. Staufenbiel, eds., 1978, pp. 152-161.

3. Miller, David S.; and Wood, Richard M.: Lee-Side Flow Over Delta Wings at Supersonic Speeds. NASA TP-2430, 1985.

4. Rizzetta, Donald P.; and Shang, Joseph S.: Numerical Simulation of Leading-Edge Vortex Flows. AIAA-84-1544, June 1984.

5. Murman, Earll M.: Solutions of the Conical Euler Equations for Flat Plate Geometries - Preliminary Results. CFDL-TR-84-4, Dep. of Aeronautics and Astronautics, Massachusetts Inst. of Technology, Aug. 1984.

6. Wood, Richard M.; and Miller, David S.: Assessment of Preliminary Prediction Techniques for Wing Leading-Edge Vortex Flows at Supersonic Speeds. AIAA-84-2208, Aug. 1984.

7. Murman, Earll M.; Powell, Kenneth G.; Miller, David S.; and Wood, Richard M.: Comparison of Computations and Experimental Data for Leading Edge Vortices - Effects of Yaw and Vortex Flaps. AIAA-86-0439, Jan. 1986.

8. Jackson, Charlie M., Jr.; Corlett, William A.; and Monta, William J.: Description and Calibration of the Langley Unitary Plan Wind Tunnel. NASA TP-1905, 1981.

9. Braslow, Albert L.; and Knox, Eugene C.: Simplified Method for Determination of Critical Height of Distributed Roughness Particles for Boundary-Layer Transition at Mach Numbers From 0 to 5. NACA TN 4363, 1958.

10. Lambourne, N. C.; and Bryer, D. W.: Some Measurements in the Vortex Flow Generated by a Sharp Leading Edge Having 65 Degrees Sweep. C.P. No. 477, British Aeronautical Research Council, 1960.

11. Manro, Marjorie E.: Transonic Pressure Measurements and Comparison of Theory to Experiment for Three Arrow-Wing Configurations. Volume I: Experimental Data Report - Basic Data and Effect of Wing Shape. NASA CR-165701, 1981.

12. Rao, Dhanvada M.: Leading-Edge 'Vortex Flaps' for Enhanced Subsonic Aerodynamics of Slender Wings. ICAS Proceedings 1980 - 12th Congress of the International Council of the Aeronautical Sciences (ICAS), J. Singer and R. Staufenbiel, eds., 1980, pp. 554-562. (Available as ICAS-80-13.5.)

13. Wood, Richard M.; and Miller, David S.: Impact of Airfoil Profile on the Supersonic Aerodynamics of Delta Wings. AIAA-85-4073, Oct. 1985.

14. Miller, David S.; and Wood, Richard M.: Aerodynamic Design Considerations for Efficient High-Lift Supersonic Wings. AIAA-85-4076, Oct. 1985.

TABLE I.- GEOMETRIC CHARACTERISTICS OF WING MODELS

Characteristic	$\delta_F = 0°$	$\delta_F = 5°$	$\delta_F = 10°$	$\delta_F = 15°$
Surface area, in^2	302.292	302.292	302.292	302.292
Planform area, in^2	302.202	293.475	277.437	264.069
Span, in.	18.000	17.475	16.520	15.724
Length, in.	33.588	33.637	33.725	33.799
Leading-edge sweep, deg	75.000	75.440	76.240	76.910
Flap surface area, in^2	93.039	93.039	93.039	93.039
Flap planform area, in^2	93.039	84.222	68.184	54.816

TABLE II.- LOCATION OF SURFACE PRESSURE ORIFICES

x/l	η	x/l	η	x/l	η	x/l	η	x/l	η	x/l	η
0.1	0.00	0.2	0.00	0.3	0.00	0.6	0.00	0.8	0.00	0.9	0.00
.1	.05	.2	-.05	.3	-.05	.6	.05	.8	.05	.9	.05
.1	-.10	.2	-.10	.3	-.10	.6	.10	.8	.10	.9	.10
.1	.15	.2	-.15	.3	-.15	.6	.15	.8	.15	.9	.15
.1	-.20	.2	-.20	.3	-.20	.6	.20	.8	.20	.9	.20
.1	.25	.2	-.25	.3	-.25	.6	.25	.8	.25	.9	.25
.1	-.30	.2	-.30	.3	-.30	.6	.30	.8	.30	.9	.30
.1	.35	.2	-.35	.3	-.35	.6	.35	.8	.35	.9	.35
.1	-.40	.2	-.40	.3	-.40	.6	.40	.8	.40	.9	.40
.1	.45	.2	-.45	.3	-.45	.6	.45	.8	.45	.9	.45
.1	-.50	.2	-.50	.3	-.50	.6	.50	.8	.50	.9	.50
.1	.55	.2	-.55	.3	-.55	.6	.55	.8	.55	.9	.55
.1	-.60	.2	-.60	.3	-.60	.6	.60	.8	.60	.9	.60
.1	.65	.2	-.65	.3	-.65	.6	.65	.8	.65	.9	.65
.1	-.70	.2	-.70	.3	-.70	.6	.70	.8	.70	.9	.70
		.2	-.75	.3	-.75	.6	.75	.8	.75	.9	.75
		.2	-.80	.3	-.80	.6	.80	.8	.80	.9	.80
		.2	-.85	.3	-.85	.6	.85	.8	.85	.9	.85
		.2	-.90	.3	-.90	.6	.90	.8	.90	.9	.90

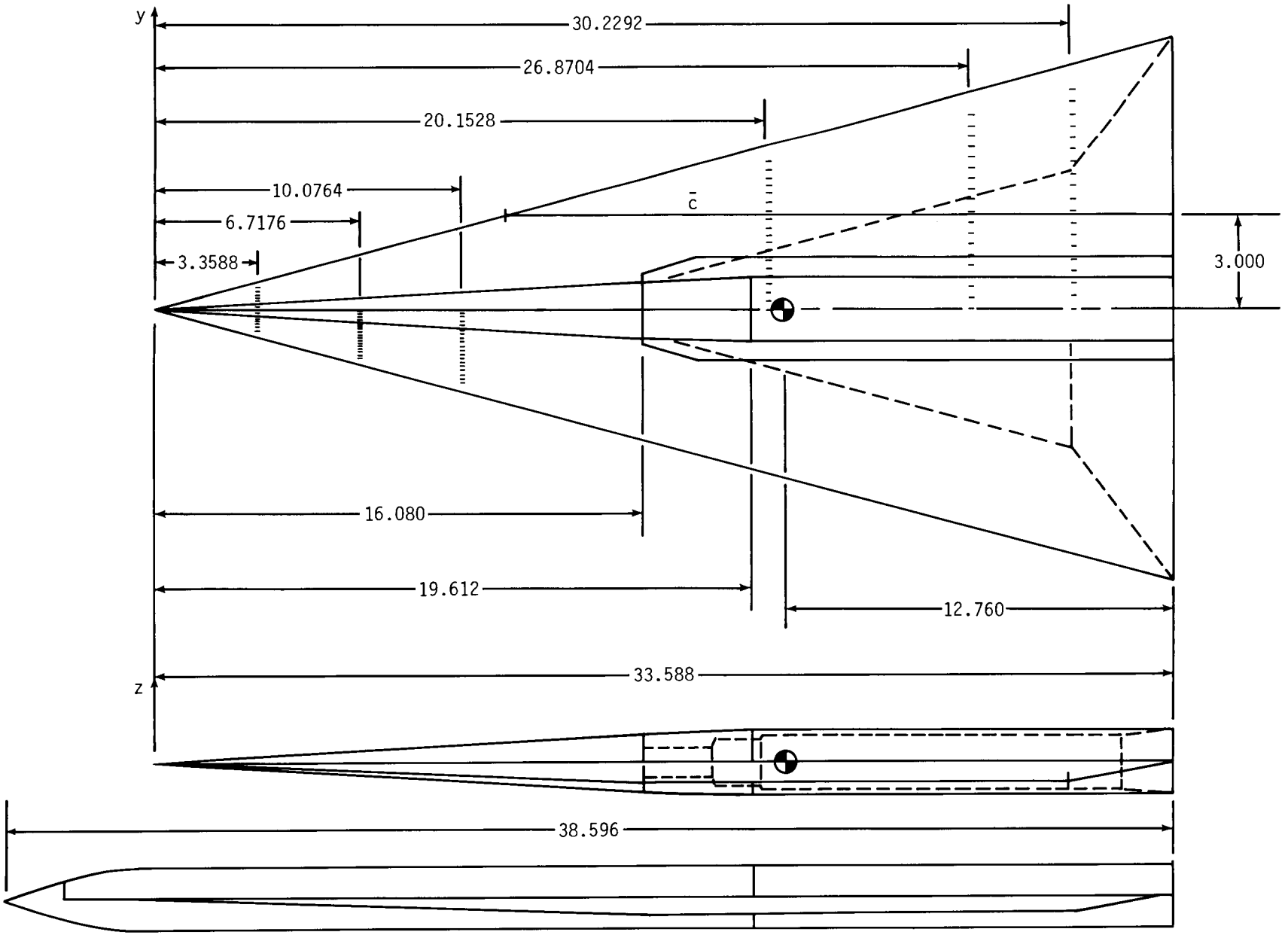

Figure 1.- Details of wind-tunnel model. All dimensions are in inches.

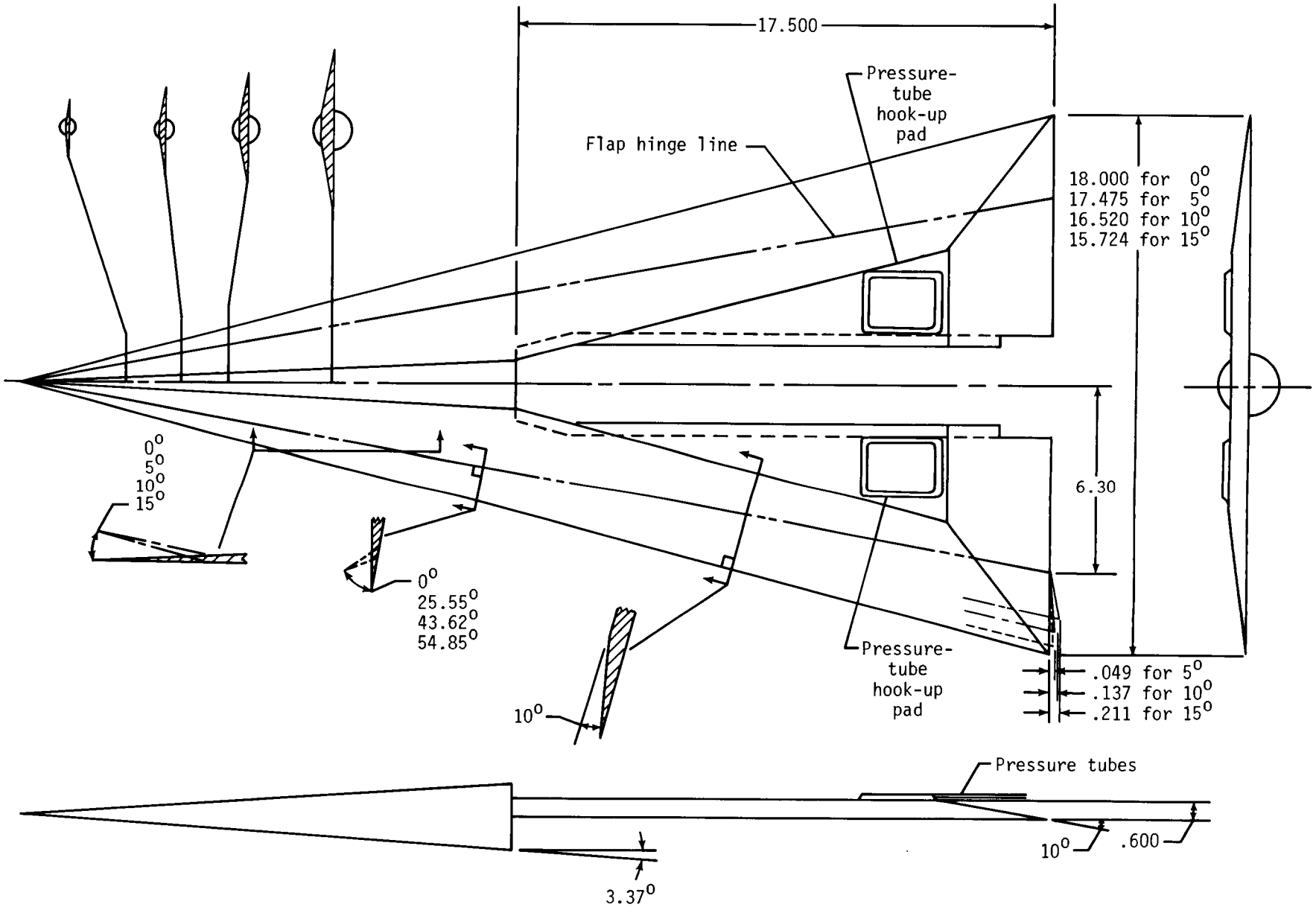

Figure 2.- Details of 75° swept delta wings. All dimensions are in inches.

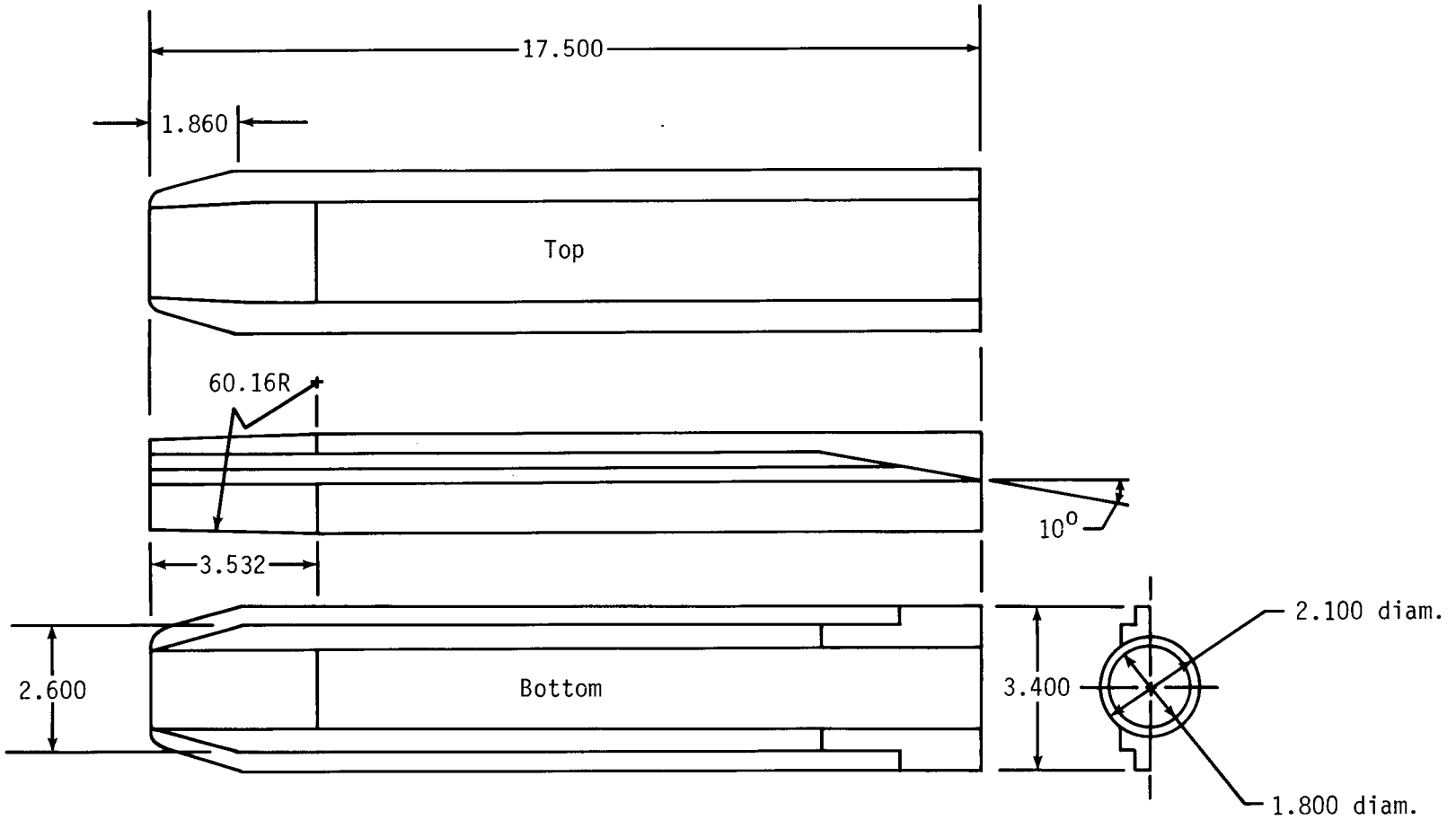

Figure 3.- Details of balance block. All dimensions are in inches.

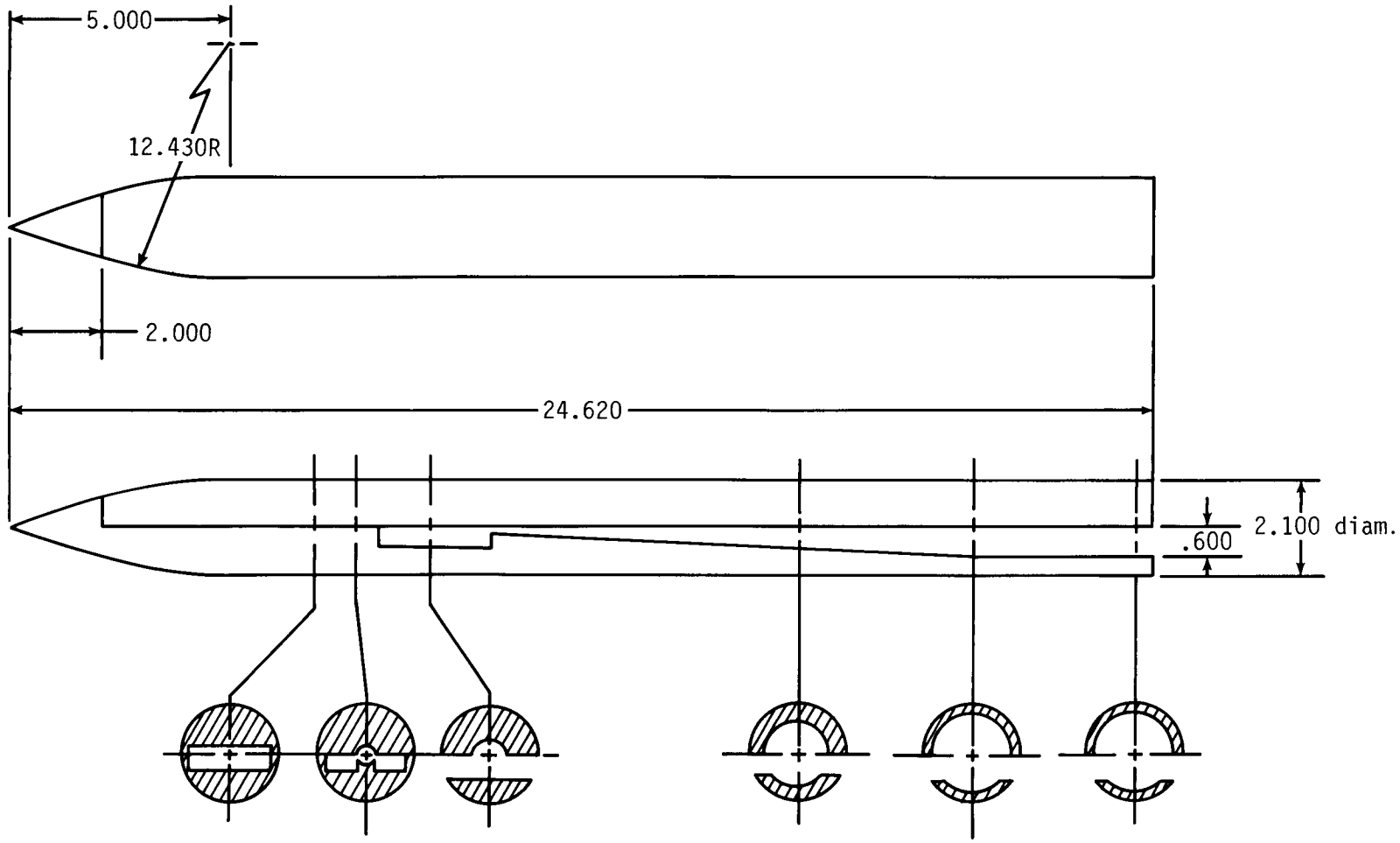

Figure 4.- Details of extended fuselage. All dimensions are in inches.

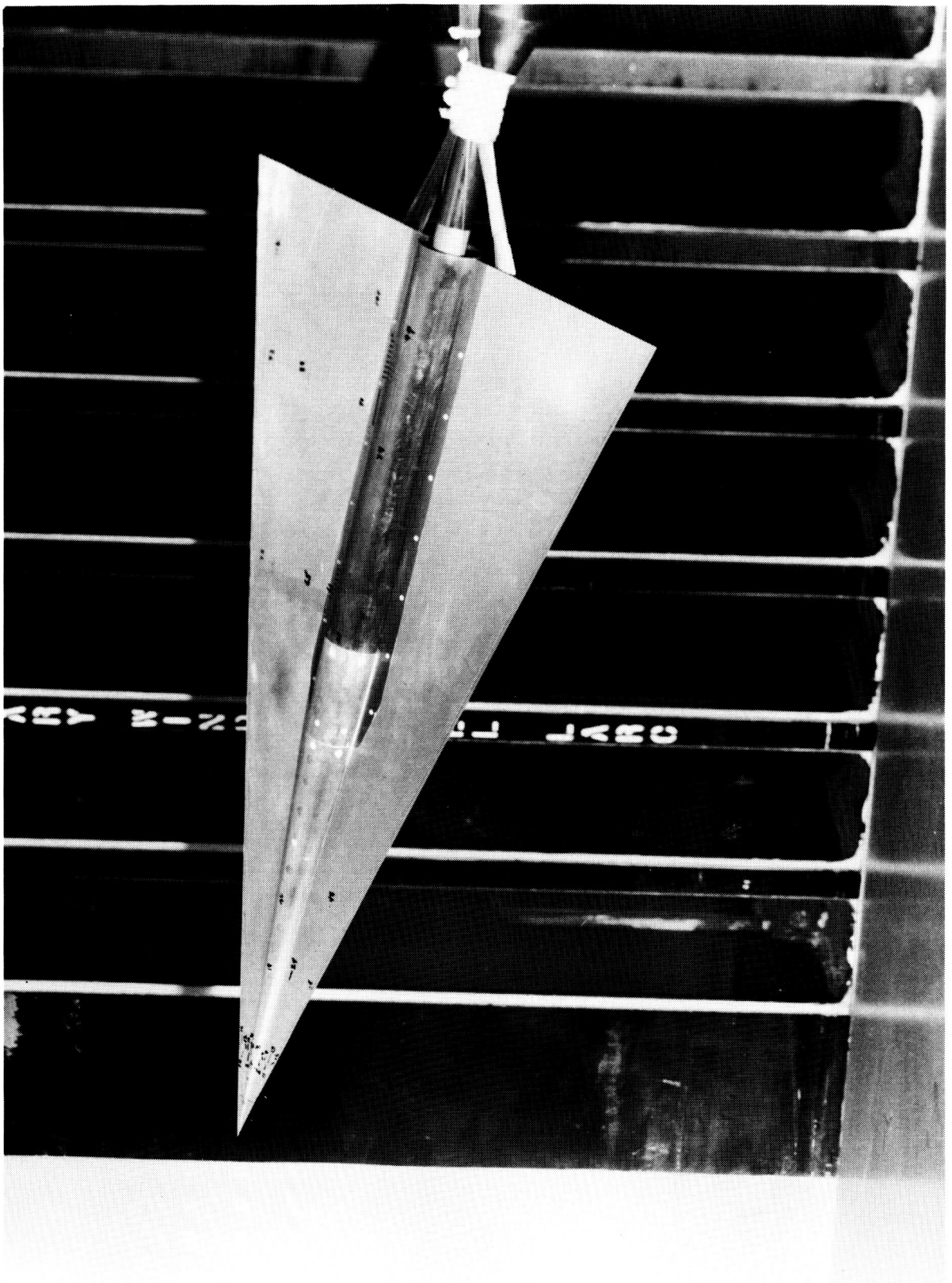

L-85-2205

Figure 5.- Photograph of 75° delta wing with $\delta_F = 0°$.

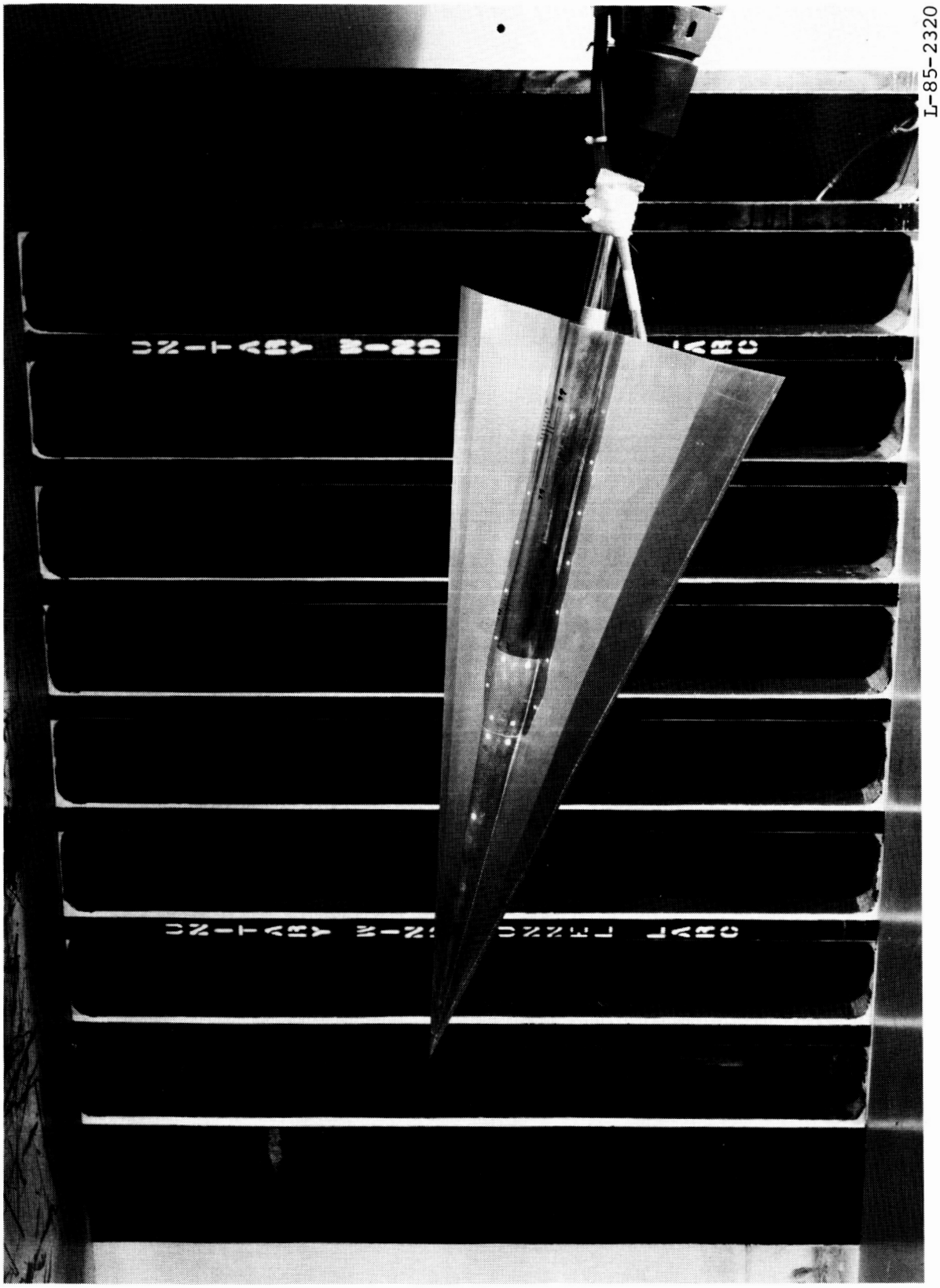

L-85-2320

(a) Upper surface.

Figure 6.- Photograph of 75° delta wing with $\delta_F = 10°$.

L-85-2318

(b) Lower surface.

Figure 6.- Concluded.

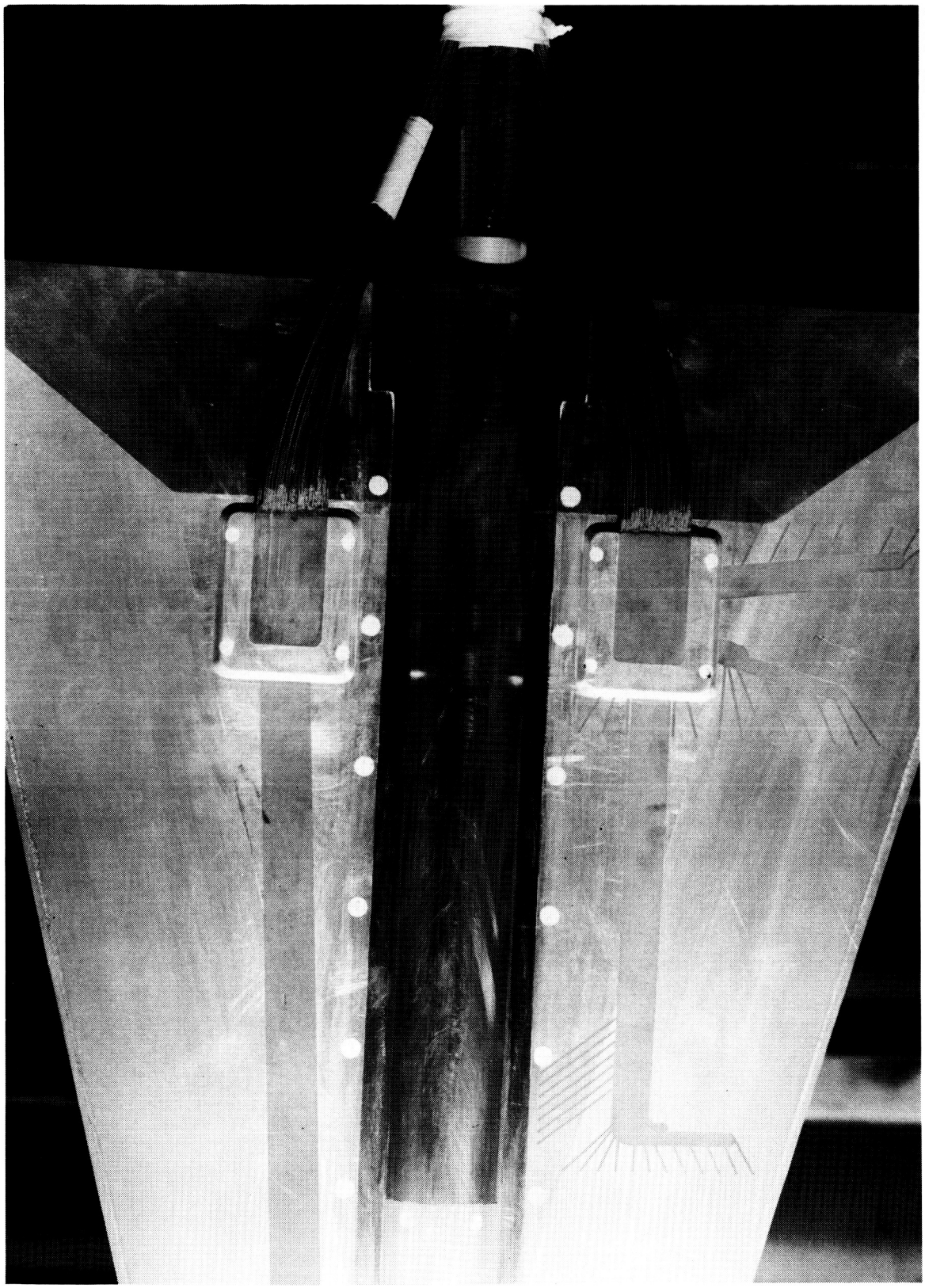

L-85-2201

Figure 7.- Photograph of pressure tube connector.

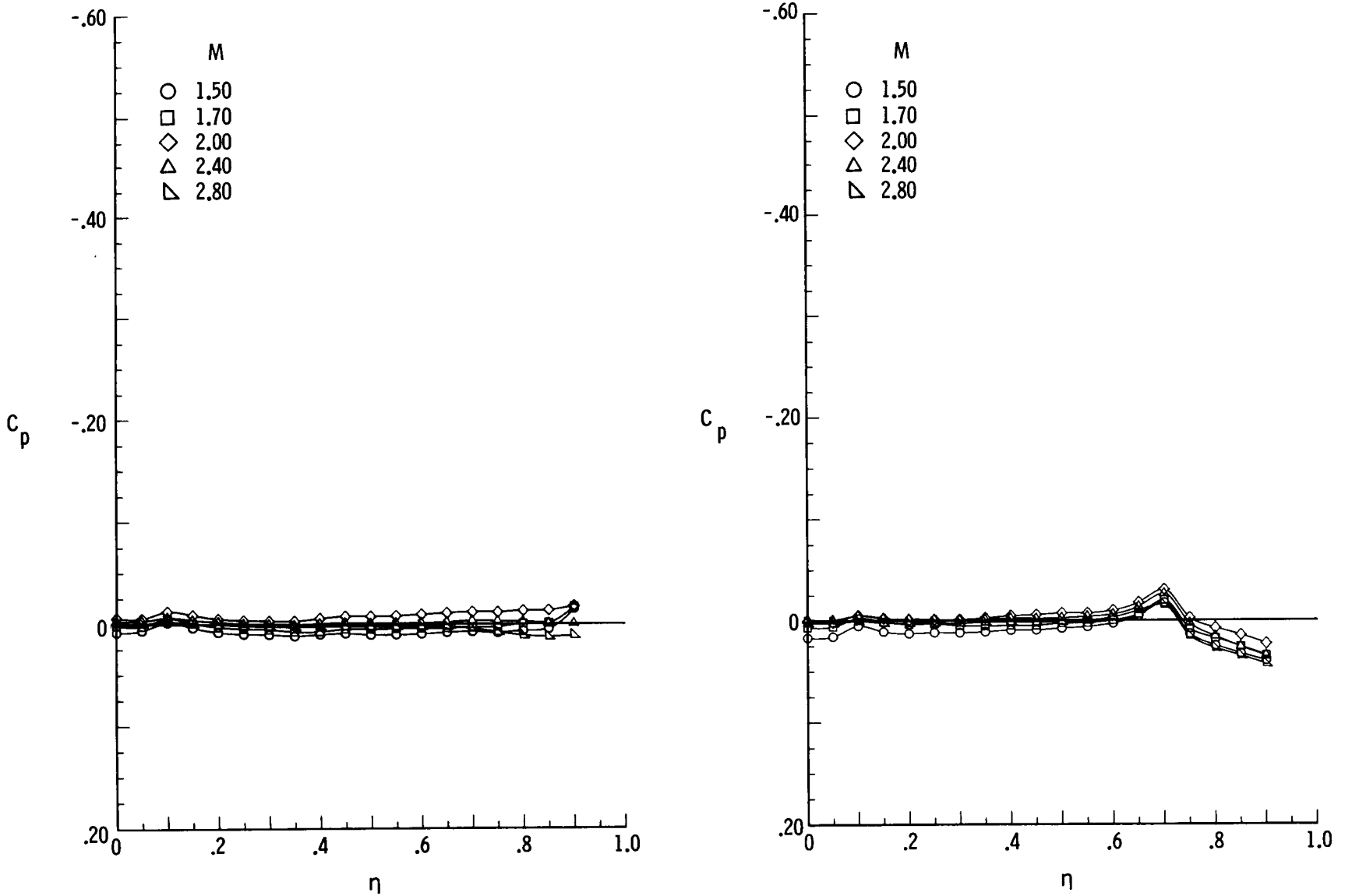

(a) $\delta_F = 0°$.

(b) $\delta_F = 5°$.

Figure 8.- Effect of M on spanwise pressure distribution at $\alpha = 0°$, $R = 2 \times 10^6$, and $x/\ell = 0.90$.

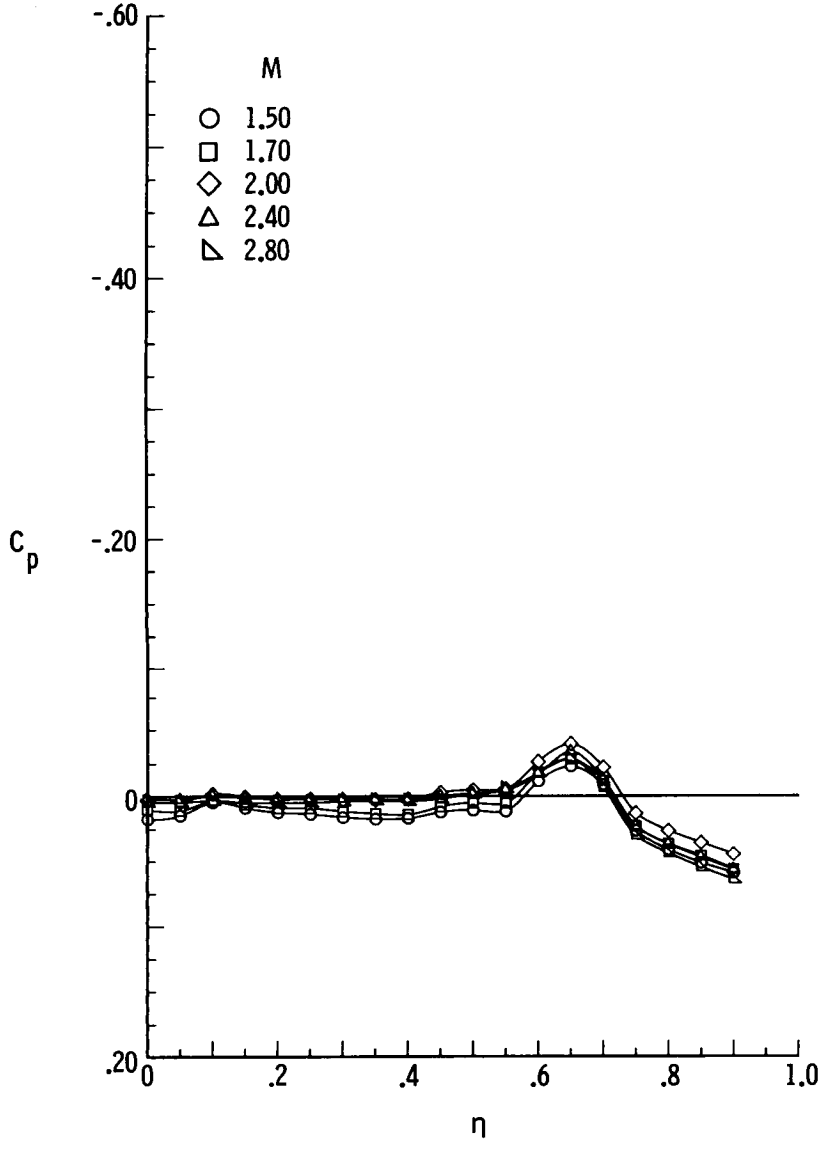

(c) δ_F = 10°.

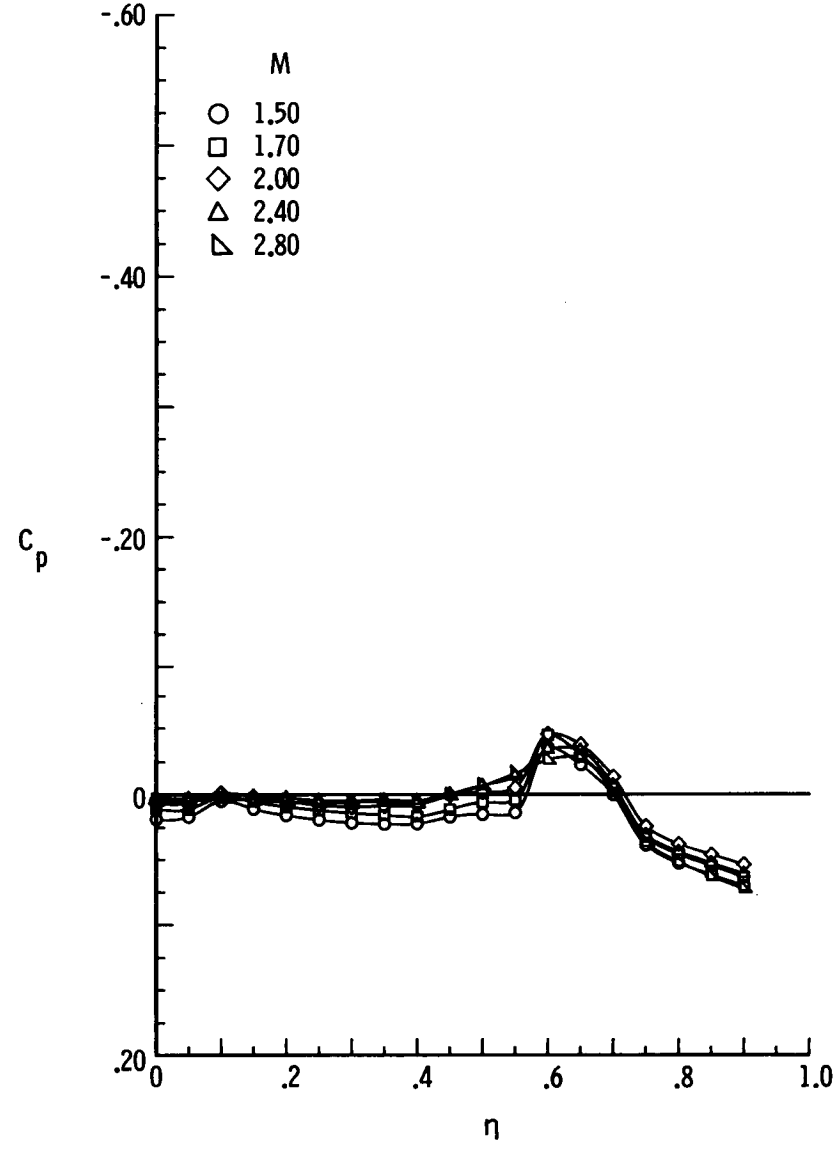

(d) δ_F = 15°.

Figure 8.- Concluded.

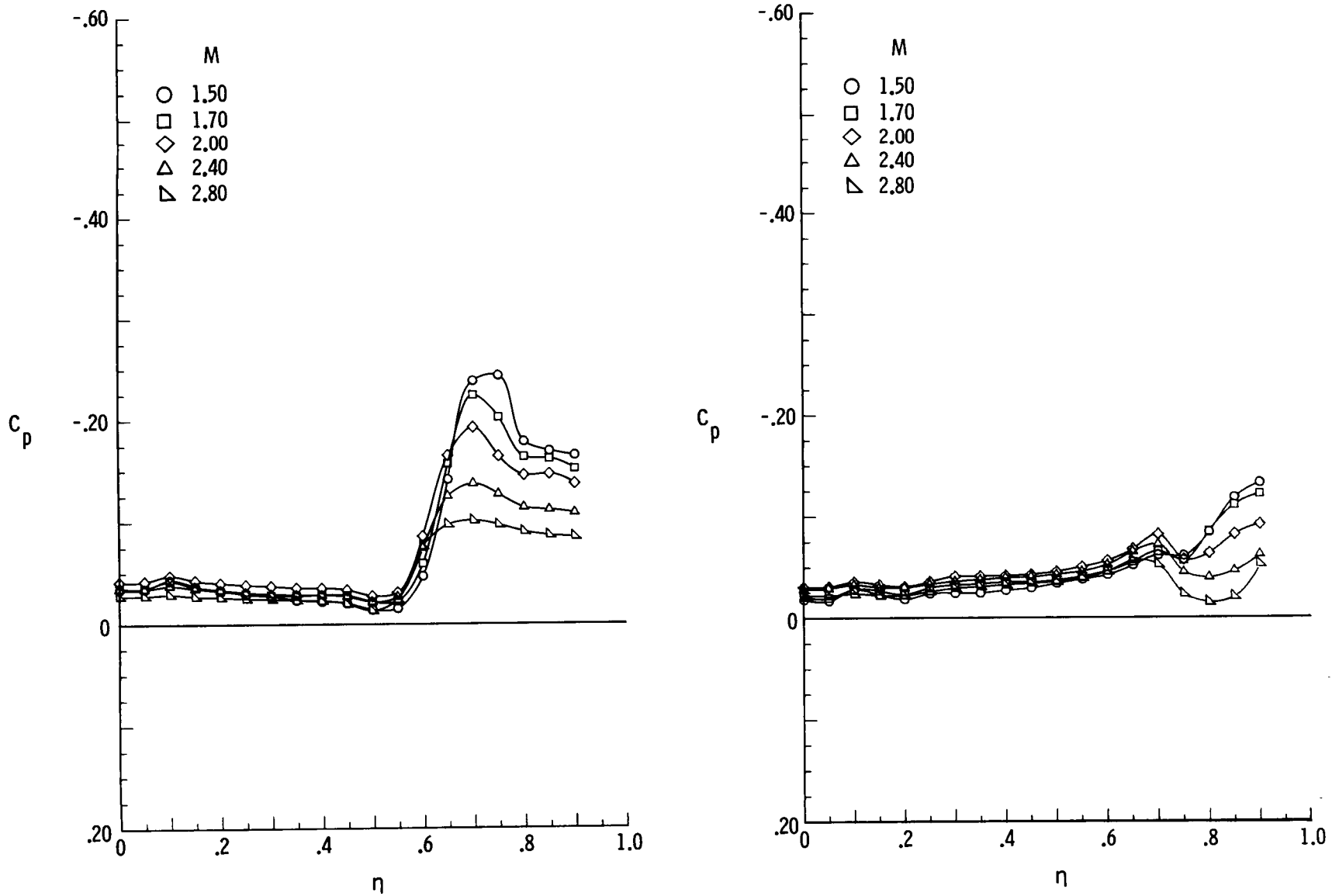

(a) $\delta_F = 0°$.

(b) $\delta_F = 5°$.

Figure 9.- Effect of M on spanwise pressure distribution at $\alpha = 4°$, $R = 2 \times 10^6$, and $x/\ell = 0.90$.

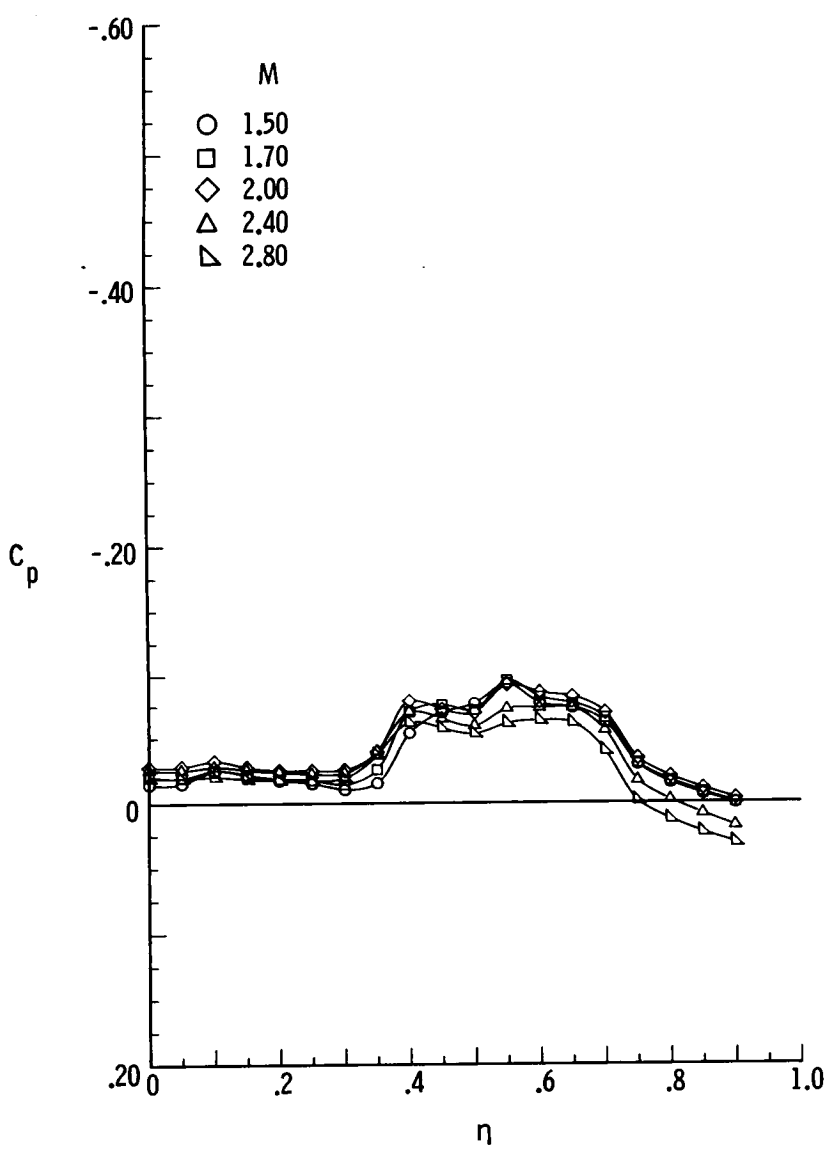

(c) $\delta_F = 10°$.

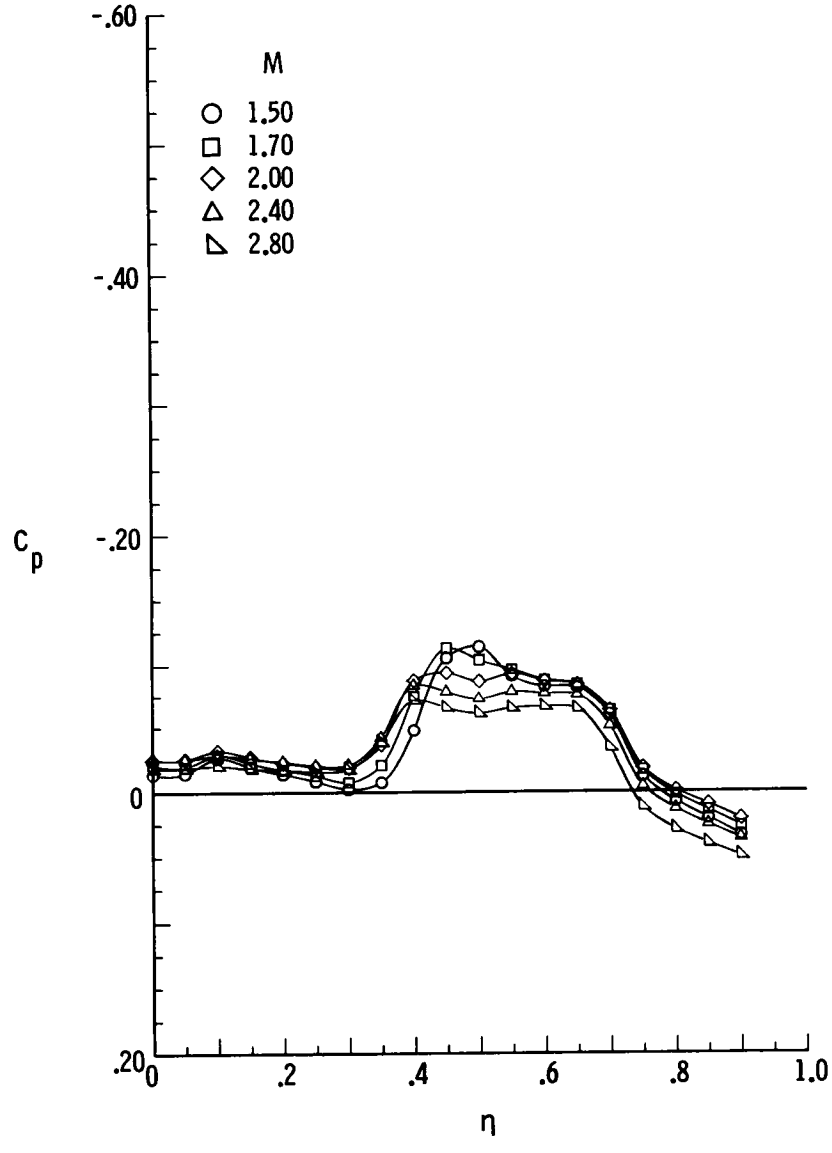

(d) $\delta_F = 15°$.

Figure 9.- Concluded.

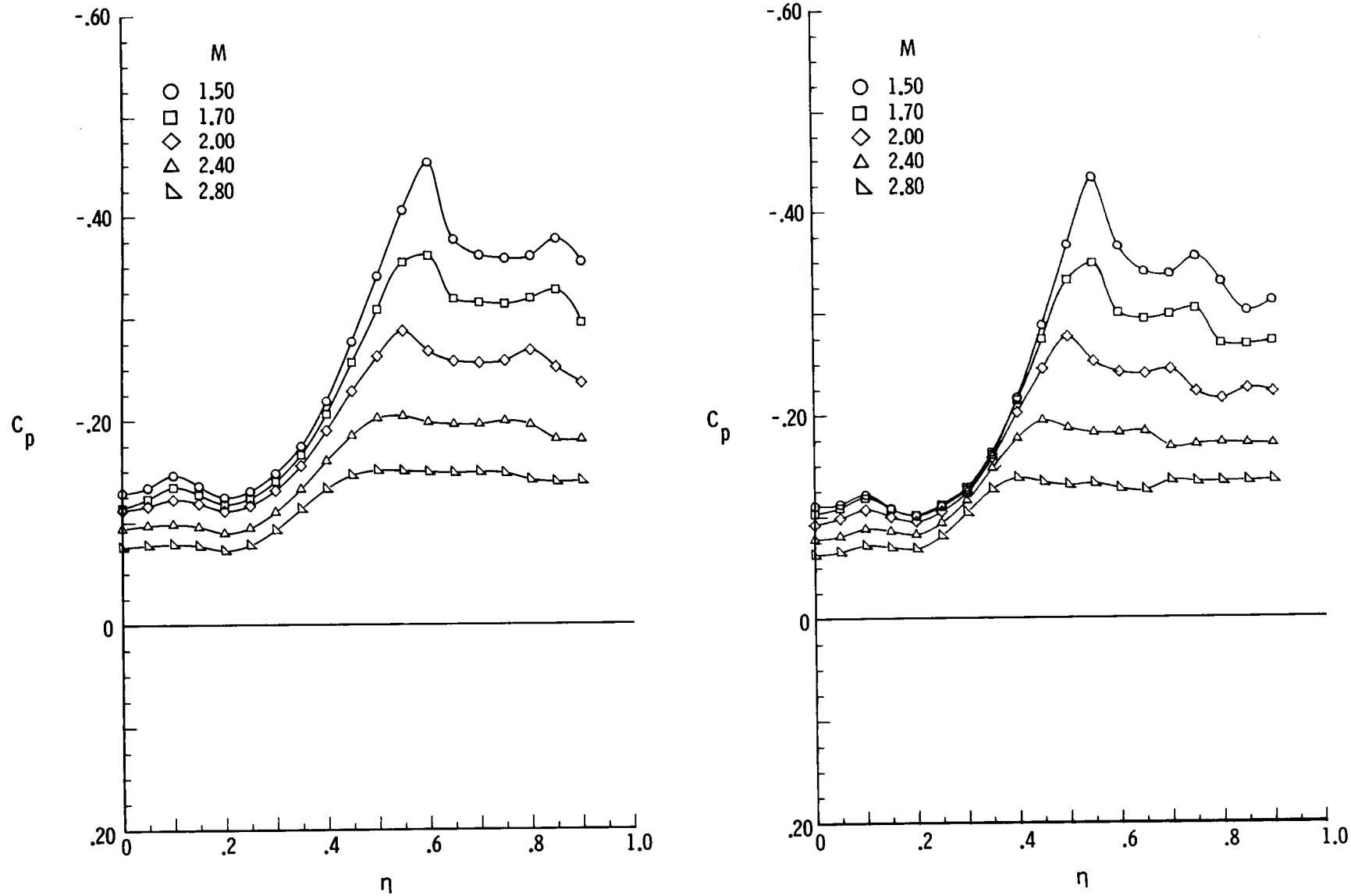

(a) $\delta_F = 0°$.

(b) $\delta_F = 5°$.

Figure 10.- Effect of M on spanwise surface pressure distribution at $\alpha = 12°$, $R = 2 \times 10^6$, and $x/\ell = 0.90$.

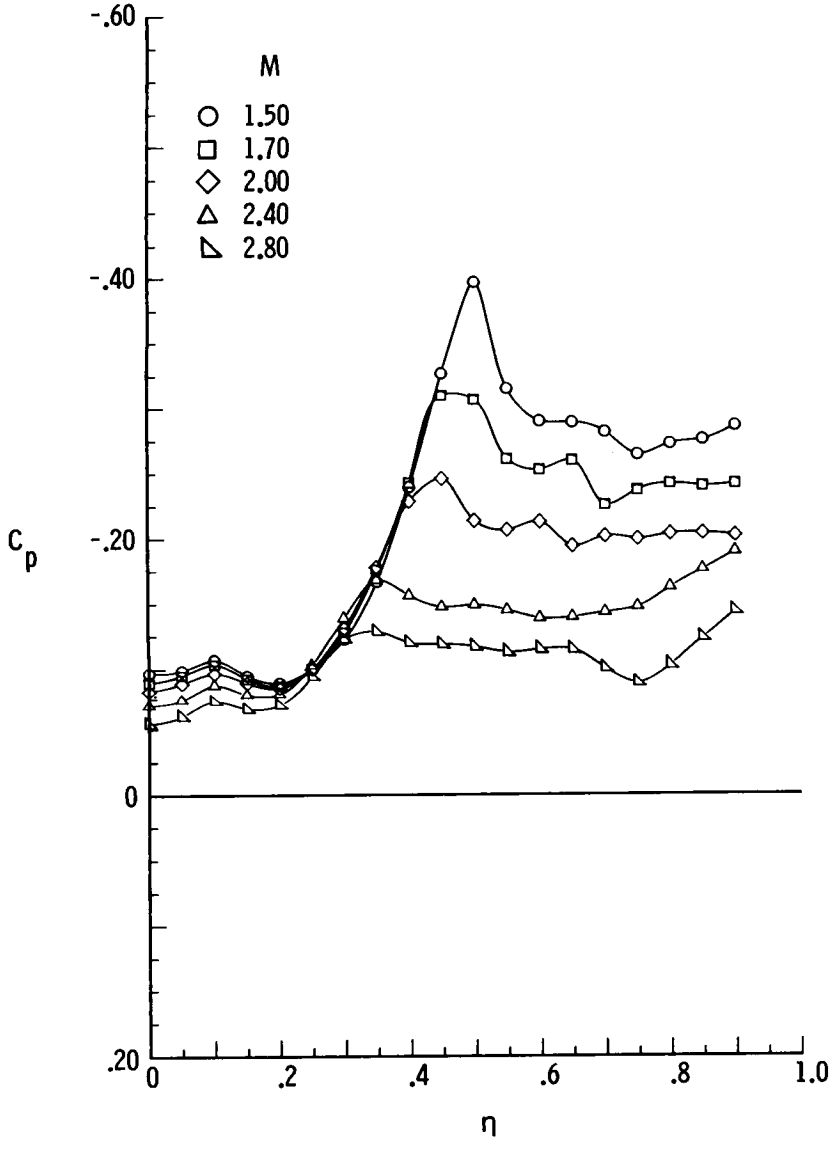

(c) δ_F = 10°.

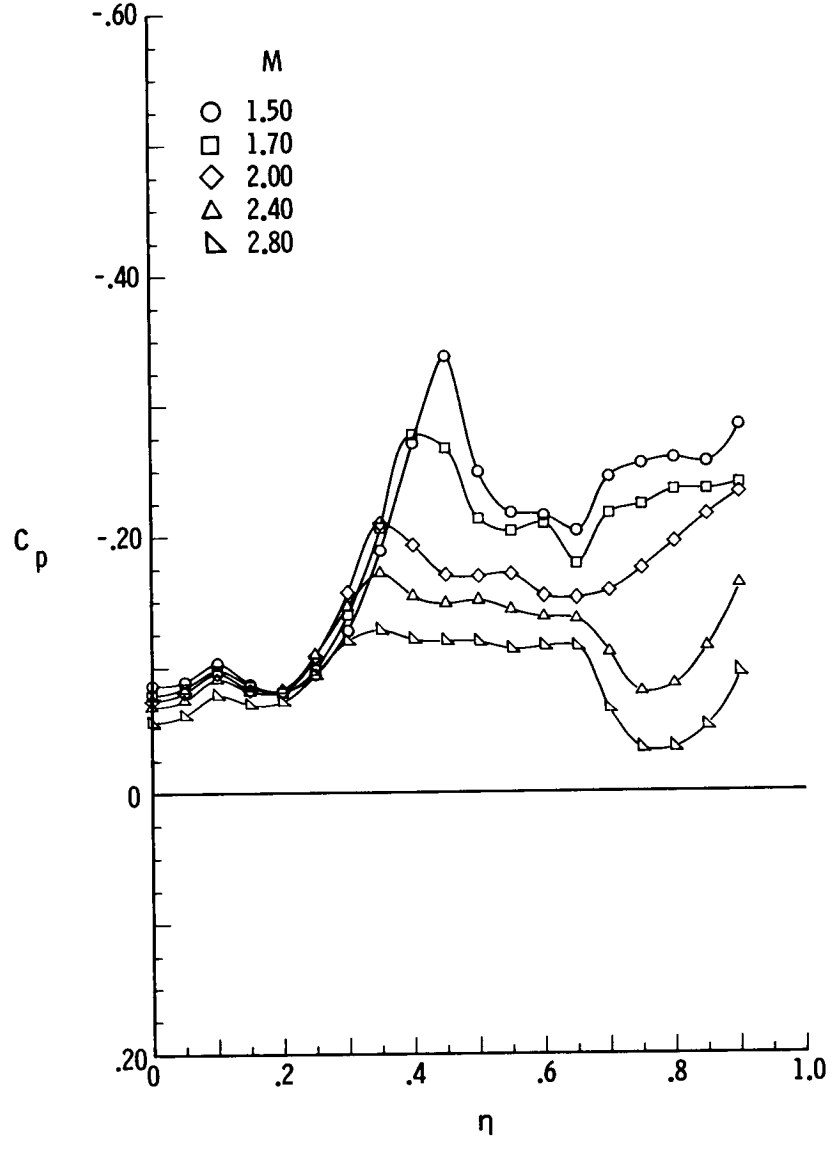

(d) δ_F = 15°.

Figure 10.- Concluded.

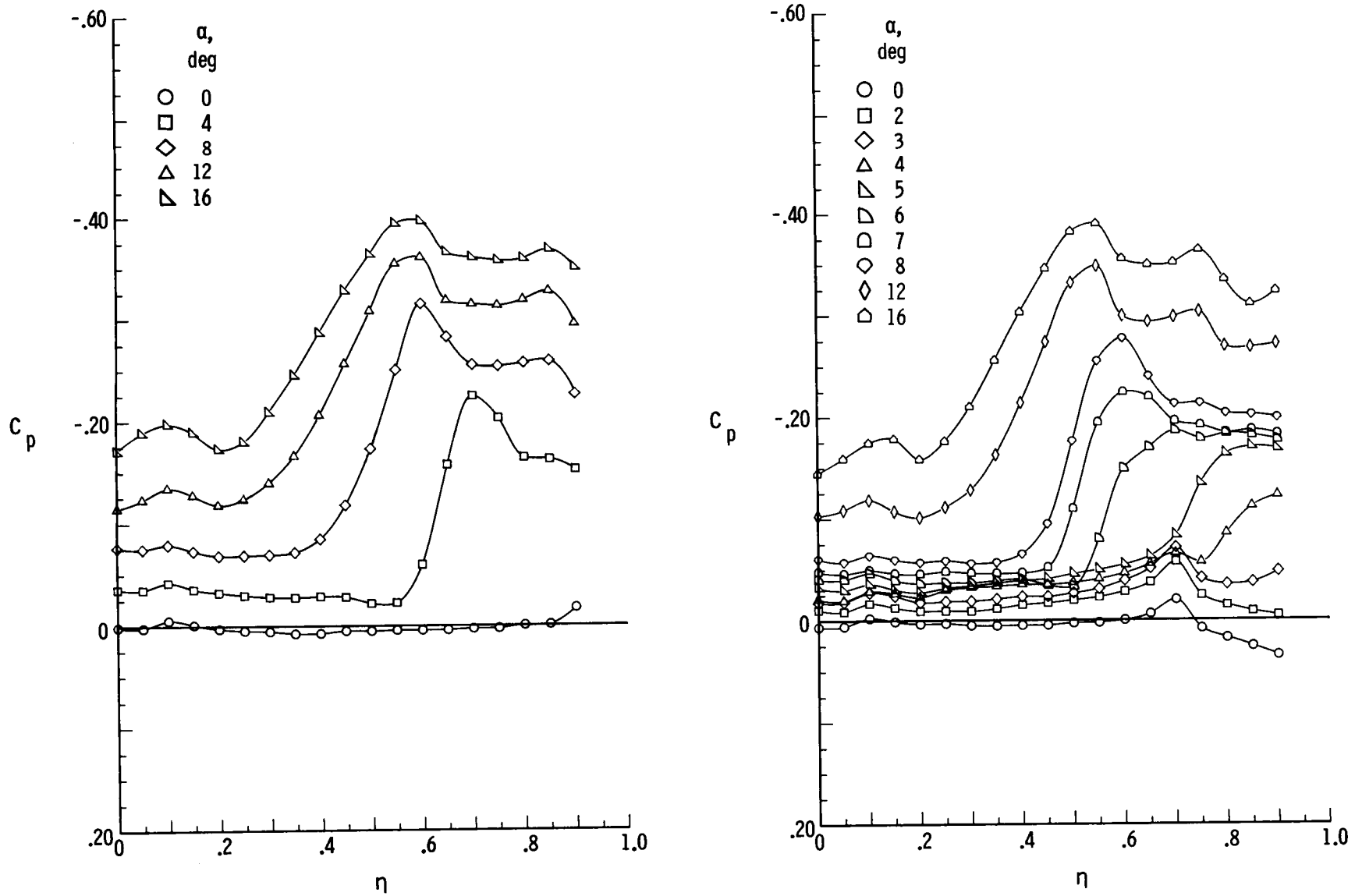

(a) $\delta_F = 0°$.

(b) $\delta_F = 5°$.

Figure 11.- Effect of α on spanwise surface pressure distribution at $M = 1.70$, $R = 2 \times 10^6$, and $x/\ell = 0.90$.

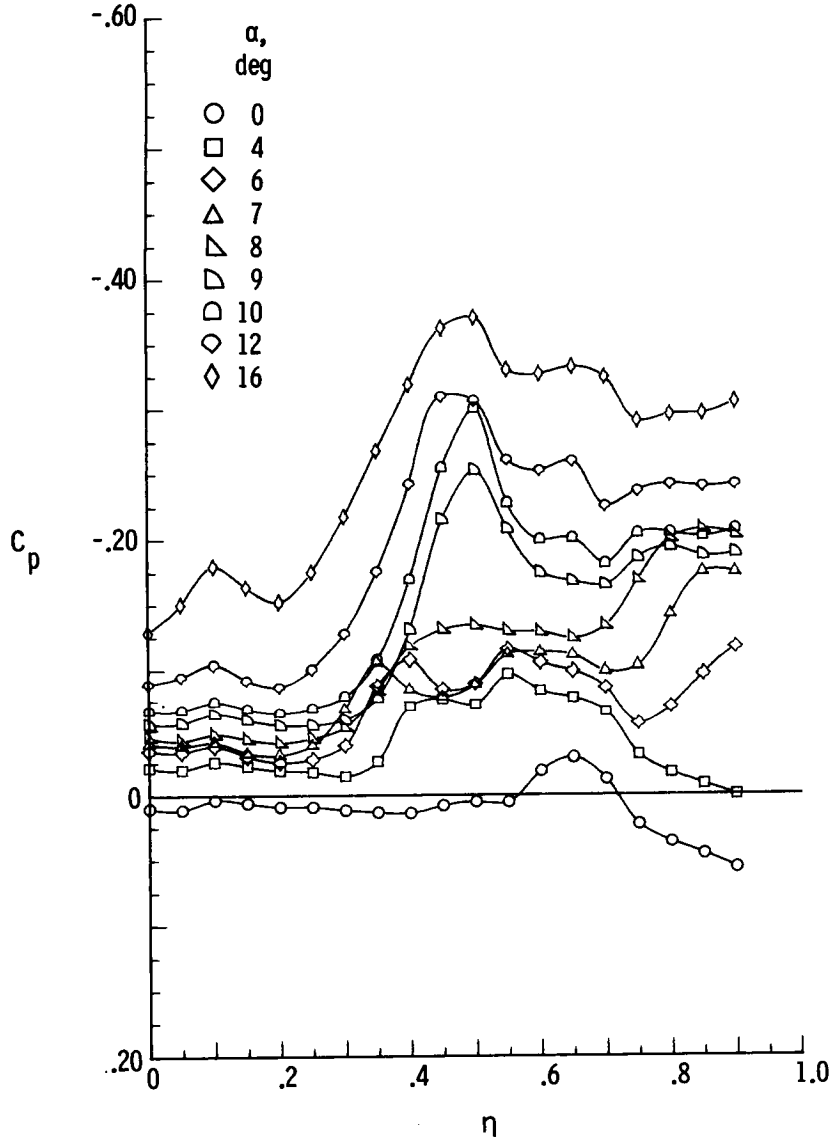

(c) $\delta_F = 10°$.

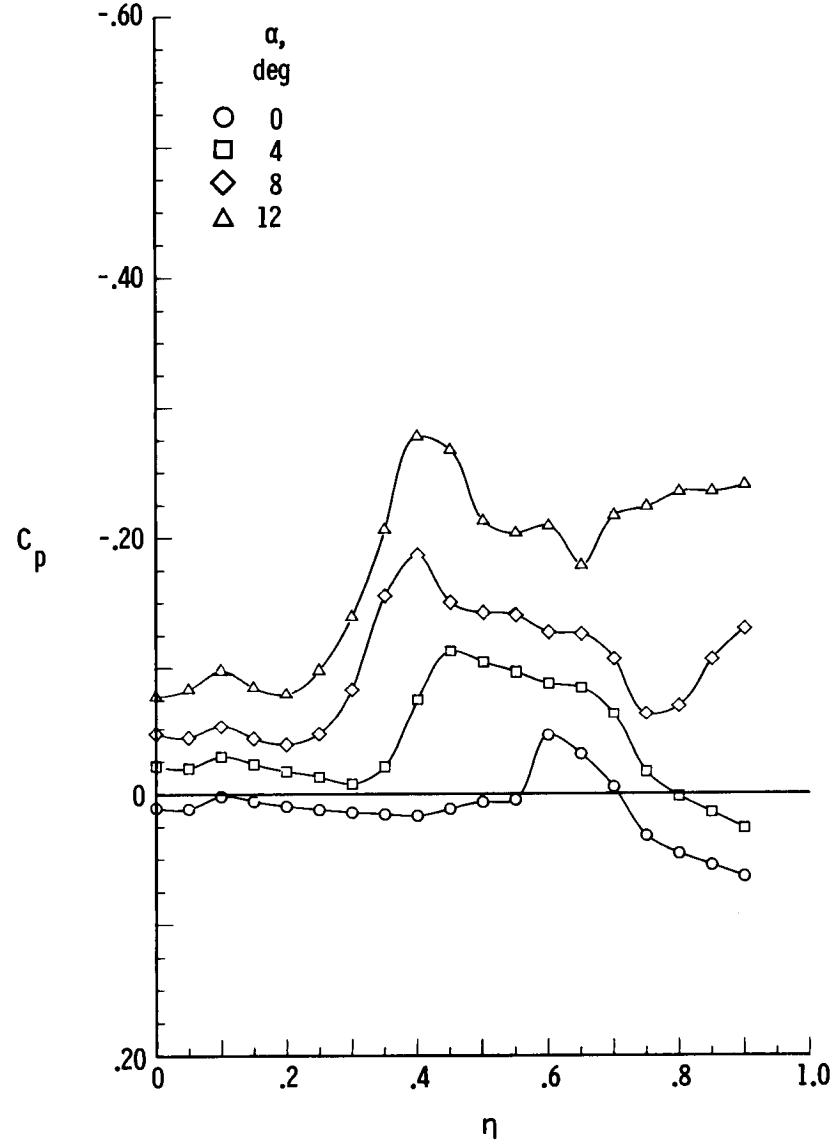

(d) $\delta_F = 15°$.

Figure 11.- Concluded.

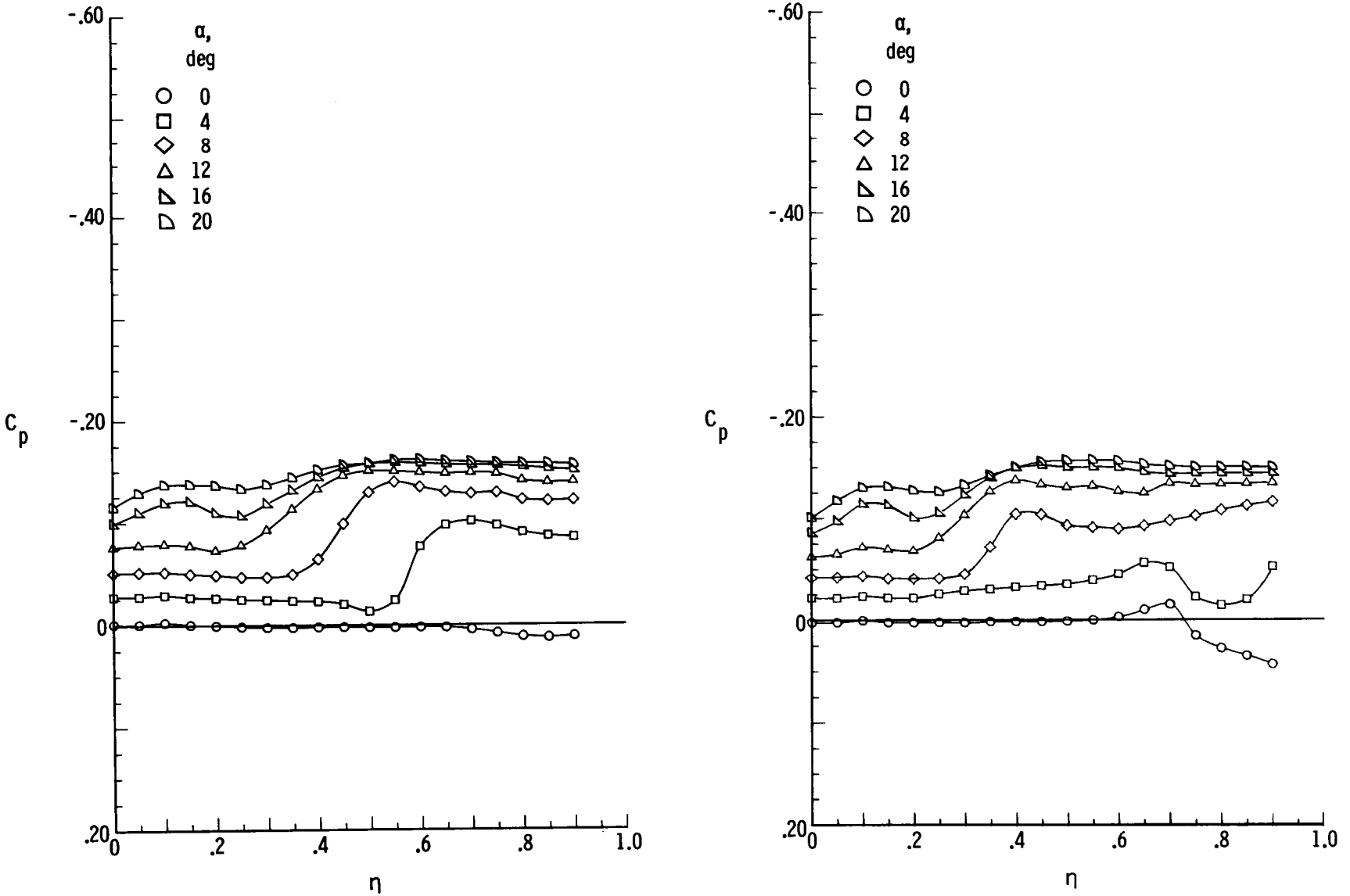

(a) $\delta_F = 0°$.

(b) $\delta_F = 5°$.

Figure 12.- Effect of α on spanwise surface pressure distribution at $M = 2.80$, $R = 2 \times 10^6$, and $x/l = 0.90$.

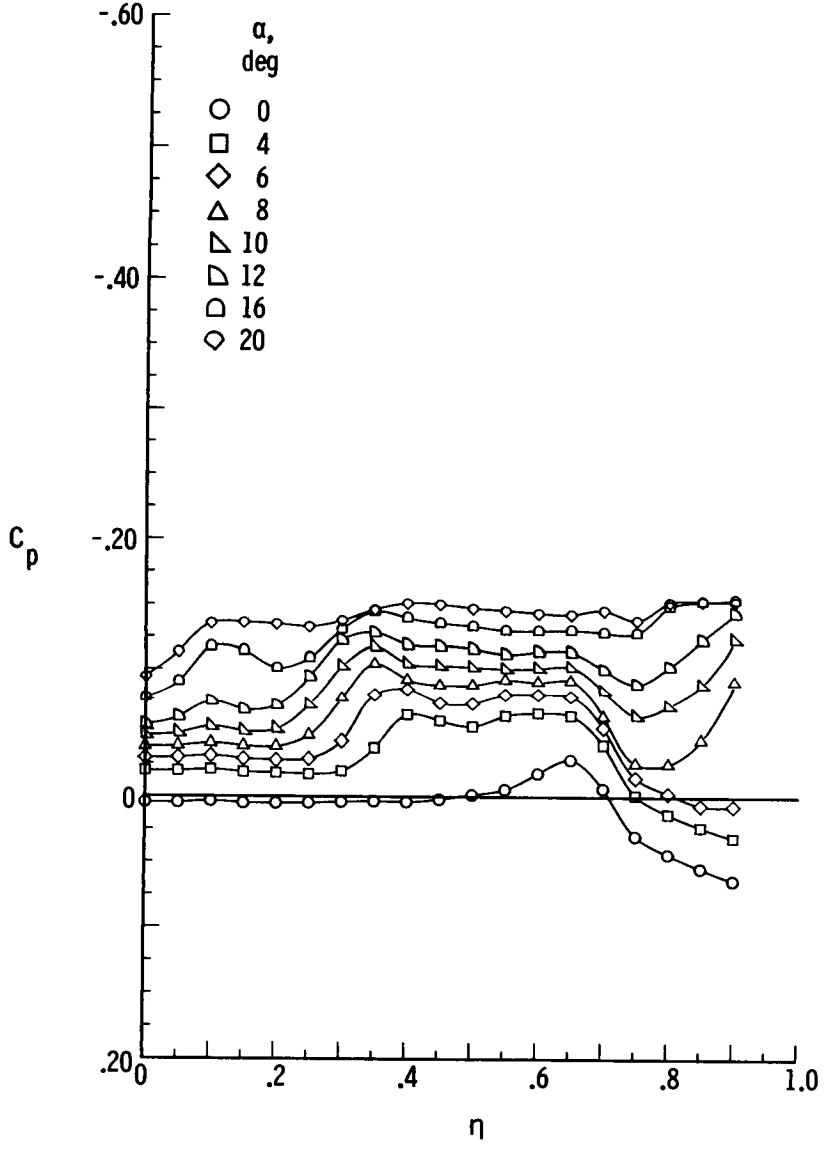

(c) δ_F = 10°.

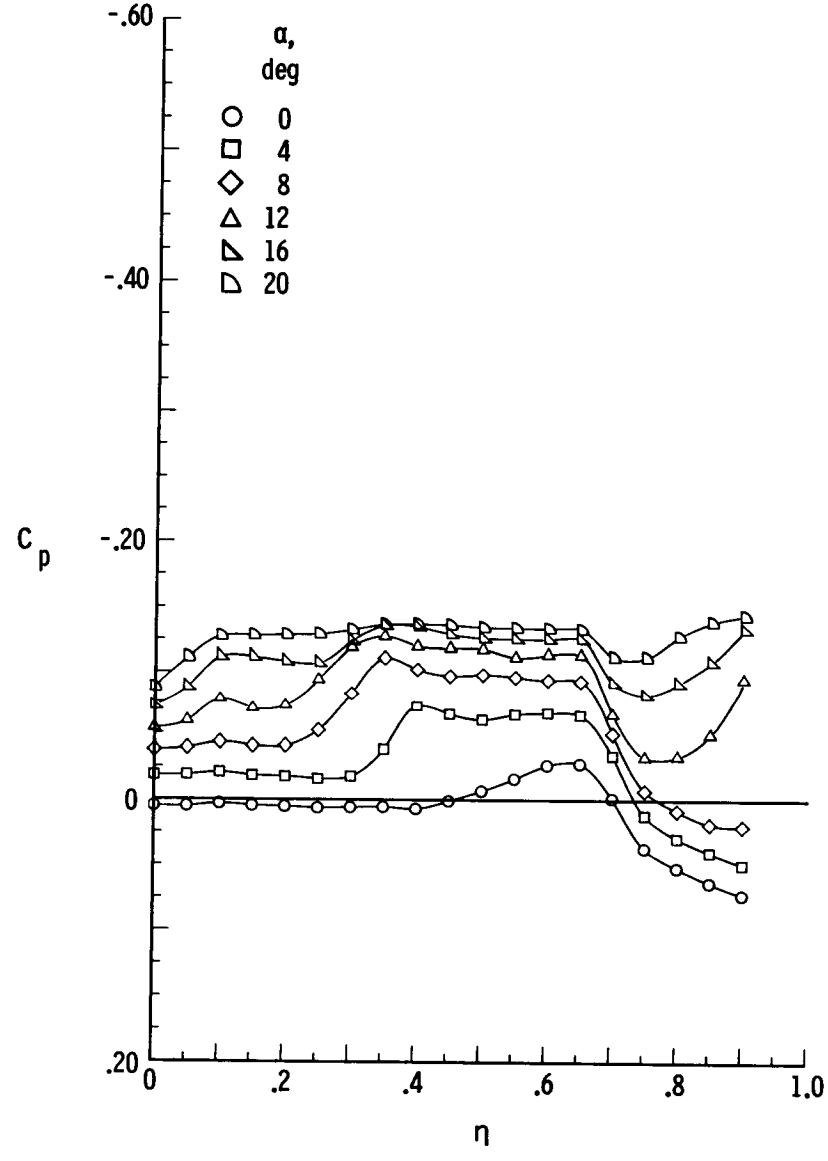

(d) δ_F = 15°.

Figure 12.- Concluded.

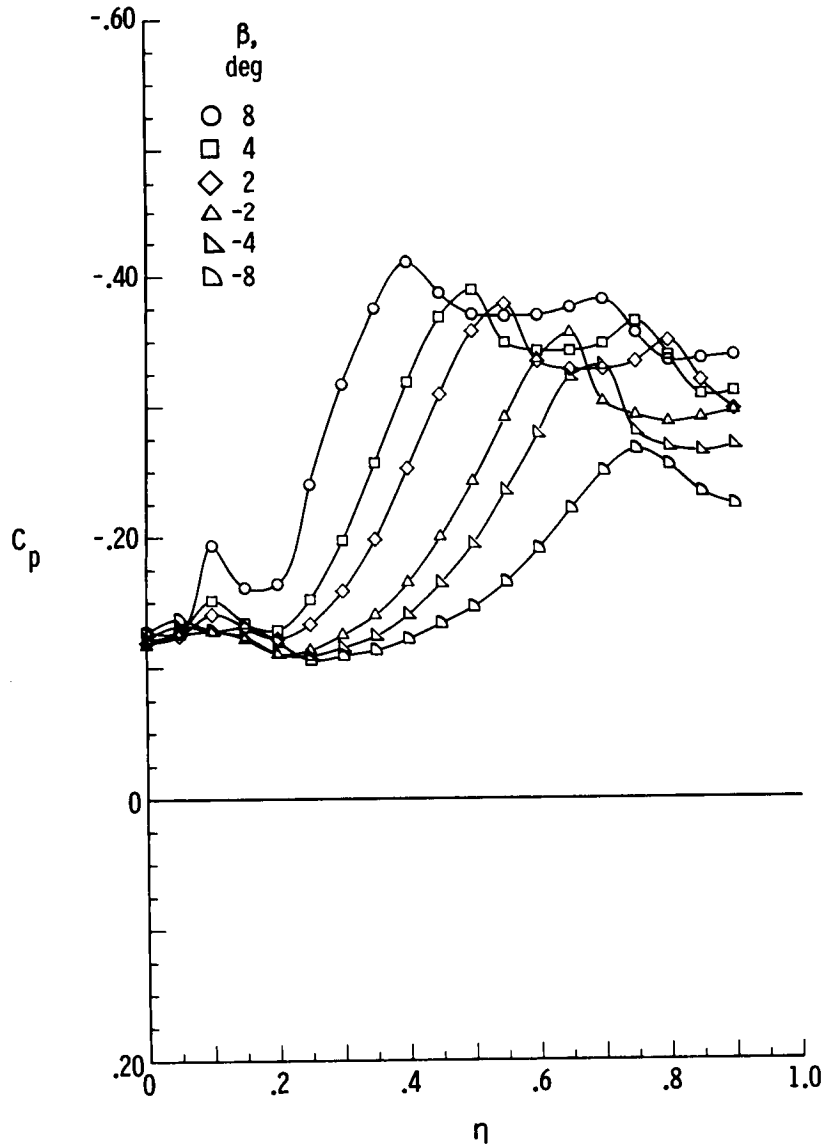

(a) $\delta_F = 0°$.

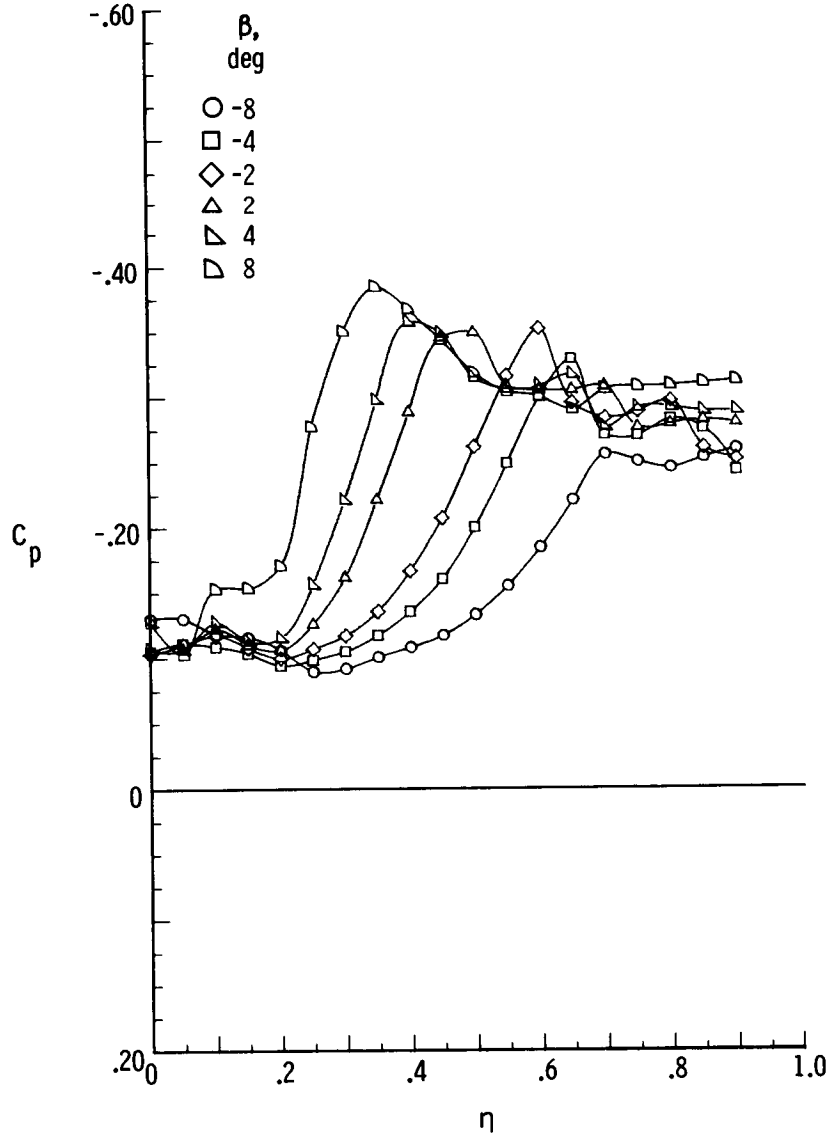

(b) $\delta_F = 5°$.

Figure 13.- Effect of β on spanwise surface pressure distribution at $M = 1.70$, $\alpha = 12°$, $R = 2 \times 10^6$, and $x/\ell = 0.90$.

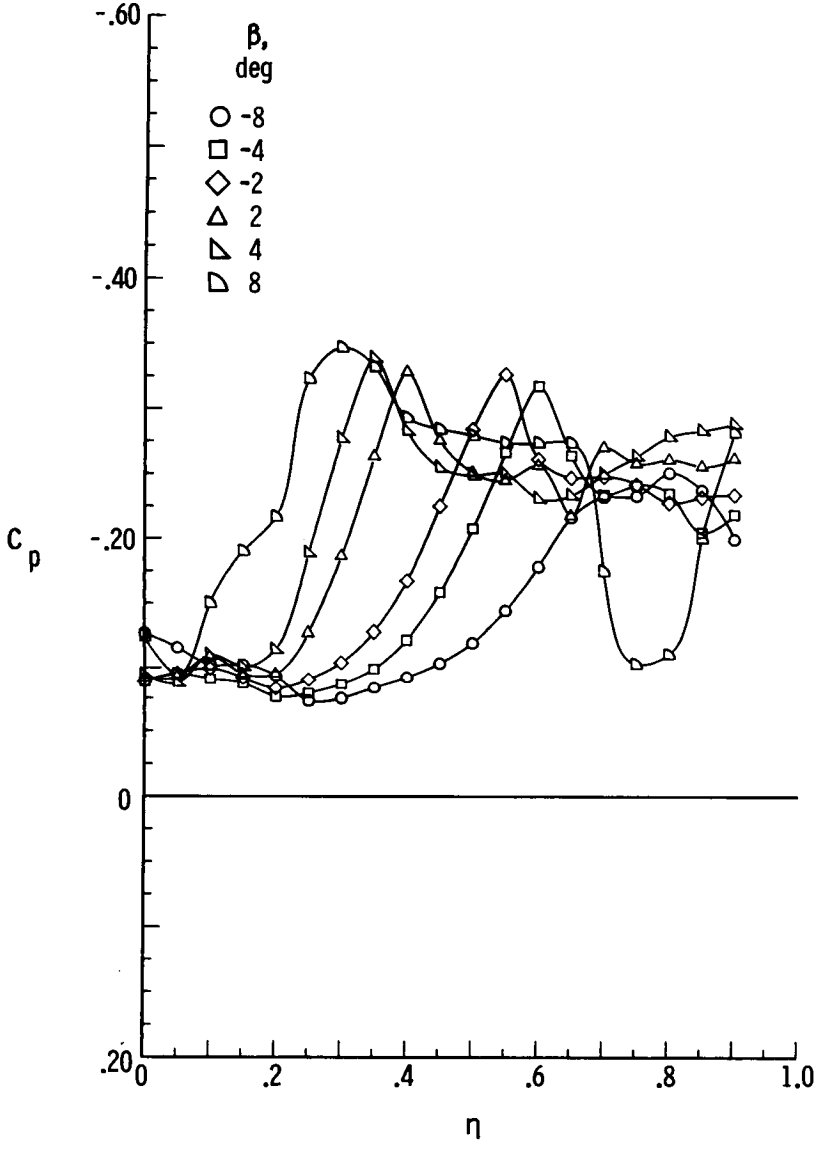

(c) δ_F = 10°.

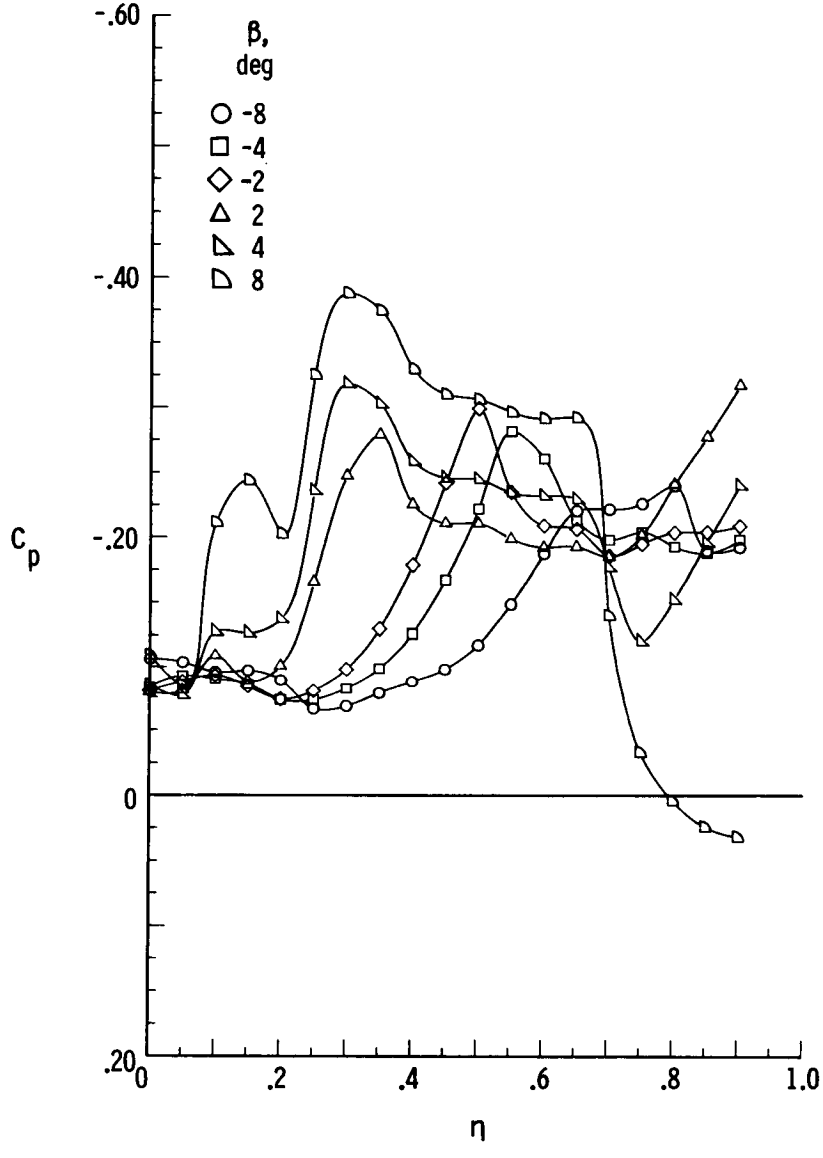

(d) δ_F = 15°.

Figure 13.- Concluded.

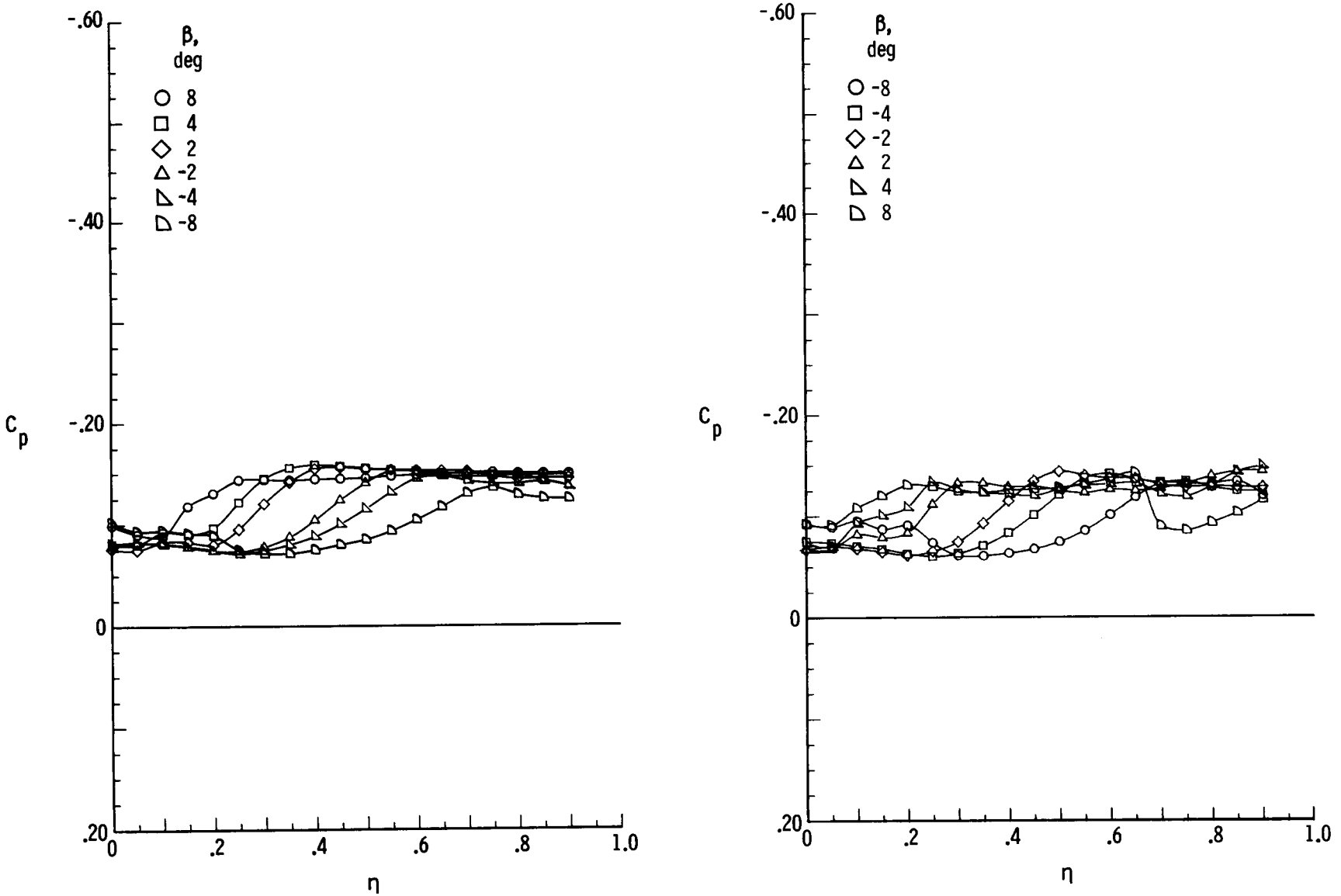

(a) $\delta_F = 0°$.

(b) $\delta_F = 5°$.

Figure 14.- Effect of β on spanwise surface pressure distribution at $M = 2.80$, $\alpha = 12°$, $R = 2 \times 10^6$, and $x/\ell = 0.90$.

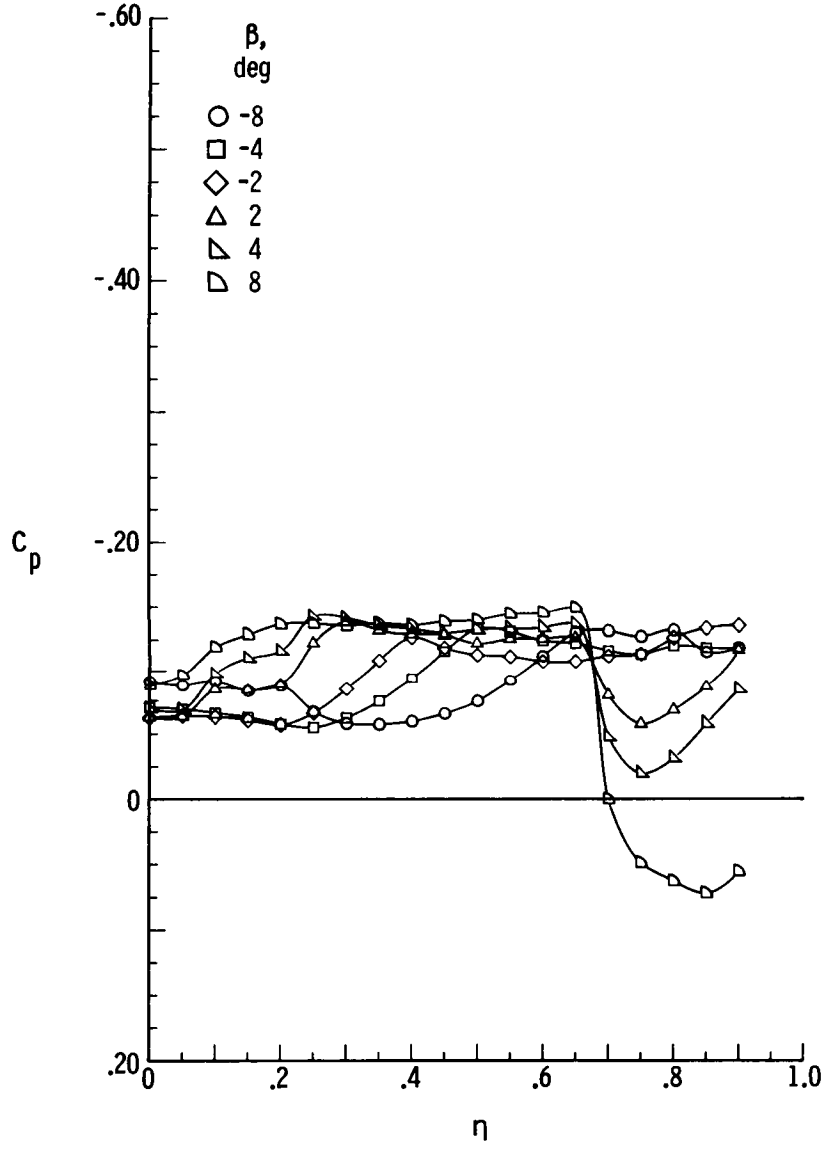

(c) δ_F = 10°.

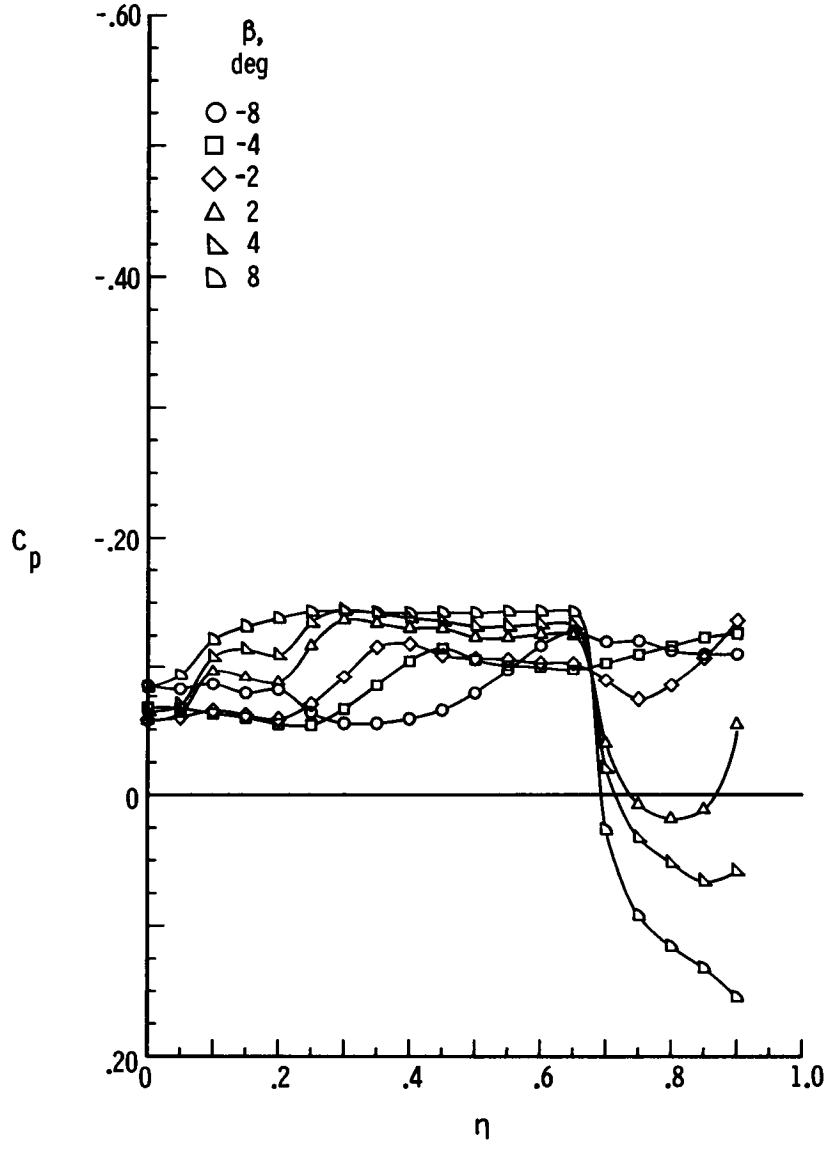

(d) δ_F = 15°.

Figure 14.- Concluded.

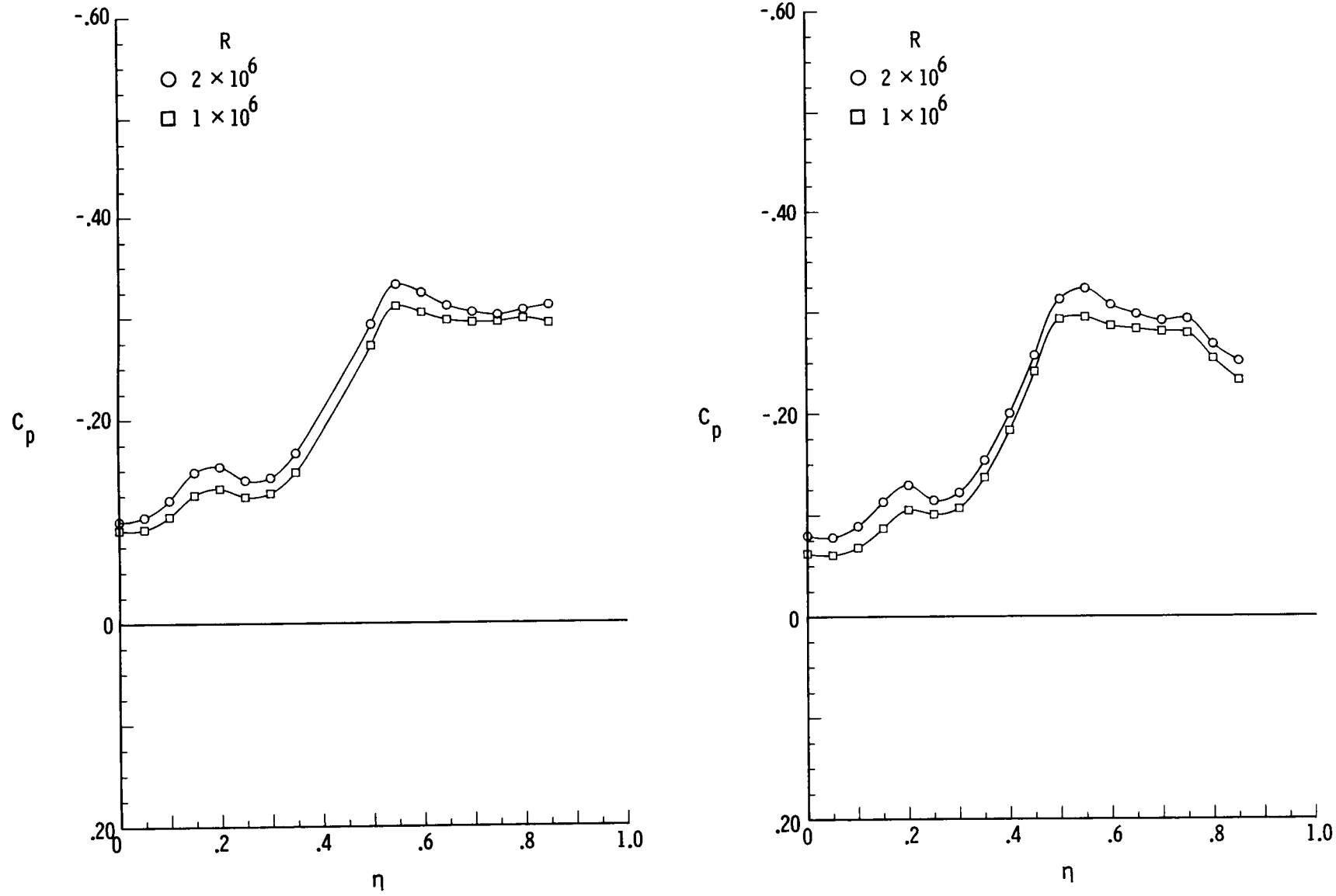

(a) $\delta_F = 0°$.

(b) $\delta_F = 5°$.

Figure 15.- Effect of R on spanwise surface pressure distribution at M = 1.70, $\alpha = 12°$, and $x/\ell = 0.20$.

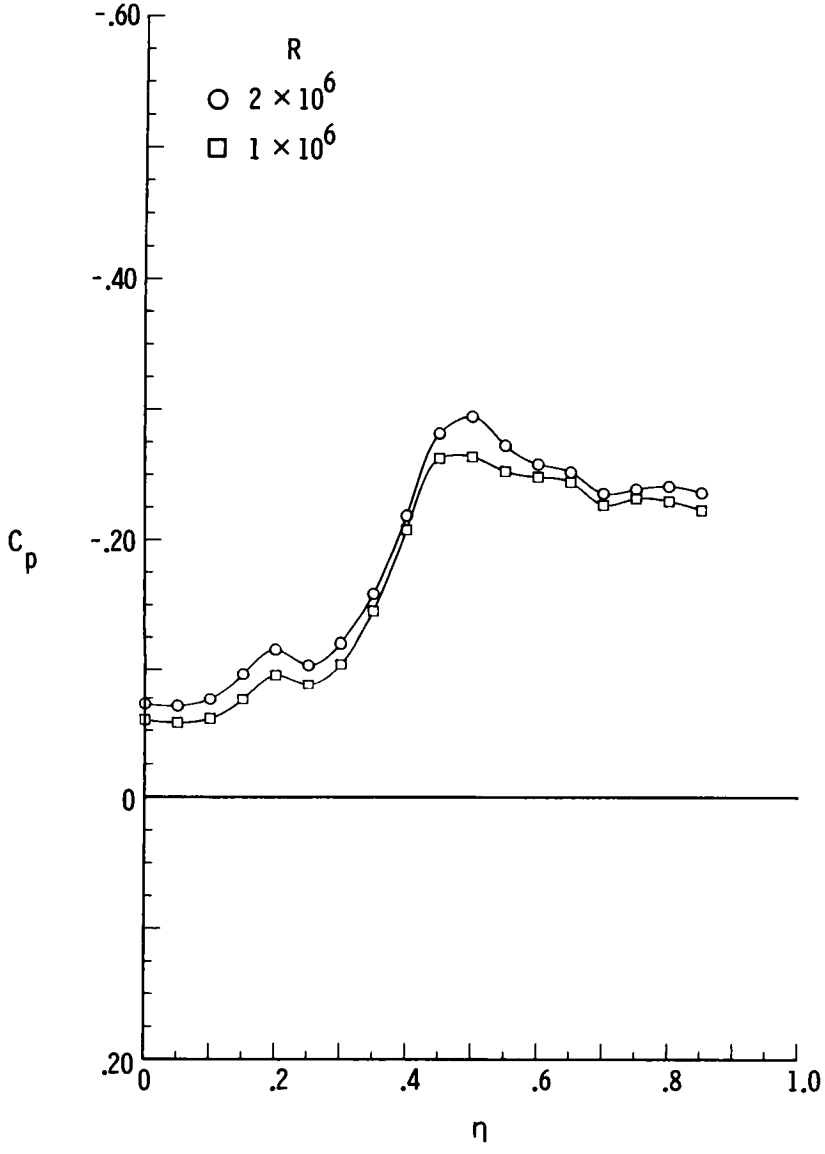

(c) δ_F = 10°.

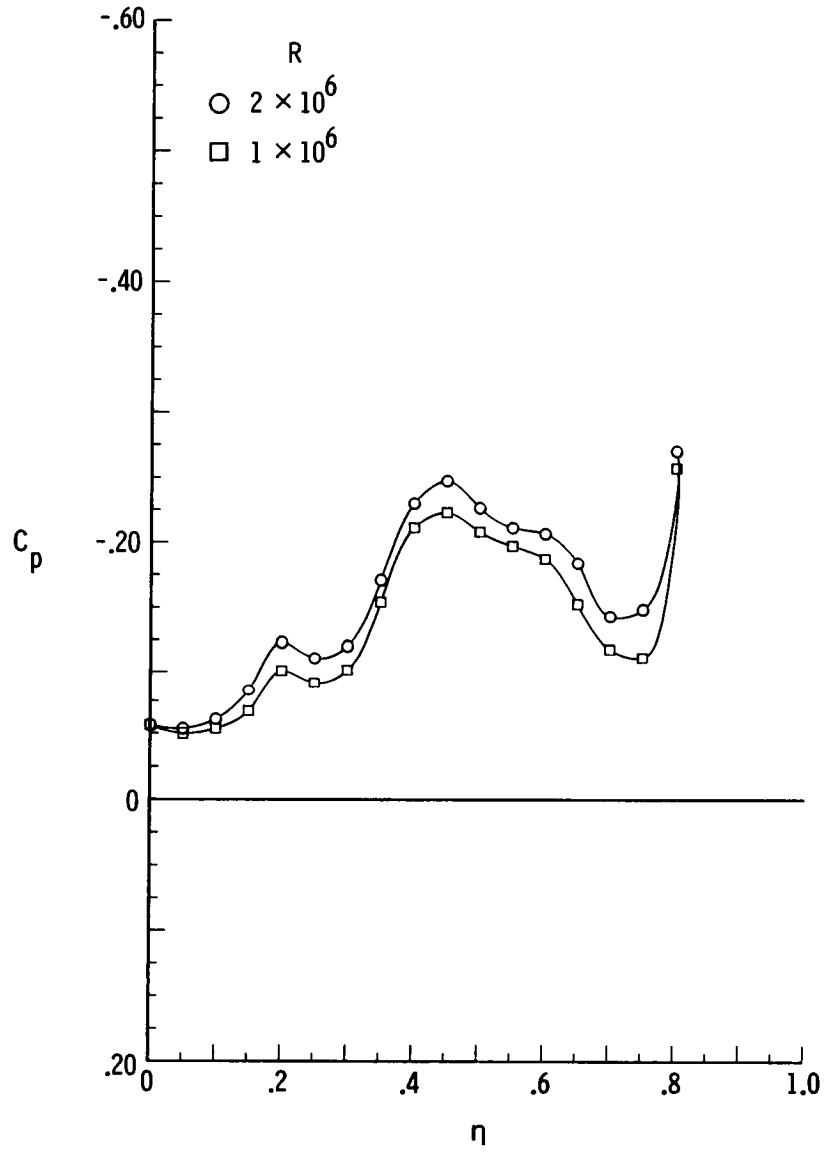

(d) δ_F = 15°.

Figure 15.- Concluded.

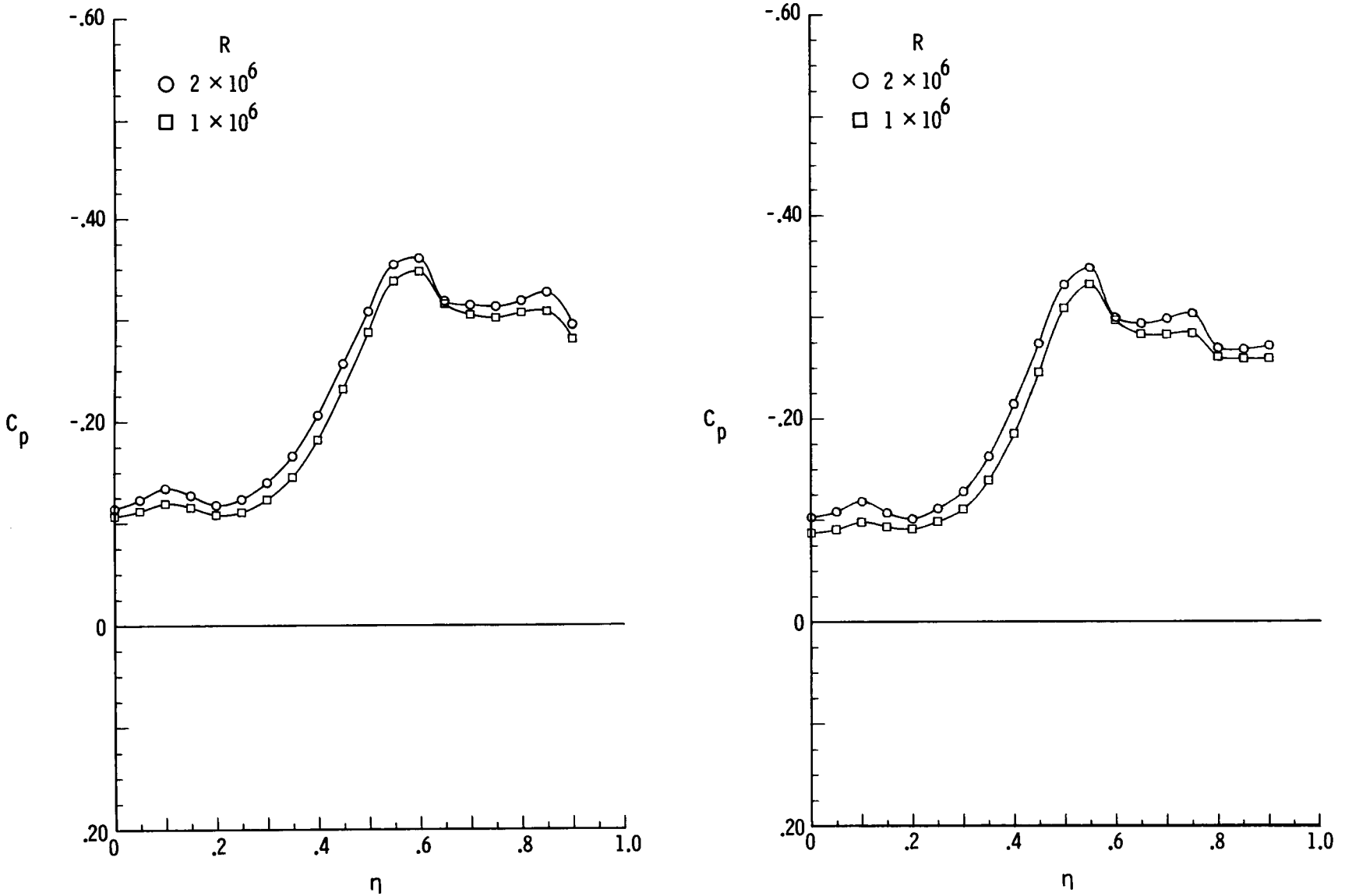

(a) $\delta_F = 0°$.

(b) $\delta_F = 5°$.

Figure 16.- Effect of R on spanwise surface pressure distribution at M = 1.70, $\alpha = 12°$, and $x/\ell = 0.90$.

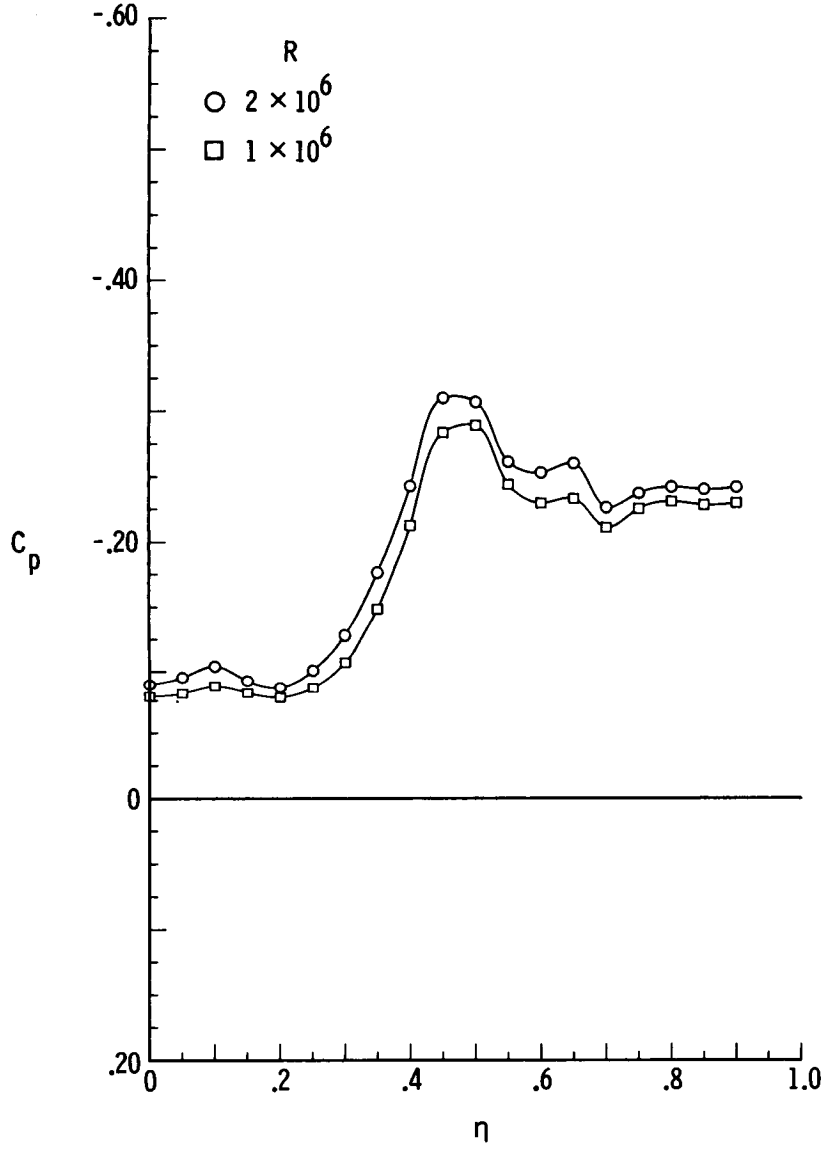

(c) δ_F = 10°.

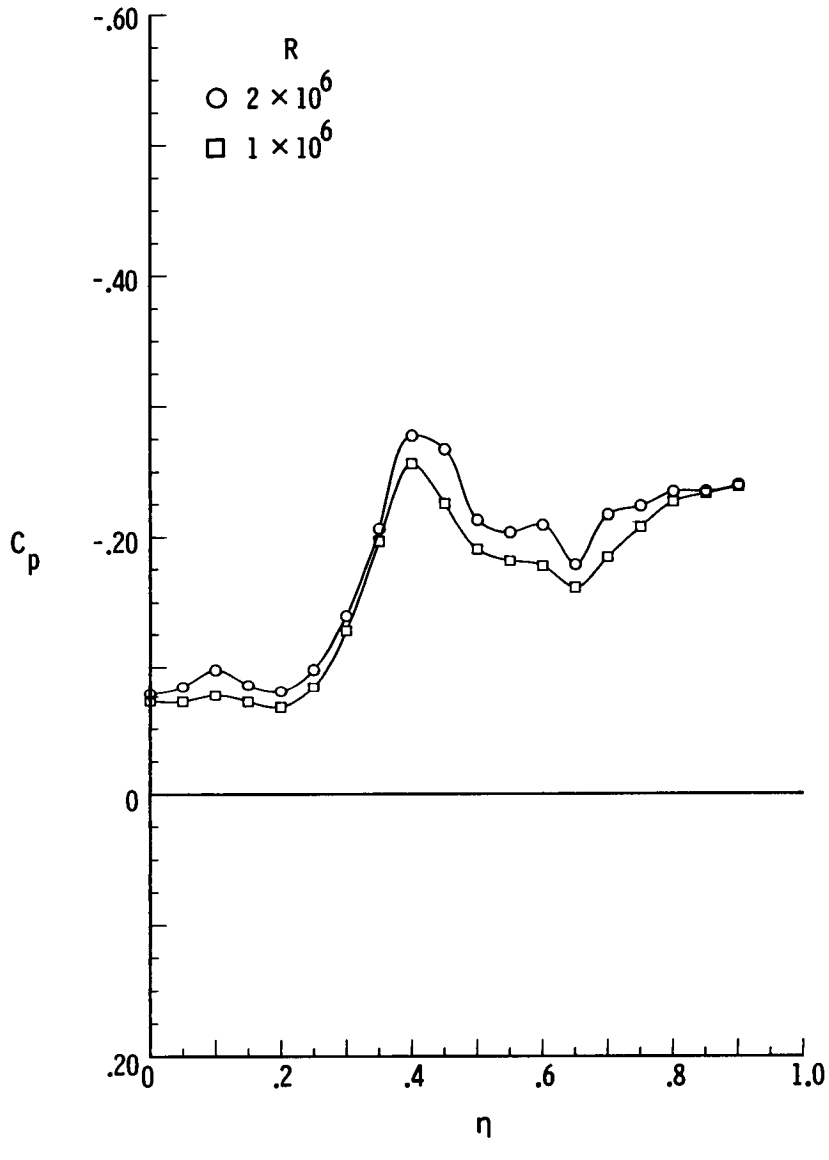

(d) δ_F = 15°.

Figure 16.- Concluded.

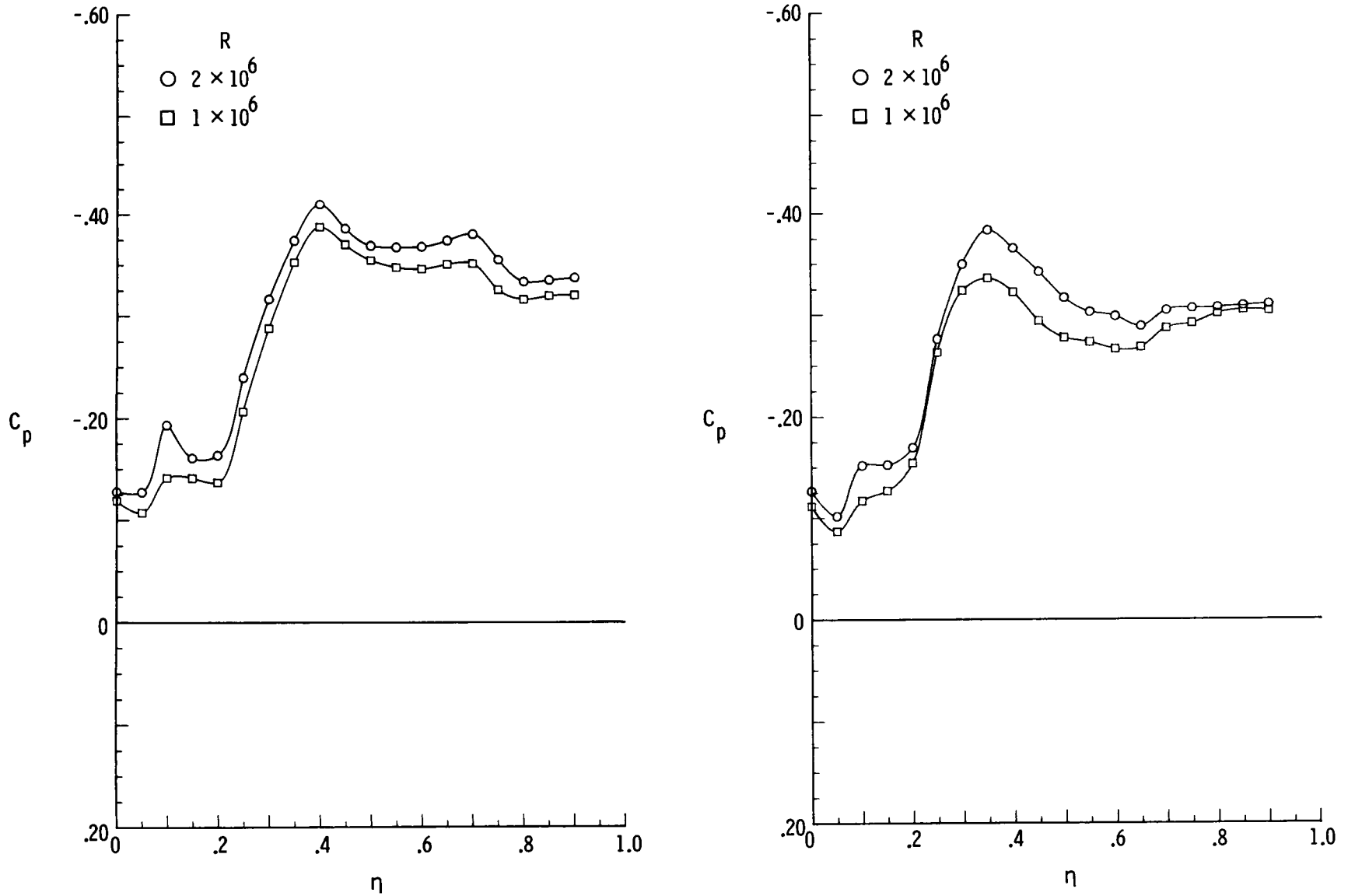

(a) $\delta_F = 0°$.

(b) $\delta_F = 5°$.

Figure 17.- Effect of R on spanwise pressure distribution at M = 1.70, $\alpha = 12°$, $\beta = 8°$, and $x/\ell = 0.90$.

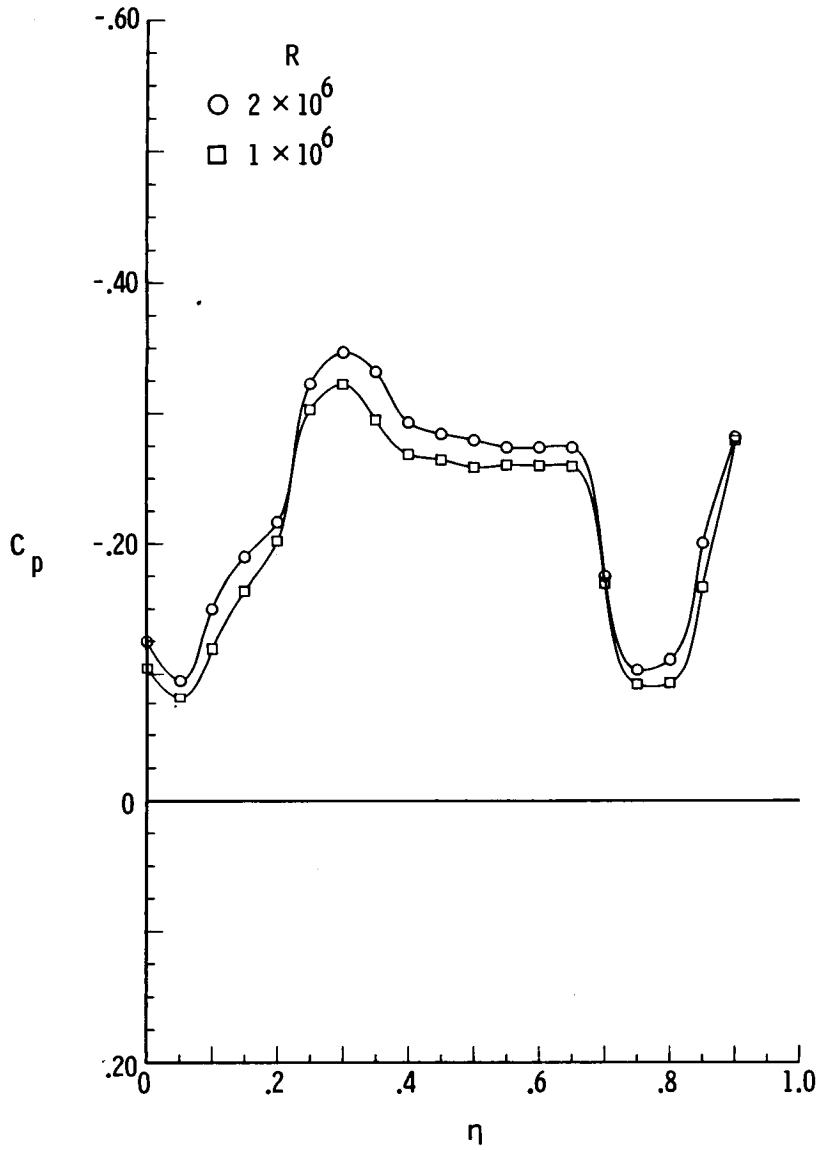

(c) $\delta_F = 10°$.

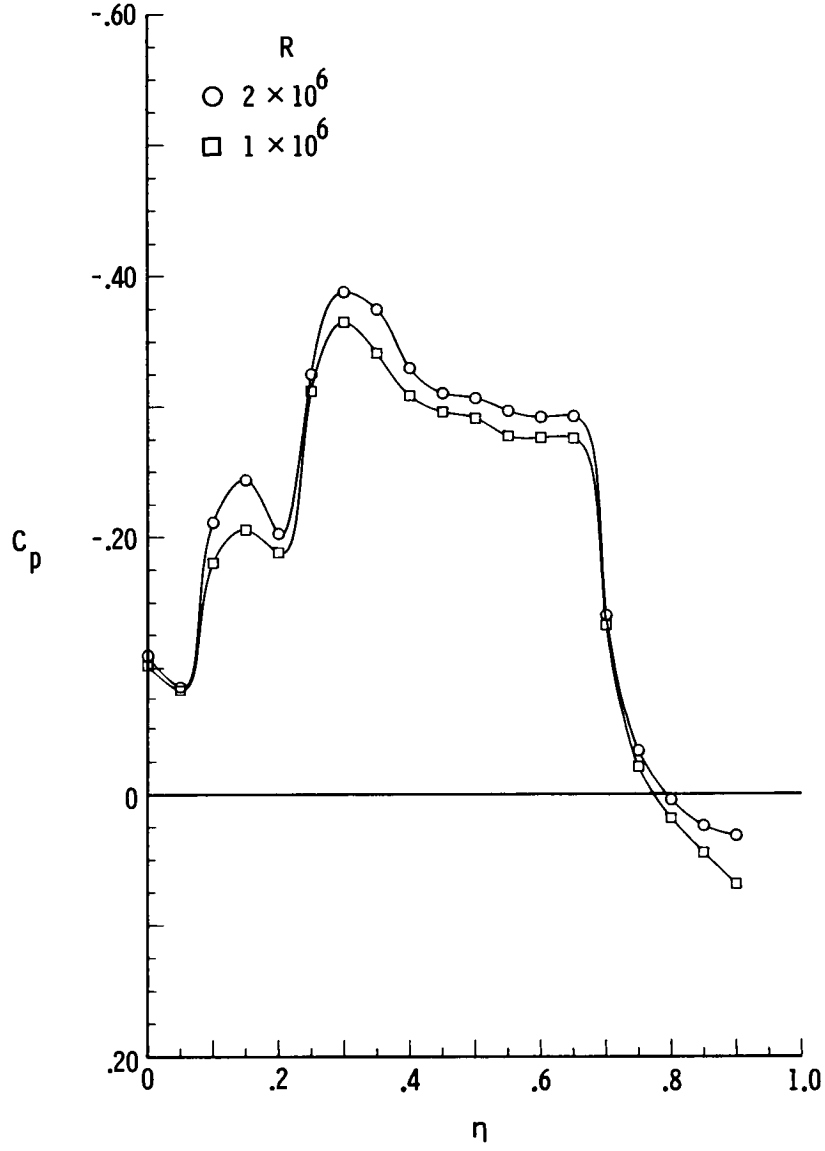

(d) $\delta_F = 15°$.

Figure 17.- Concluded.

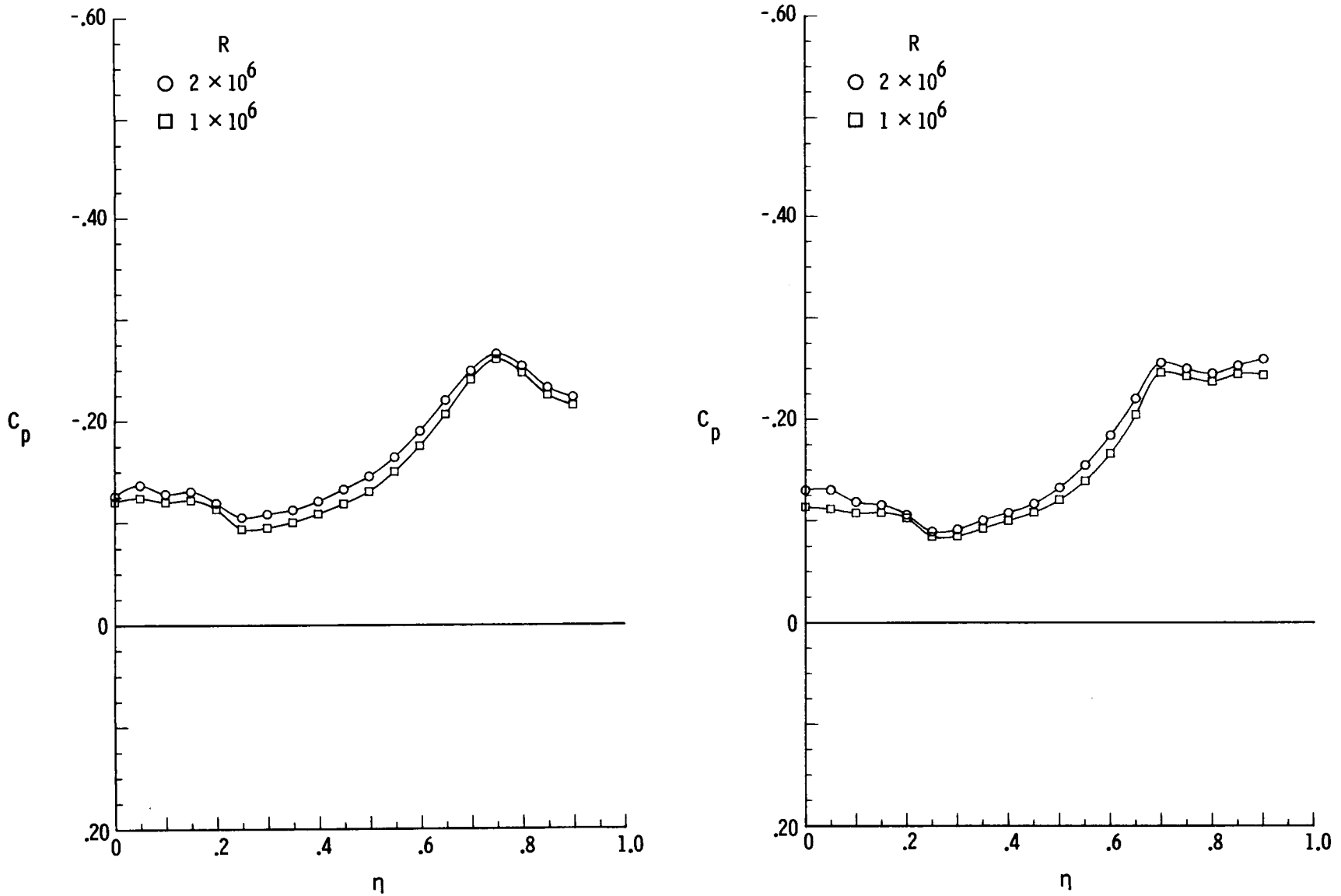

(a) $\delta_F = 0°$.

(b) $\delta_F = 5°$.

Figure 18.- Effect of R on spanwise surface pressure distribution at M = 1.70, $\alpha = 12°$, $\beta = -8°$, and $x/\ell = 0.90$.

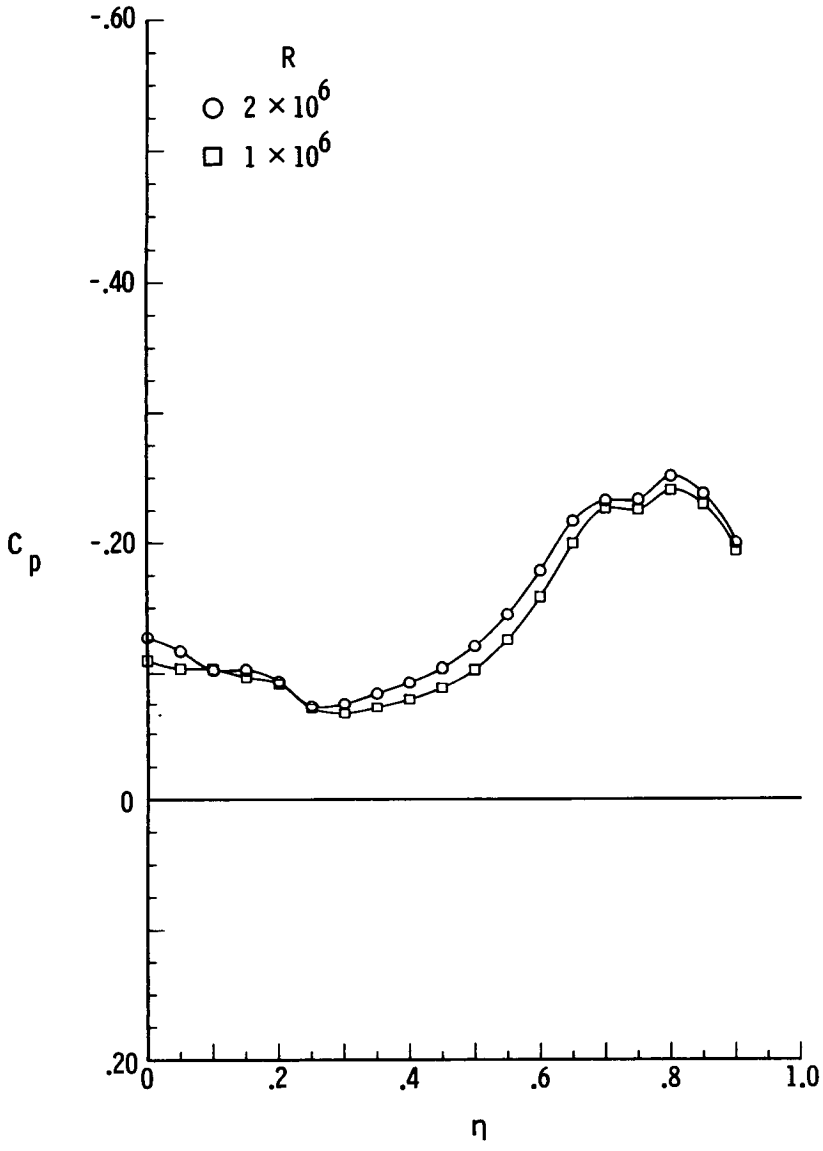

(c) δ_F = 10°.

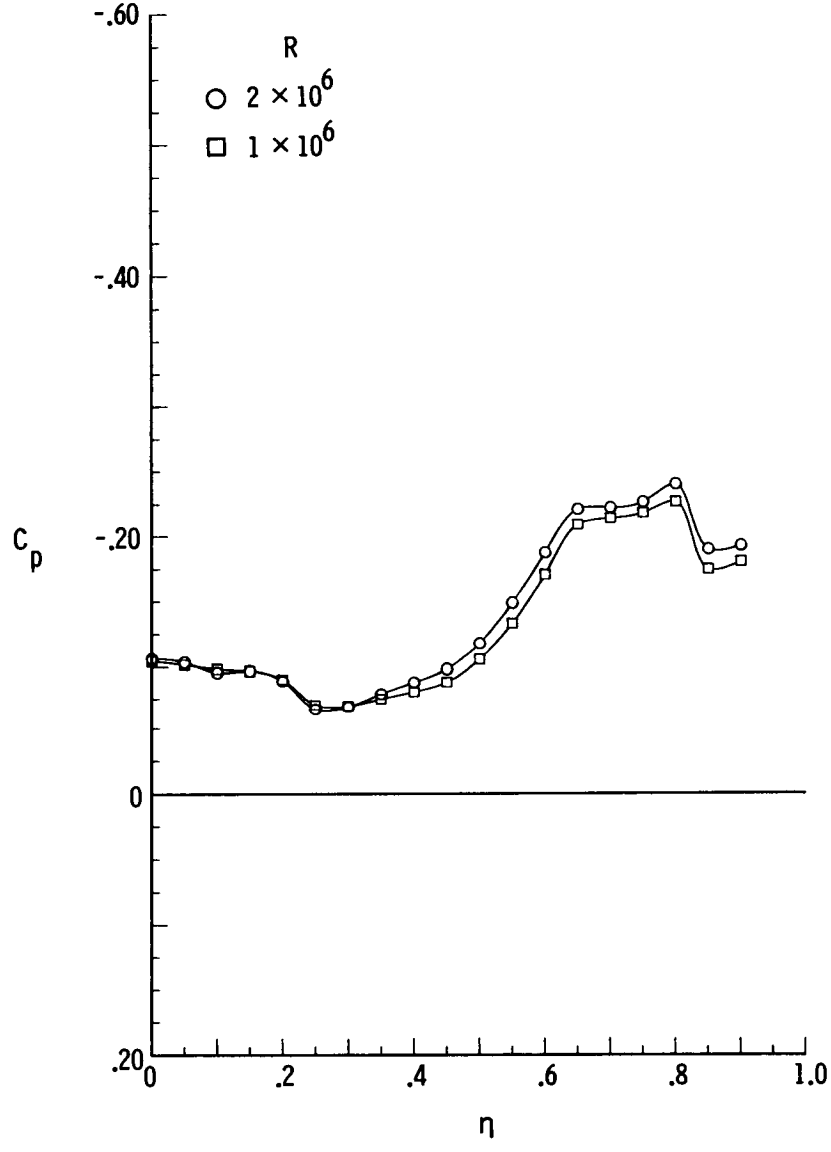

(d) δ_F = 15°.

Figure 18.- Concluded.

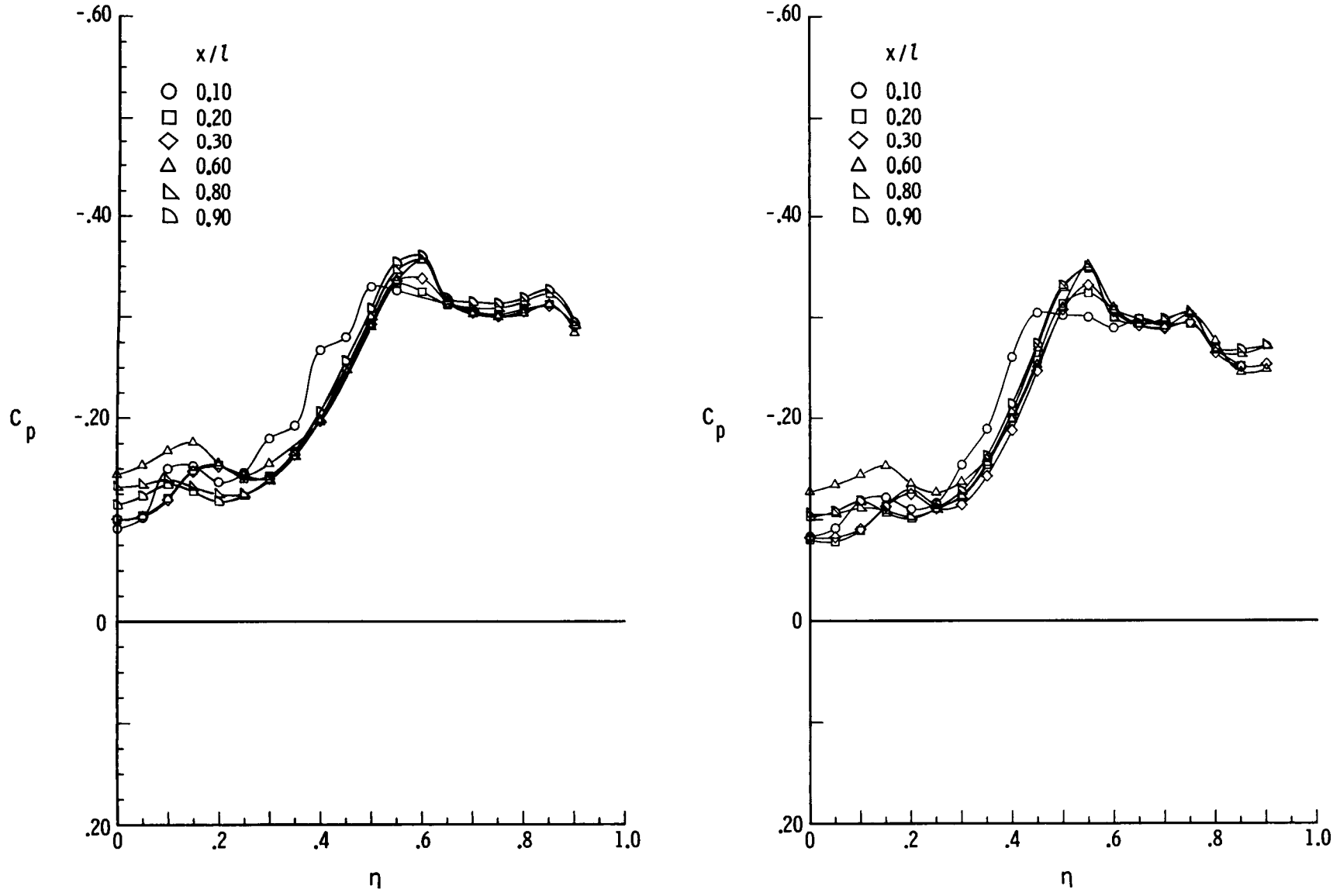

(a) $\delta_F = 0°$.

(b) $\delta_F = 5°$.

Figure 19.- Evaluation of flow conicity at M = 1.70, $\alpha = 12°$, and $R = 2 \times 10^6$.

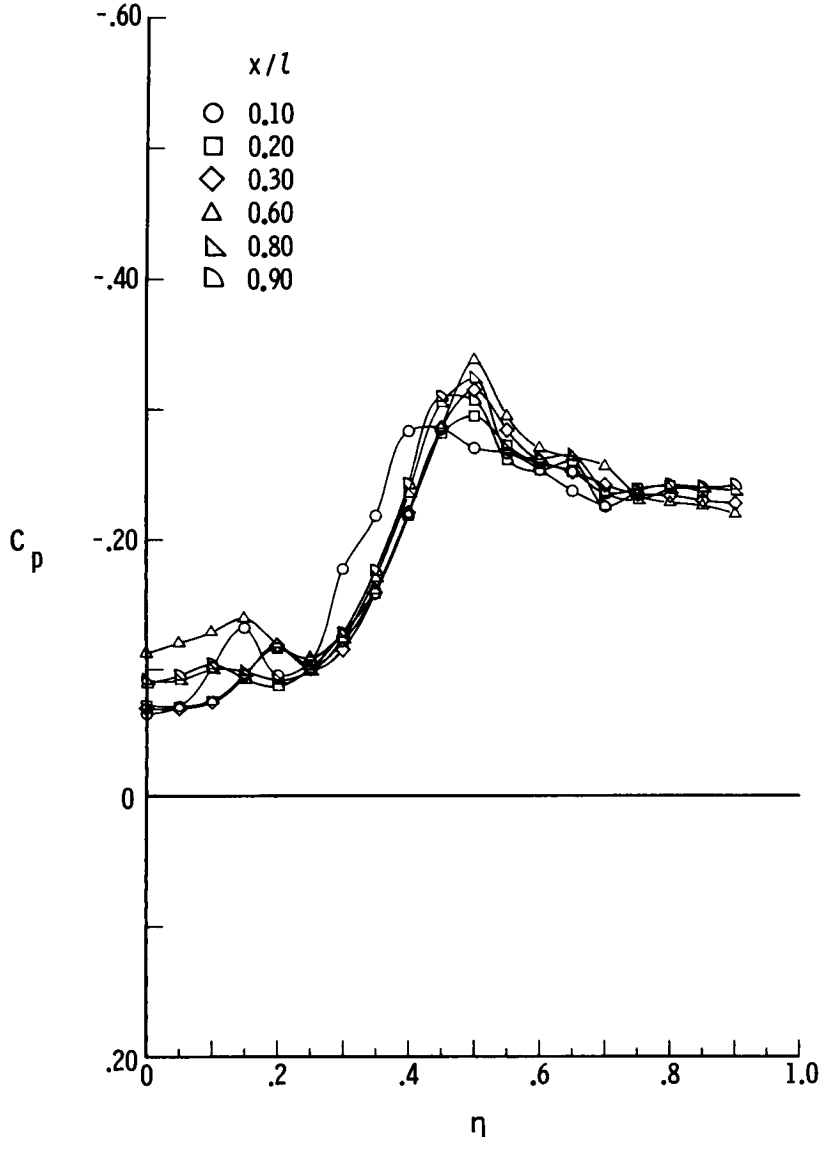

(c) $\delta_F = 10°$.

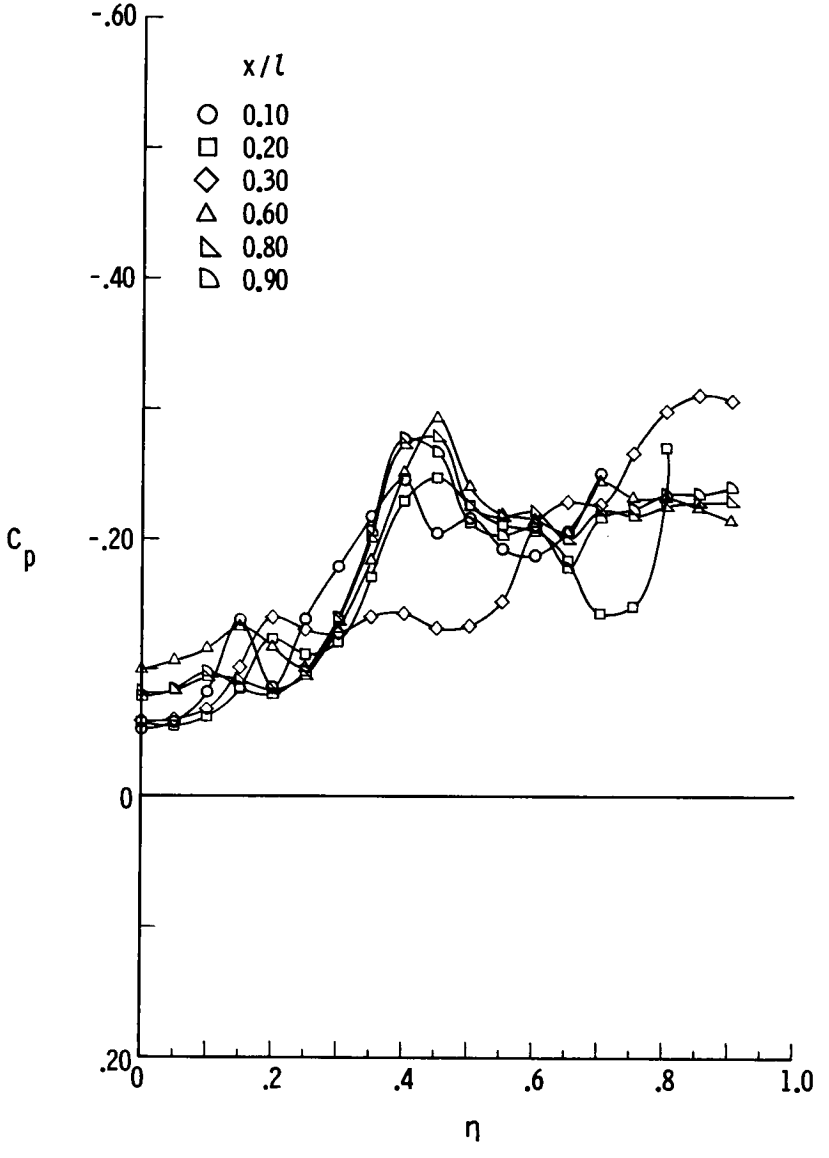

(d) $\delta_F = 15°$.

Figure 19.- Concluded.

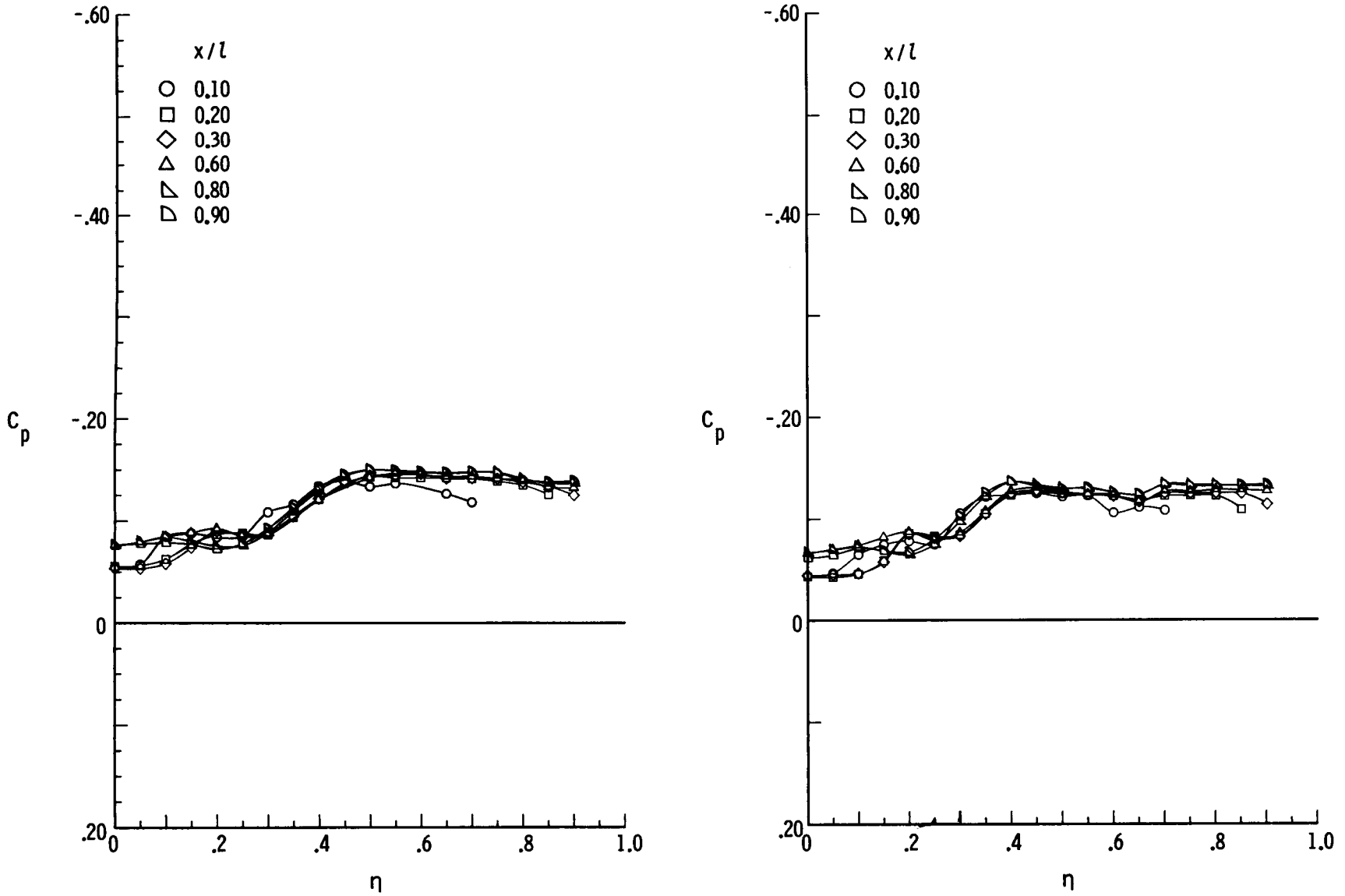

(a) $\delta_F = 0°$.

(b) $\delta_F = 5°$.

Figure 20.- Evaluation of flow conicity at M = 2.80, $\alpha = 12°$. and $R = 2 \times 10^6$.

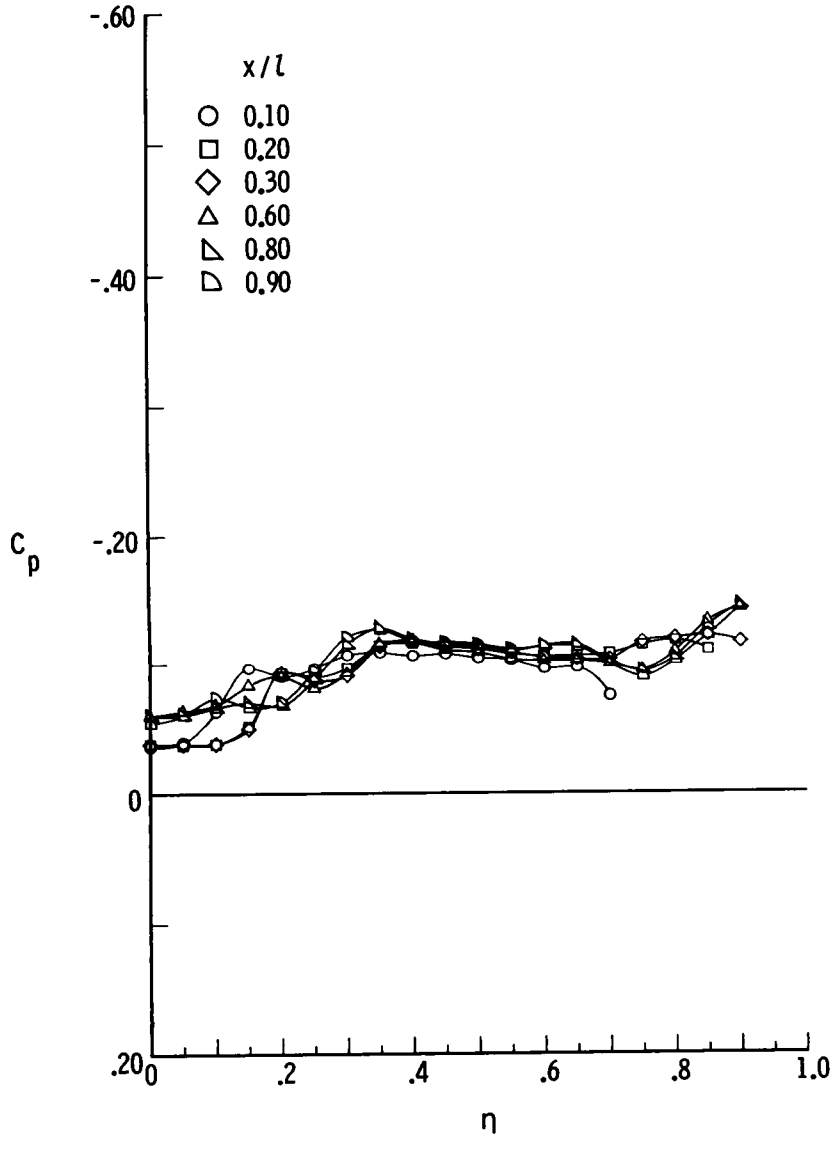

(c) δ_F = 10°.

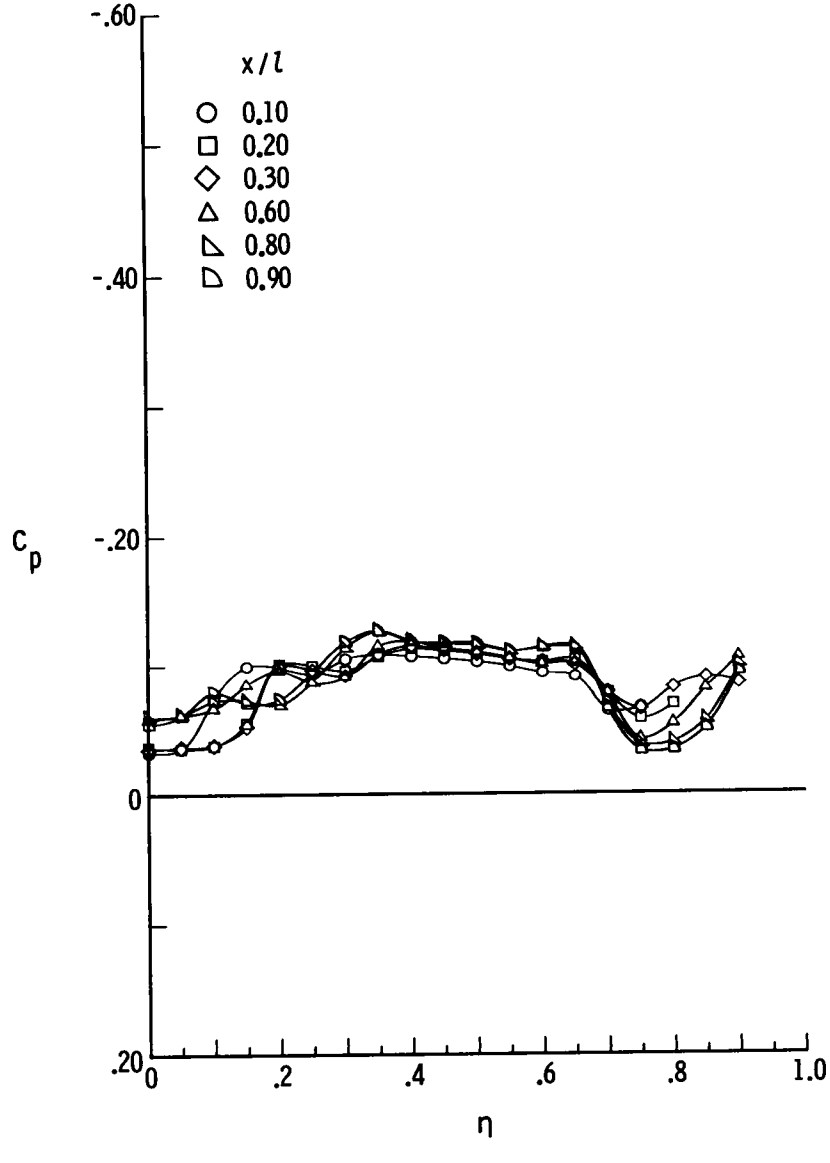

(d) δ_F = 15°.

Figure 20.- Concluded.

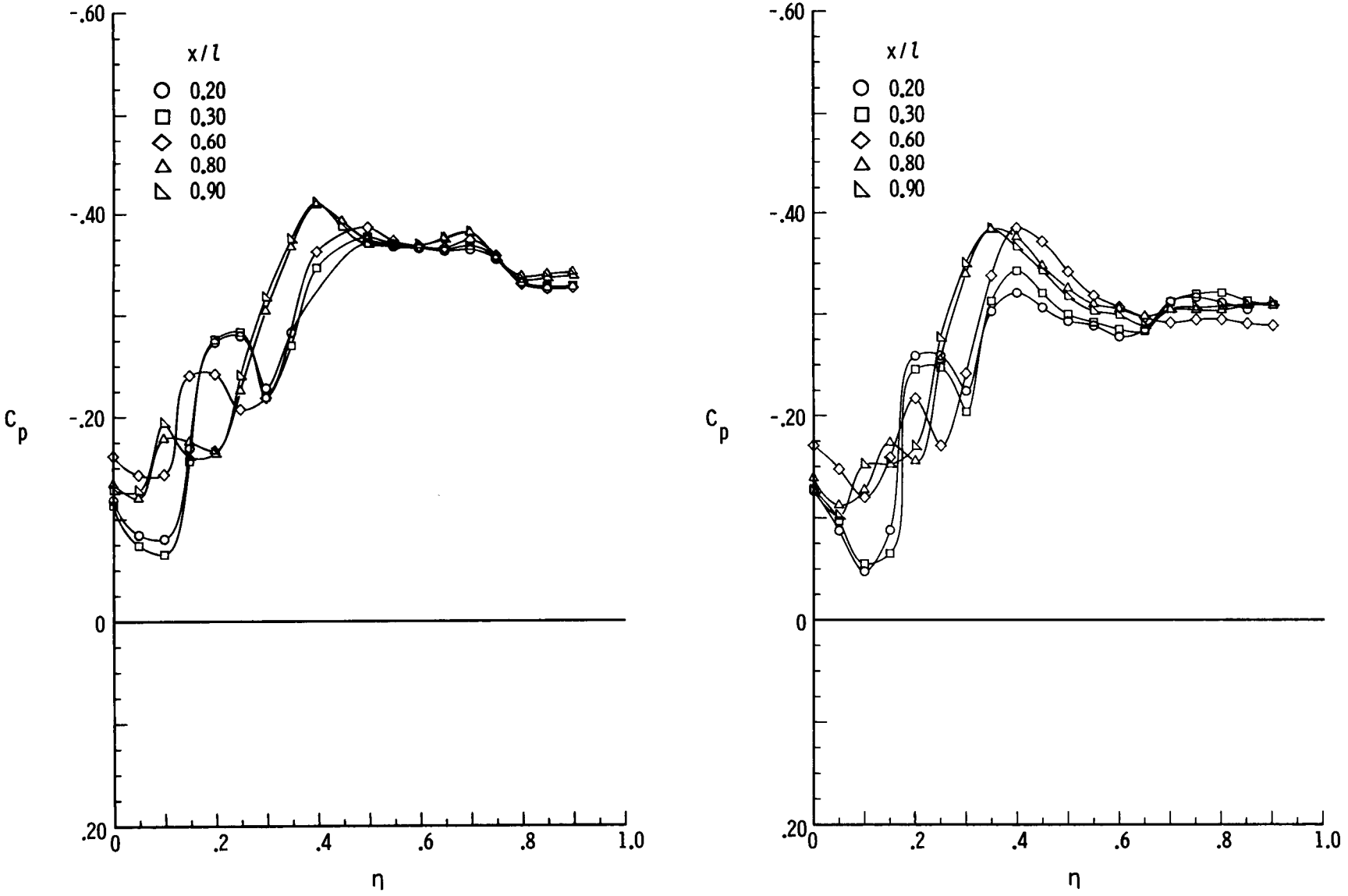

(a) $\delta_F = 0°$.

(b) $\delta_F = 5°$.

Figure 21.- Evaluation of flow conicity at $M = 1.70$, $\alpha = 12°$, $\beta = 8°$, and $R = 2 \times 10^6$.

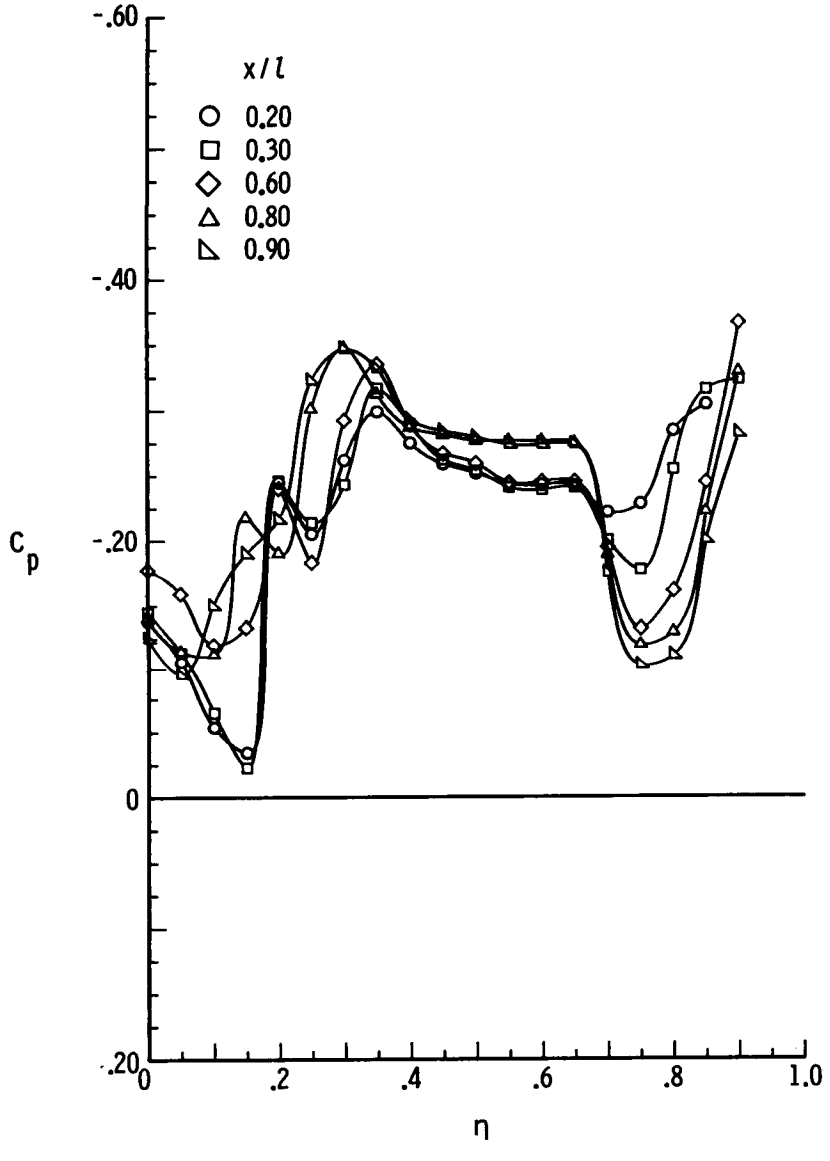

(c) δ_F = 10°.

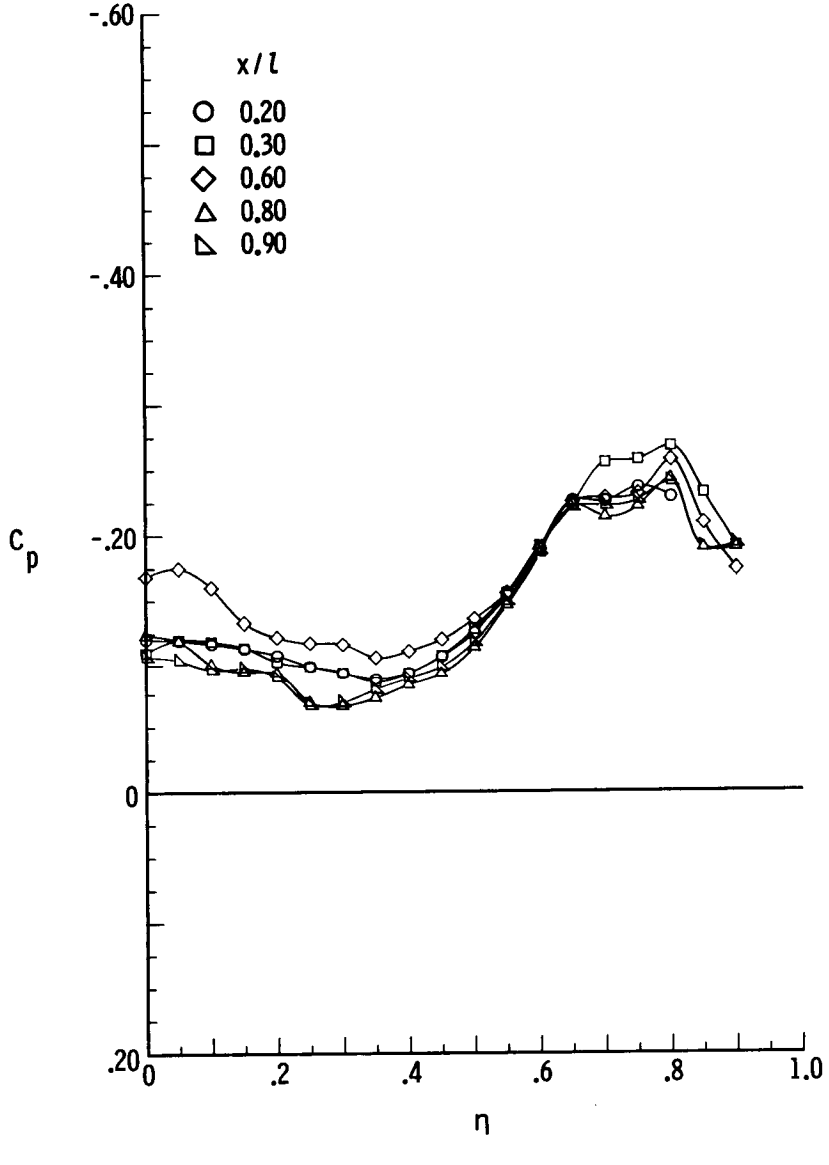

(d) δ_F = 15°.

Figure 21.- Concluded.

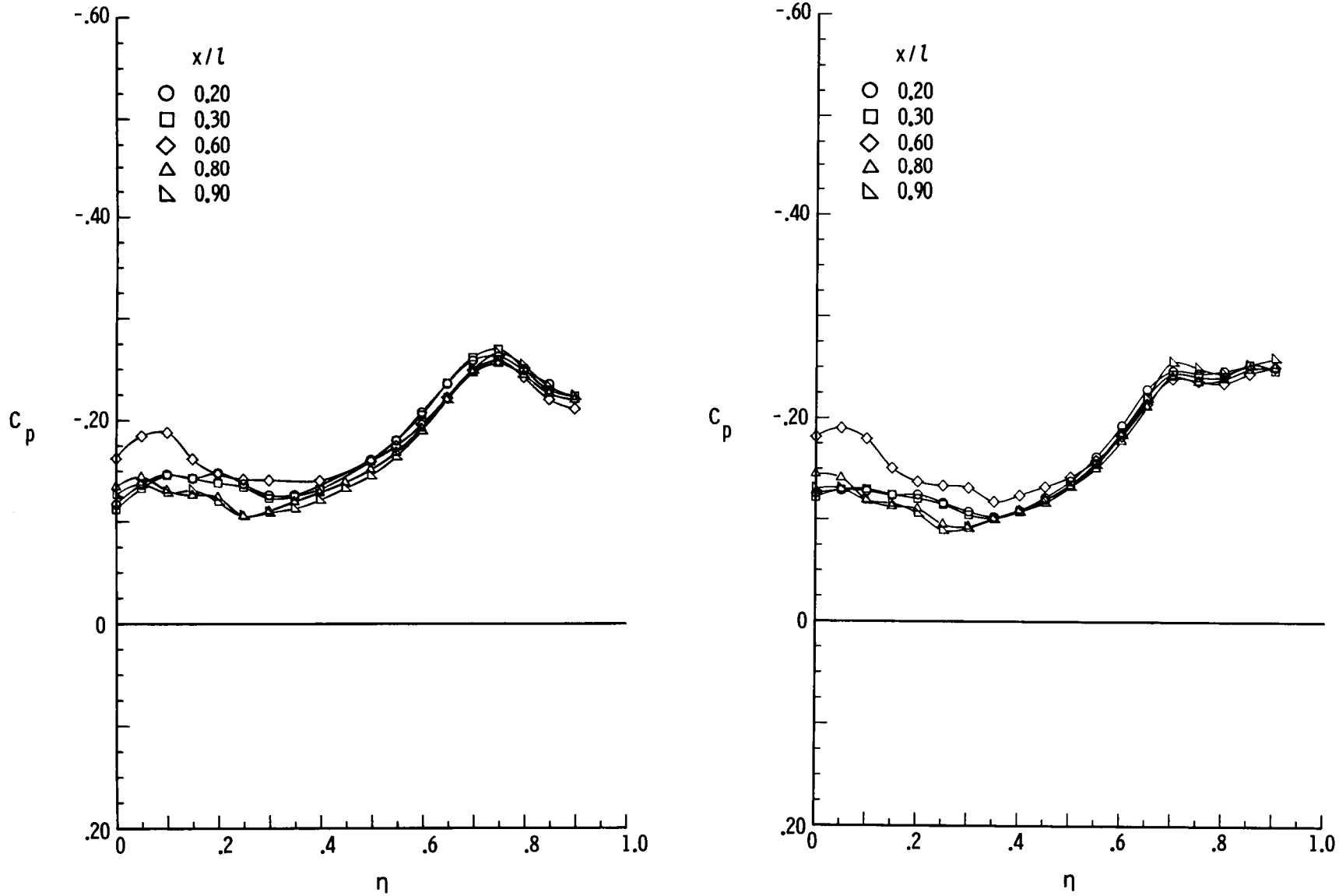

(a) $\delta_F = 0°$.

(b) $\delta_F = 5°$.

Figure 22.- Evaluation of flow conicity at $M = 1.70$, $\alpha = 12°$, $\beta = -8°$, and $R = 2 \times 10^6$.

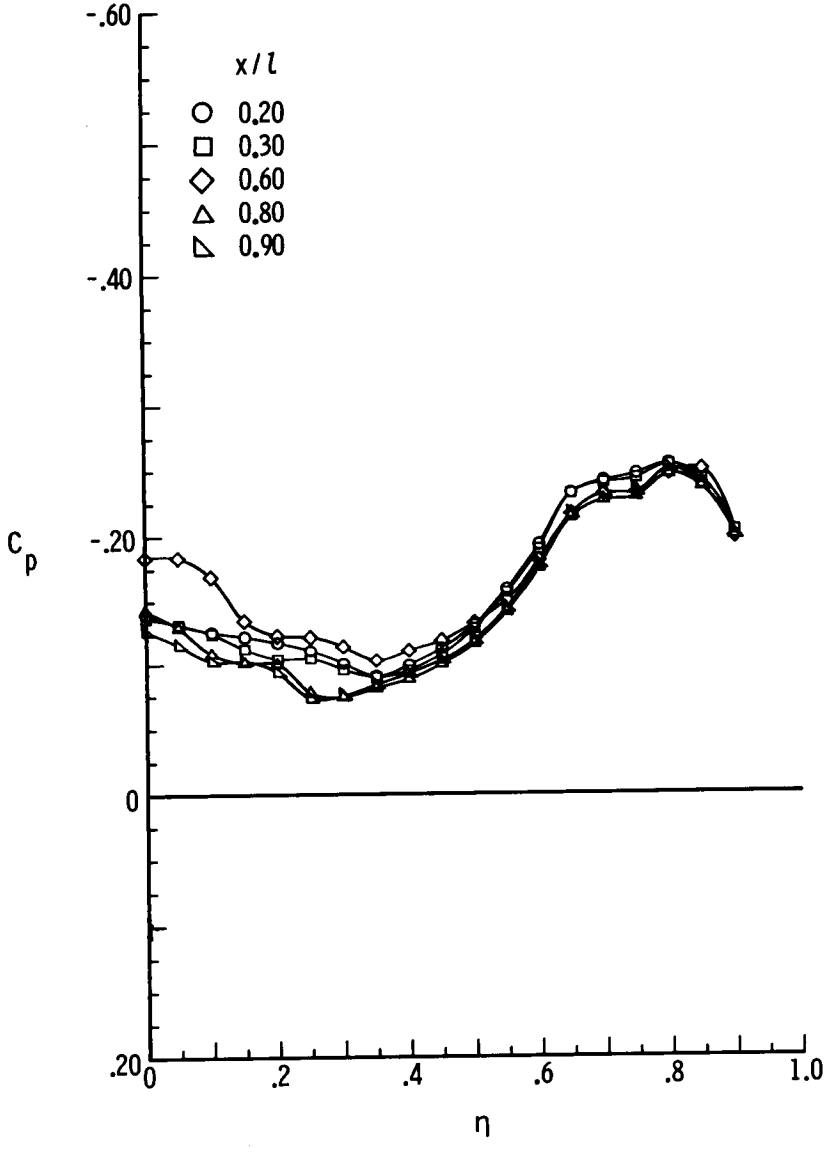

(c) δ_F = 10°.

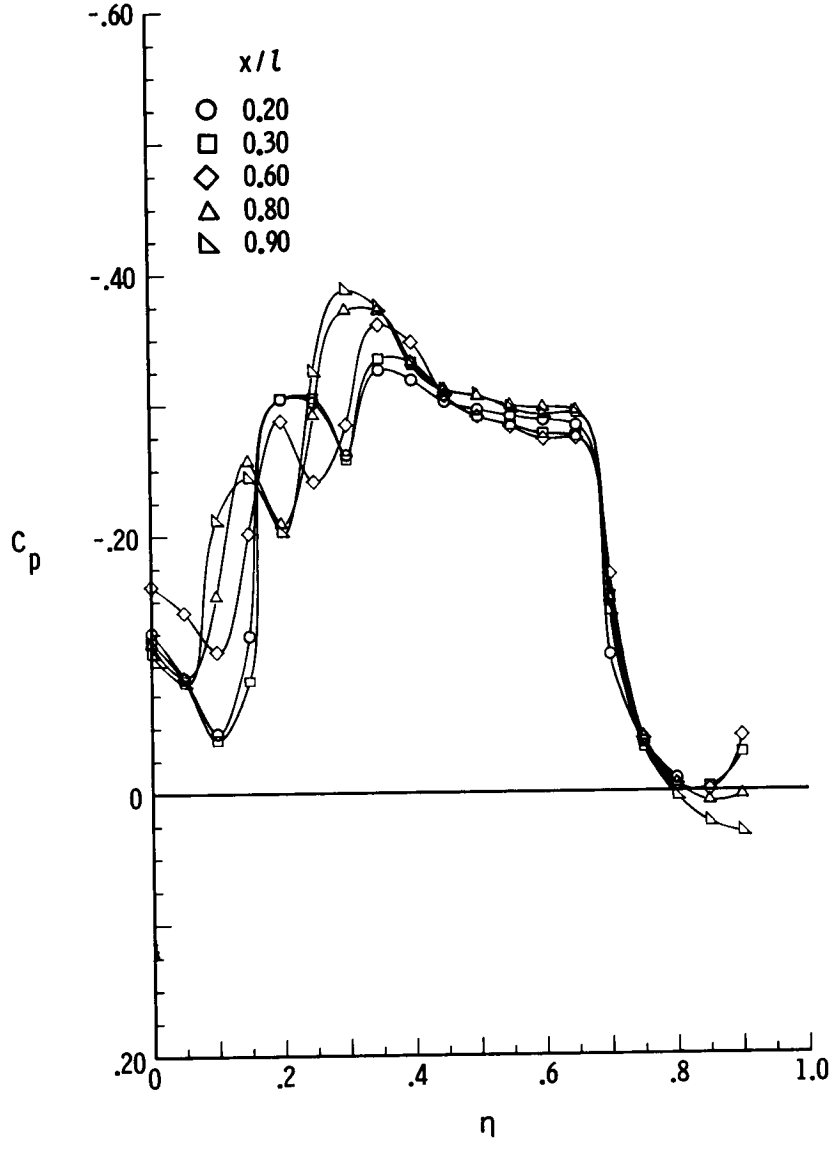

(d) δ_F = 15°.

Figure 22.- Concluded.

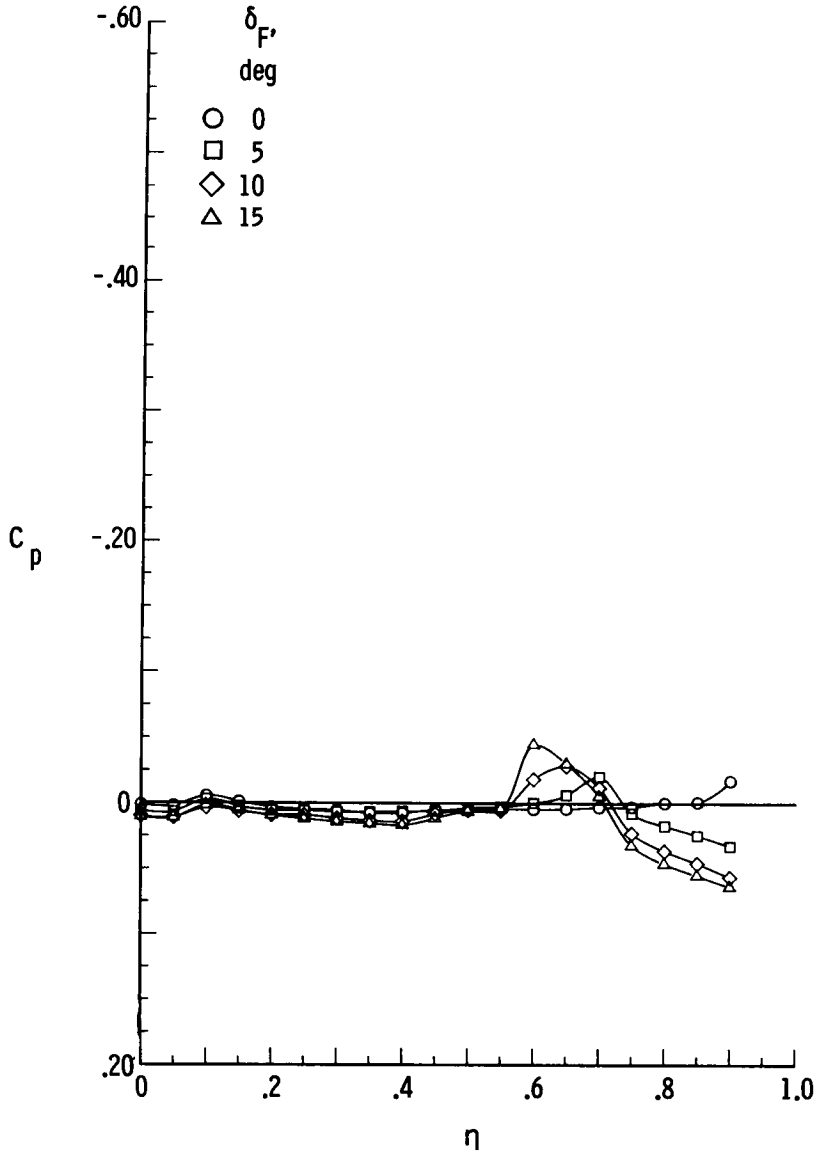

(a) $\alpha = 0°$.

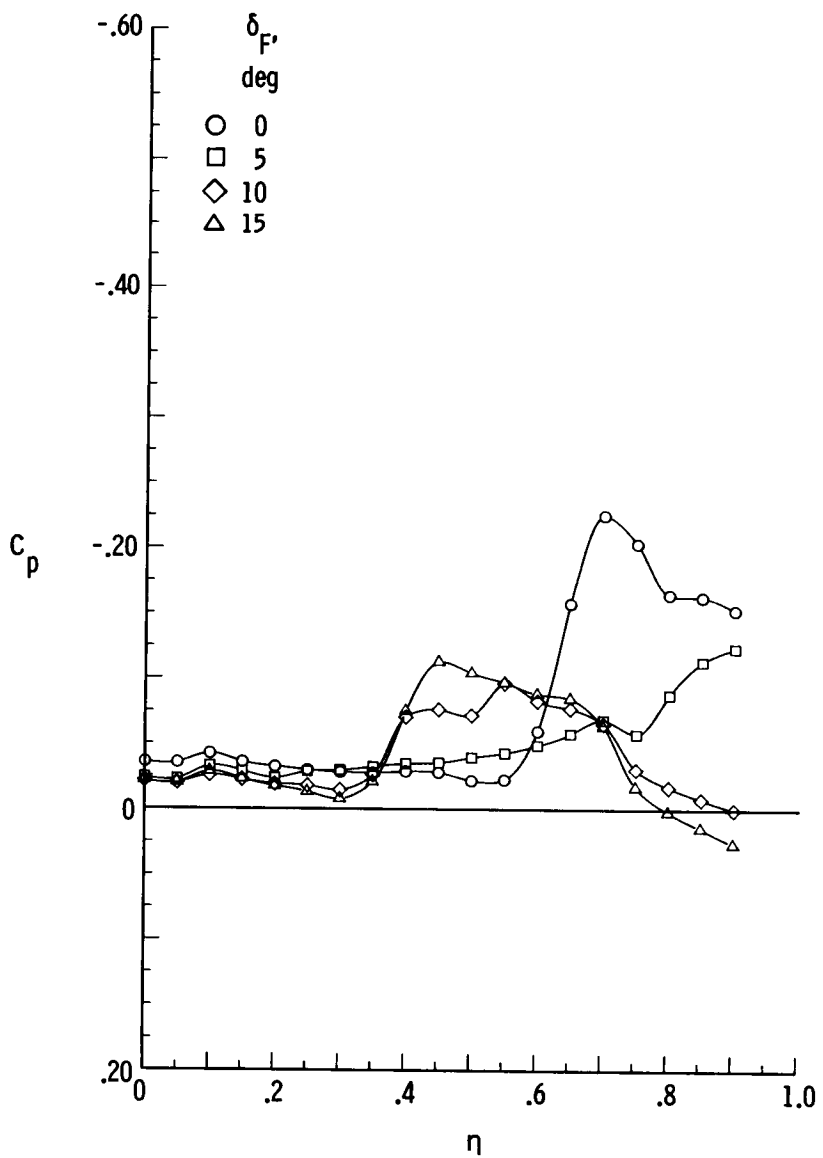

(b) $\alpha = 4°$.

Figure 23.- Effect of δ_F on spanwise pressure distribution at $M = 1.70$, $R = 2 \times 10^6$, and $x/l = 0.90$.

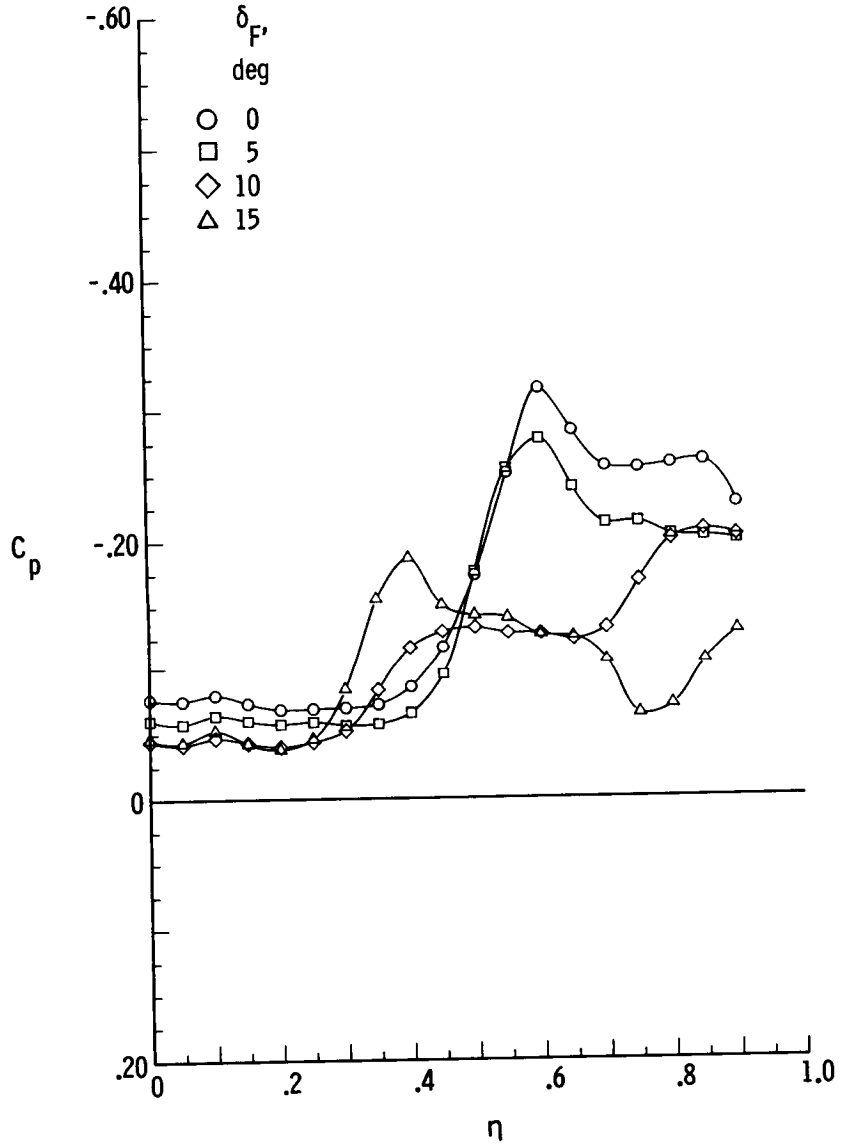

(c) $\alpha = 8°$.

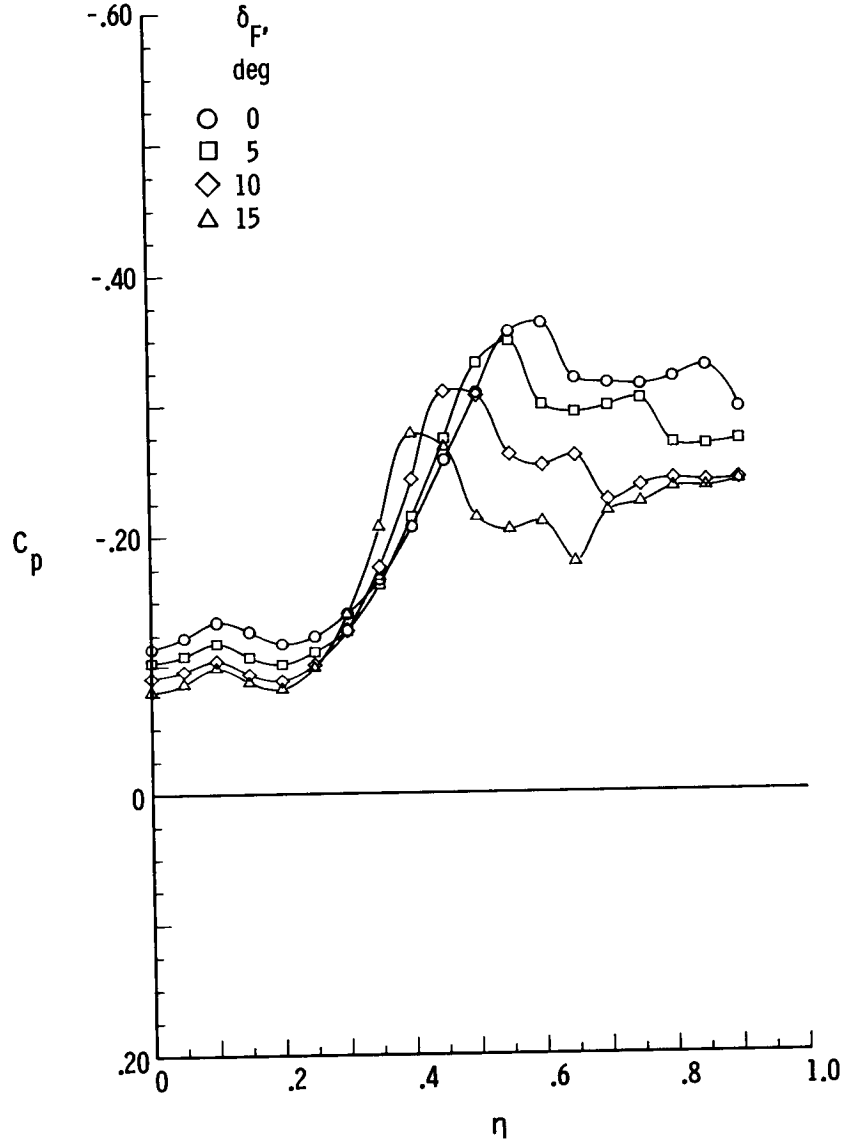

(d) $\alpha = 12°$.

Figure 23.- Concluded.

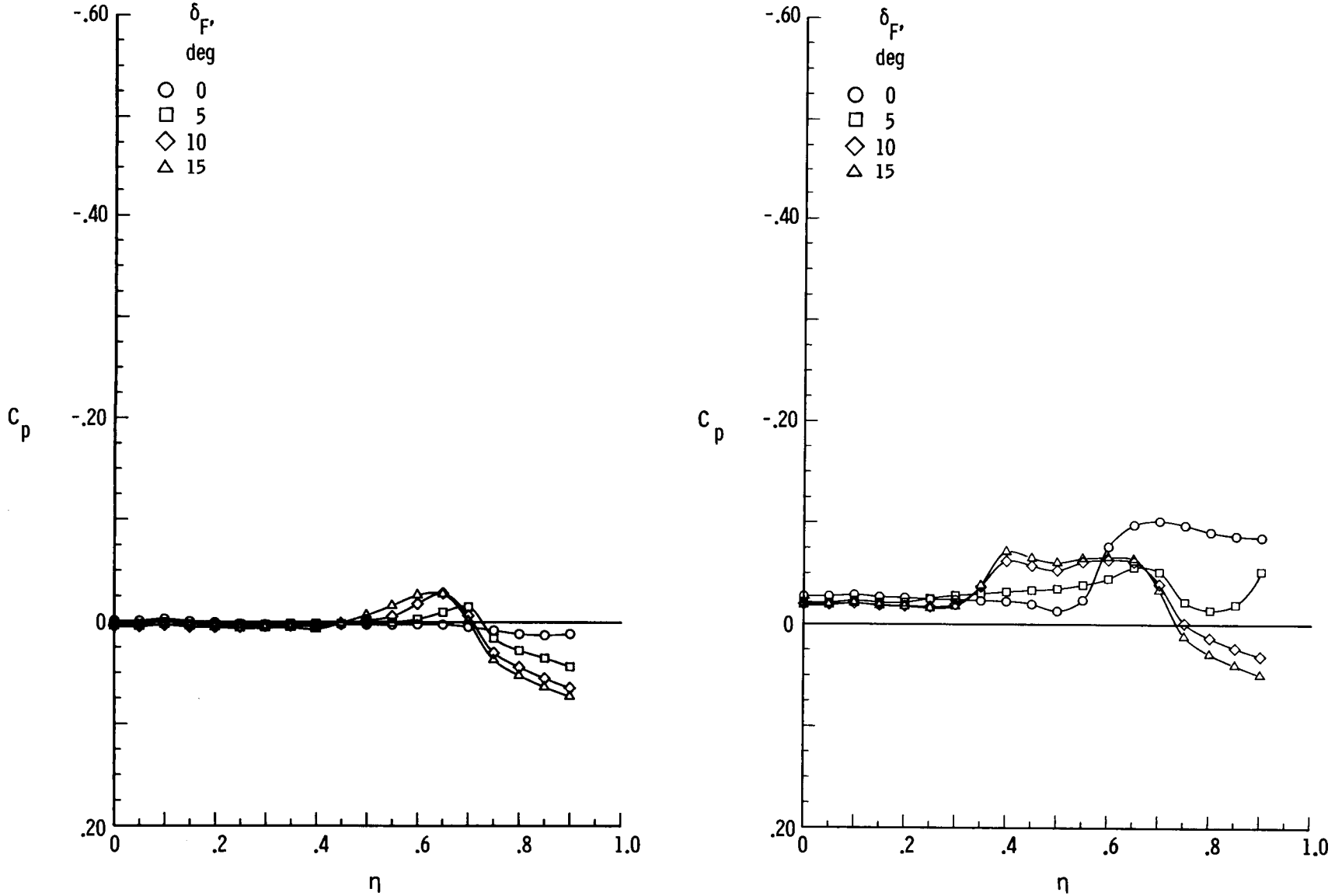

(a) $\alpha = 0°$.

(b) $\alpha = 4°$.

Figure 24.- Effect of δ_F on spanwise pressure distribution at $M = 2.80$, $R = 2 \times 10^6$, and $x/\ell = 0.90$.

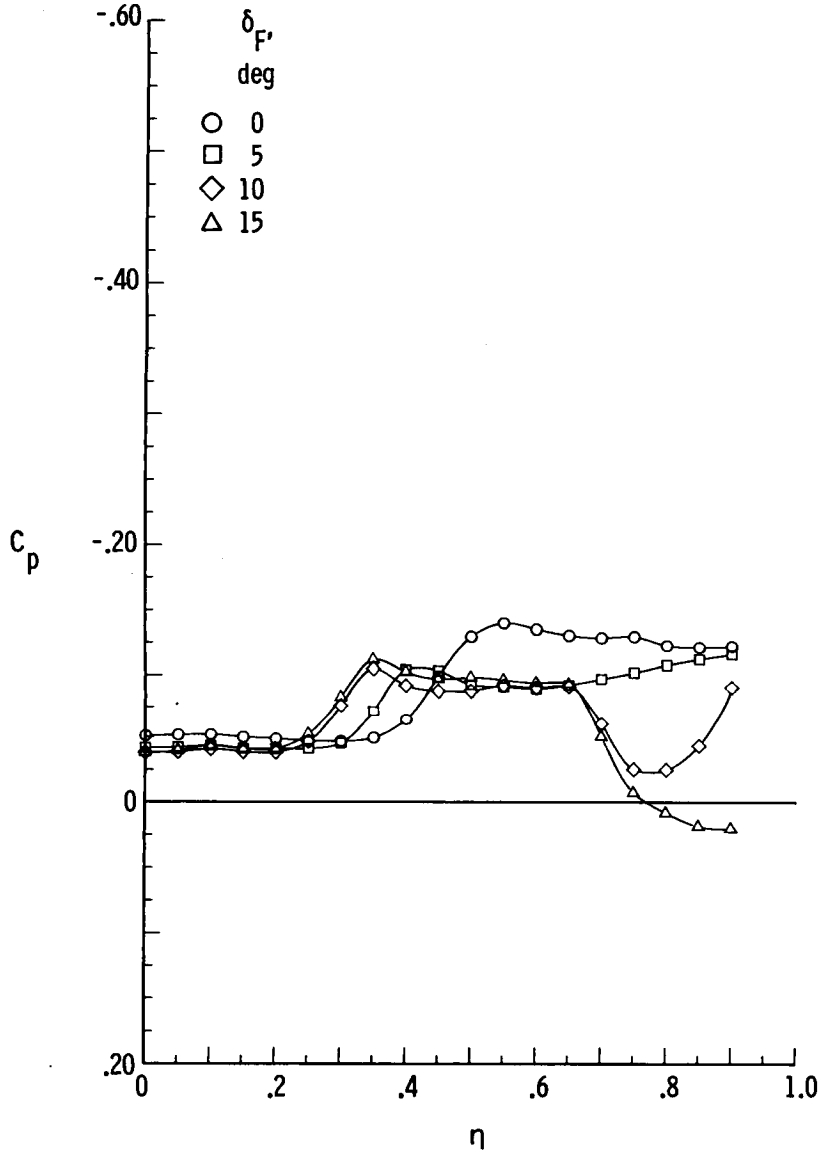

(c) $\alpha = 8°$.

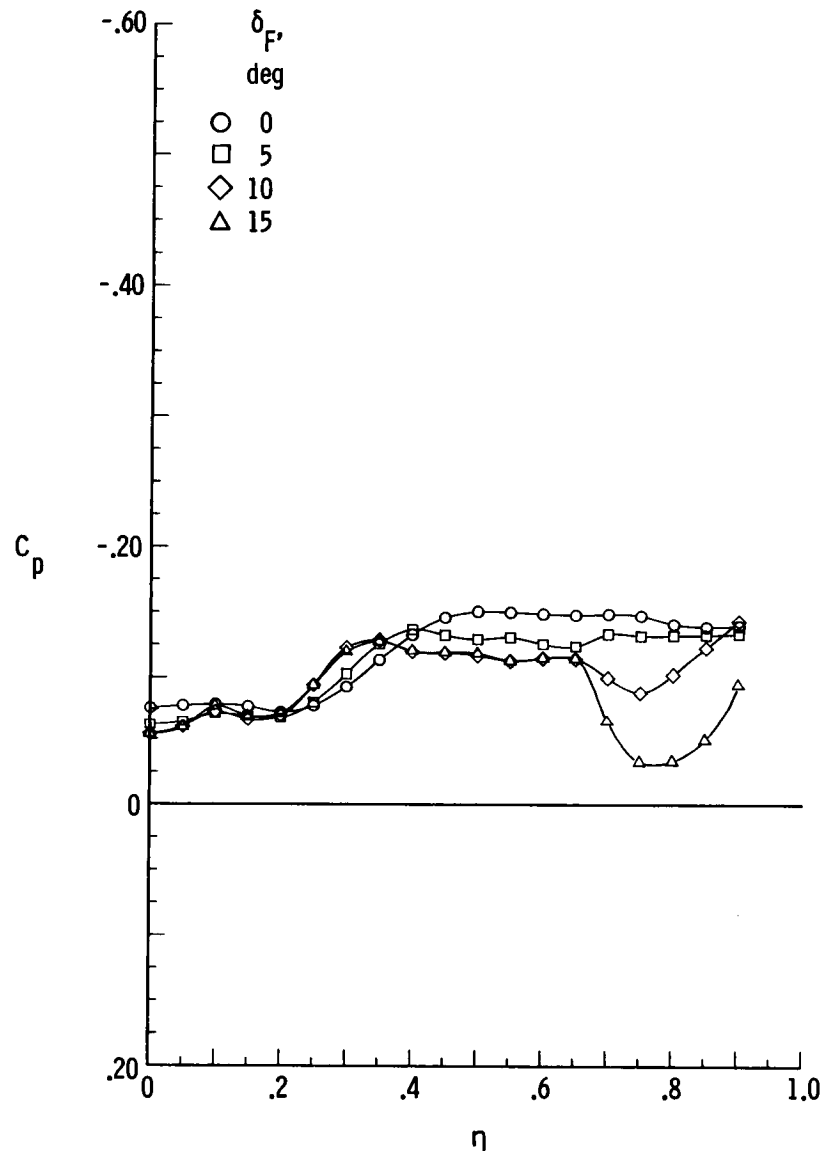

(d) $\alpha = 12°$.

Figure 24.- Concluded.

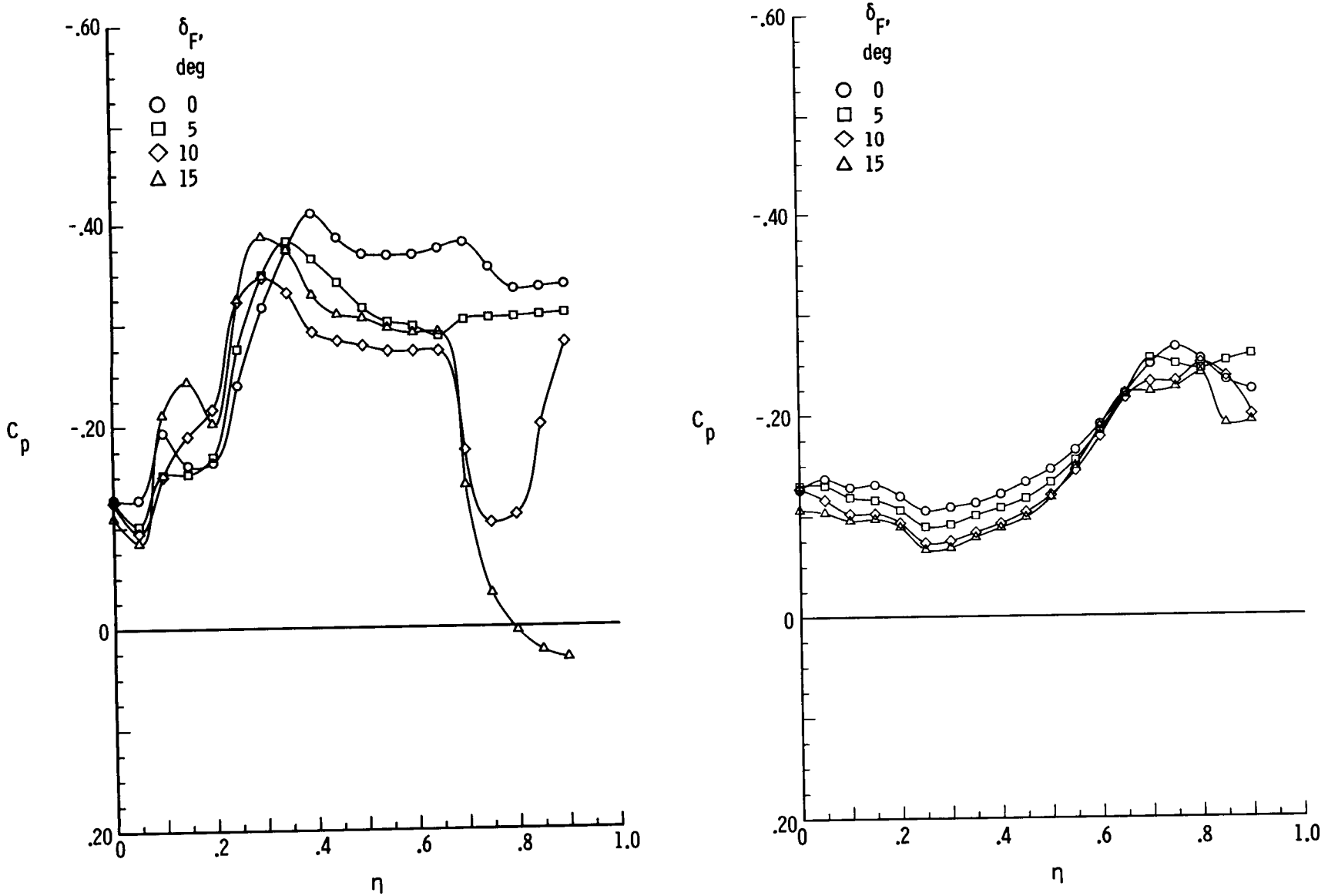

(a) Windward.

(b) Leeward.

Figure 25.- Effect of δ_F on spanwise pressure distribution at M = 1.70, α = 12°, β = 8°, R = 2 × 10^6, and x/ℓ = 0.90.

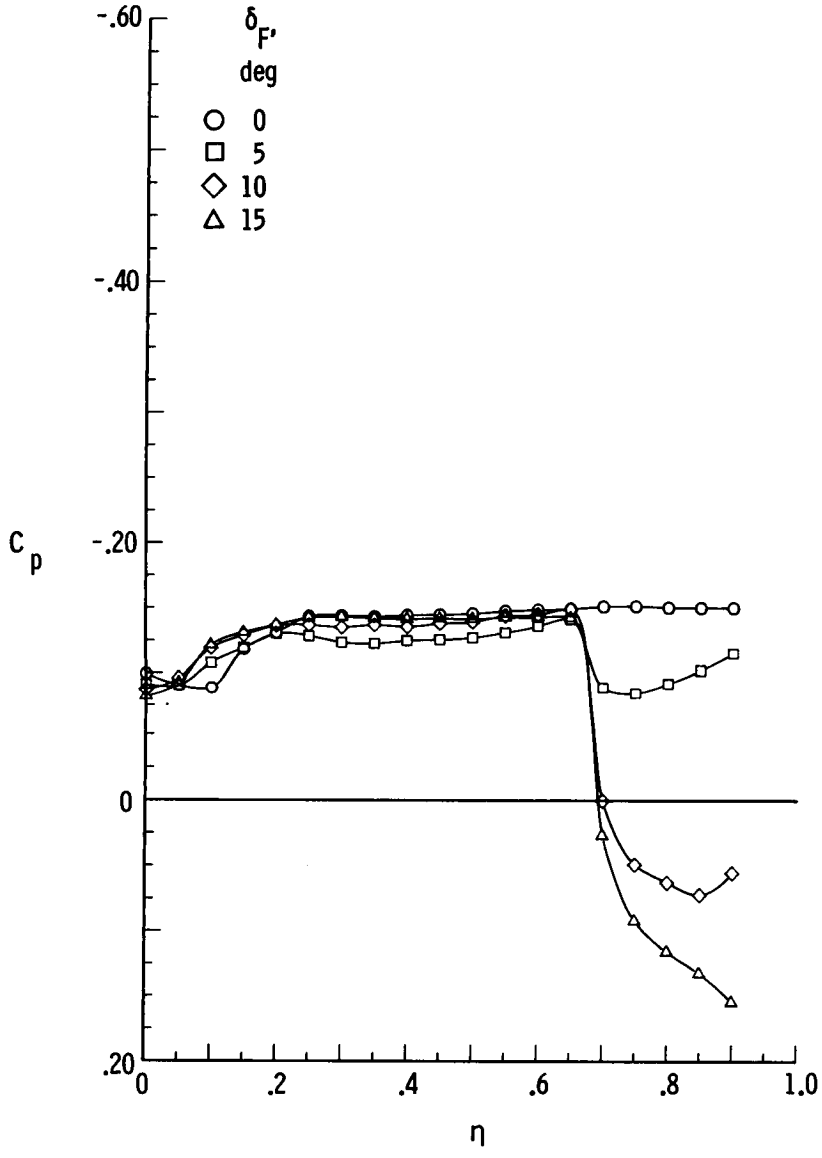

(a) Windward.

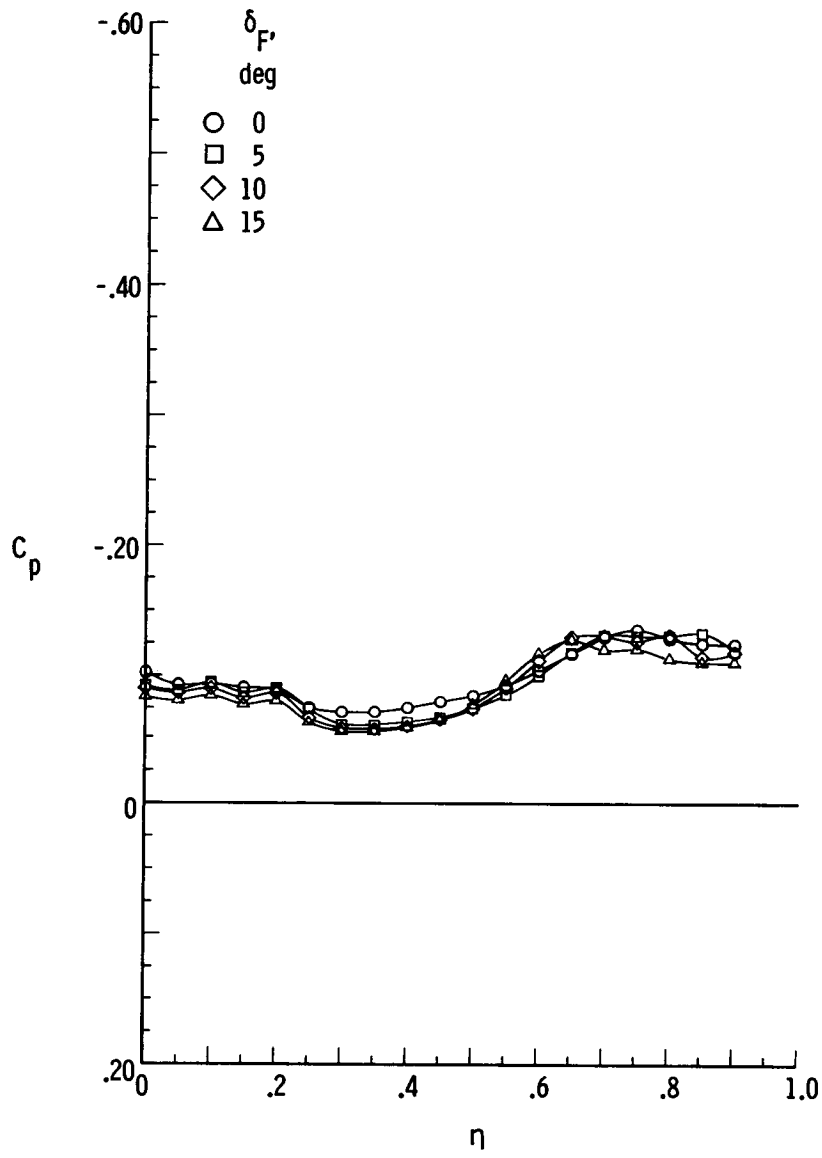

(b) Leeward.

Figure 26.- Effect of δ_F on spanwise surface pressure distribution at $M = 2.80$, $\alpha = 12°$, $\beta = 8°$, $R = 2 \times 10^6$, and $x/l = 0.90$.

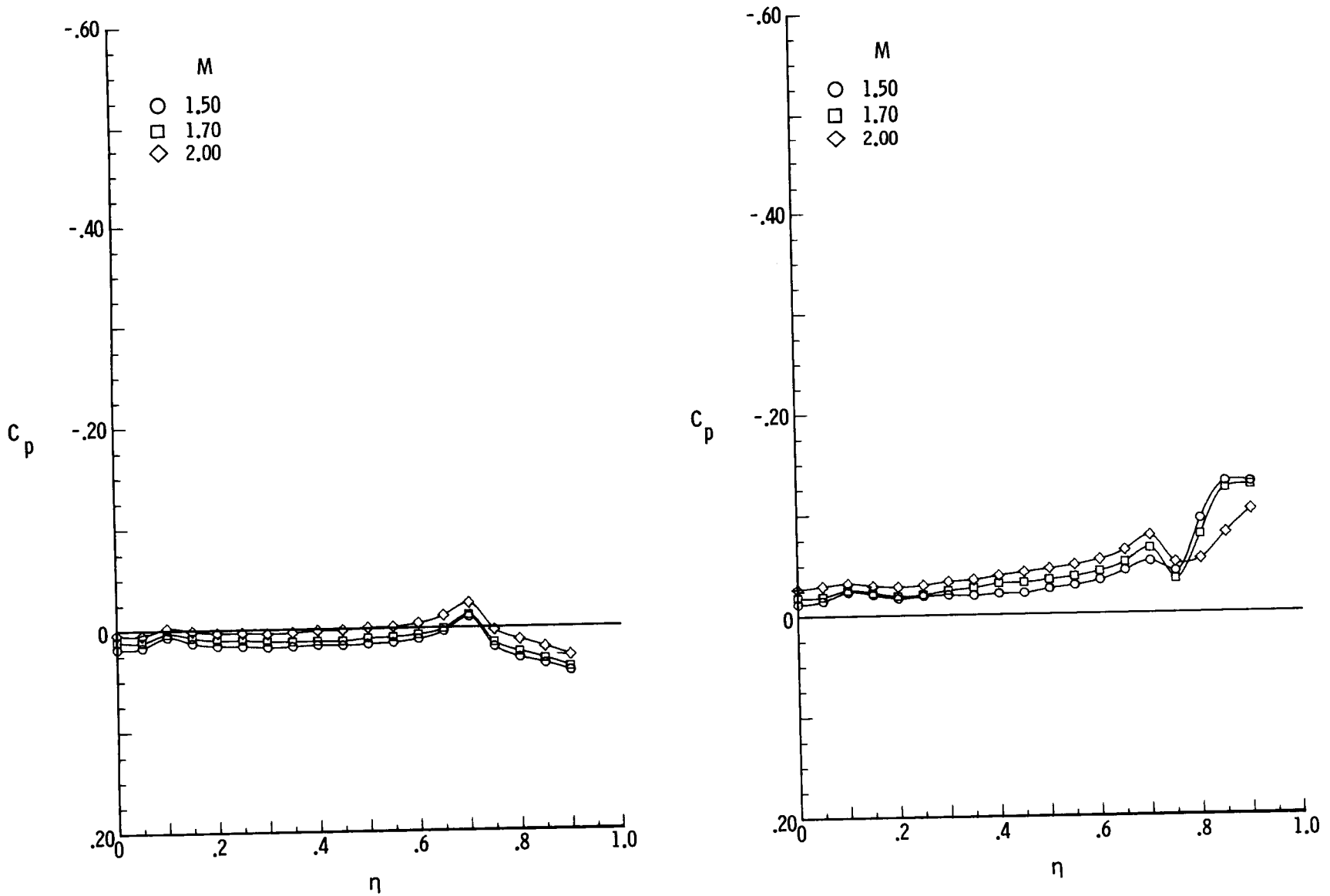

(a) $\alpha = 0°$.

(b) $\alpha = 4°$.

Figure 27.- Effect of M on spanwise surface pressure distribution for wing with $\delta_F = 5°$ with forebody at $R = 2 \times 10^6$ and $x/\ell = 0.90$.

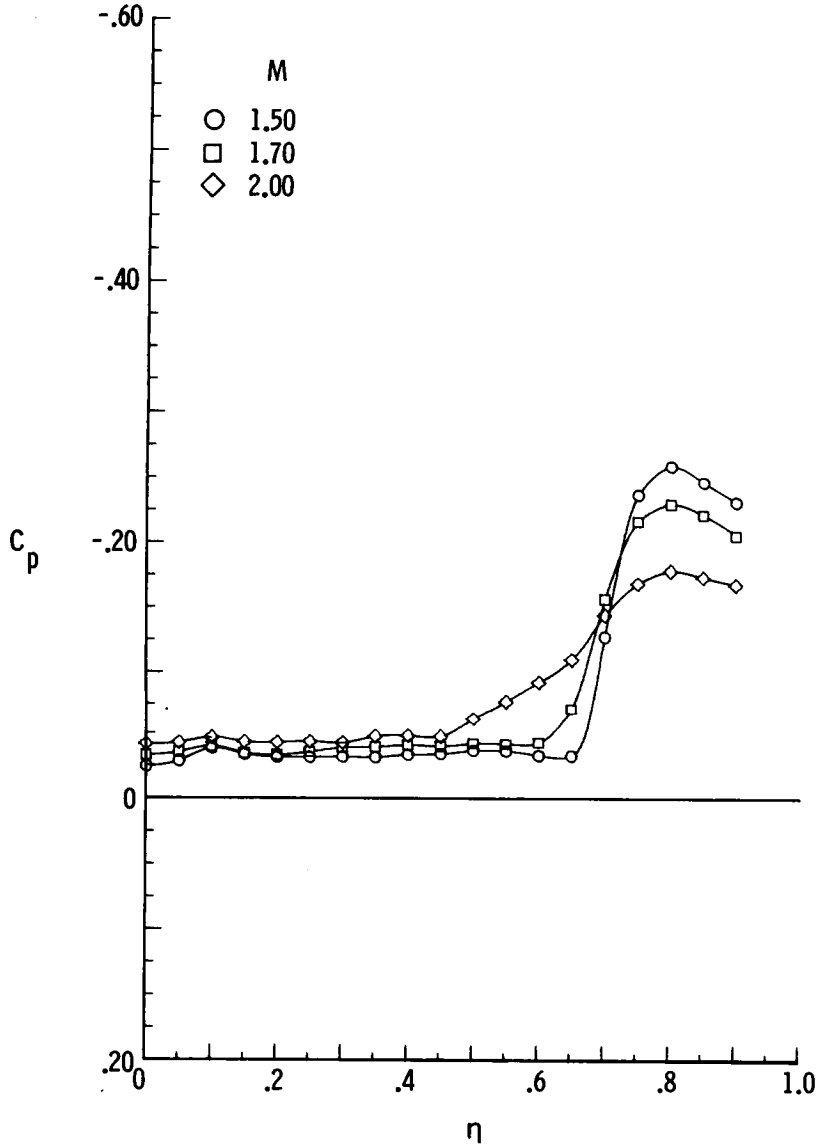

(c) $\alpha = 6°$.

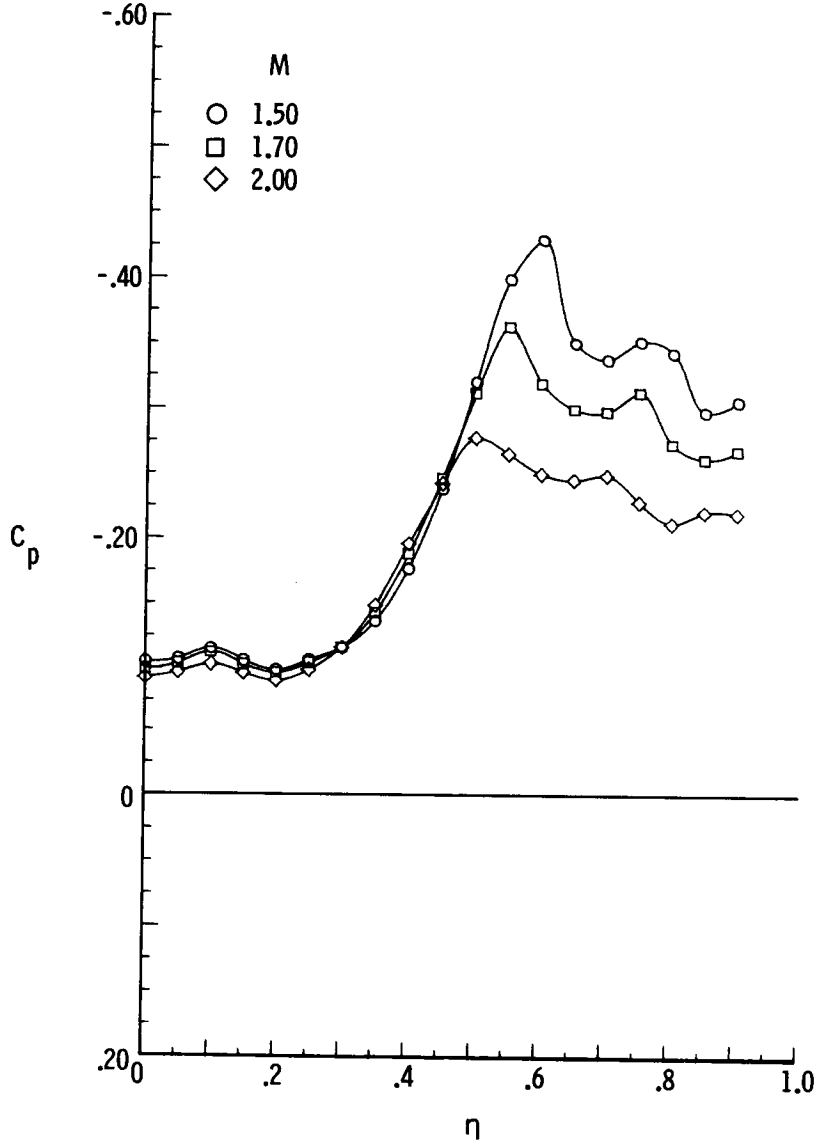

(d) $\alpha = 12°$.

Figure 27.- Concluded.

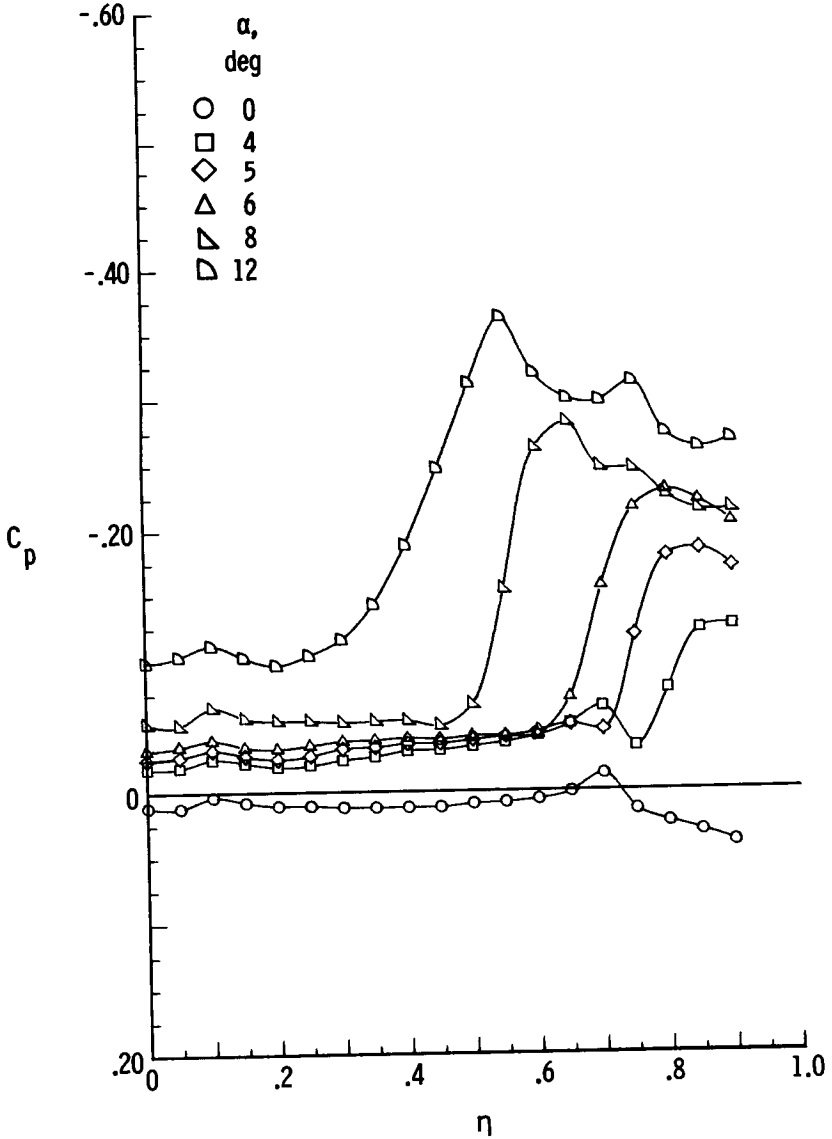

Figure 28.- Effect of α on spanwise surface pressure distribution for wing with $\delta_F = 5°$ with forebody at $M = 1.70$, $R = 2 \times 10^6$, and $x/\ell = 0.90$.

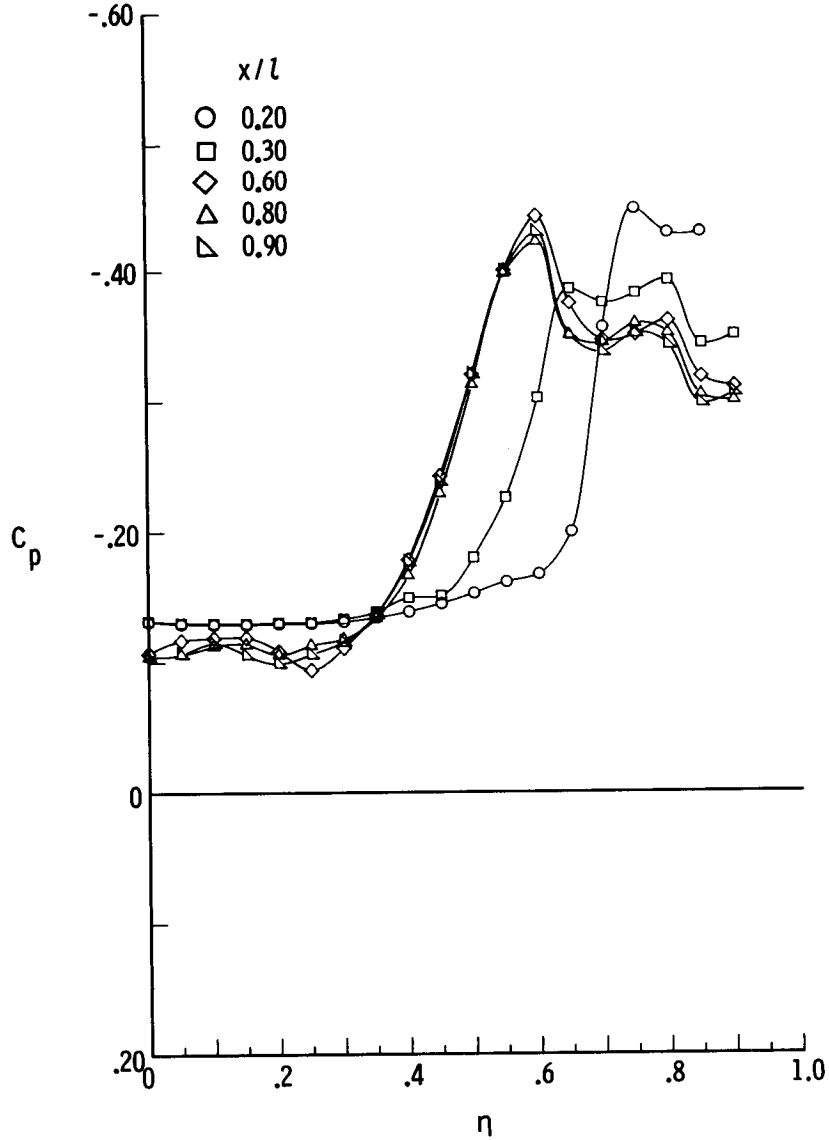

Figure 29.- Evaluation of flow conicity for wing with $\delta_F = 5°$ with forebody at $M = 1.70$, $\alpha = 12°$, and $R = 2 \times 10^6$.

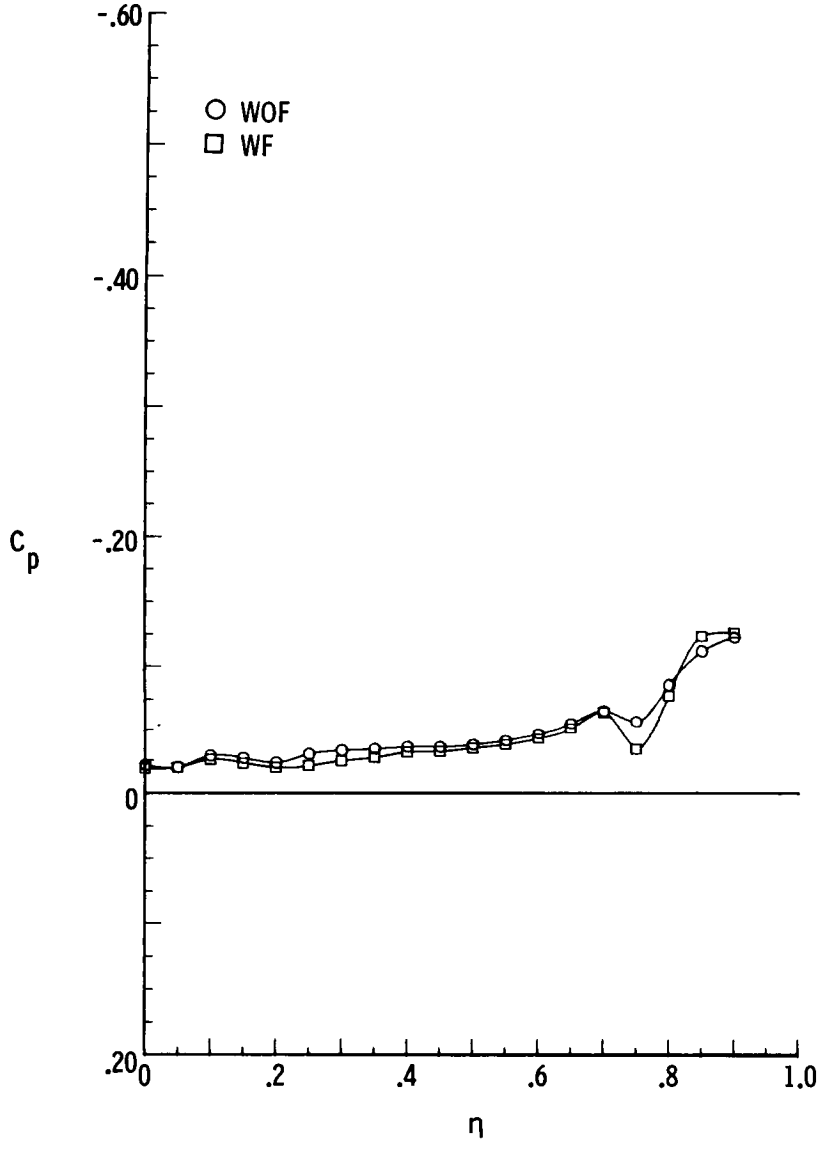

(a) $\alpha = 4°$.

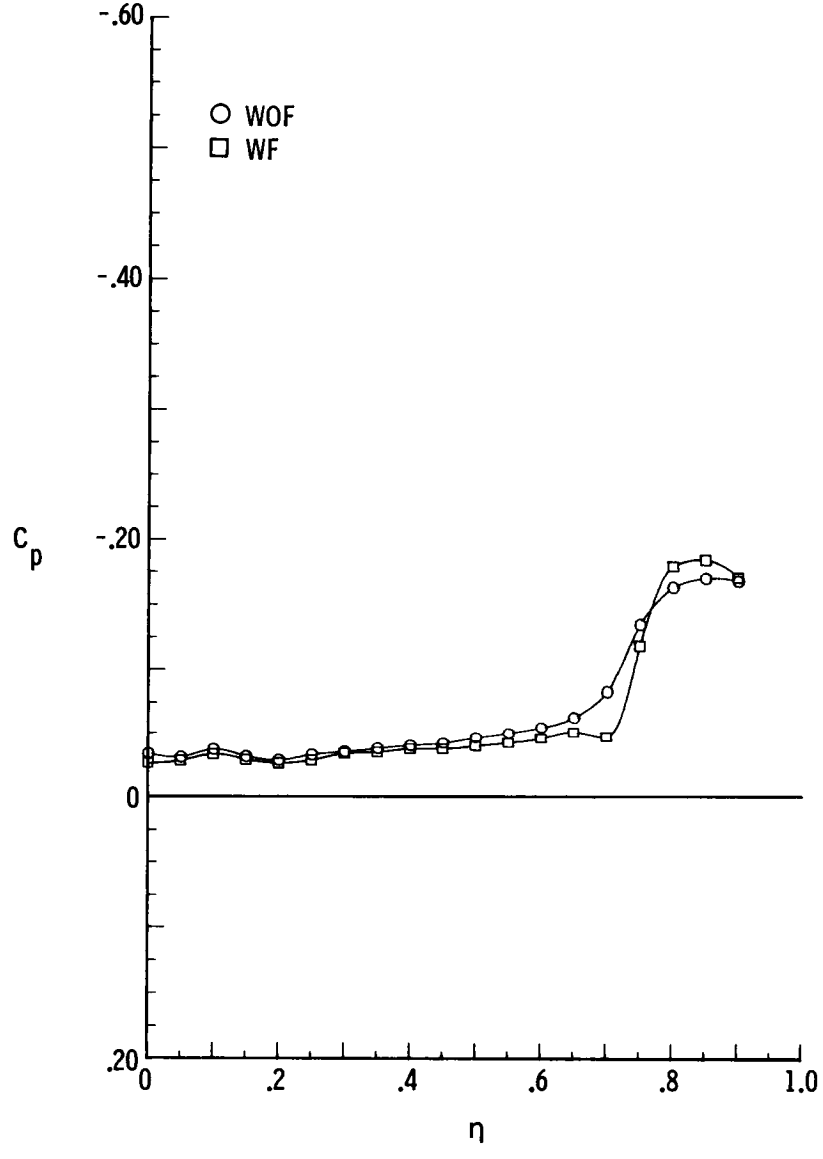

(b) $\alpha = 5°$.

Figure 30.- Effect of forebody on spanwise surface pressure distribution at $M = 1.70$, $R = 2 \times 10^6$, and $x/\ell = 0.90$.

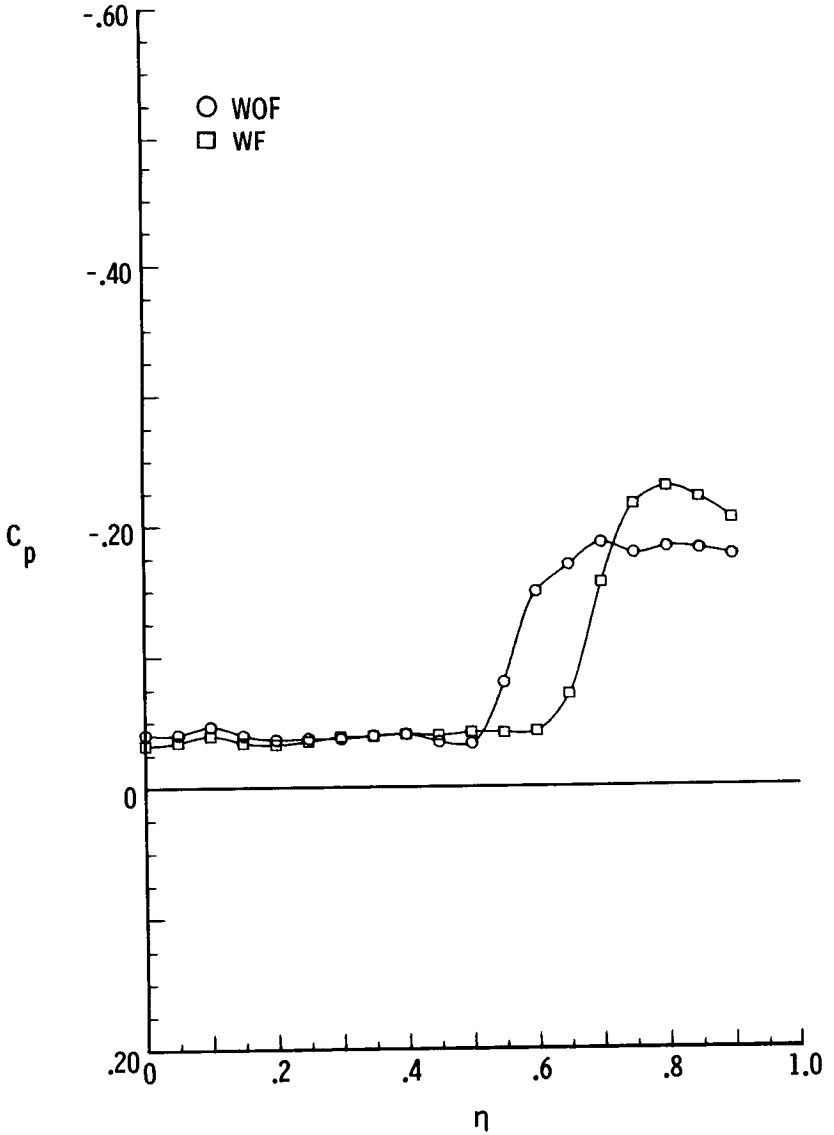

(c) $\alpha = 6°$.

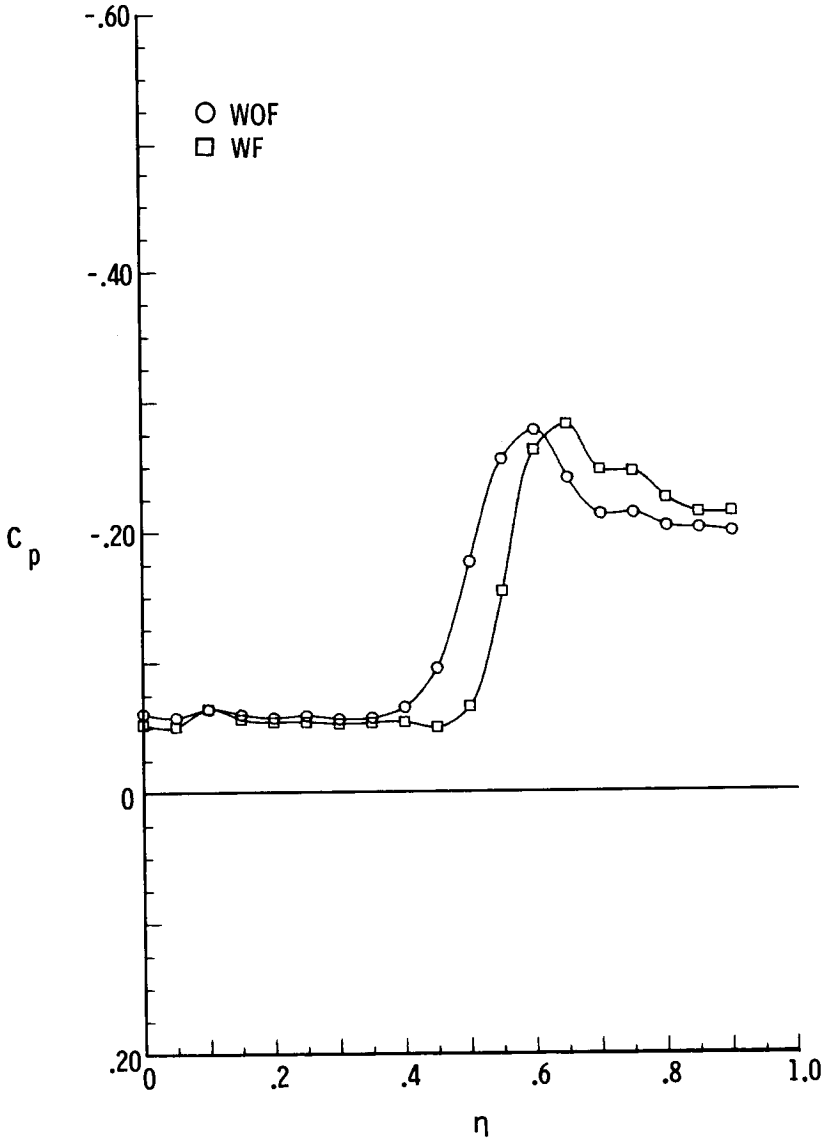

(d) $\alpha = 8°$.

Figure 30.- Continued.

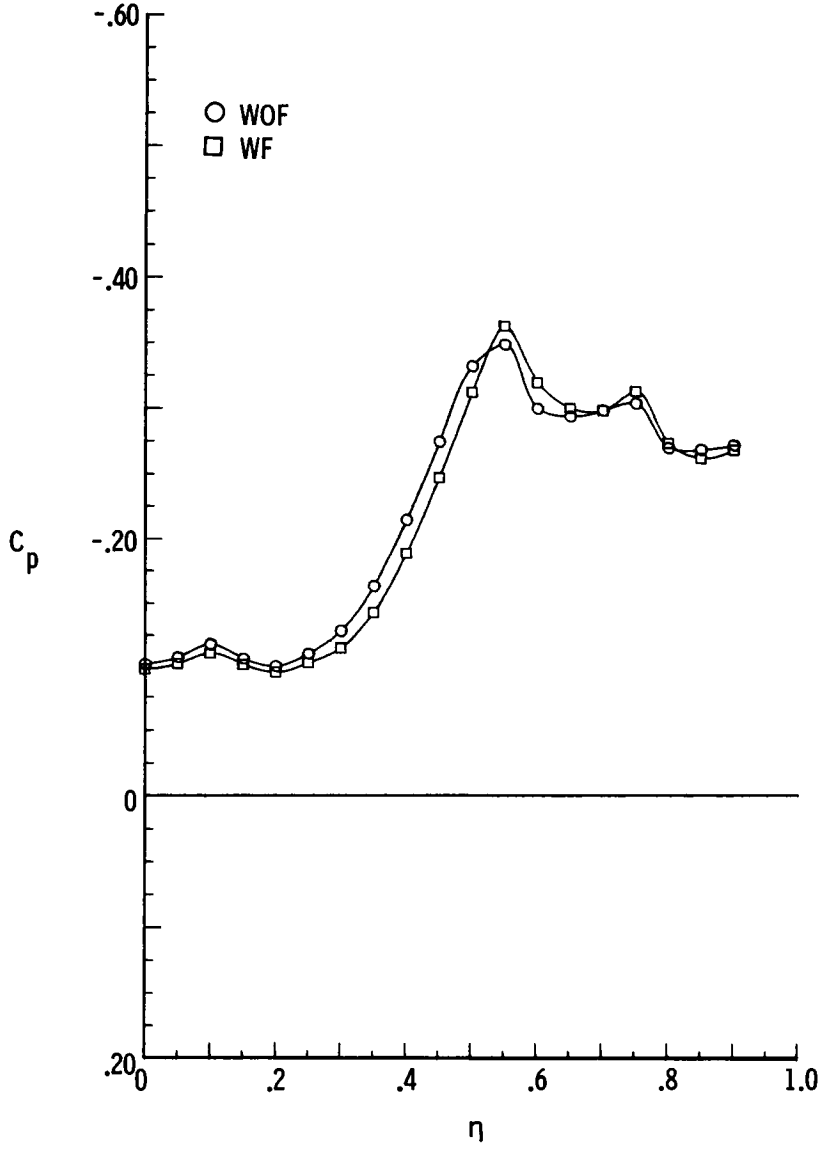

(e) $\alpha = 12°$.

Figure 30.- Concluded.

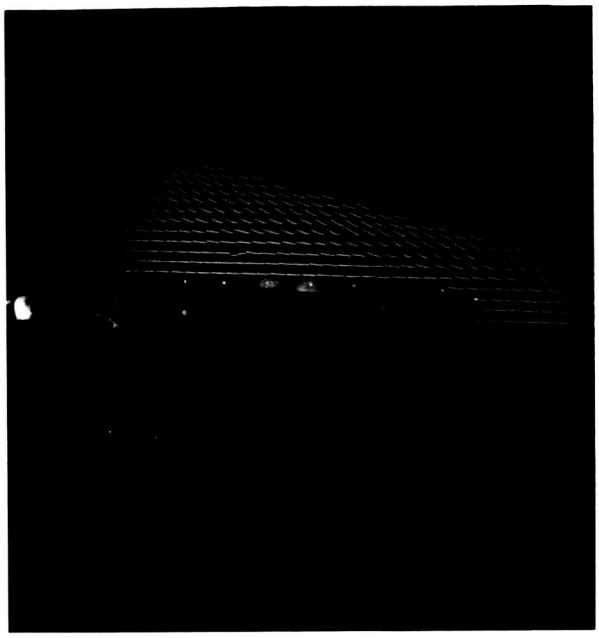

Tufts

Oil flow

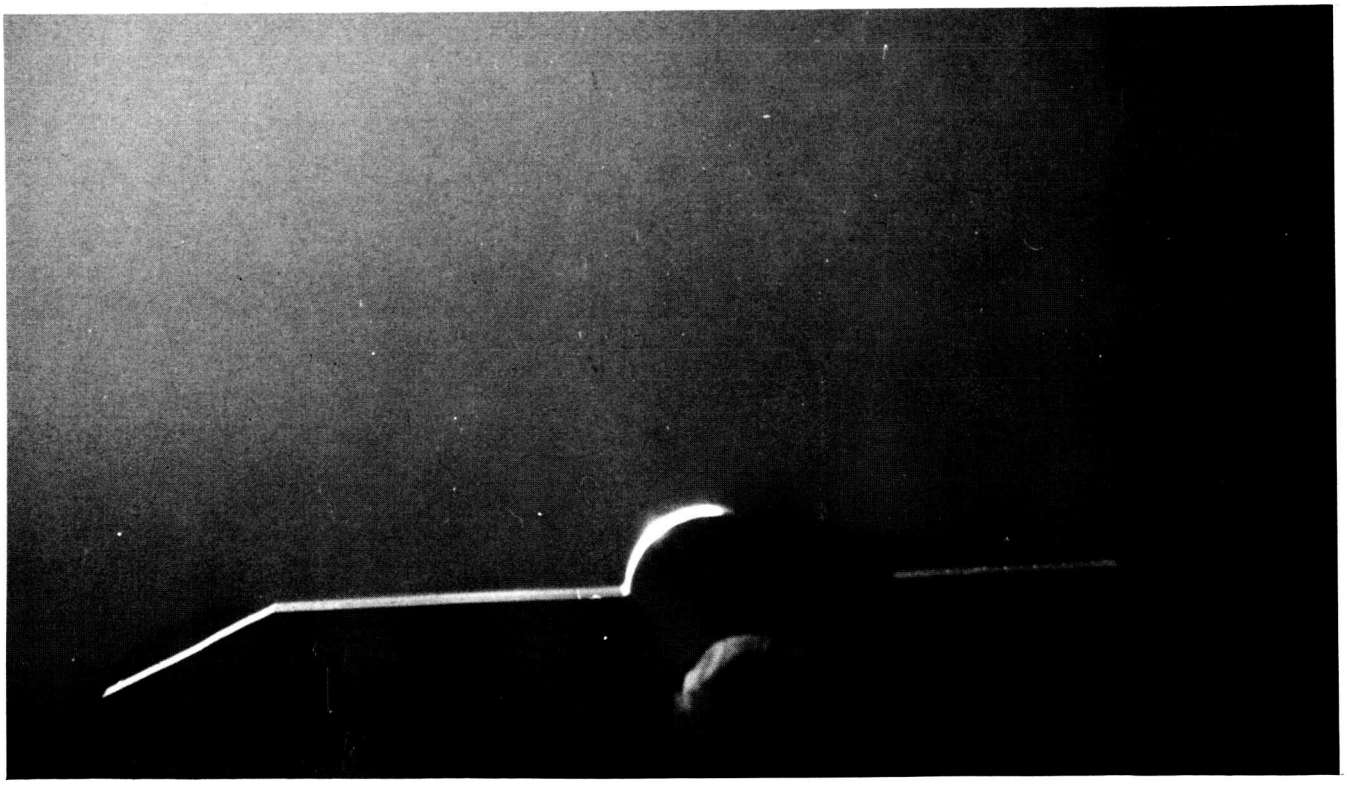

Vapor screen

Figure 31.- Representative flow visualization data for wing with $\delta_F = 5°$ at $M = 1.70$, $\alpha = 6°$, and $R = 2 \times 10^6$.

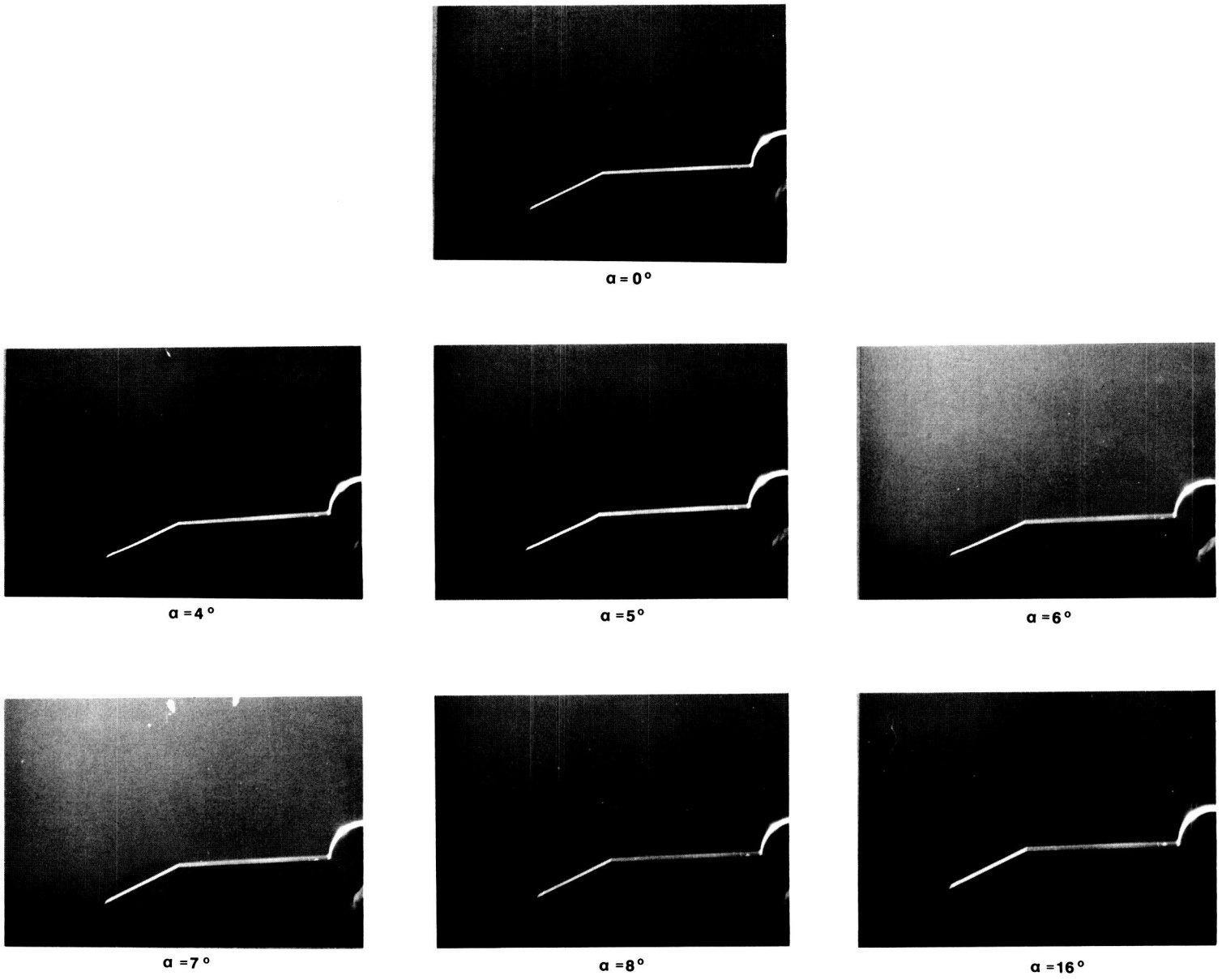

Figure 32.- Effect of α on lee-side flow characteristics of delta wing with $\delta_F = 5°$ with forebody at $M = 1.70$ and $R = 2 \times 10^6$.

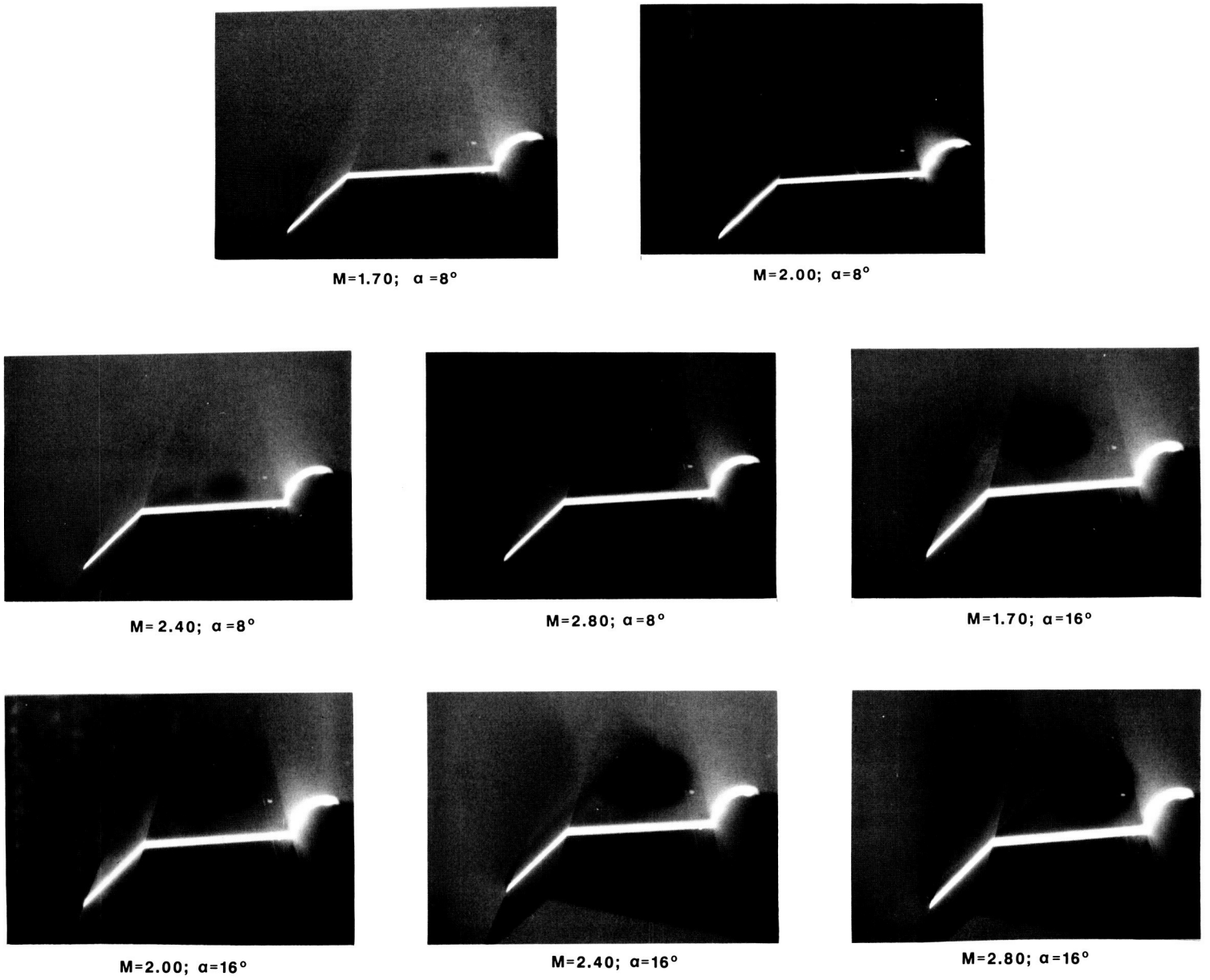

Figure 33.- Effect of M on lee-side flow characteristics of delta wing with δ_F = 10°.

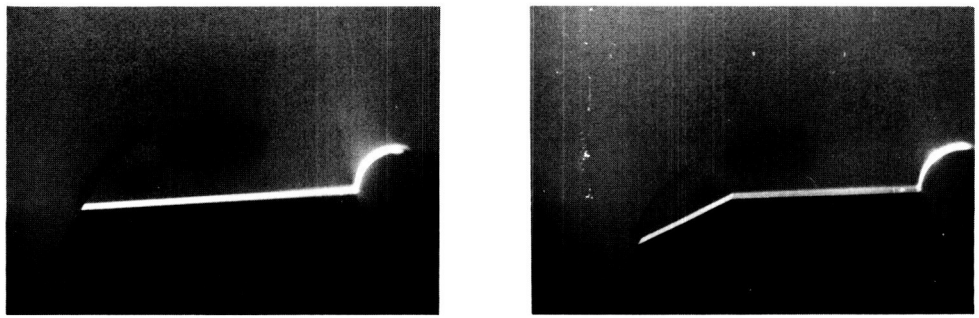

M=1.70; δ_F=0°

M=1.70; δ_F=5°

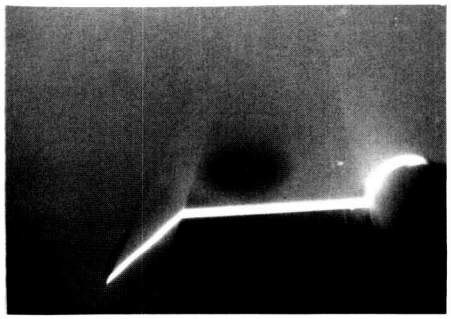

M=1.70; δ_F=10°

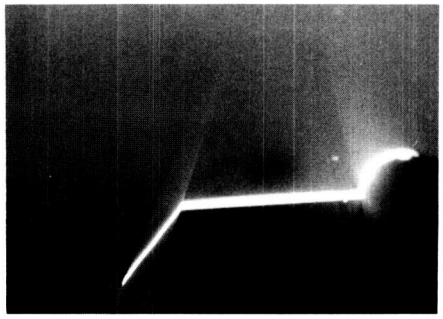

M=1.70; δ_F=15°

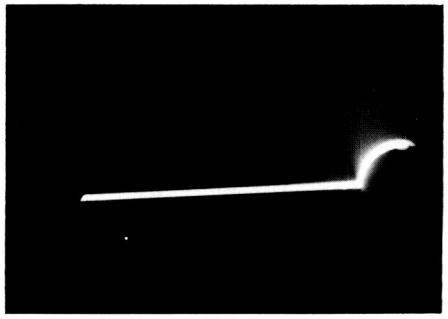

M=2.80; δ_F=0°

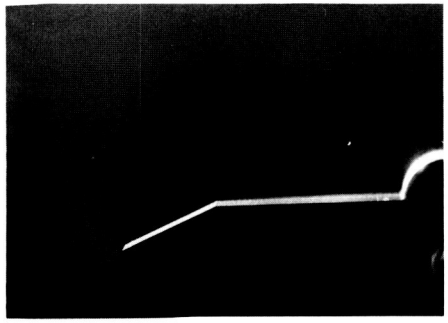

M=2.80; δ_F=5°

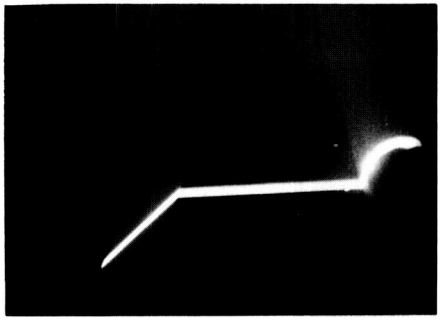

M=2.80; δ_F=10°

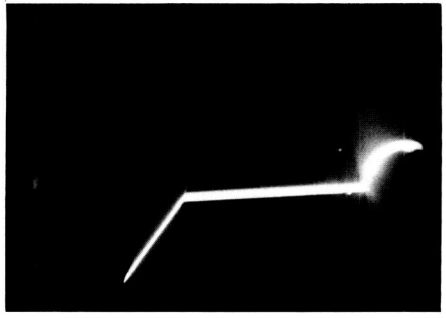

M=2.80; δ_F=15°

Figure 34.- Effect of δ_F on lee-side flow characteristics at α = 12°.

Figure 35.- Lee-side flows with one dominate feature.

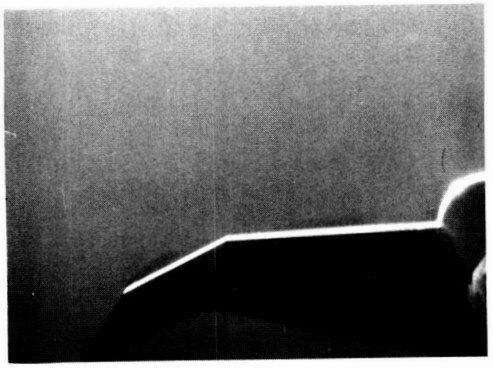

Leading-edge bubble and hinge-line bubble

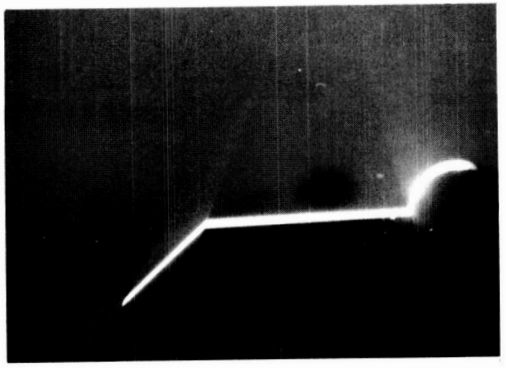

Leading-edge bubble and hinge-line vortex

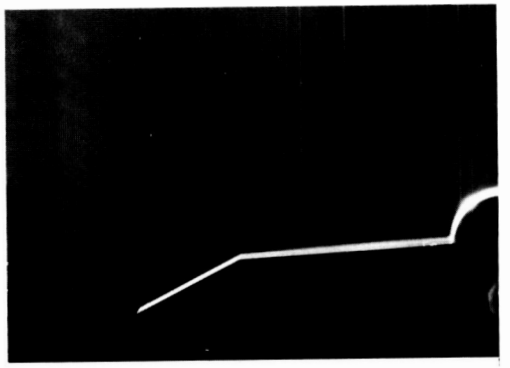

Leading-edge bubble with shock and hinge-line bubble

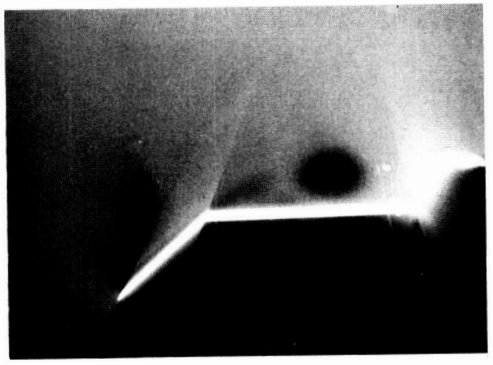

Leading-edge bubble with shock and hinge-line vortex

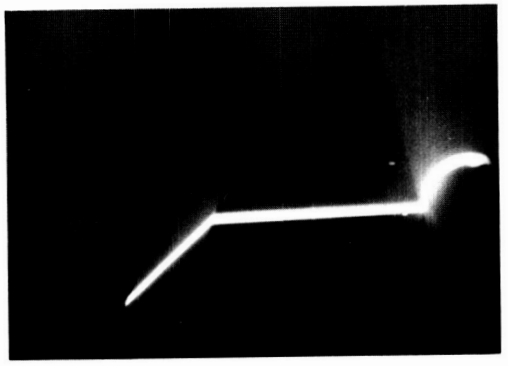

Shock and hinge-line vortex

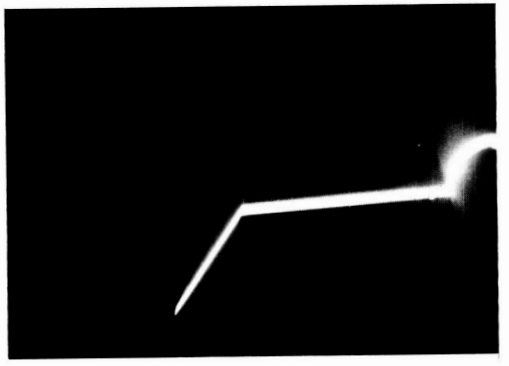

Shock and hinge-line vortex with shock

Figure 36.- Leading-edge flows with two dominate features.

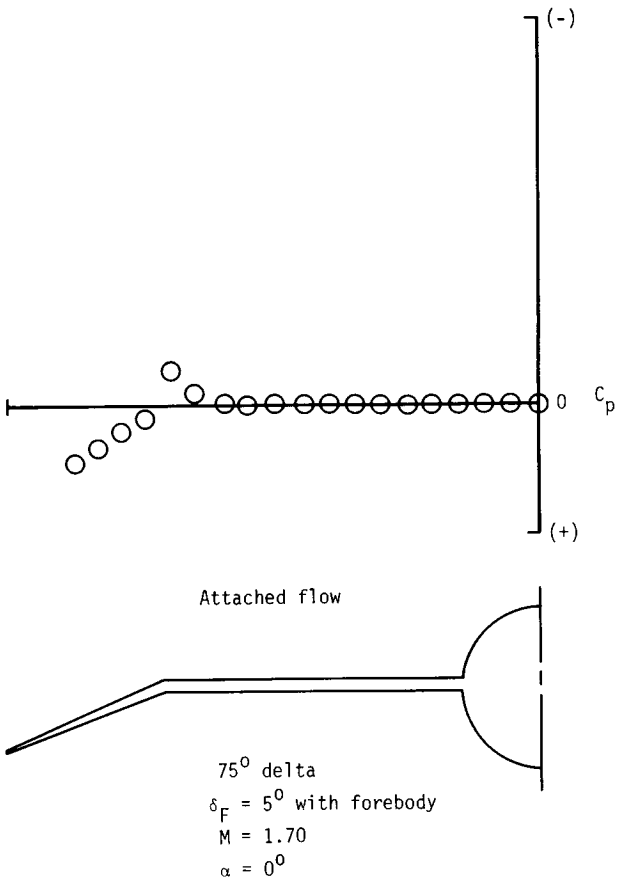

Figure 37.- Pressure distribution and sketch of attached flow condition.

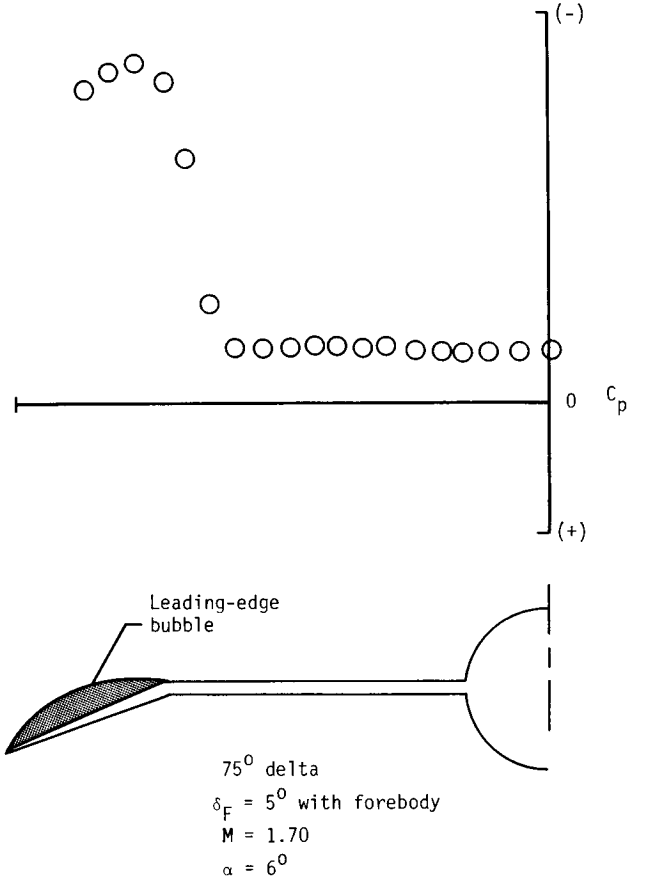

Figure 38.- Pressure distribution and sketch of leading-edge bubble condition.

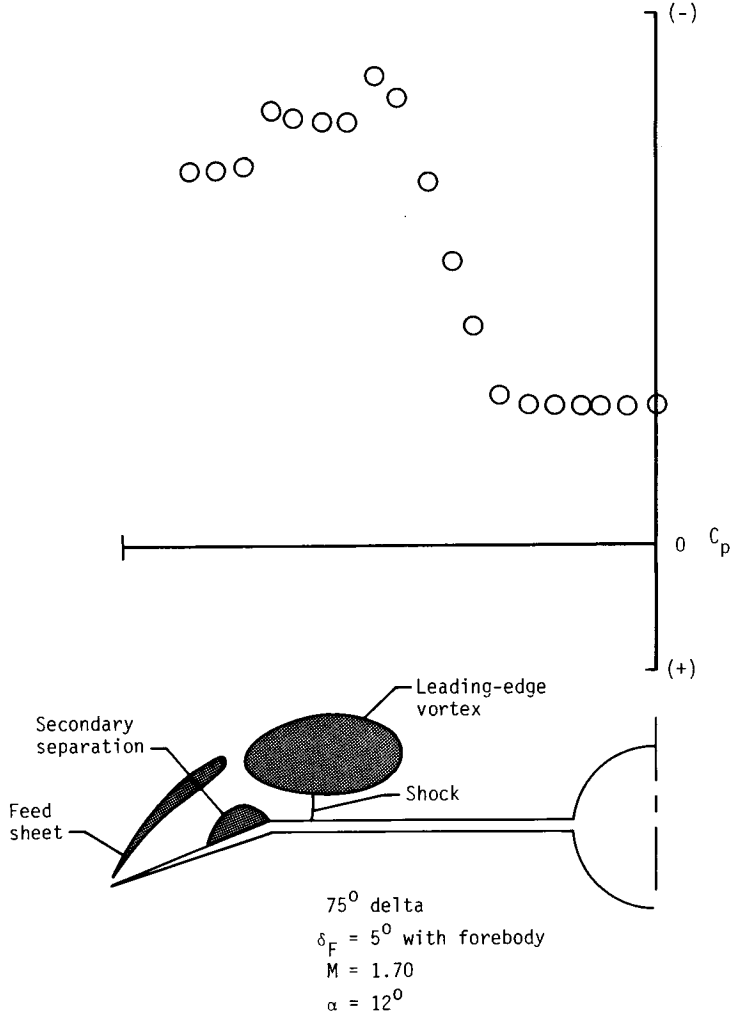

Figure 39.- Pressure distribution and sketch of leading-edge vortex condition.

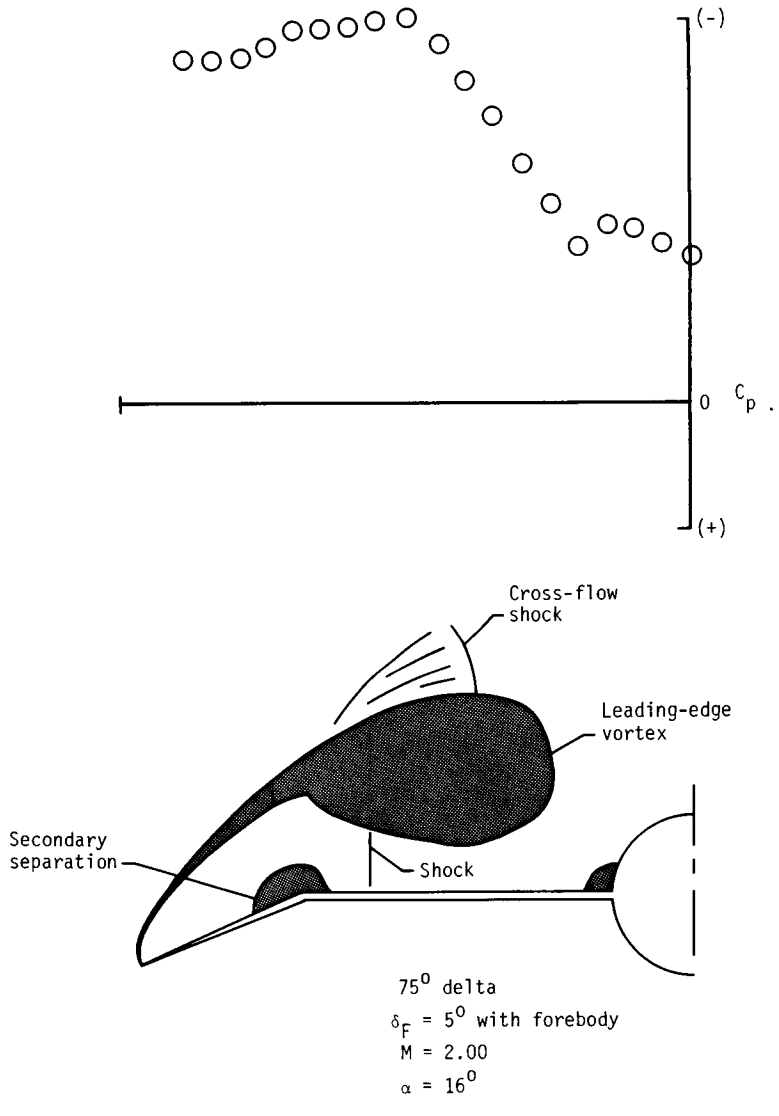

Figure 40.- Pressure distribution and sketch of leading-edge vortex with shock condition.

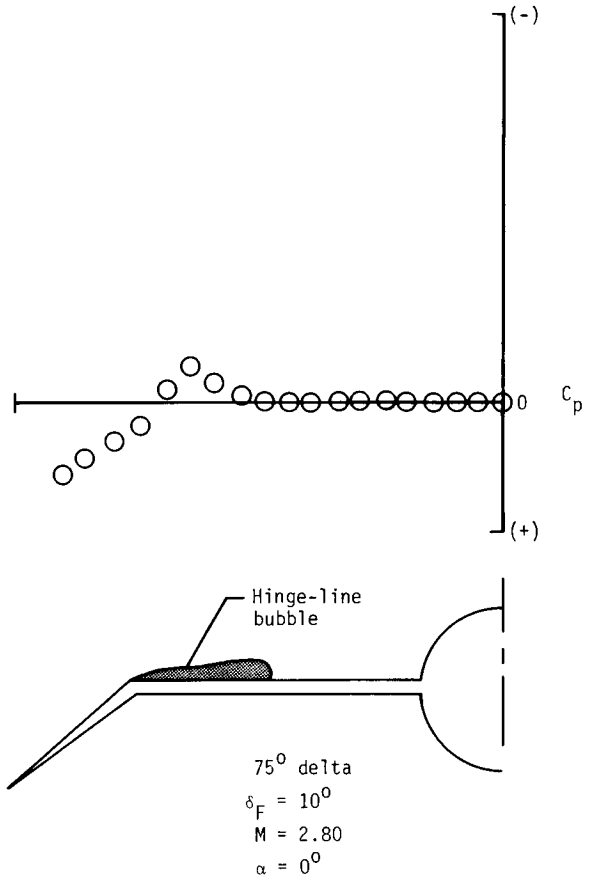

Figure 41.- Pressure distribution and sketch of hinge-line bubble condition.

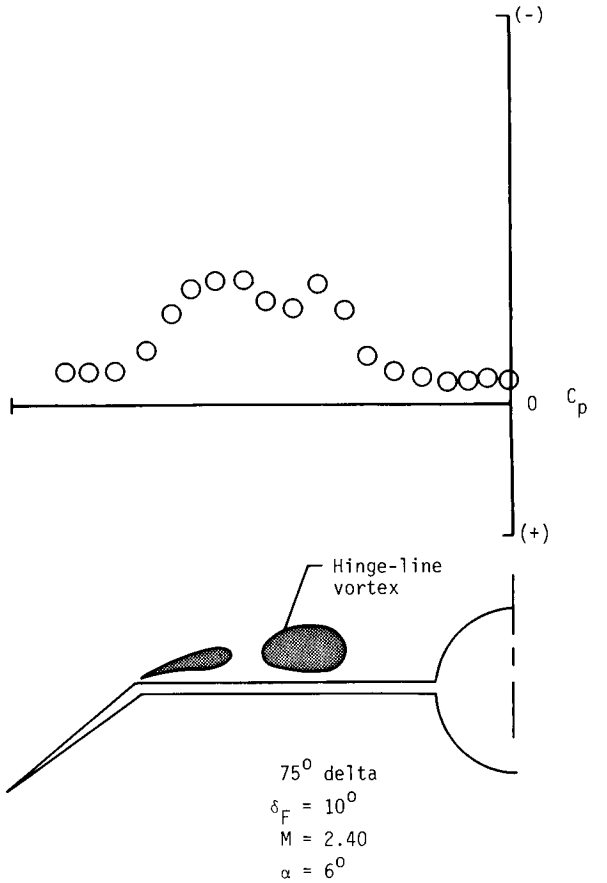

Figure 42.- Pressure distribution and sketch of hinge-line vortex condition.

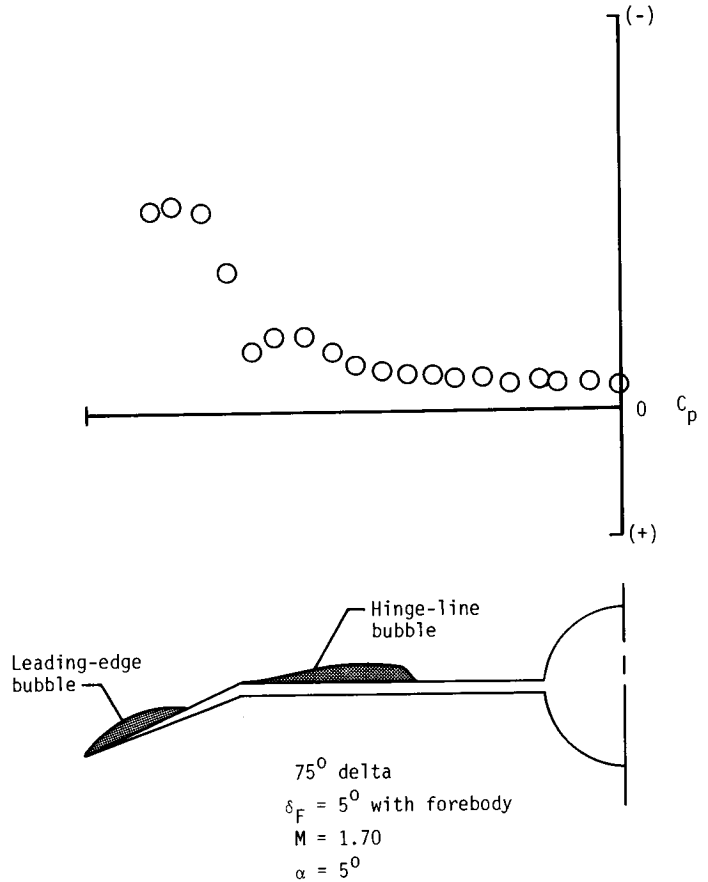

Figure 43.- Pressure distribution and sketch of leading-edge bubble and hinge-line bubble condition.

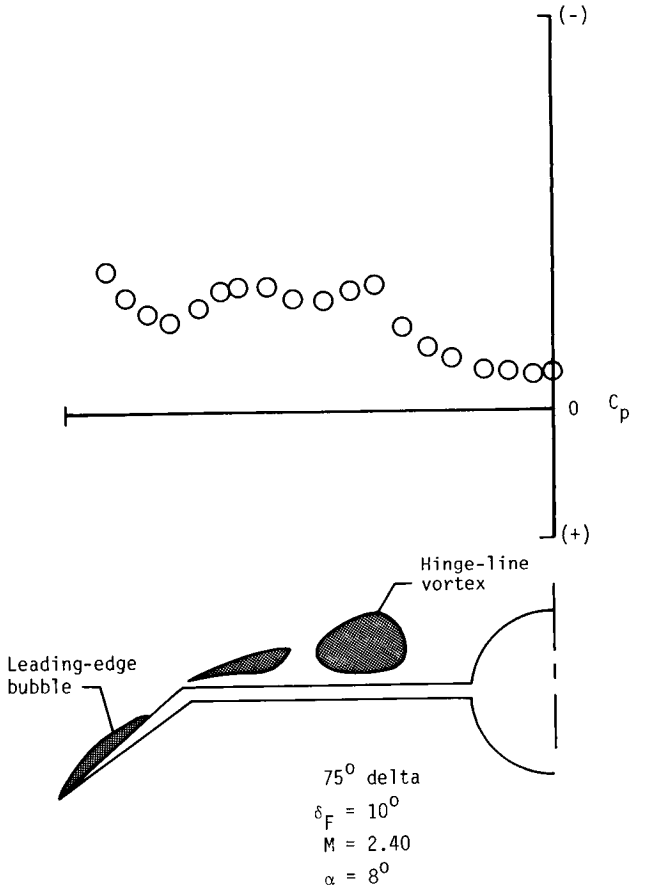

Figure 44.- Pressure distribution and sketch of leading-edge bubble and hinge-line vortex condition.

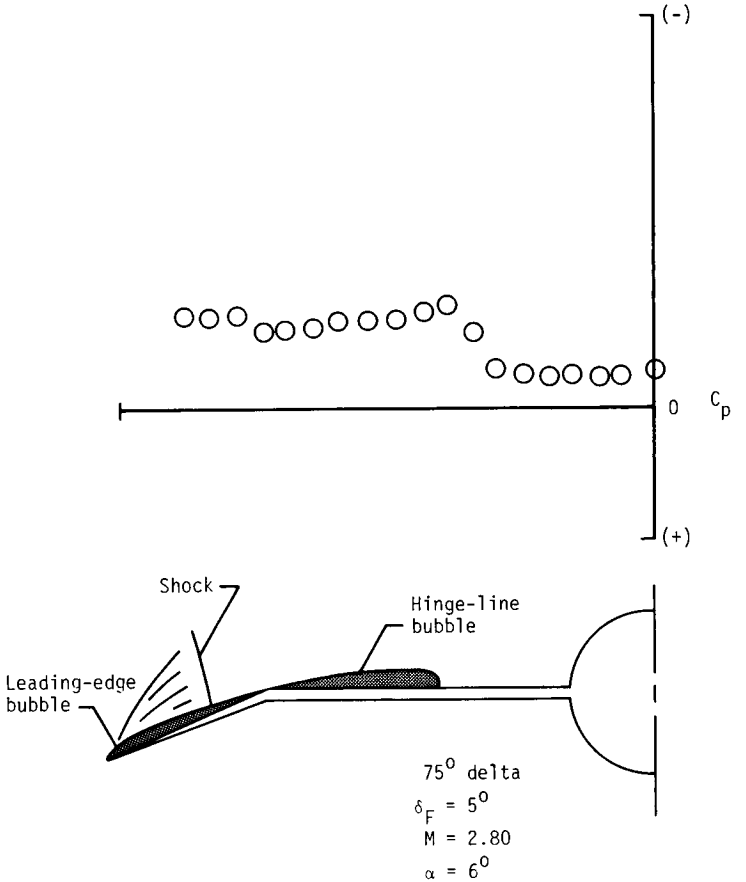

Figure 45.- Pressure distribution and sketch of leading-edge bubble with shock and hinge-line bubble condition.

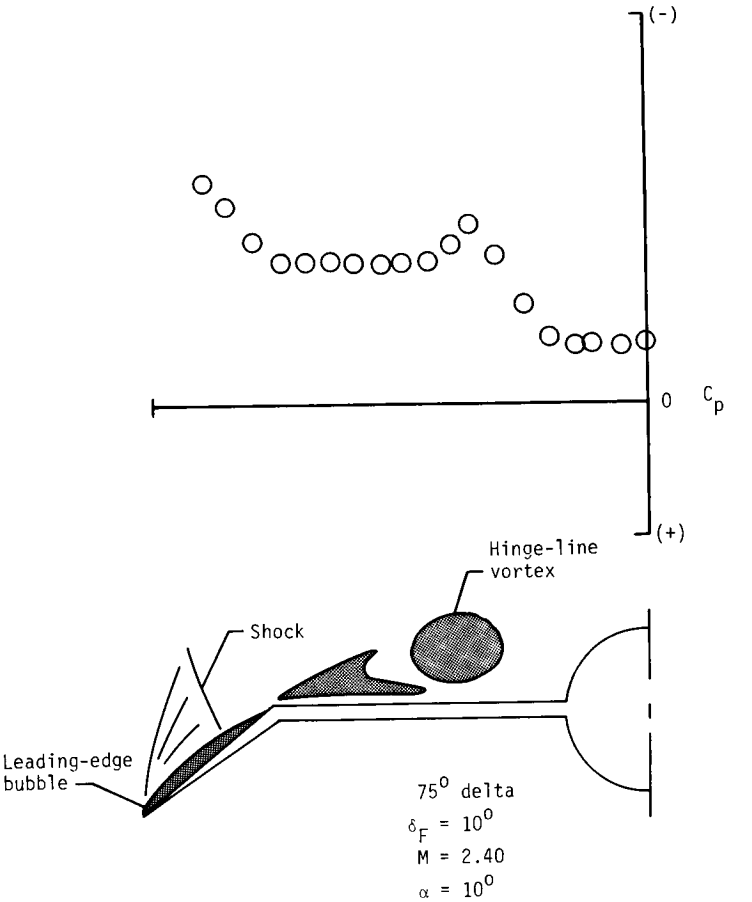

Figure 46.- Pressure distribution and sketch of leading-edge bubble with shock and hinge-line vortex condition.

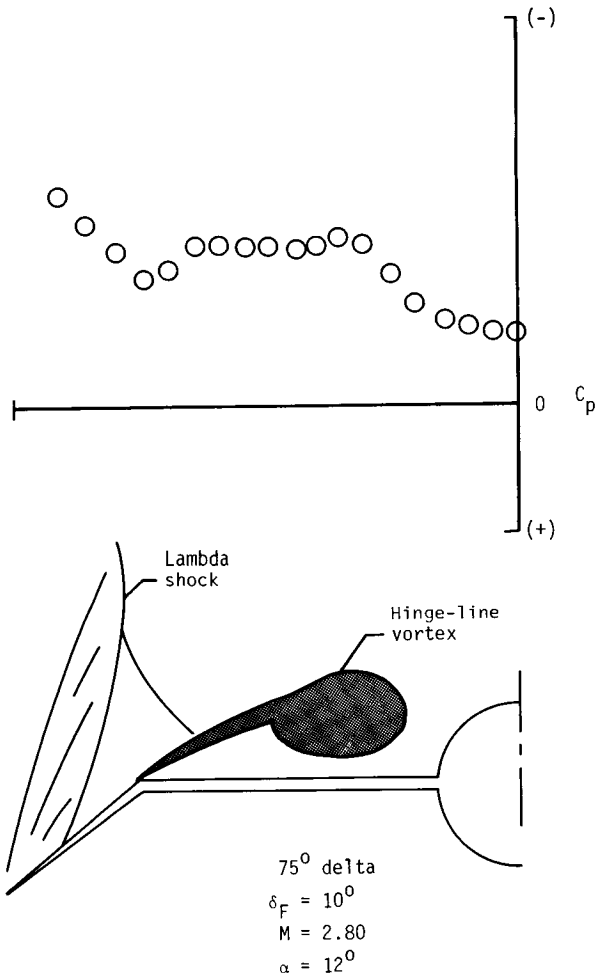

Figure 47.- Pressure distribution and sketch of shock and hinge-line vortex condition.

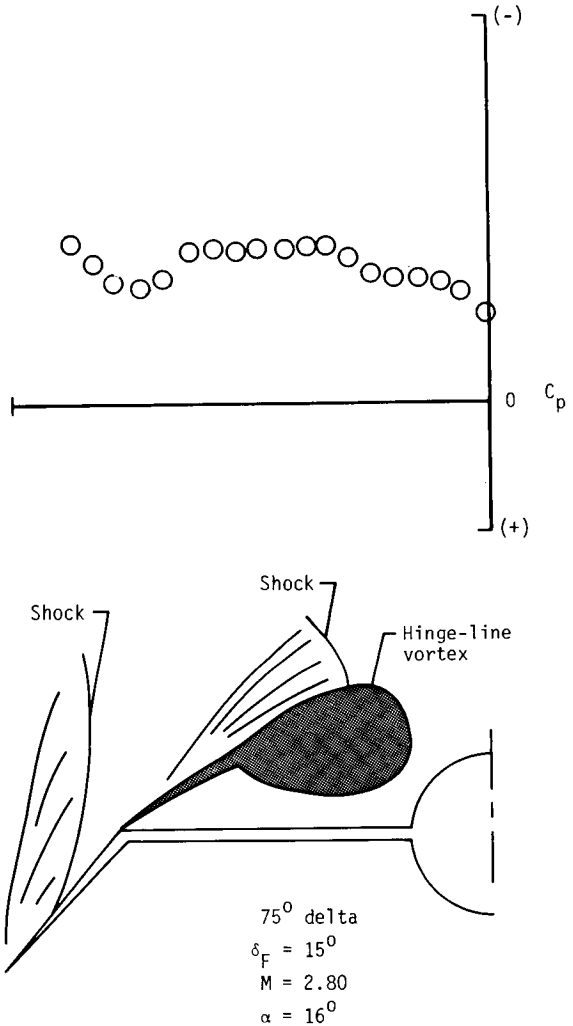

Figure 48.- Pressure distribution and sketch of shock and hinge-line vortex with shock condition.

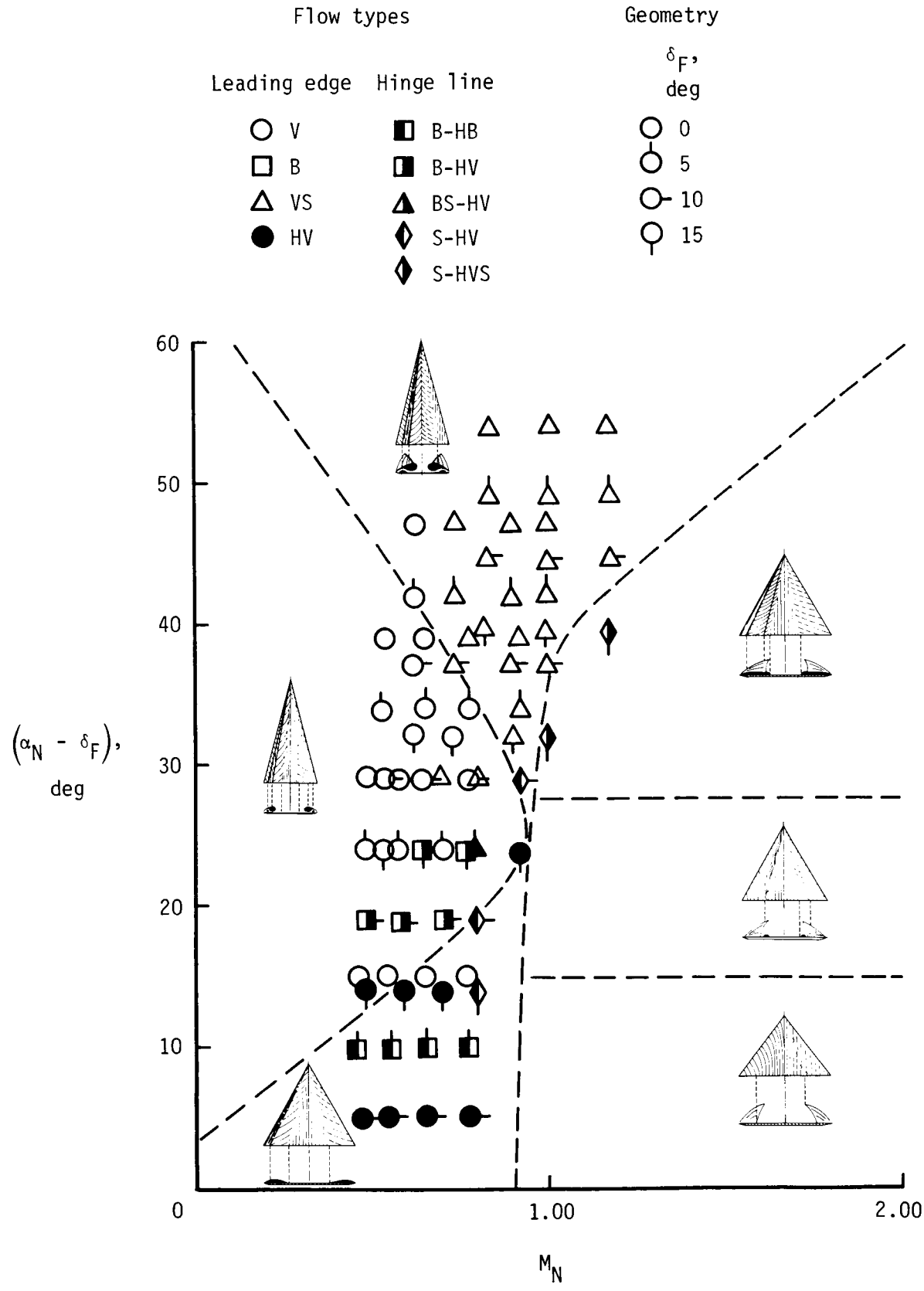

Figure 49.- Lee-side flow classification.

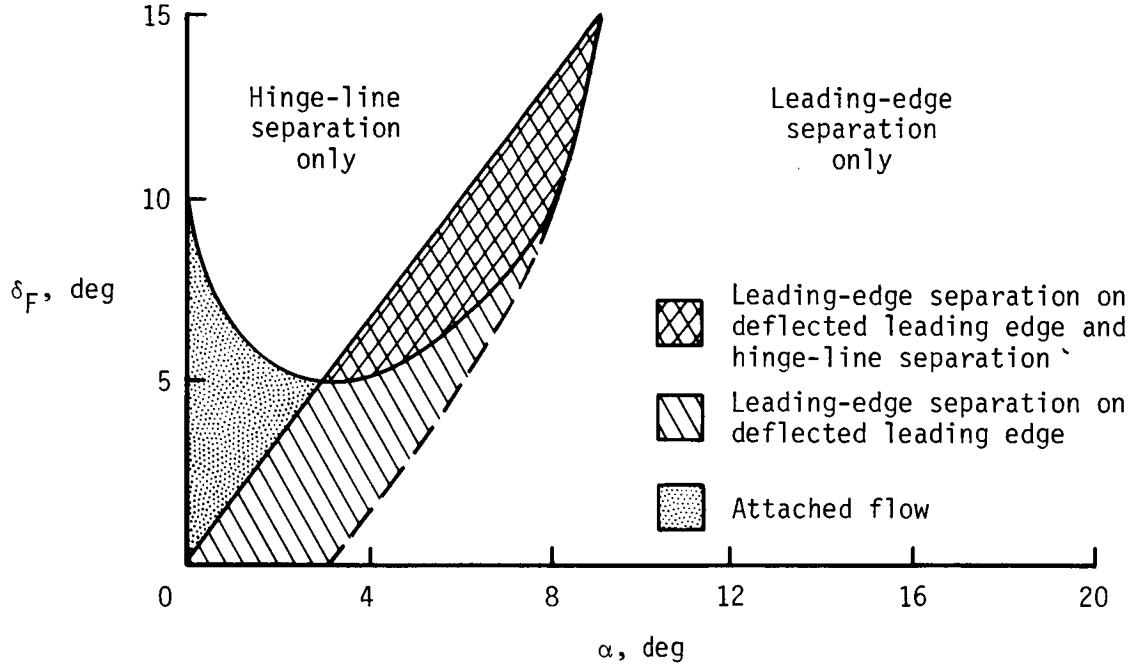

Figure 50.- Vortex flap lee-side flow characteristics at M = 1.70.

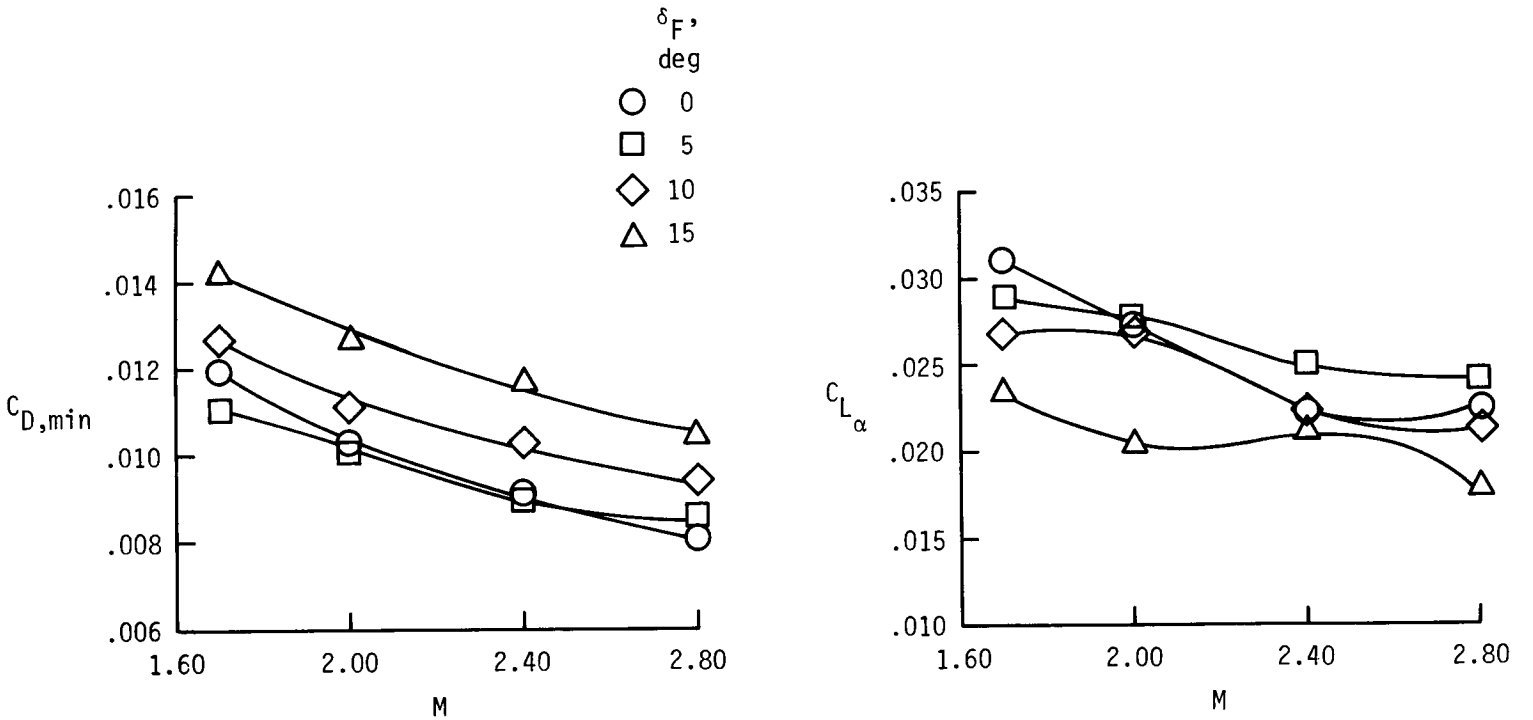

Figure 51.- Variation in $C_{D,min}$ and C_{L_α} with Mach number.

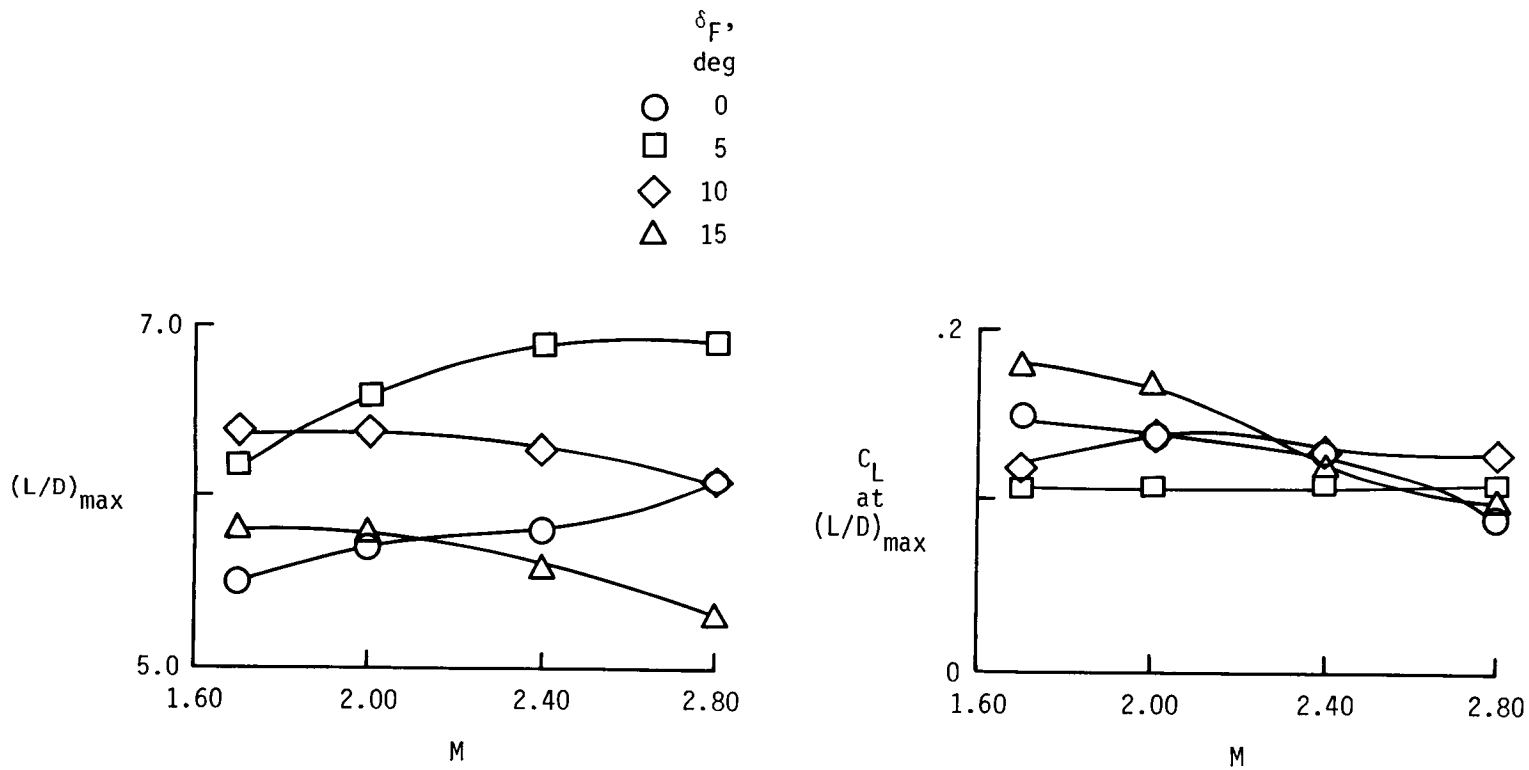

Figure 52.- Effect of Mach number on the aerodynamic performance.

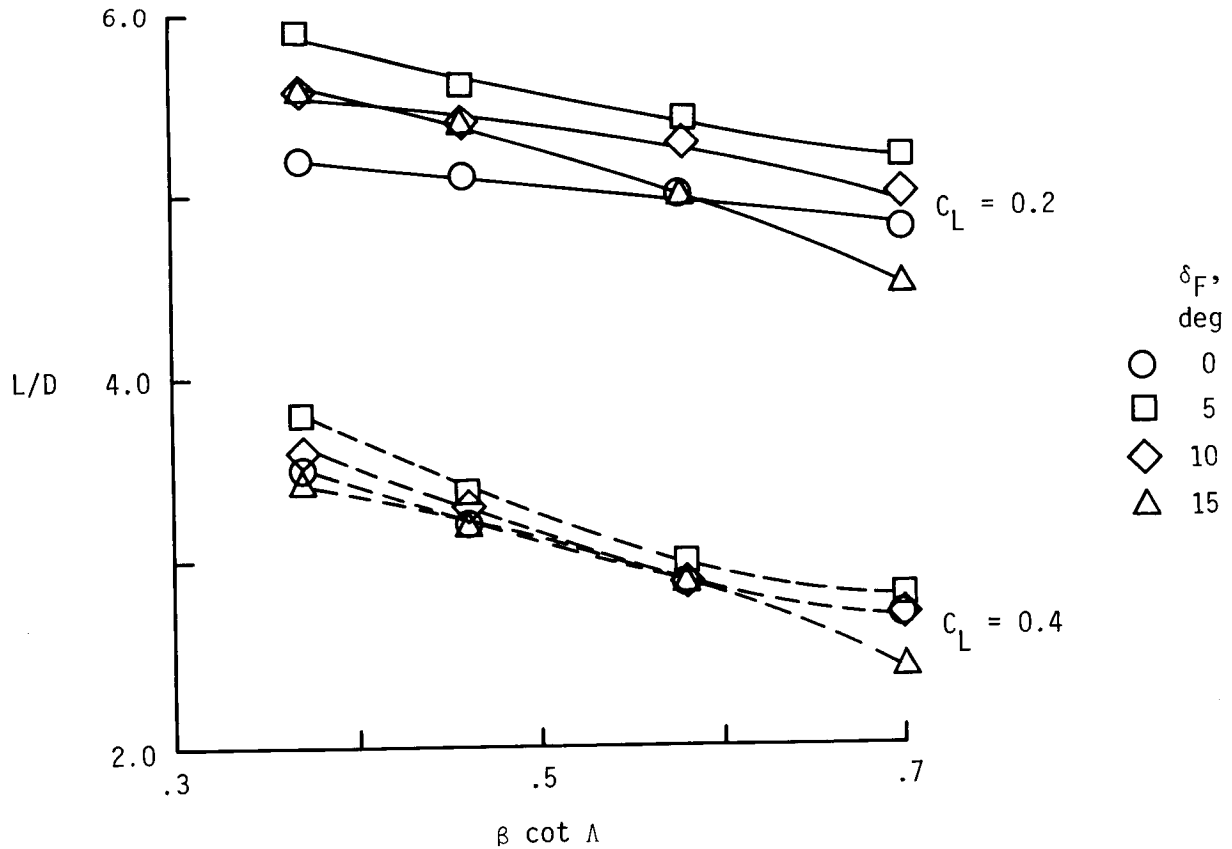

Figure 53.- Variation in lift-drag ratio with lift coefficient.

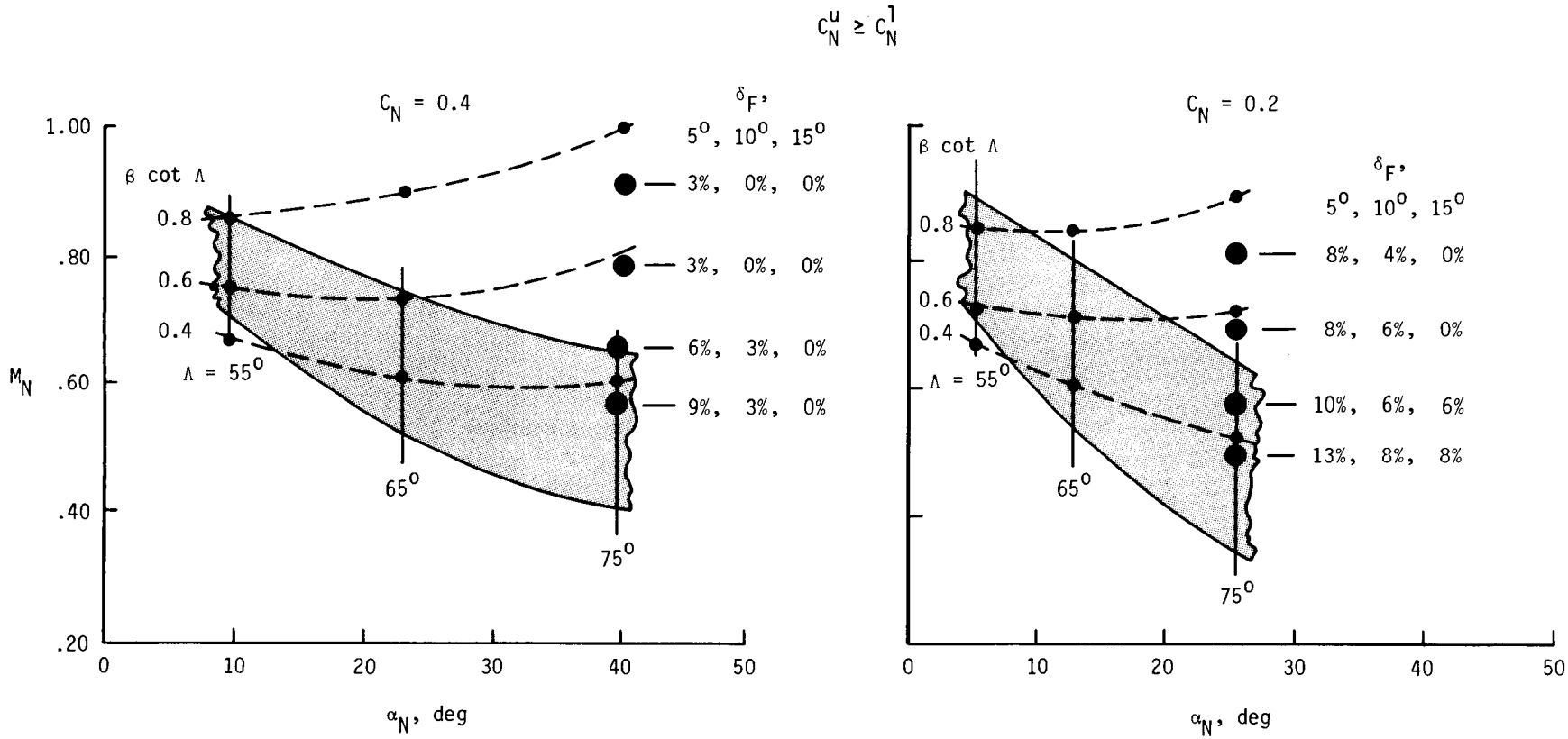

Figure 54.- Evaluation of wing design space concept.

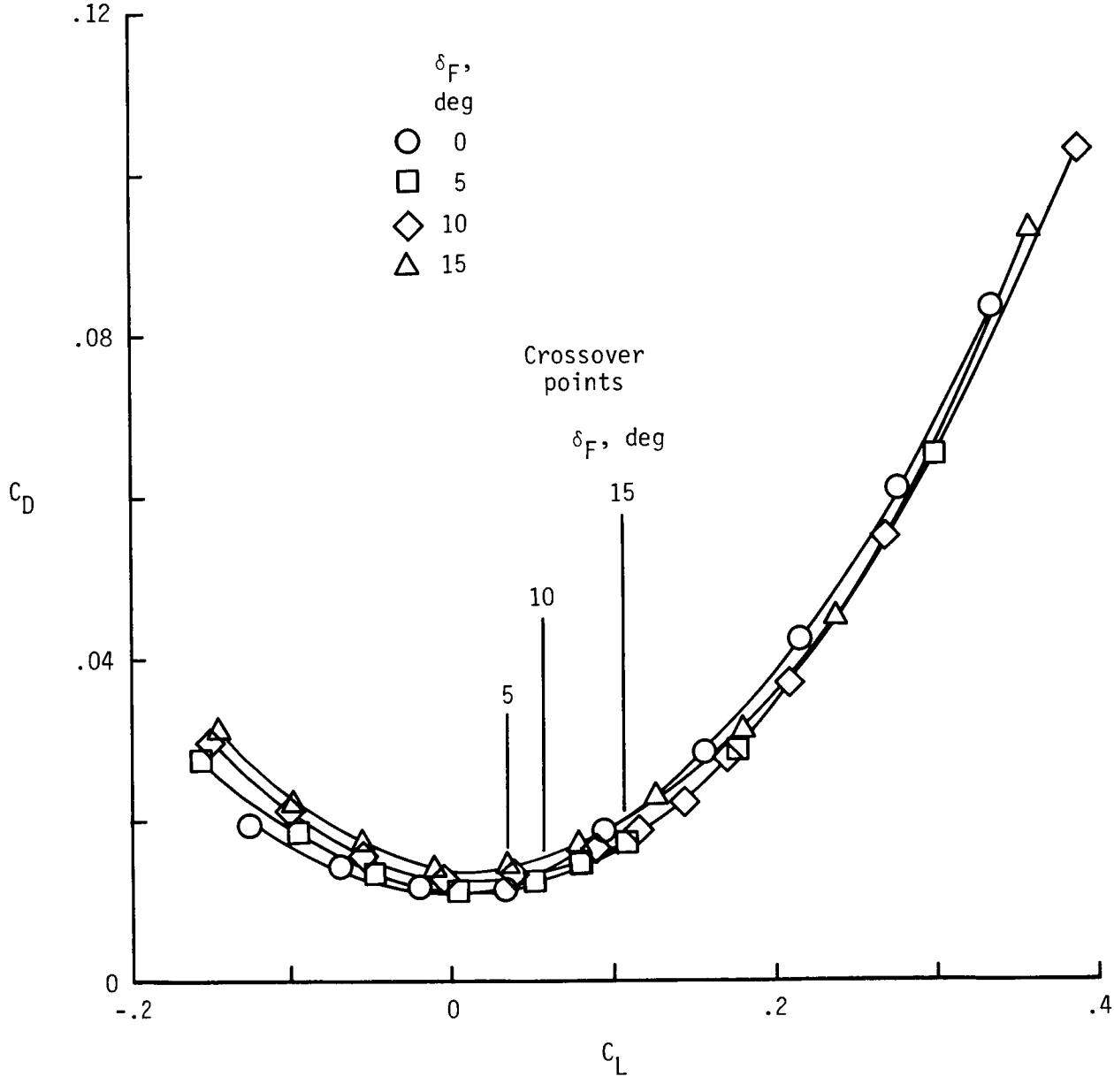

Figure 55.- Effect of δ_F on drag characteristics at M = 1.70.

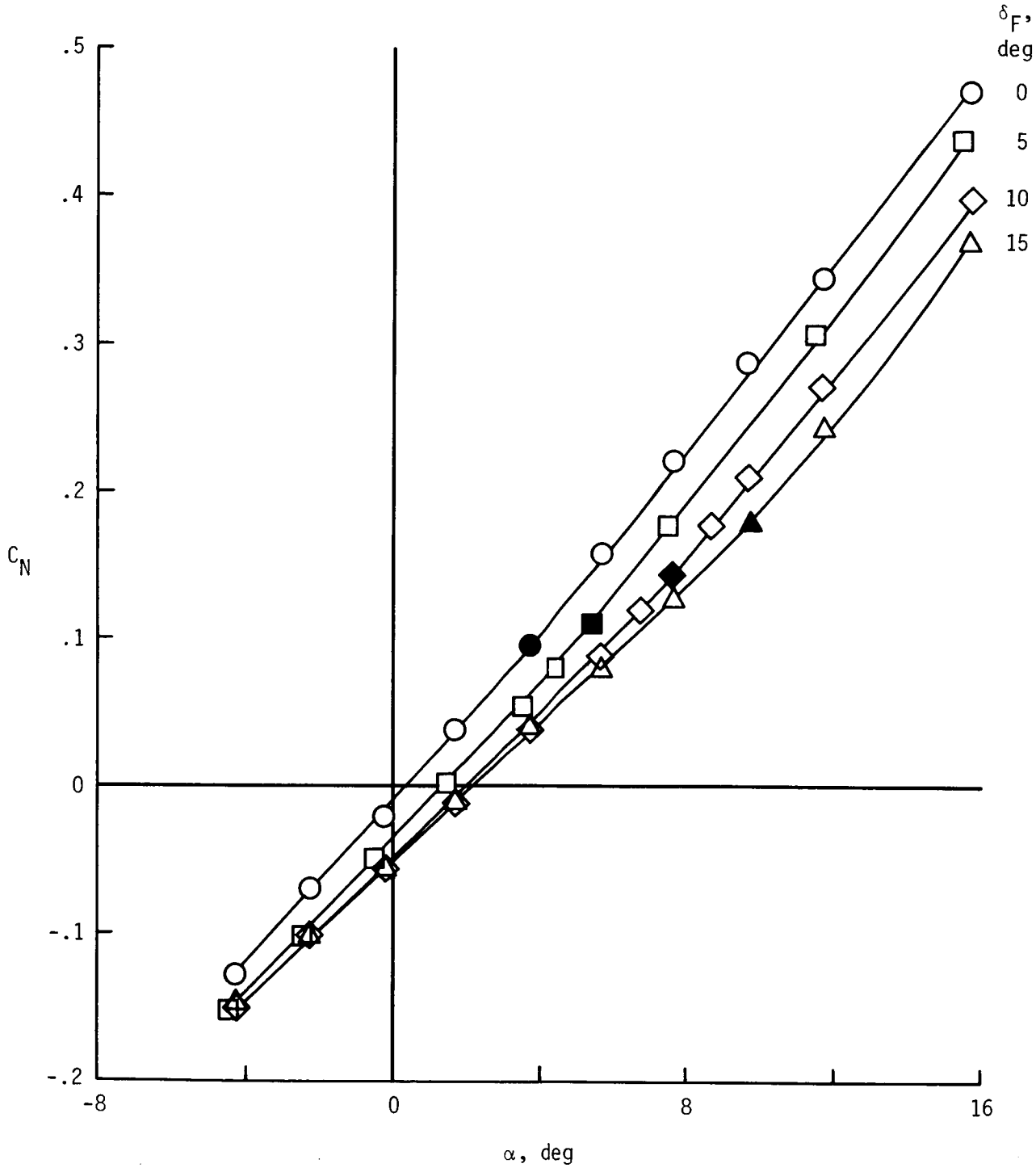

Figure 56.- Effect of δ_F on normal-force characteristics at M = 1.70. Solid symbols indicate break points.

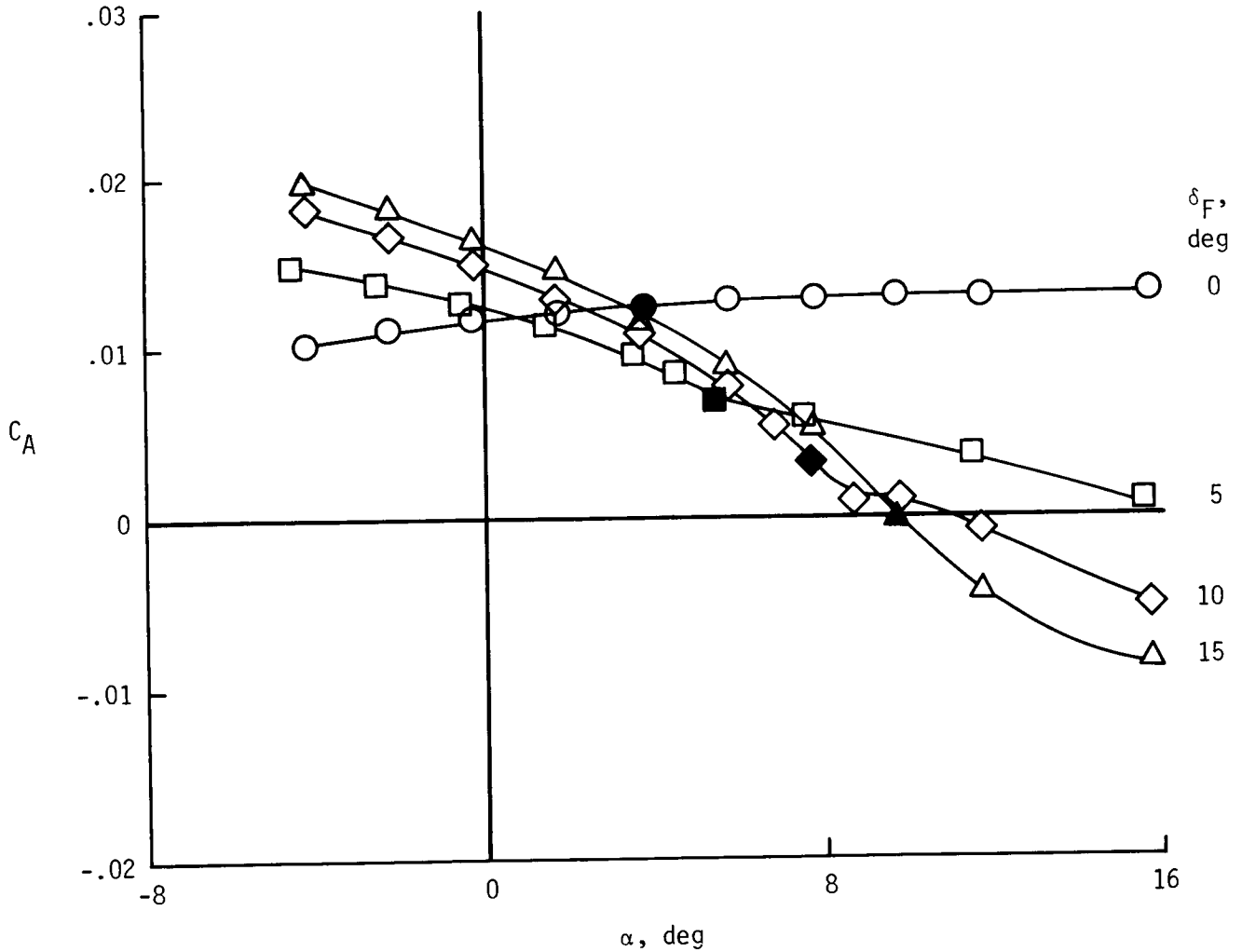

Figure 57.- Effect of δ_F on axial-force characteristics at M = 1.70. Solid symbols indicate break points.

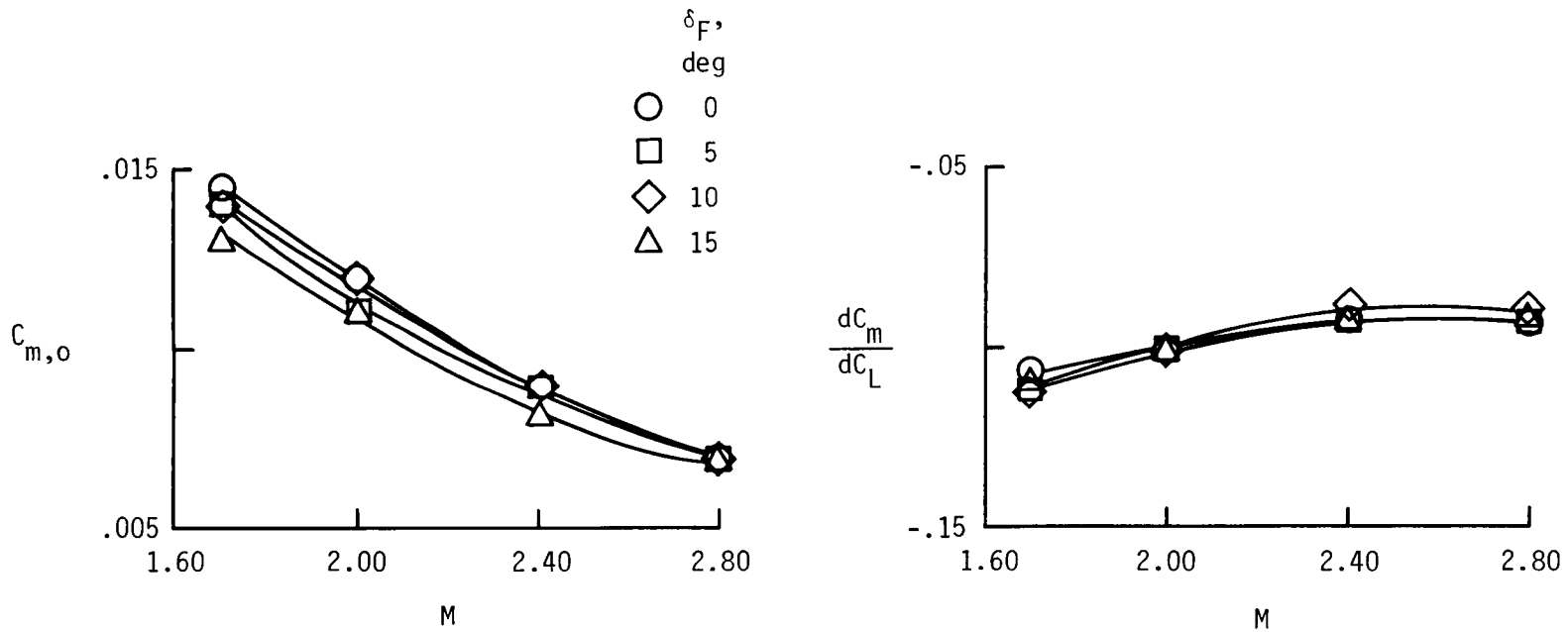

Figure 58.- Variation in longitudinal stability with Mach number.

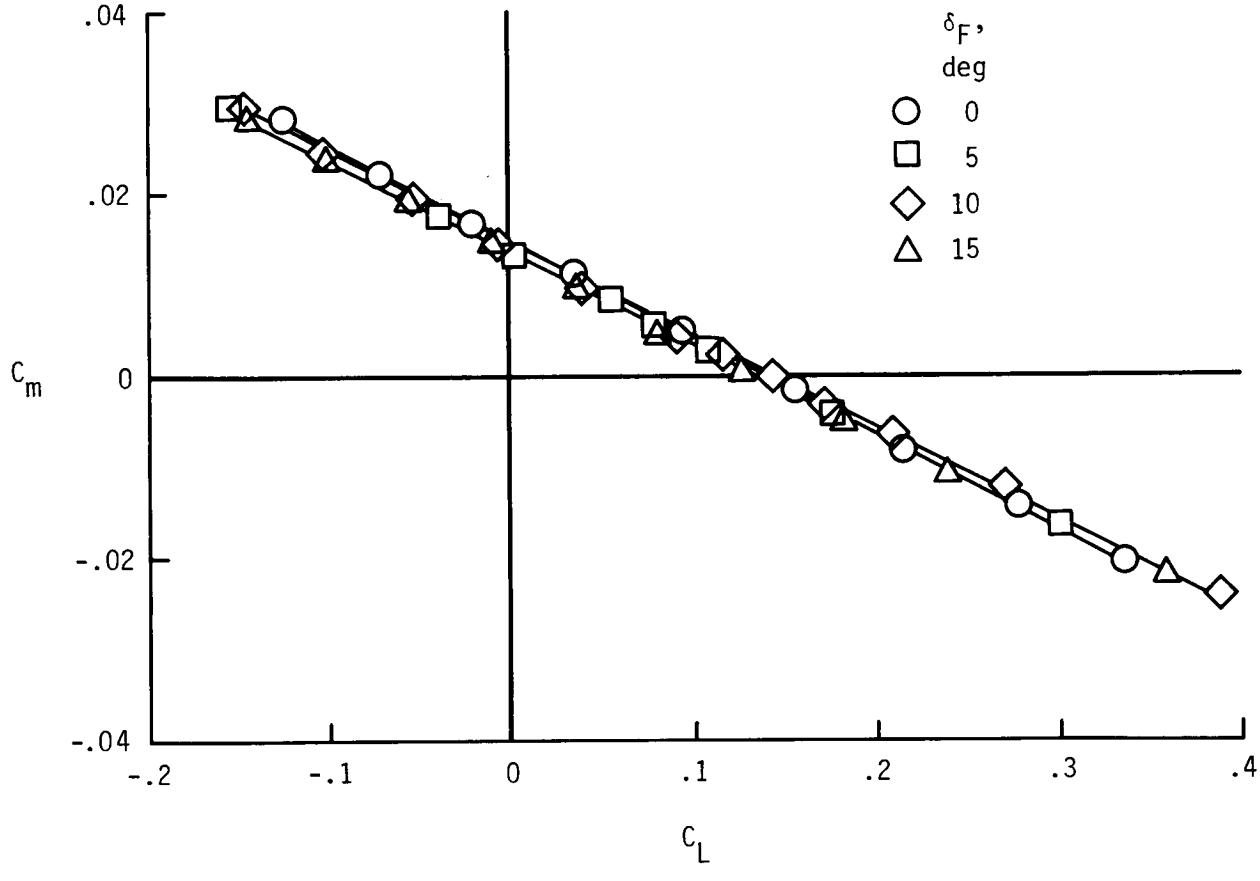

Figure 59.- Effect of δ_F on pitching-moment characteristics at M = 1.70.

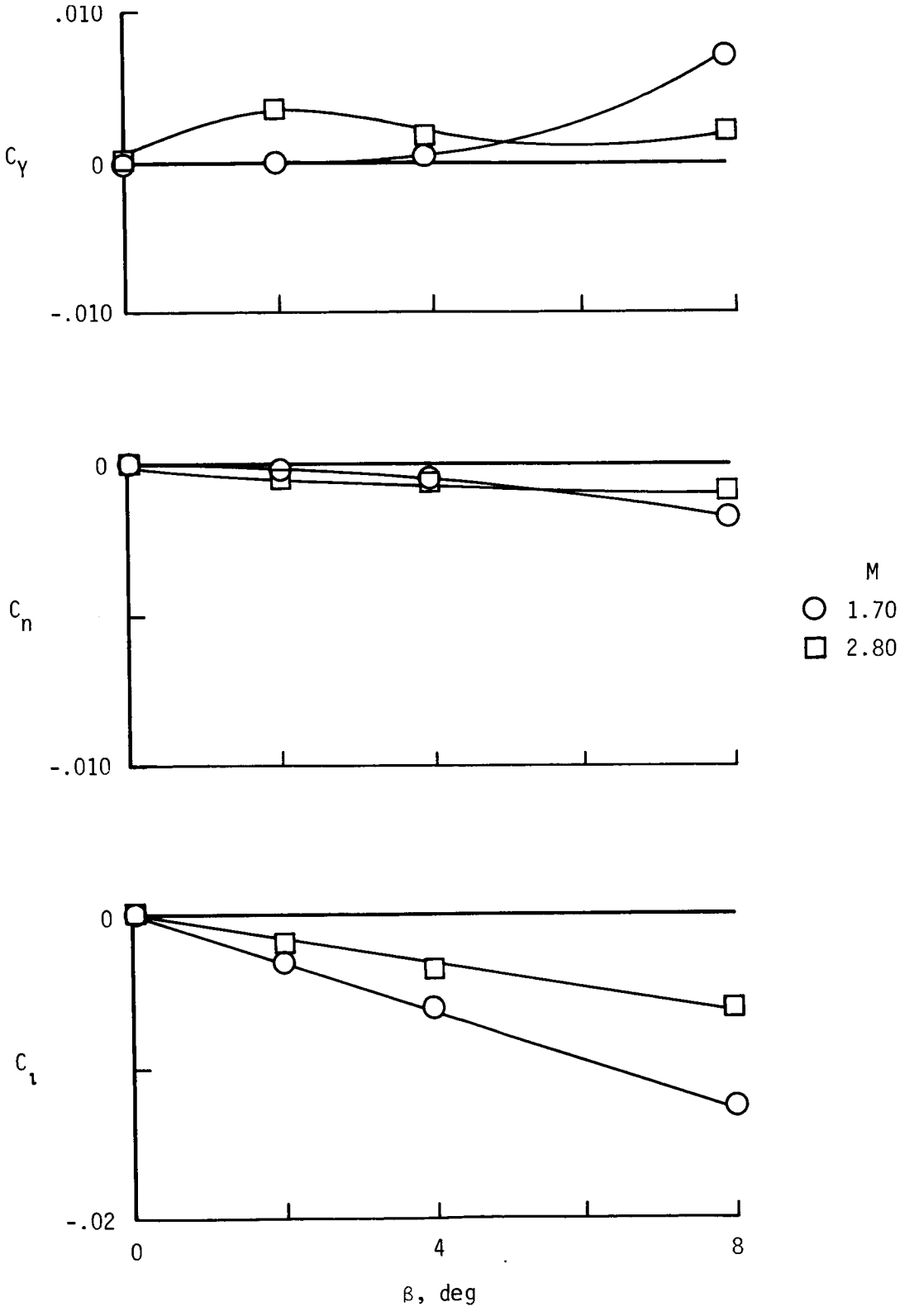

Figure 60.- Effect of M on C_Y, C_n, and C_l for wing with $\delta_F = 5°$. $\alpha = 12°$.

APPENDIX A

PRESSURE TEST ANGLE-OF-ATTACK CORRECTION

It is difficult to accurately assess the true angle of attack for pressure tests of wind-tunnel models which require large numbers of pressure tubing to be routed from the model to an externally mounted pressure transducer. The requirement to route the pressure tubing external to the model creates both a nonmetric test setup and a distortion to the model lower surface which would be expected to effect both the measured balance loads and the deflections of the balance and sting. For the present test, an accelerometer could not be located within the model due to the slenderness of the geometry. The only remaining solution to the problem of assessing the correct angle of attack would be to employ the balance and sting deflection coefficients to approximate a correction to the angles of attack and angles of sideslip. It should be noted that the application of such a correction is questionable due to the nonmetric model setup which existed during pressure testing. The nonmetric arrangement is contradictory to the metric model arrangement from which the balance and sting deflection coefficient were derived. In addition, there is also a concern as to the ability to obtain repeatable deflection characteristics due to the binding or slipping of the rigid tube bundles as the model is rotated through an angle of attack and/or sideslip.

Despite these known deficiencies, it was deemed appropriate to include enough information to allow for balance and sting deflection correction to the experimental data. The balance and sting deflection coefficients obtained for the metric model setup (force test) are as follows:

Normal force	0.005308 deg/lb
Pitching moment	0.001074 deg/in-lb
Side force	0.005300 deg/lb
Yawing moment	0.001155 deg/in-lb

Nonmetric model setup (pressure test) balance and sting deflection coefficients, which represent test conditions, cannot be obtained. Pressure test forces and moments are not presented due to the nonmetric arrangement of the test system.

APPENDIX B

SURFACE PRESSURE COEFFICIENT PLOTS

Experimental pressure coefficient plots for the four delta wings are presented. Table BI is an index to the plots.

TABLE BI.- INDEX TO SURFACE PRESSURE PLOTS

Figure	Configuration	M	R	α, deg	β, deg	x/ℓ	Page
B1(a)	75° delta wing with δ_F = 0°	Vary	2×10^6	0	0	0.90	108
(b)				4			108
(c)				12			109
B2(a)	75° delta wing with δ_F = 0°	1.50	2×10^6	Vary	0	0.90	110
(b)		1.70					110
(c)		2.00					111
(d)		2.40					111
(e)		2.80					112
B3(a)	75° delta wing with δ_F = 0°	1.70	2×10^6	12	Vary	0.90	113
(b)		2.80					113
B4(a)	75° delta wing with δ_F = 0°	1.70	Vary	12	0	0.10	114
(b)		1.70				.20	114
(c)		1.70				.30	115
(d)		1.70				.60	115
(e)		1.70				.80	116
(f)		1.70				.90	116
(g)		2.80				.10	117
(h)		2.80				.20	117
(i)		2.80				.30	118
(j)		2.80				.60	118
(k)		2.80				.80	119
(l)		2.80				.90	119
B5(a)	75° delta wing with δ_F = 0°	1.70	Vary	12	-8	0.90	120
(b)		1.70			8	.90	120
(c)		2.80			-8	.90	121
(d)		2.80			8	.90	121
B6(a)	75° delta wing with δ_F = 0°	1.50	2×10^6	12	0	Vary	122
(b)		1.70					122
(c)		2.00					123
(d)		2.40					123
(e)		2.80					124

TABLE BI.- Continued

Figure	Configuration	M	R	α, deg	β, deg	x/l	Page
B7(a)	75° delta wing with δ_F = 0°	1.70	2×10^6	12	8	Vary	125
(b)		1.70			4		125
(c)		1.70			2		126
(d)		1.70			-2		126
(e)		1.70			-4		127
(f)		1.70			-8		127
(g)		2.80			8		128
(h)		2.80			4		128
(i)		2.80			2		129
(j)		2.80			-2		129
(k)		2.80			-4		130
(l)		2.80			-8		130
B8(a)	75° delta wing with δ_F = 5°	Vary	2×10^6	0	0	0.90	131
(b)					4		131
(c)					6		132
(d)					12		132
B9(a)	75° delta wing with δ_F = 5°	1.50	2×10^6	Vary	0	0.90	133
(b)		1.70					133
(c)		2.00					134
(d)		2.40					134
(e)		2.80					135
B10(a)	75° delta wing with δ_F = 5°	1.70	2×10^6	12	Vary	0.90	136
(b)		2.80					136
B11(a)	75° delta wing with δ_F = 5°	1.70	Vary	12	0	0.10	137
(b)		1.70				.20	137
(c)		1.70				.30	138
(d)		1.70				.60	138
(e)		1.70				.80	139
(f)		1.70				.90	139
(g)		2.80				.10	140
(h)		2.80				.20	140
(i)		2.80				.30	141
(j)		2.80				.60	141
(k)		2.80				.80	142
(l)		2.80				.90	142
B12(a)	75° delta wing with δ_F = 5°	1.70	Vary	12	-8	0.90	143
(b)		1.70			8		143
(c)		2.80			-8		144
(d)		2.80			8		144

TABLE BI.- Continued

Figure	Configuration	M	R	α, deg	β, deg	x/l	Page
B13(a)	75° delta wing with δ_F = 5°	1.50	2×10^6	12	0	Vary	145
(b)		1.70					145
(c)		2.00					146
(d)		2.40					146
(e)		2.80					147
B14(a)	75° delta wing with δ_F = 5°	1.70	2×10^6	12	8	Vary	148
(b)		1.70			4		148
(c)		1.70			2		149
(d)		1.70			-2		149
(e)		1.70			-4		150
(f)		1.70			-8		150
(g)		2.80			8		151
(h)		2.80			4		151
(i)		2.80			2		152
(j)		2.80			-2		152
(k)		2.80			-4		153
(l)		2.80			-8		153
B15(a)	75° delta wing with δ_F = 10°	Vary	2×10^6	0	0	0.90	154
(b)					4		154
(c)					8		155
(d)					12		155
B16(a)	75° delta wing with δ_F = 10°	1.50	2×10^6	Vary	0	0.90	156
(b)		1.70					156
(c)		2.00					157
(d)		2.40					157
(e)		2.80					158
B17(a)	75° delta wing with δ_F = 10°	1.70	2×10^6	12	Vary	0.90	159
(b)		2.80					159
B18(a)	75° delta wing with δ_F = 10°	1.70	Vary	12	0	0.10	160
(b)		1.70				.20	160
(c)		1.70				.30	161
(d)		1.70				.60	161
(e)		1.70				.80	162
(f)		1.70				.90	162
(g)		2.80				.10	163
(h)		2.80				.20	163
(i)		2.80				.30	164
(j)		2.80				.60	164
(k)		2.80				.80	165
(l)		2.80				.90	165
B19(a)	75° delta wing with δ_F = 10°	1.70	Vary	12	-8	0.90	166
(b)		1.70			8		166
(c)		2.80			-8		167
(d)		2.80			8		167

TABLE BI.- Continued

Figure	Configuration	M	R	α, deg	β, deg	x/l	Page
B20(a)	75° delta wing with δ_F = 10°	1.50	2 × 10^6	0	0	Vary	168
(b)		1.70					168
(c)		2.00					169
(d)		2.40					169
(e)		2.80					170
B21(a)	75° delta wing with δ_F = 10°	1.50	2 × 10^6	12	0	Vary	171
(b)		1.70					171
(c)		2.00					172
(d)		2.40					172
(e)		2.80					173
B22(a)	75° delta wing with δ_F = 10°	1.70	2 × 10^6	12	8	Vary	174
(b)		1.70			4		174
(c)		1.70			2		175
(d)		1.70			-2		175
(e)		1.70			-4		176
(f)		1.70			-8		176
(g)		2.80			8		177
(h)		2.80			4		177
(i)		2.80			2		178
(j)		2.80			-2		178
(k)		2.80			-4		179
(l)		2.80			-8		179
B23(a)	75° delta wing with δ_F = 15°	Vary	2 × 10^6	0	0	0.90	180
(b)				4			180
(c)				8			181
(d)				12			181
B24(a)	75° delta wing with δ_F = 15°	1.50	2 × 10^6	Vary	0	0.90	182
(b)		1.70					182
(c)		2.00					183
(d)		2.40					183
(e)		2.80					184
B25(a)	75° delta wing with δ_F = 15°	1.70	2 × 10^6	12	Vary	0.90	185
(b)		2.80					185
B26(a)	75° delta wing with δ_F = 15°	1.70	Vary	12	0	0.10	186
(b)		1.70				.20	186
(c)		1.70				.30	187
(d)		1.70				.60	187
(e)		1.70				.80	188
(f)		1.70				.90	188
(g)		2.80				.10	189
(h)		2.80				.20	189
(i)		2.80				.30	190
(j)		2.80				.60	190
(k)		2.80				.80	191
(l)		2.80				.90	191

TABLE BI.- Concluded

Figure	Configuration	M	R	α, deg	β, deg	x/l	Page
B27(a)	75° delta wing with δ_F = 15°	1.70	Vary	12	-8	0.90	192
(b)		1.70			8		192
(c)		2.80			-8		193
(d)		2.80			8		193
B28(a)	75° delta wing with δ_F = 15°	1.50	2×10^6	12	0	Vary	194
(b)		1.70					194
(c)		2.00					195
(d)		2.40					195
(e)		2.80					196
B29(a)	75° delta wing with δ_F = 15°	1.70	2×10^6	12	8	Vary	197
(b)		1.70			4		197
(c)		1.70			2		198
(d)		1.70			-2		198
(e)		1.70			-4		199
(f)		1.70			-8		199
(g)		2.80			8		200
(h)		2.80			4		200
(i)		2.80			2		201
(j)		2.80			-2		201
(k)		2.80			-4		202
(l)		2.80			-8		202
B30(a)	75° delta wing with δ_F = 5° with forebody	Vary	2×10^6	0	0	0.90	203
(b)				4			203
(c)				6			204
(d)				12			204
B31(a)	75° delta wing with δ_F = 5° with forebody	1.50	2×10^6	Vary	0	0.90	205
(b)		1.70					205
(c)		2.00					206
B32(a)	75° delta wing with δ_F = 5° with forebody	1.50	2×10^6	12	0	Vary	207
(b)		1.70					207
(c)		2.00					208

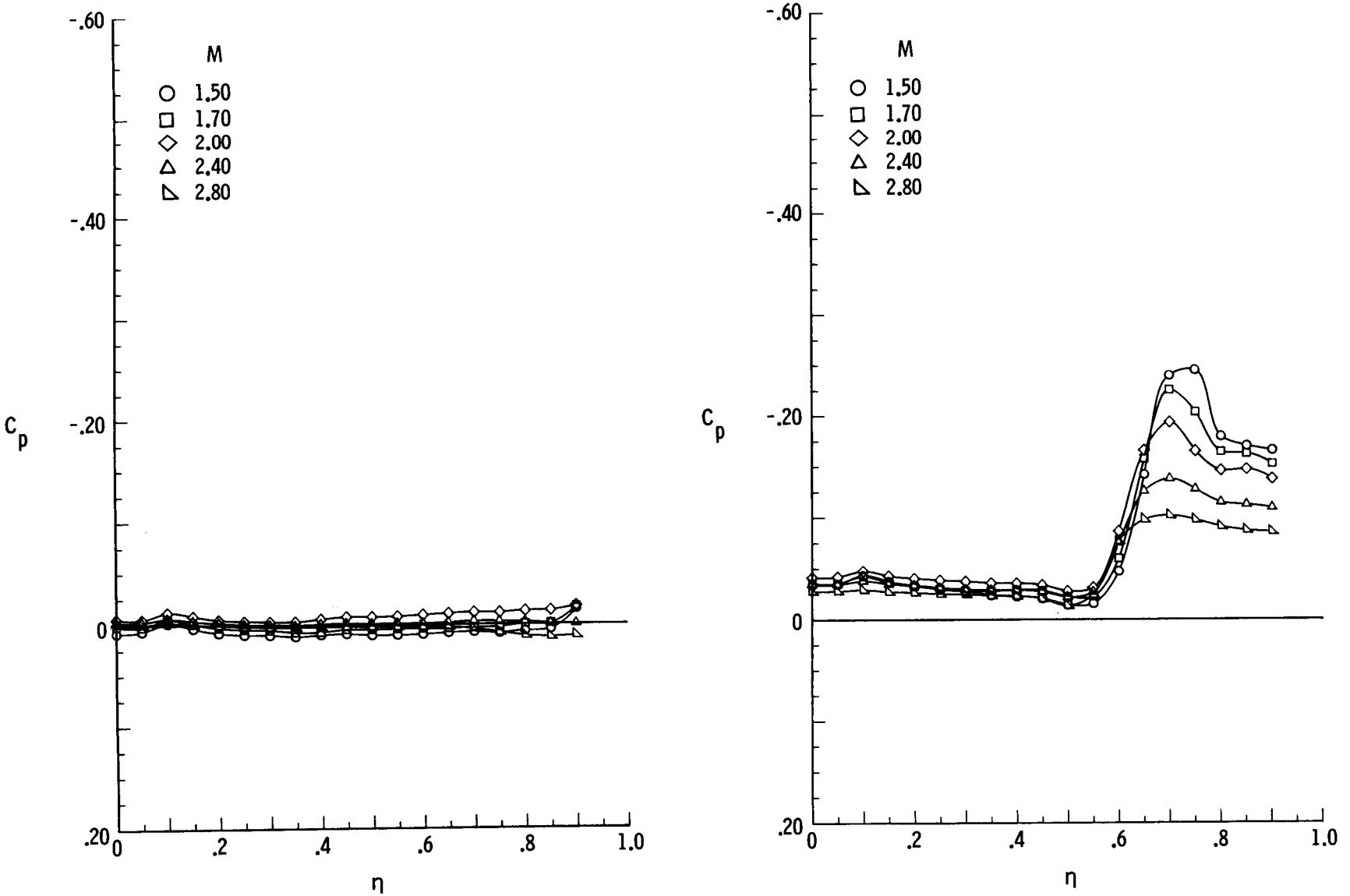

(a) $\alpha = 0°$.

(b) $\alpha = 4°$.

Figure B1.- Pressure plots for 75° delta wing with $\delta_F = 0°$ for varying M, $R = 2 \times 10^6$, $\beta = 0°$, and $x/\ell = 0.90$.

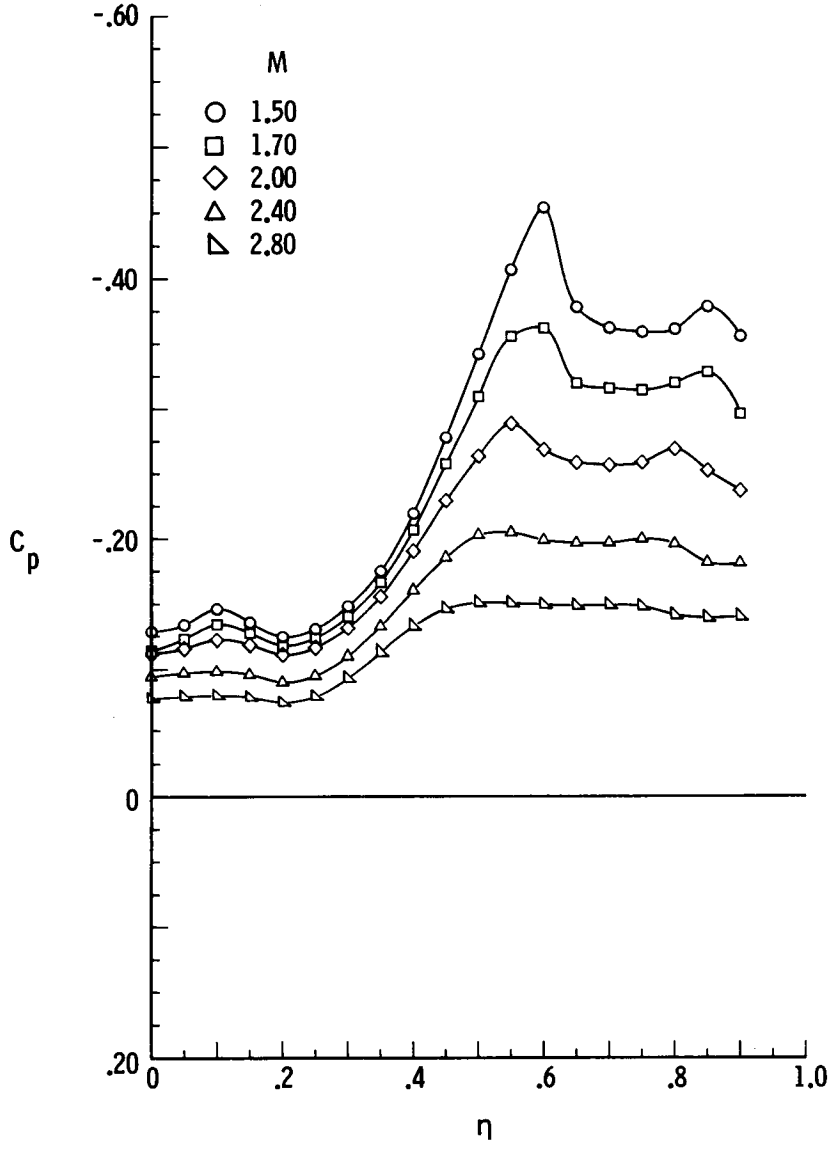

(c) $\alpha = 12°$.

Figure B1.- Concluded.

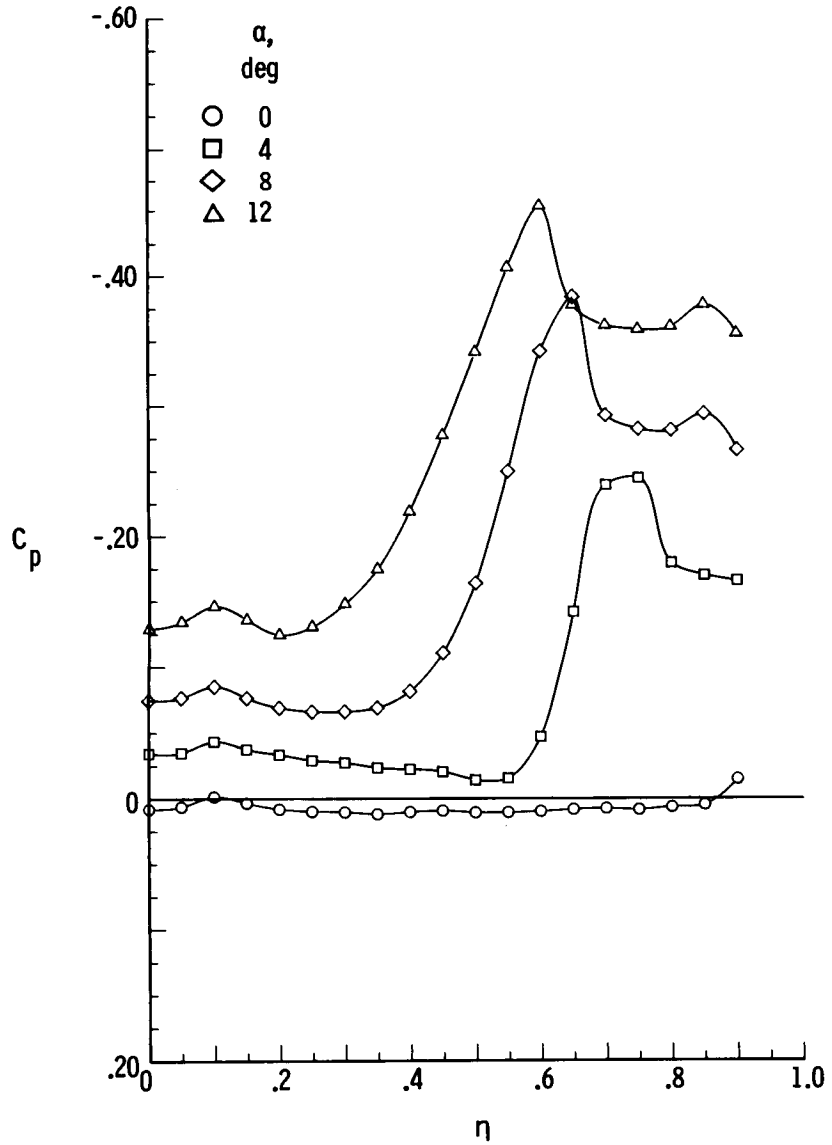

(a) M = 1.50.

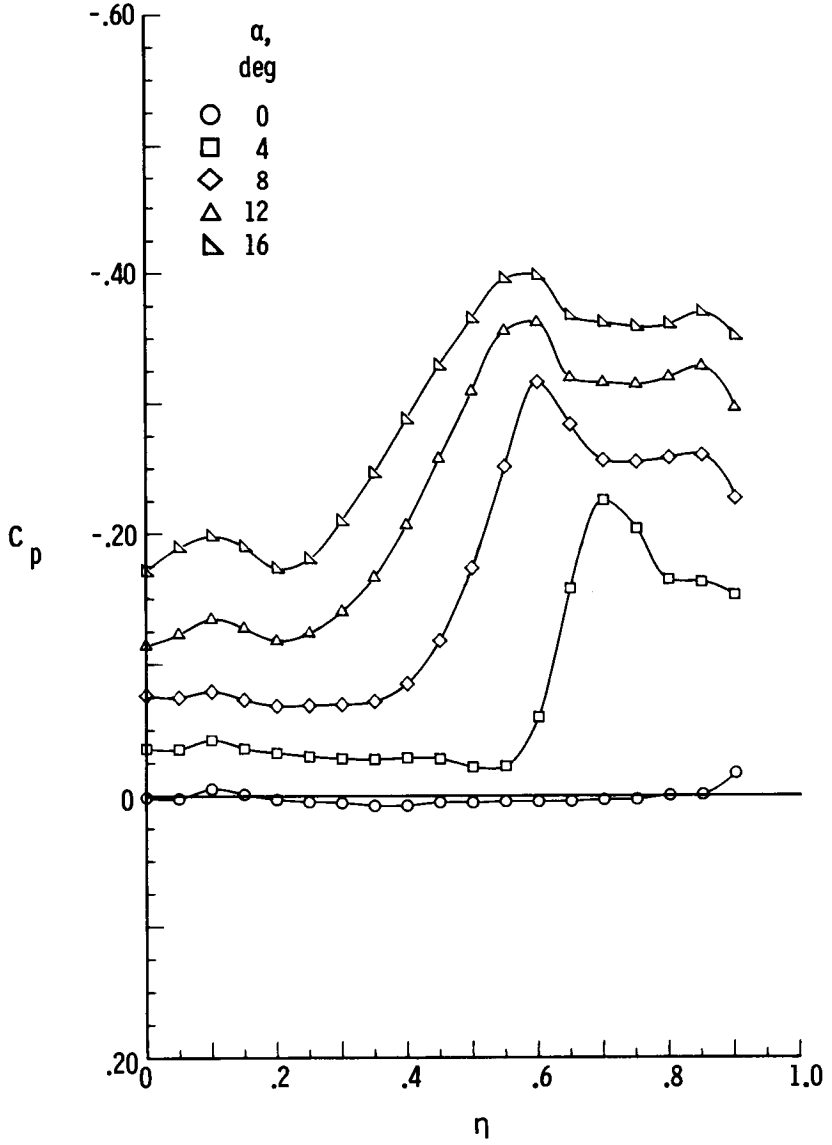

(b) M = 1.70.

Figure B2.- Pressure plots for 75° delta wing with $\delta_F = 0°$ for varying α, $R = 2 \times 10^6$, $\beta = 0°$, and $x/\ell = 0.90$.

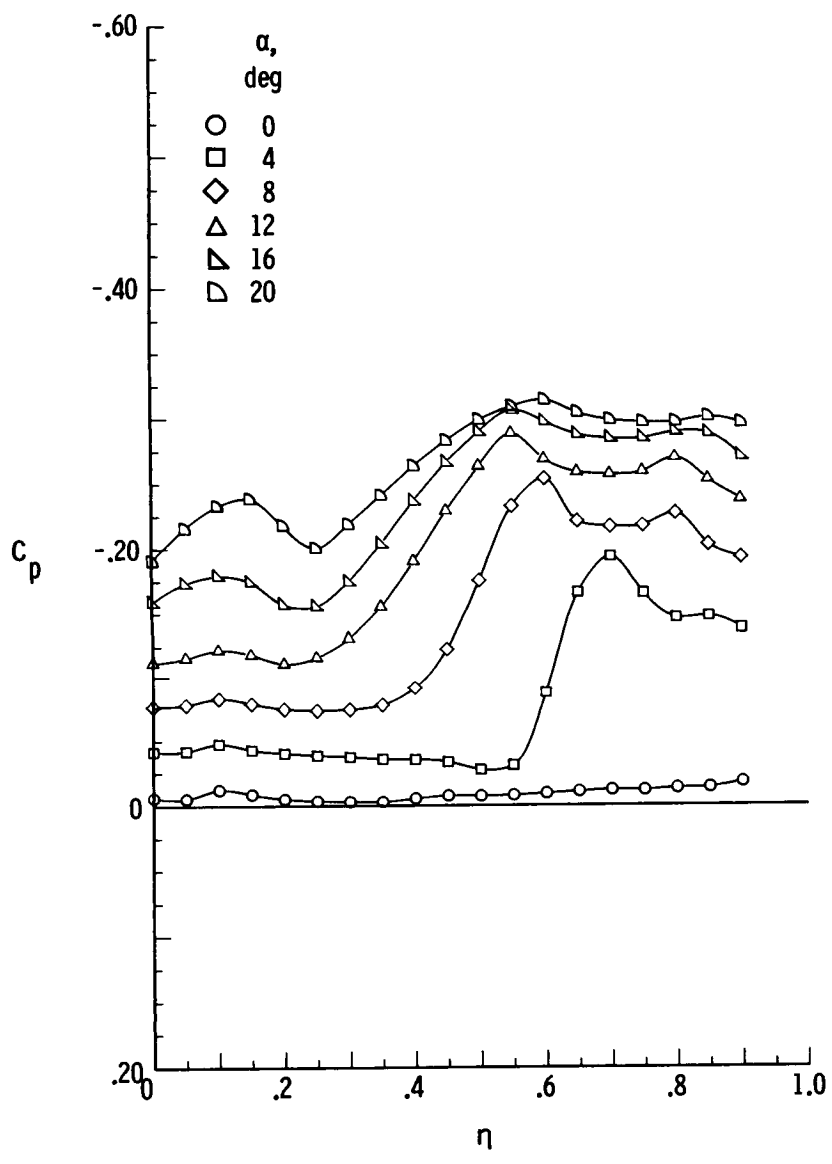

(c) M = 2.00.

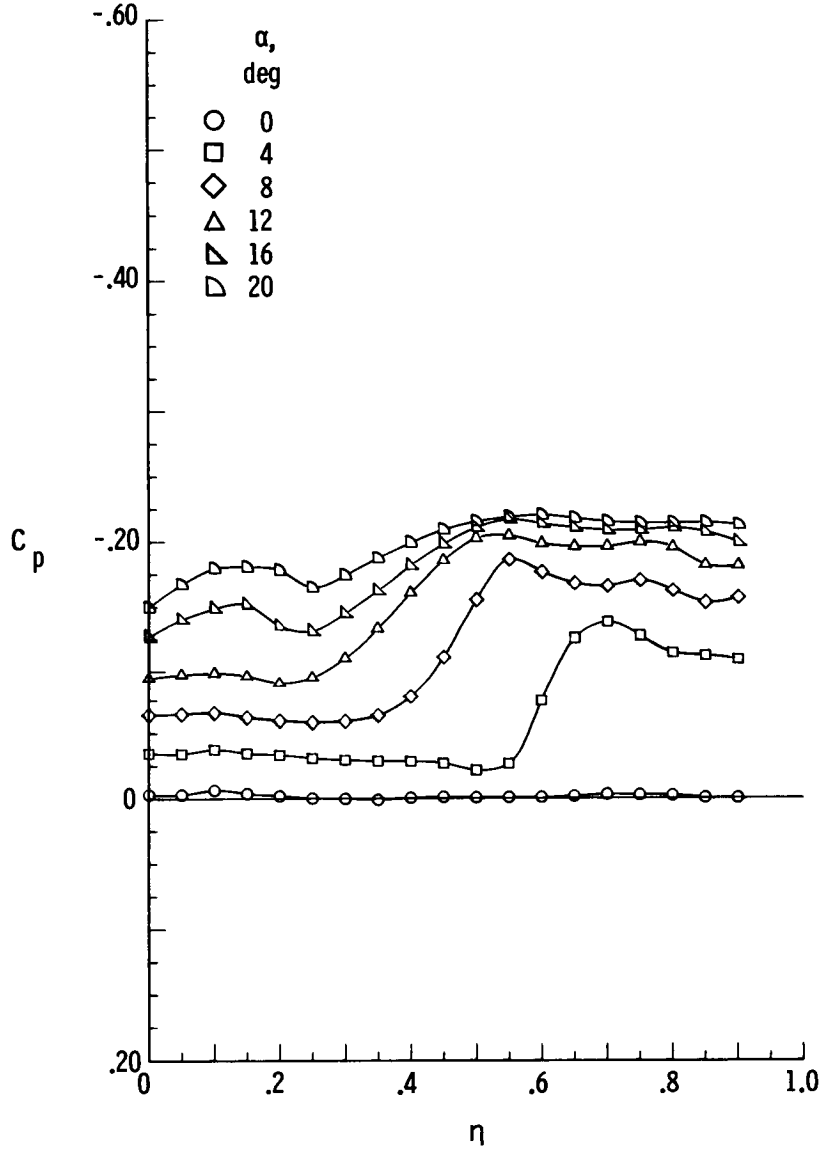

(d) M = 2.40.

Figure B2.- Continued.

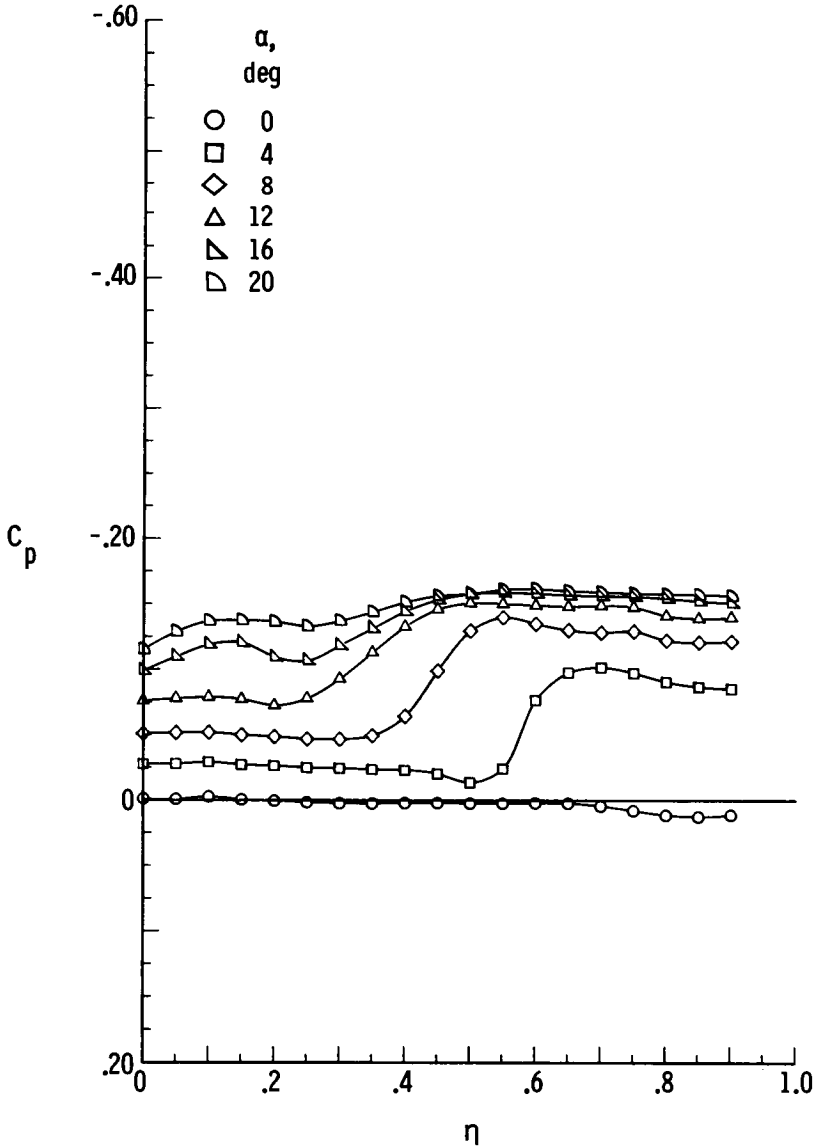

(e) M = 2.80.

Figure B2.- Concluded.

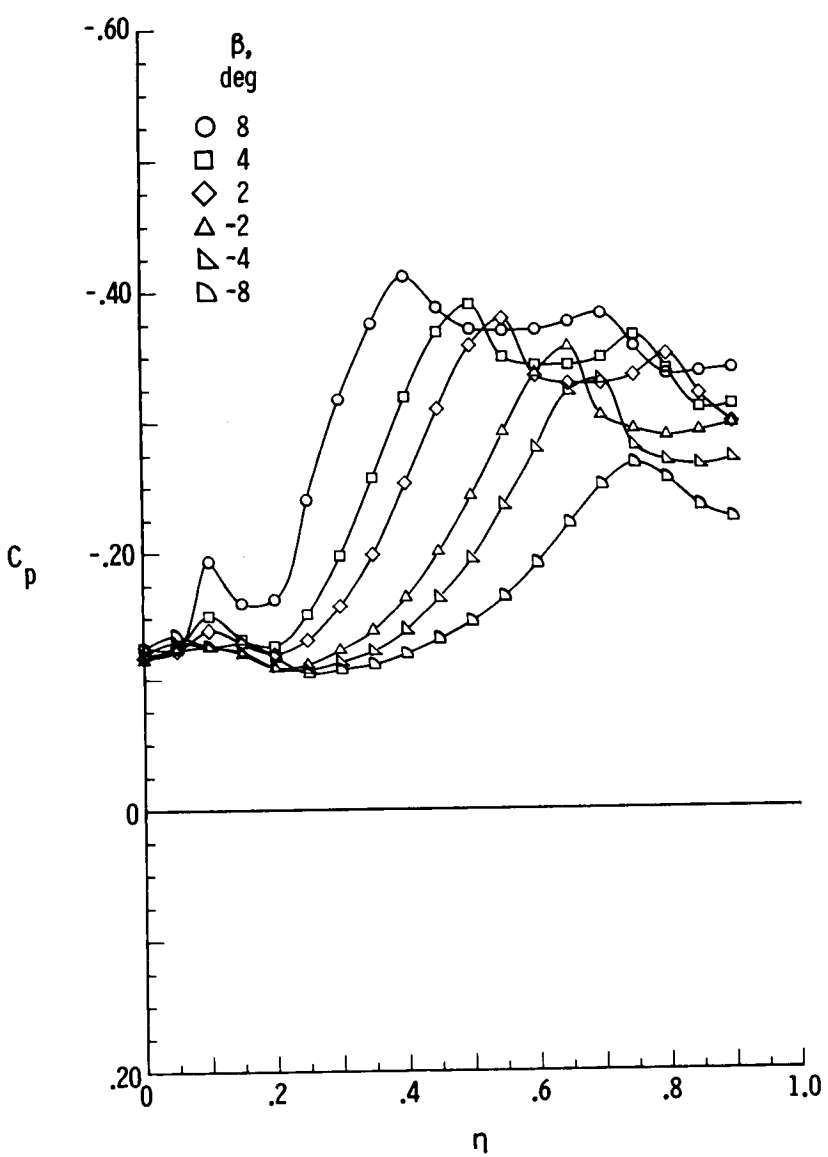

(a) M = 1.70.

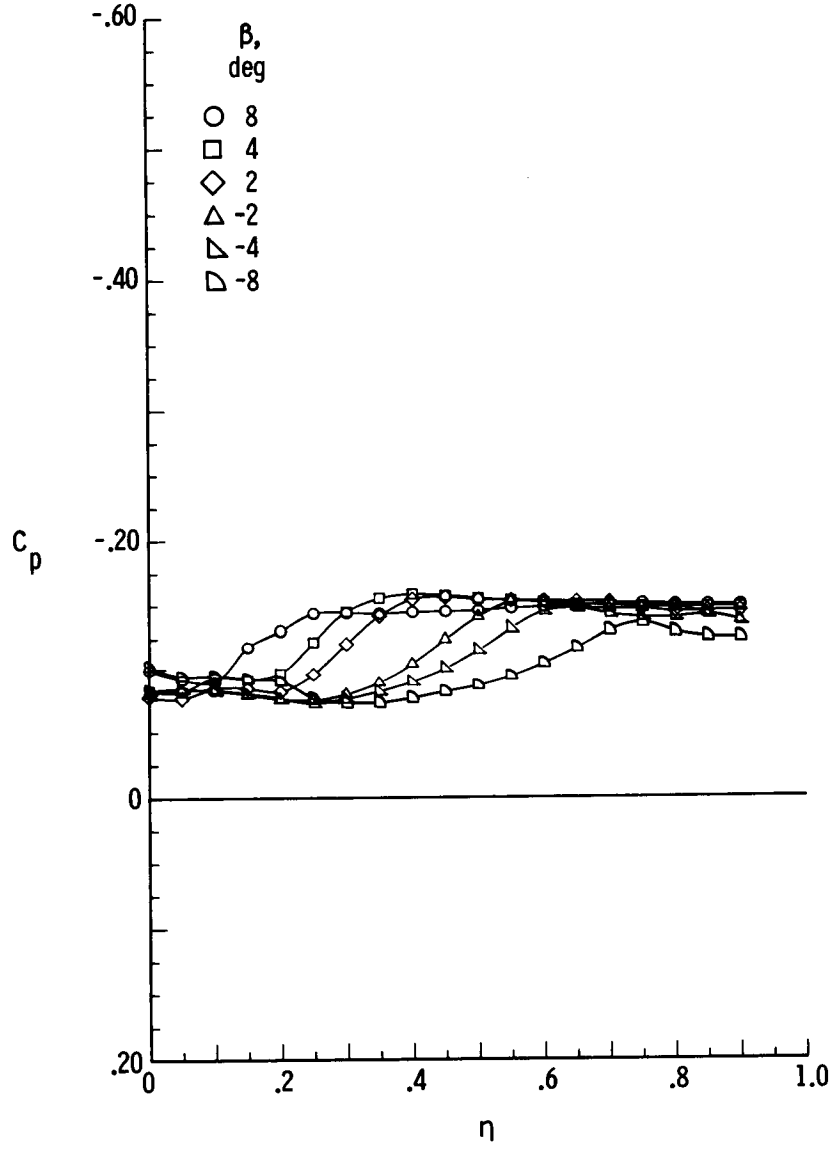

(b) M = 2.80.

Figure B3.- Pressure plots for 75° delta wing with $\delta_F = 0°$ for varying β, $R = 2 \times 10^6$, $\alpha = 12°$, and $x/\ell = 0.90$.

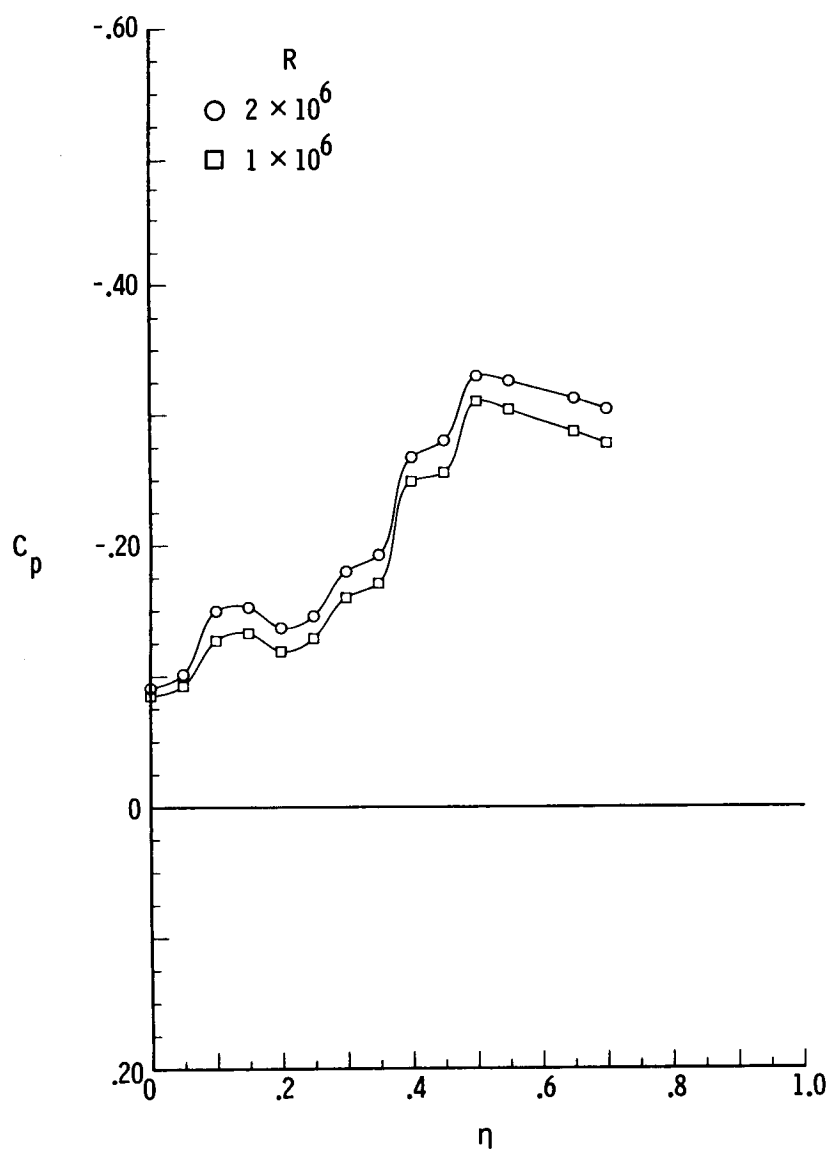

(a) M = 1.70; x/ℓ = 0.10.

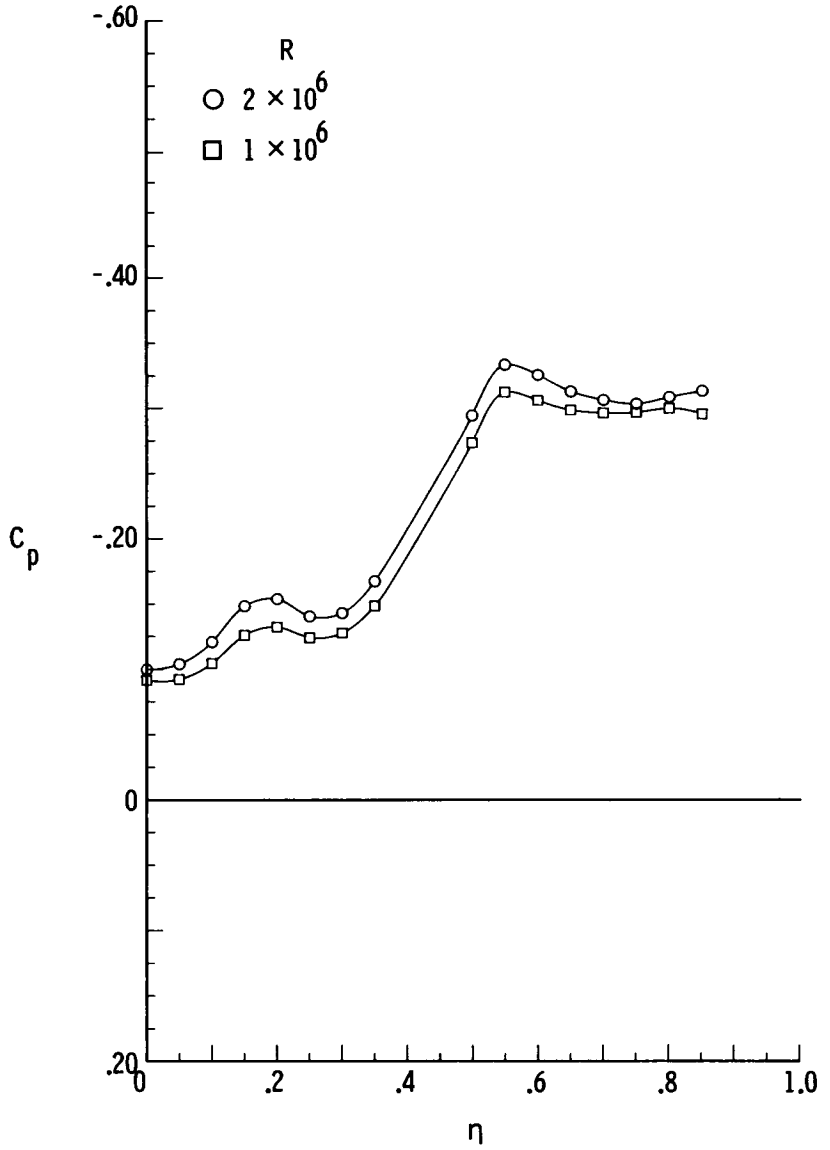

(b) M = 1.70; x/ℓ = 0.20.

Figure B4.- Pressure plots for 75° delta wing with δ_F = 0° for varying R, α = 12°, and β = 0°.

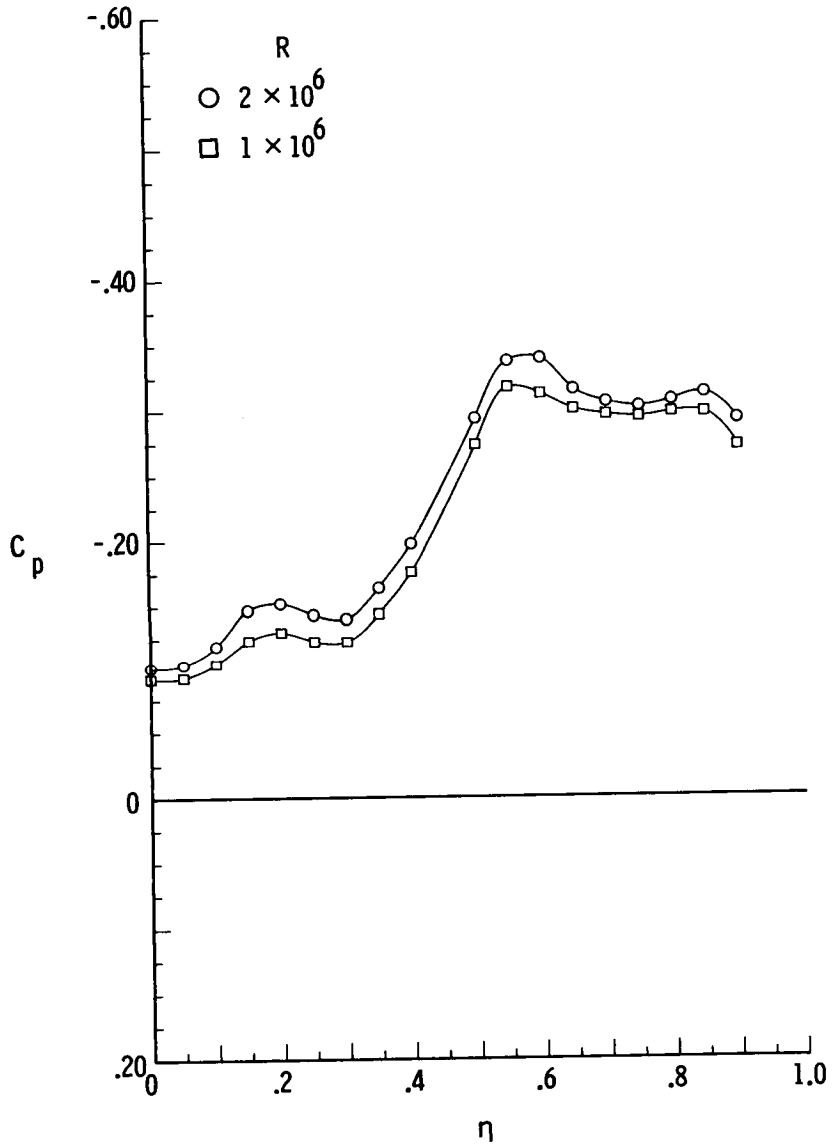

(c) M = 1.70; x/ℓ = 0.30.

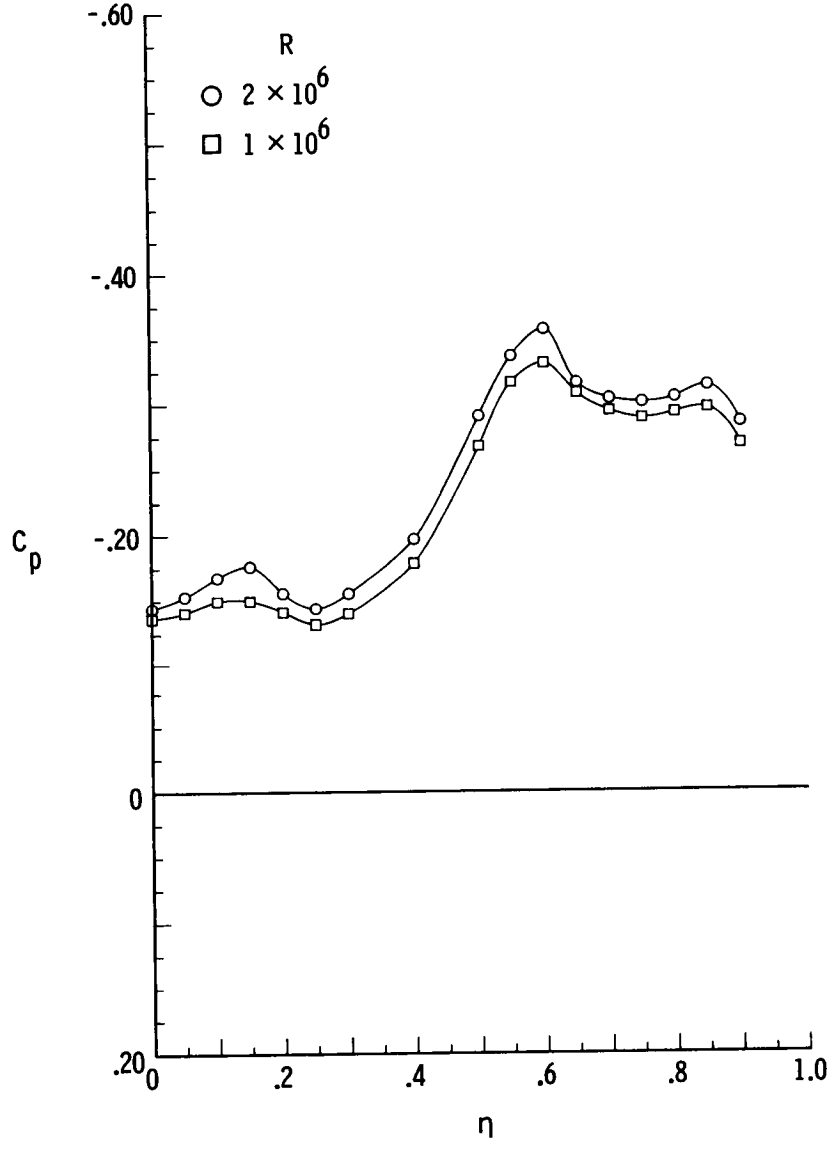

(d) M = 1.70; x/ℓ = 0.60.

Figure B4.- Continued.

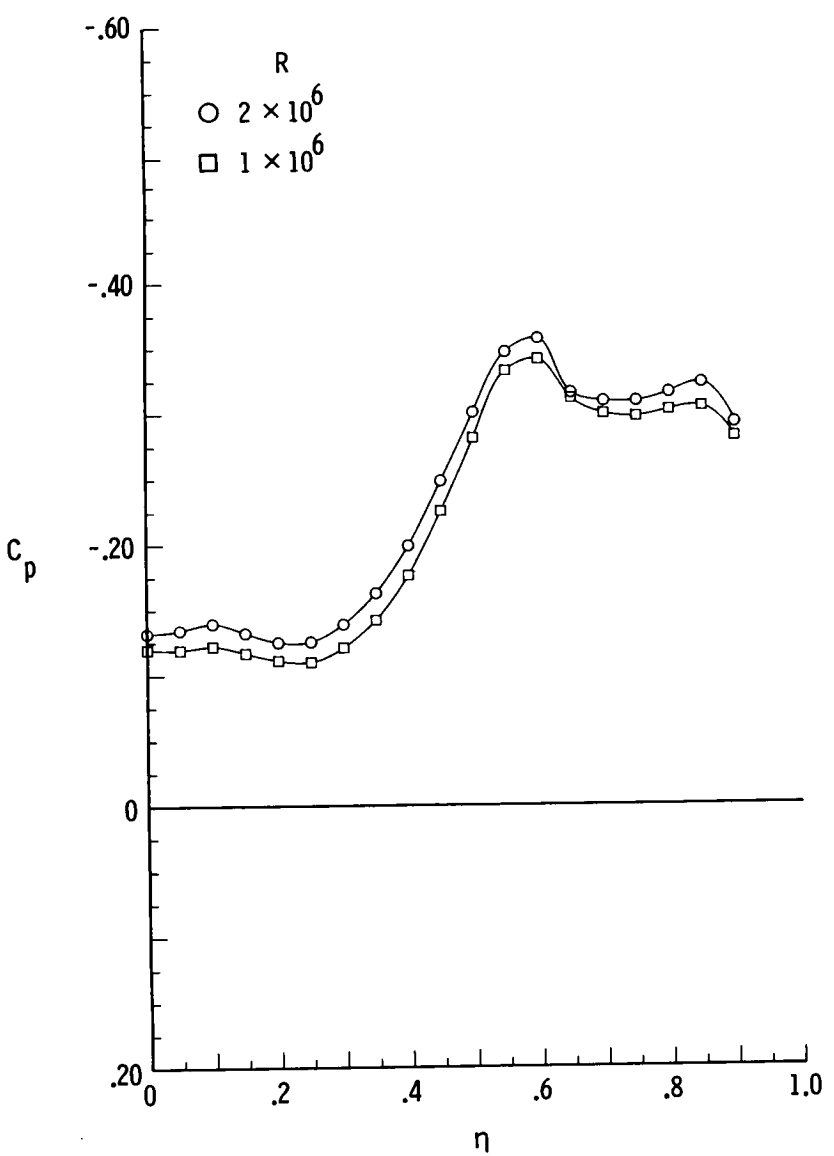

(e) M = 1.70; x/ℓ = 0.80.

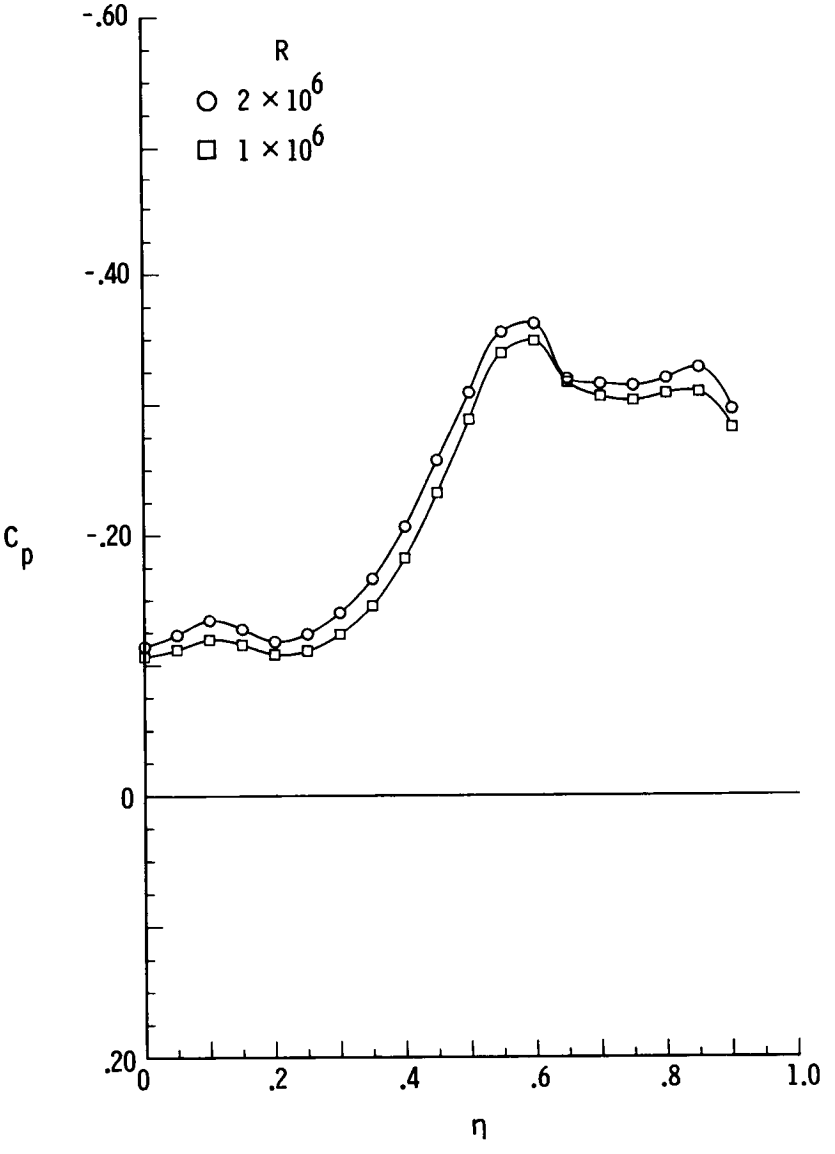

(f) M = 1.70; x/ℓ = 0.90.

Figure B4.- Continued.

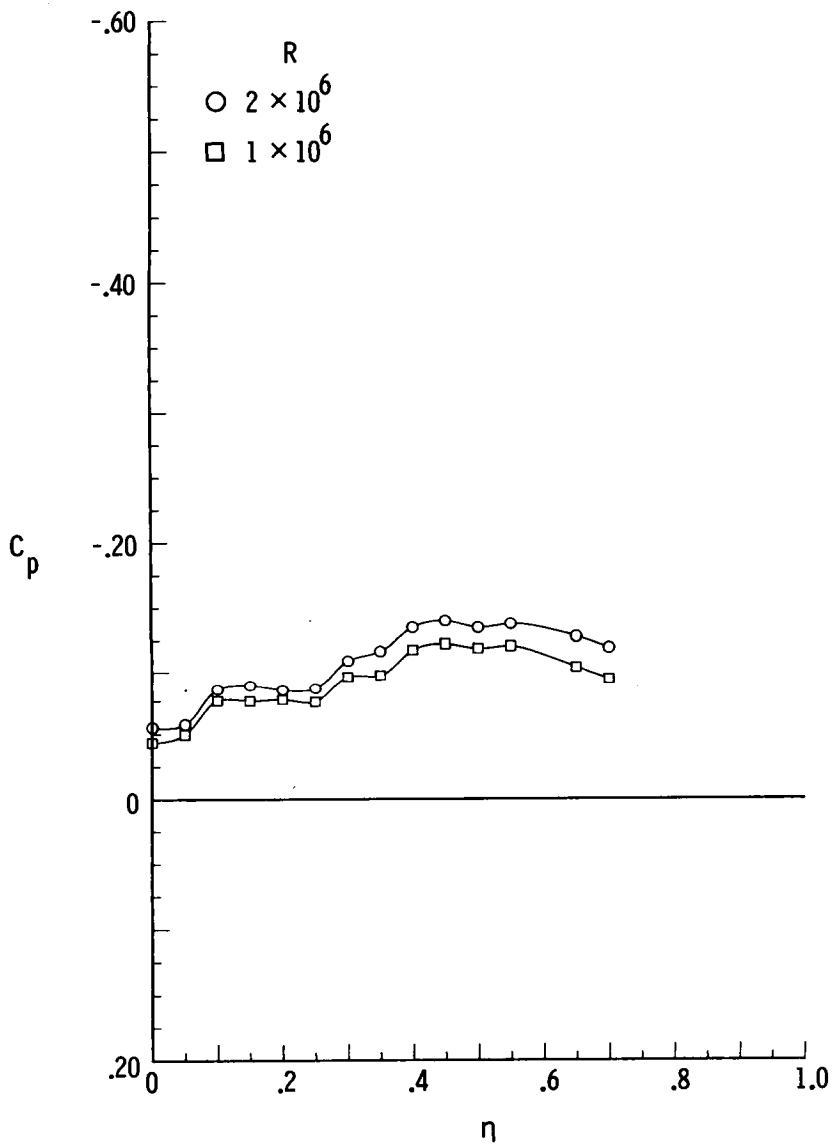

(g) M = 2.80; x/ℓ = 0.10.

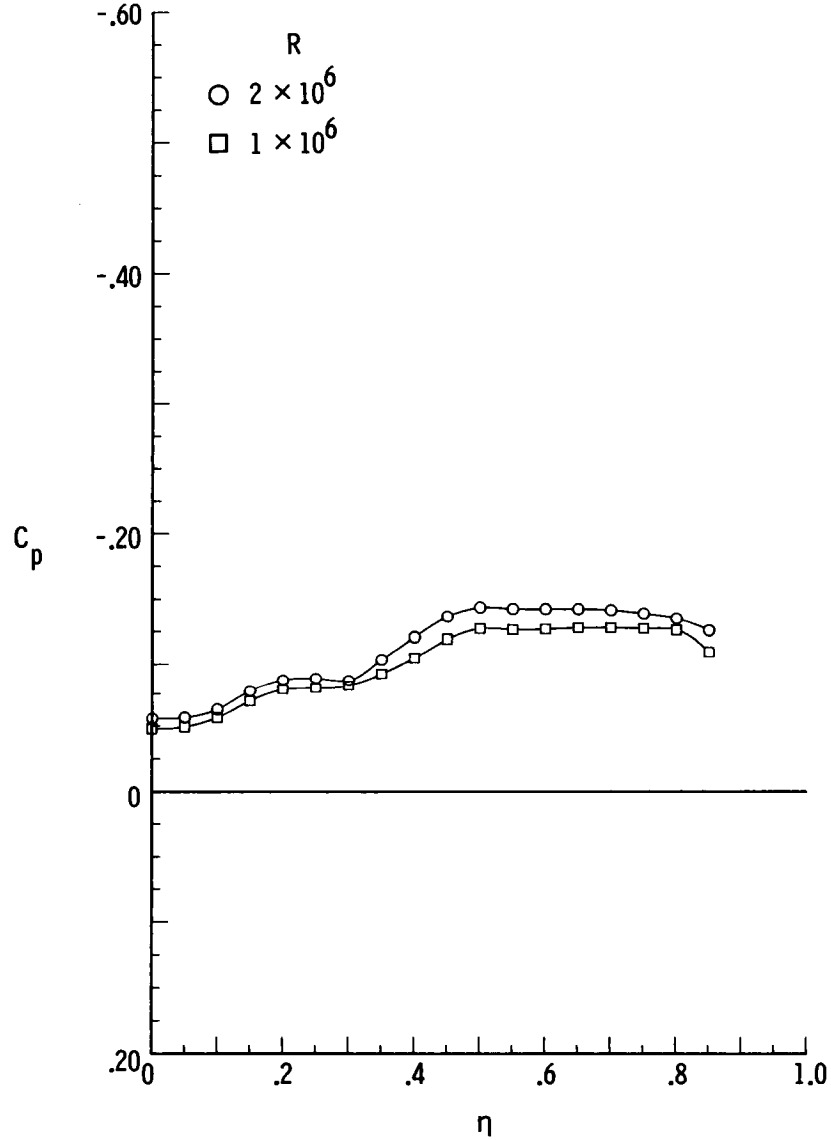

(h) M = 2.80; x/ℓ = 0.20.

Figure B4.- Continued.

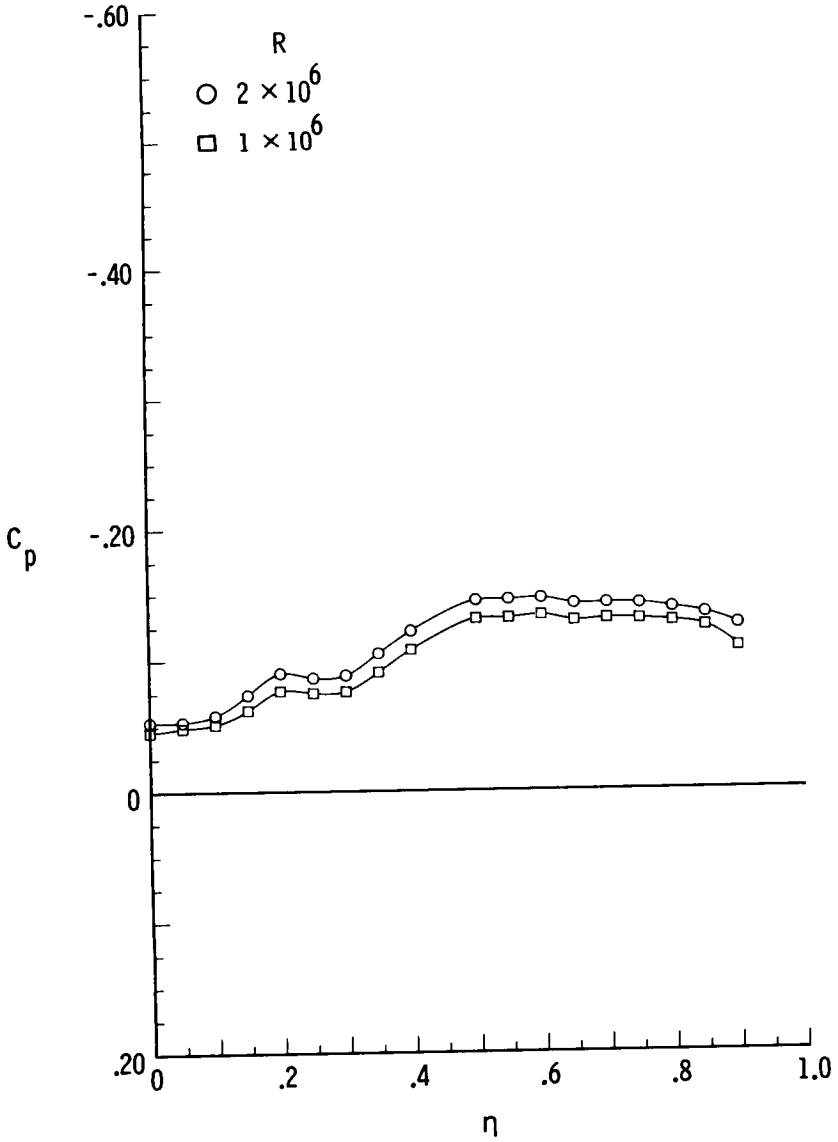

(i) M = 2.80; x/ℓ = 0.30.

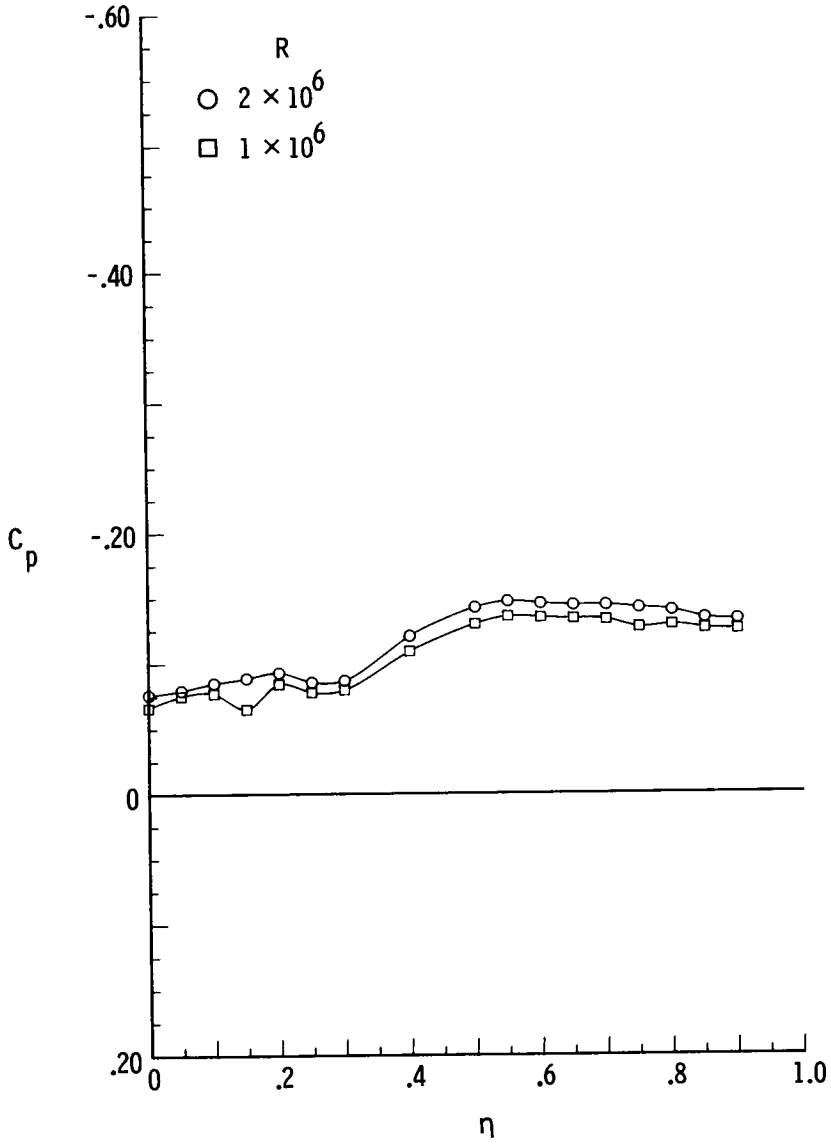

(j) M = 2.80; x/ℓ = 0.60.

Figure B4.- Continued.

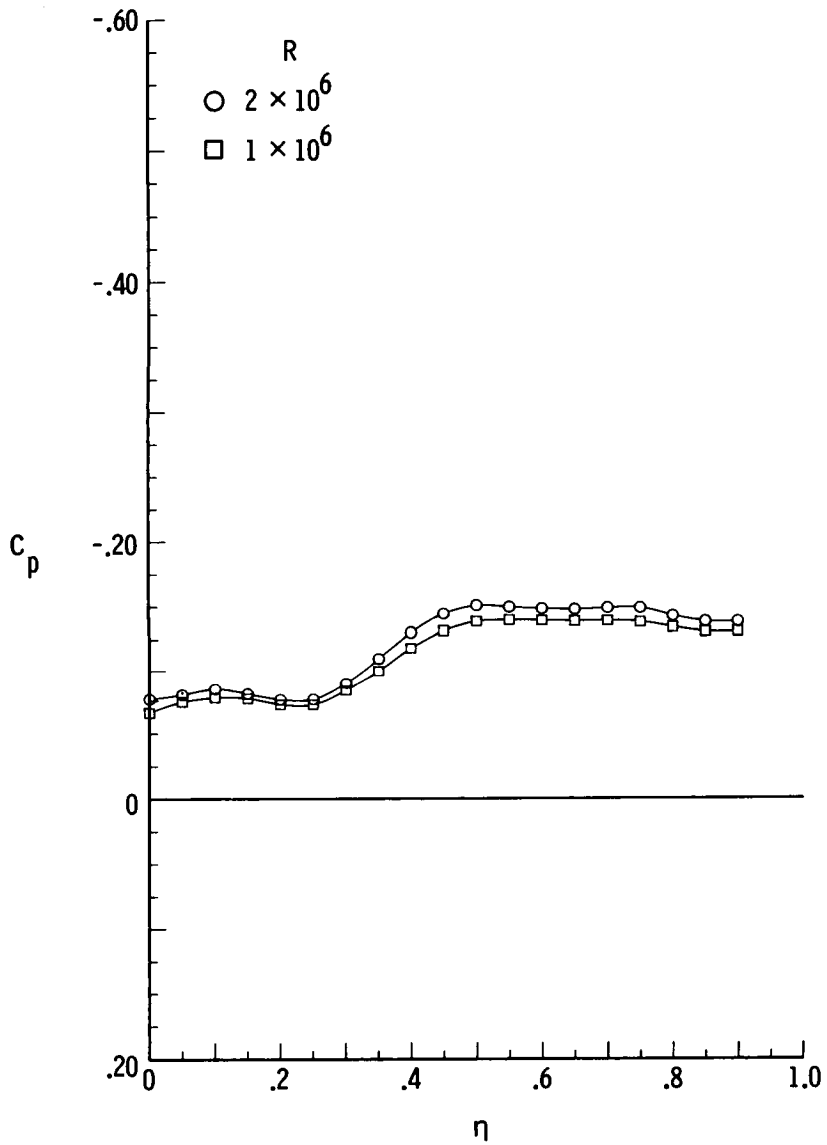

(k) M = 2.80; x/ℓ = 0.80.

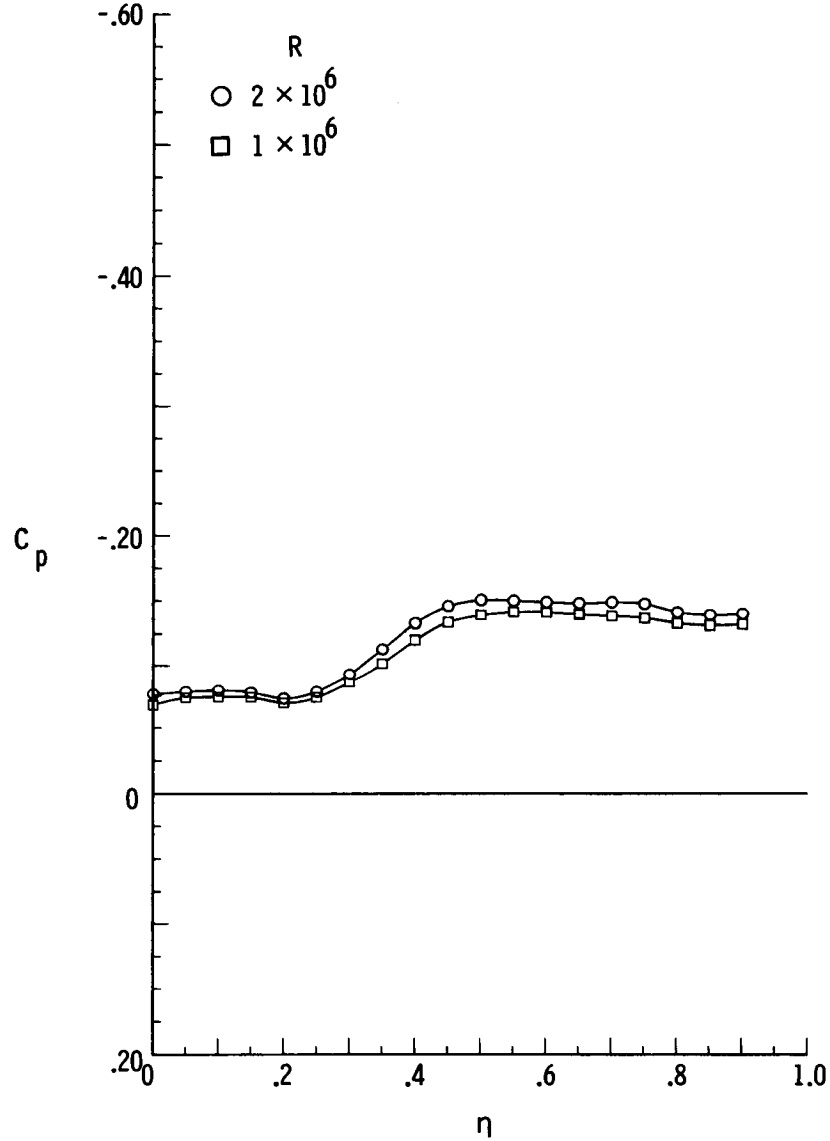

(l) M = 2.80; x/ℓ = 0.90.

Figure B4.- Concluded.

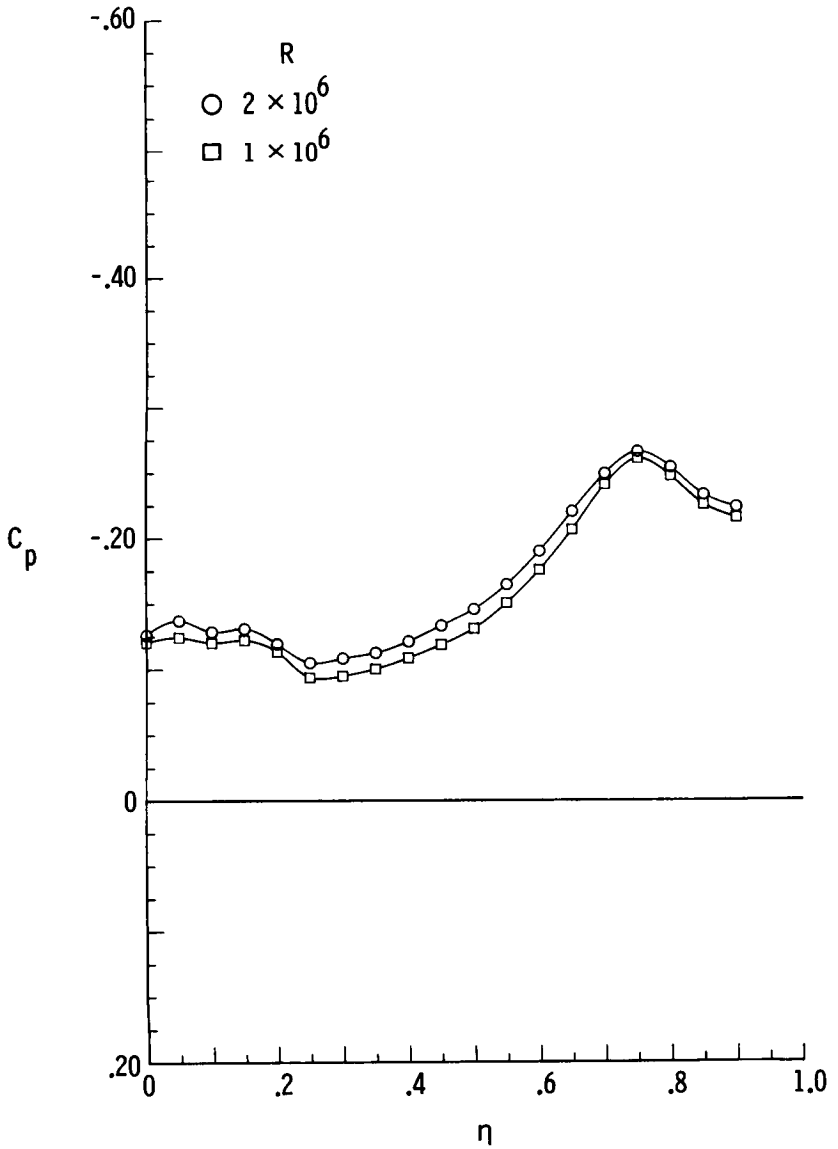

(a) M = 1.70; β = -8°.

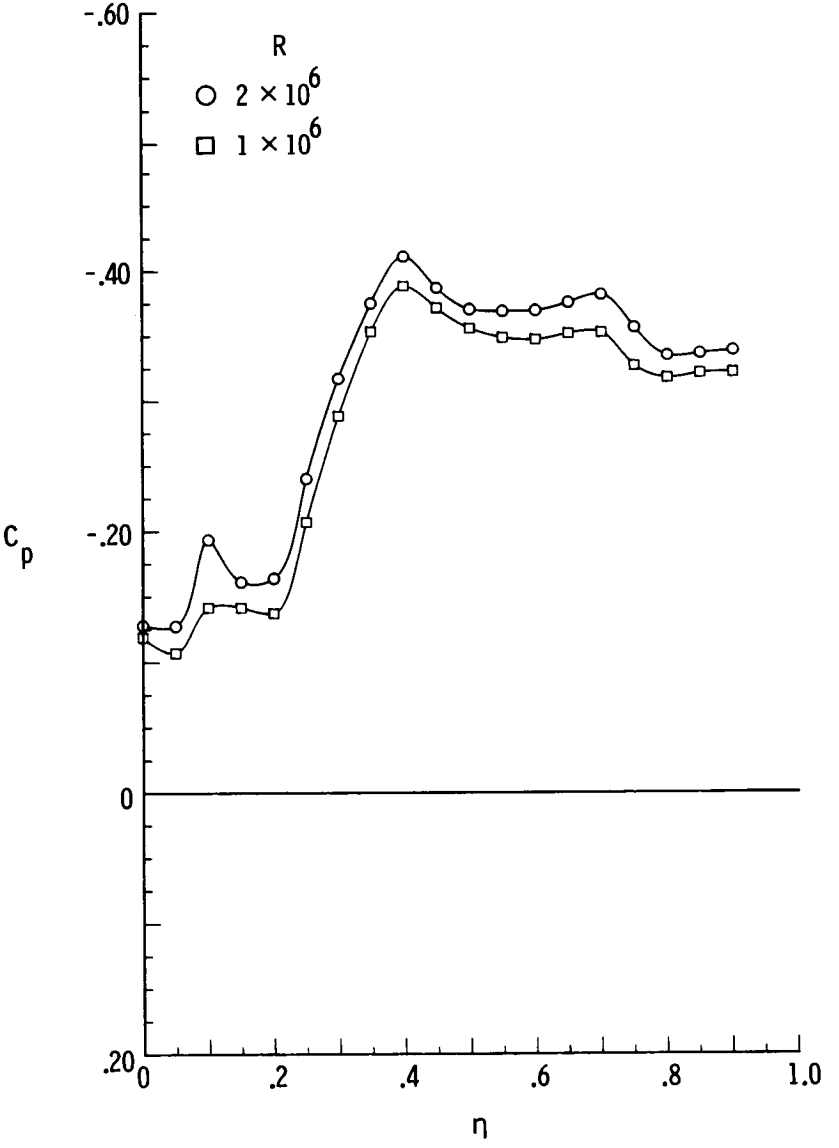

(b) M = 1.70; β = 8°.

Figure B5.- Pressure plots for 75° delta wing with δ_F = 0° for varying R, α = 12°, and x/ℓ = 0.90.

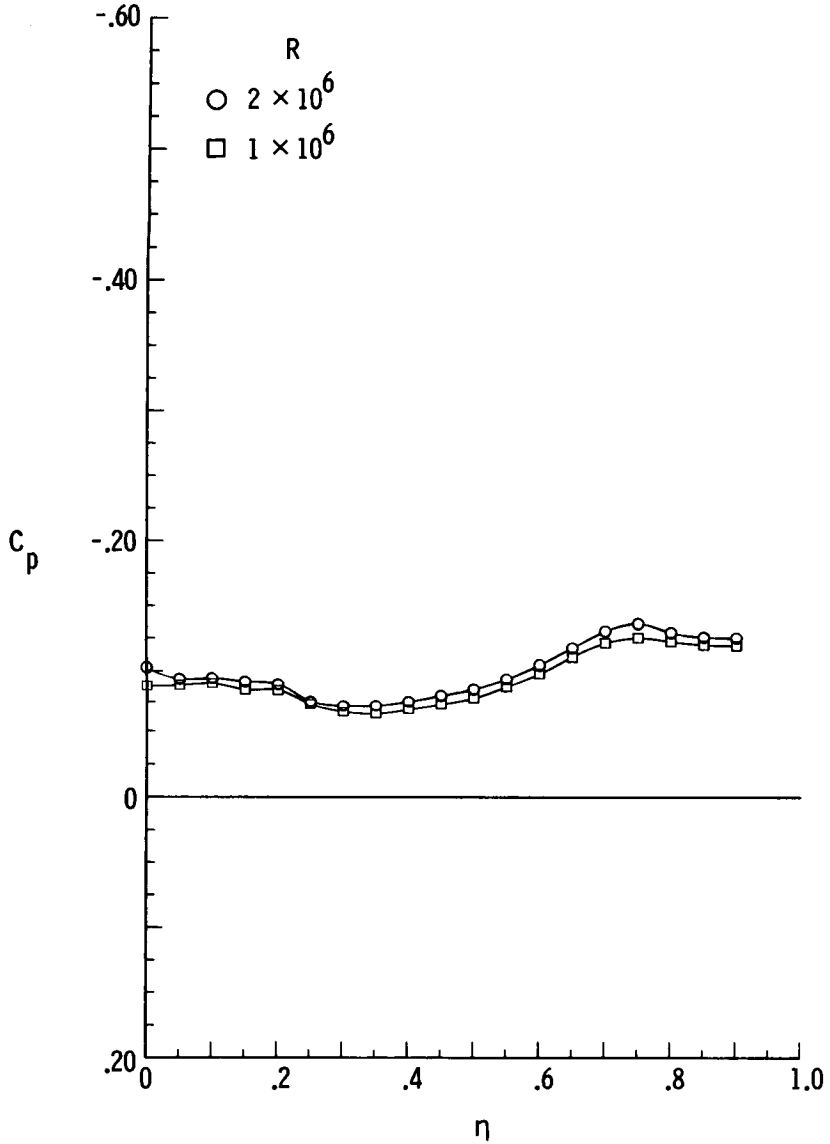

(c) M = 2.80; β = -8°.

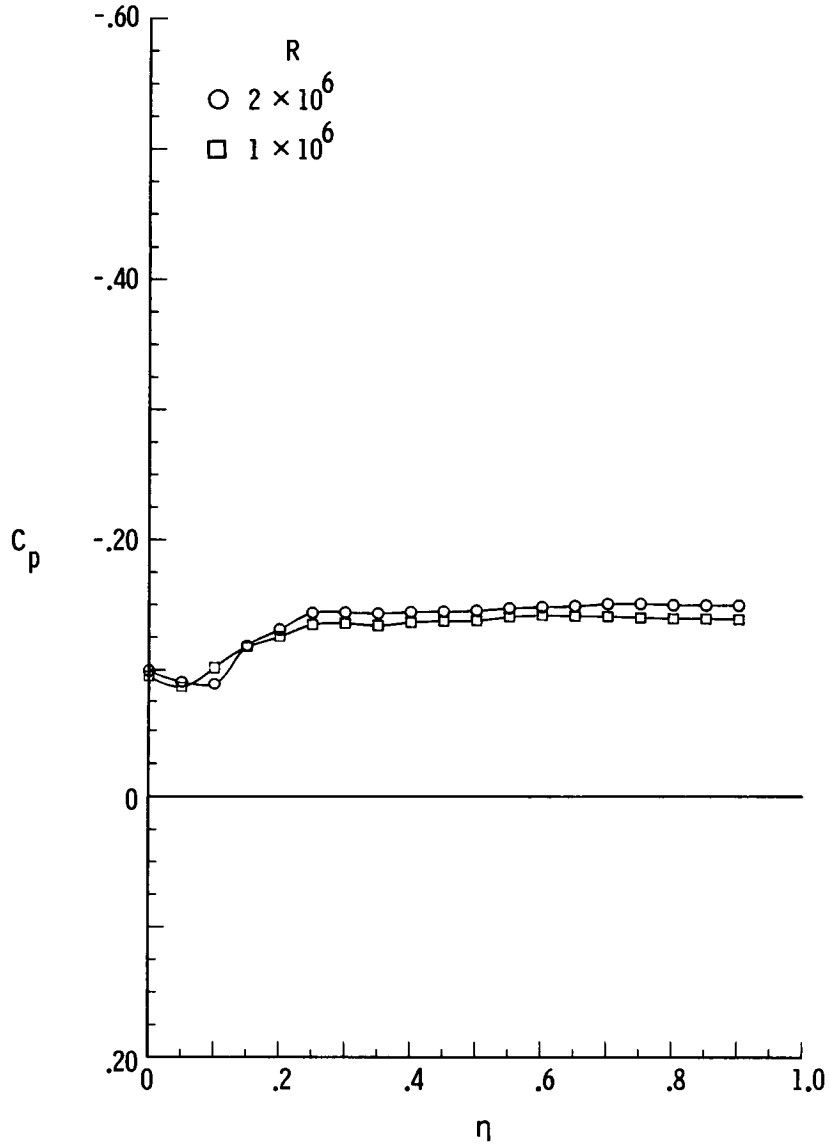

(d) M = 2.80; β = 8°.

Figure B5.- Concluded.

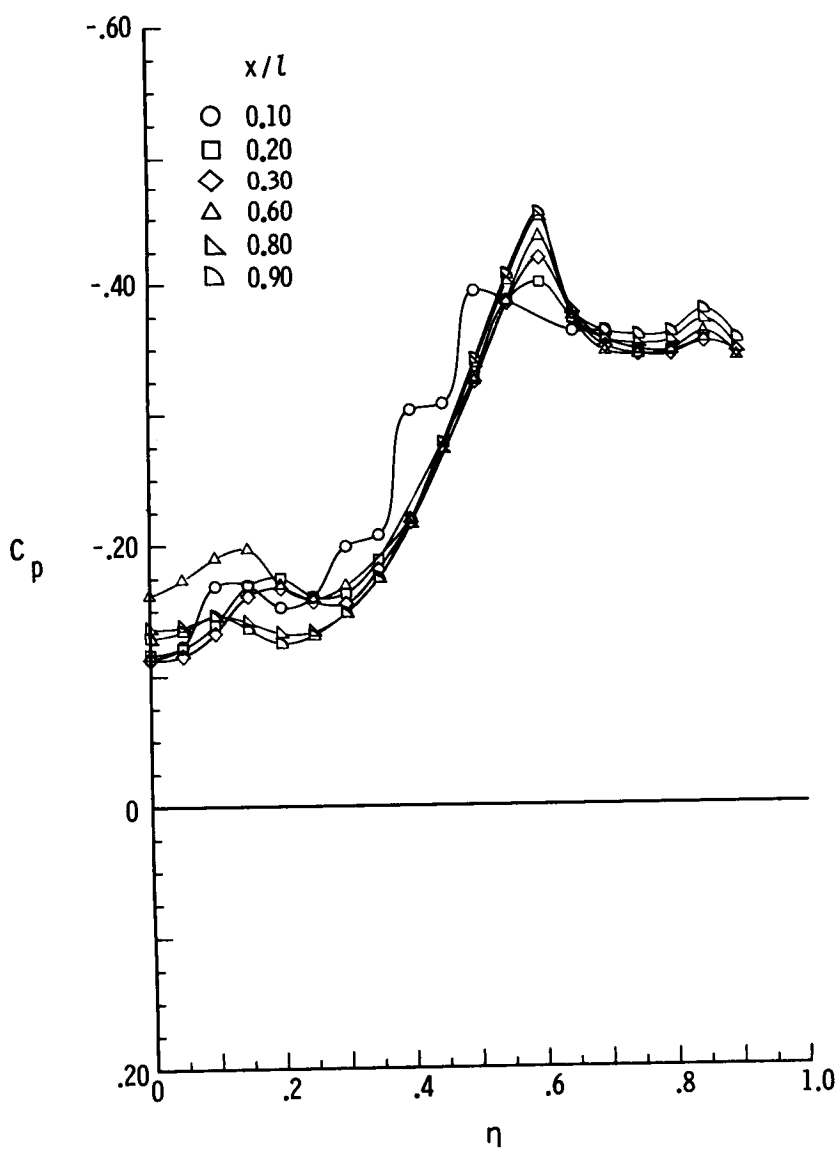

(a) M = 1.50; α = 12°.

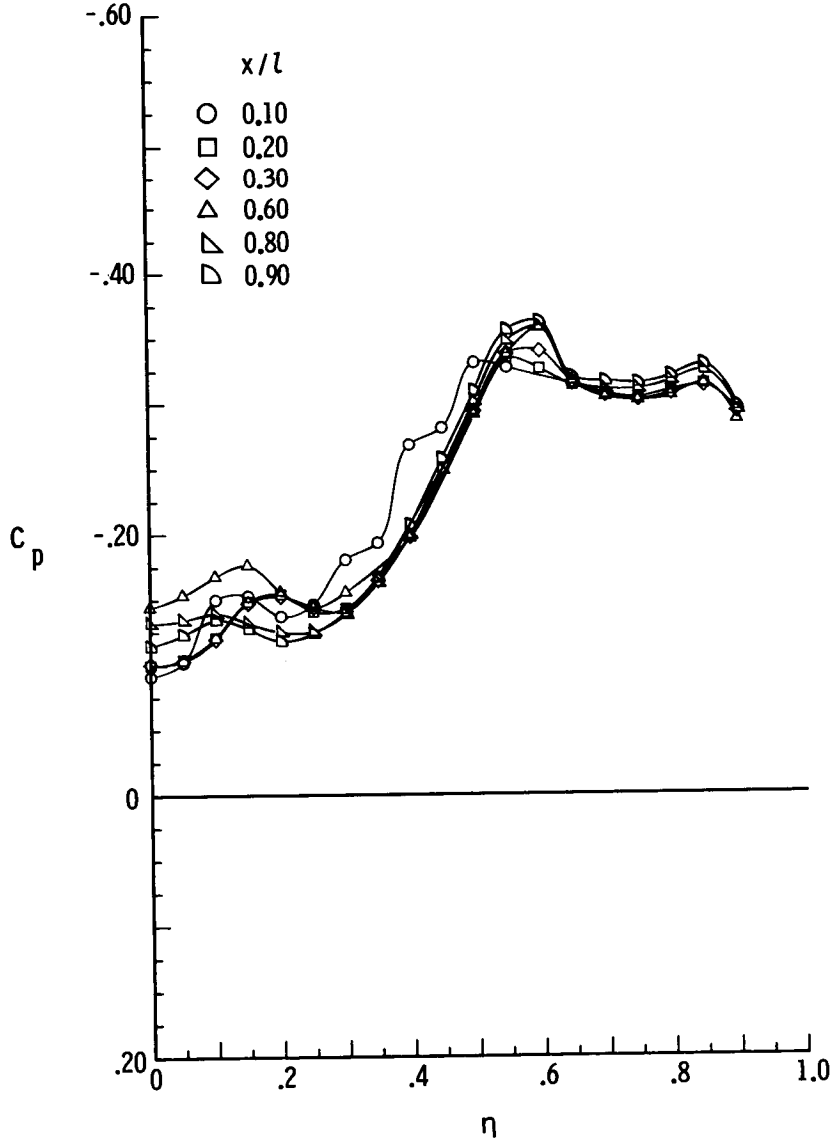

(b) M = 1.70; α = 12°.

Figure B6.- Pressure plots for 75° delta wing with δ_F = 0° for varying x/l, R = 2 × 10^6, and β = 0°.

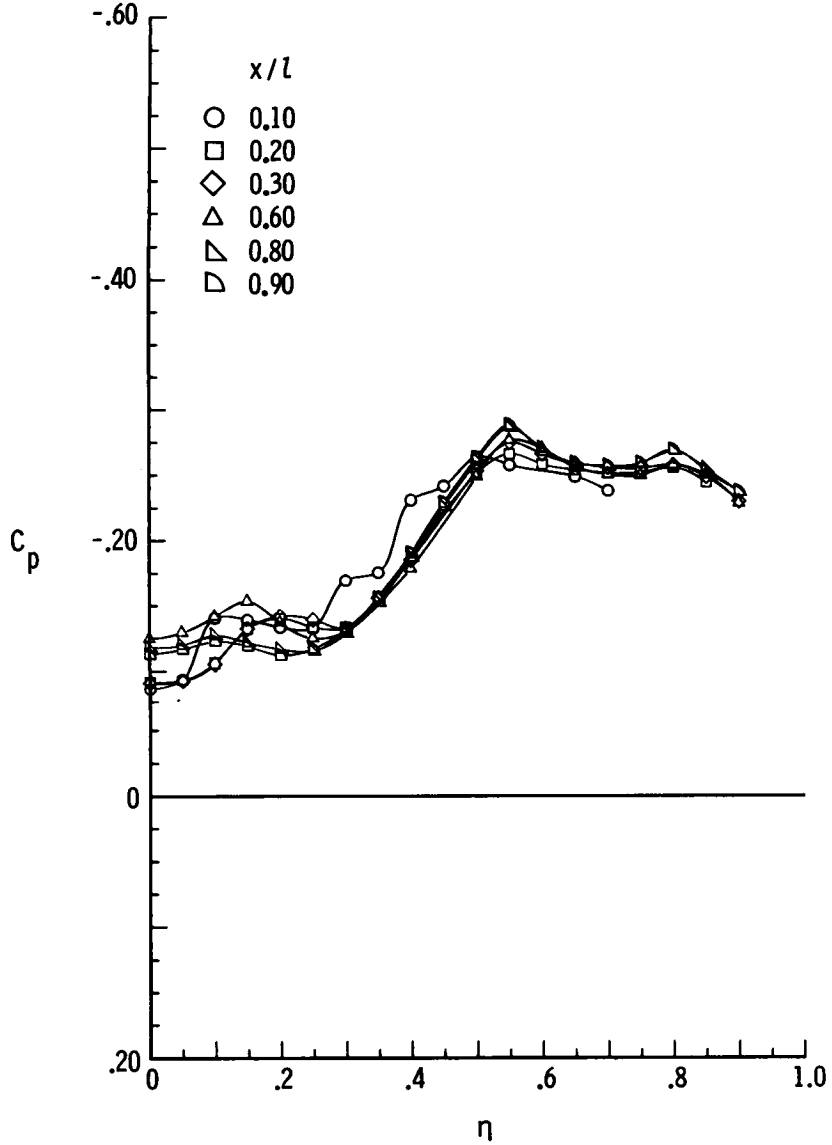

(c) M = 2.00; α = 12°.

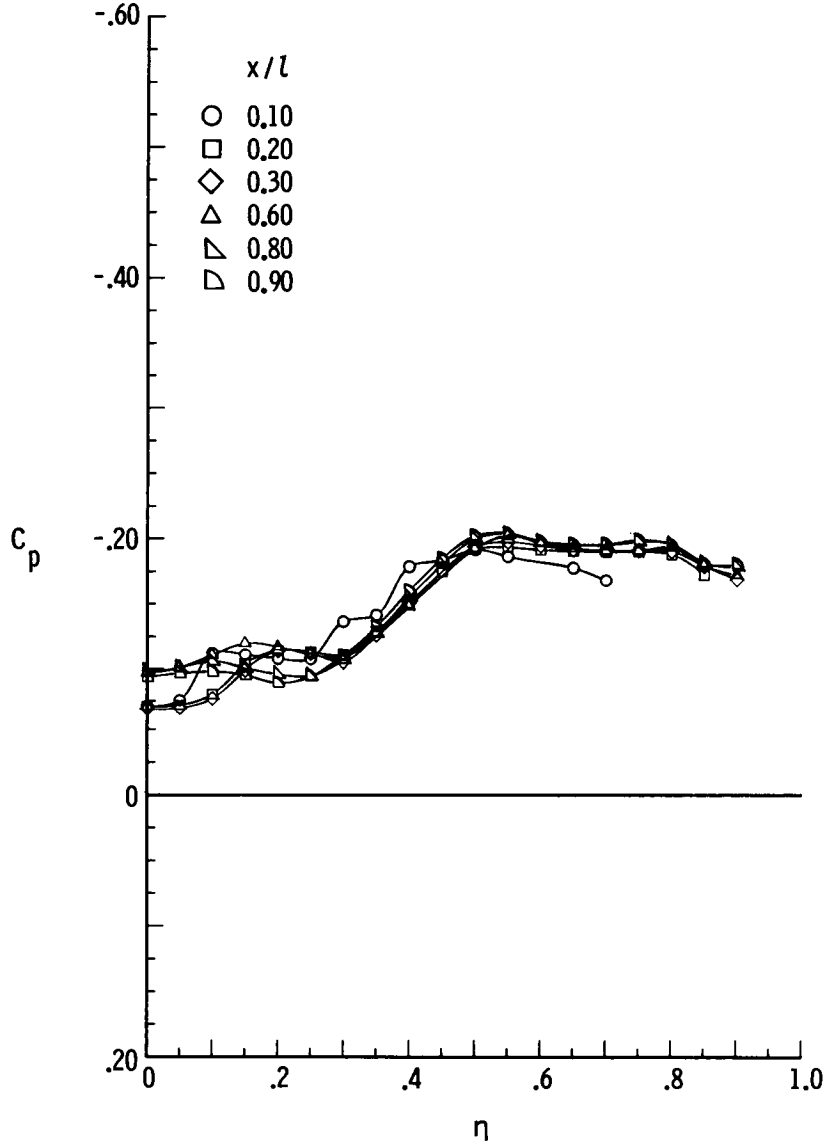

(d) M = 2.40; α = 12°.

Figure B6.- Continued.

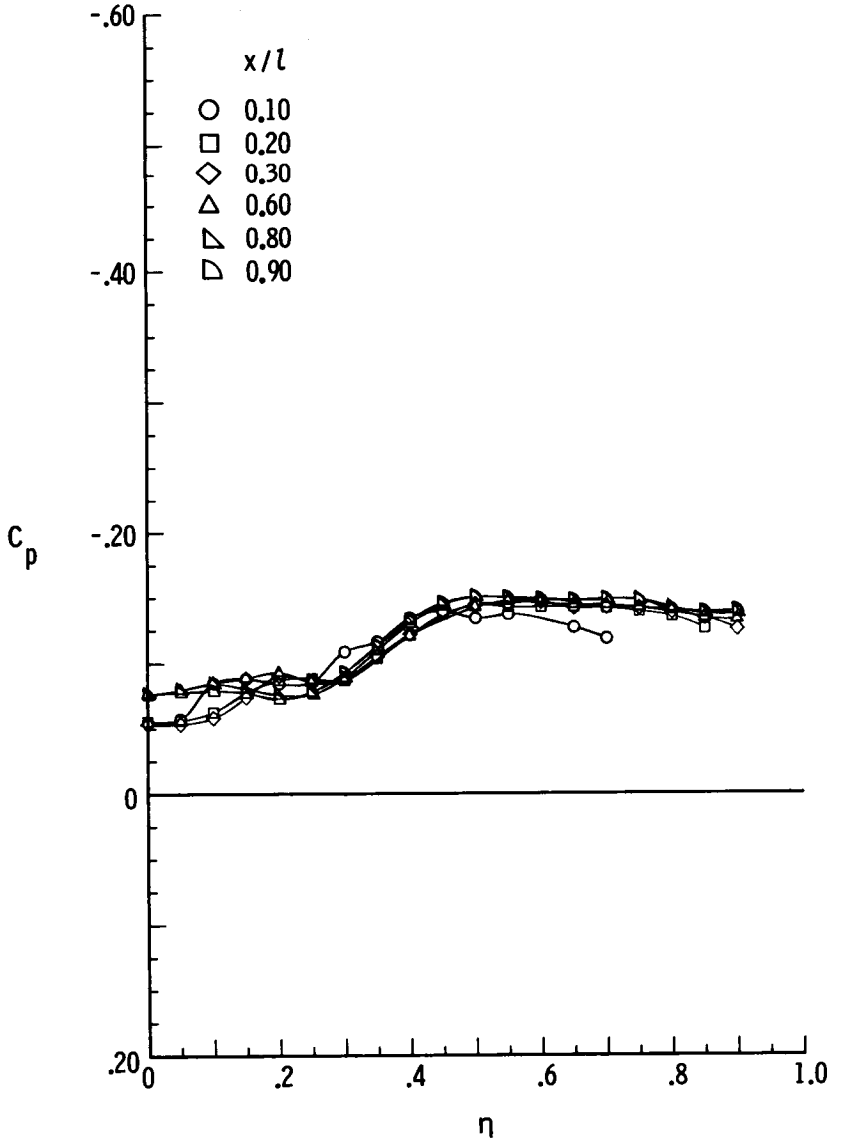

(e) M = 2.80; α = 12°.

Figure B6.- Concluded.

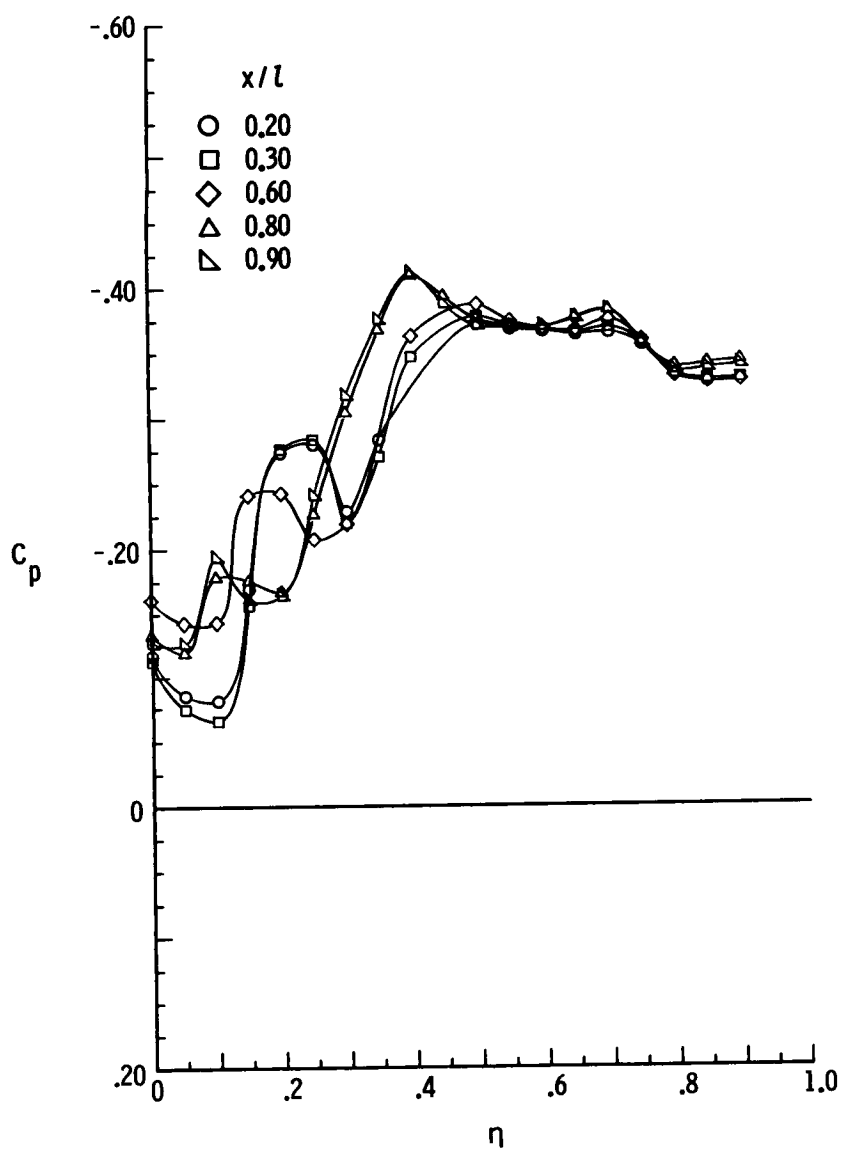

(a) M = 1.70; β = 8°.

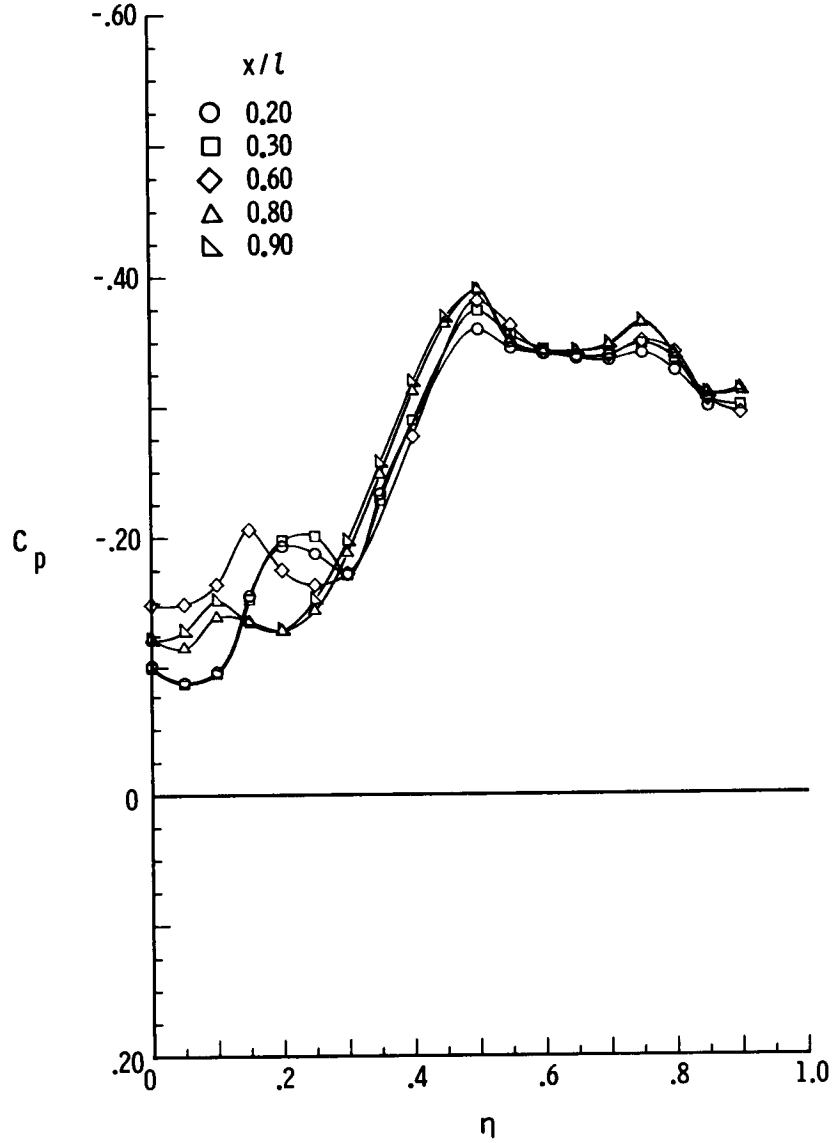

(b) M = 1.70; β = 4°.

Figure B7.- Pressure plots for 75° delta wing with $\delta_F = 0°$ for varying x/l, $R = 2 \times 10^6$, and $\alpha = 12°$.

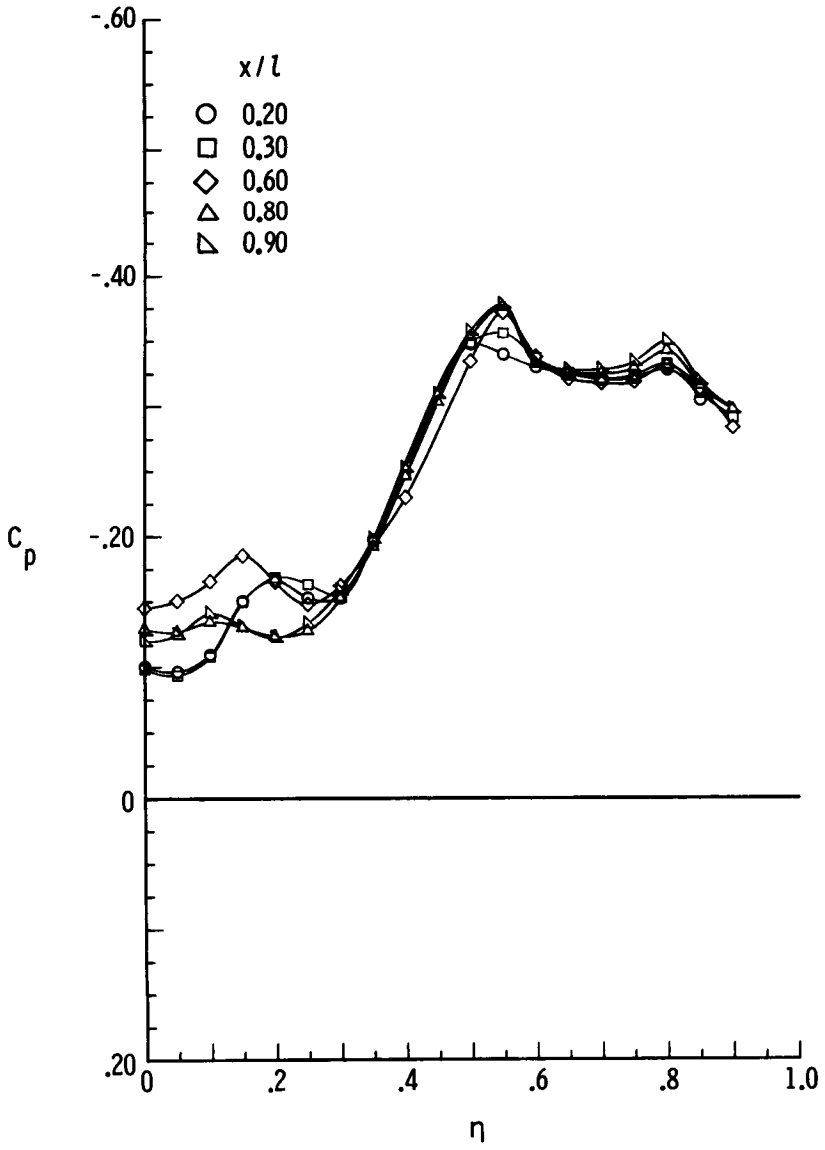

(c) M = 1.70; β = 2°.

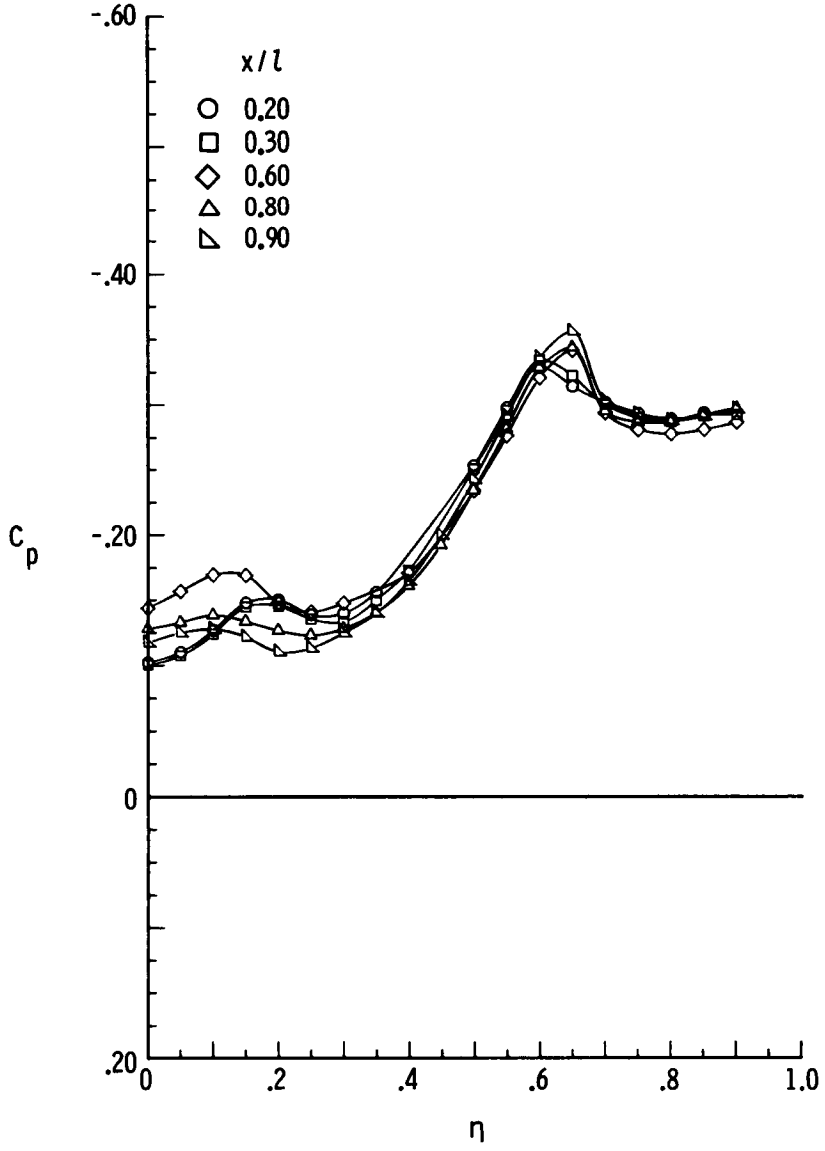

(d) M = 1.70; β = -2°.

Figure B7.- Continued.

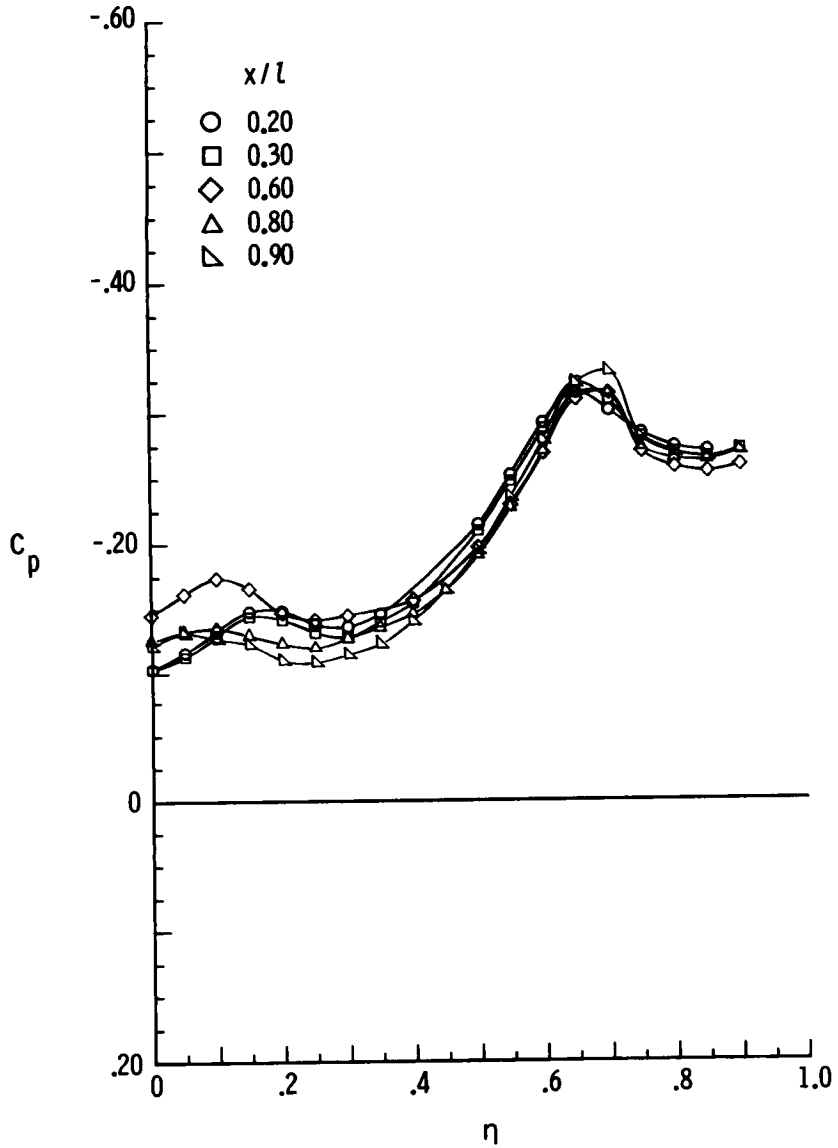

(e) M = 1.70; β = -4°.

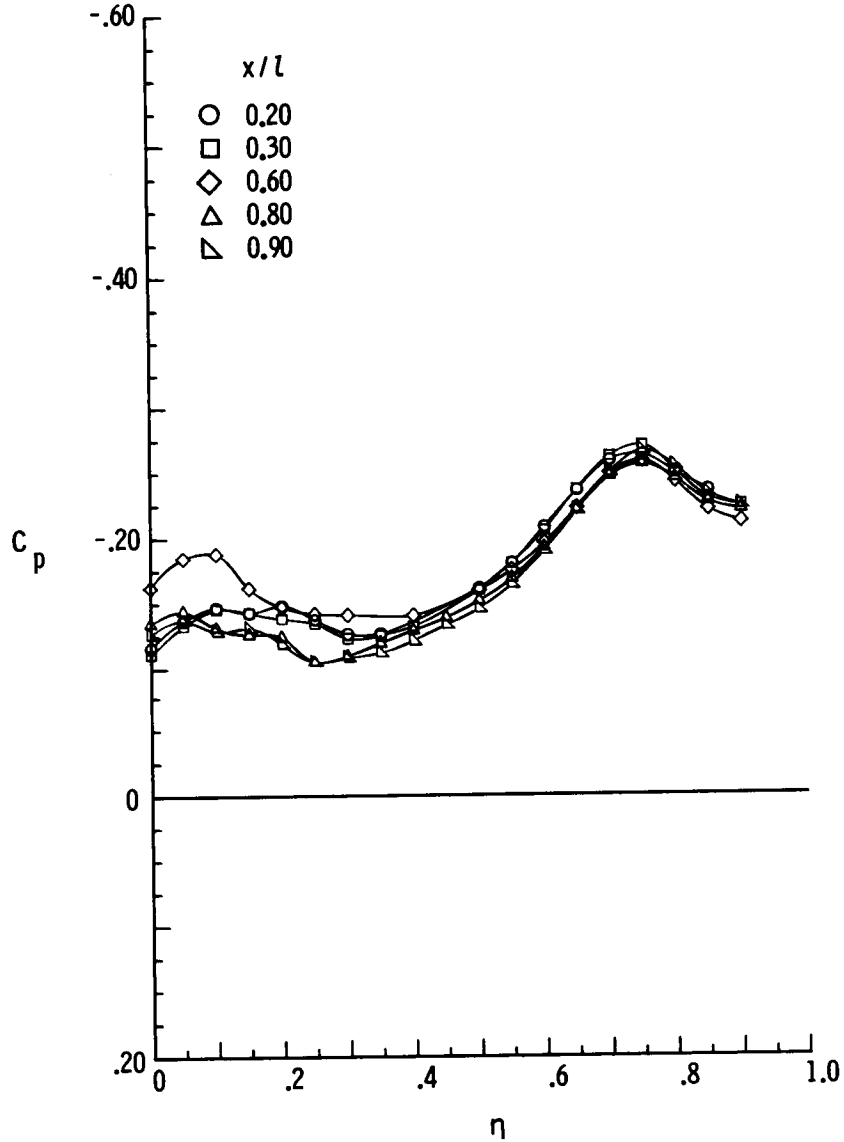

(f) M = 1.70; β = -8°.

Figure B7.- Continued.

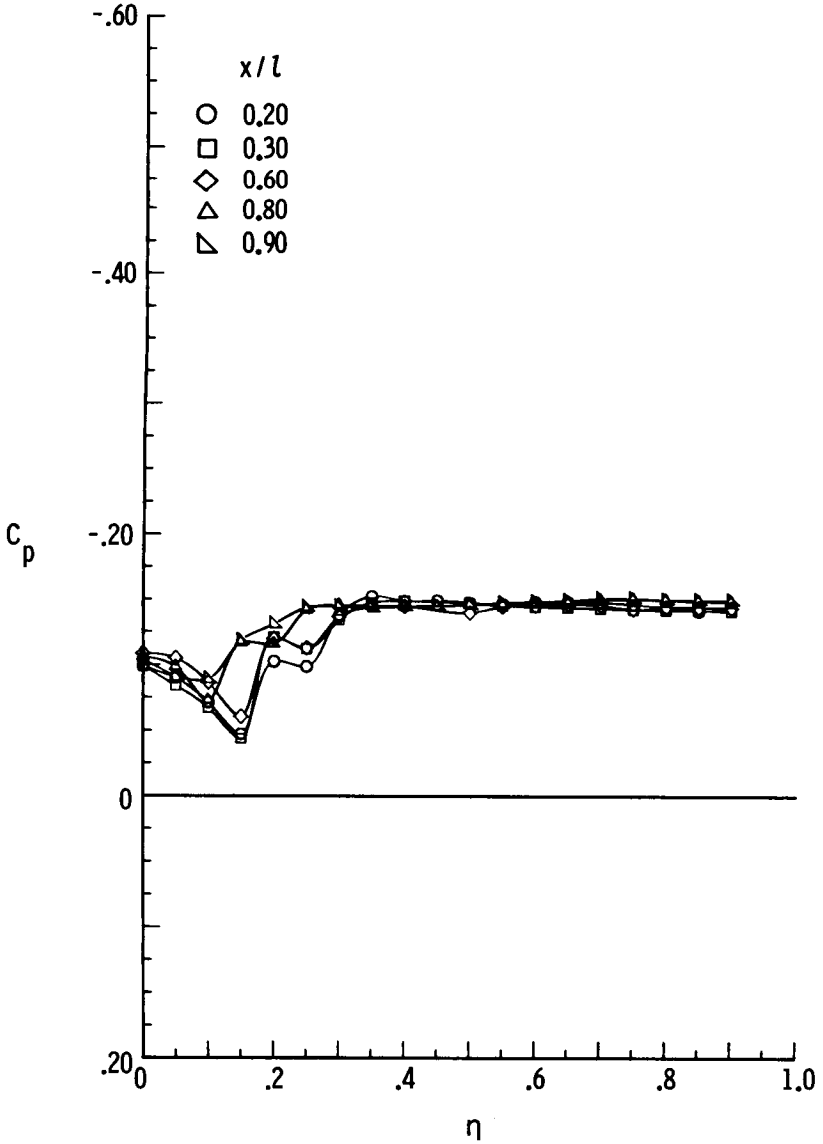

(g) M = 2.80; β = 8°.

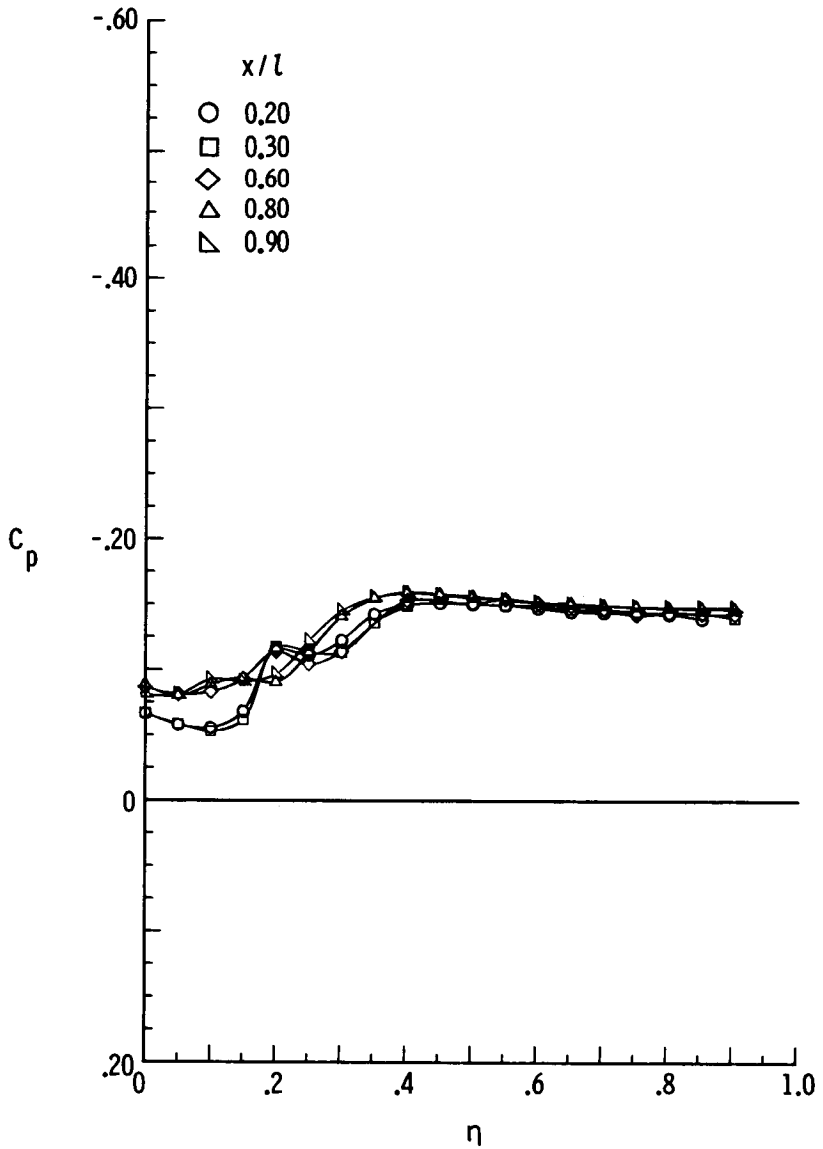

(h) M = 2.80; β = 4°.

Figure B7.- Continued.

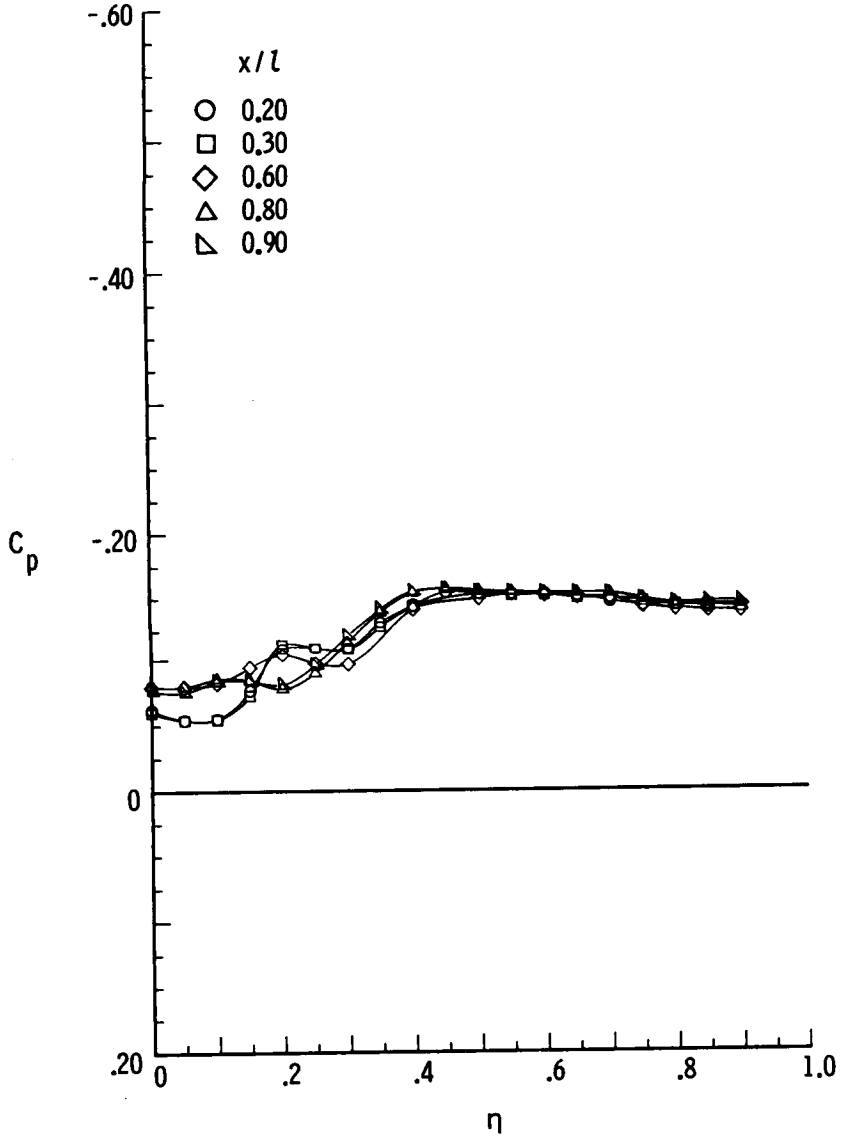

(i) M = 2.80; β = 2°.

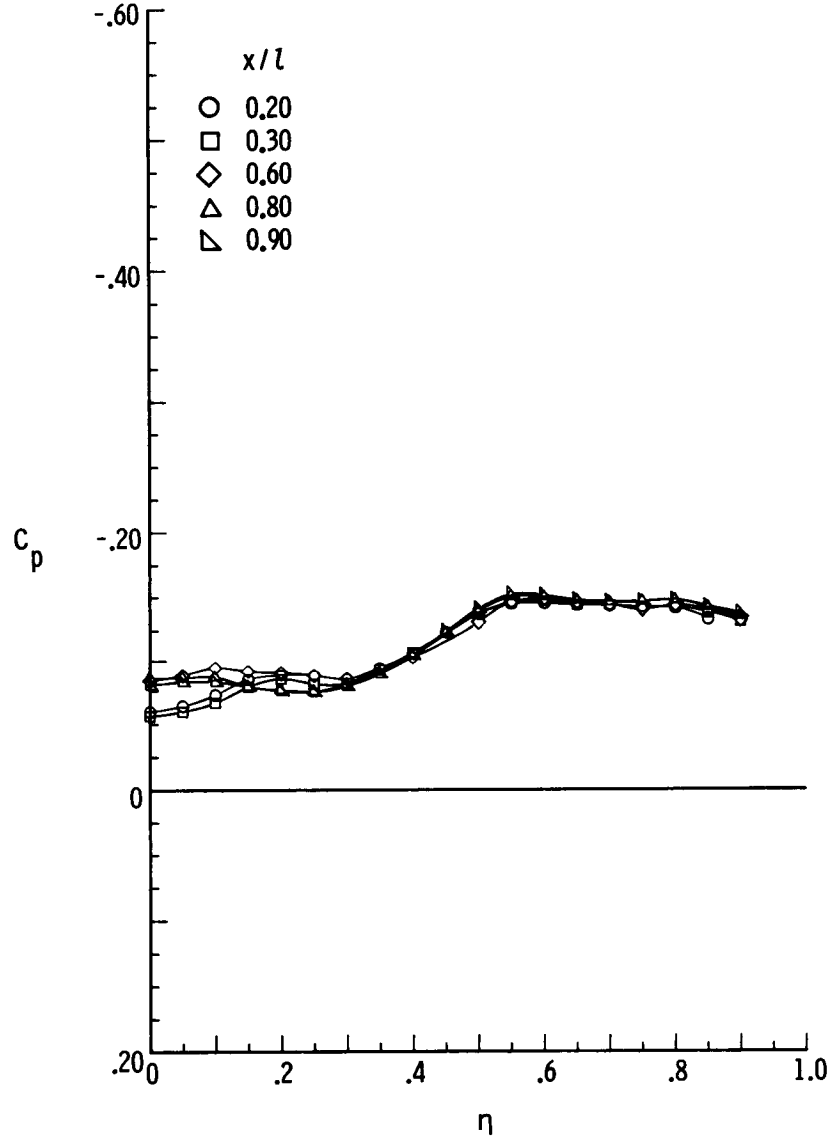

(j) M = 2.80; β = -2°.

Figure B7.- Continued.

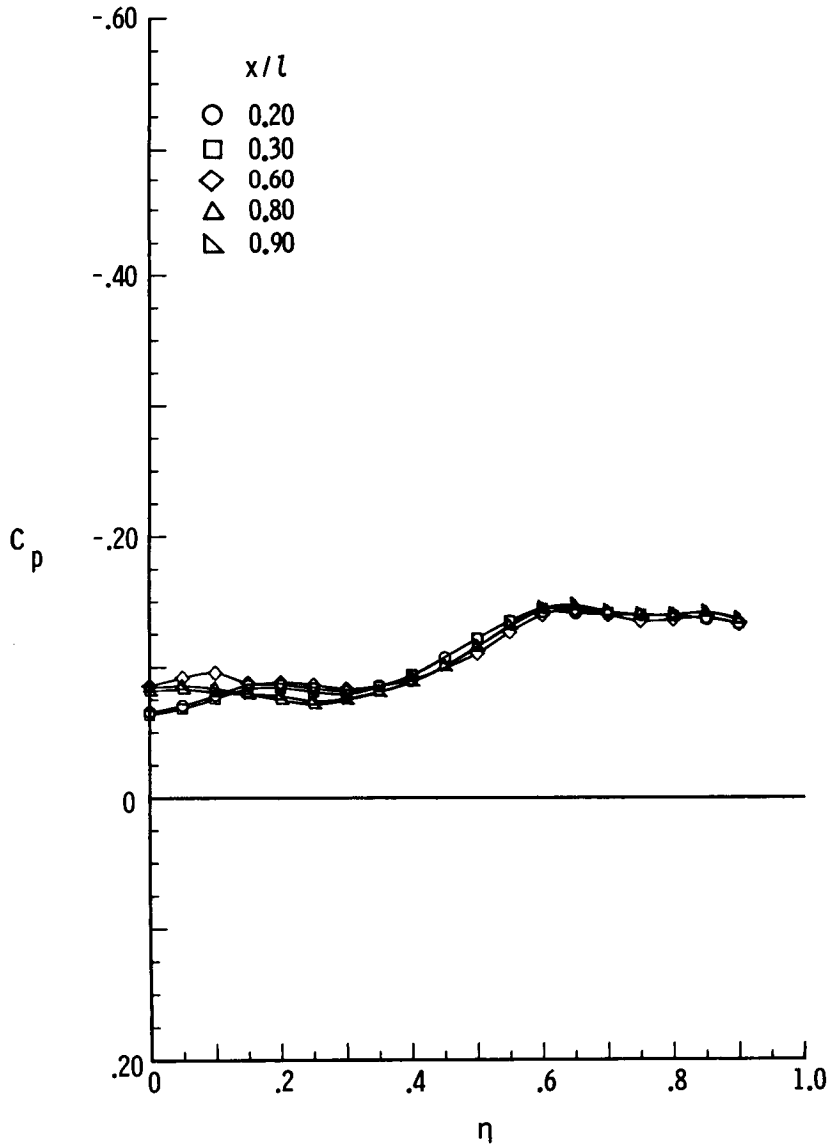

(k) M = 2.80; β = -4°.

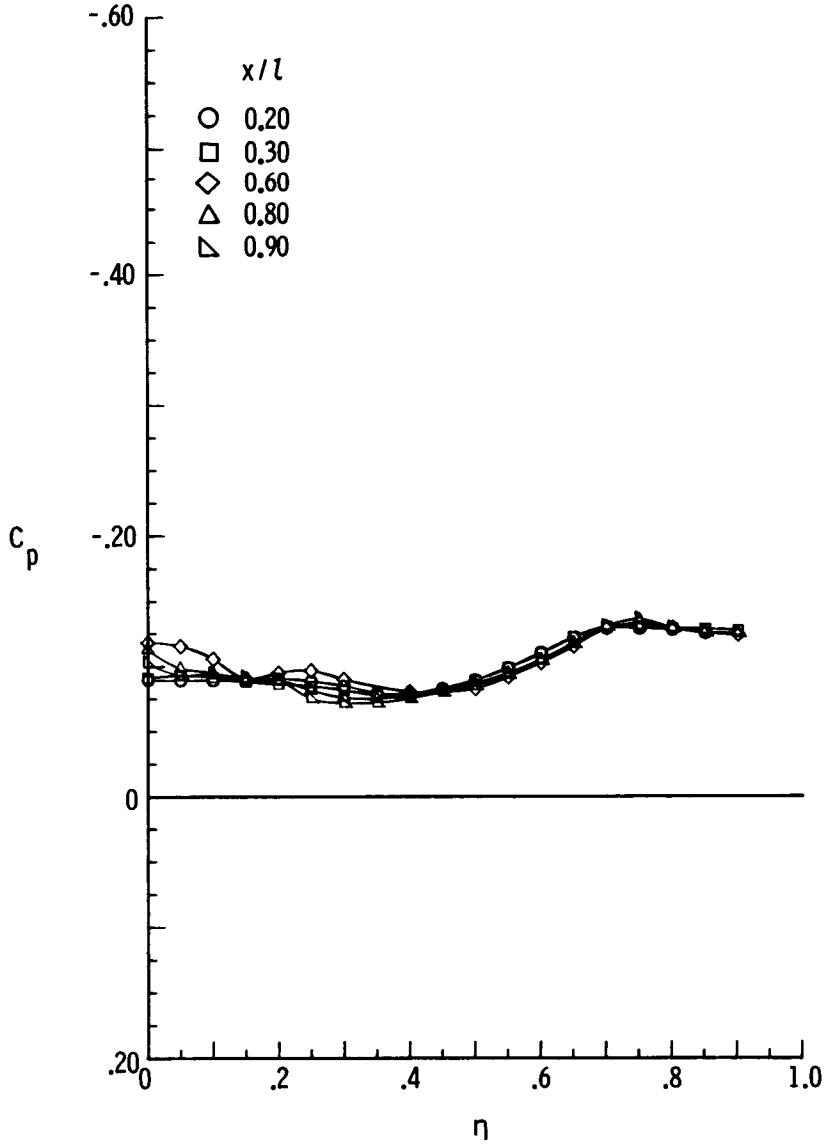

(l) M = 2.80; β = -8°.

Figure B7.- Concluded.

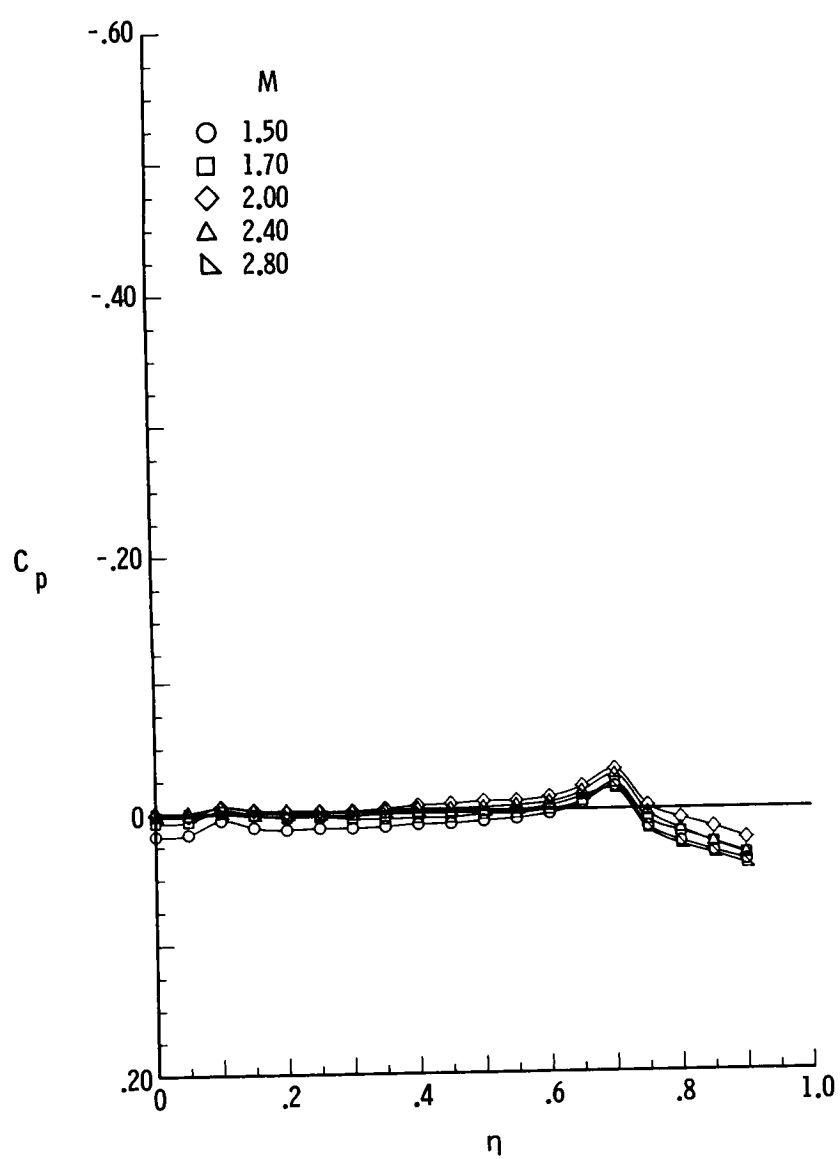

(a) $\beta = 0°$.

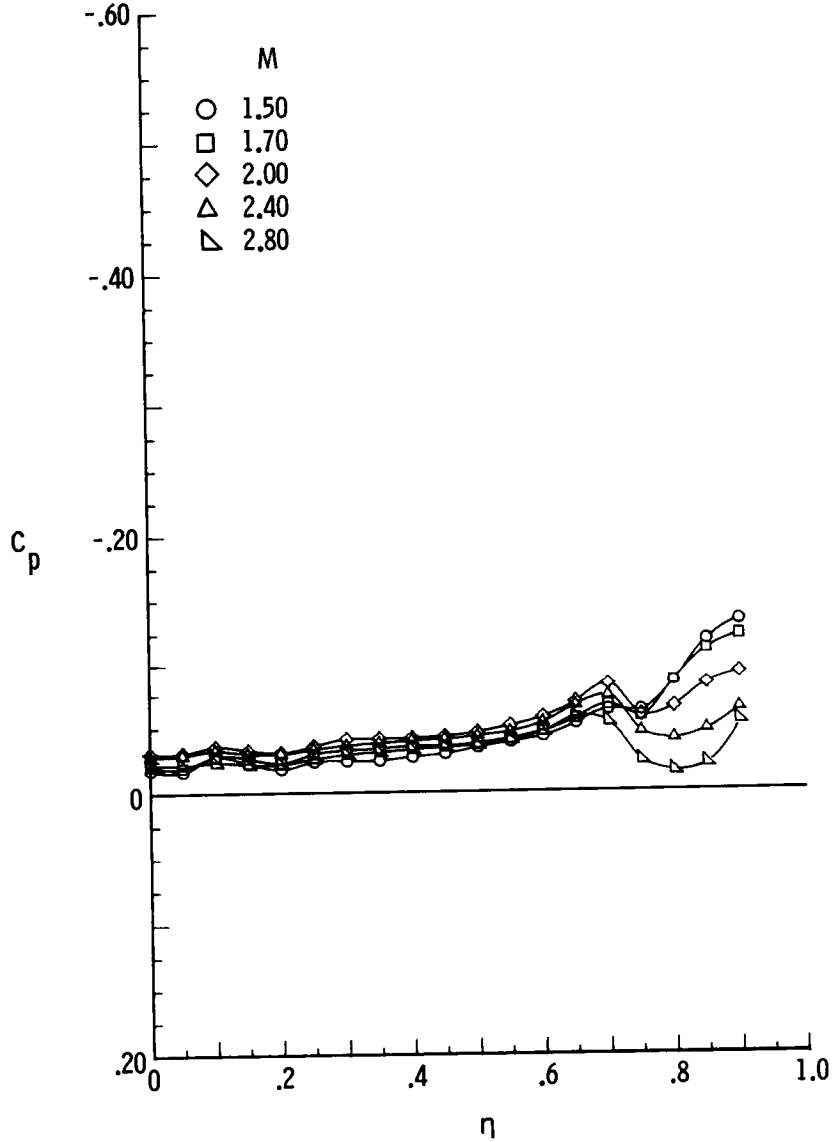

(b) $\beta = 4°$.

Figure B8.- Pressure plots for 75° delta wing with $\delta_F = 5°$ for varying M, $R = 2 \times 10^6$, $\alpha = 0°$, and $x/\ell = 0.90$.

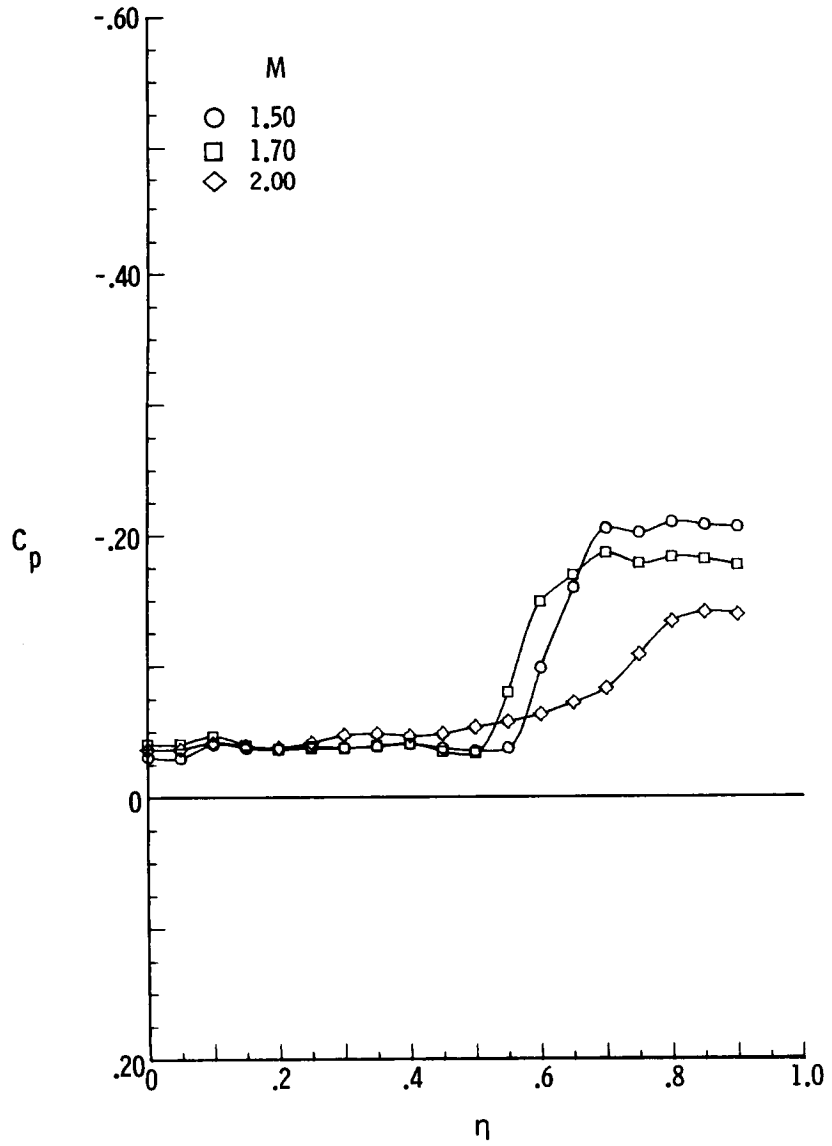

(c) $\beta = 6°$.

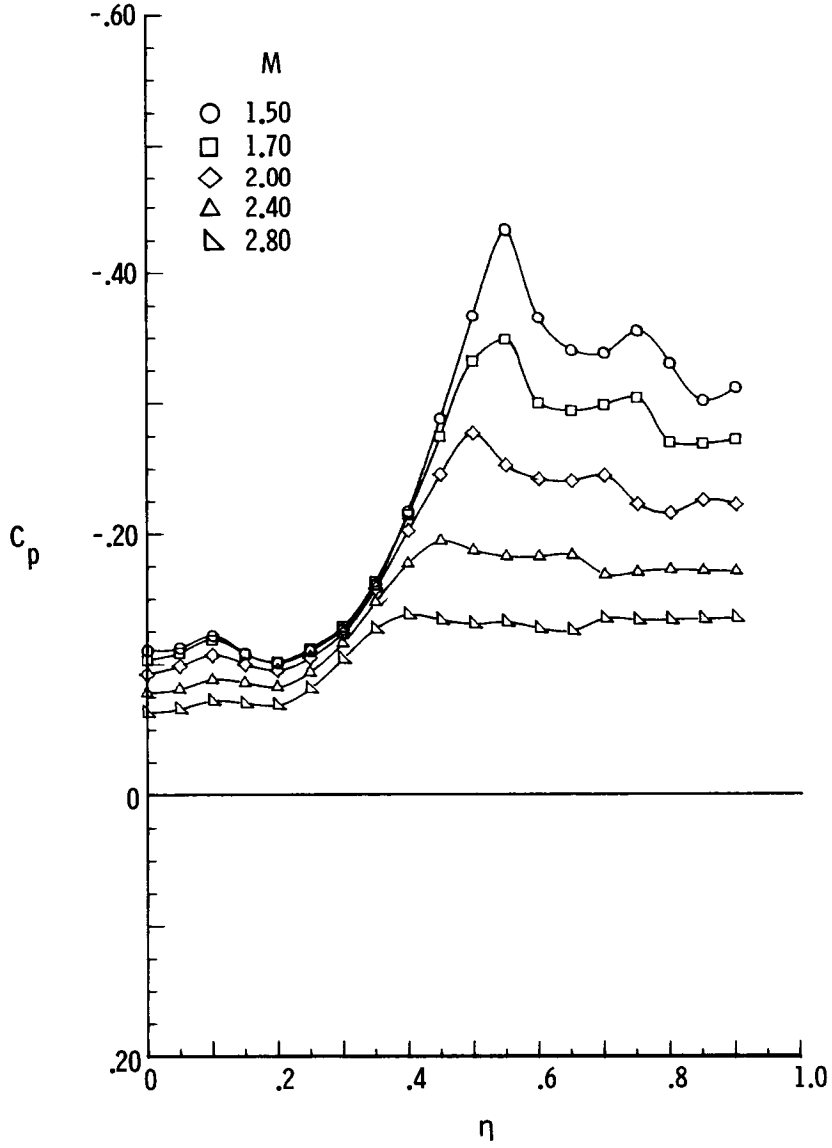

(d) $\beta = 12°$.

Figure B8.- Concluded.

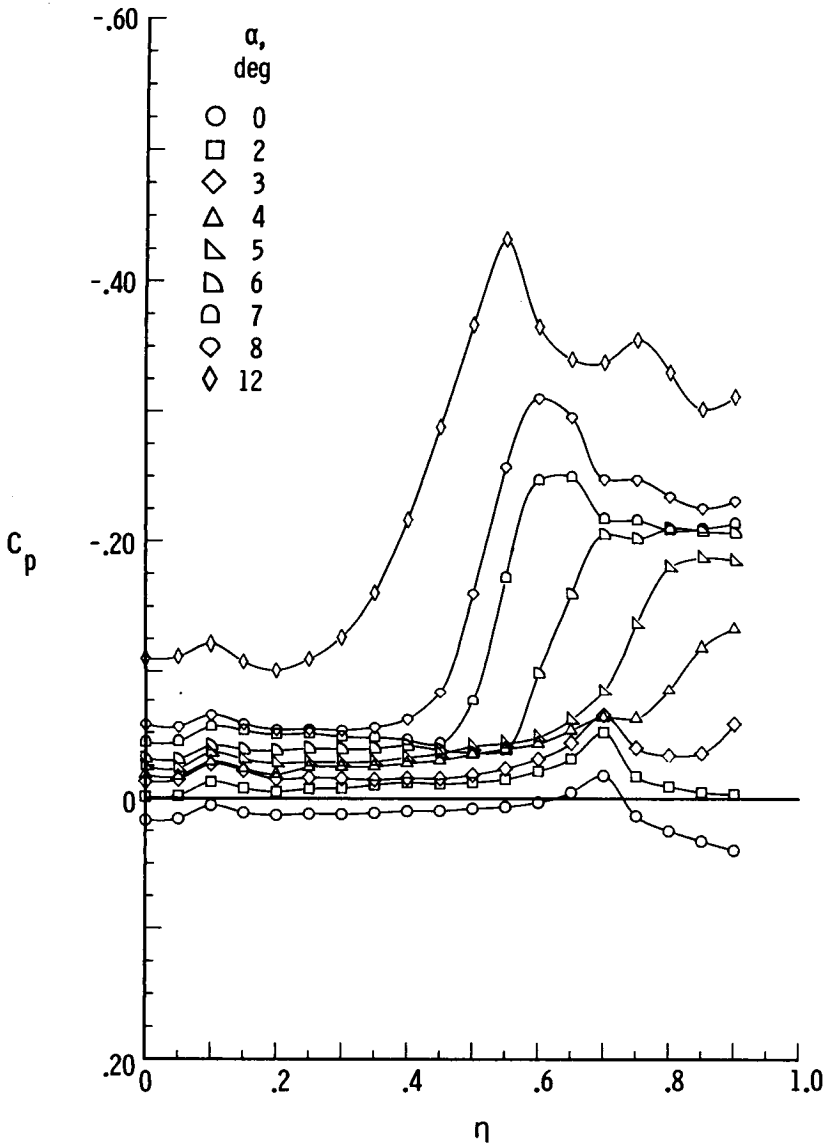

(a) M = 1.50.

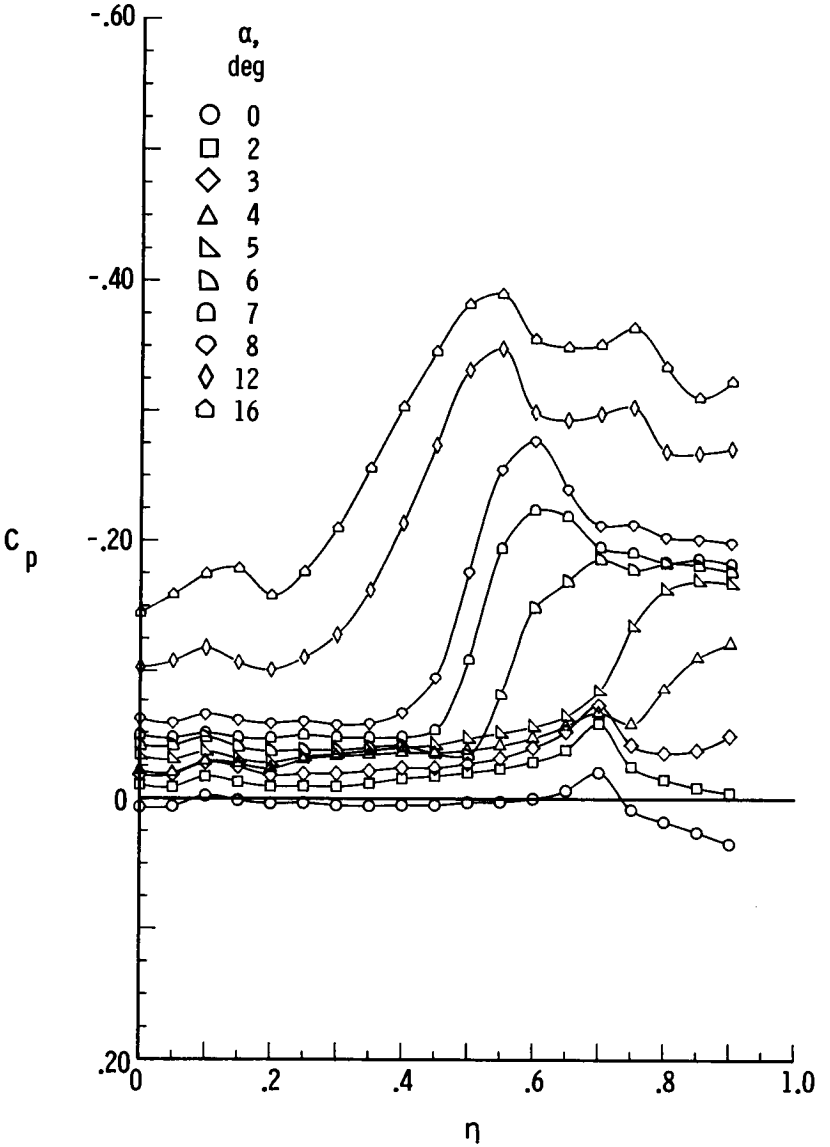

(b) M = 1.70.

Figure B9.- Pressure plots for 75° delta wing with $\delta_F = 5°$ for varying α, $R = 2 \times 10^6$, $\beta = 0°$, and $x/\ell = 0.90$.

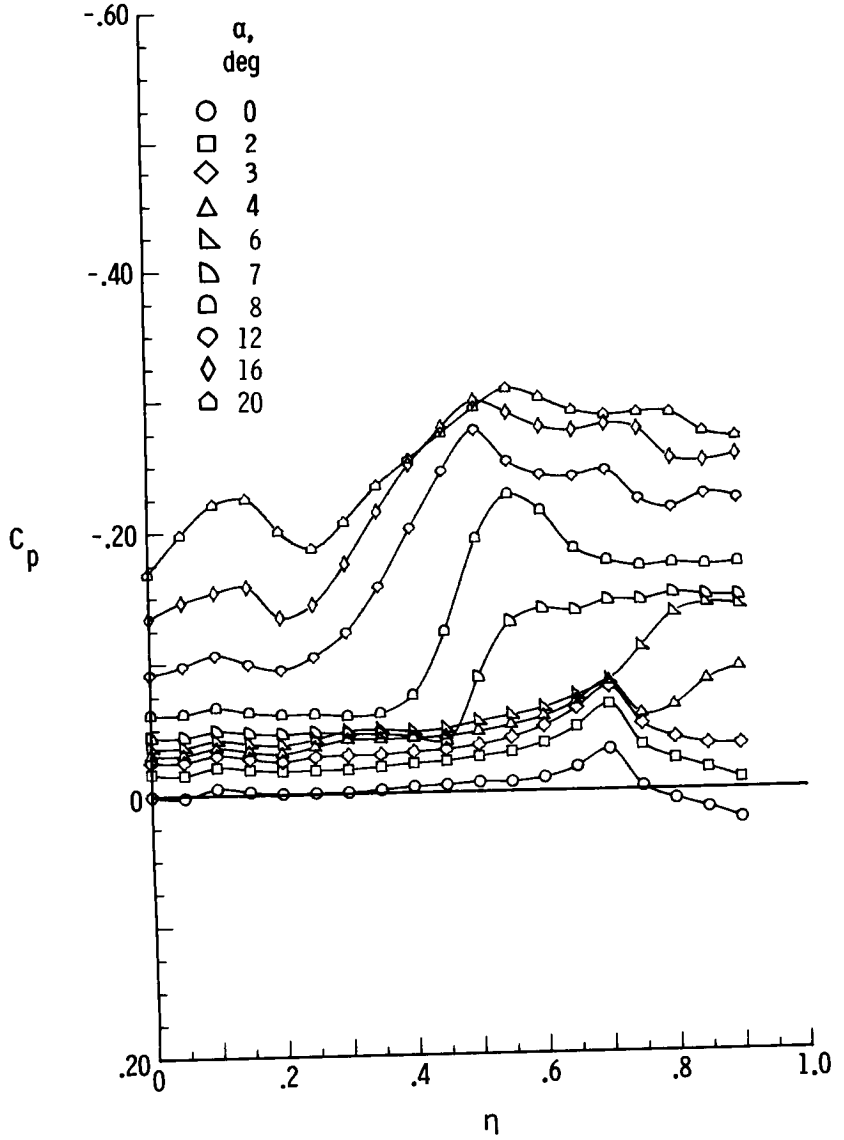

(c) M = 2.00.

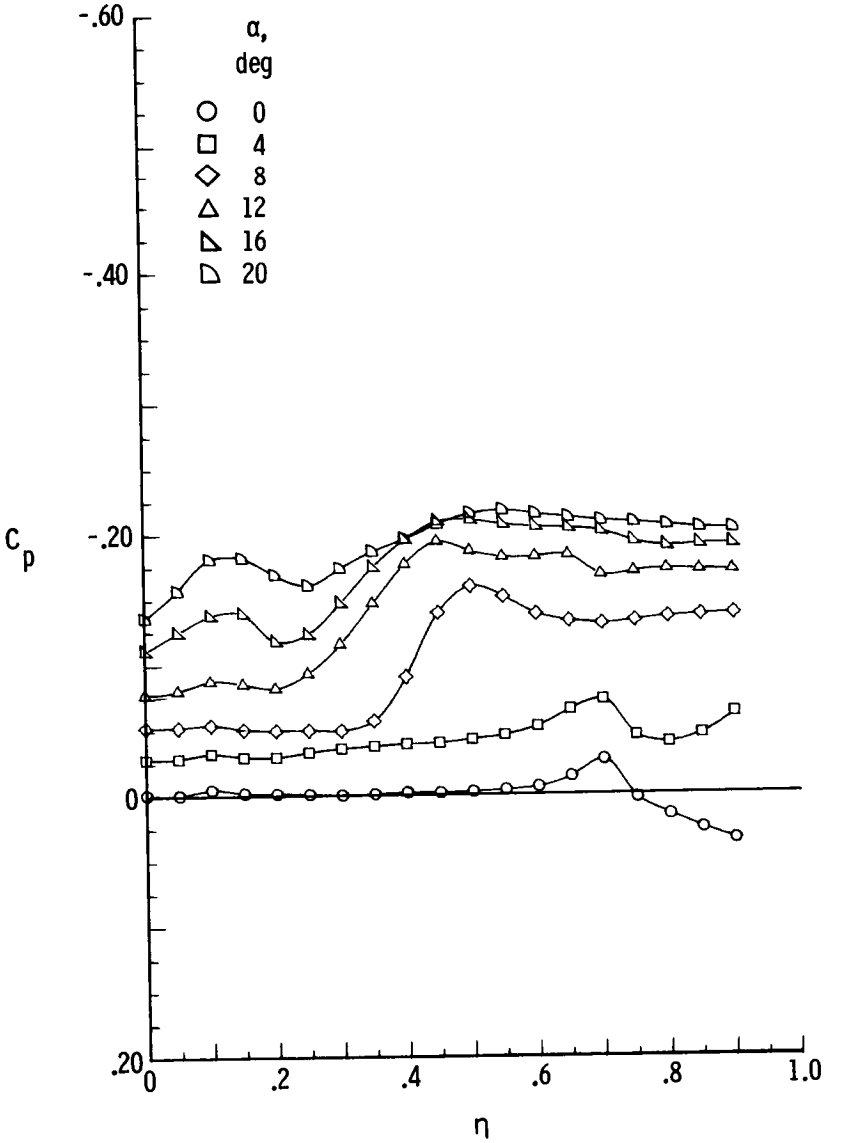

(d) M = 2.40.

Figure B9.- Continued.

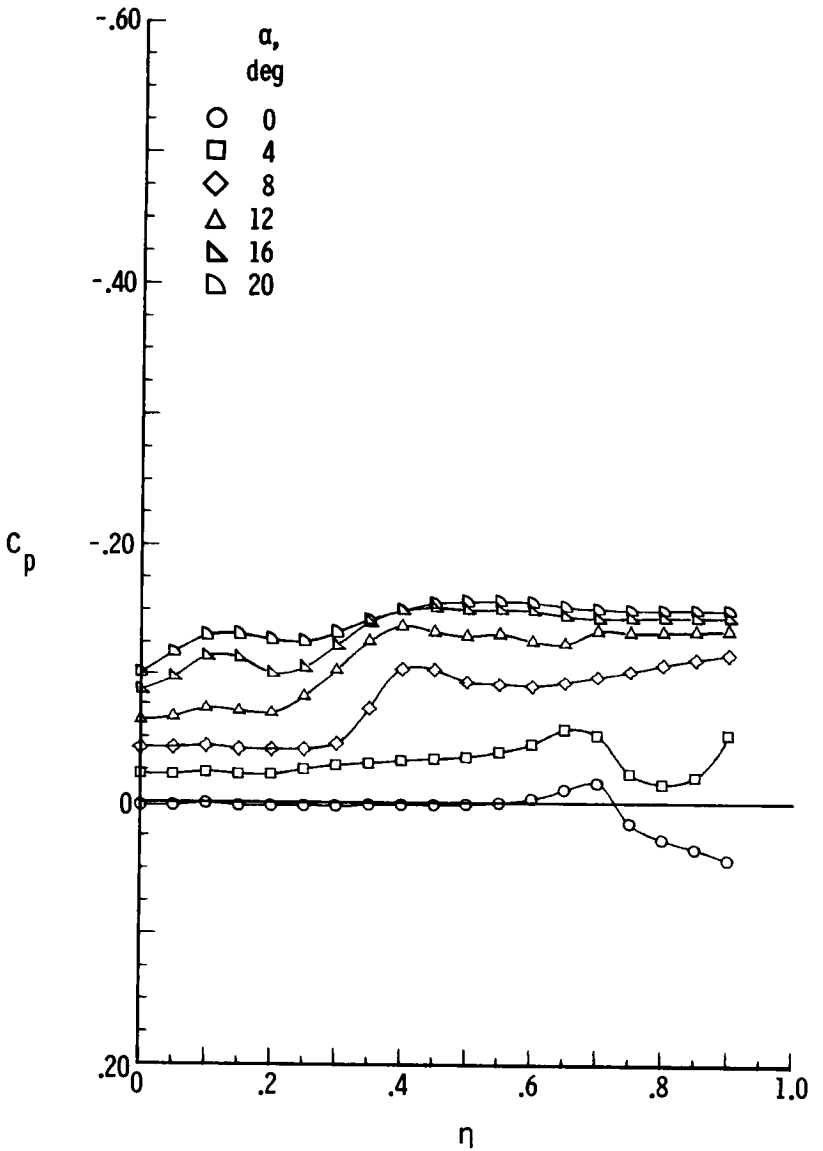

(e) M = 2.80.

Figure B9.- Concluded.

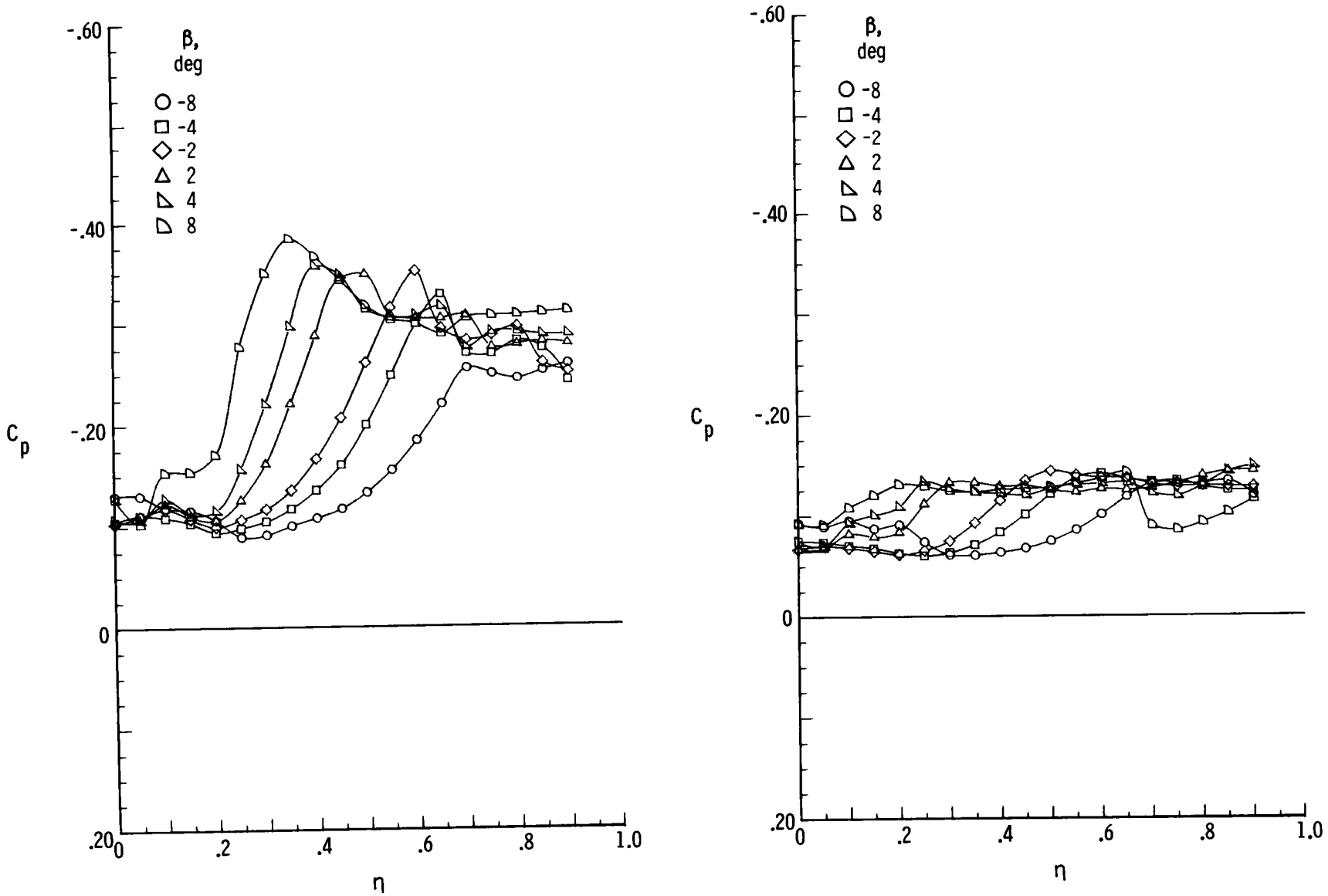

(a) M = 1.70.

(b) M = 2.80.

Figure B10.- Pressure plots for 75° delta wing with $\delta_F = 5°$ for varying β, $R = 2 \times 10^6$, $\alpha = 12°$, and $x/\ell = 0.90$.

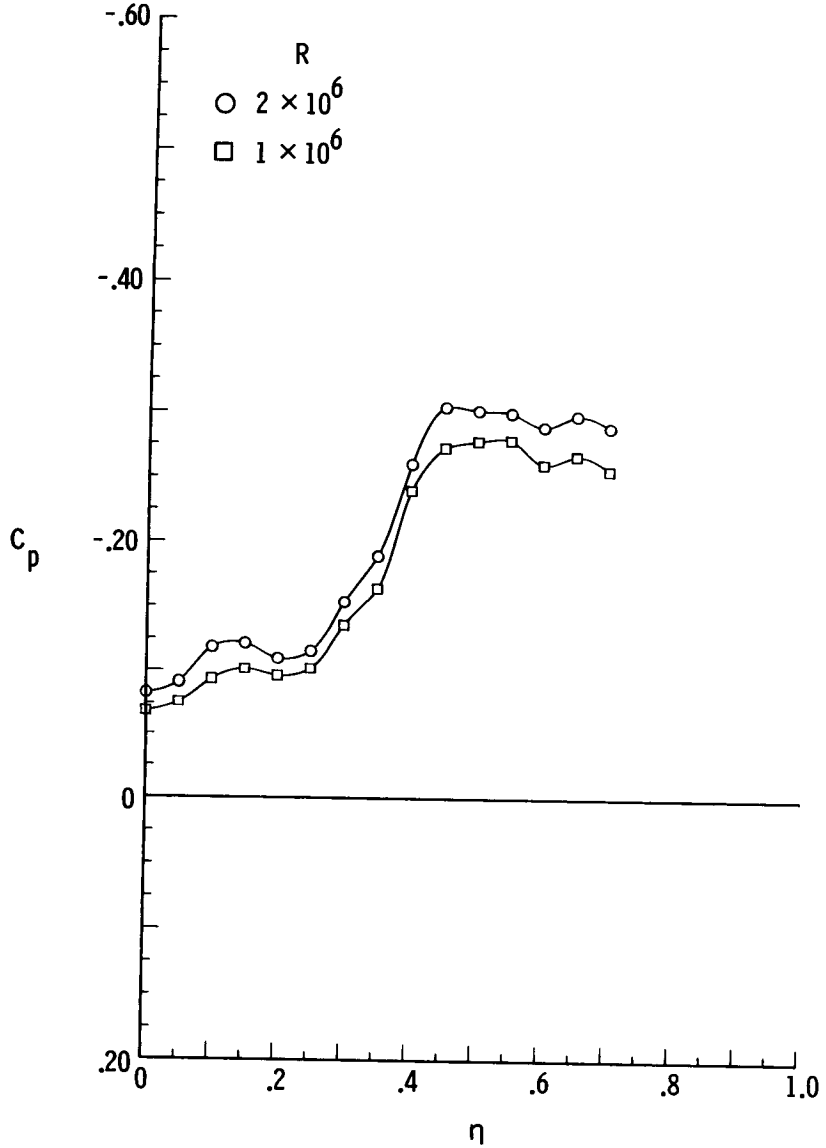

(a) M = 1.70; x/ℓ = 0.10.

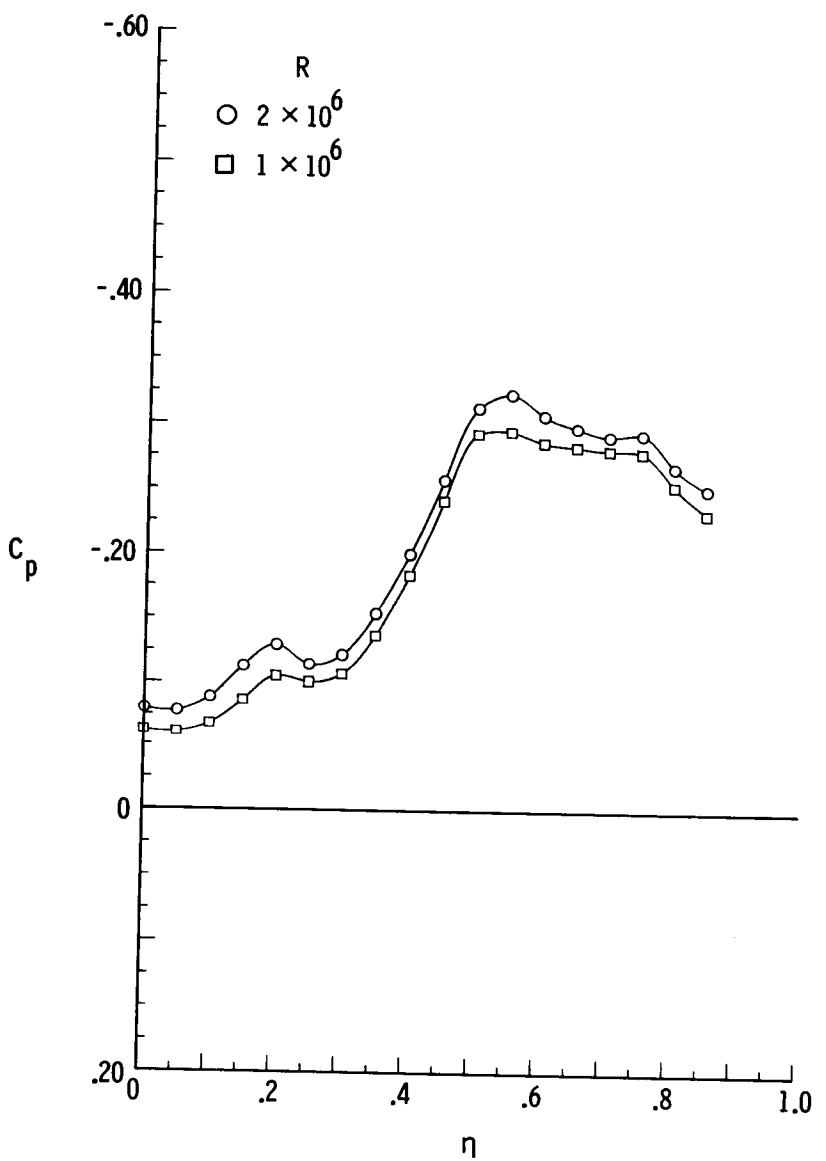

(b) M = 1.70; x/ℓ = 0.20.

Figure B11.- Pressure plots for 75° delta wing with δ_F = 5° for varying R, α = 12°, and β = 0°.

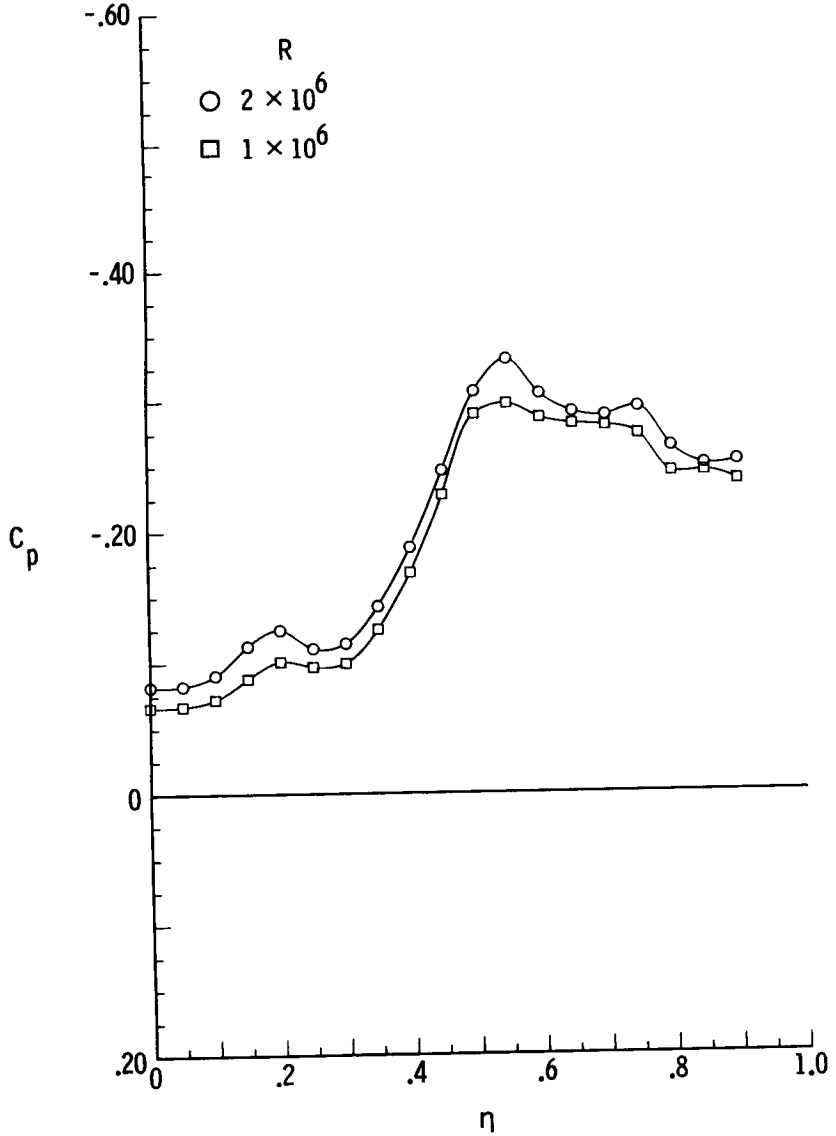

(c) M = 1.70; x/ℓ = 0.30.

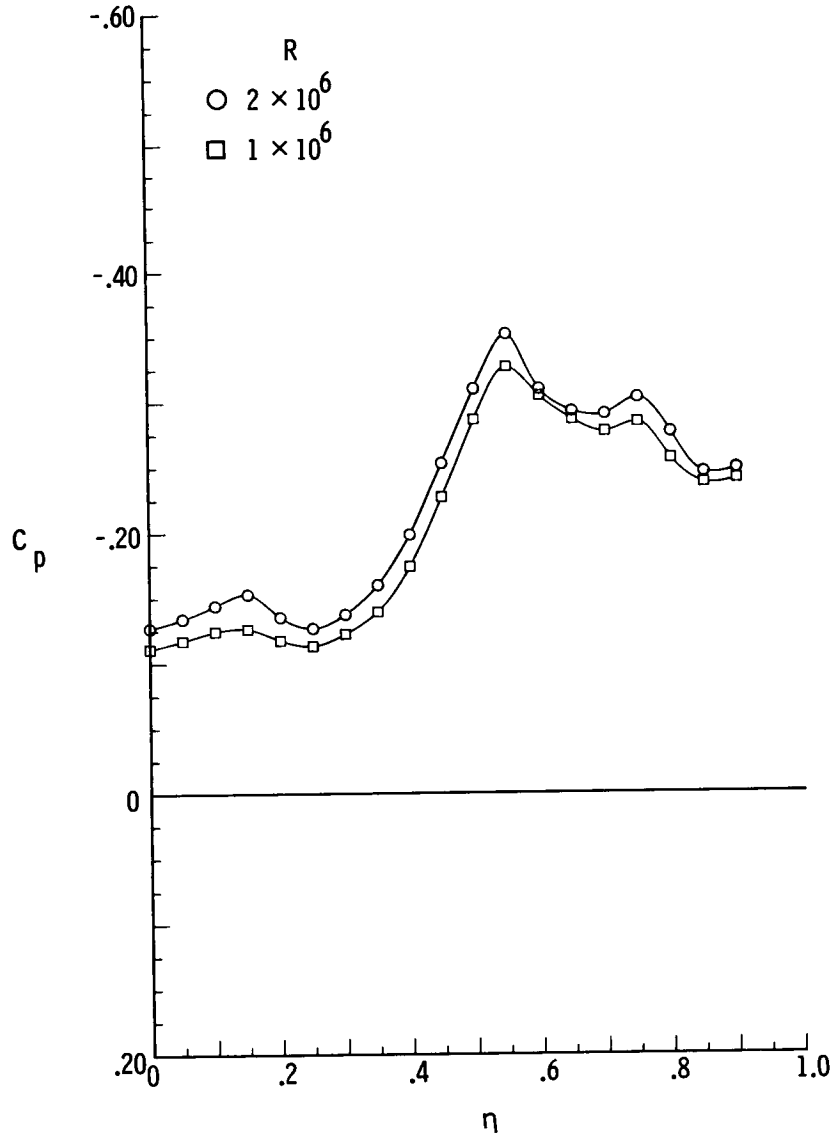

(d) M = 1.70; x/ℓ = 0.60.

Figure B11.- Continued.

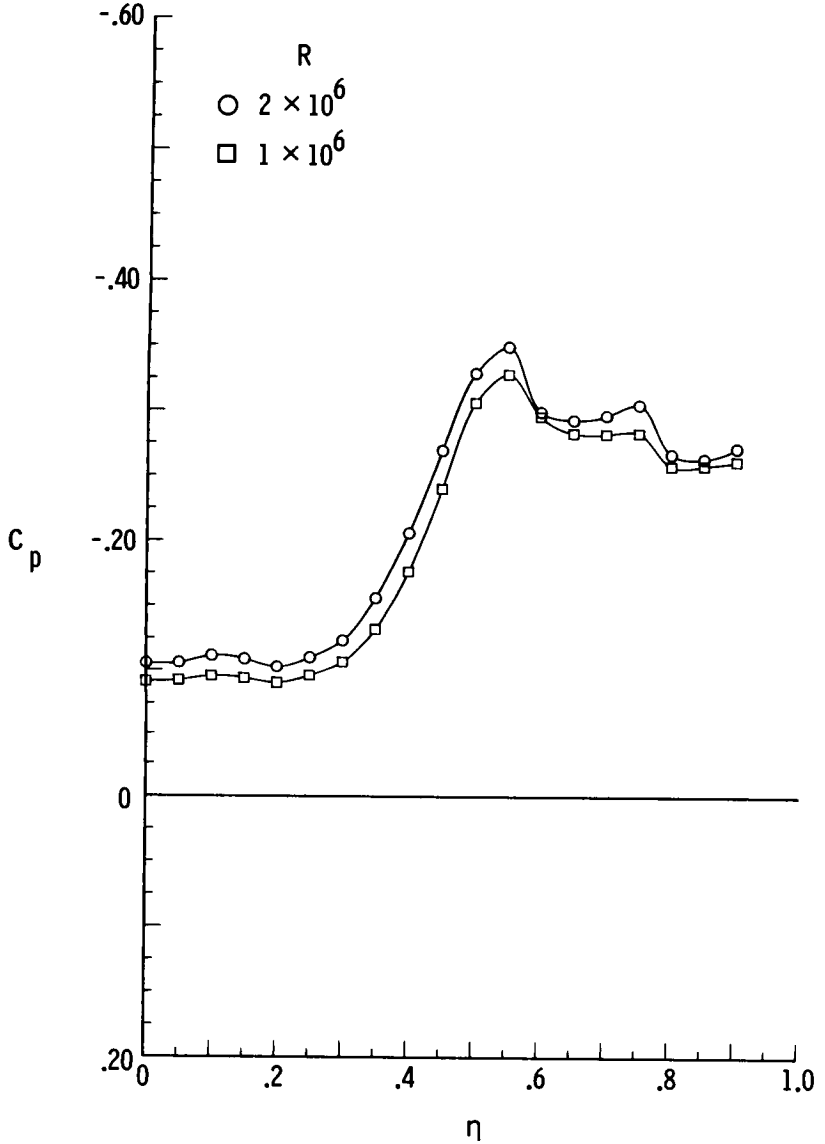

(e) M = 1.70; x/ℓ = 0.80.

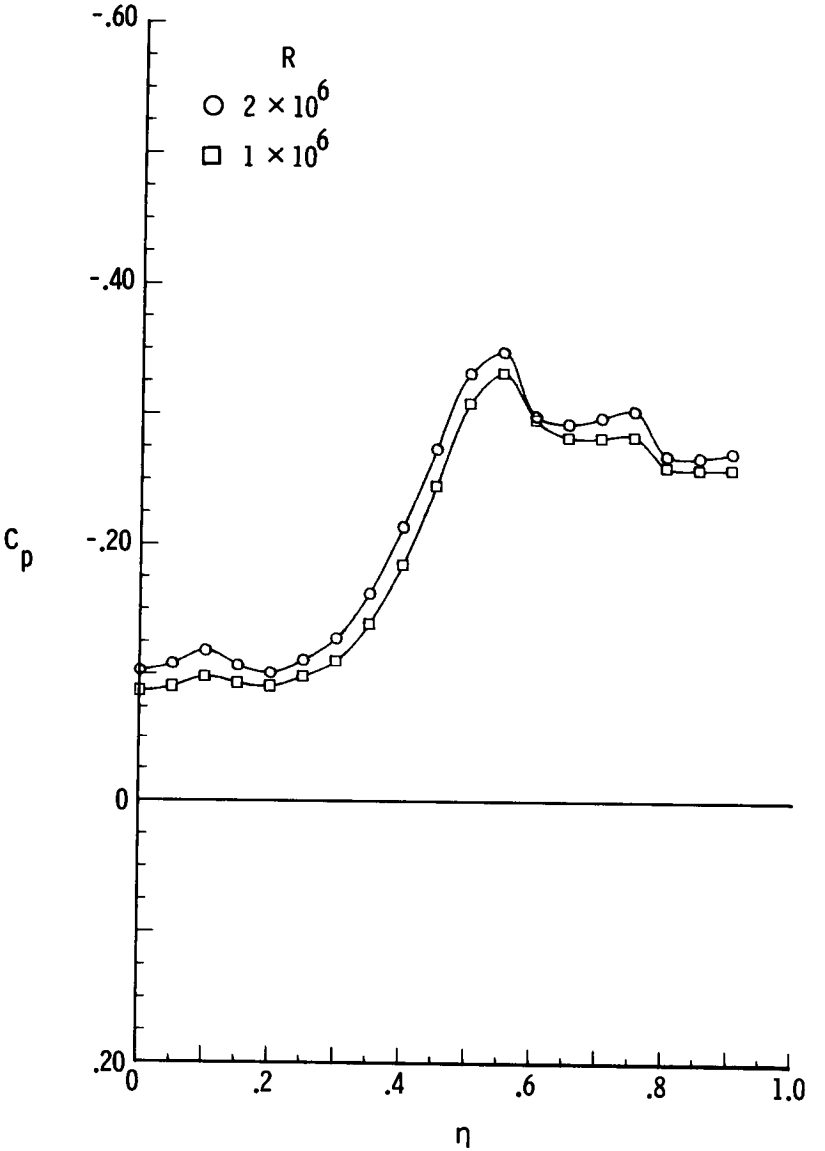

(f) M = 1.70; x/ℓ = 0.90.

Figure B11.- Continued.

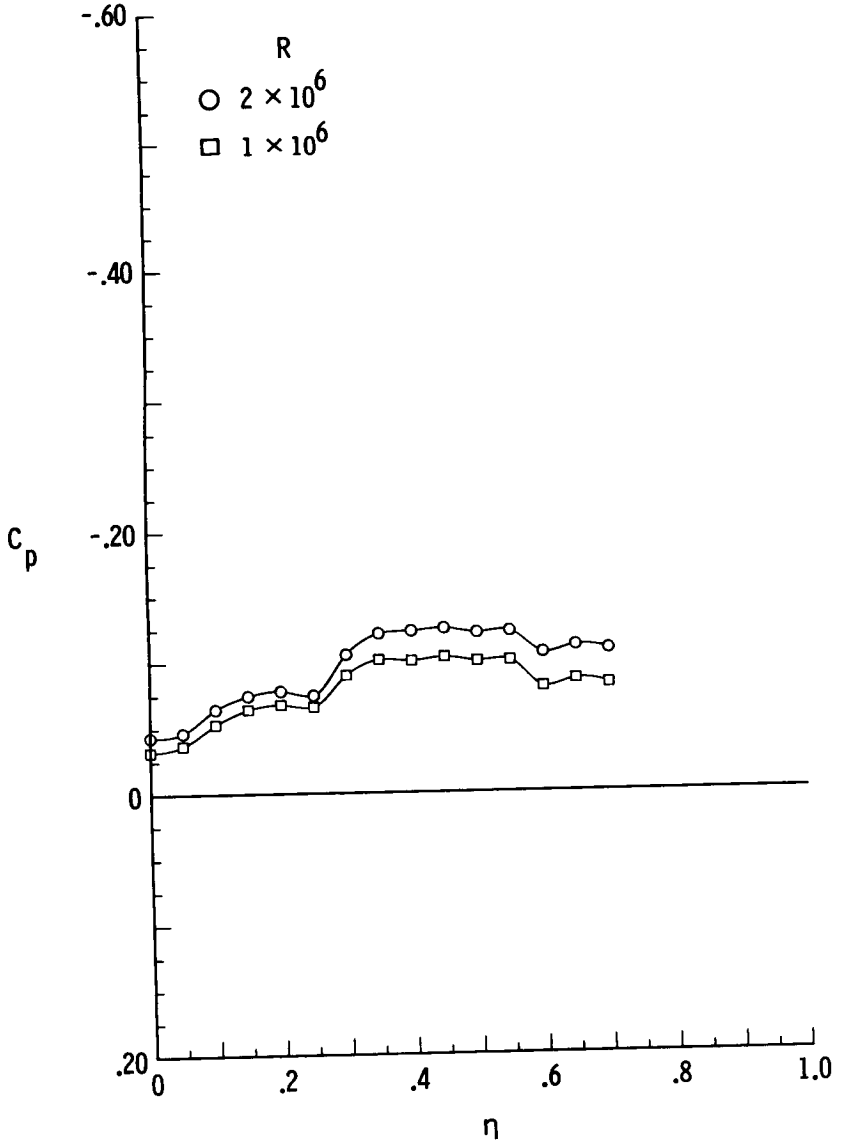

(g) M = 2.80; x/l = 0.10.

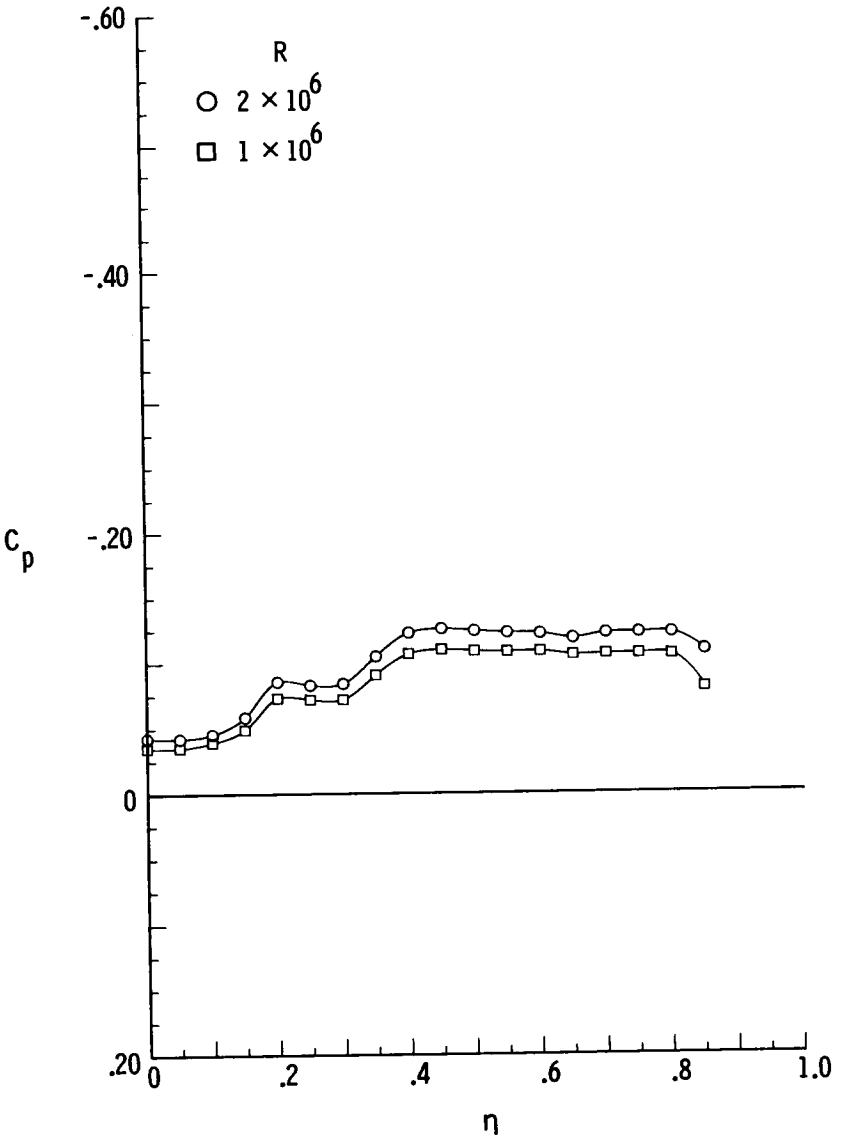

(h) M = 2.80; x/l = 0.20.

Figure B11.- Continued.

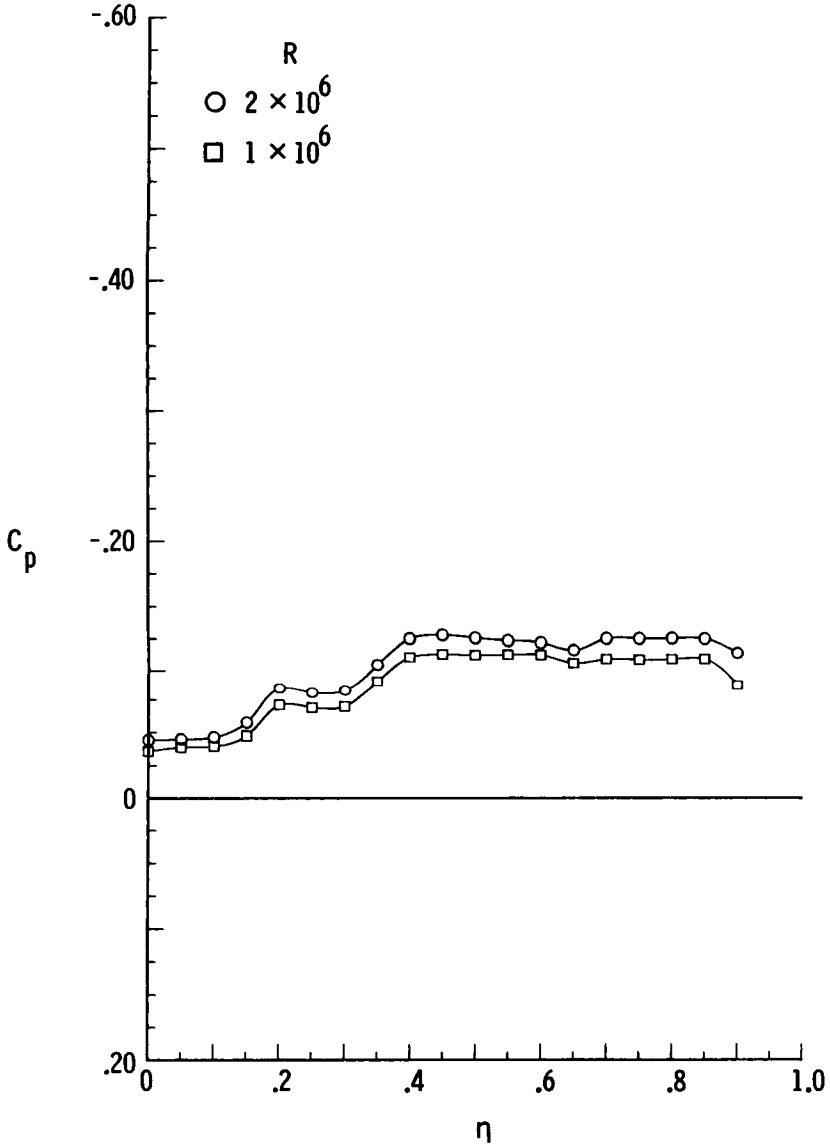

(i) M = 2.80; x/ℓ = 0.30.

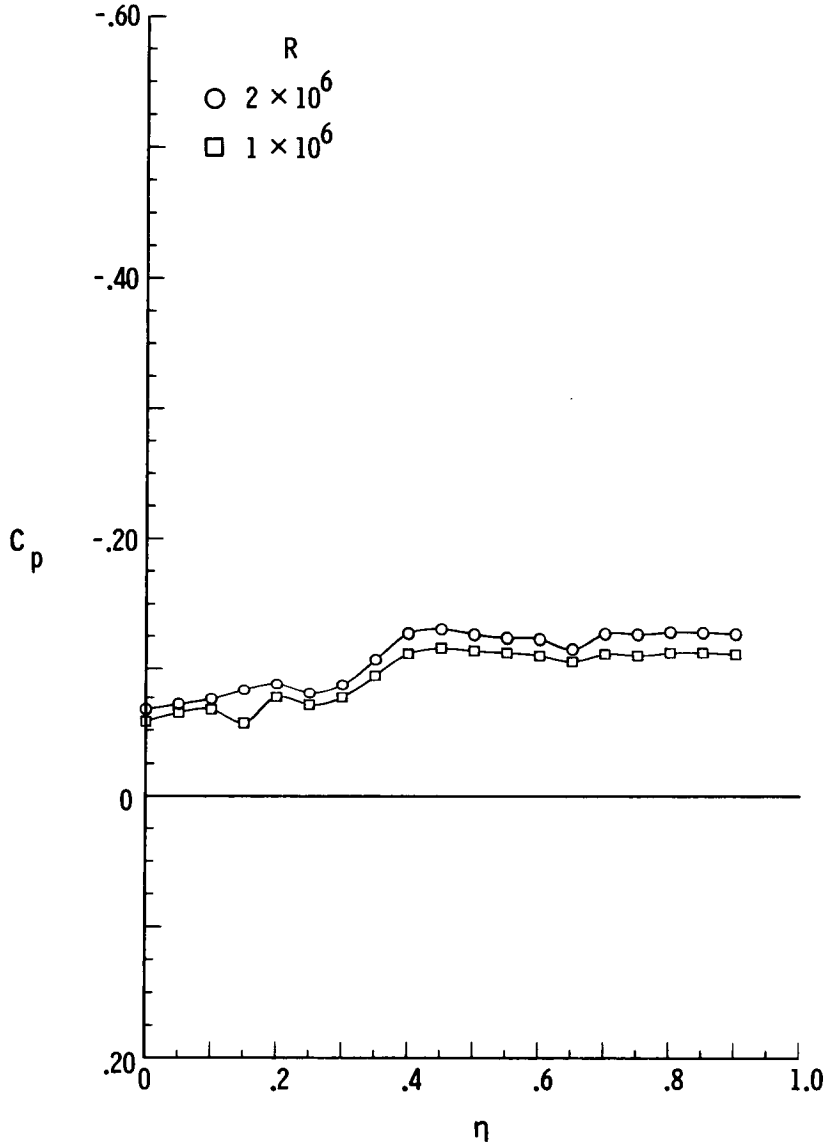

(j) M = 2.80; x/ℓ = 0.60.

Figure B11.- Continued.

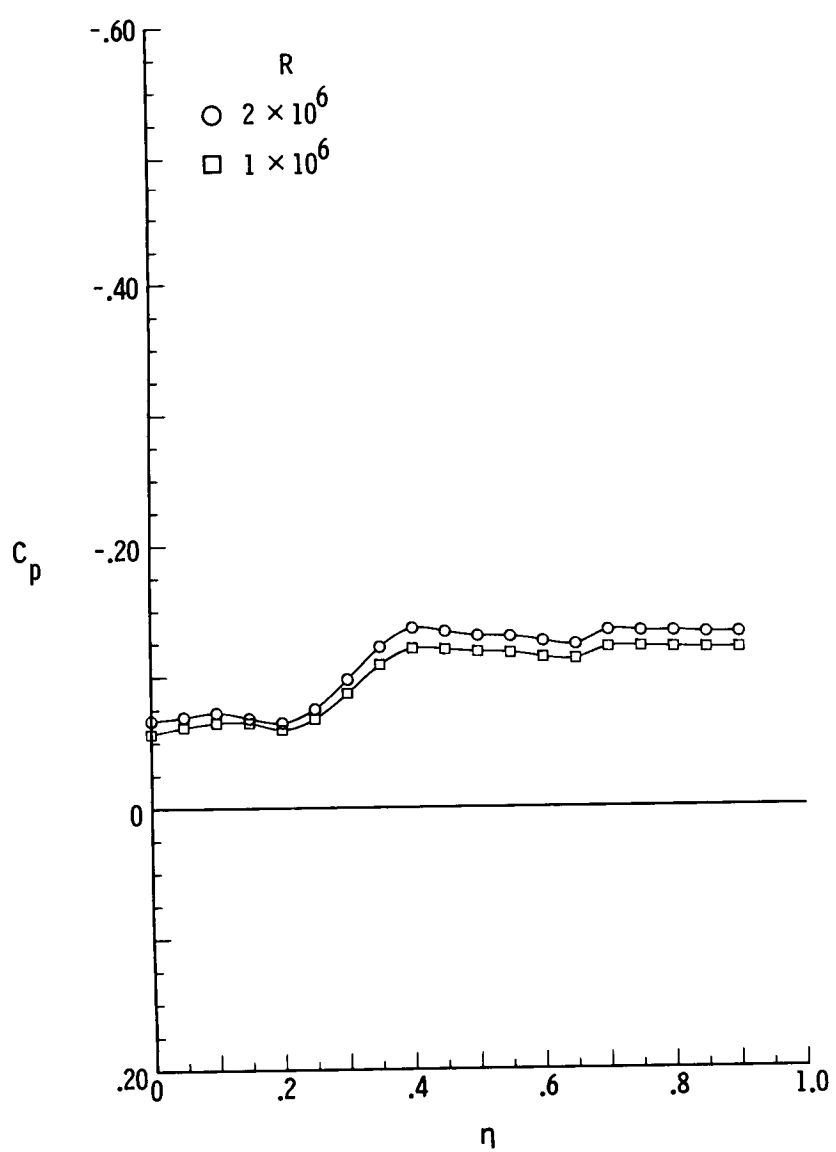

(k) M = 2.80; x/ℓ = 0.80.

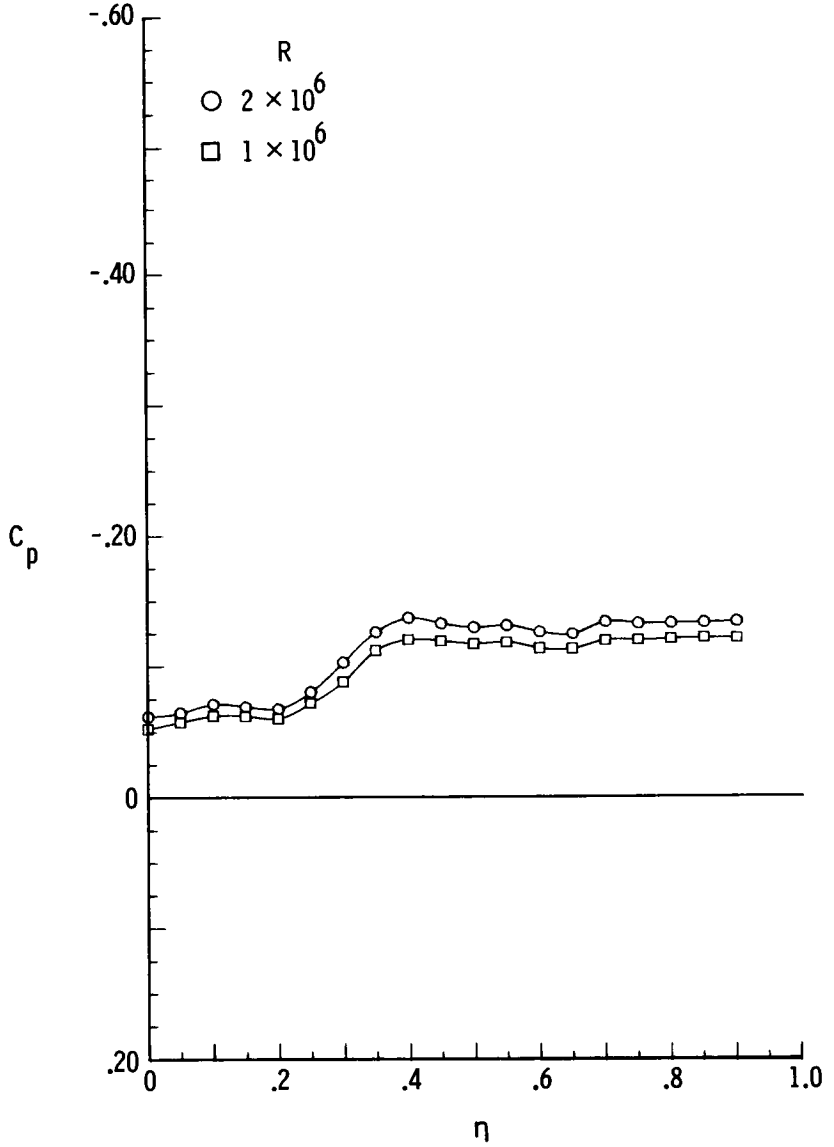

(l) M = 2.80; x/ℓ = 0.90.

Figure B11.- Concluded.

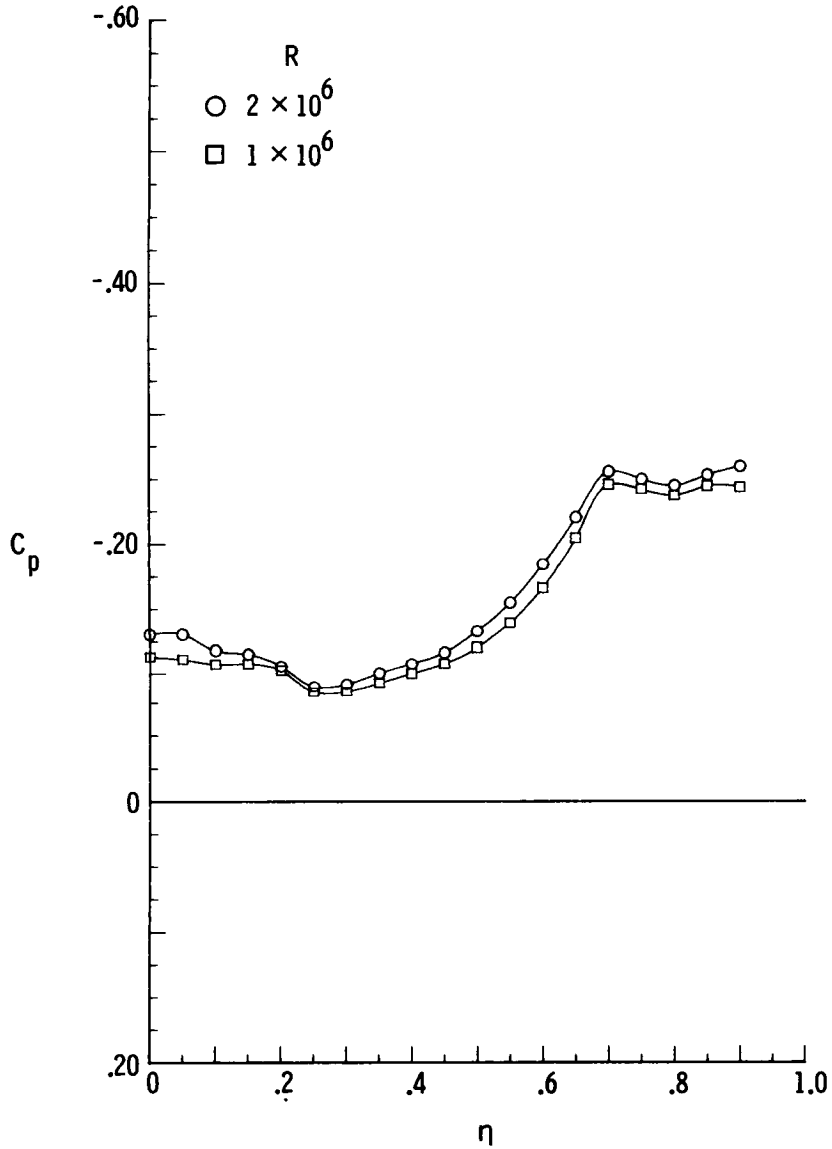

(a) M = 1.70; β = -8°.

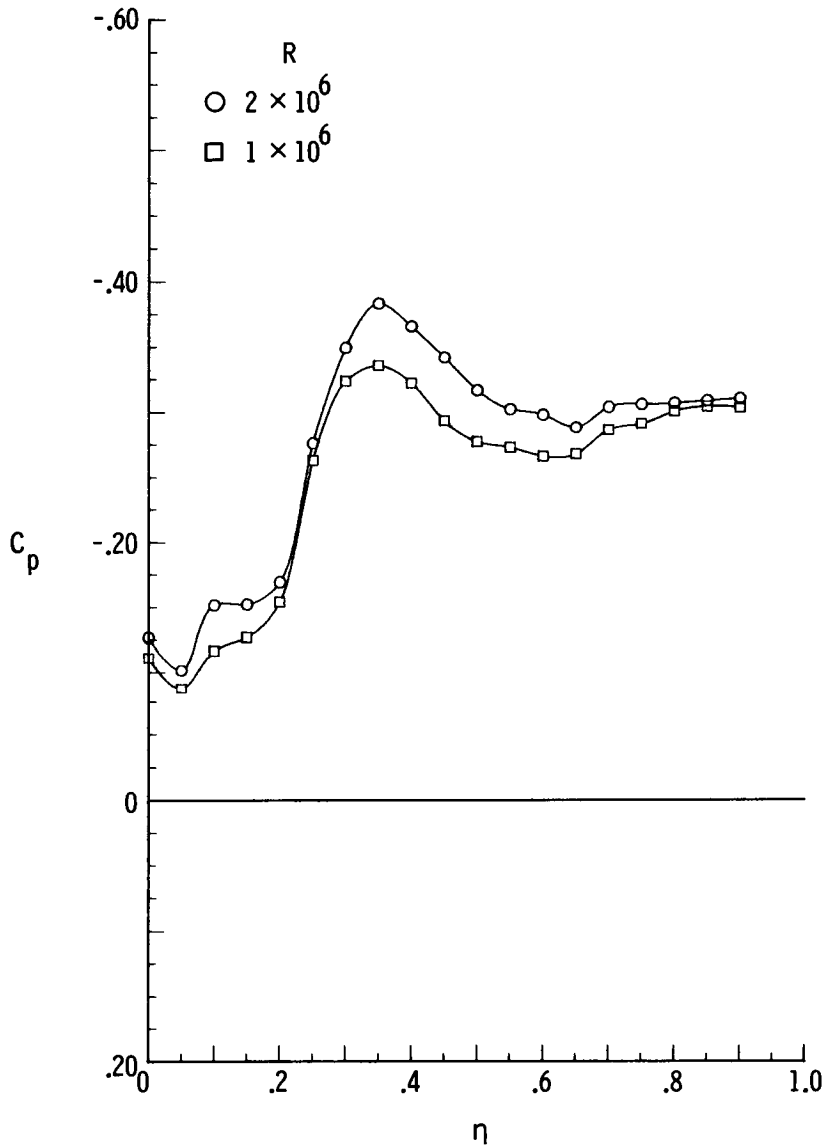

(b) M = 1.70; β = 8°.

Figure B12.- Pressure plots for 75° delta wing with δ_F = 5° for varying R, α = 12°, and x/ℓ = 0.90.

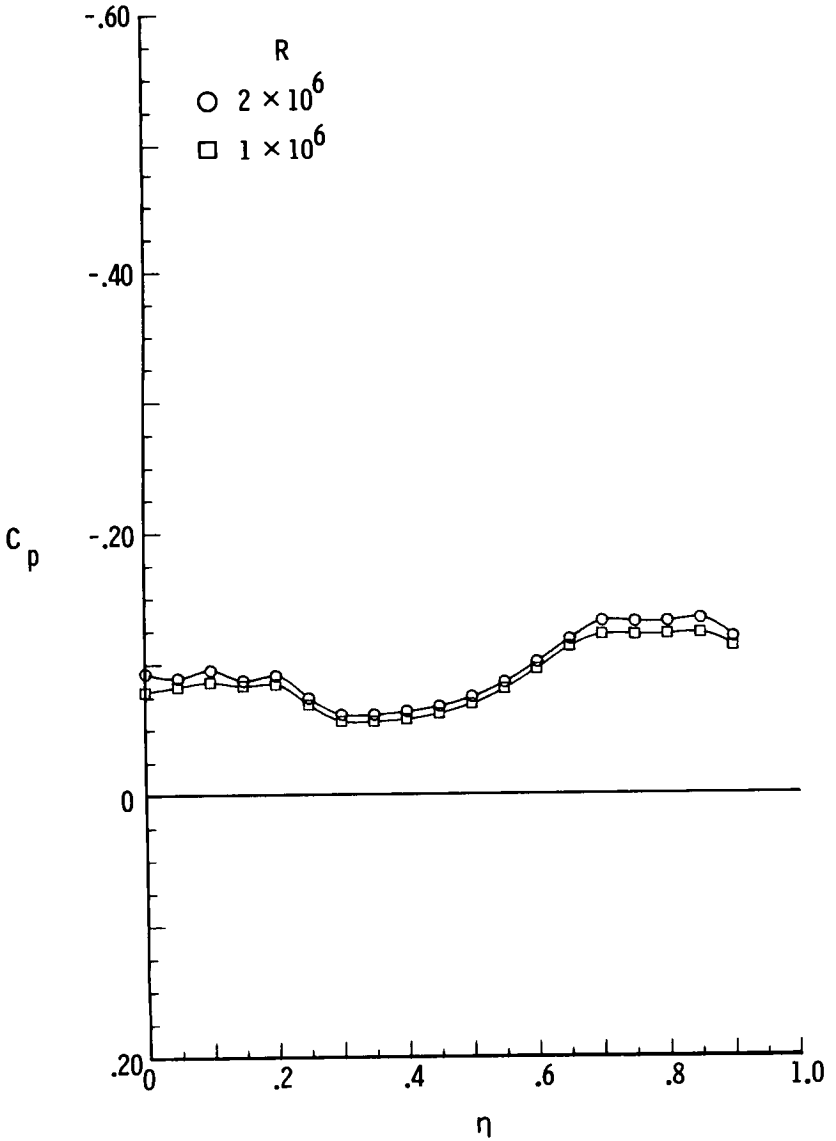

(c) M = 2.80; β = -8°.

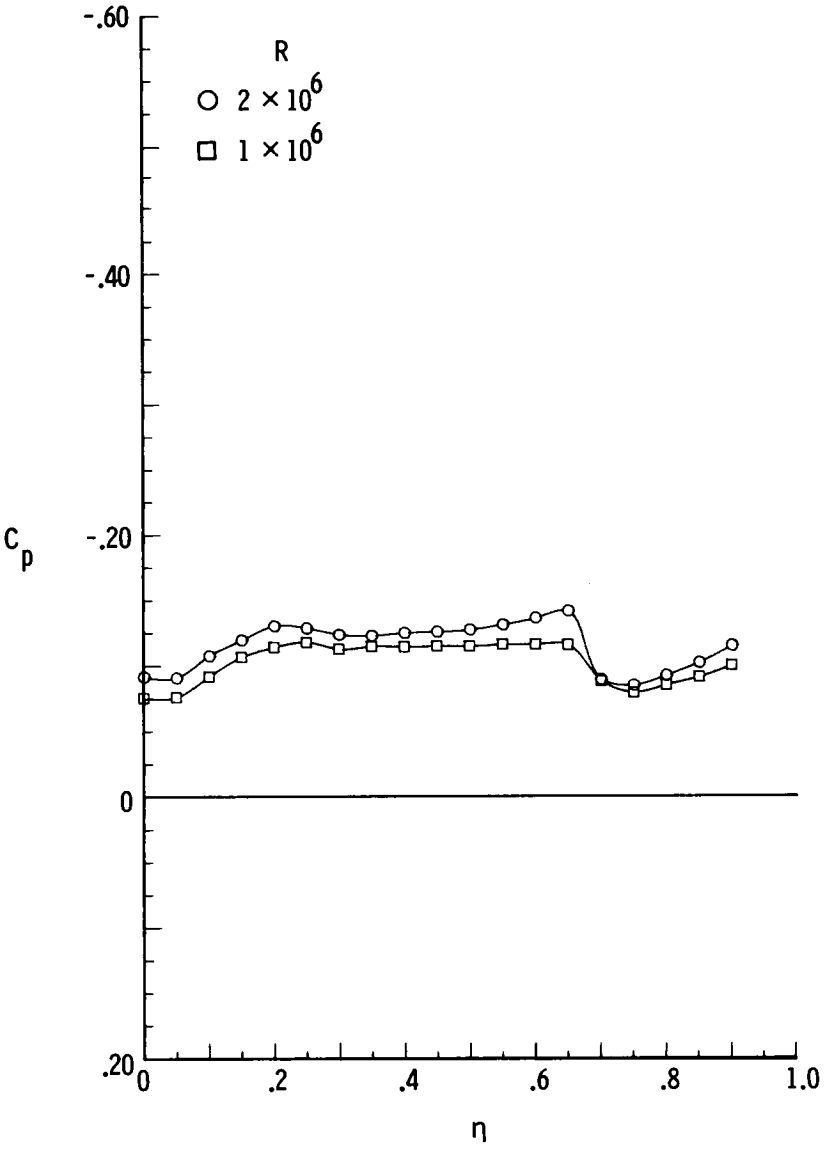

(d) M = 2.80; β = 8°.

Figure B12.- Concluded.

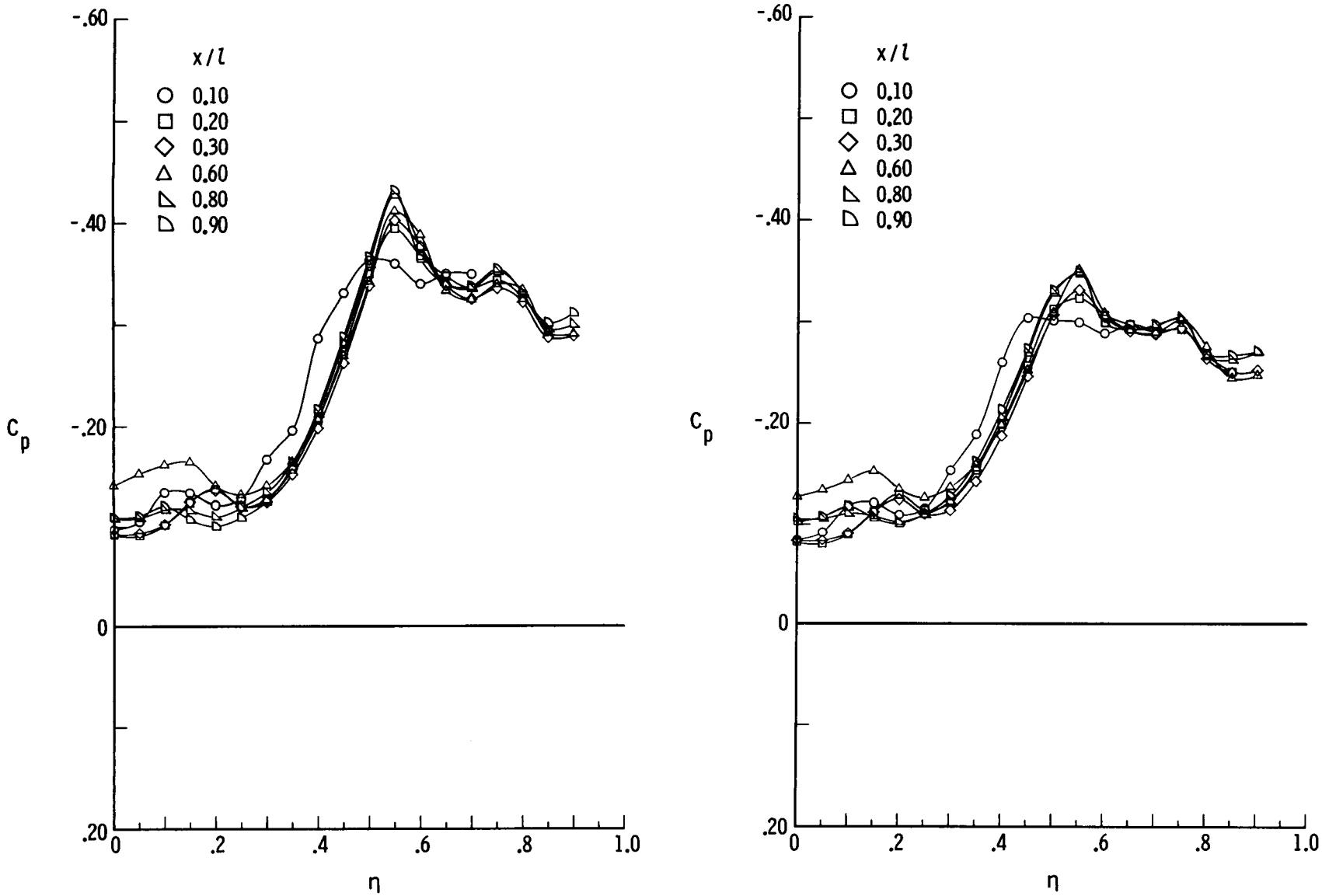

(a) M = 1.50.

(b) M = 1.70.

Figure B13.- Pressure plots for 75° delta wing with $\delta_F = 5°$ for varying x/l, $R = 2 \times 10^6$, $\alpha = 12°$, and $\beta = 0°$.

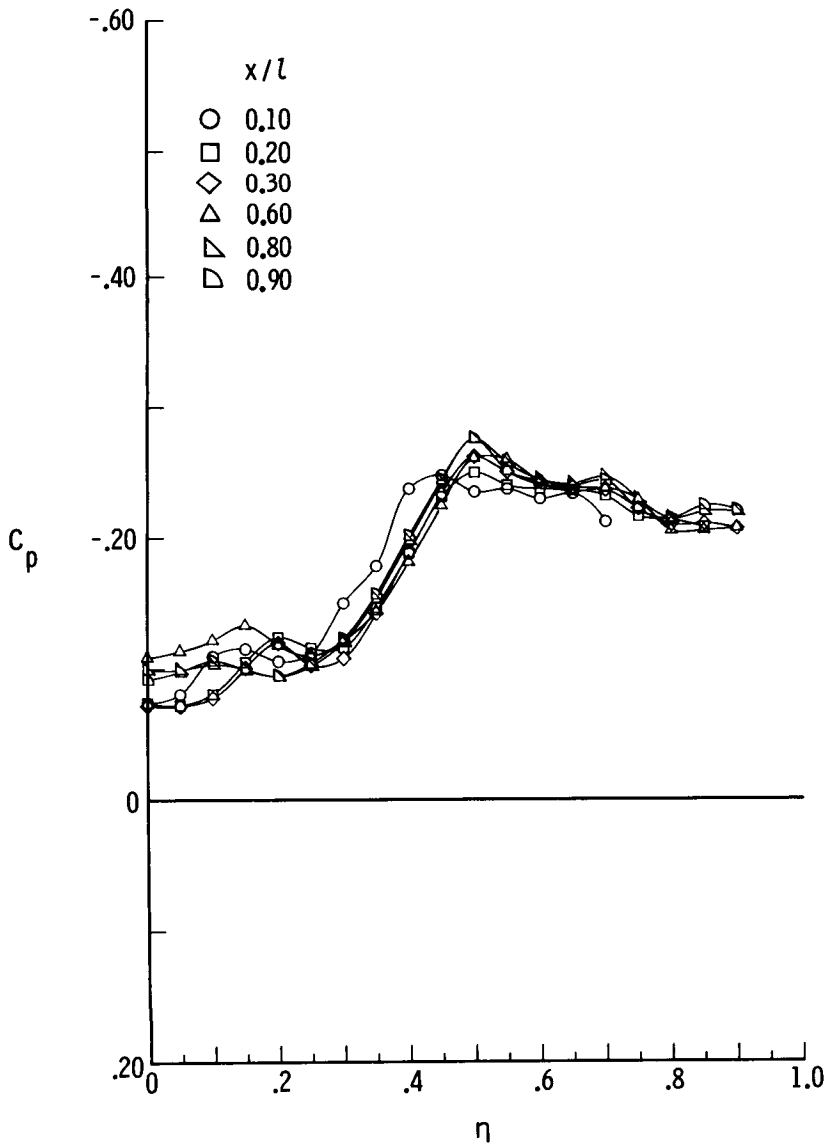

(c) M = 2.00.

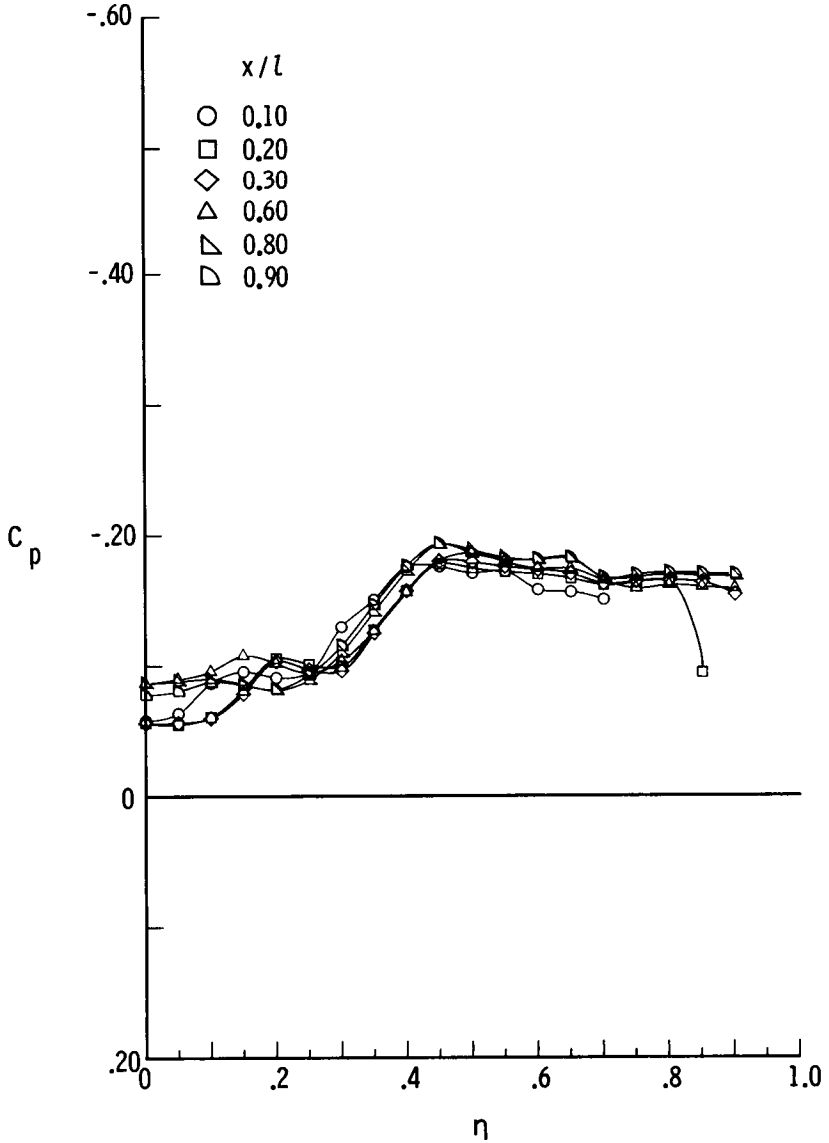

(d) M = 2.40.

Figure B13.- Continued.

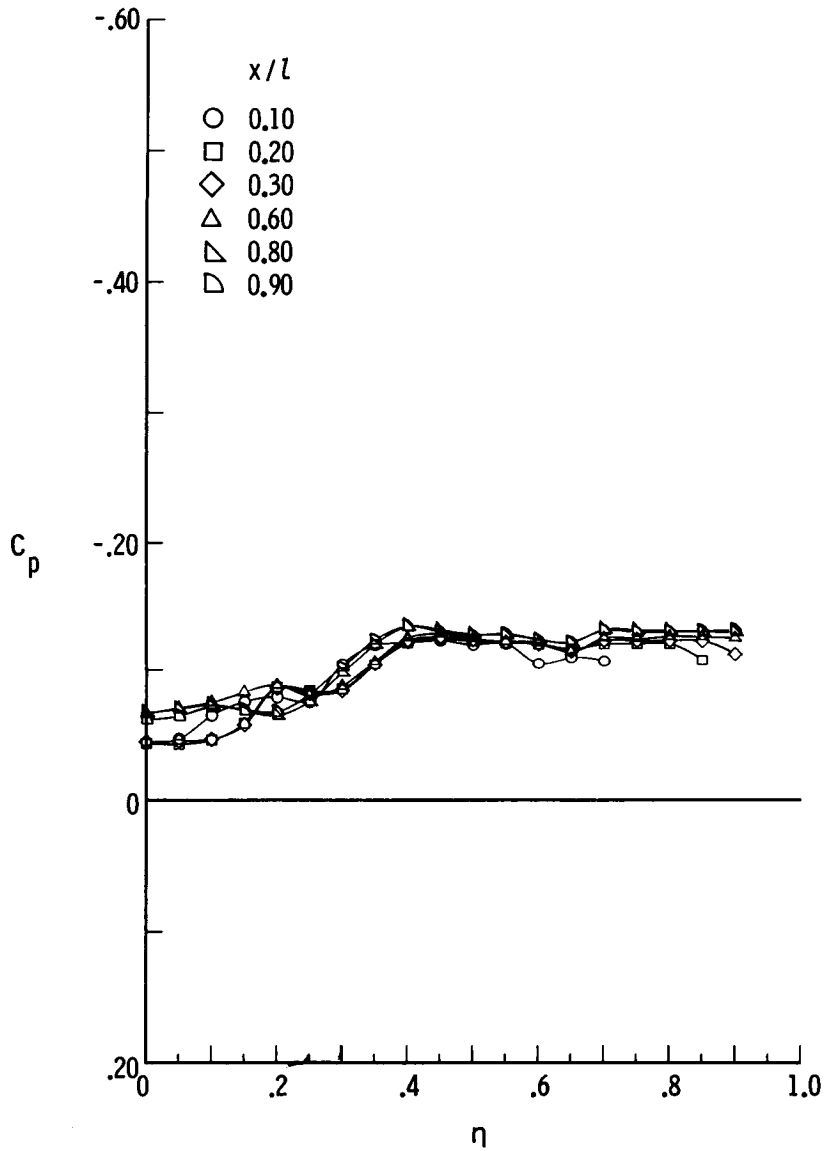

(e) M = 2.80.

Figure B13.- Concluded.

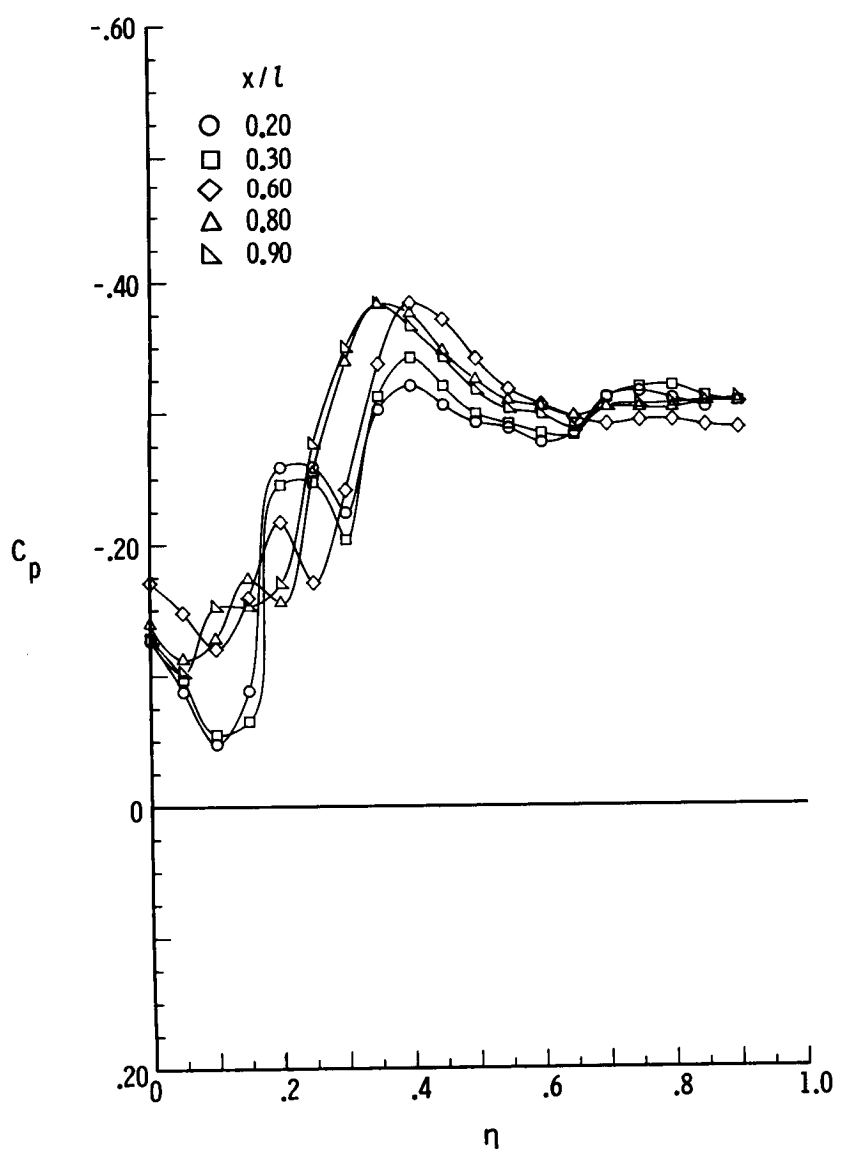

(a) M = 1.70; β = 8°.

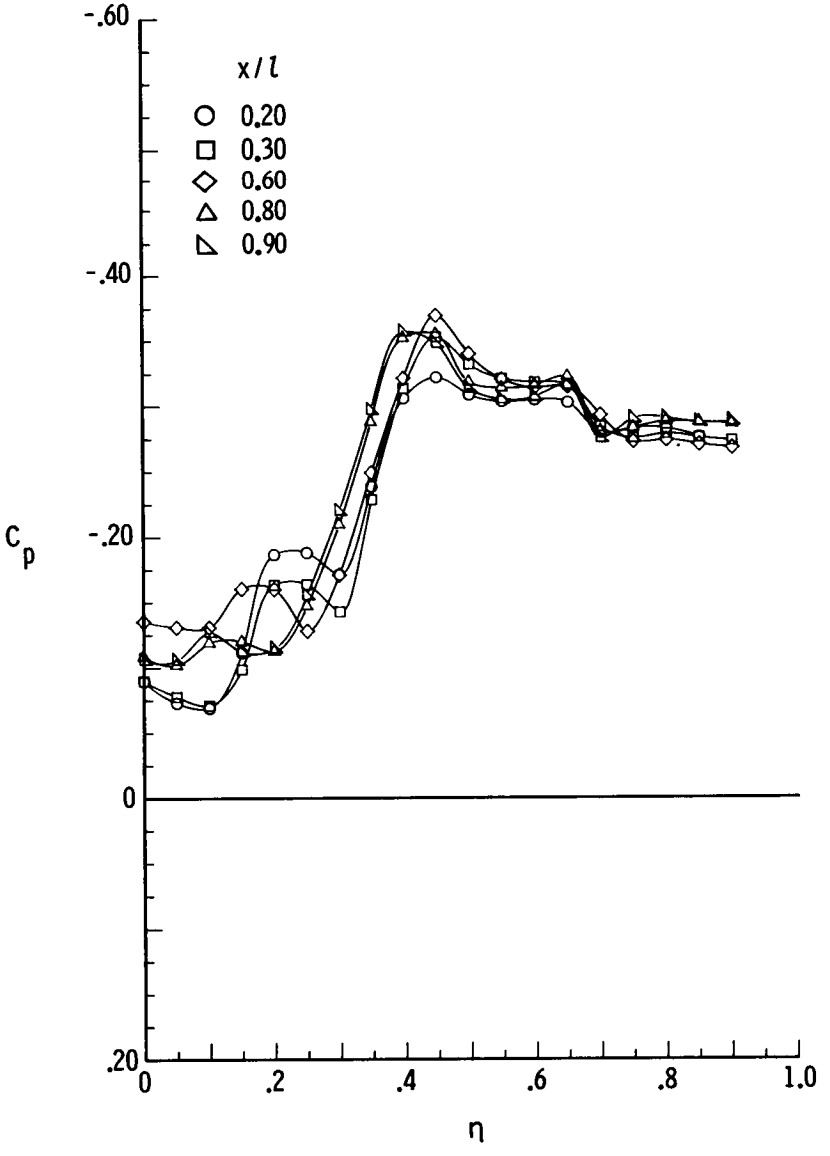

(b) M = 1.70; β = 4°.

Figure B14.- Pressure plots for 75° delta wing with δ_F = 5° for varying x/l, R = 2 × 10^6; and α = 12°.

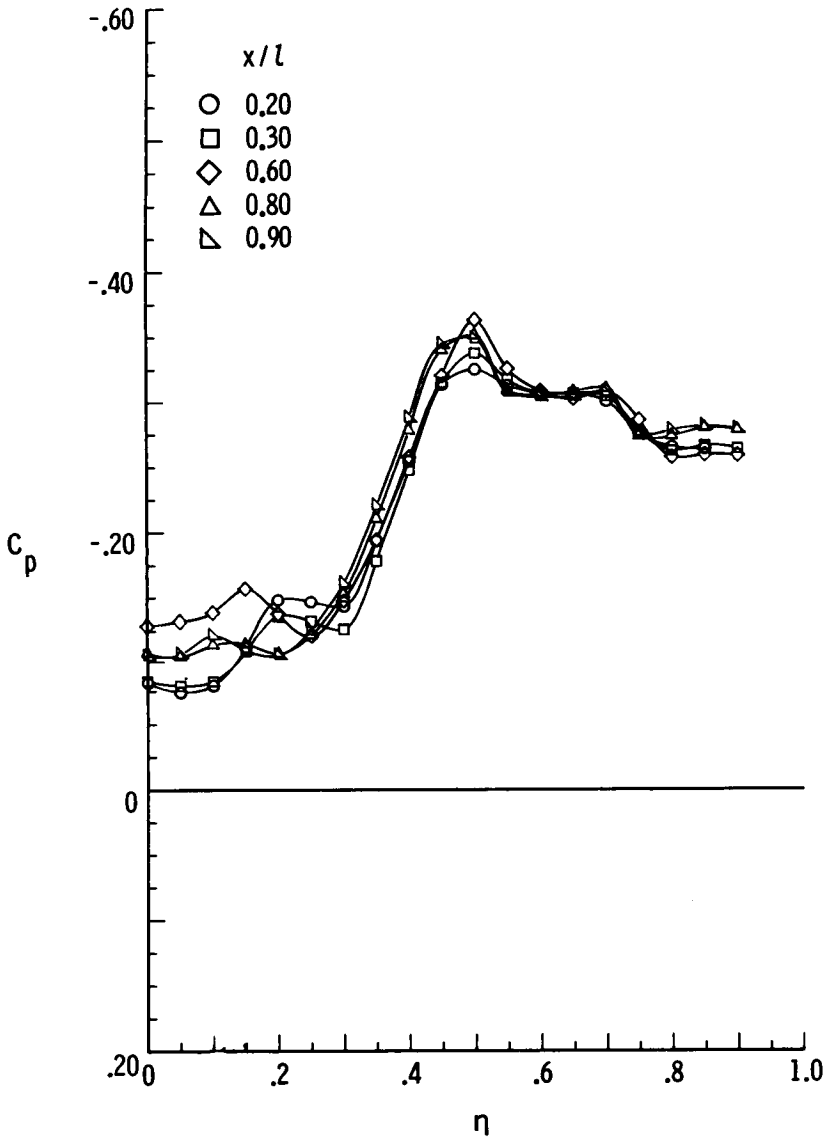

(c) M = 1.70; β = 2°.

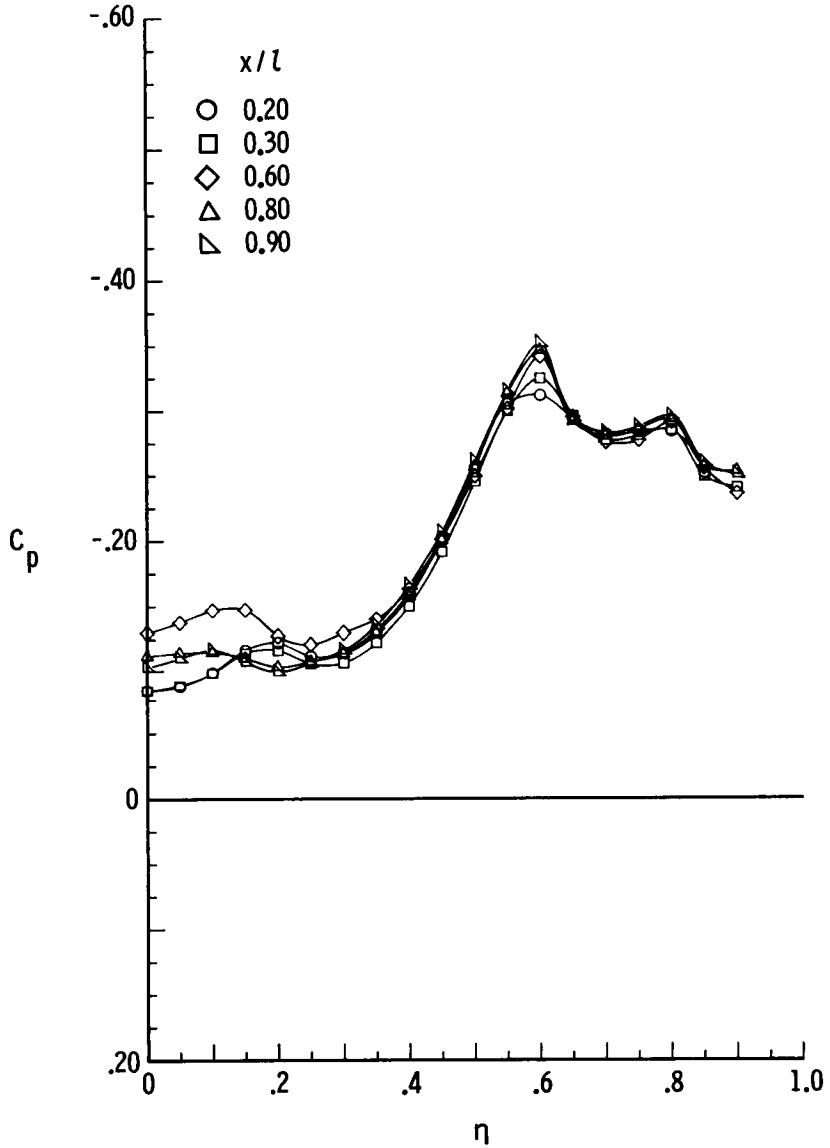

(d) M = 1.70; β = -2°.

Figure B14.- Continued.

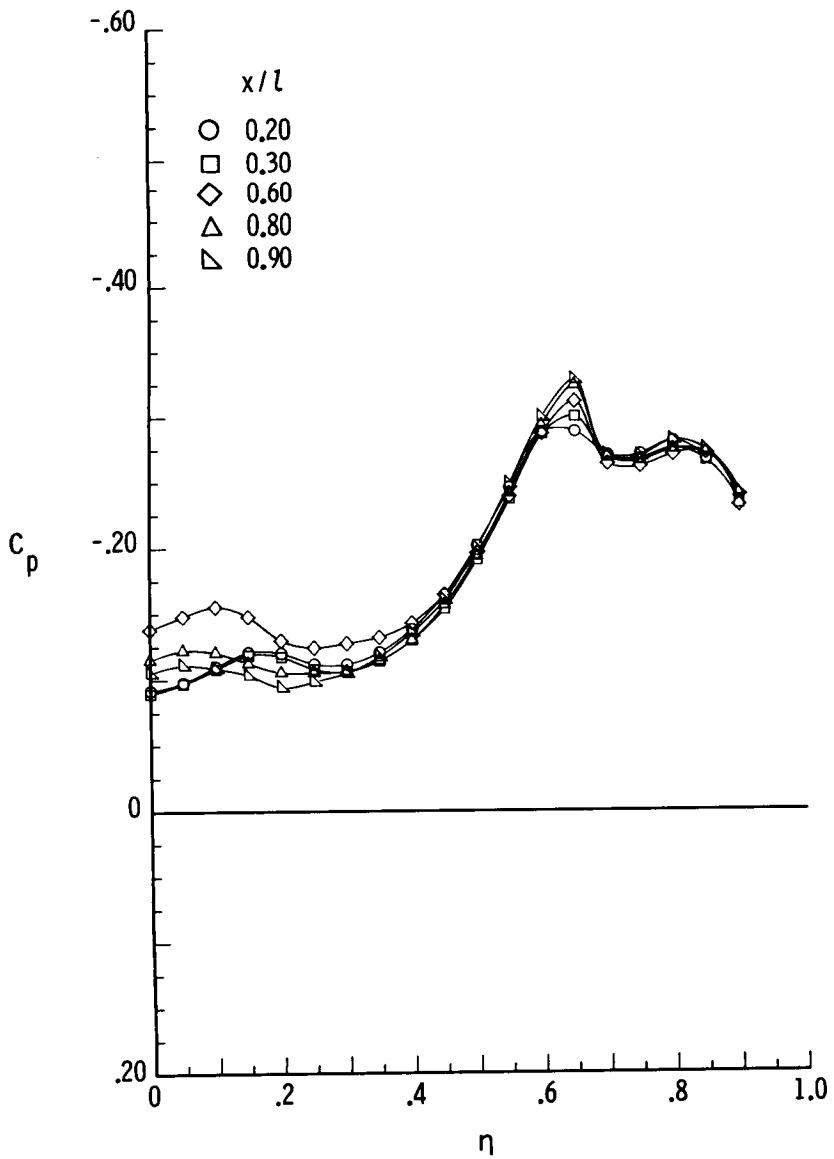

(e) M = 1.70; β = -4°.

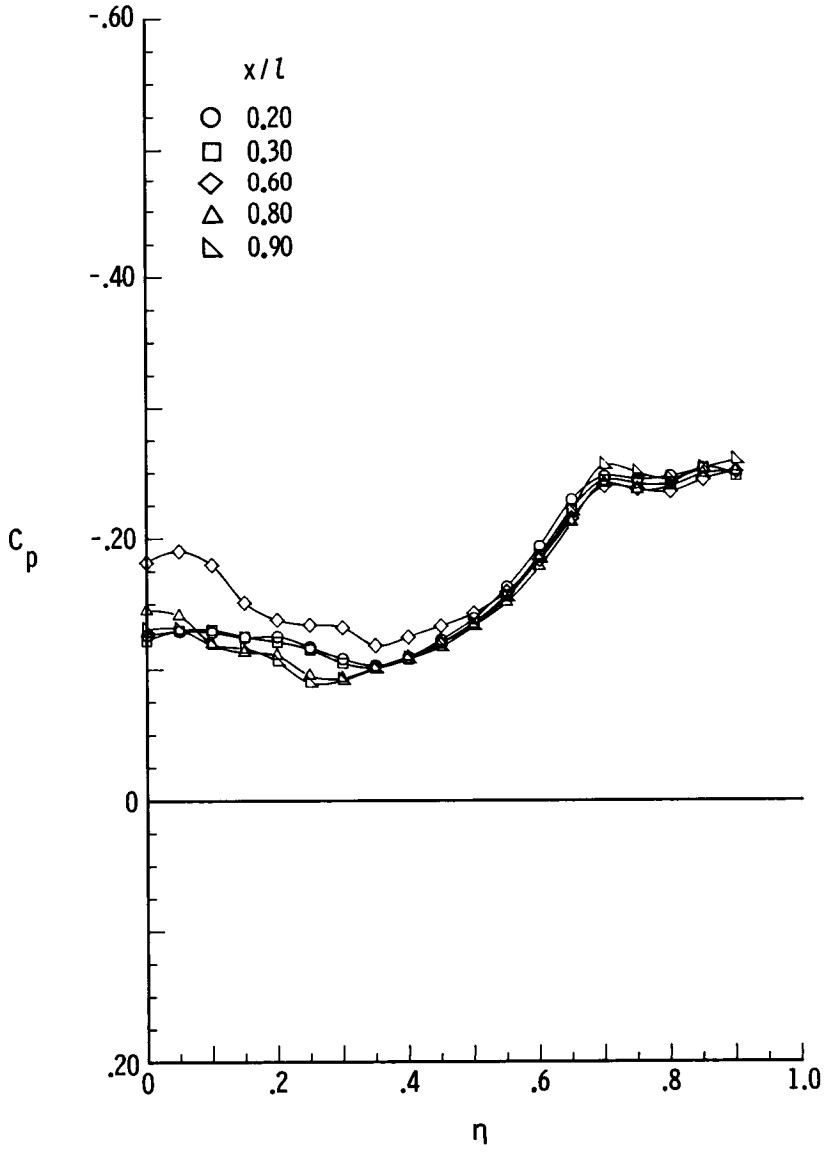

(f) M = 1.70; β = -8°.

Figure B14.- Continued.

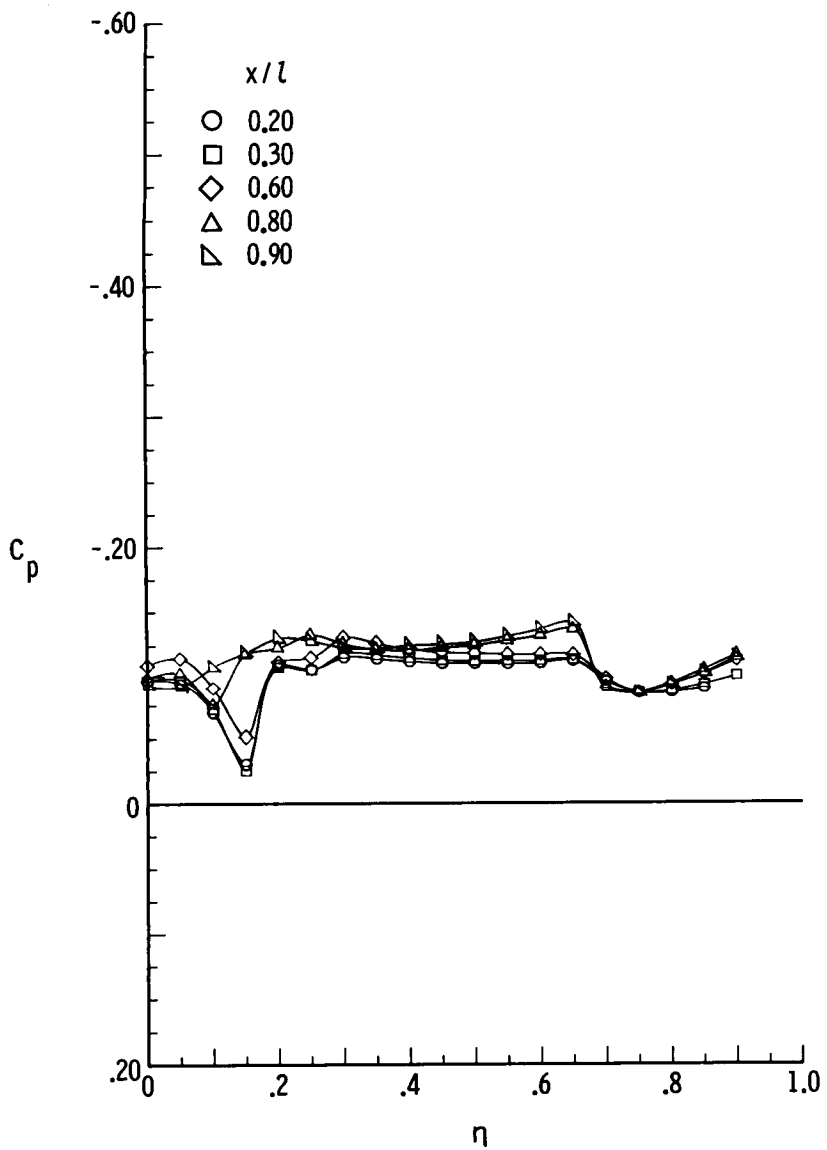

(g) M = 2.80; β = 8°.

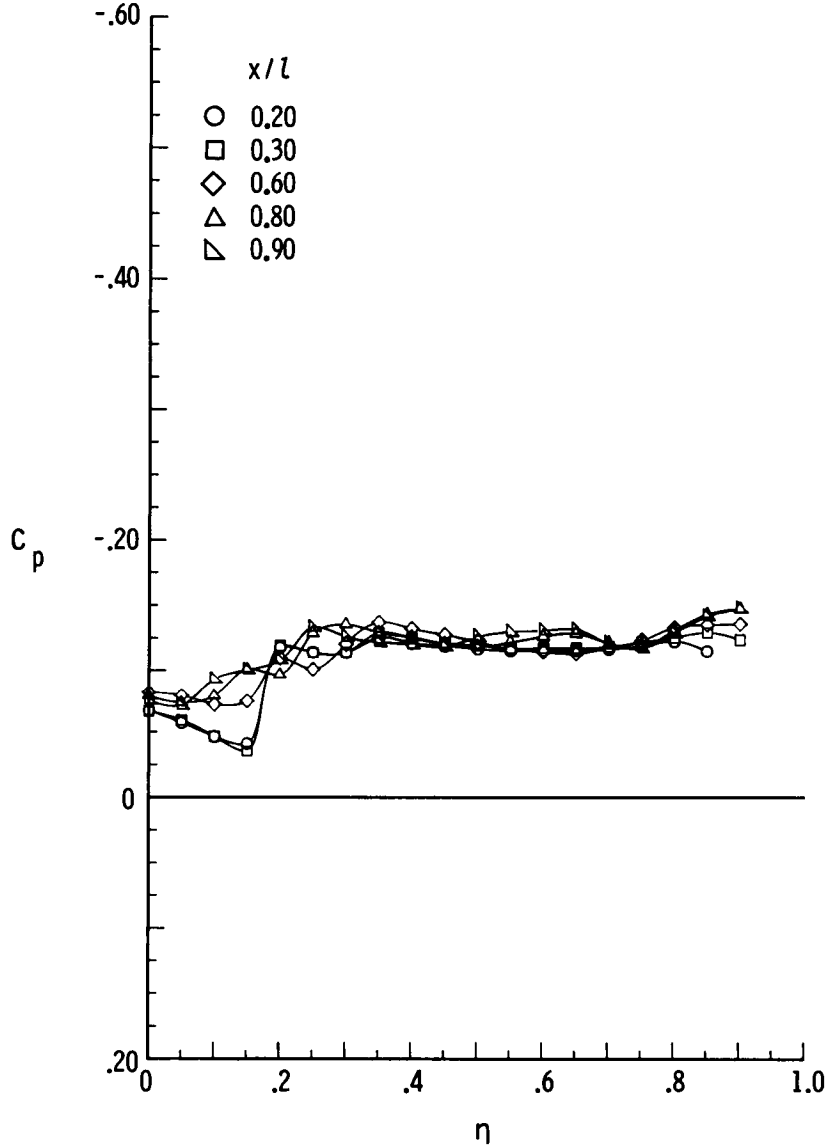

(h) M = 2.80; β = 4°.

Figure B14.- Continued.

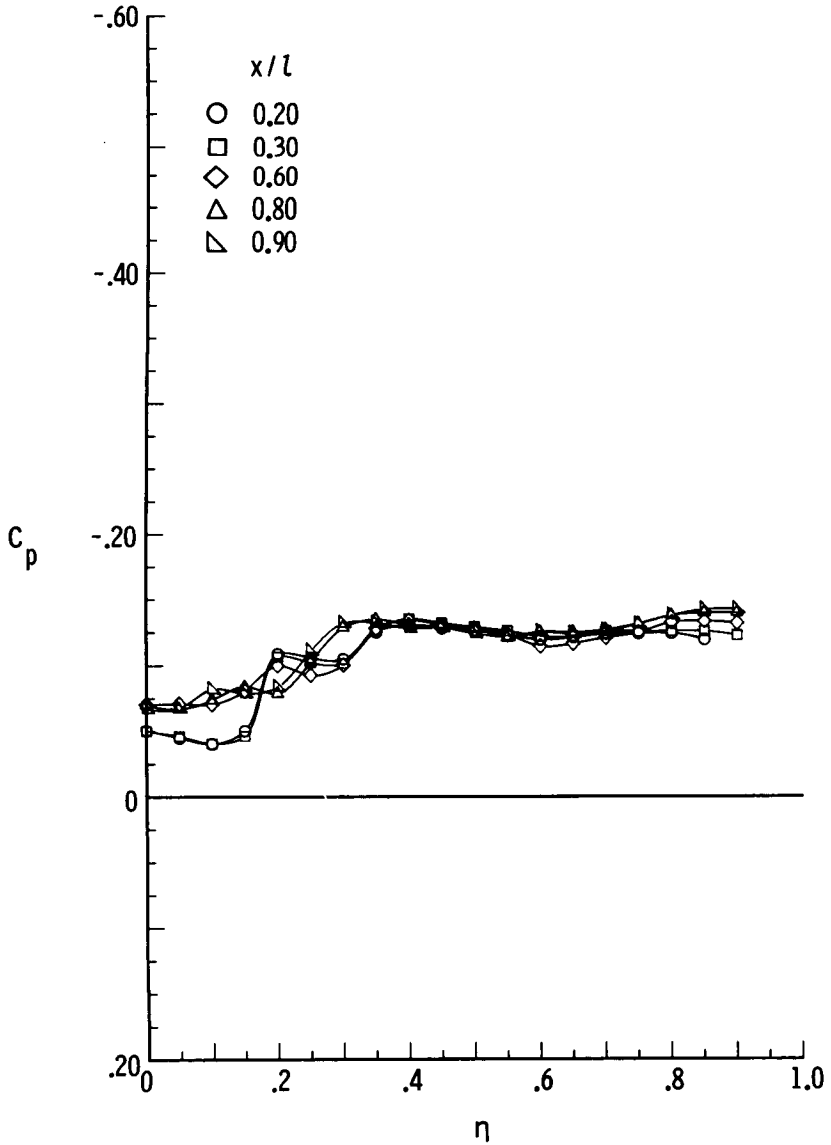

(i) M = 2.80; β = 2°.

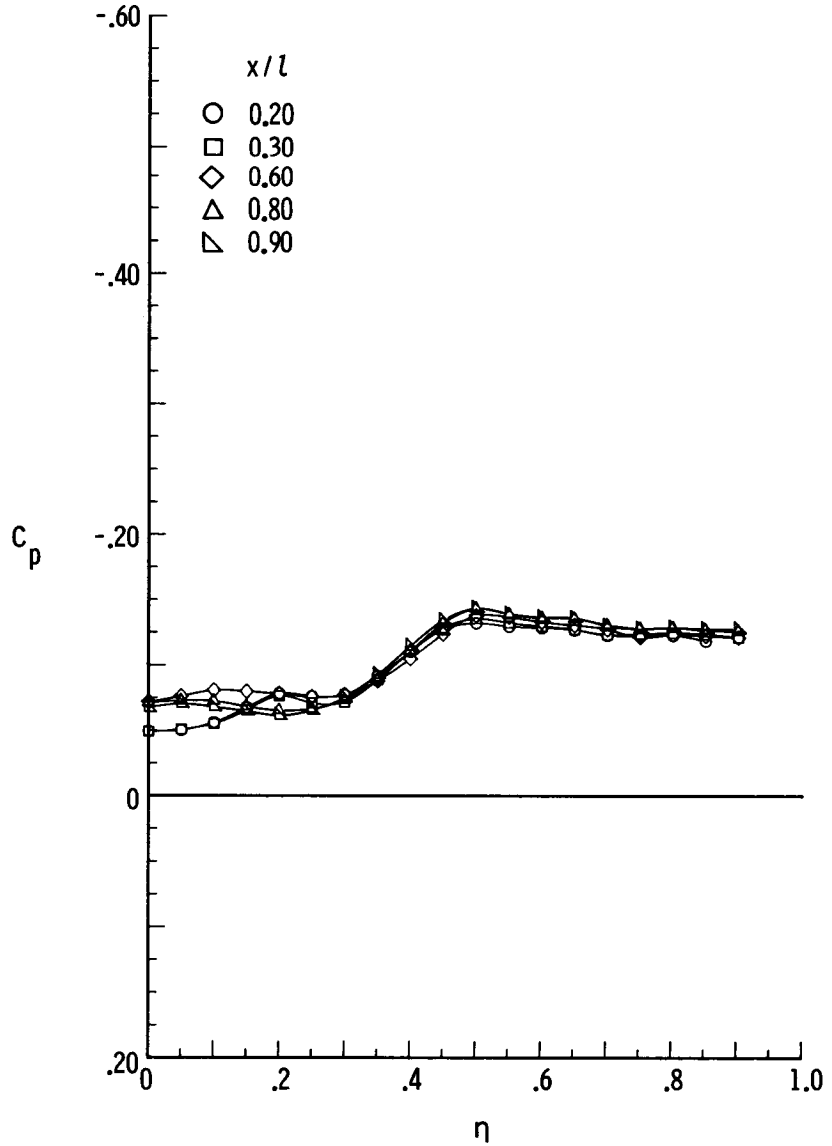

(j) M = 2.80; β = -2°.

Figure B14.- Continued.

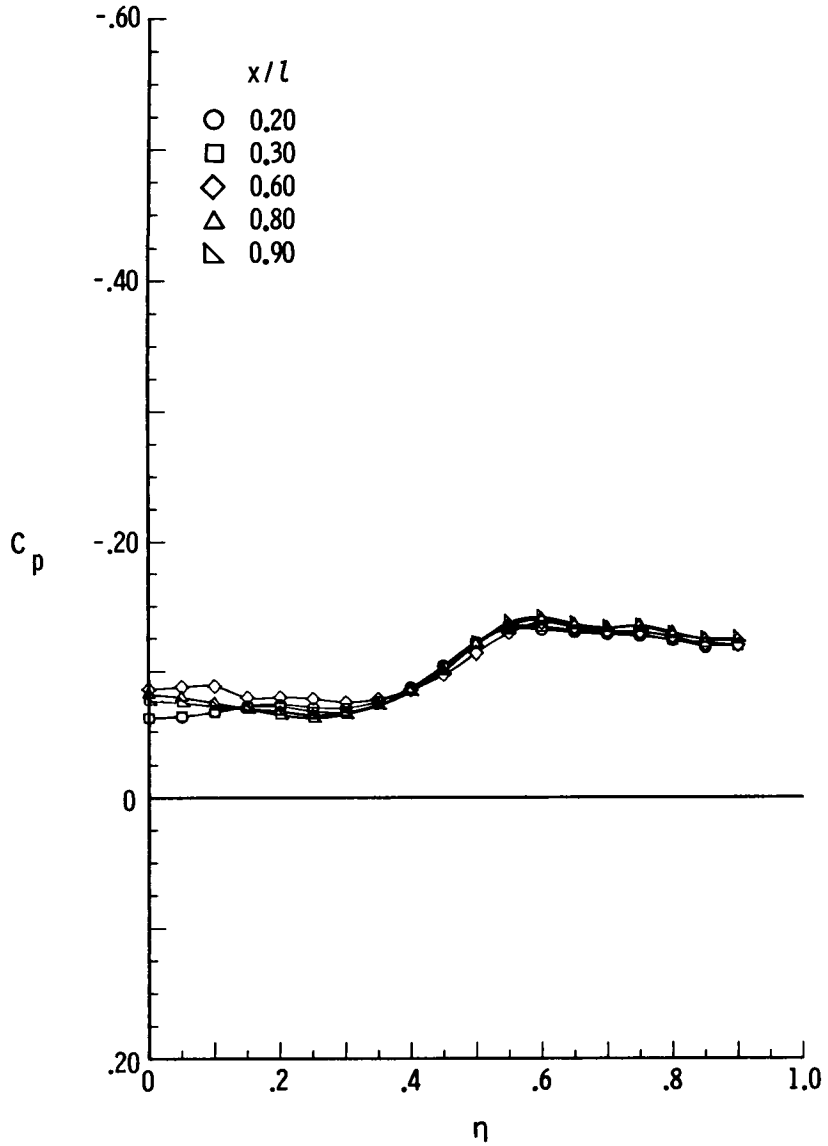

(k) M = 2.80; β = -4°.

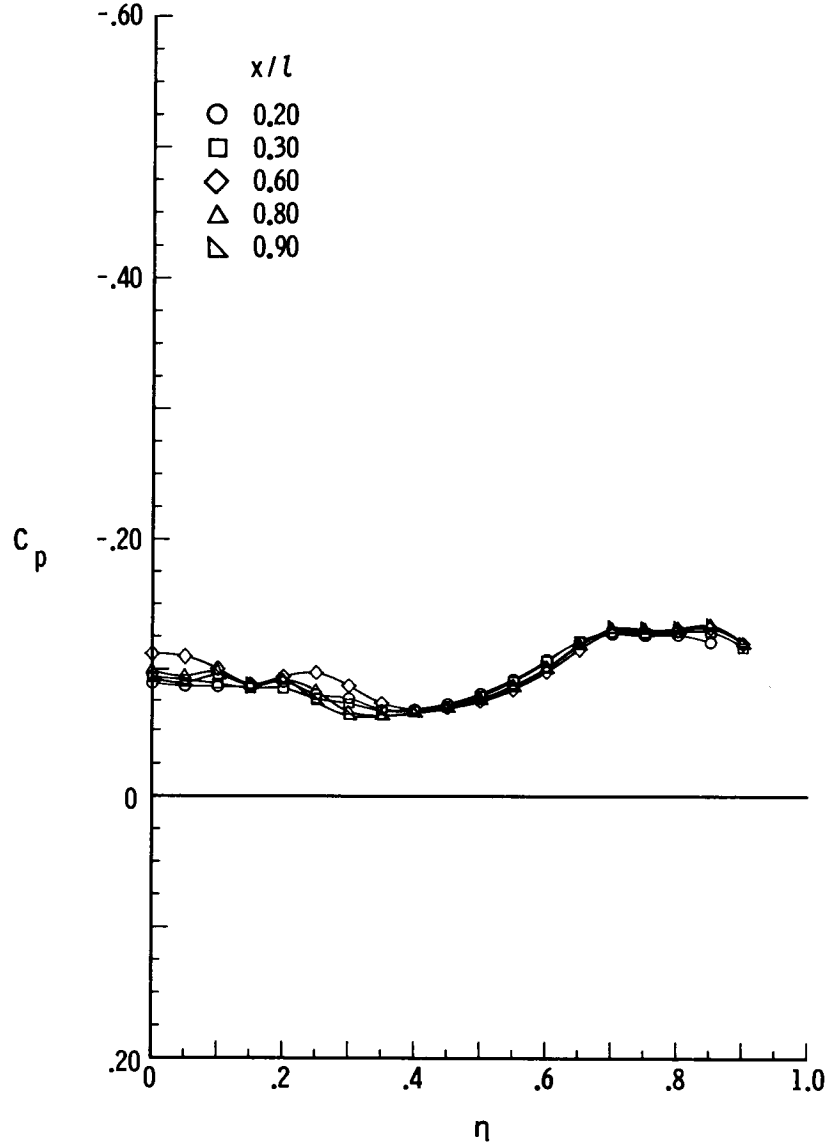

(l) M = 2.80; β = -8°.

Figure B14.- Concluded.

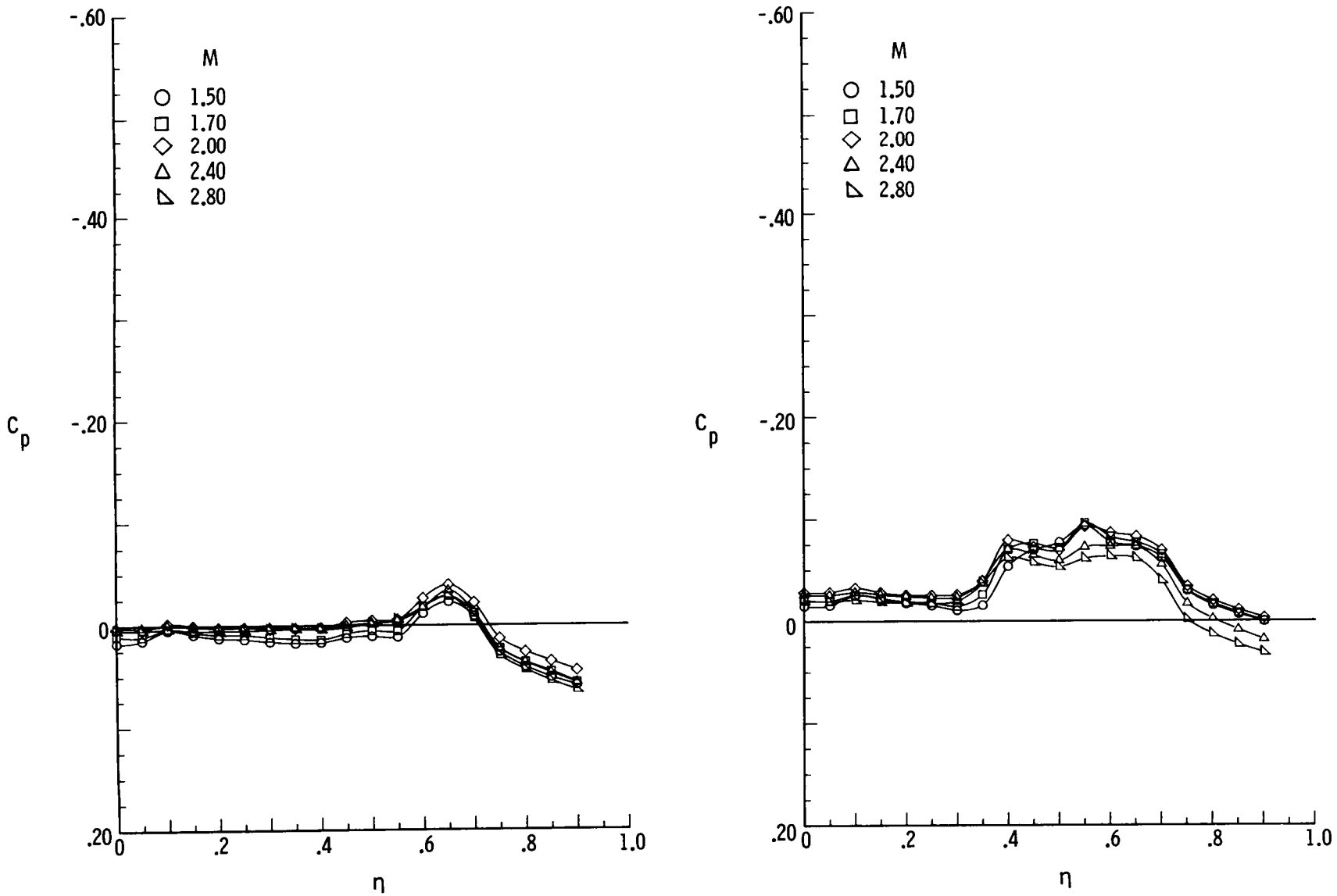

(a) $\beta = 0°$.

(b) $\beta = 4°$.

Figure B15.- Pressure plots for 75° delta wing with $\delta_F = 10°$ for varying M, $R = 2 \times 10^6$, $\alpha = 0°$, and $x/\ell = 0.90$.

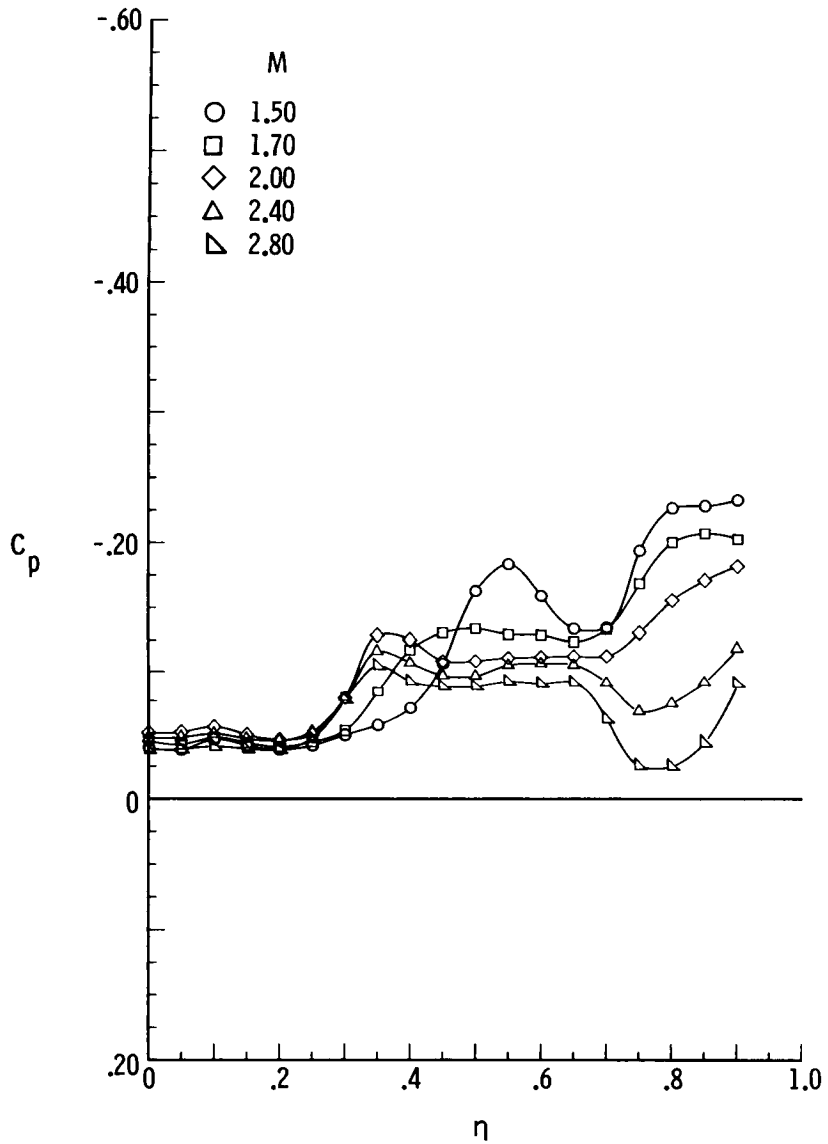

(c) $\beta = 8°$.

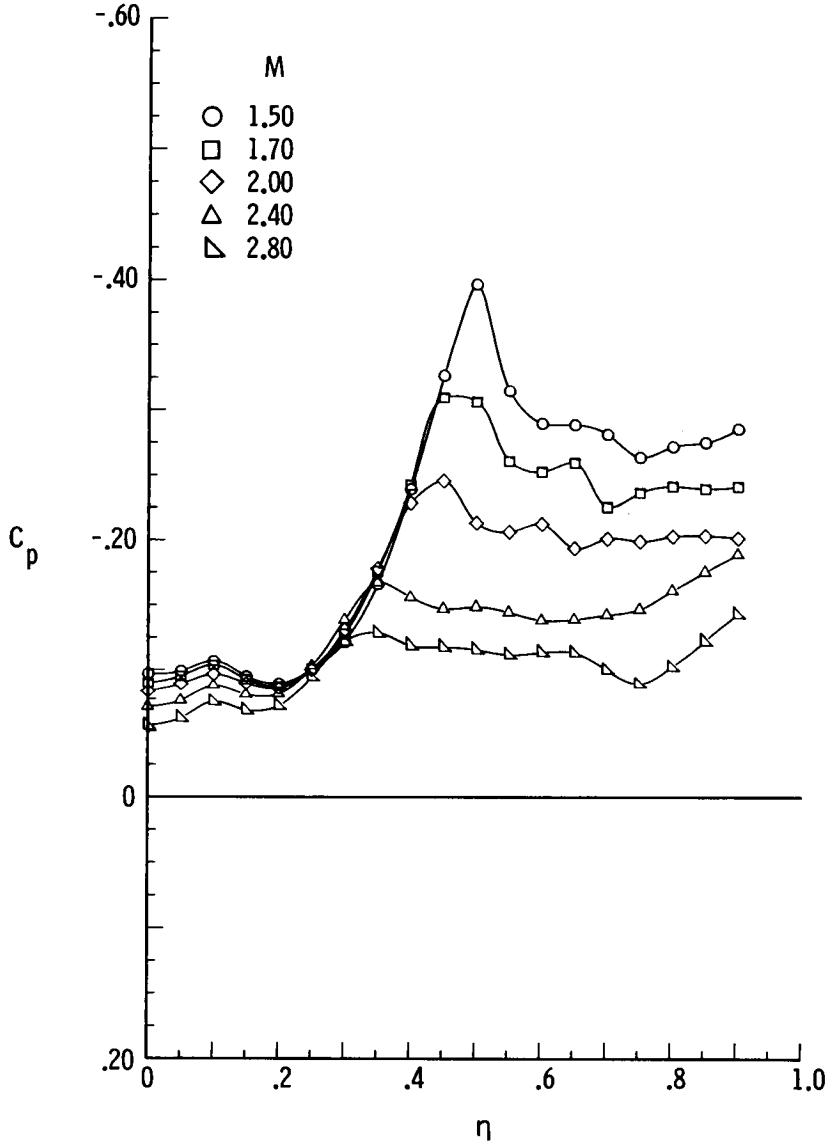

(d) $\beta = 12°$.

Figure B15.- Concluded.

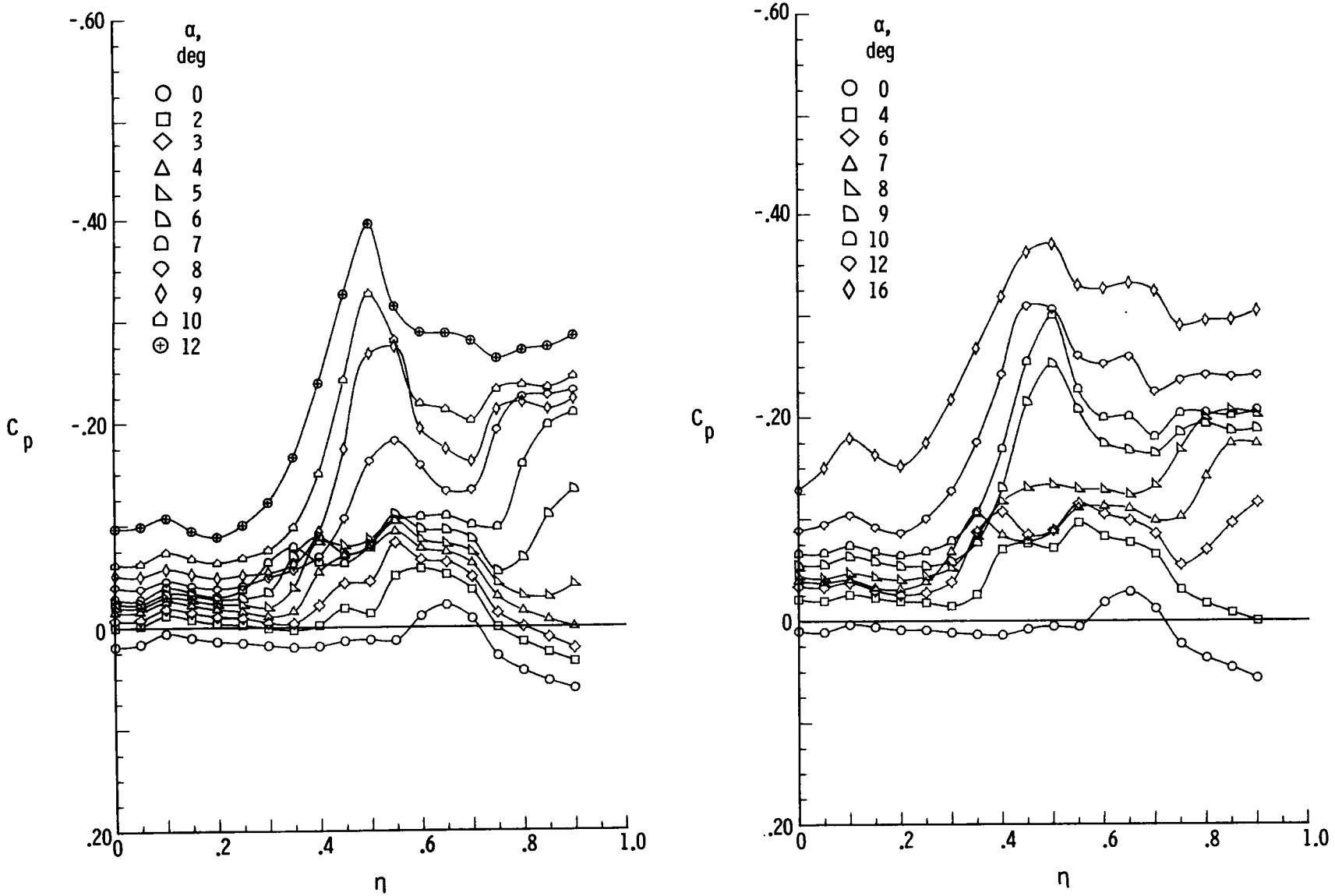

(a) M = 1.50.

(b) M = 1.70.

Figure B16.- Pressure plots for 75° delta wing with $\delta_F = 10°$ for varying α, $R = 2 \times 10^6$, $\beta = 0°$, and $x/\ell = 0.90$.

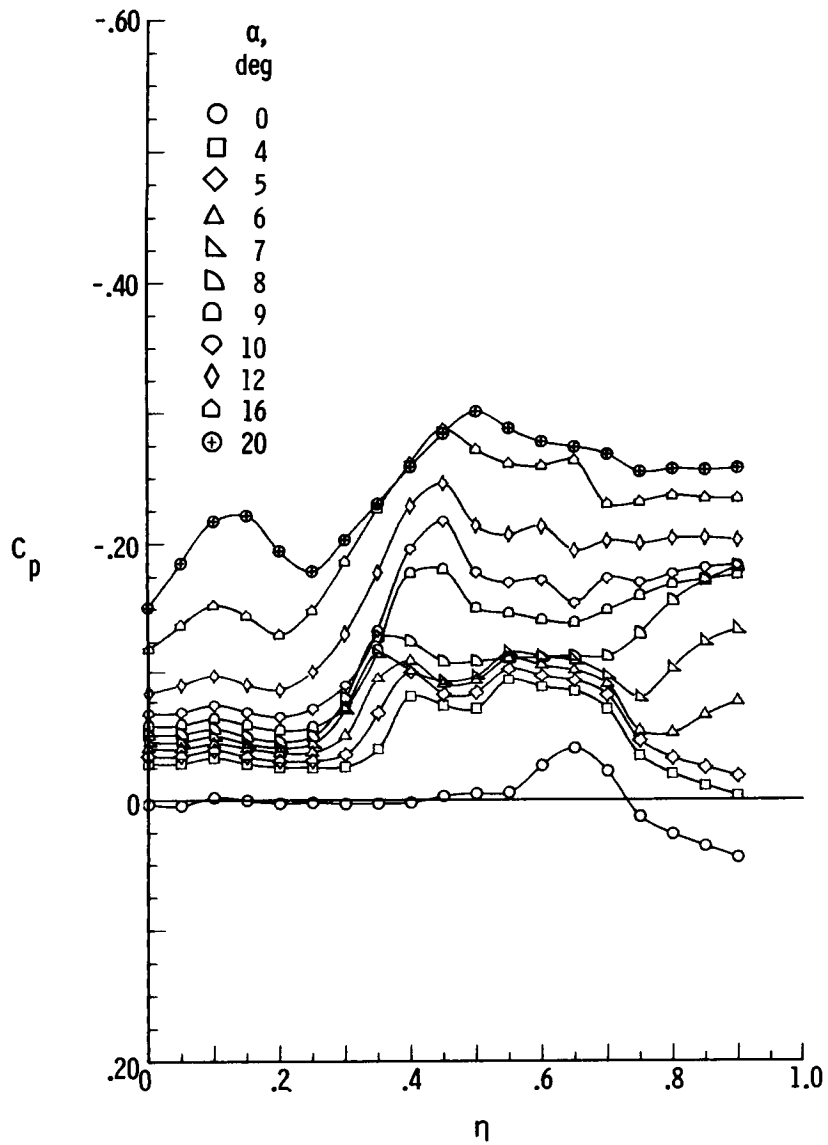

(c) M = 2.00.

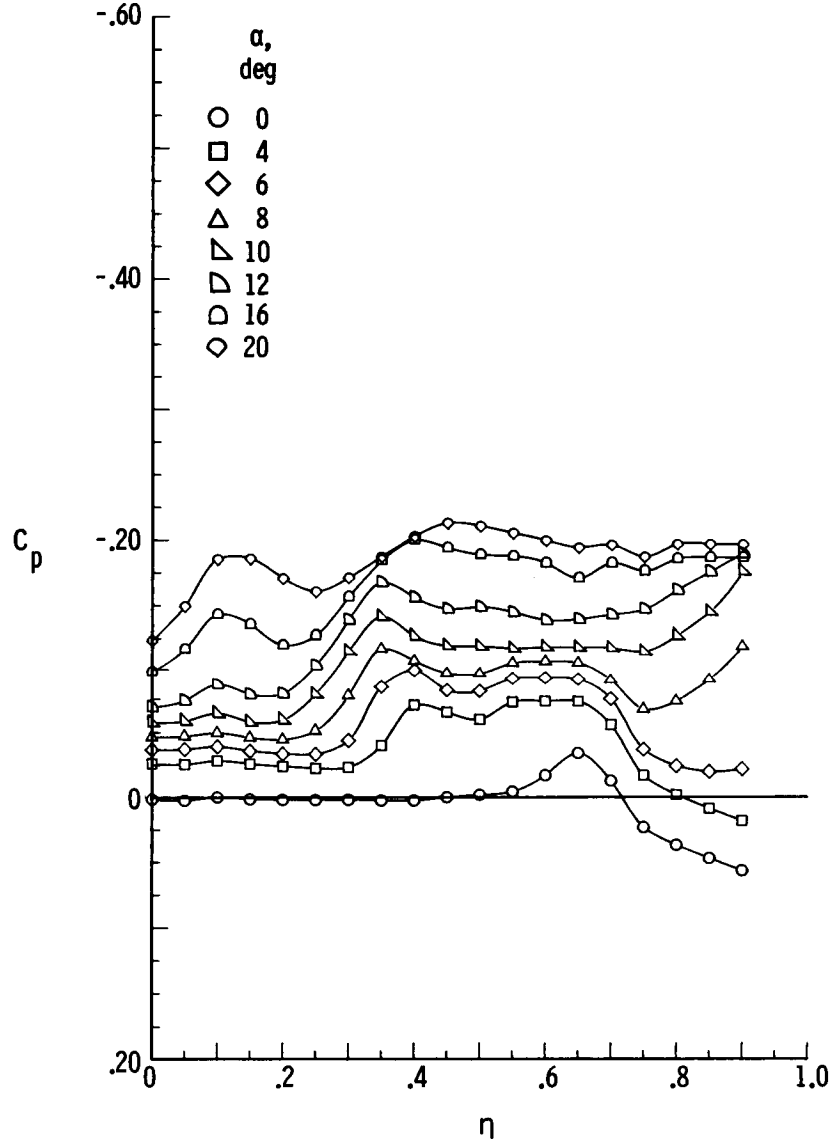

(d) M = 2.40.

Figure B16.- Continued.

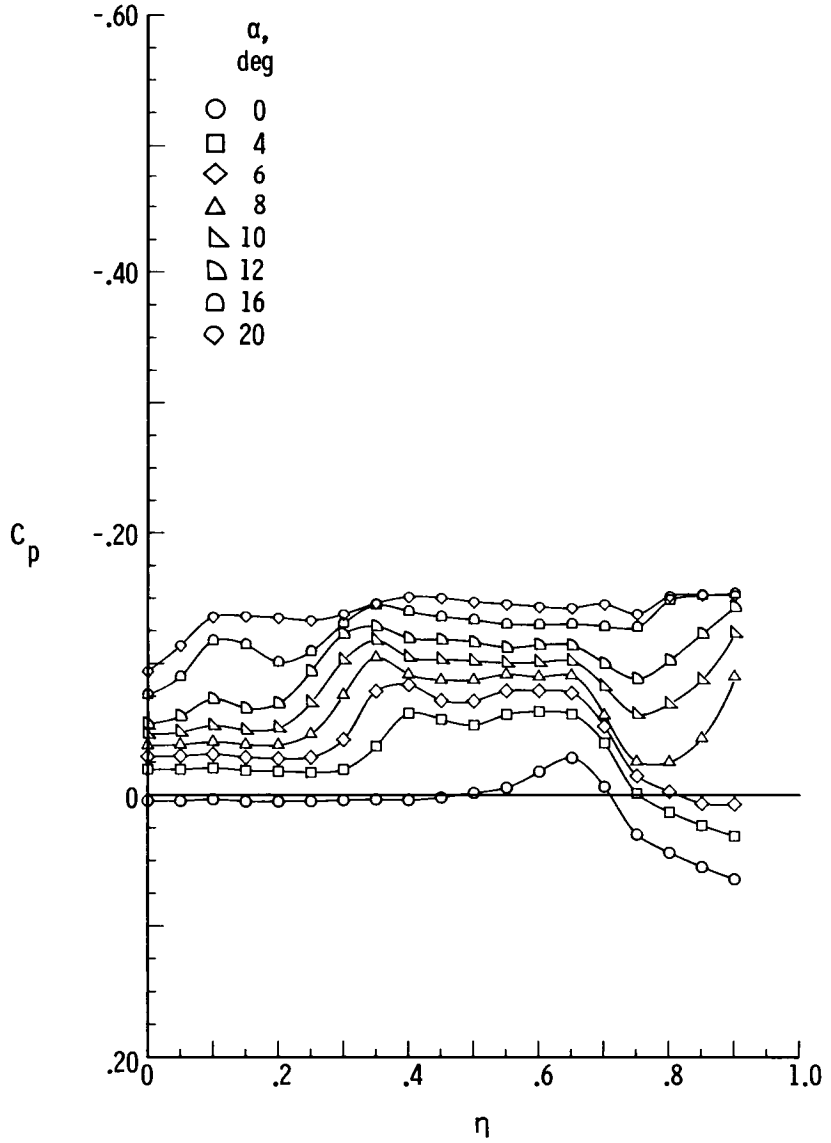

(e) M = 2.80.

Figure B16.- Concluded.

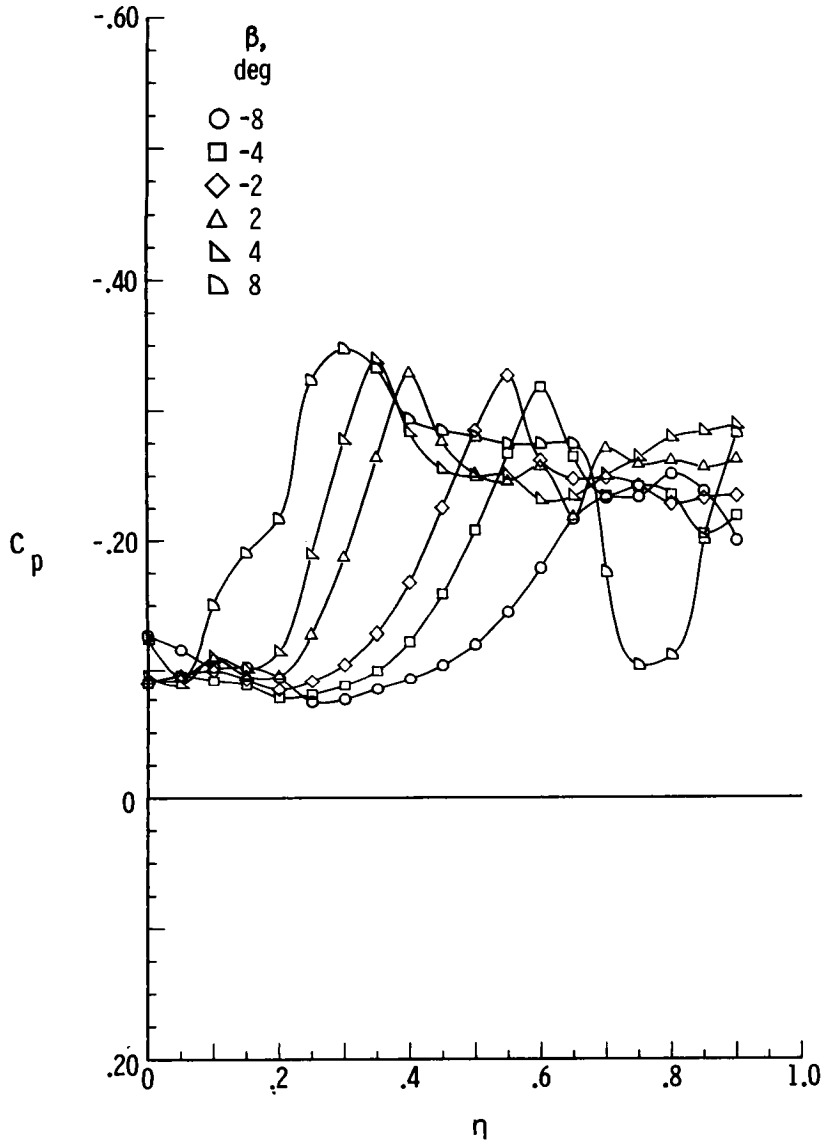

(a) M = 1.70.

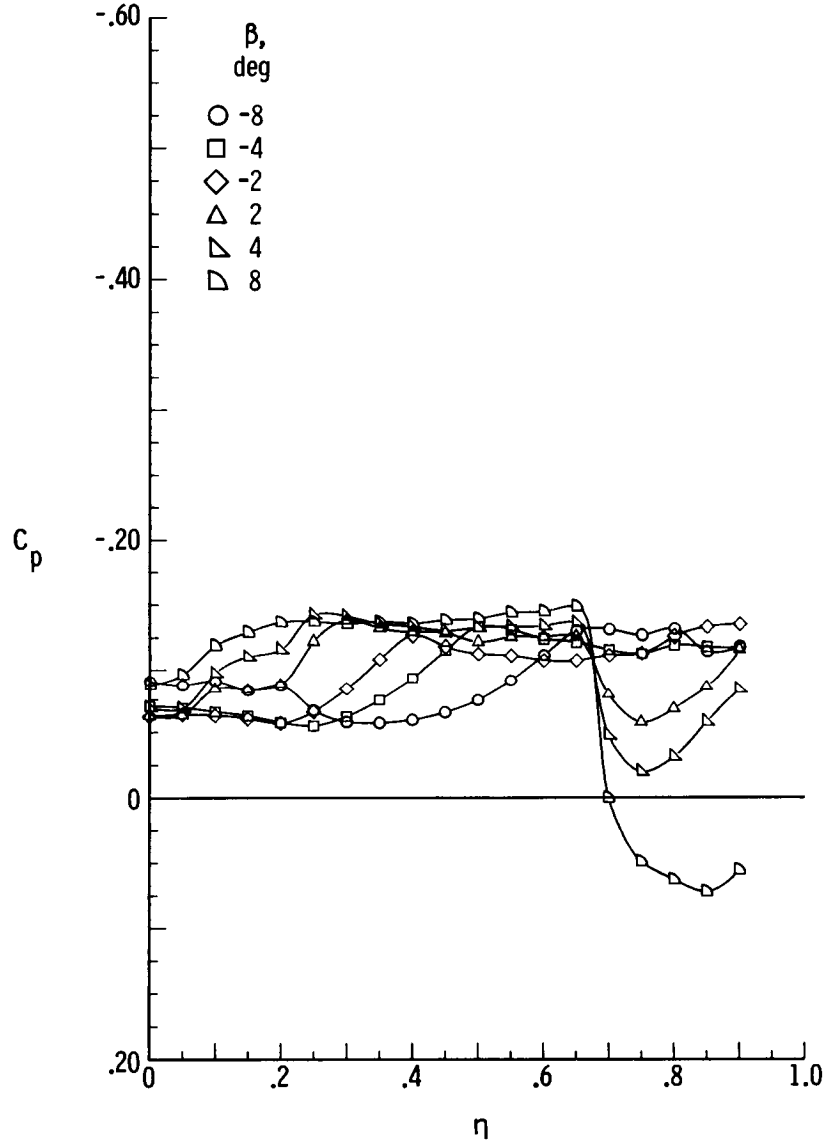

(b) M = 2.80.

Figure B17.- Pressure plots for 75° delta wing with $\delta_F = 10°$ for varying β, $R = 2 \times 10^6$, $\alpha = 12°$, and $x/\ell = 0.90$.

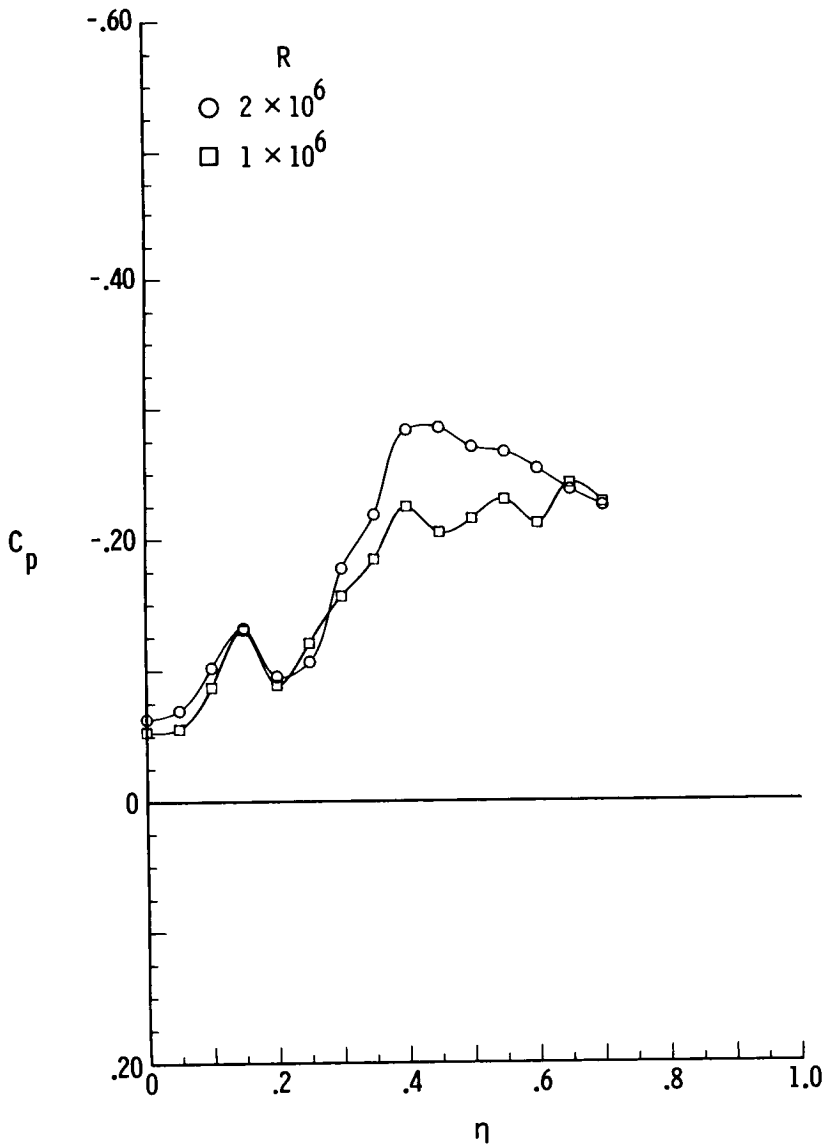

(a) M = 1.70; x/ℓ = 0.10.

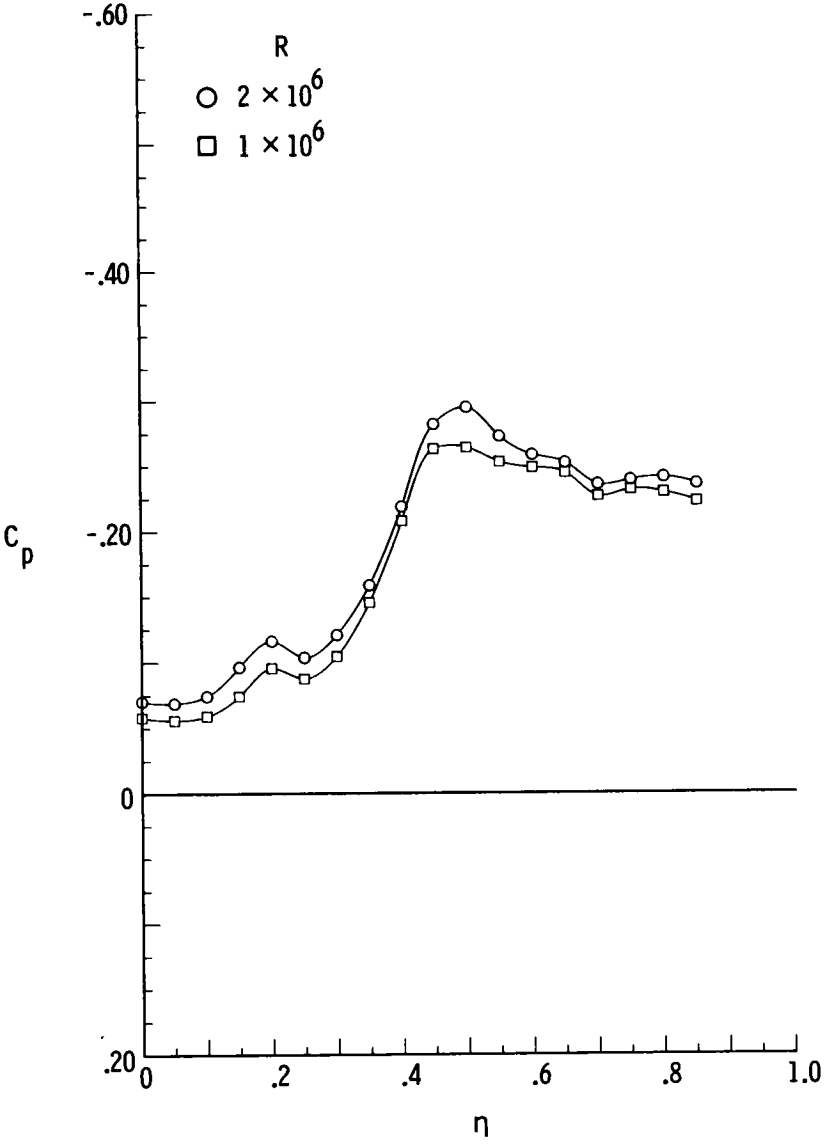

(b) M = 1.70; x/ℓ = 0.20.

Figure B18.- Pressure plots for 75° delta wing with δ_F = 10° for varying R, α = 12°, and β = 0°.

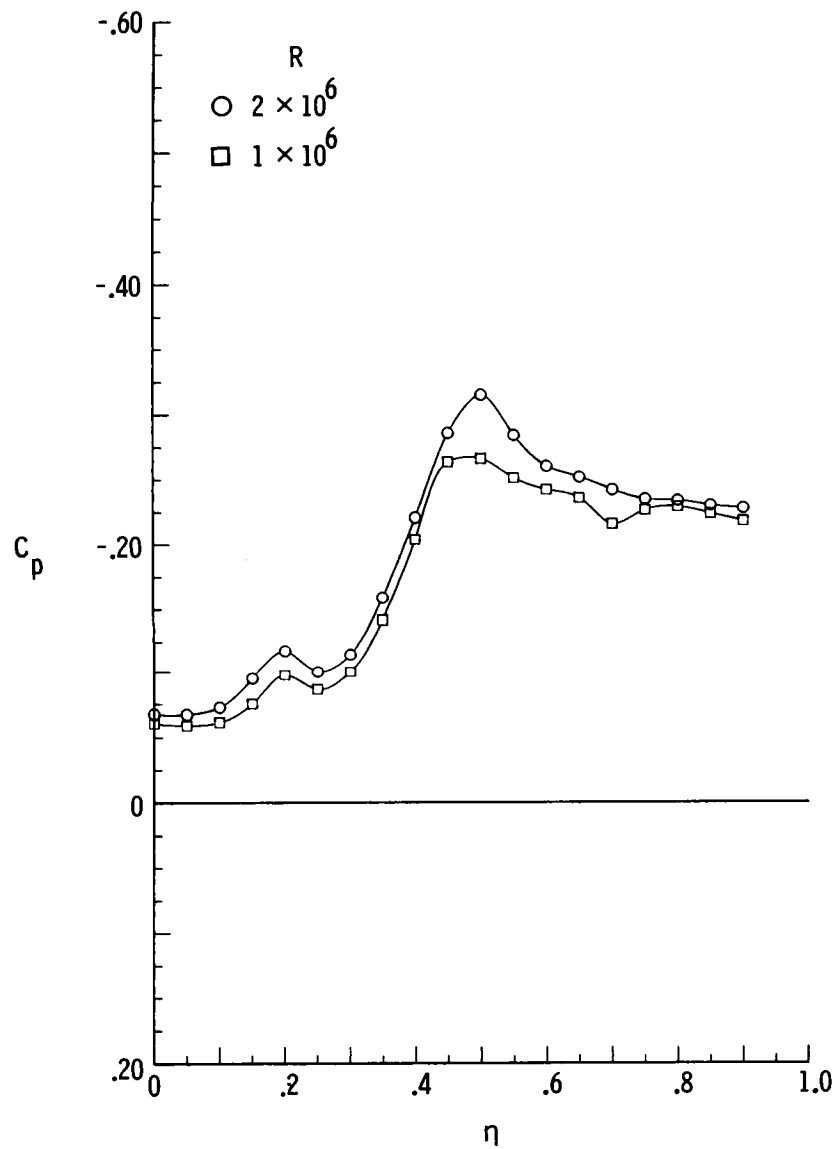

(c) M = 1.70; x/ℓ = 0.30.

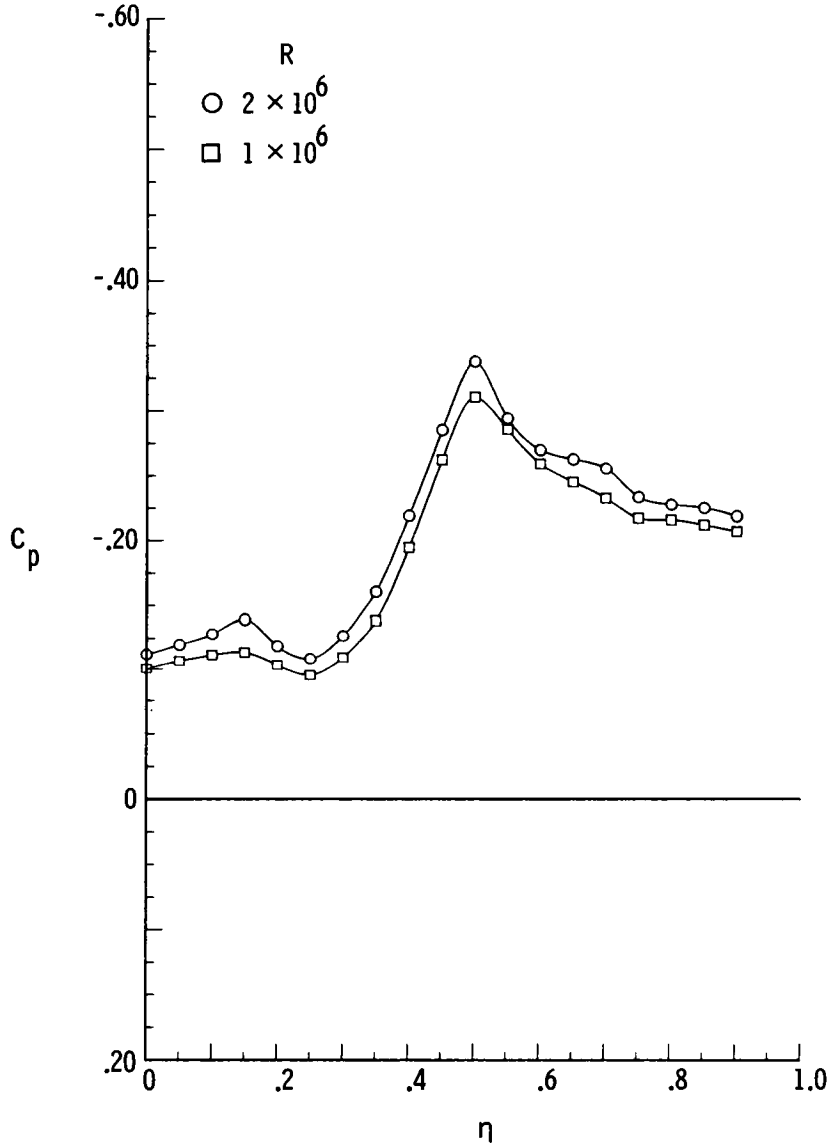

(d) M = 1.70; x/ℓ = 0.60.

Figure B18.- Continued.

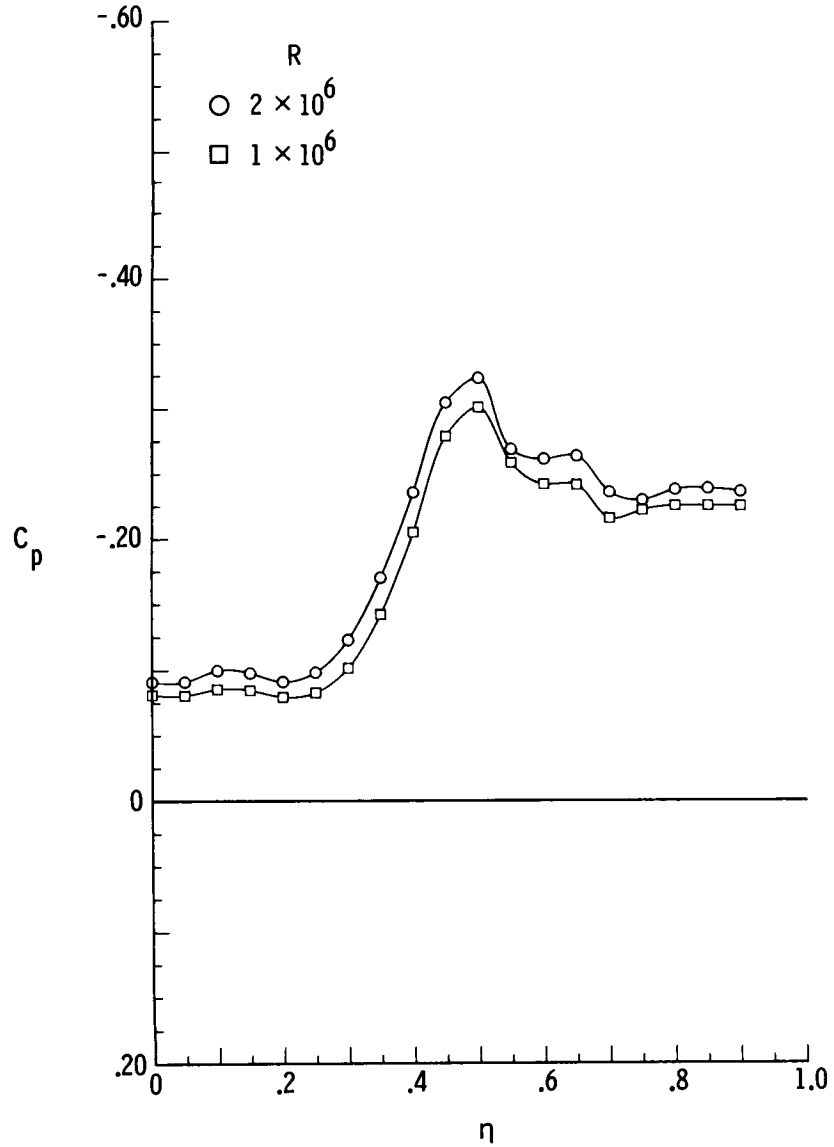

(e) M = 1.70; x/ℓ = 0.80.

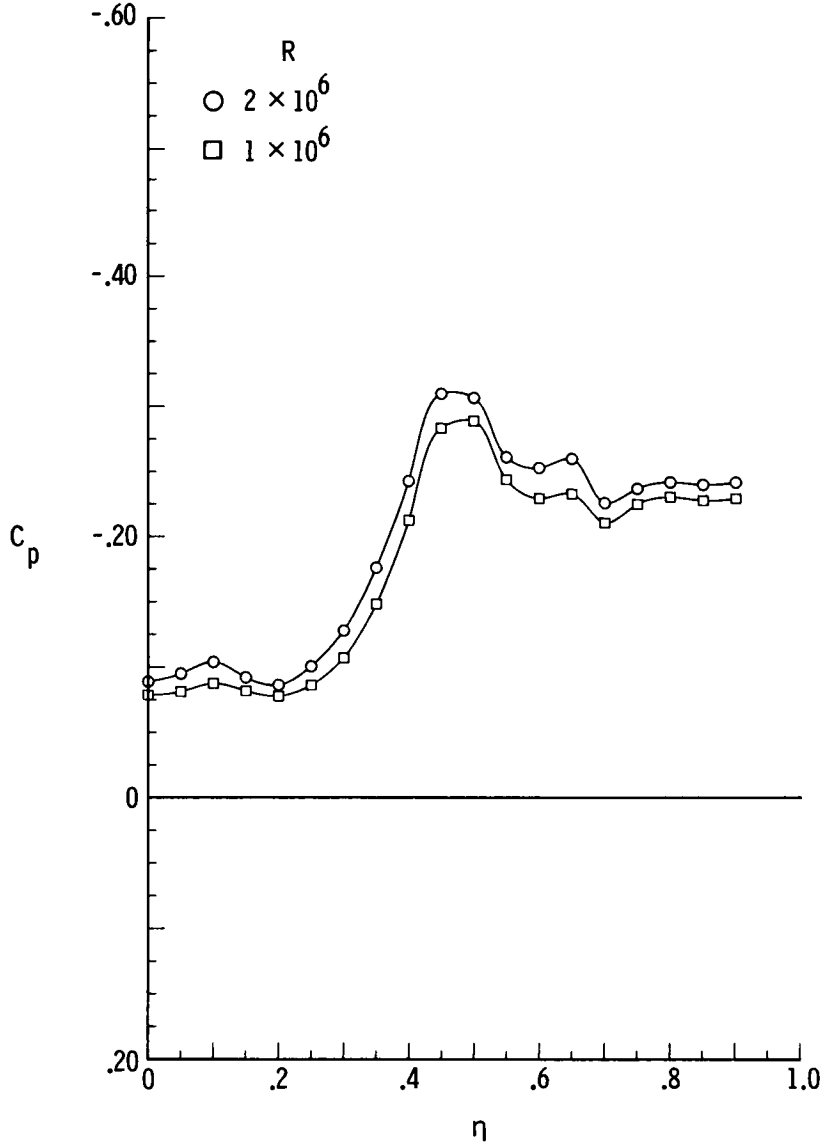

(f) M = 1.70; x/ℓ = 0.90.

Figure B18.- Continued.

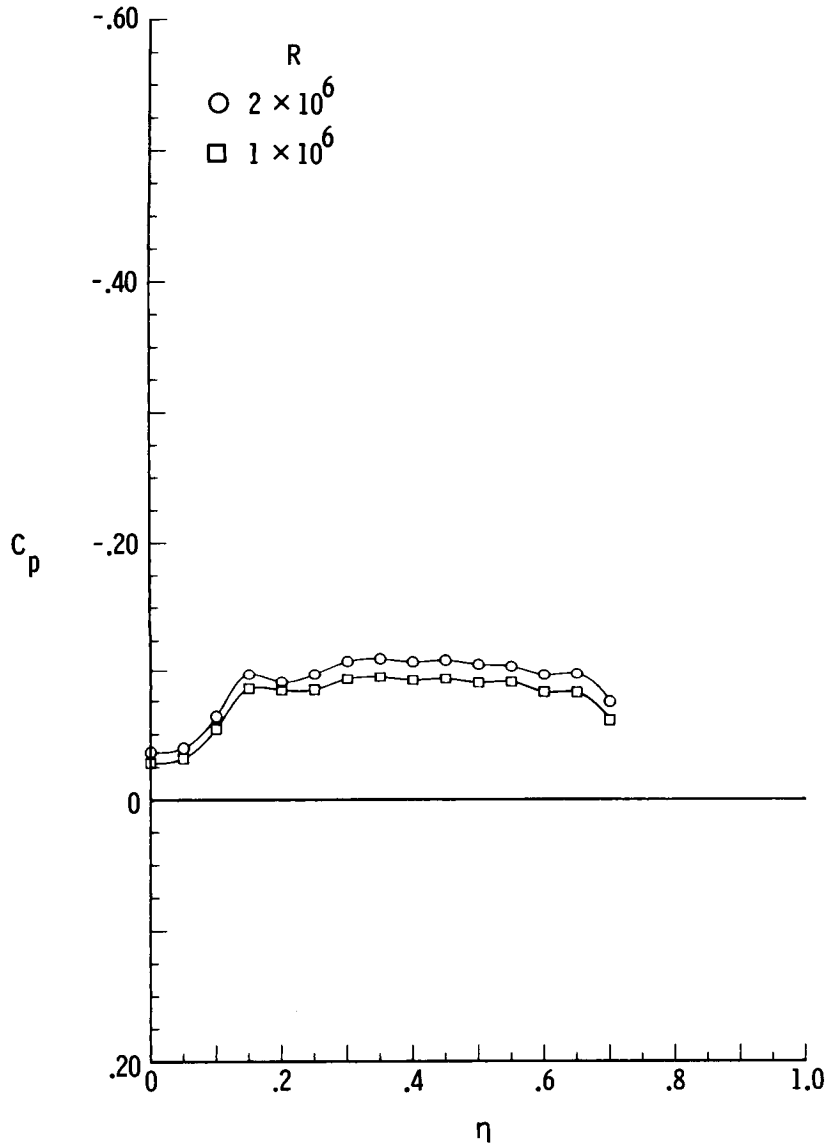

(g) M = 2.80; x/ℓ = 0.10.

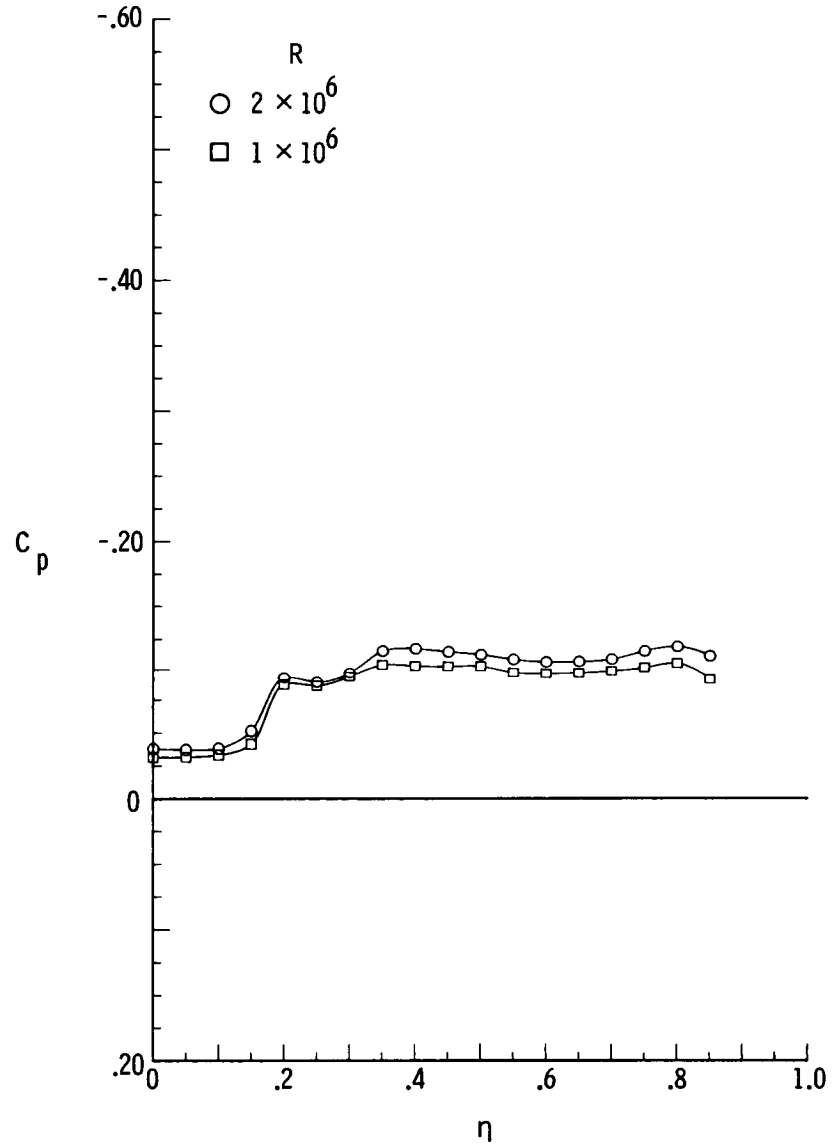

(h) M = 2.80; x/ℓ = 0.20.

Figure B18.- Continued.

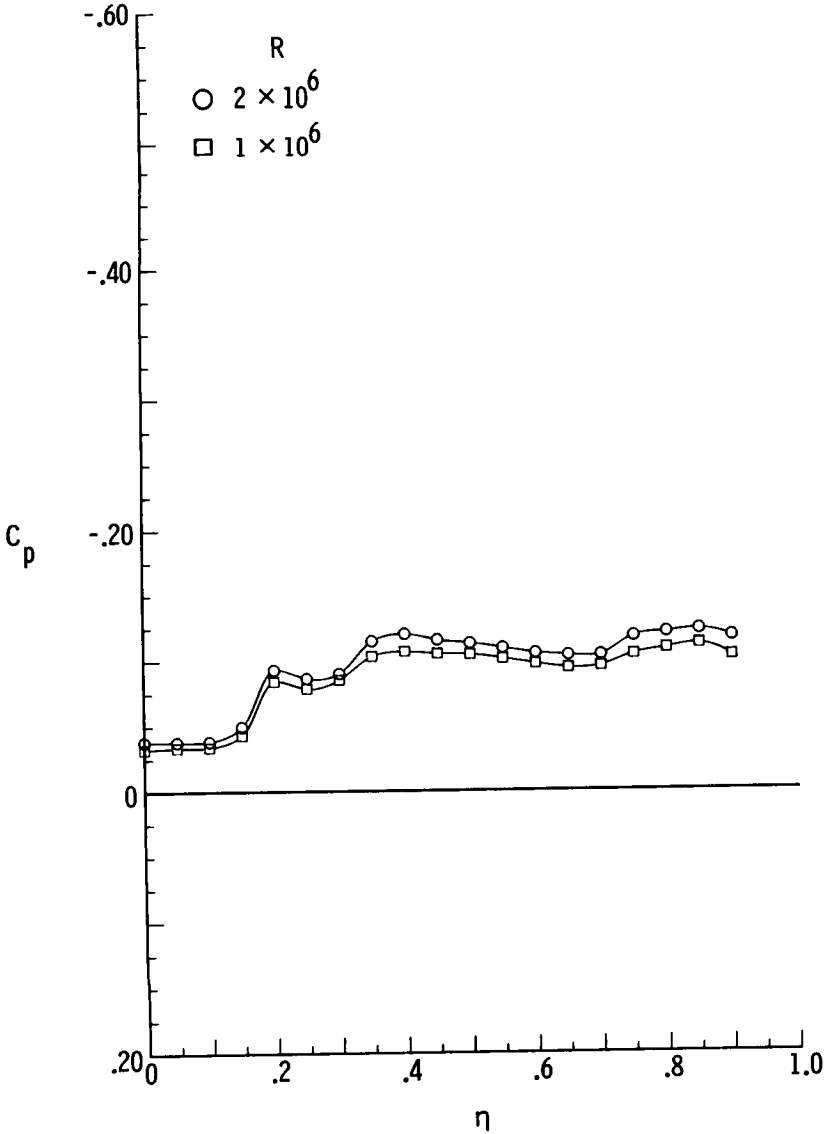

(i) M = 2.80; x/ℓ = 0.30.

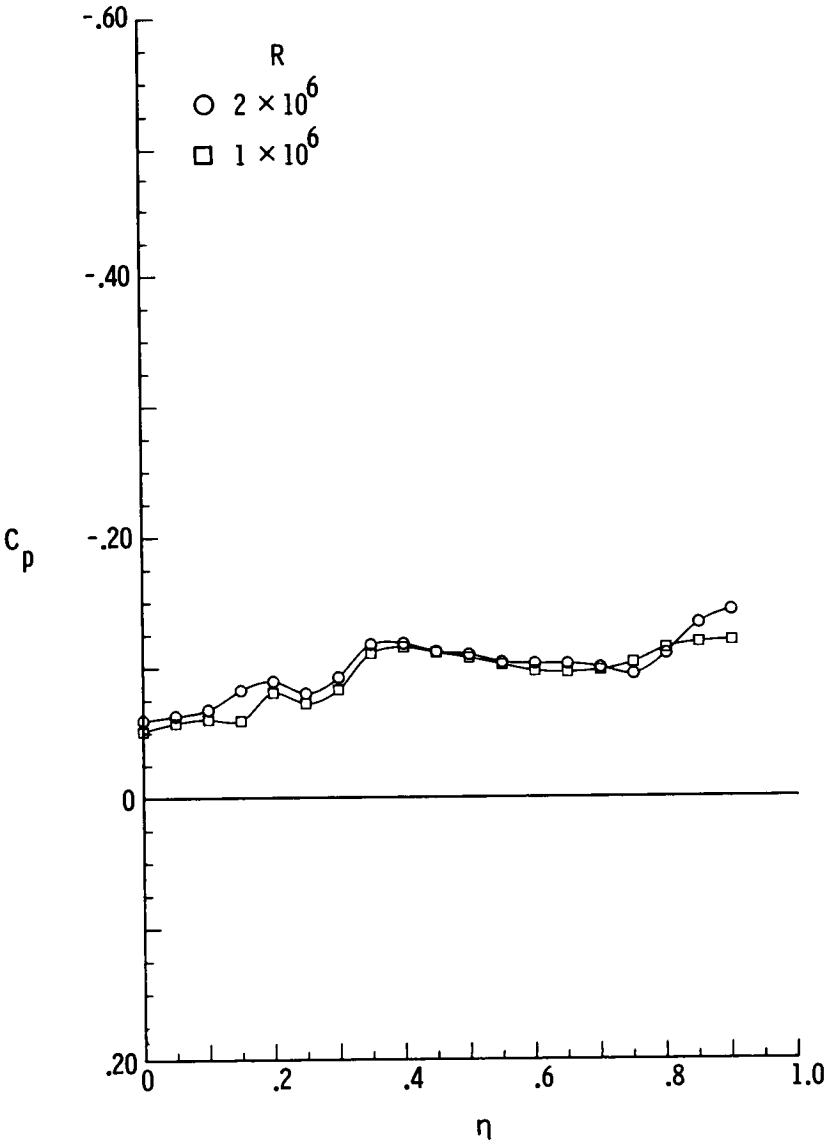

(j) M = 2.80; x/ℓ = 0.60.

Figure B18.- Continued.

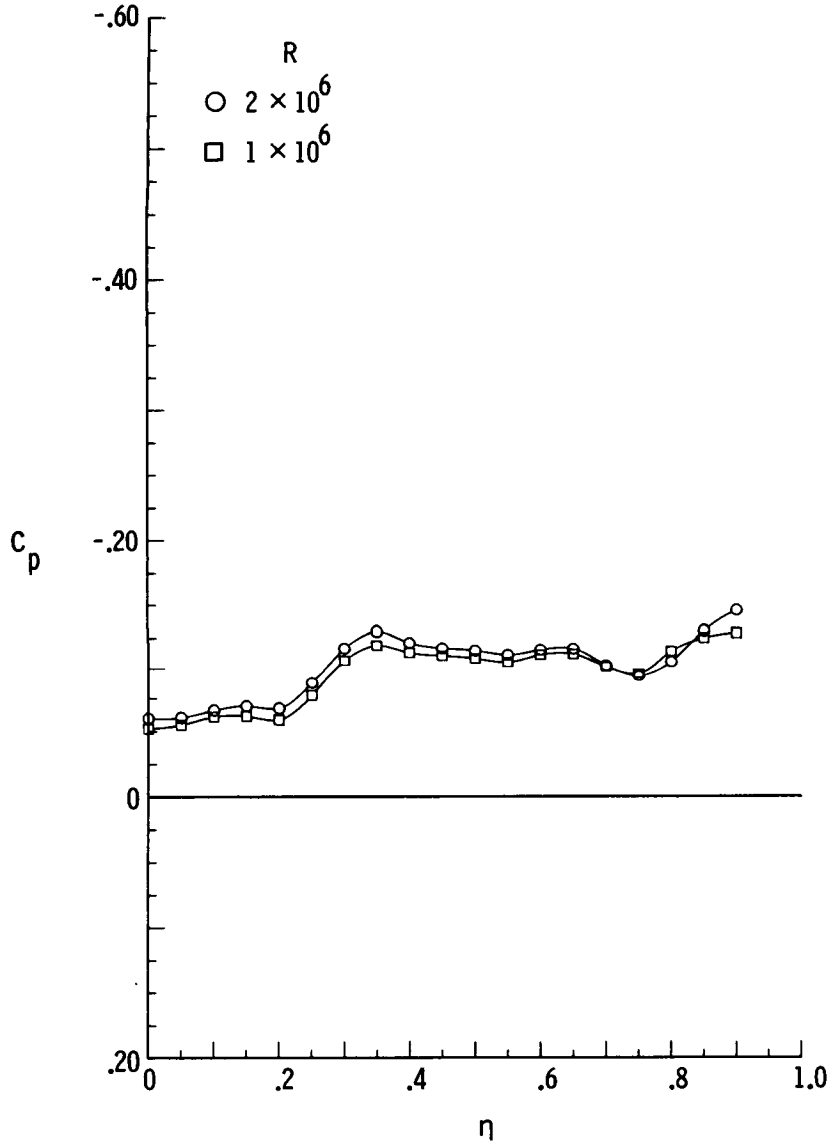

(k) M = 2.80; x/ℓ = 0.80.

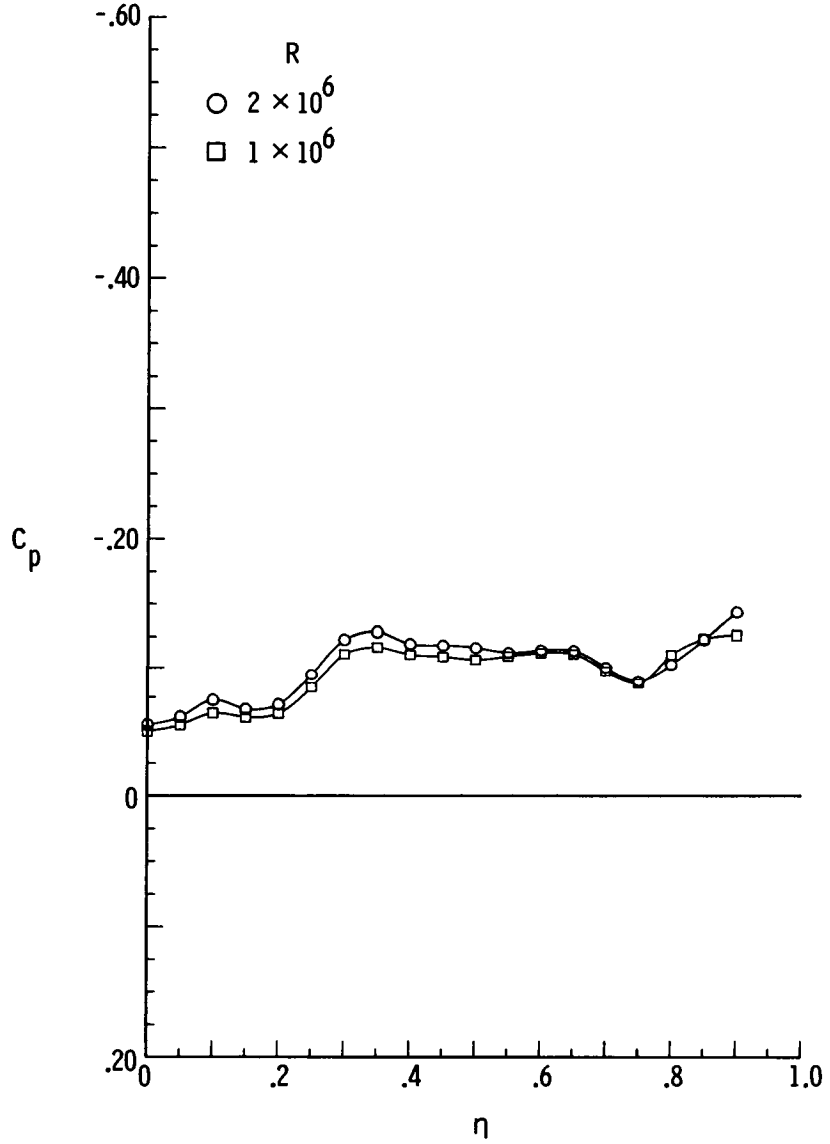

(l) M = 2.80; x/ℓ = 0.90.

Figure B18.- Concluded.

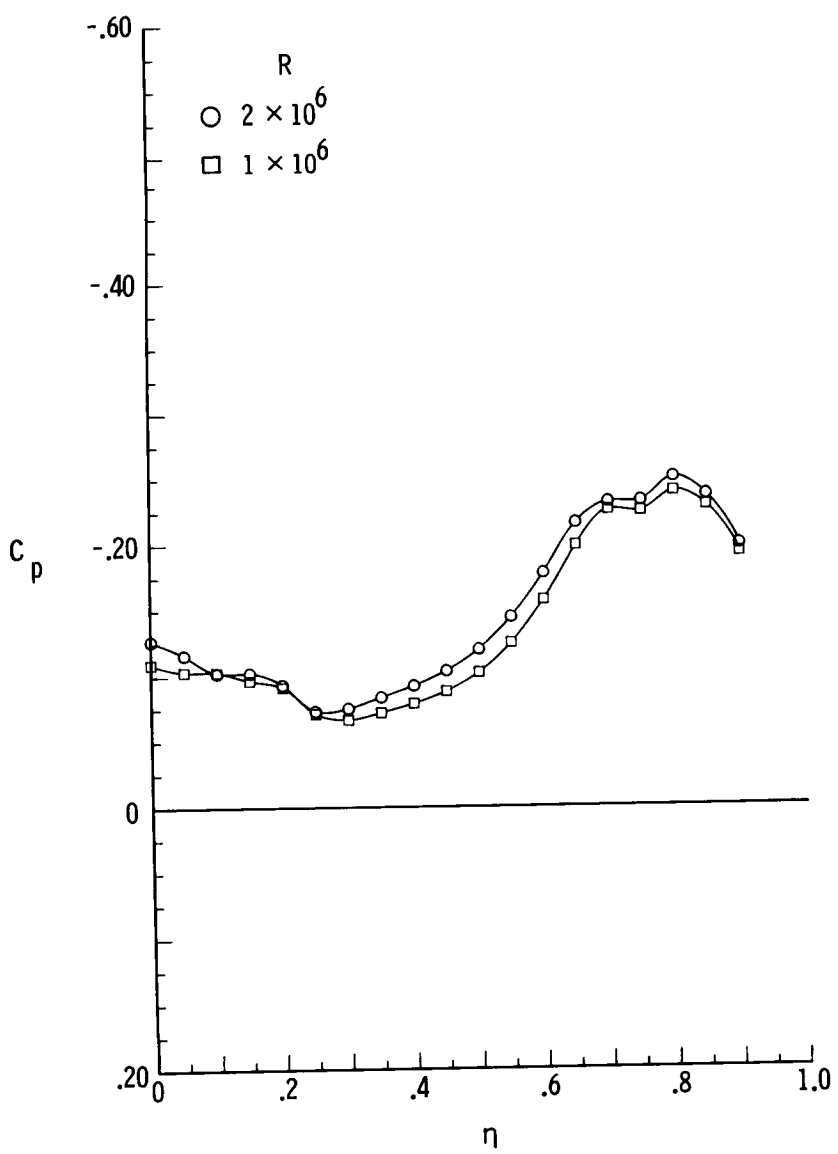

(a) M = 1.70; β = -8°.

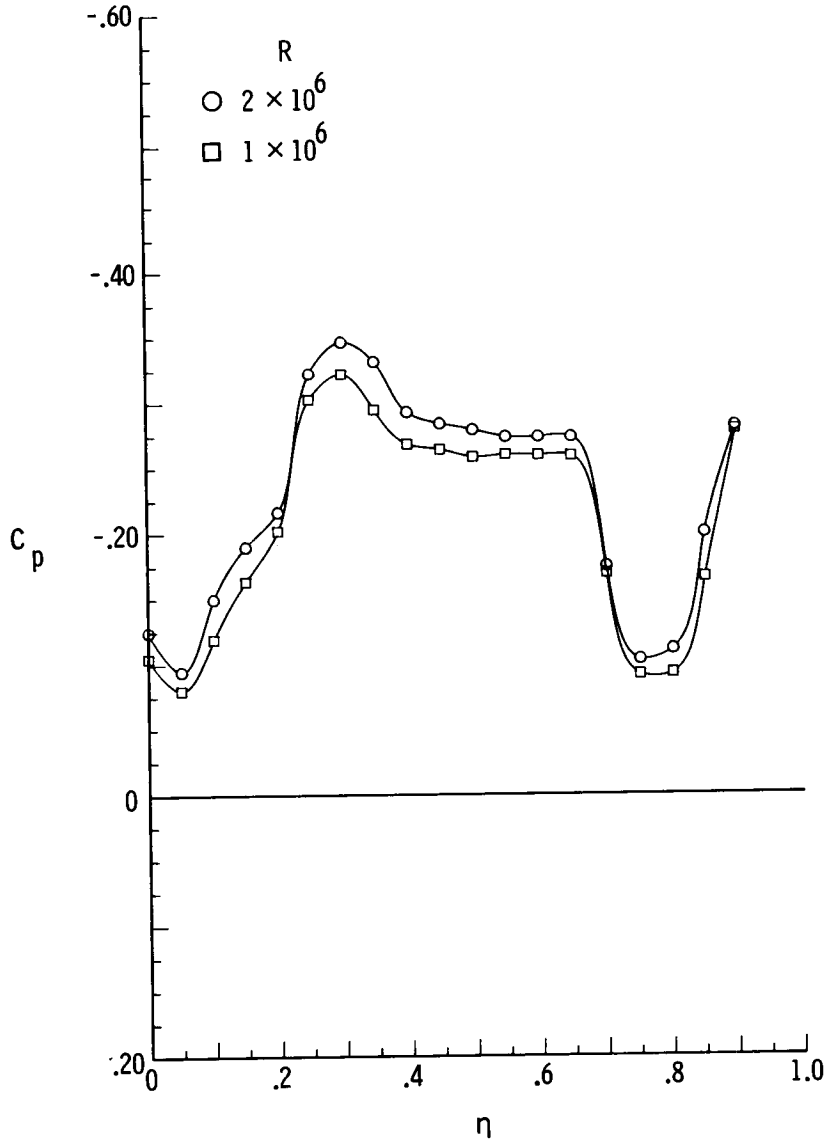

(b) M = 1.70; β = 8°.

Figure B19.- Pressure plots for 75° delta wing with δ_F = 10° for varying R, α = 12°, and x/ℓ = 0.90.

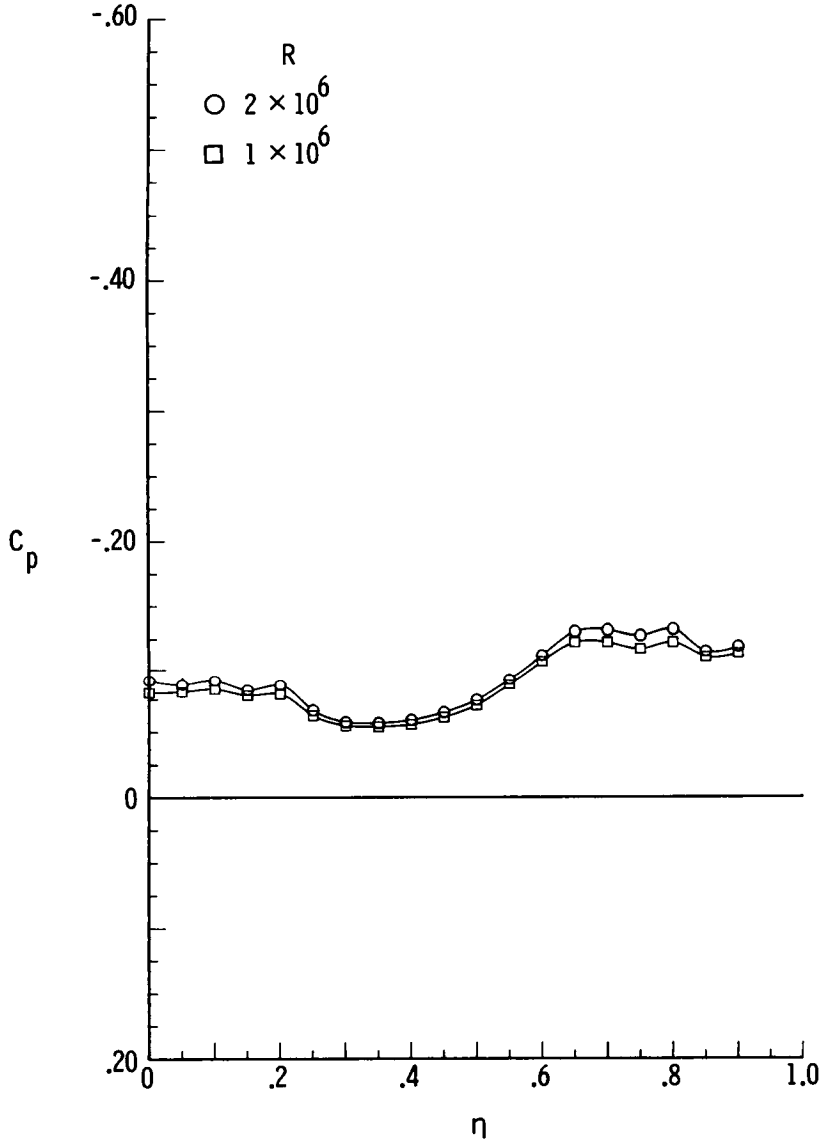

(c) M = 2.80; β = -8°.

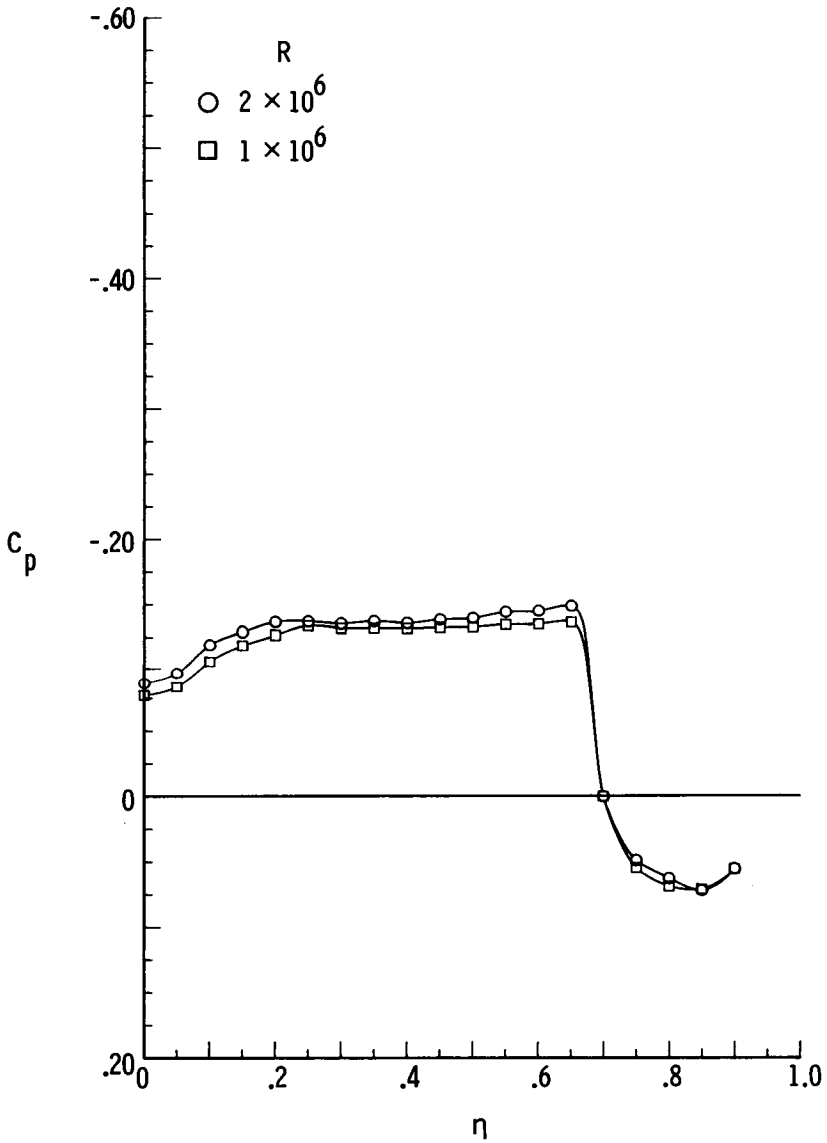

(d) M = 2.80; β = 8°.

Figure B19.- Concluded.

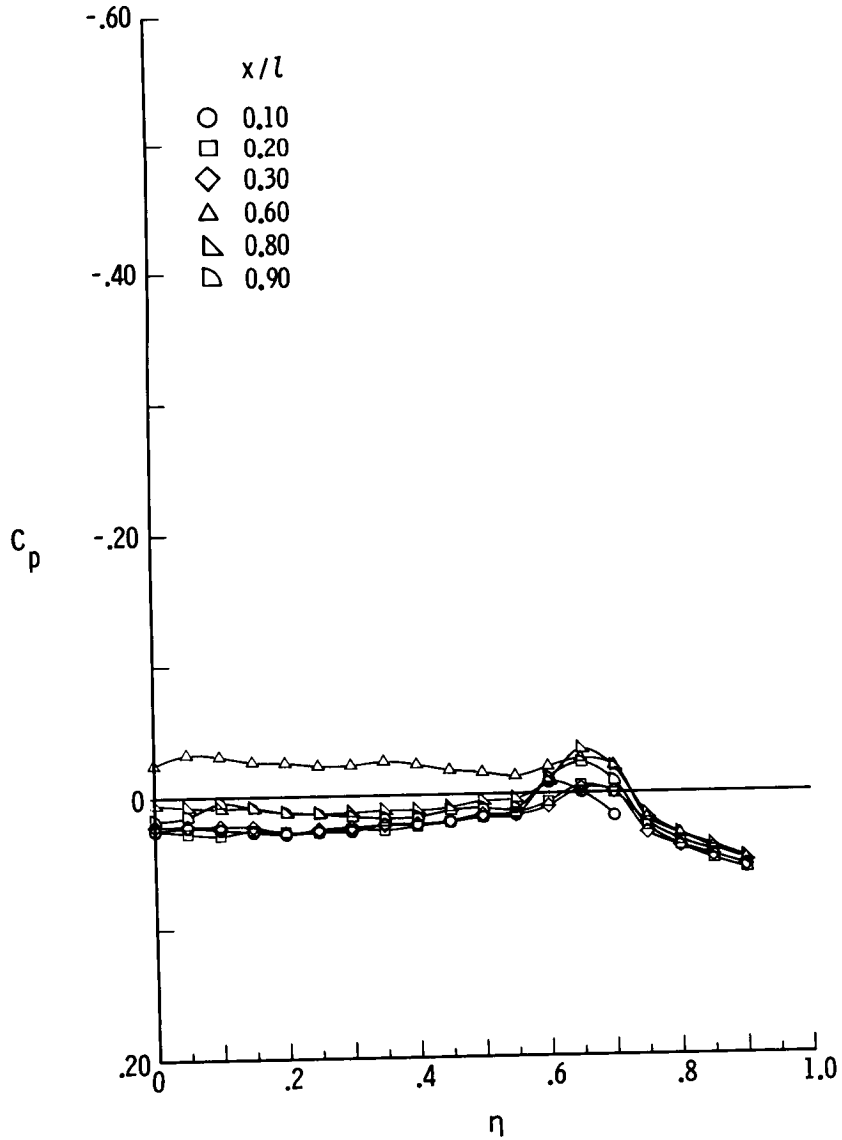

(a) M = 1.50.

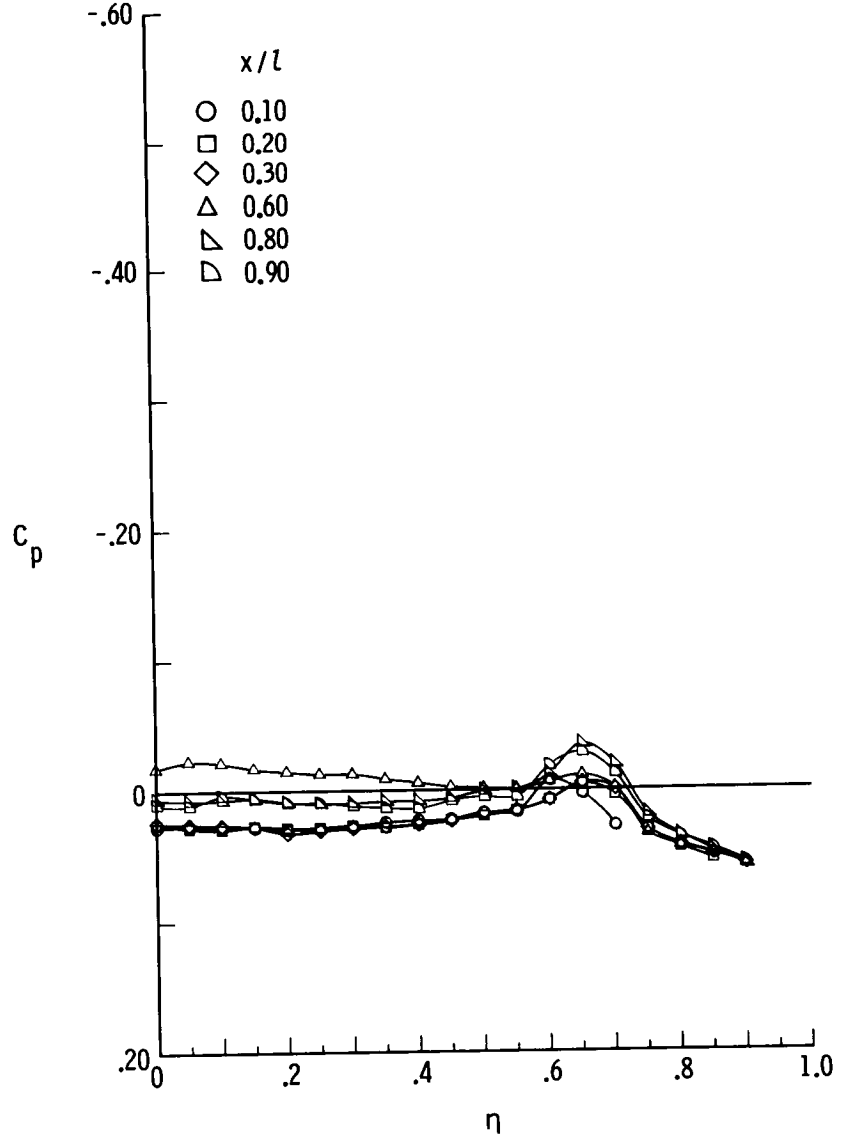

(b) M = 1.70.

Figure B20.- Pressure plots for 75° delta wing with $\delta_F = 10°$ for varying x/l, $R = 2 \times 10^6$, $\alpha = 0°$, and $\beta = 0°$.

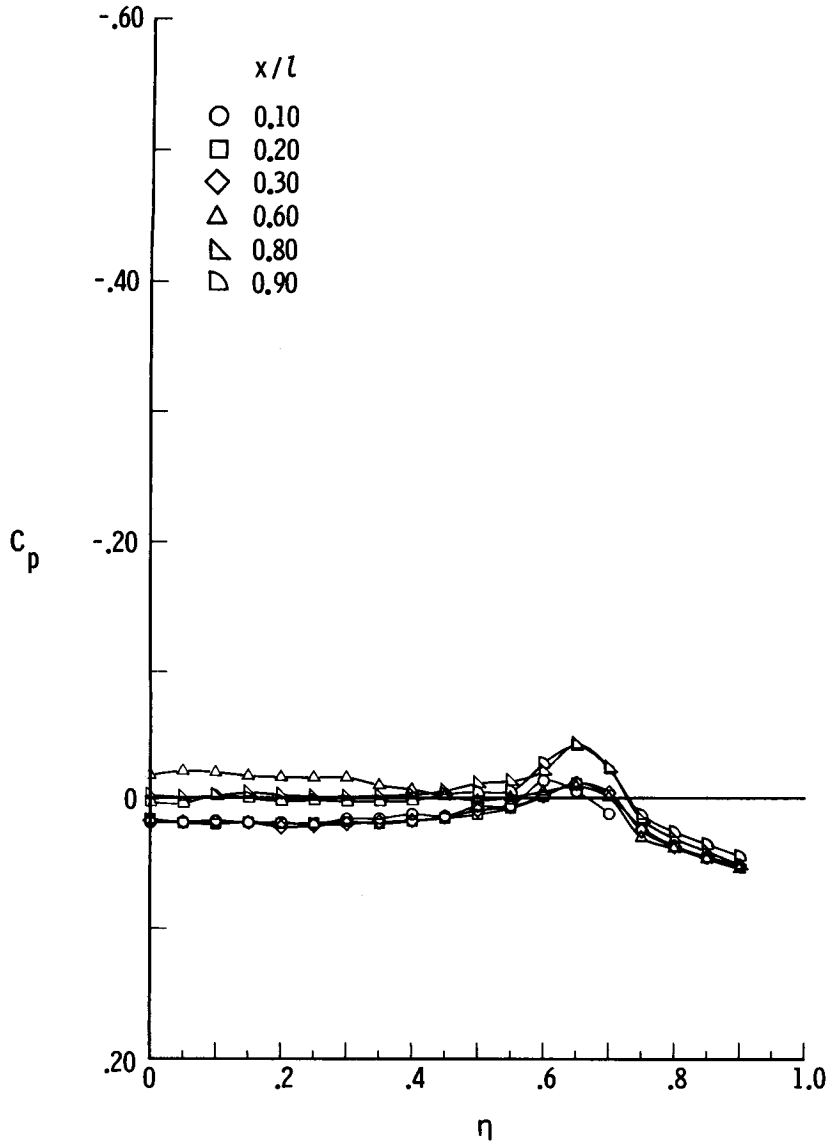

(c) M = 2.00.

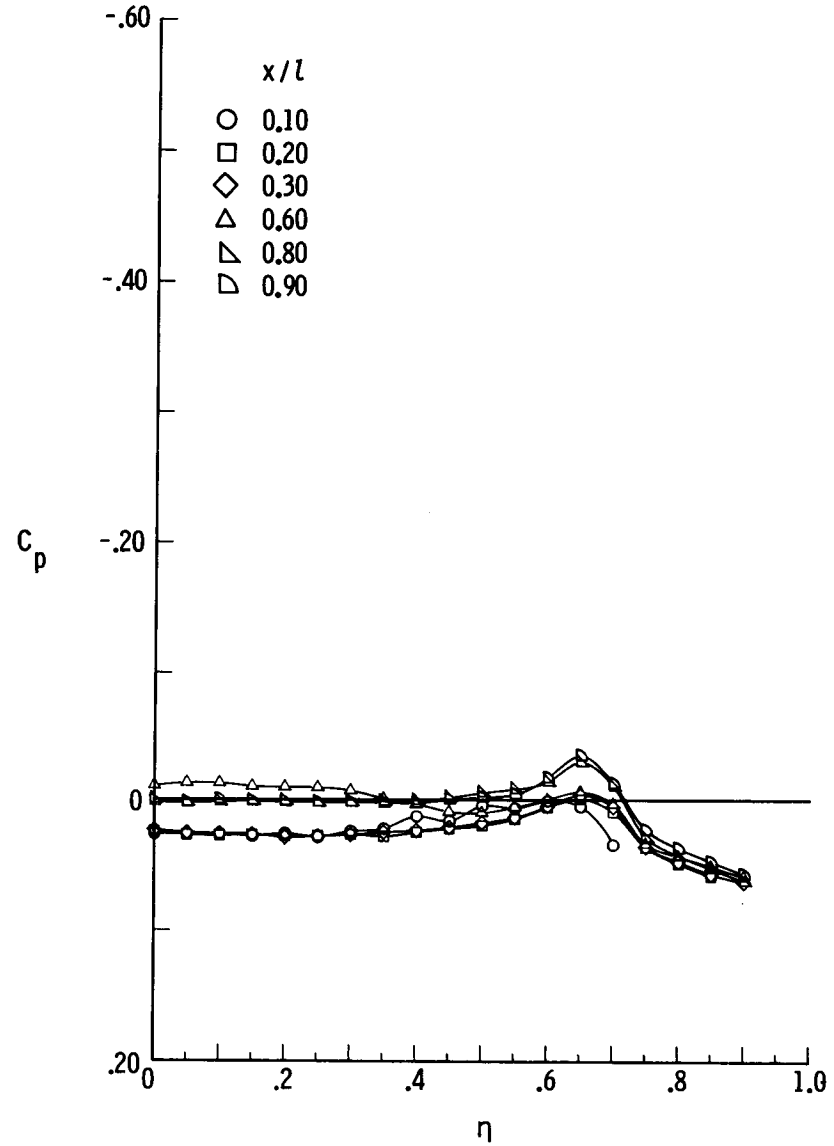

(d) M = 2.40.

Figure B20.- Continued.

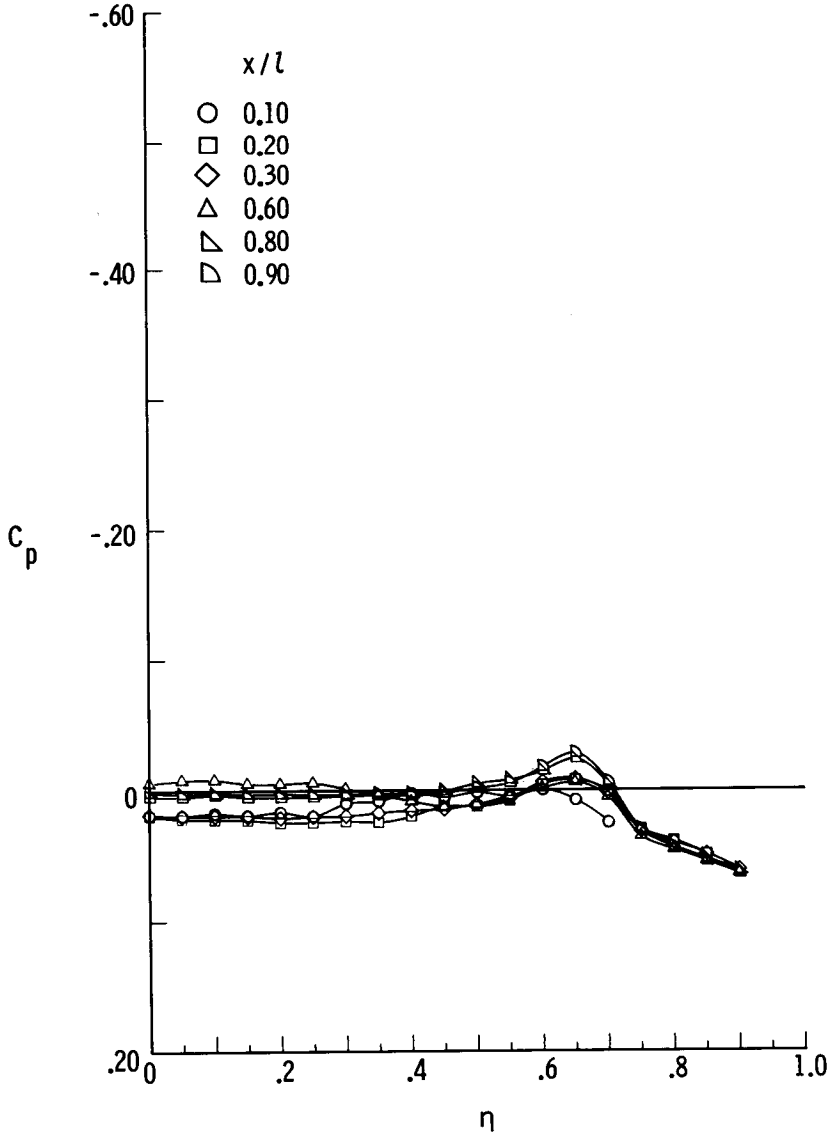

(e) M = 2.80.

Figure B20.- Concluded.

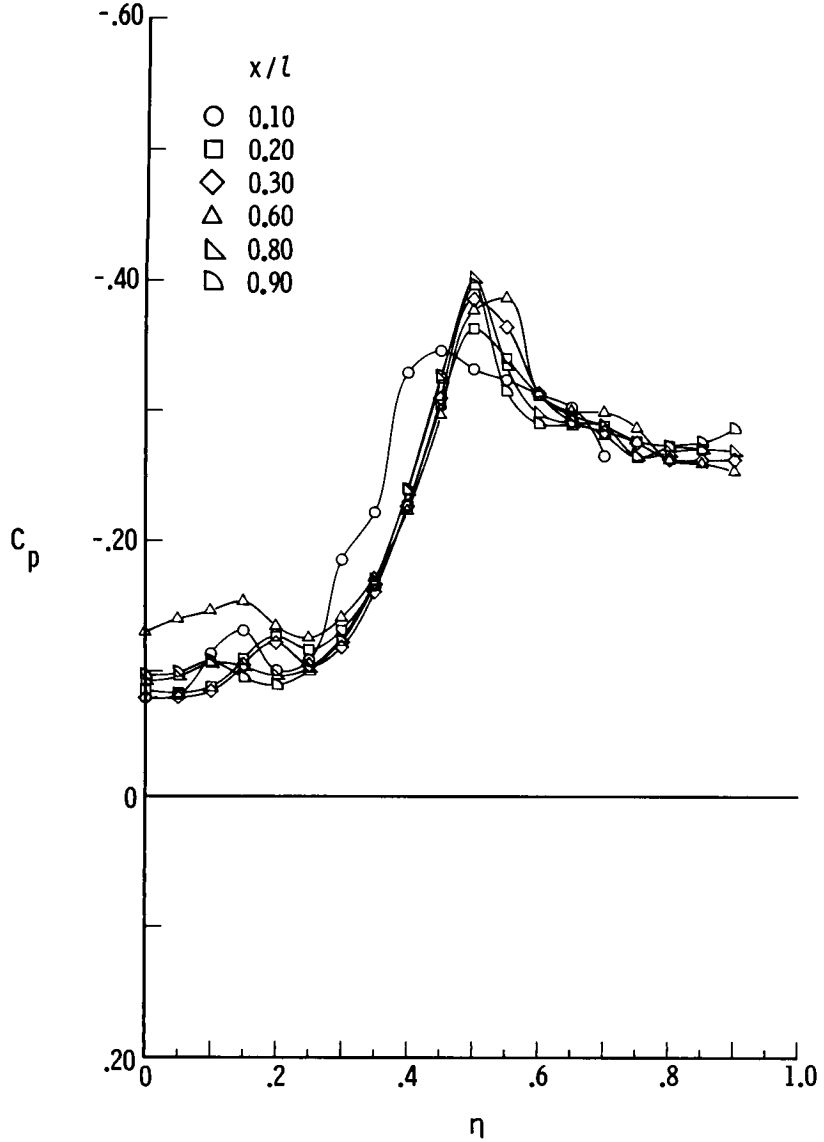

(a) M = 1.50.

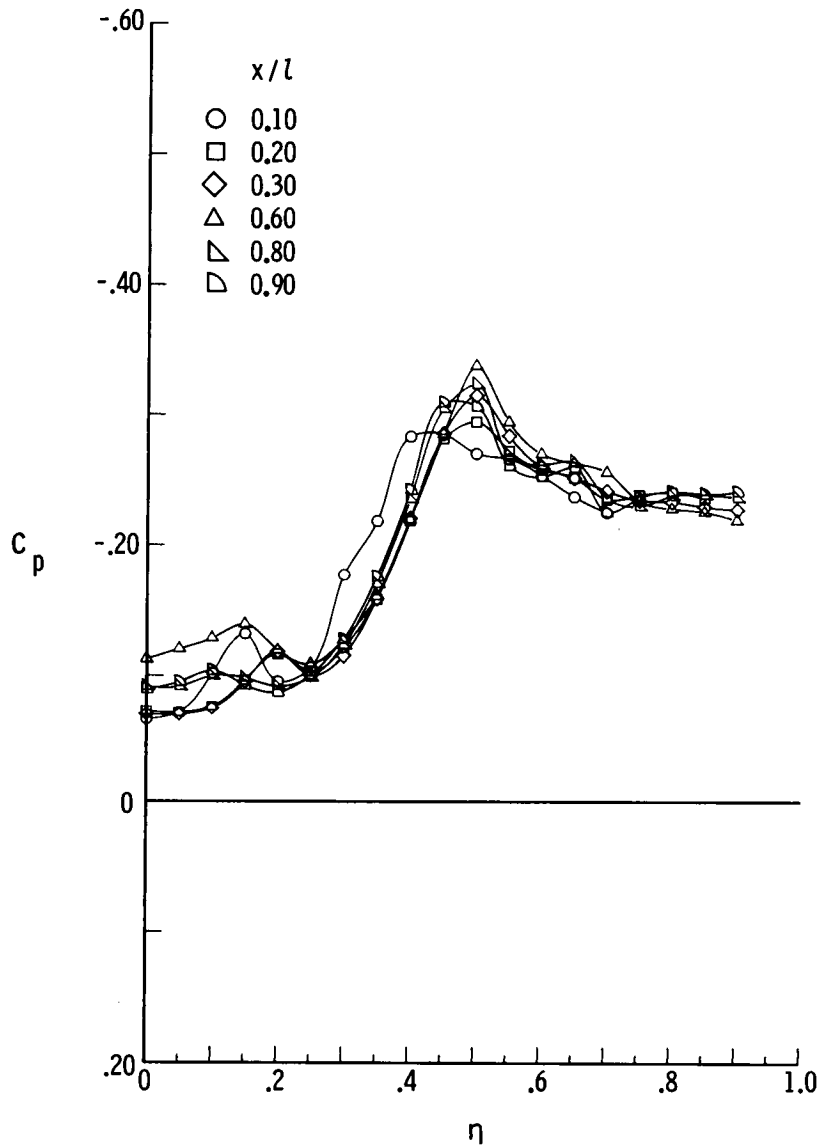

(b) M = 1.70.

Figure B21.- Pressure plots for 75° delta wing with $\delta_F = 10°$ for varying x/l, $R = 2 \times 10^6$, $\alpha = 12°$, and $\beta = 0°$.

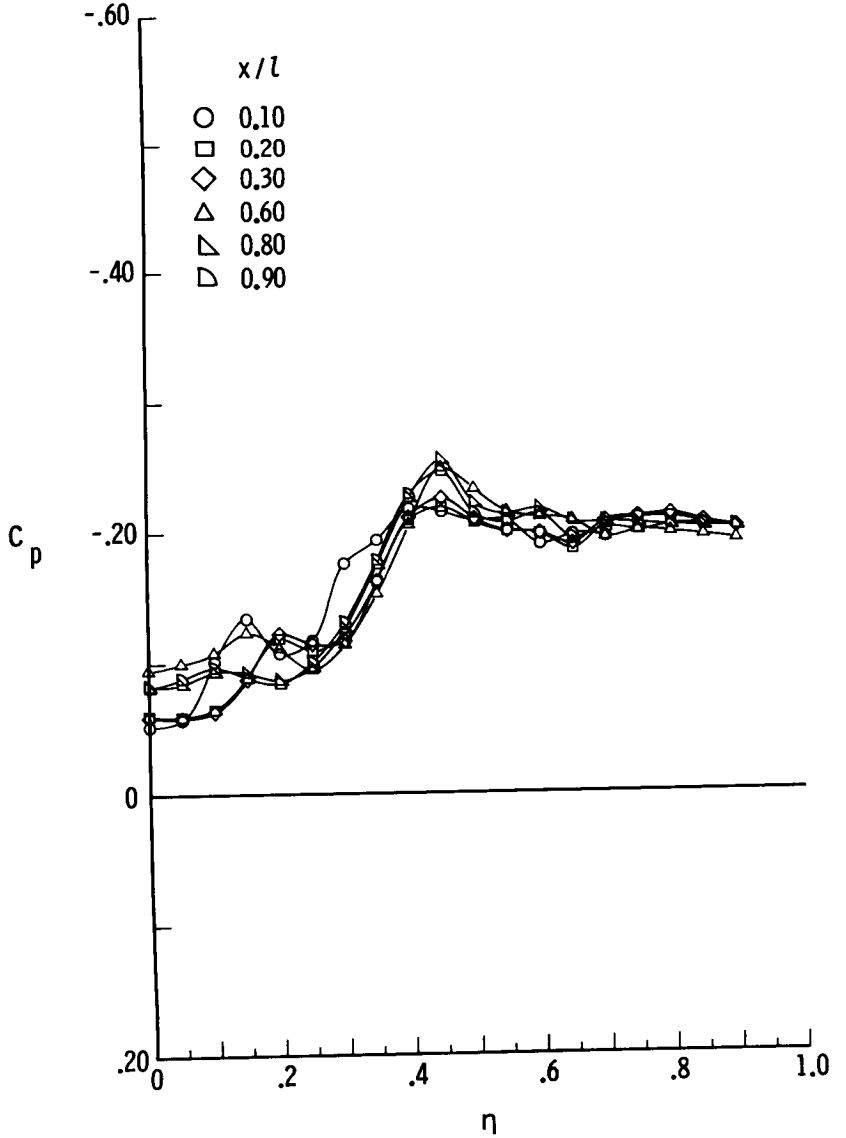

(c) M = 2.00.

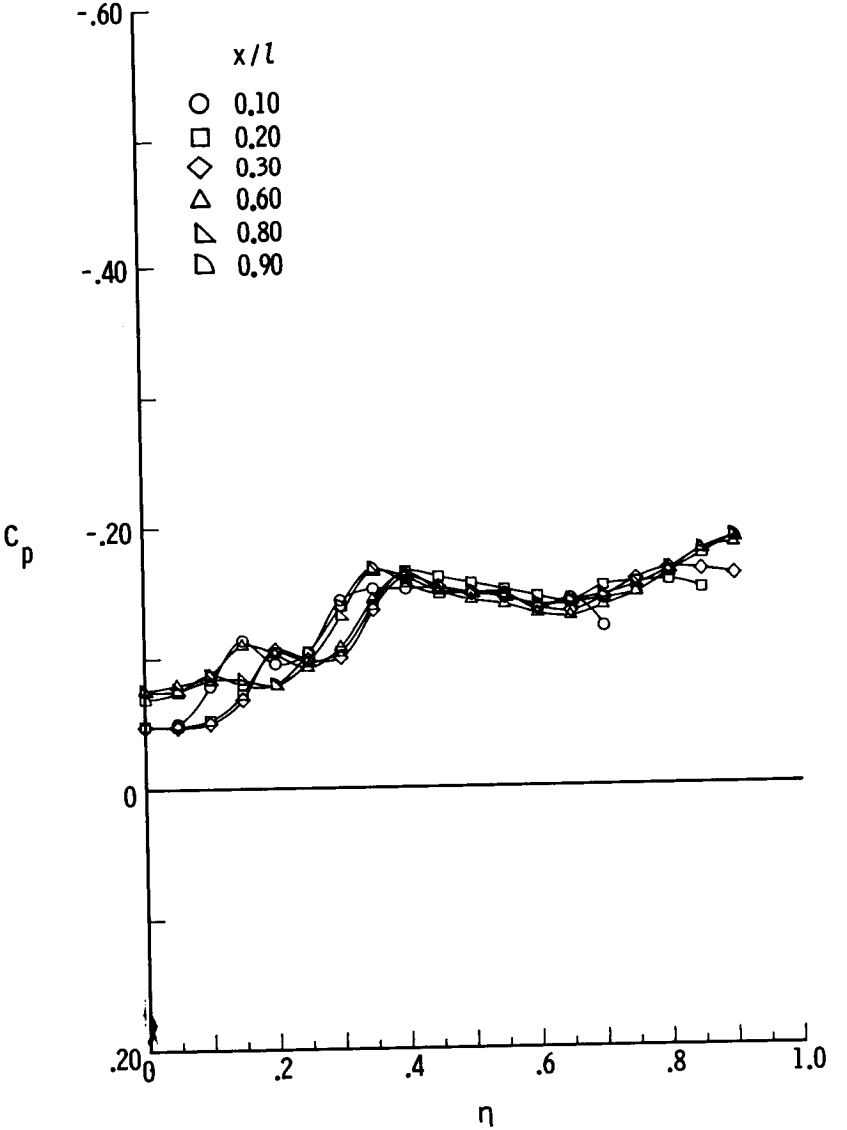

(d) M = 2.40.

Figure B21.- Continued.

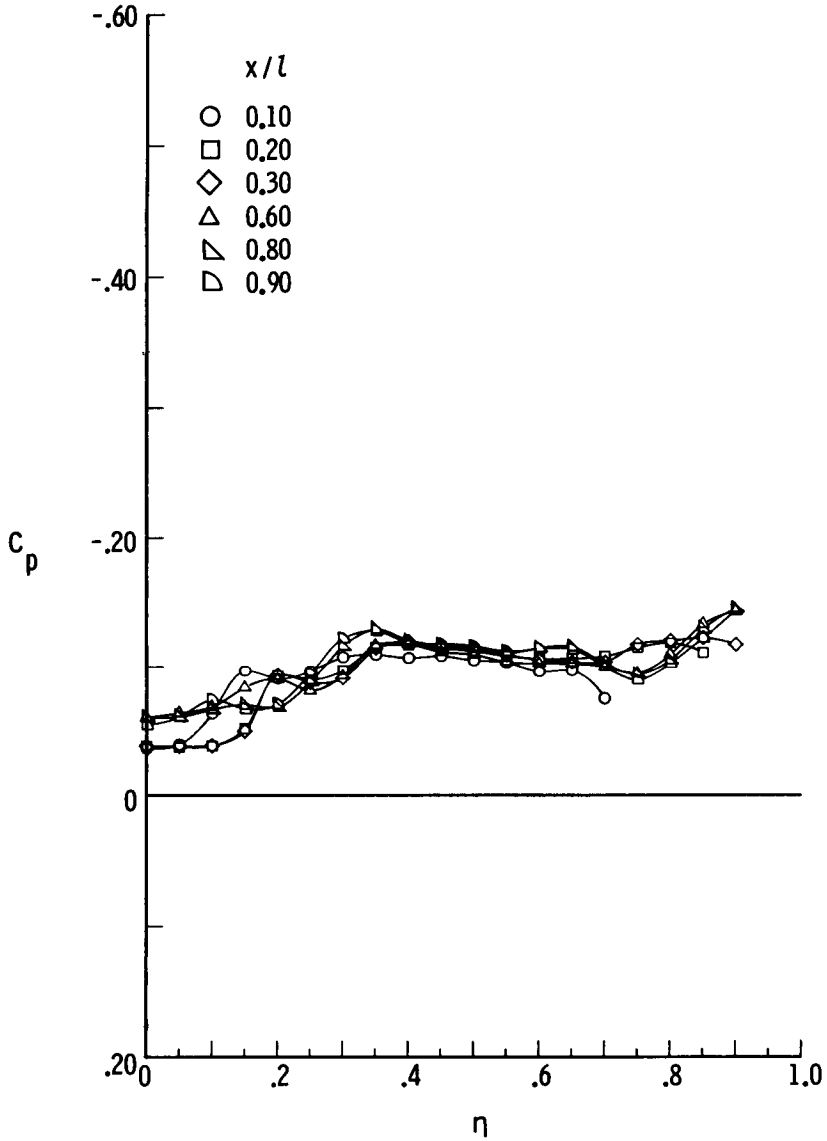

(e) M = 2.80.

Figure B21.- Concluded.

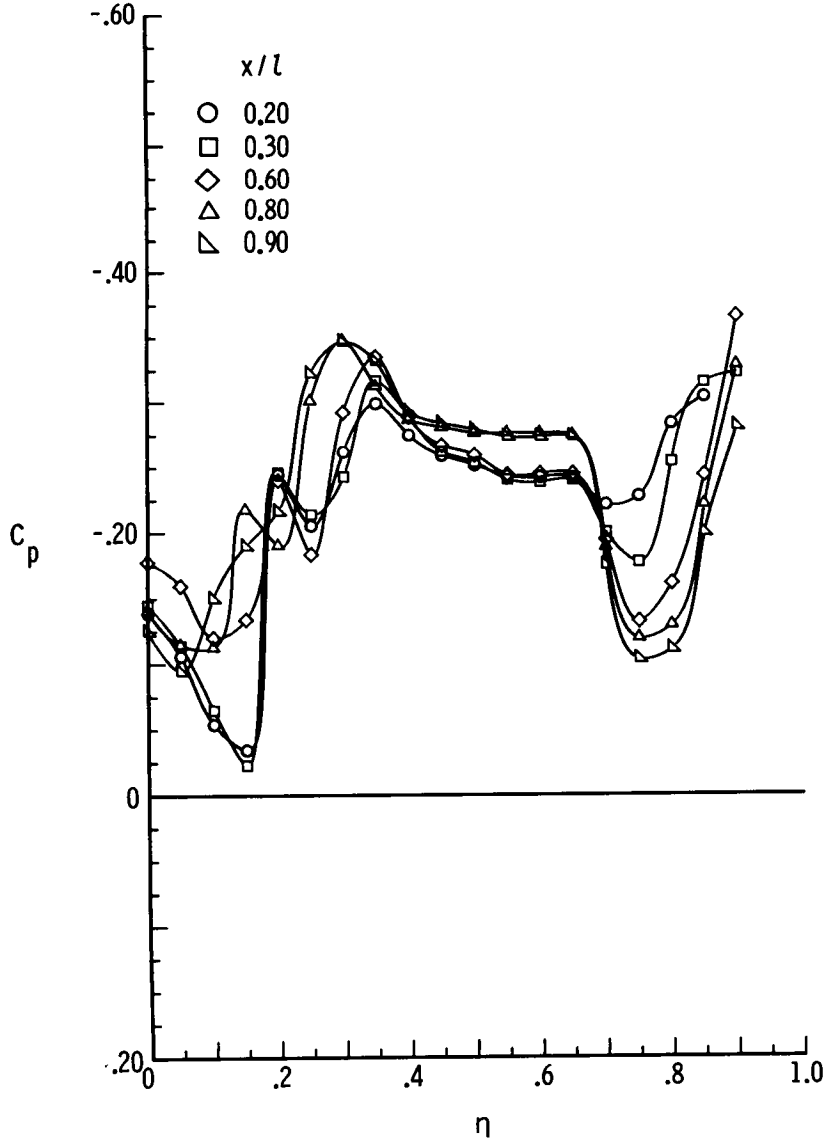

(a) M = 1.70; β = 8°.

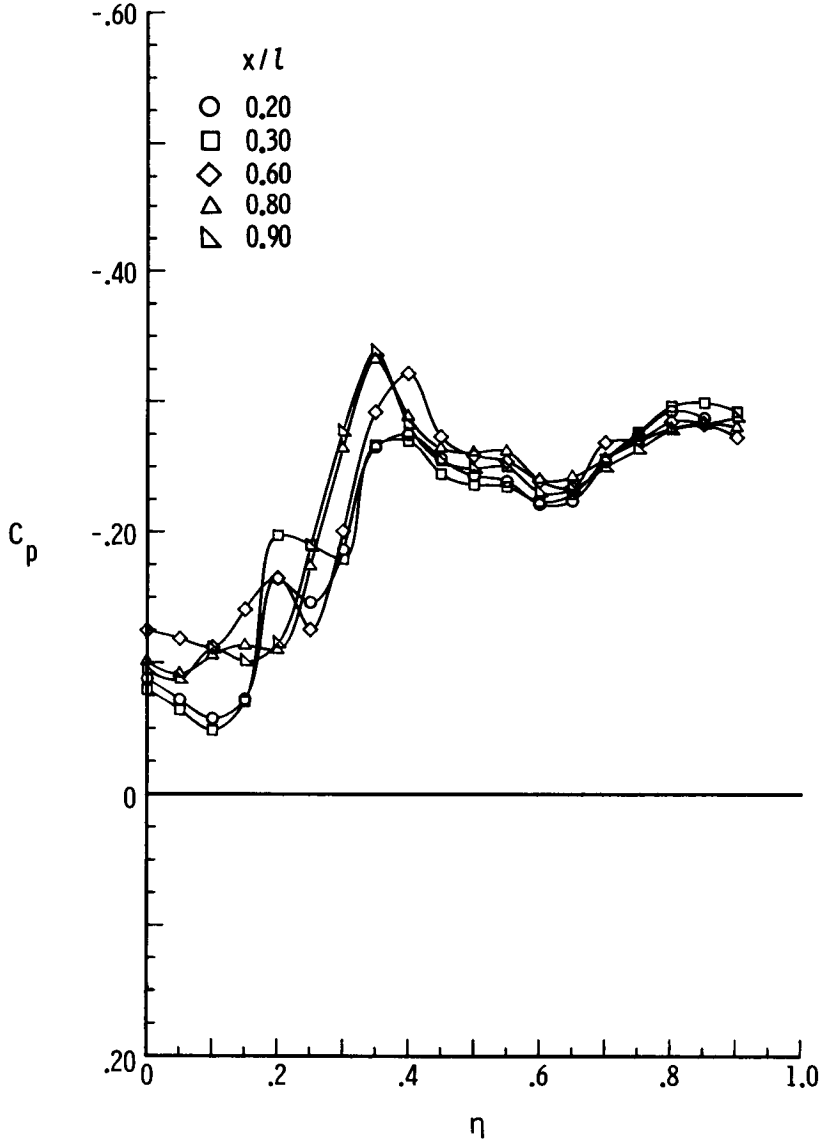

(b) M = 1.70; β = 4°.

Figure B22.- Pressure plots for 75° delta wing with δ_F = 10° for varying x/ℓ, R = 2 × 10^6, and α = 12°.

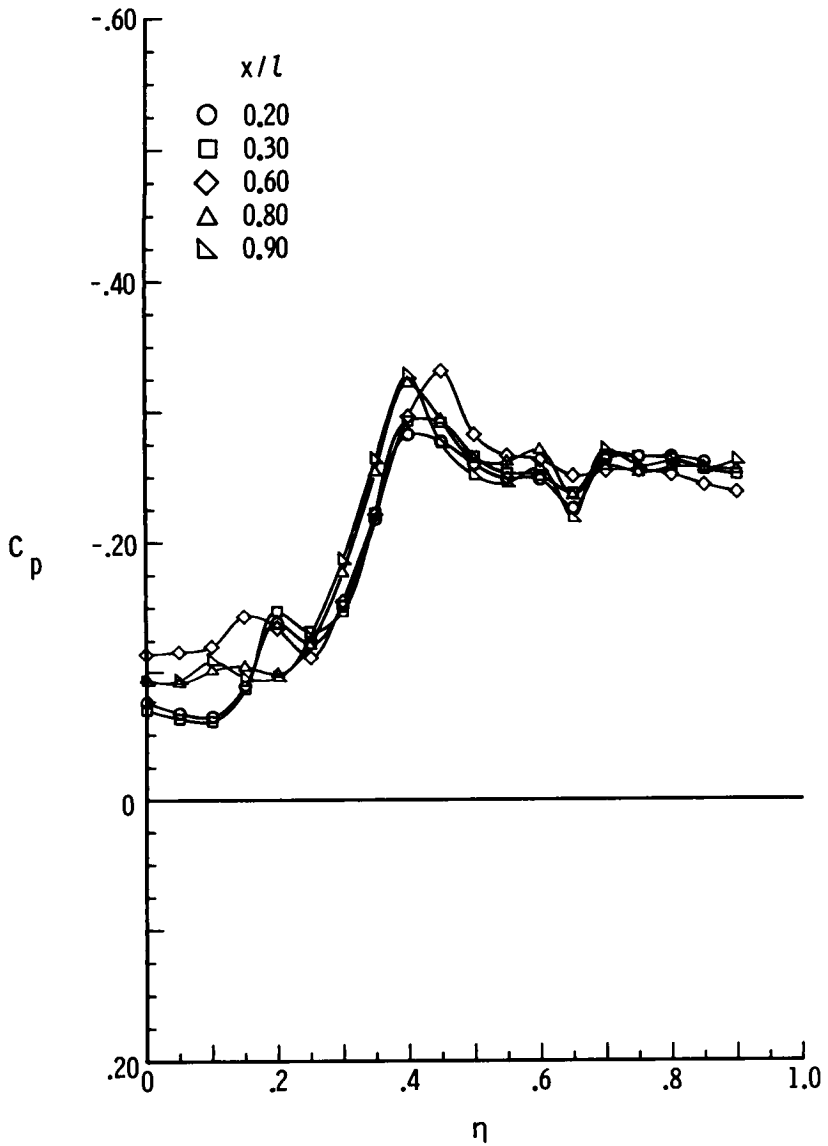

(c) M = 1.70; β = 2°.

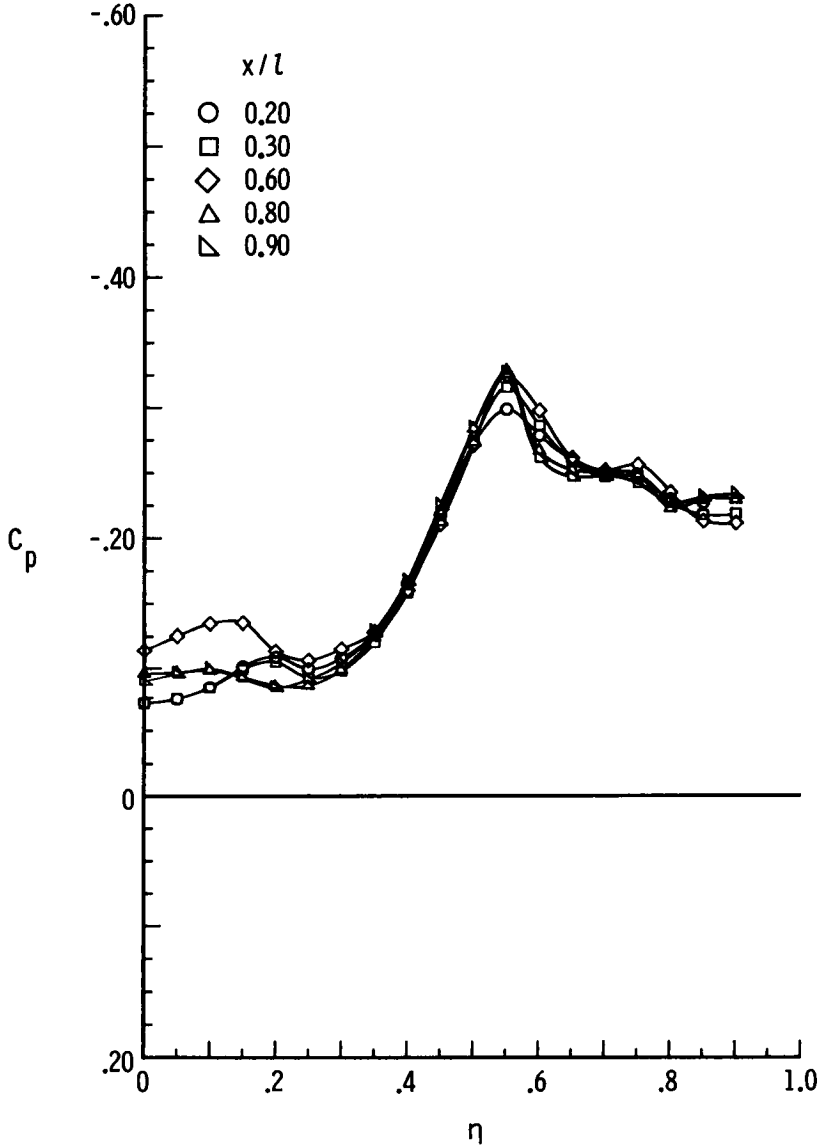

(d) M = 1.70; β = -2°.

Figure B22.- Continued.

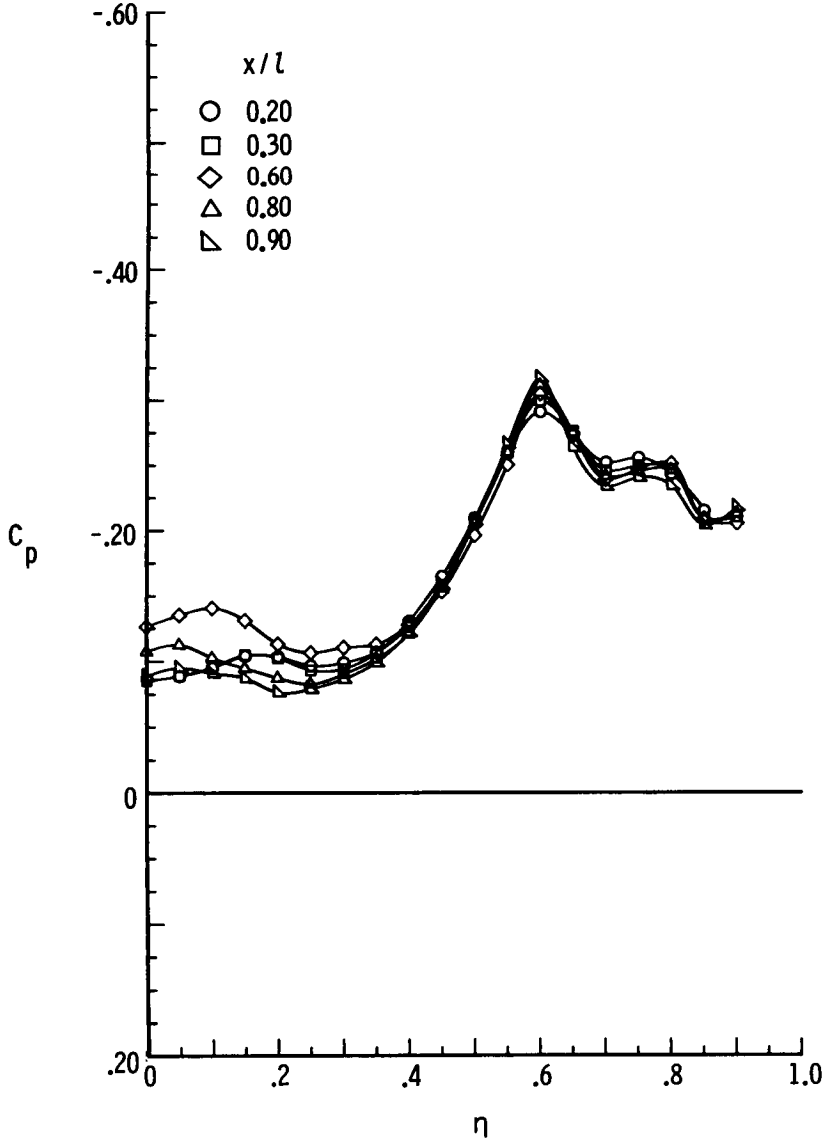

(e) M = 1.70; β = -4°.

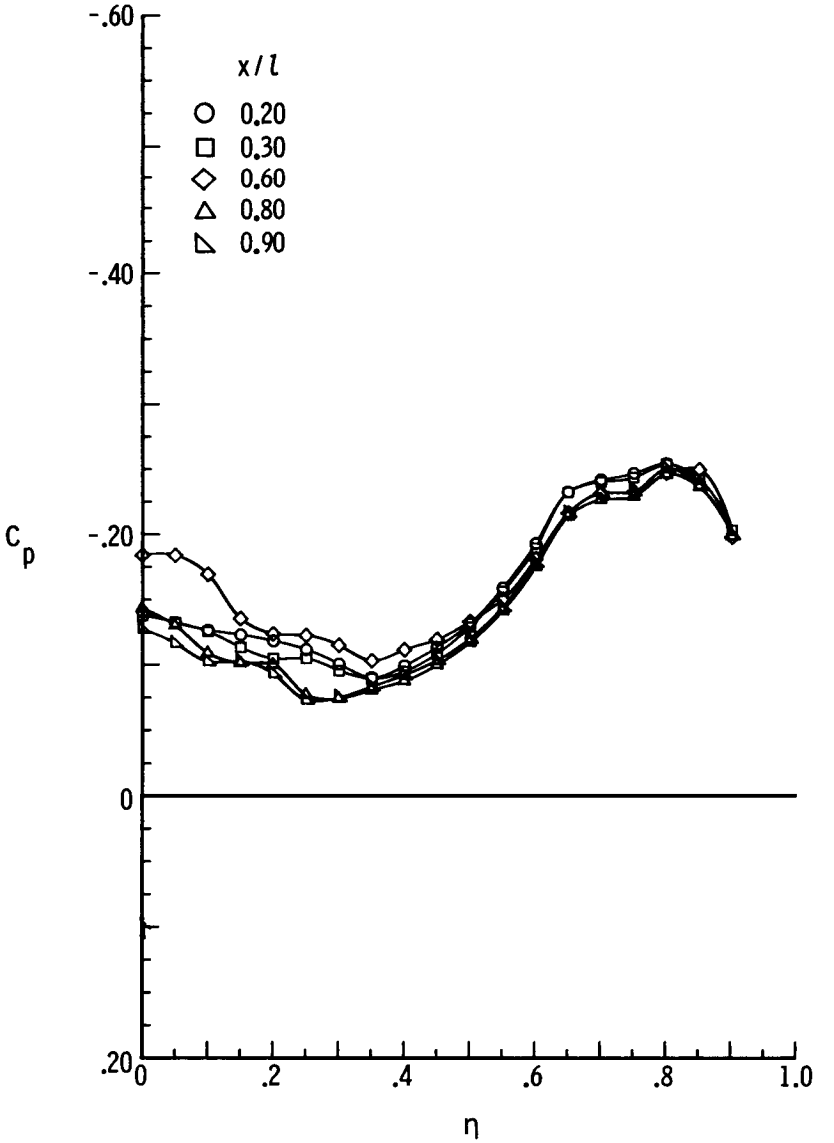

(f) M = 1.70; β = -8°.

Figure B22.- Continued.

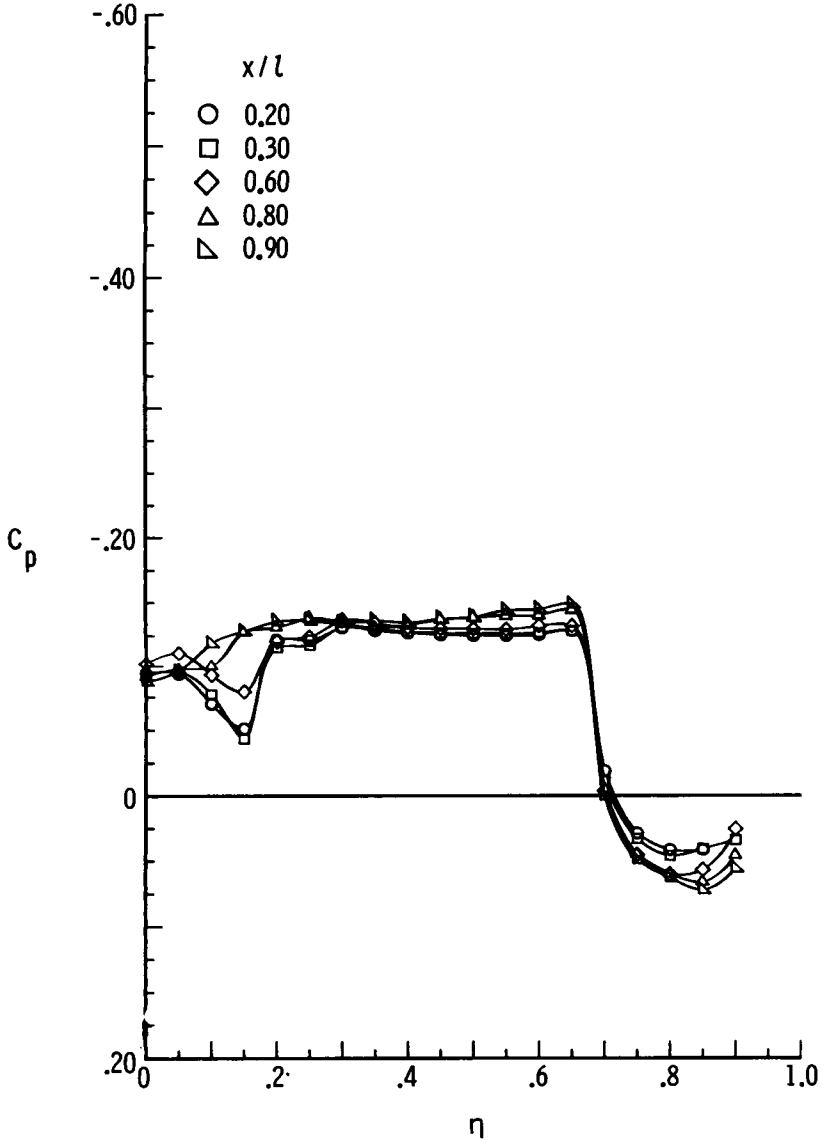

(g) M = 2.80; β = 8°.

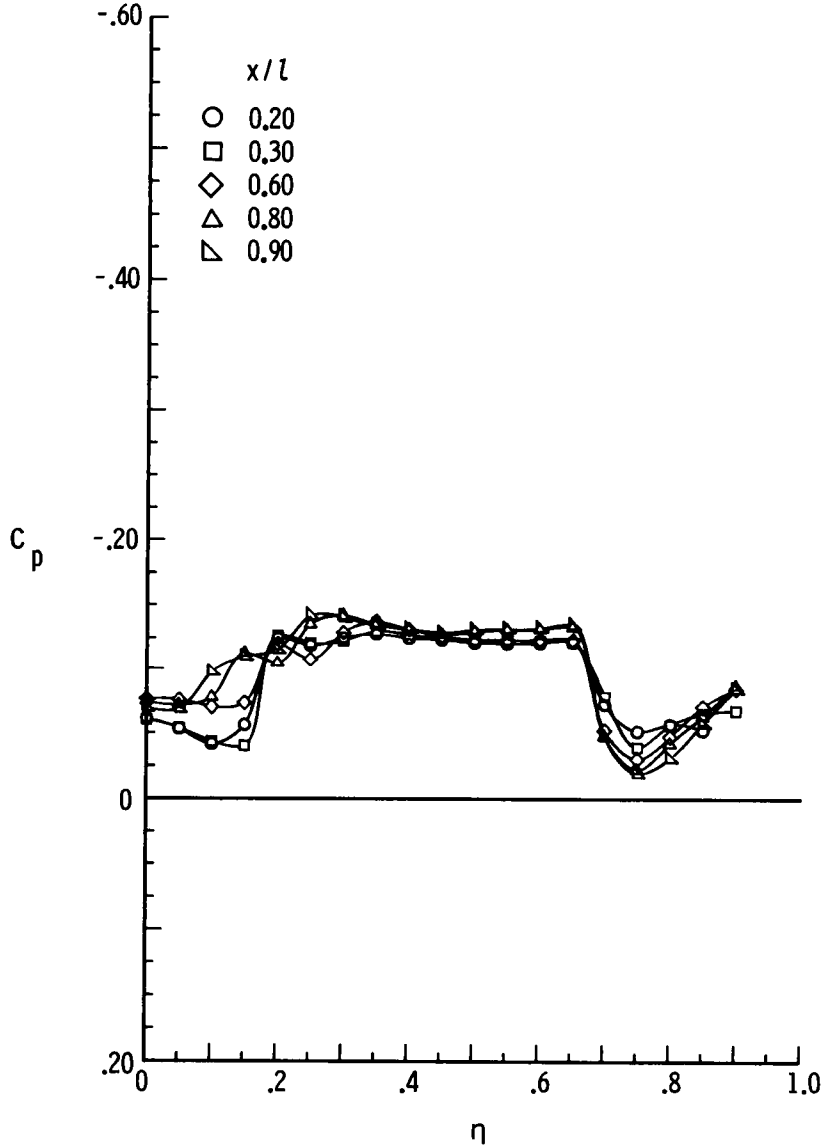

(h) M = 2.80; β = 4°.

Figure B22.- Continued.

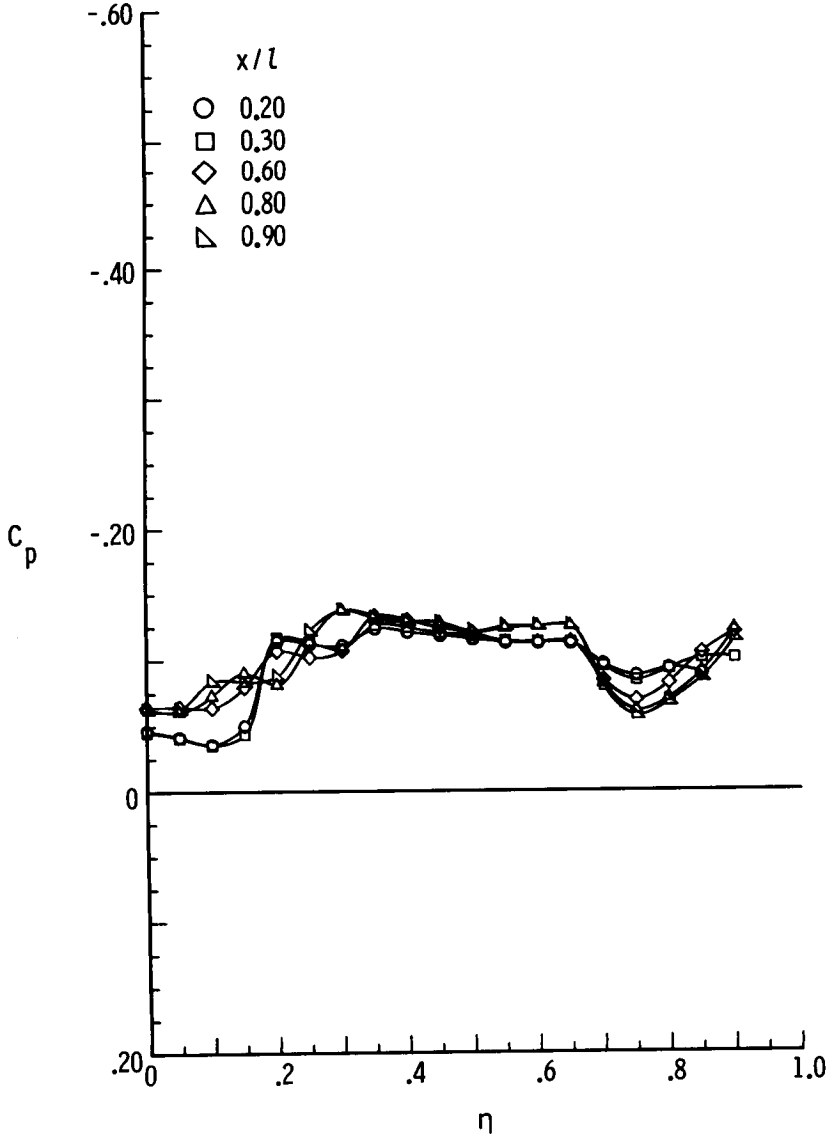

(i) M = 2.80; β = 2°.

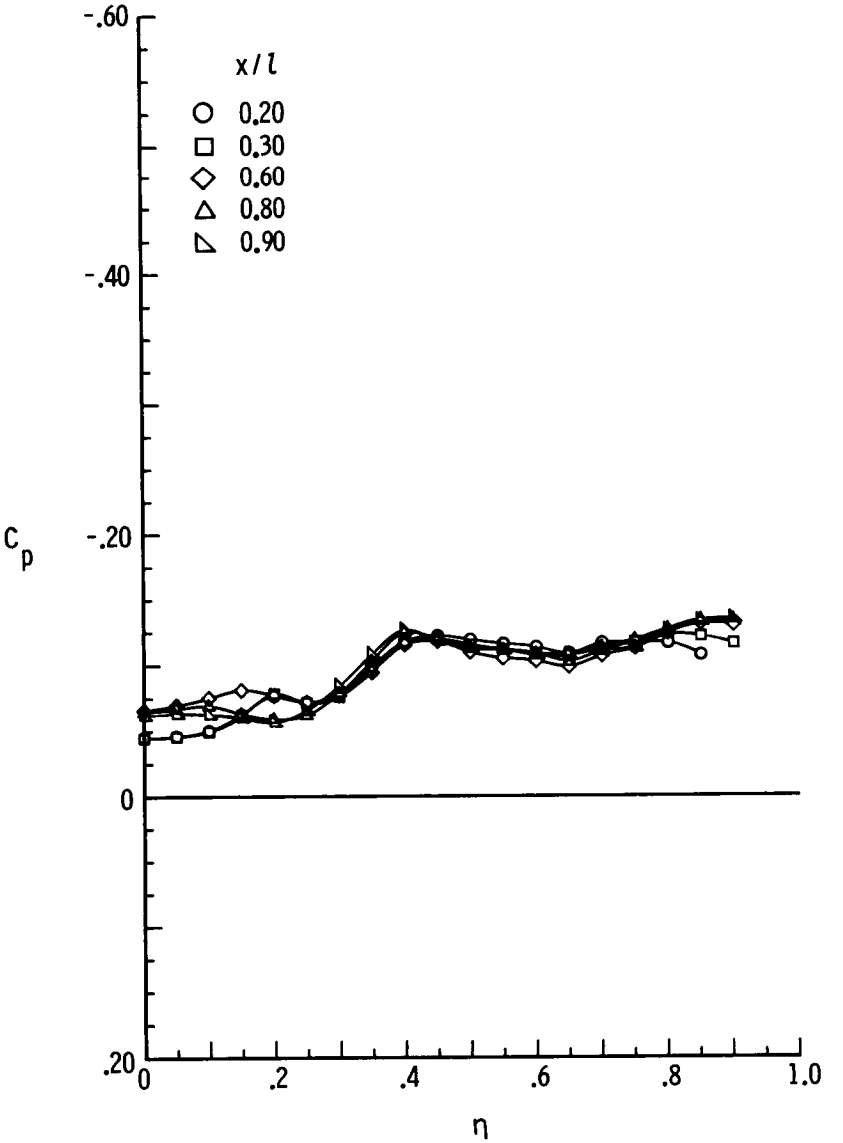

(j) M = 2.80; β = -2°.

Figure B22.- Continued.

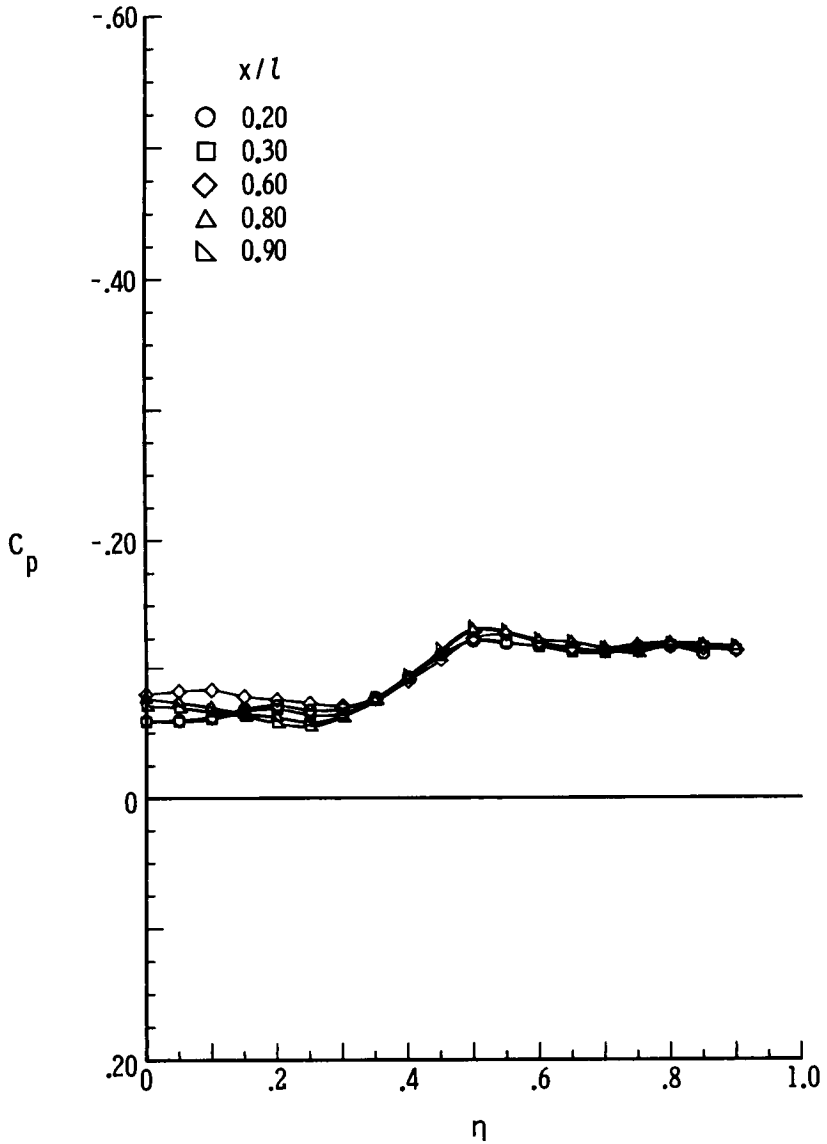

(k) M = 2.80; β = -4°.

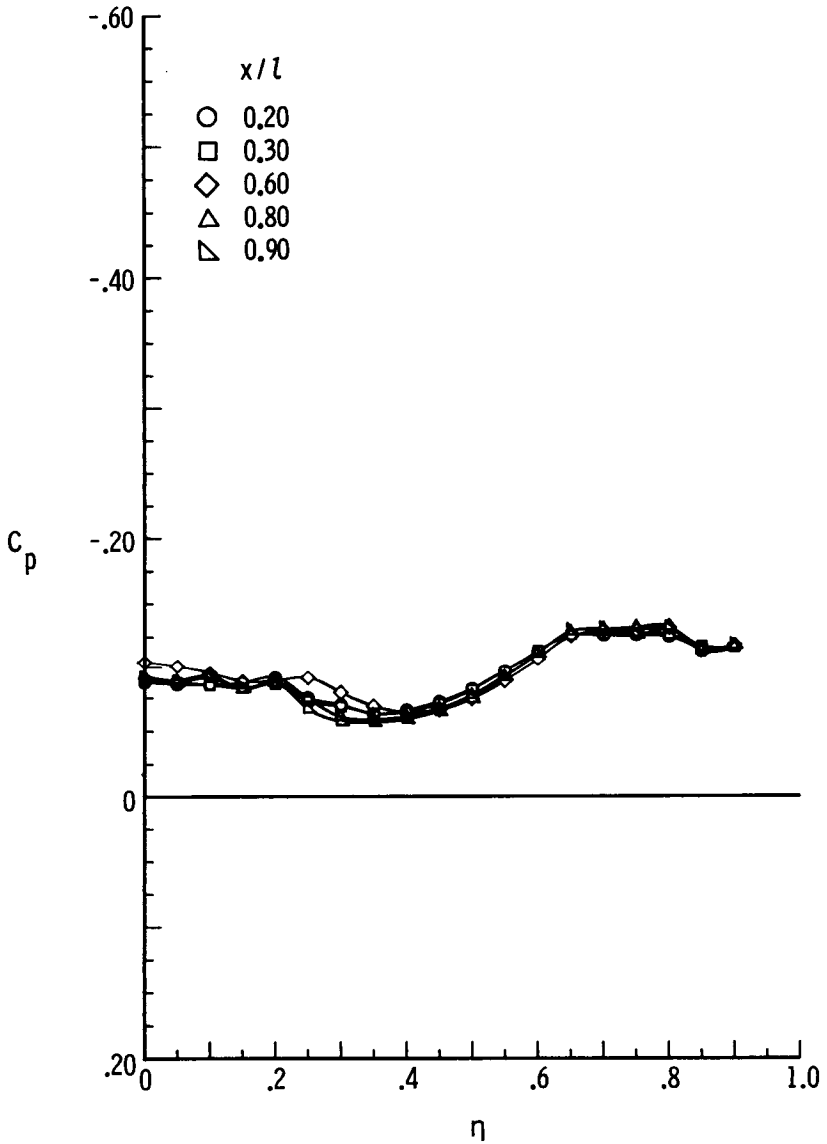

(l) M = 2.80; β = -8°.

Figure B22.- Concluded.

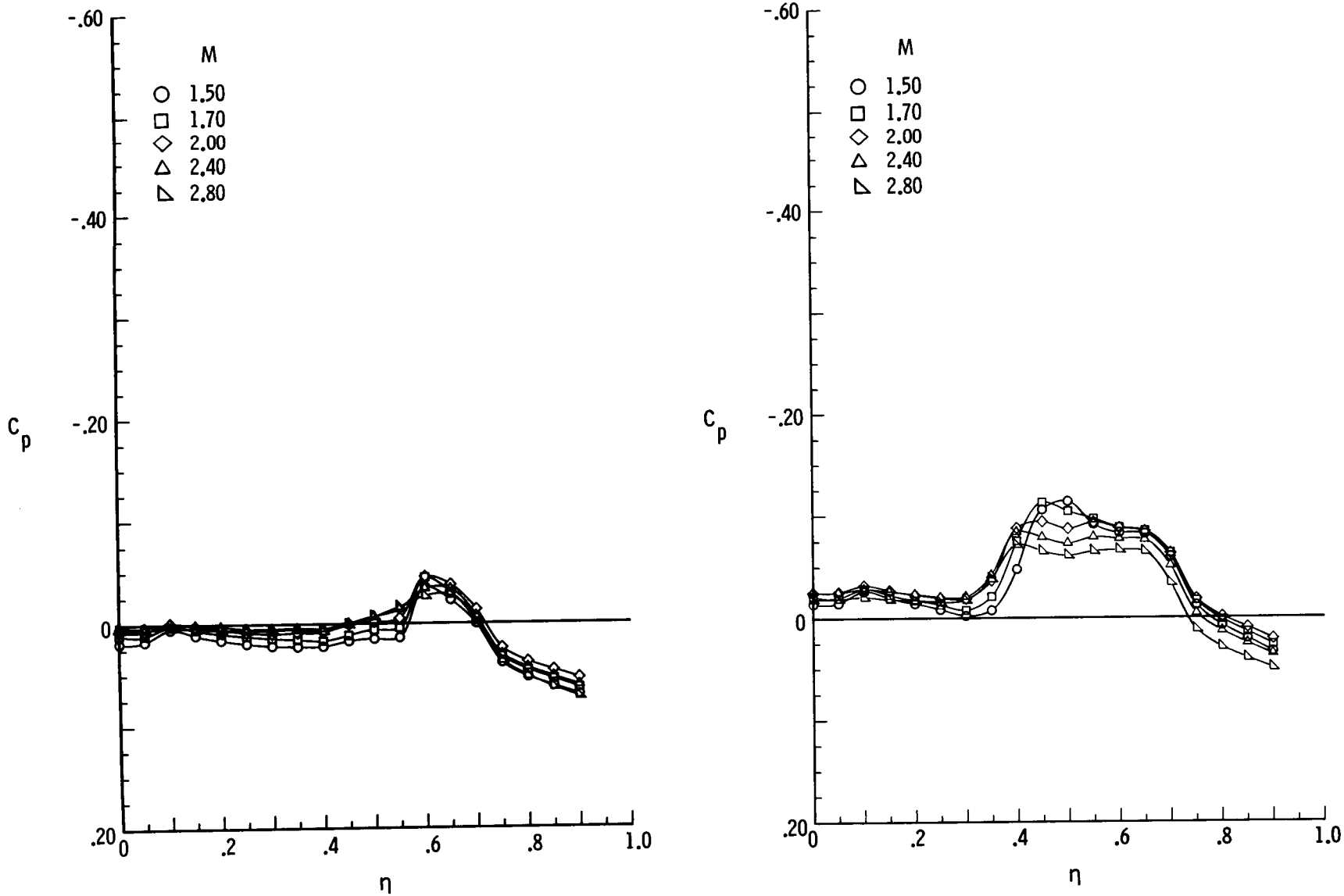

(a) $\alpha = 0°$.

(b) $\alpha = 4°$.

Figure B23.- Pressure plots for 75° delta wing with $\delta_F = 15°$ for varying M, $R = 2 \times 10^6$, $\beta = 0°$, and $x/\ell = 0.90$.

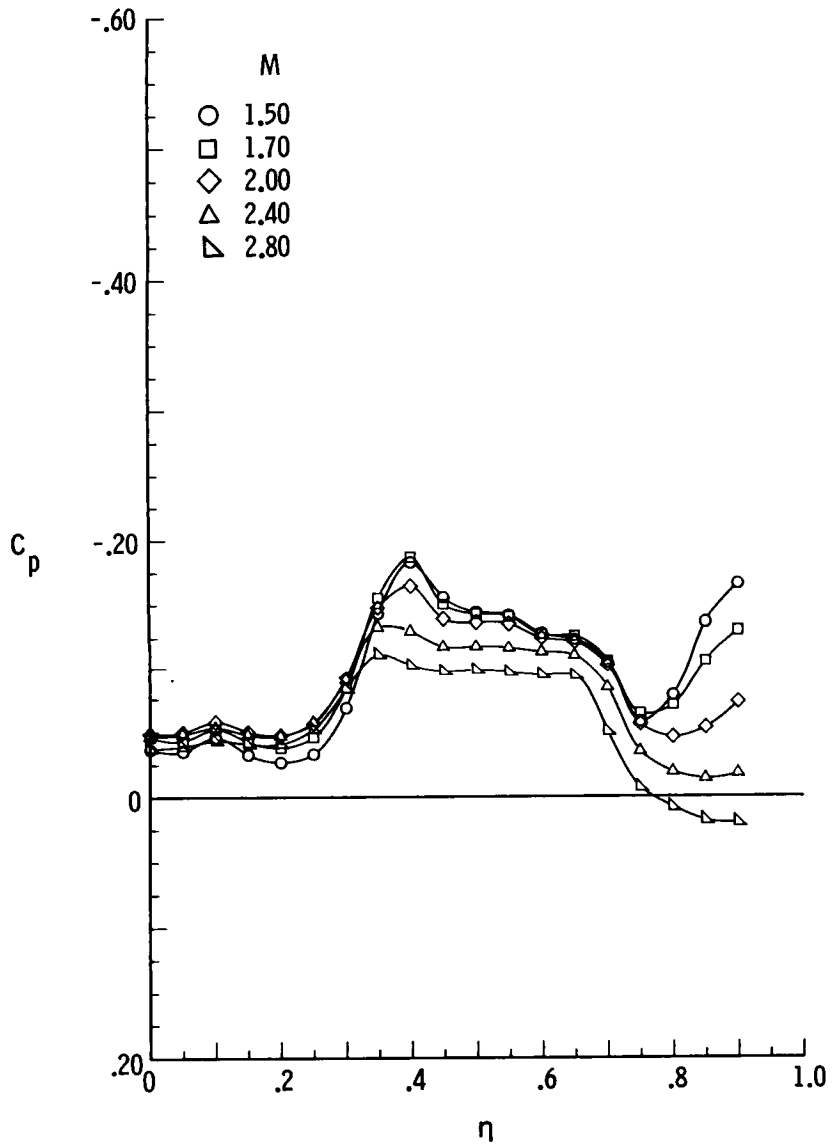

(c) $\alpha = 8°$.

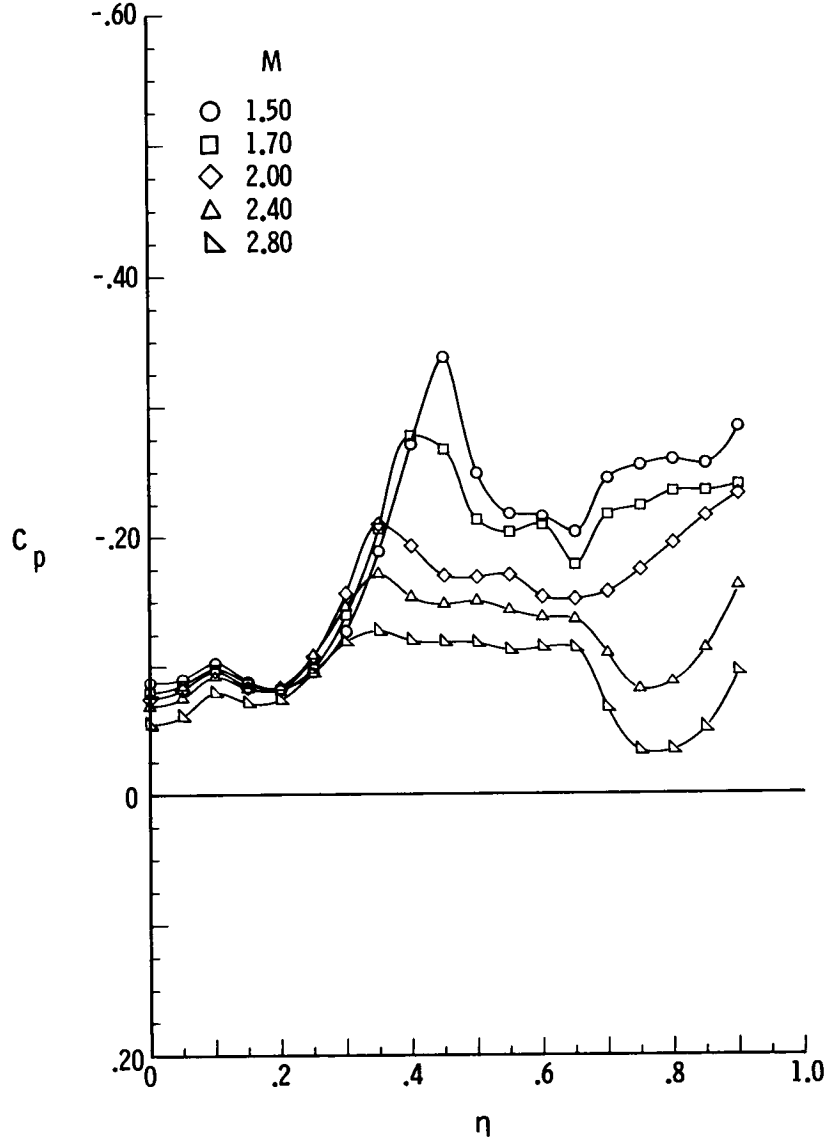

(d) $\alpha = 12°$.

Figure B23.- Concluded.

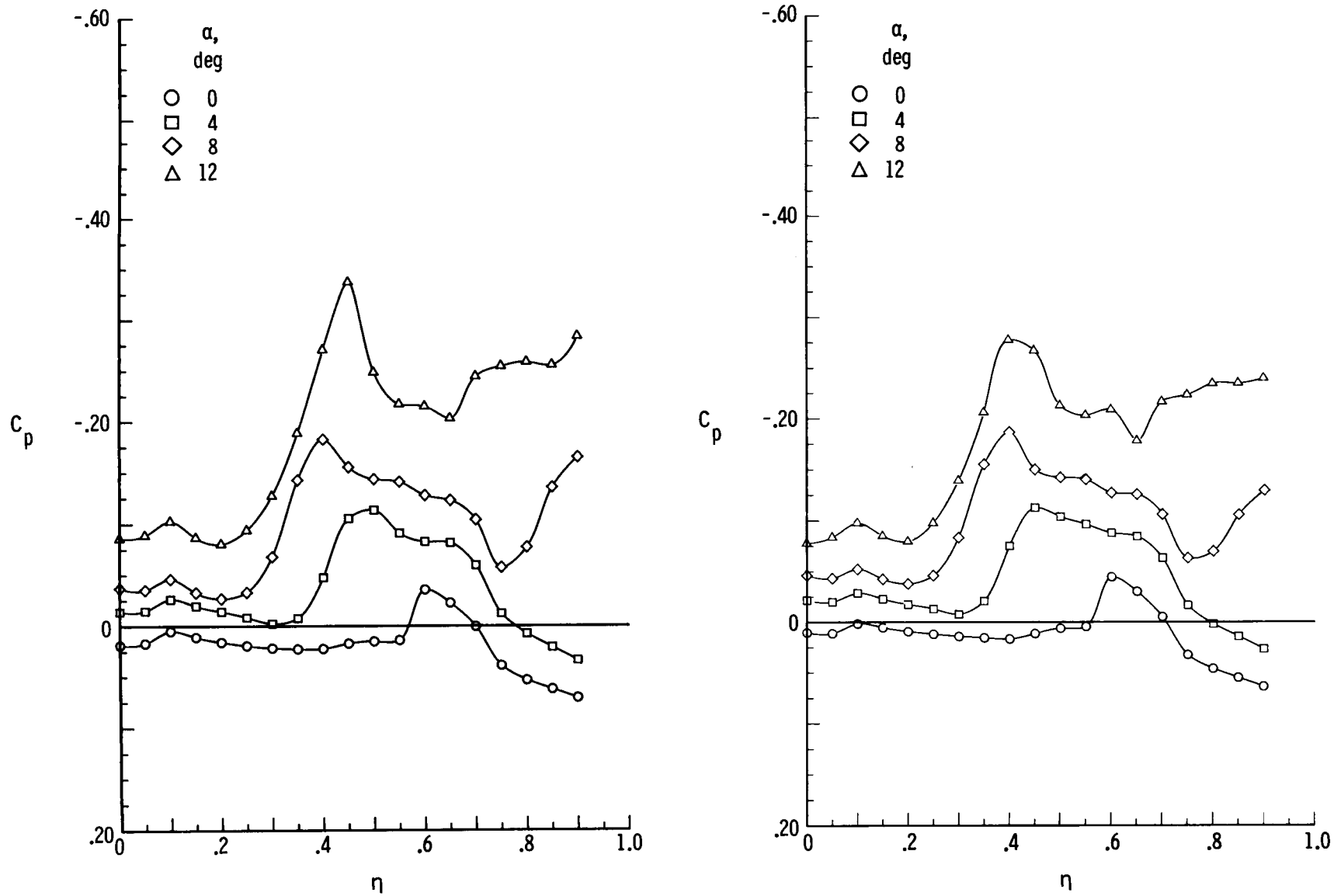

(a) M = 1.50.

(b) M = 1.70.

Figure B24.- Pressure plots for 75° delta wing with $\delta_F = 15°$ for varying α, $R = 2 \times 10^6$, $\beta = 0°$, and $x/\ell = 0.90$.

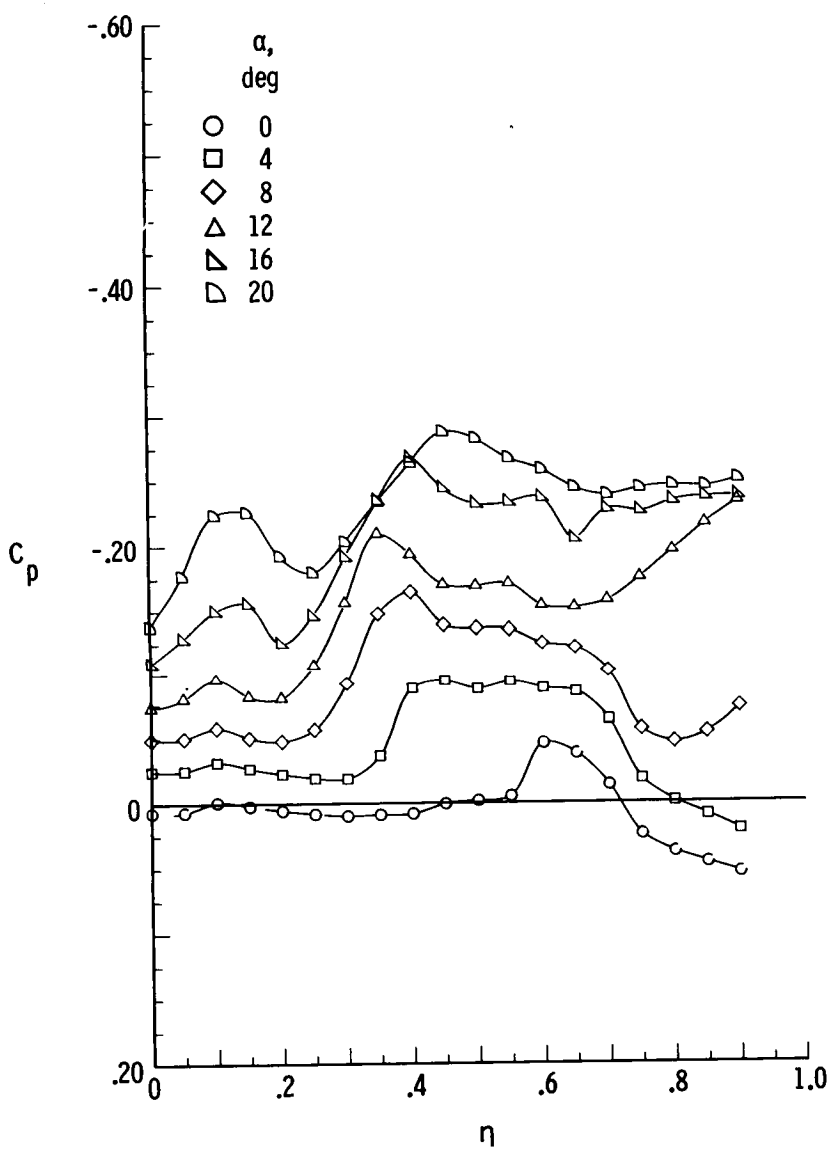

(c) M = 2.00.

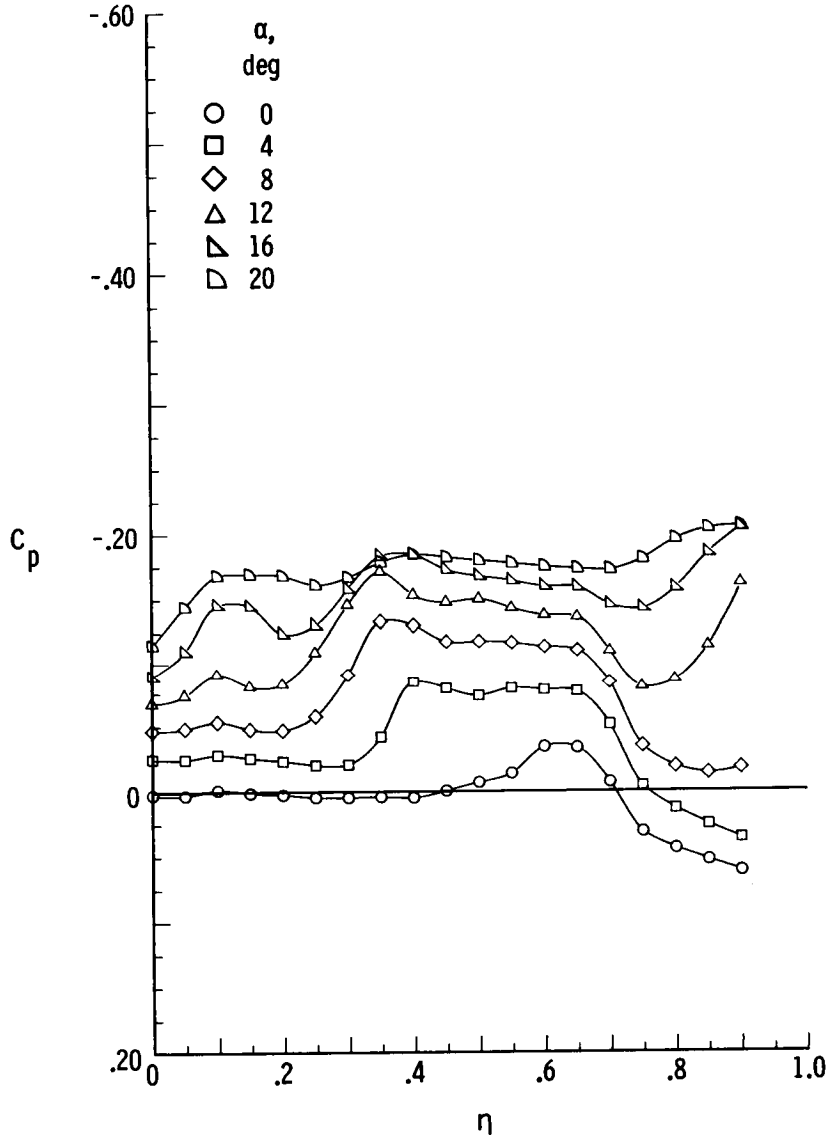

(d) M = 2.40.

Figure B24.- Continued.

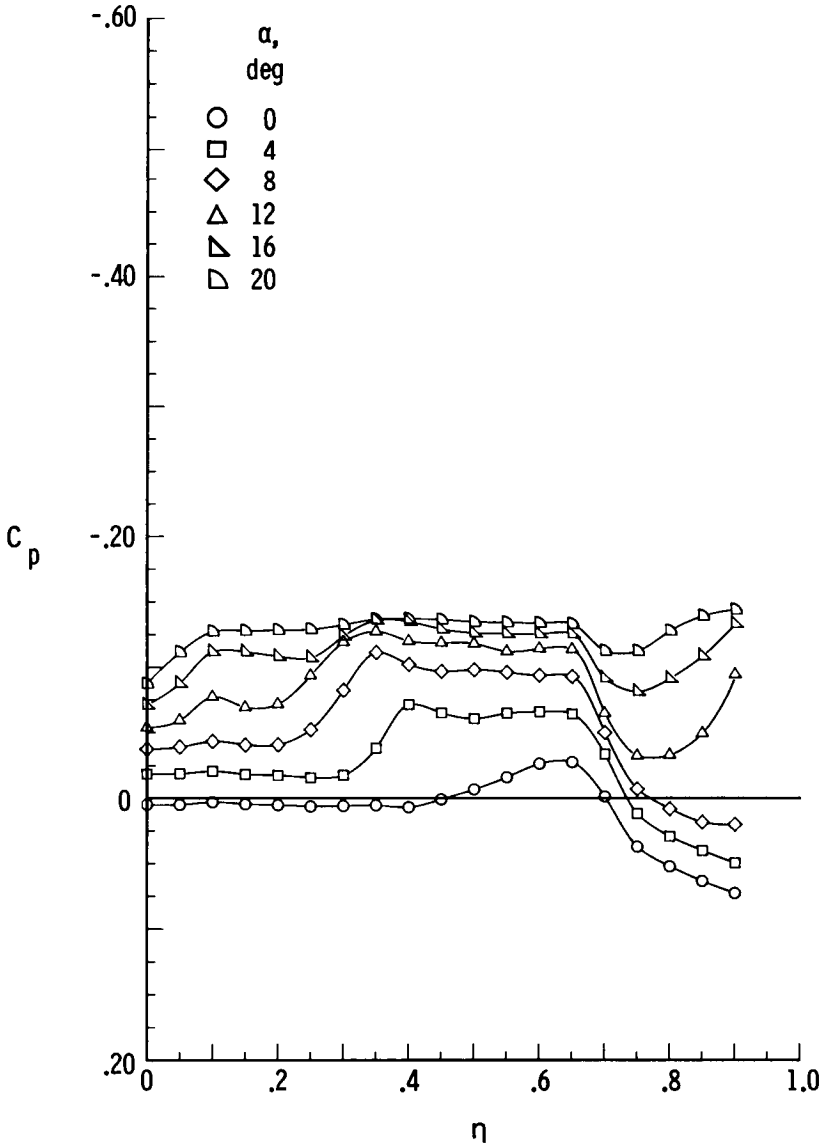

(e) M = 2.80.

Figure B24.- Concluded.

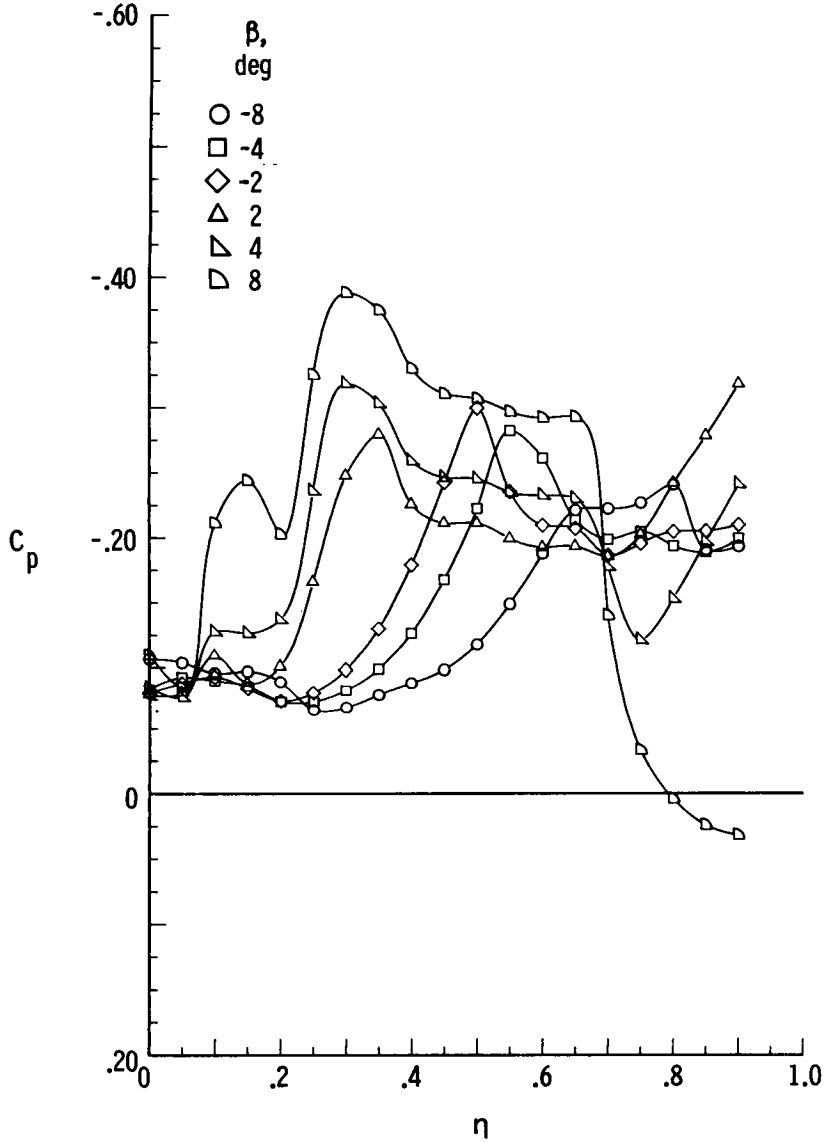

(a) M = 1.70.

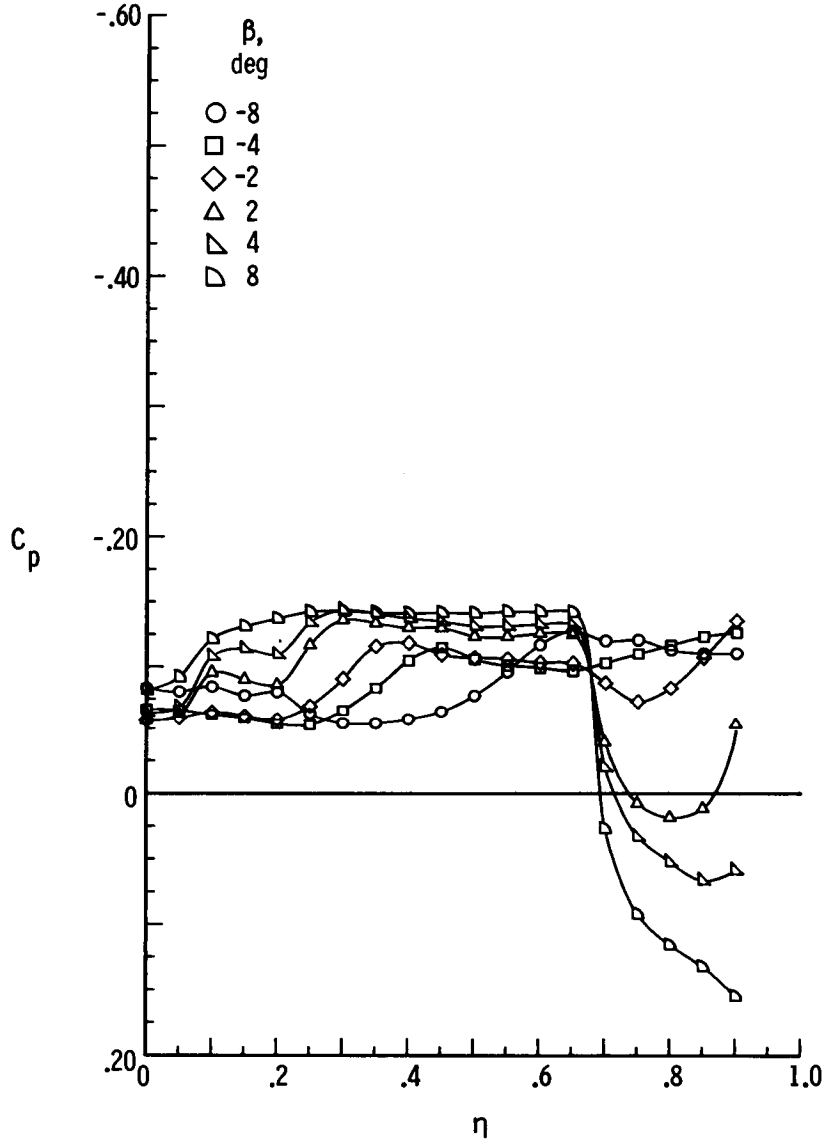

(b) M = 2.80.

Figure B25.- Pressure plots for 75° delta wing with $\delta_F = 15°$ for varying β, $R = 2 \times 10^6$, $\alpha = 12°$, and $x/\ell = 0.90$.

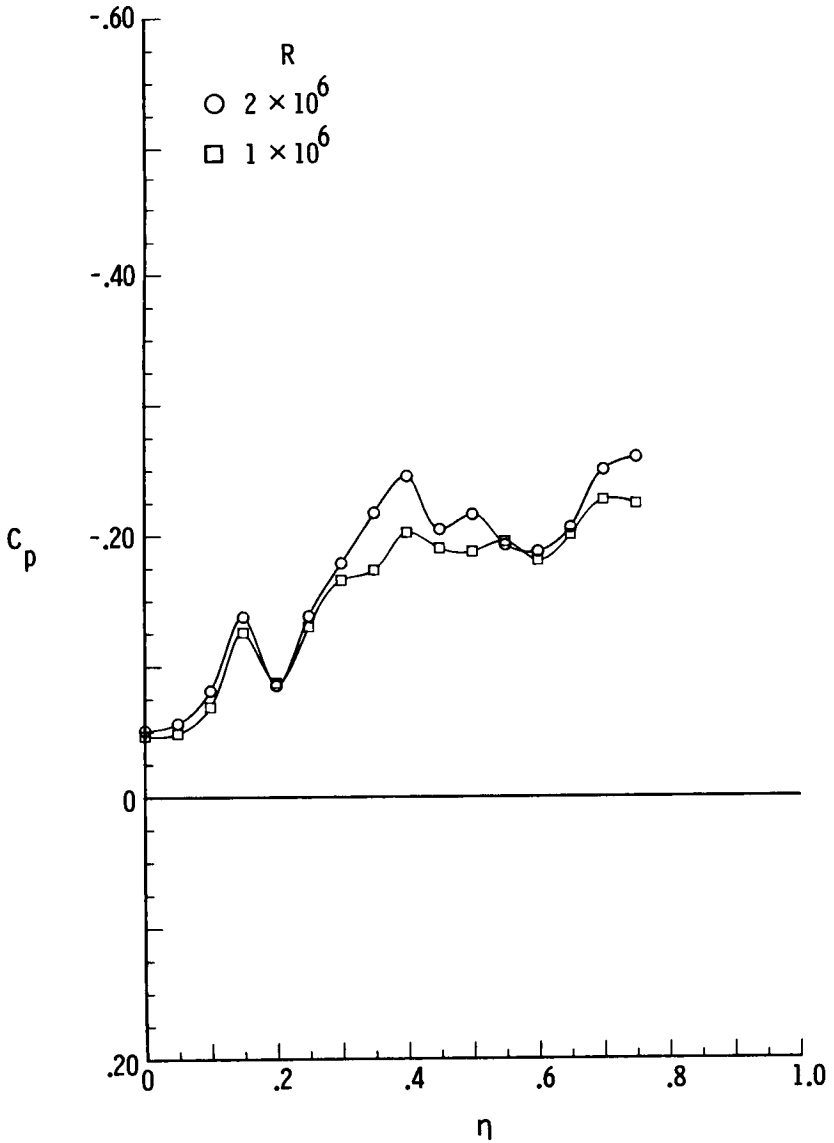

(a) M = 1.70; x/ℓ = 0.10.

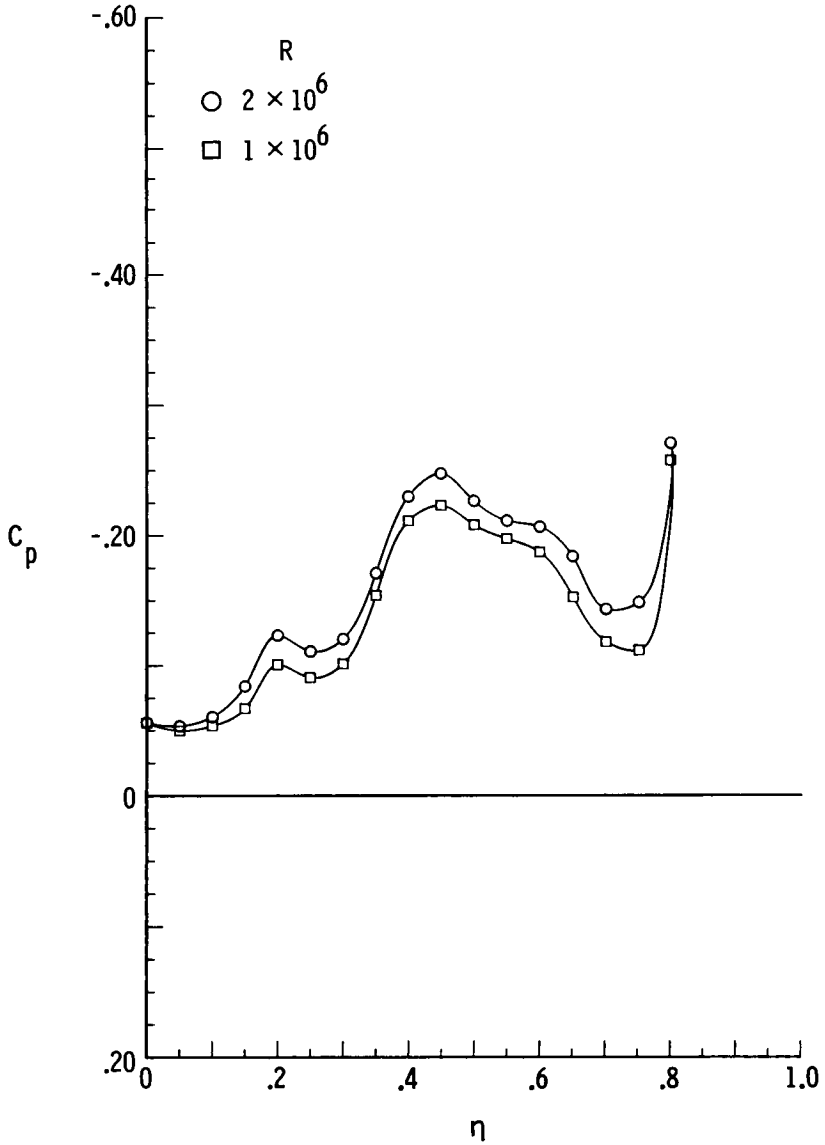

(b) M = 1.70; x/ℓ = 0.20.

Figure B26.- Pressure plots for 75° delta wing with δ_F = 15° for varying R, α = 12°, and β = 0°.

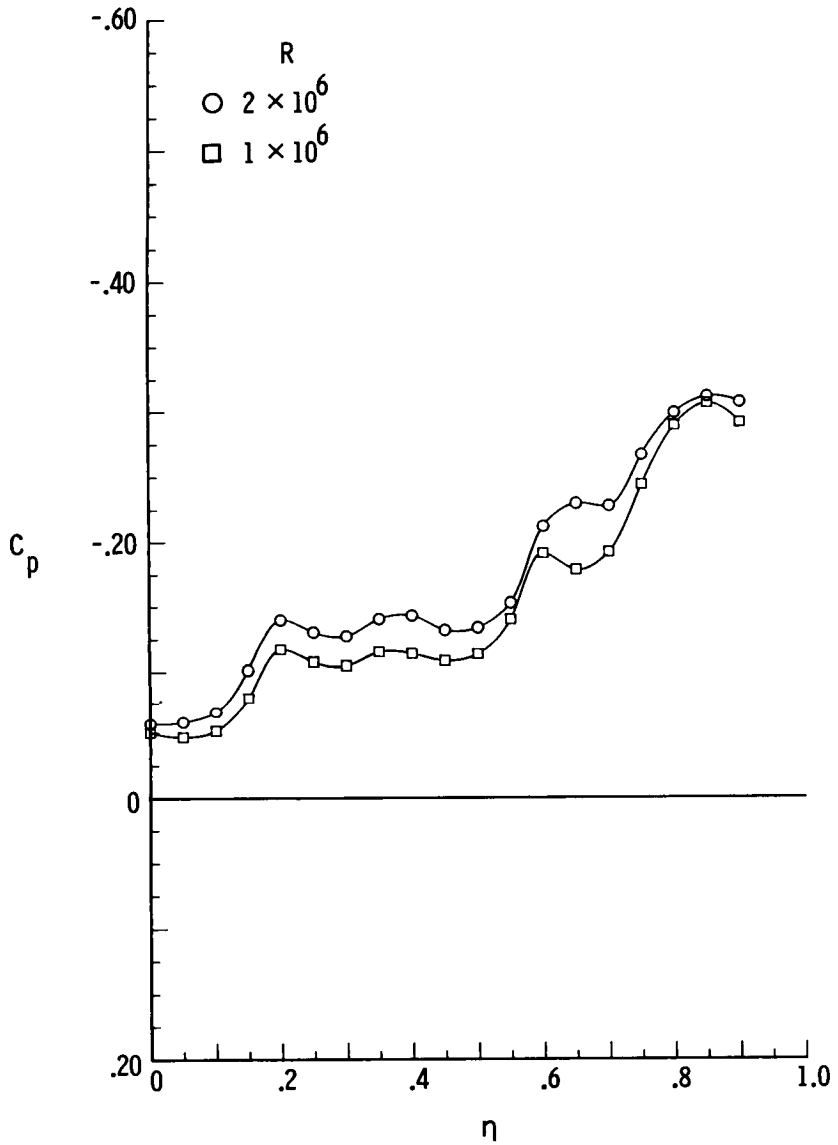

(c) M = 1.70; x/ℓ = 0.30.

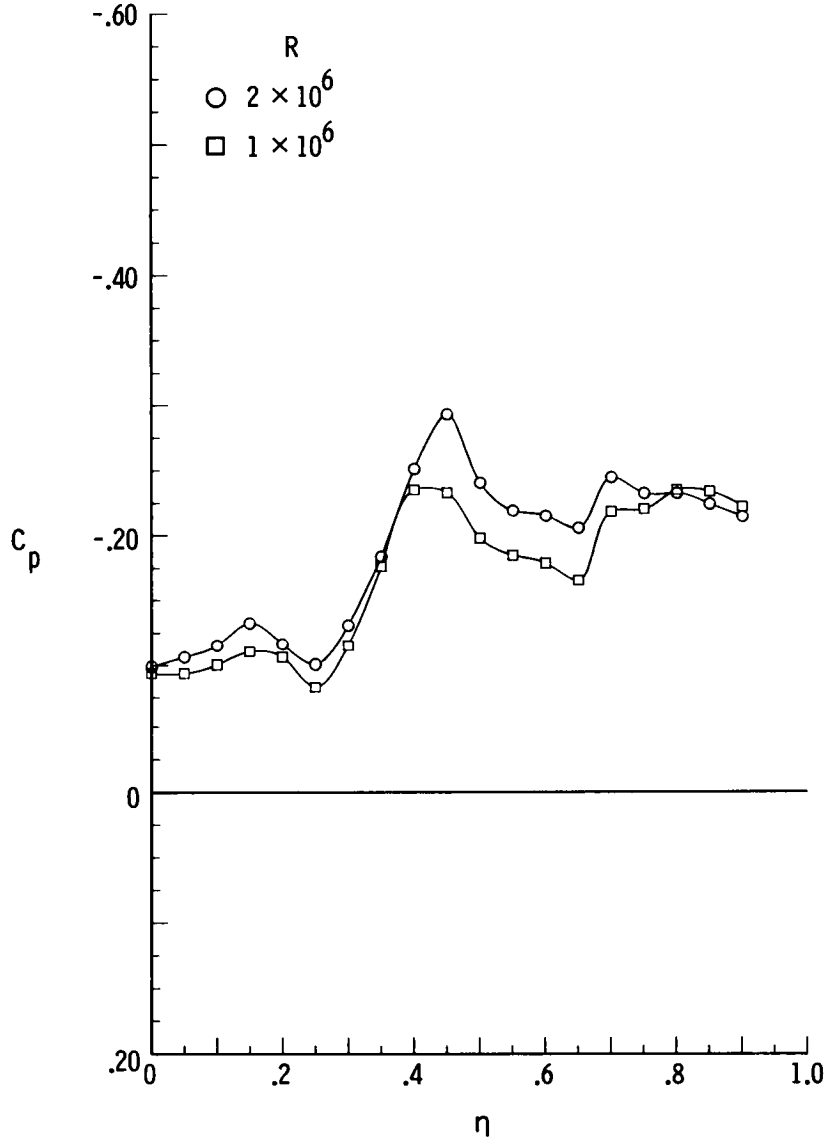

(d) M = 1.70; x/ℓ = 0.60.

Figure B26.- Continued.

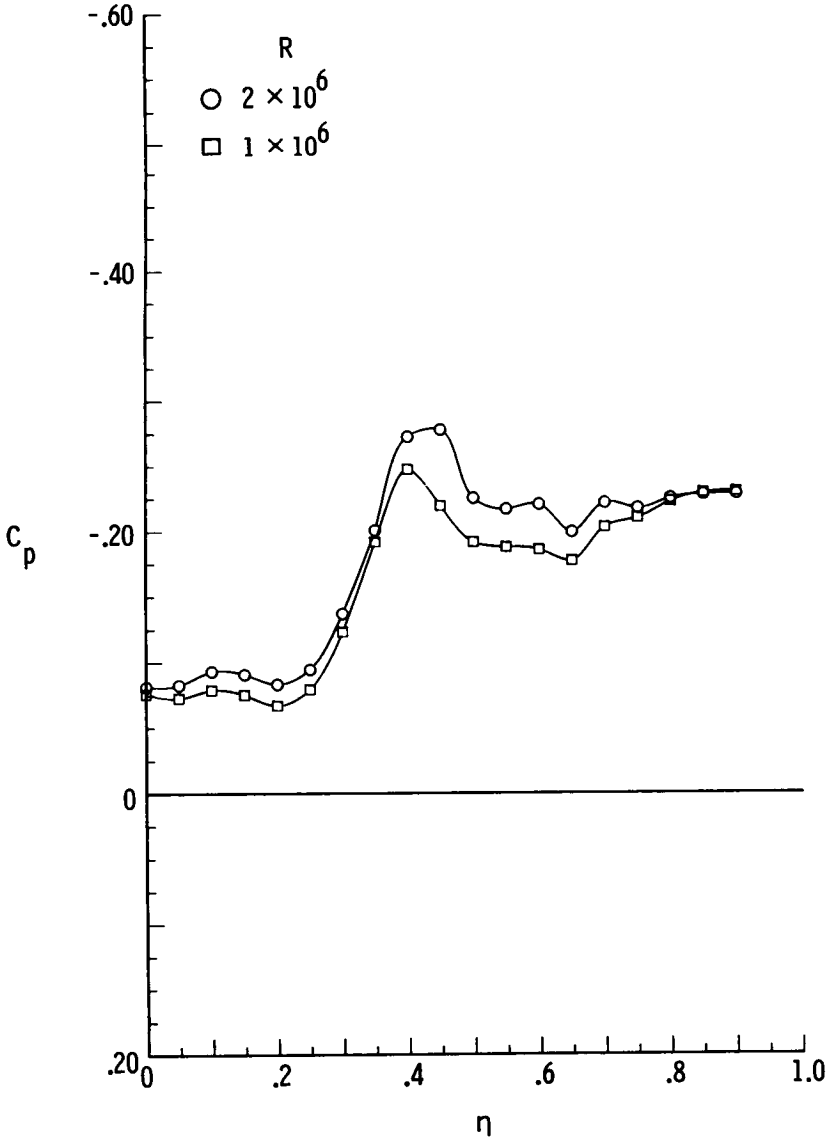

(e) M = 1.70; x/ℓ = 0.80.

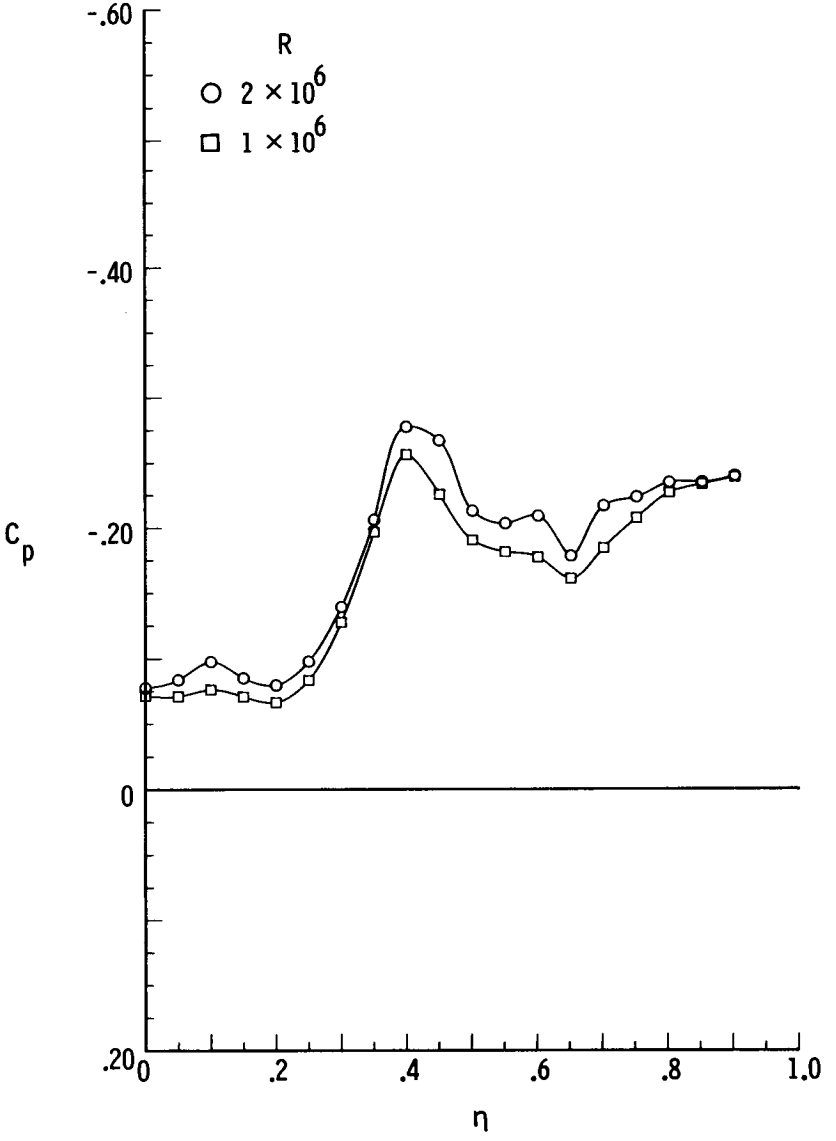

(f) M = 1.70; x/ℓ = 0.90.

Figure B26.- Continued.

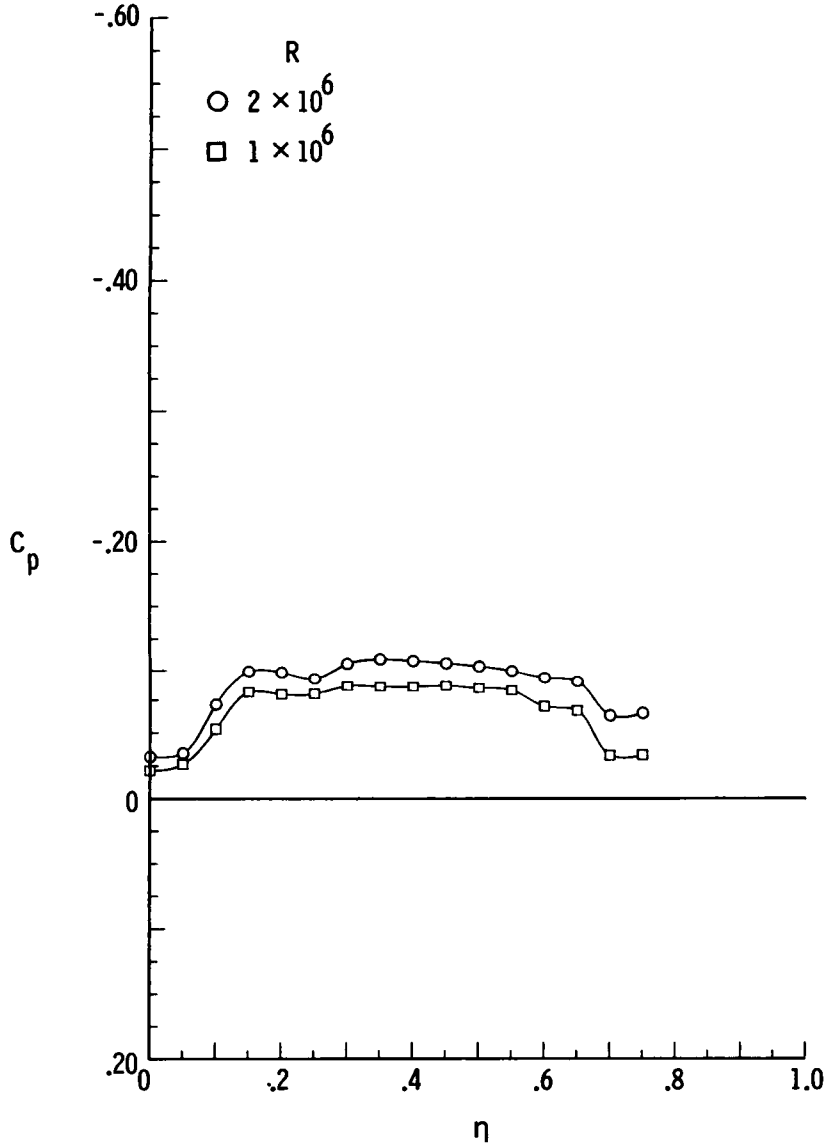

(g) M = 2.80; x/ℓ = 0.10.

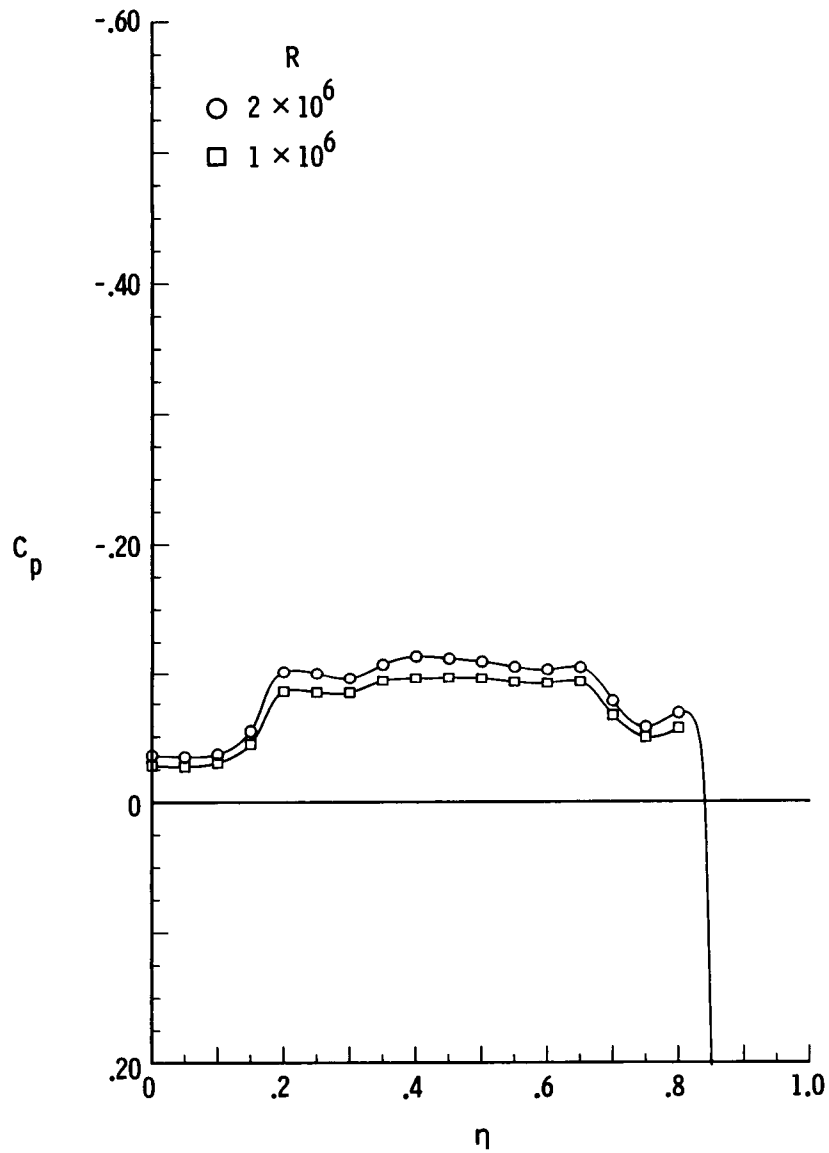

(h) M = 2.80; x/ℓ = 0.20.

Figure B26.- Continued.

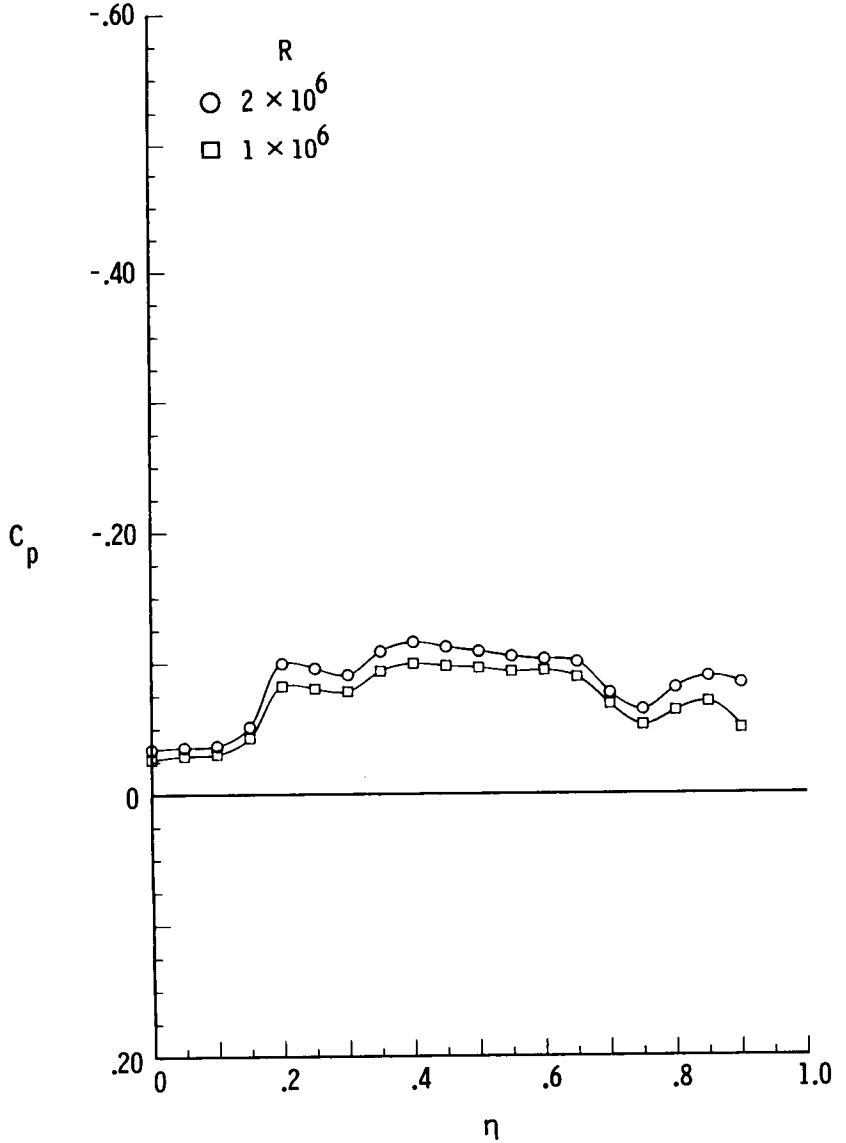

(i) M = 2.80; x/ℓ = 0.30.

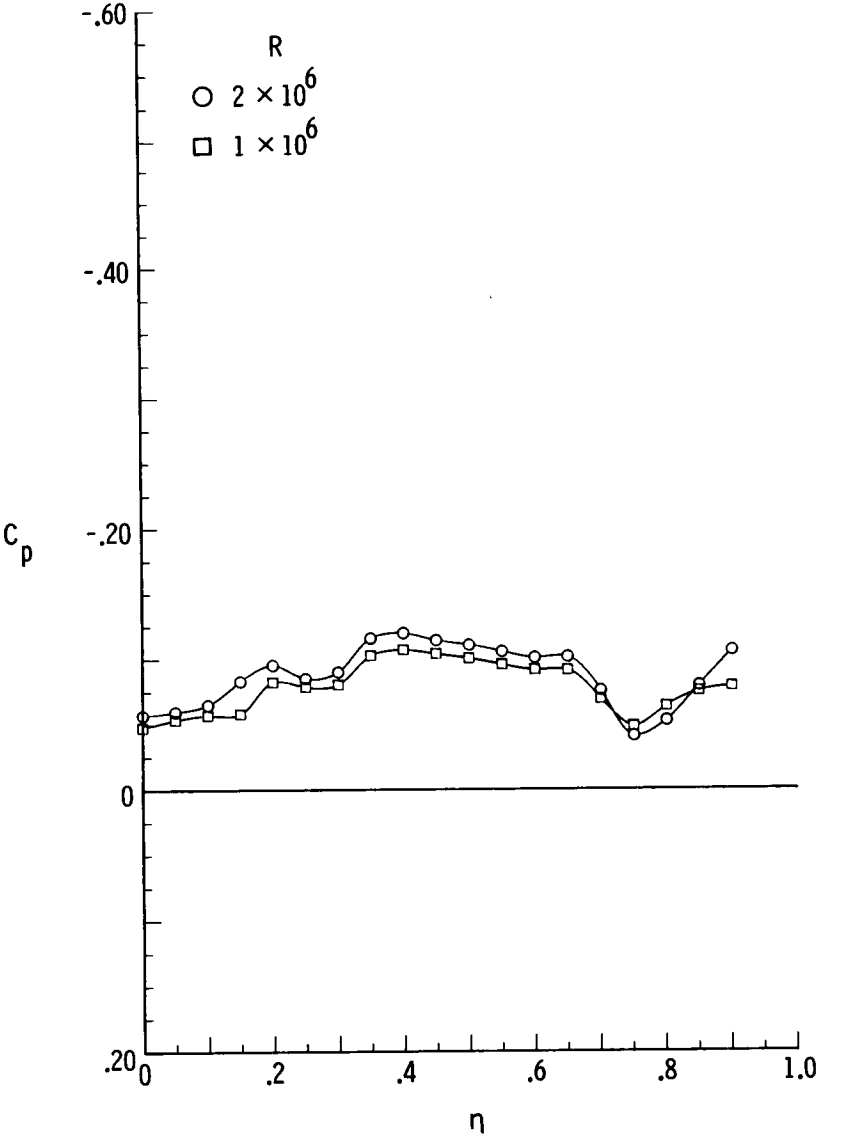

(j) M = 2.80; x/ℓ = 0.60.

Figure B26.- Continued.

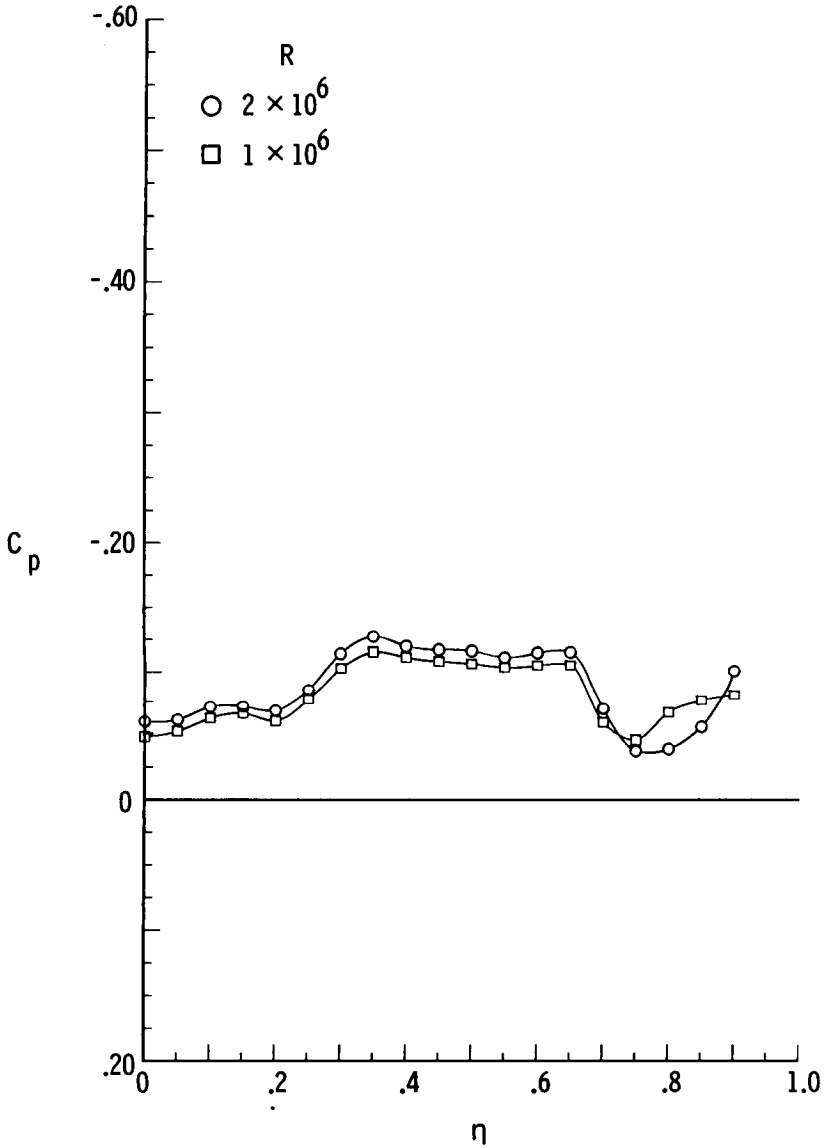

(k) M = 2.80; x/ℓ = 0.80.

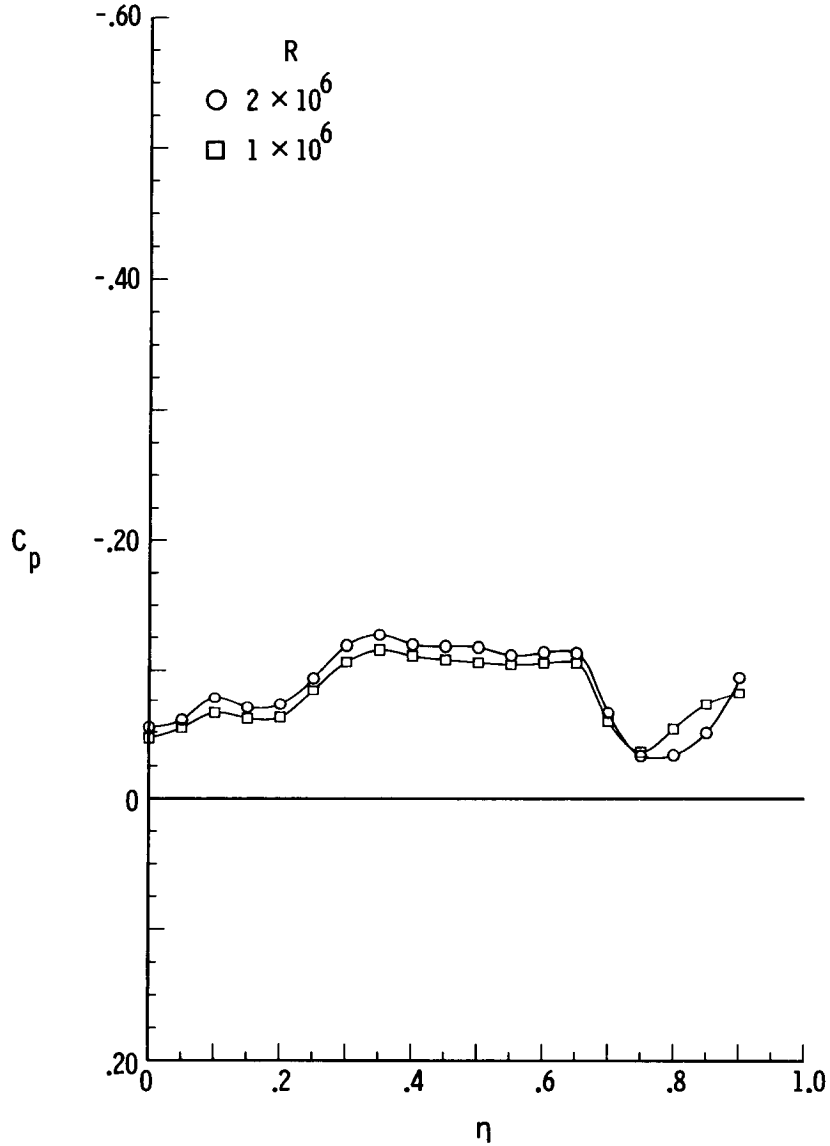

(l) M = 2.80; x/ℓ = 0.90.

Figure B26.- Concluded.

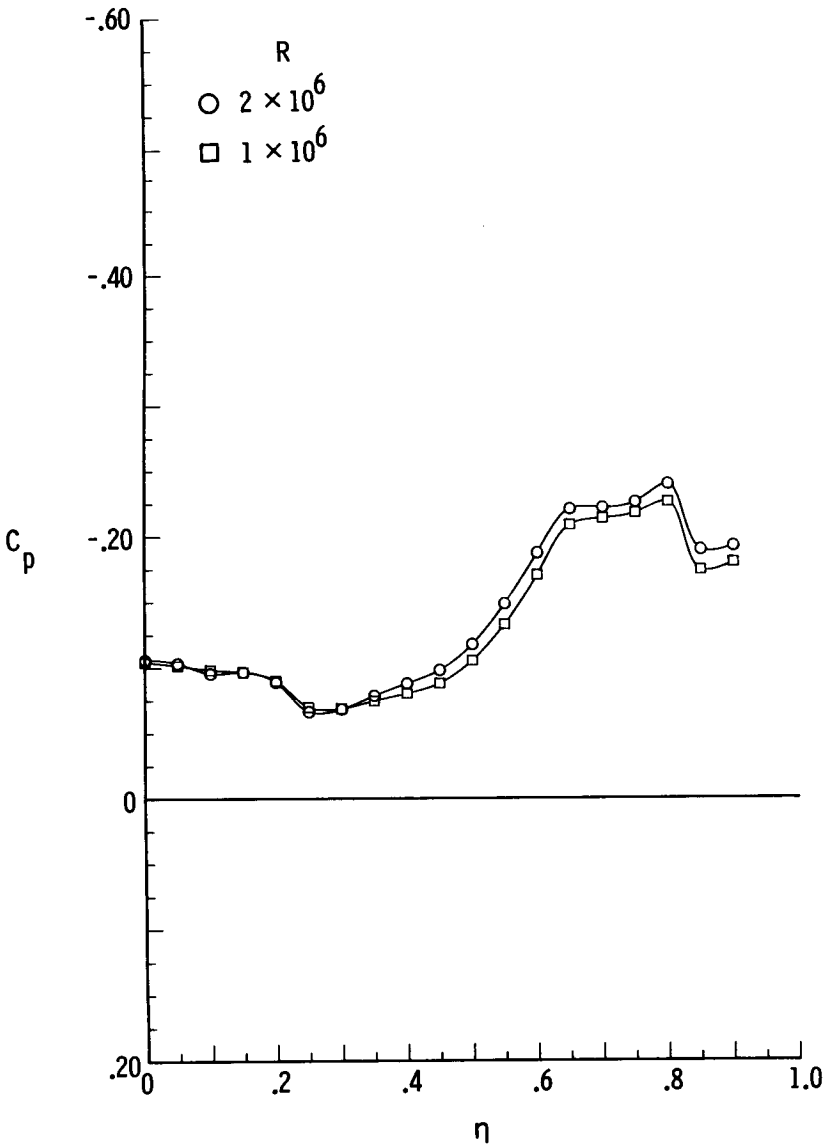

(a) M = 1.70; β = -8°.

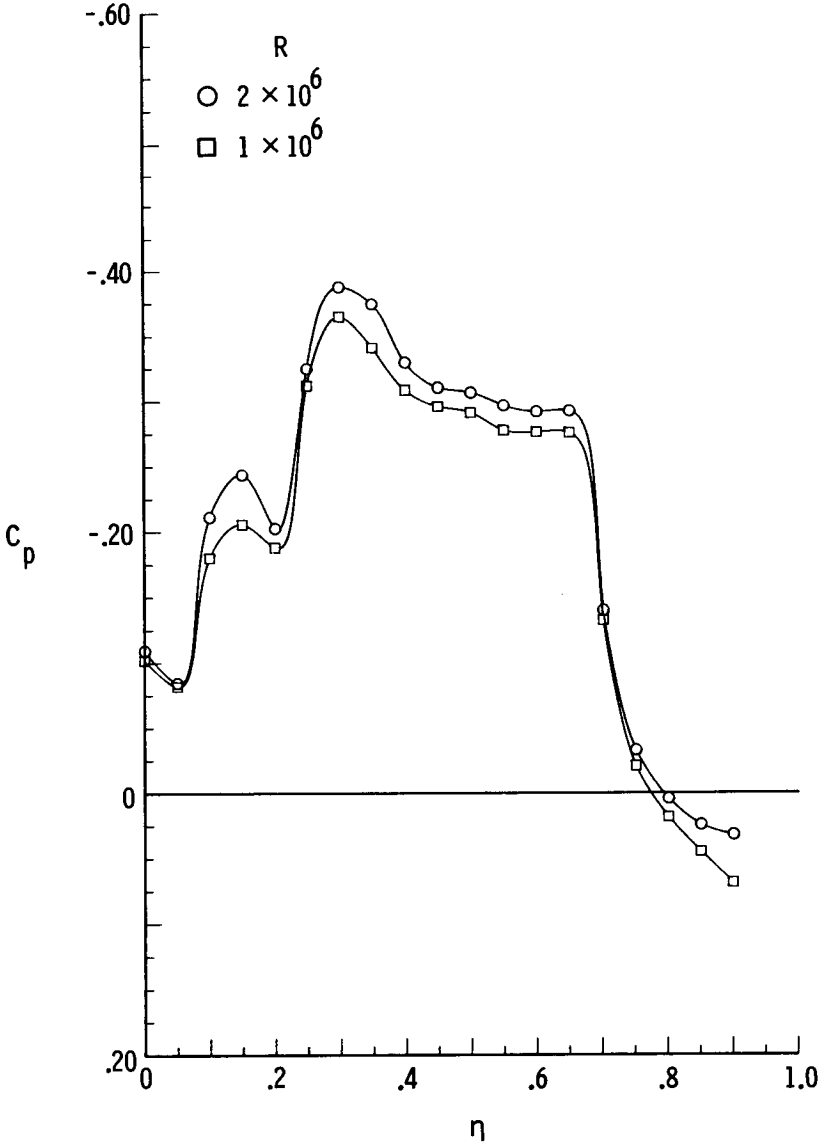

(b) M = 1.70; β = 8°.

Figure B27.- Pressure plots for 75° delta wing with δ_F = 15° for varying R, α = 12°, and x/ℓ = 0.90.

C-3

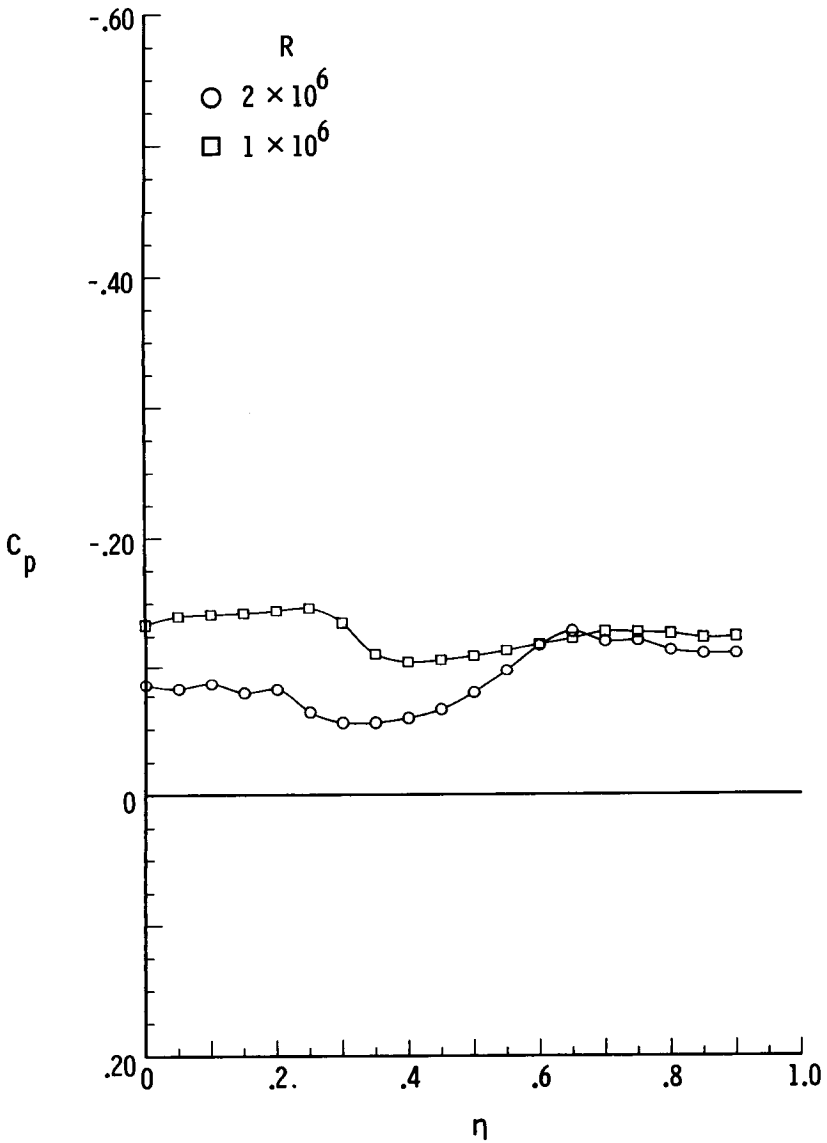

(c) M = 2.80; β = -8°.

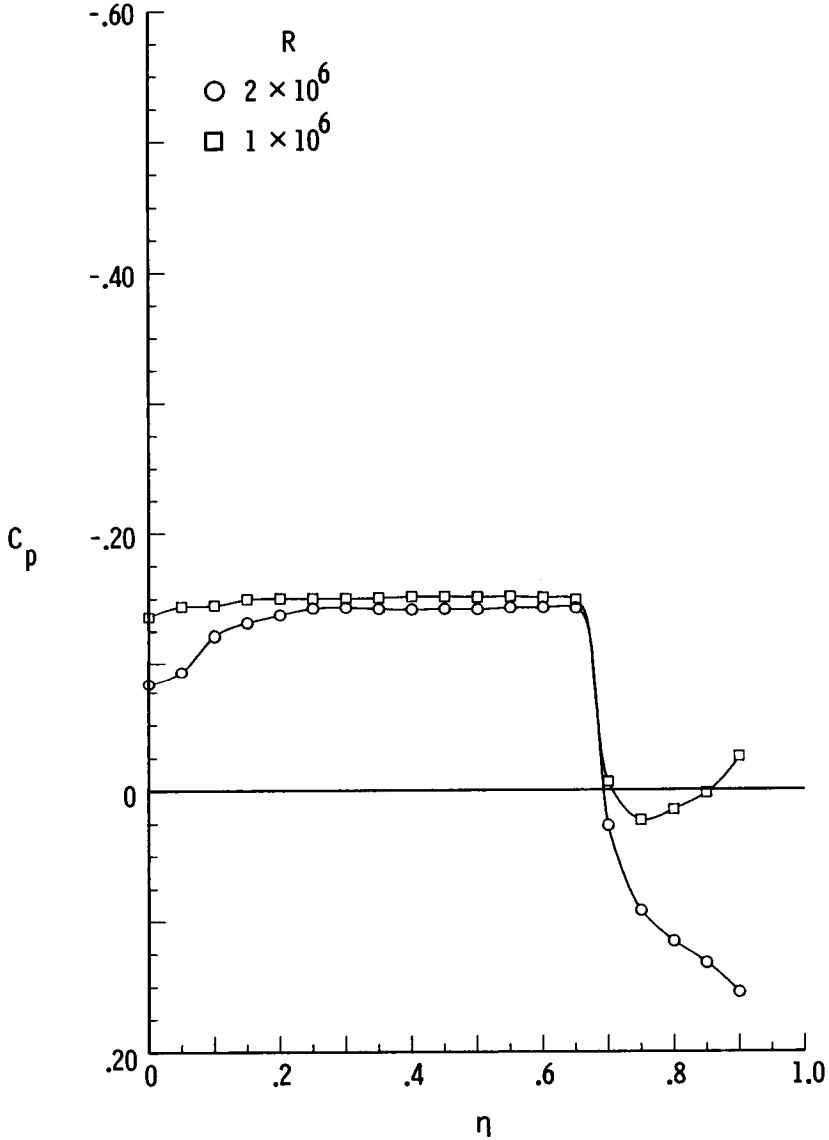

(d) M = 2.80; β = 8°.

Figure B27.- Concluded.

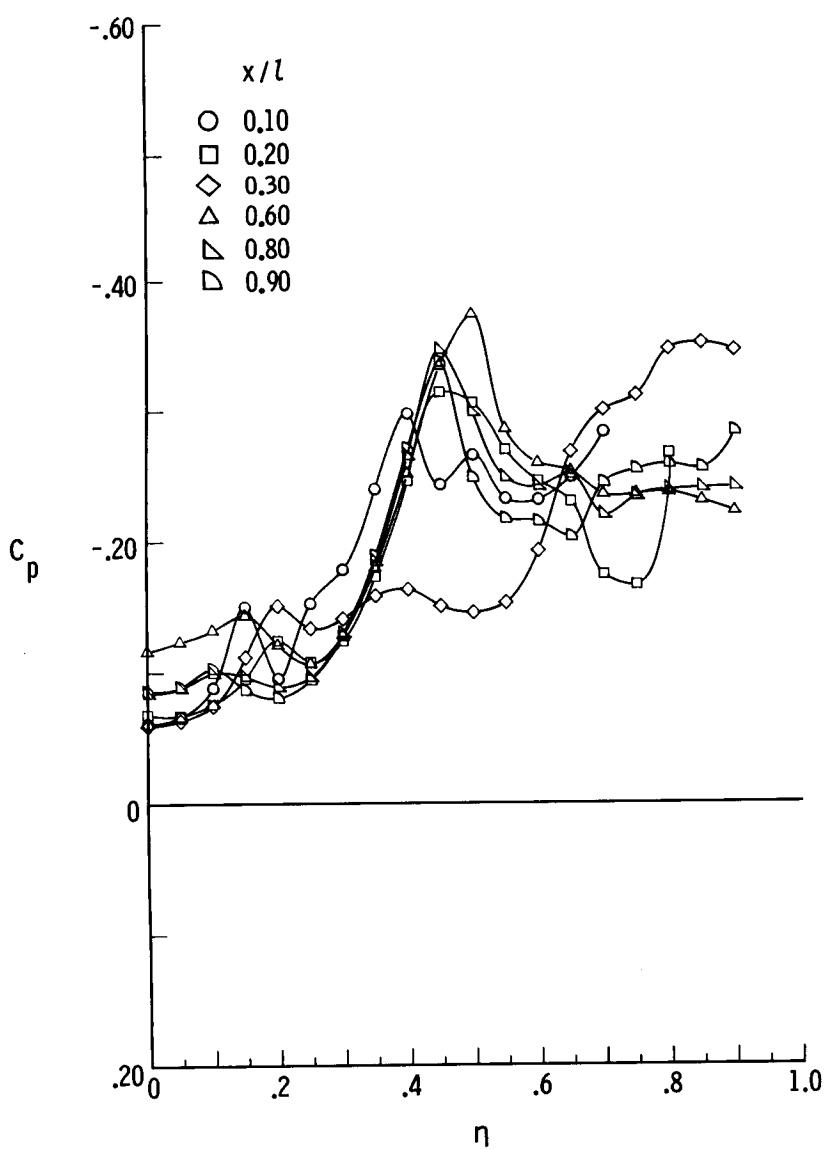

(a) M = 1.50.

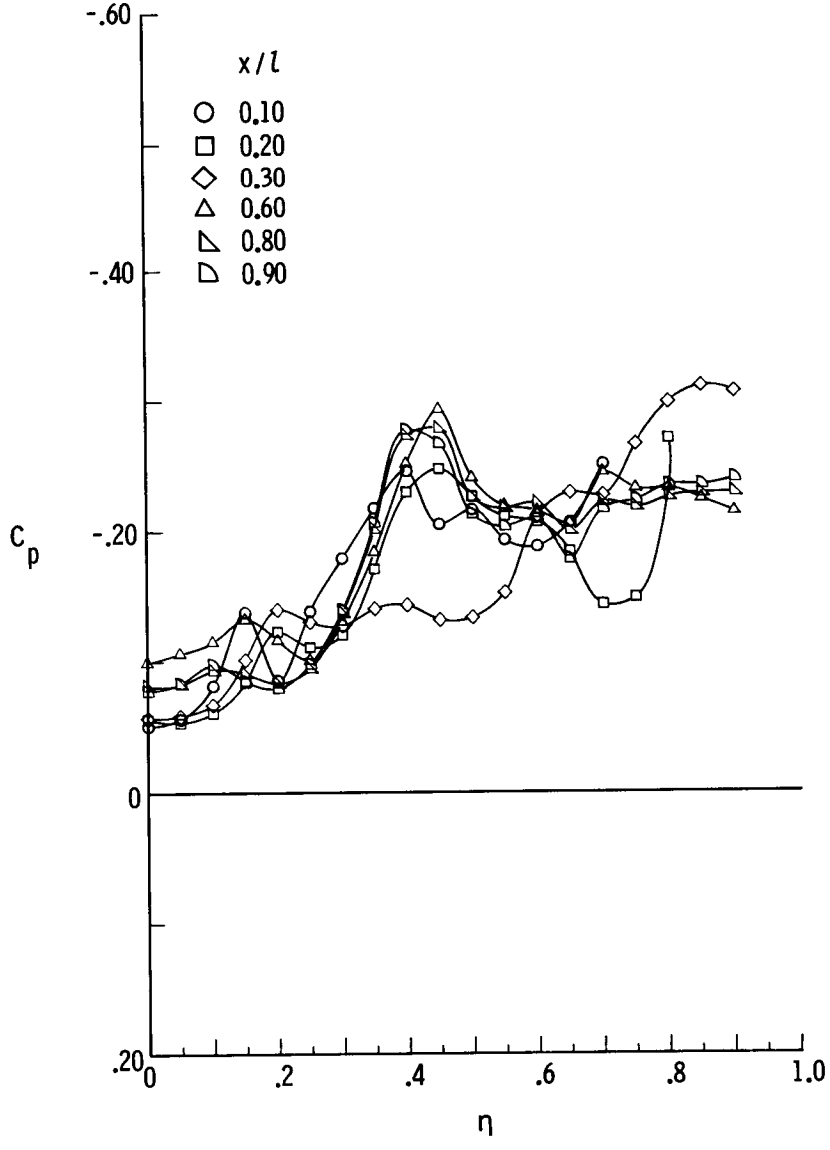

(b) M = 1.70.

Figure B28.- Pressure plots for 75° delta wing with δ_F = 15° for varying x/l, $R = 2 \times 10^6$, α = 12°, and β = 0°.

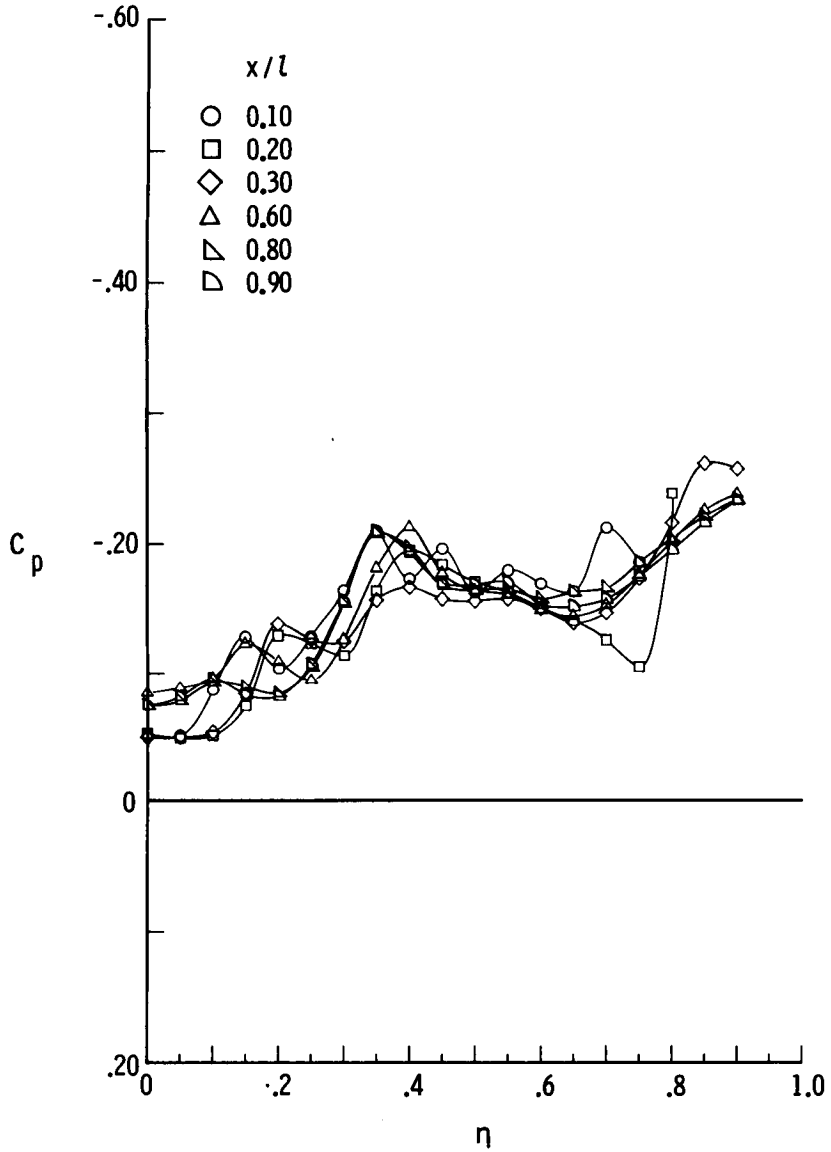

(c) M = 2.00.

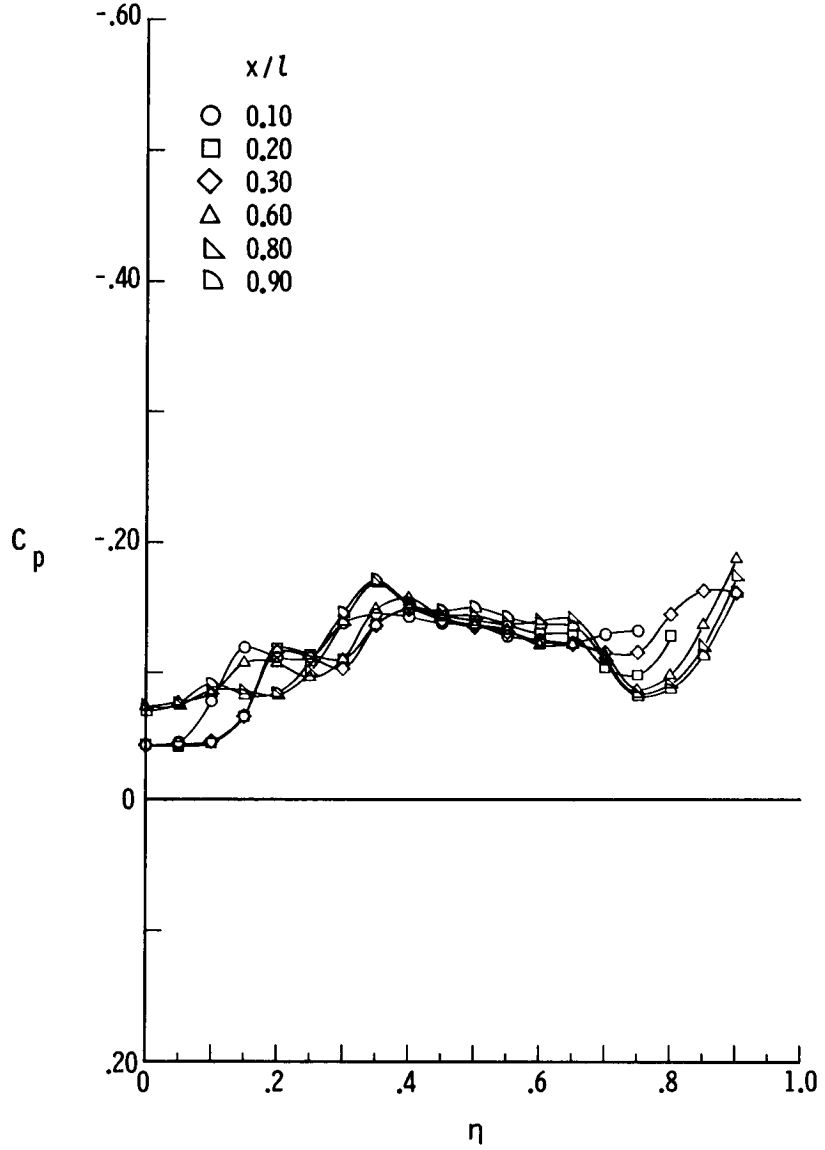

(d) M = 2.40.

Figure B28.- Continued.

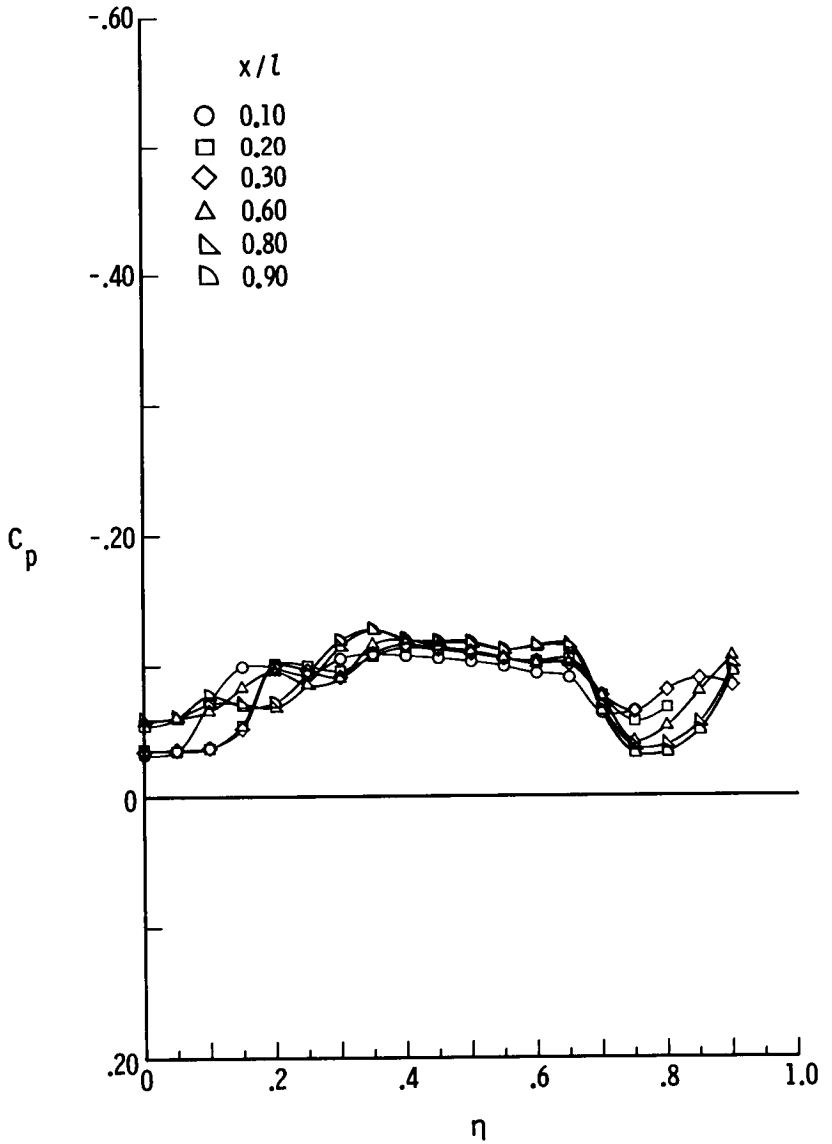

(e) M = 2.80.

Figure B28.- Concluded.

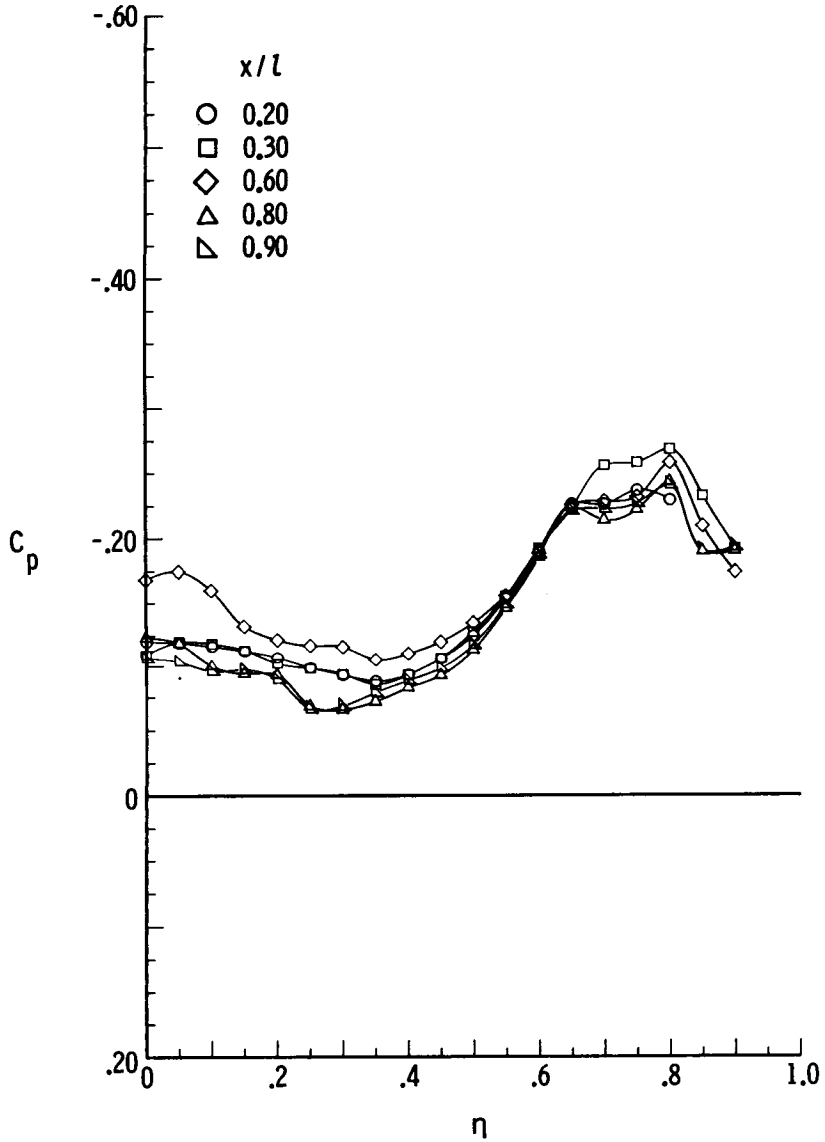

(a) M = 1.70; β = 8°.

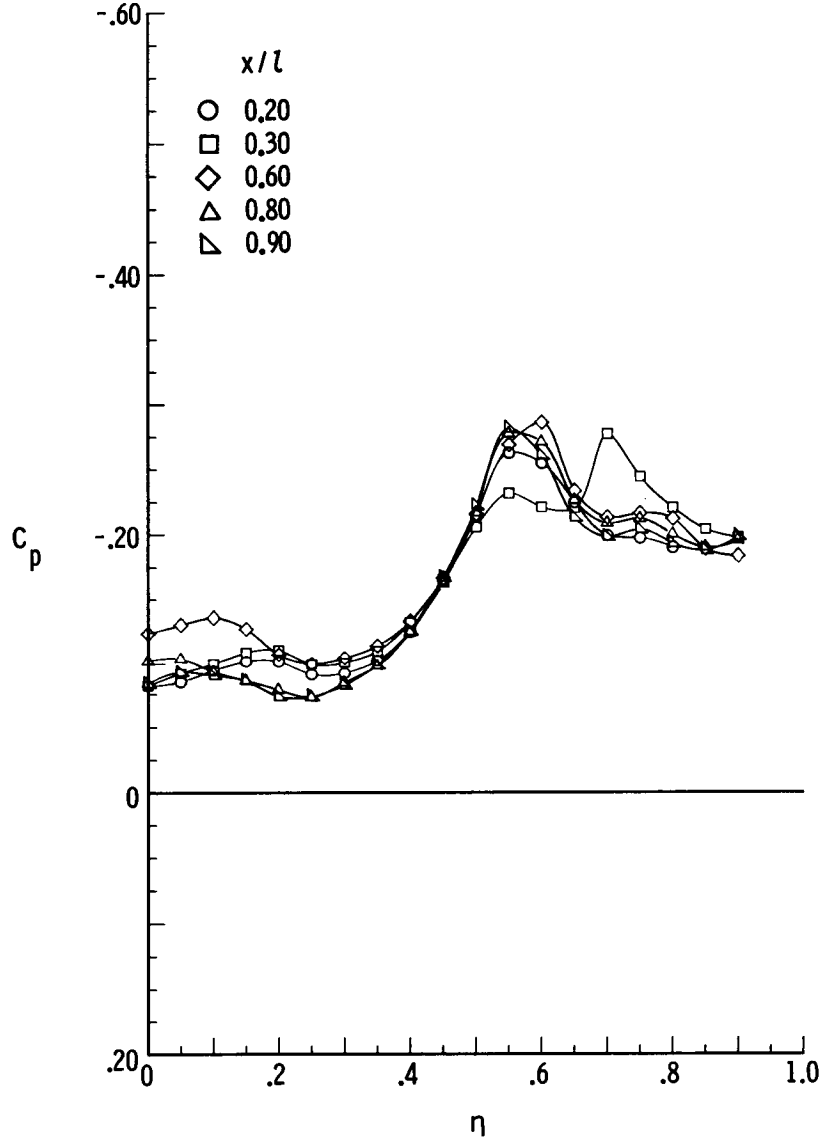

(b) M = 1.70; β = 4°.

Figure B29.- Pressure plots for 75° delta wing with δ_F = 15° for varying x/l, R = 2 × 10^6, and α = 12°.

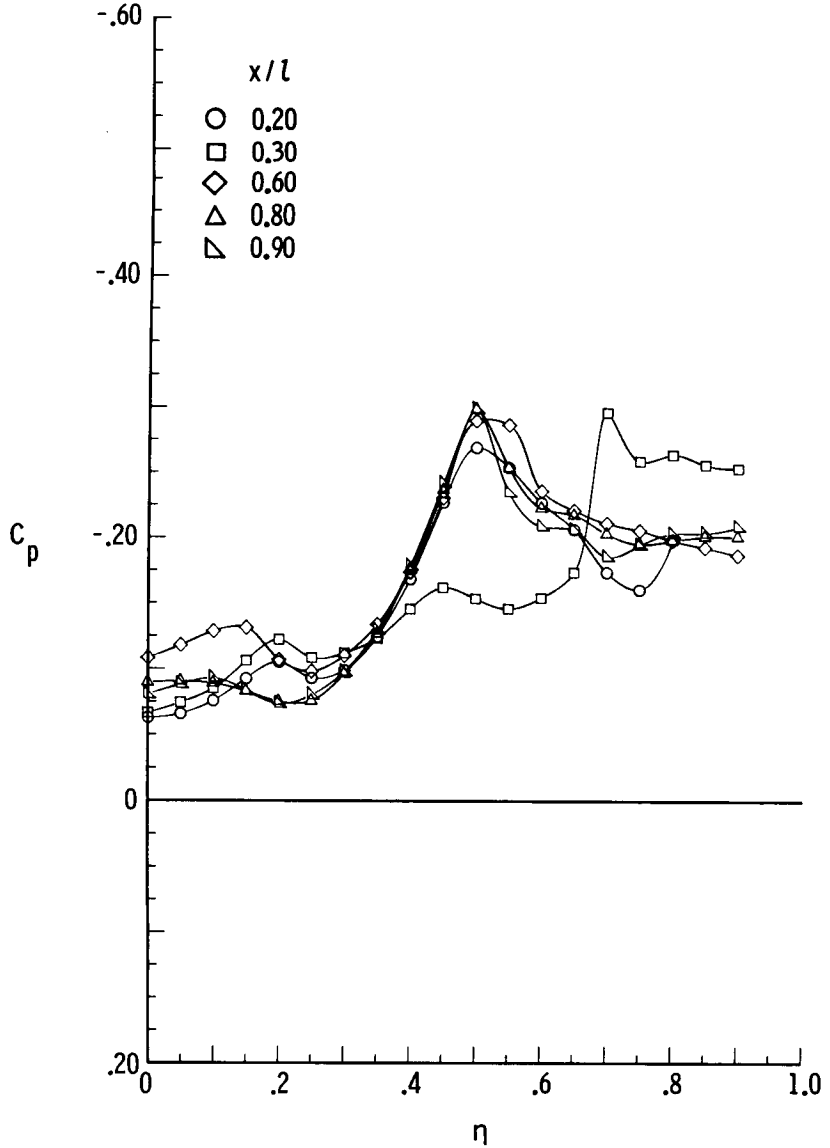

(c) M = 1.70; β = 2°.

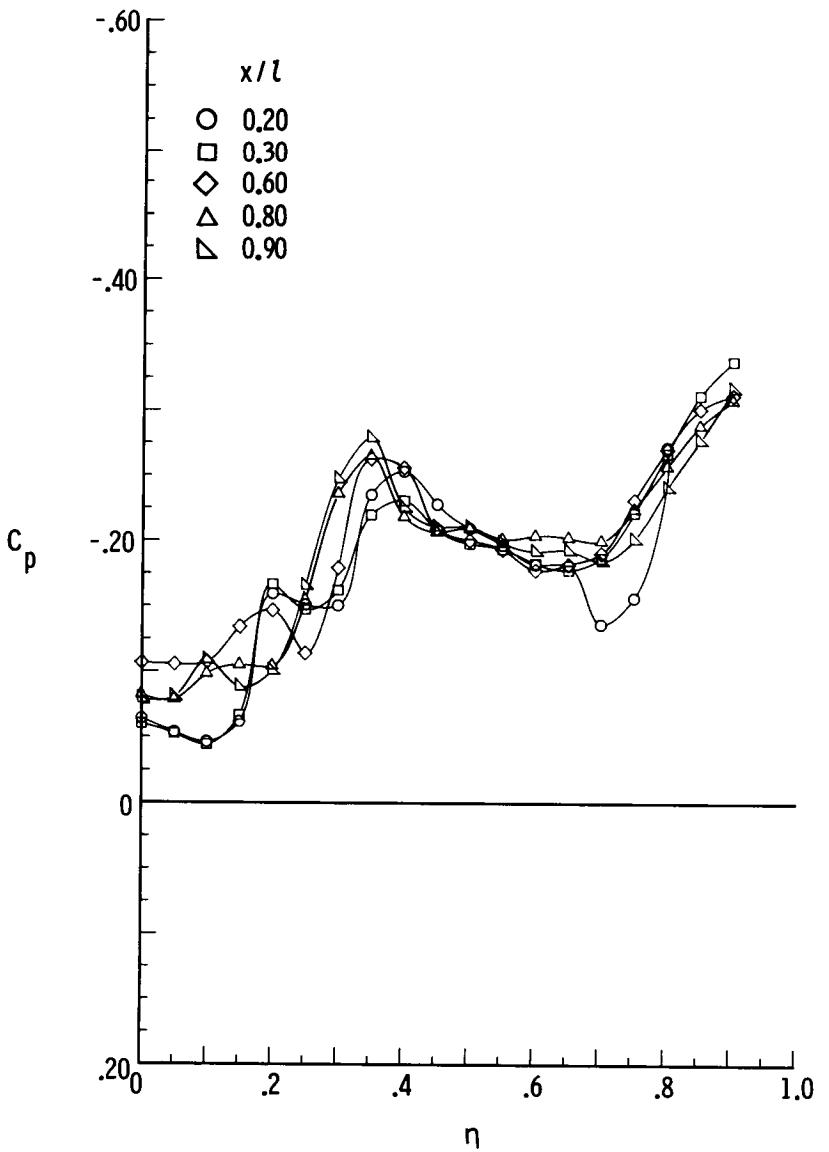

(d) M = 1.70; β = -2°.

Figure B29.- Continued.

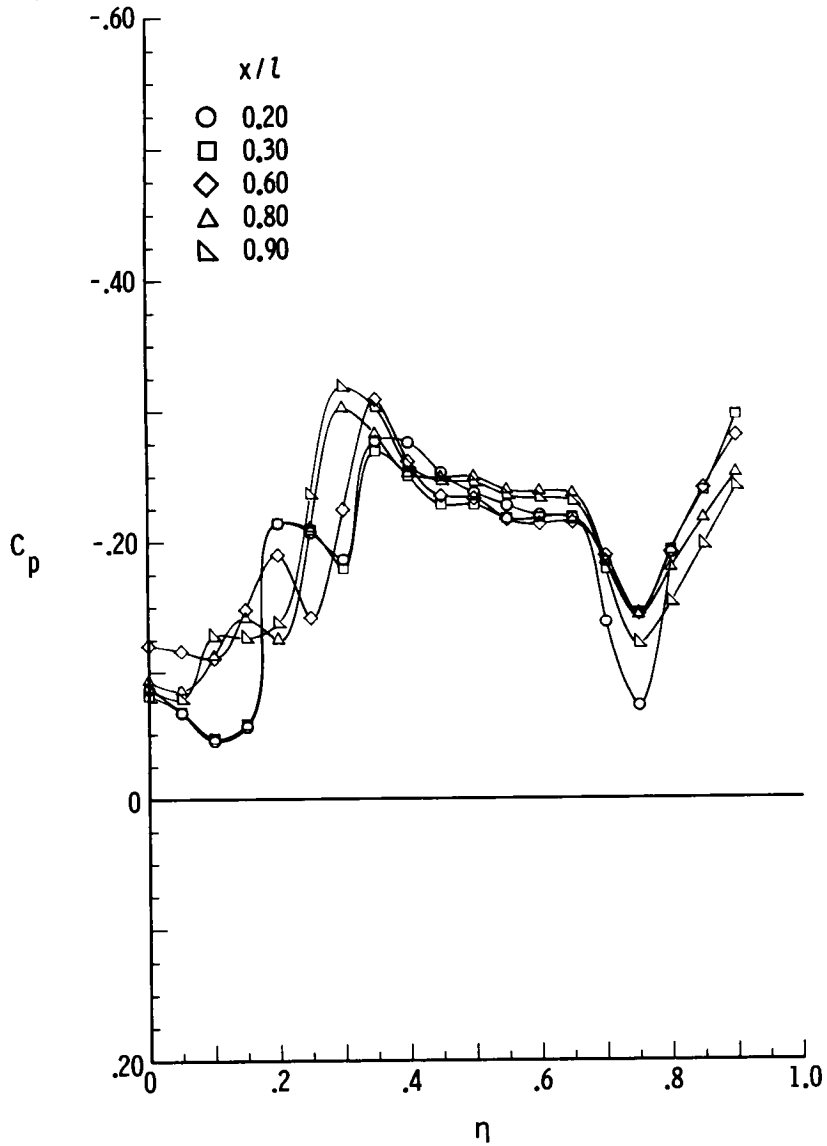

(e) M = 1.70; β = -4°.

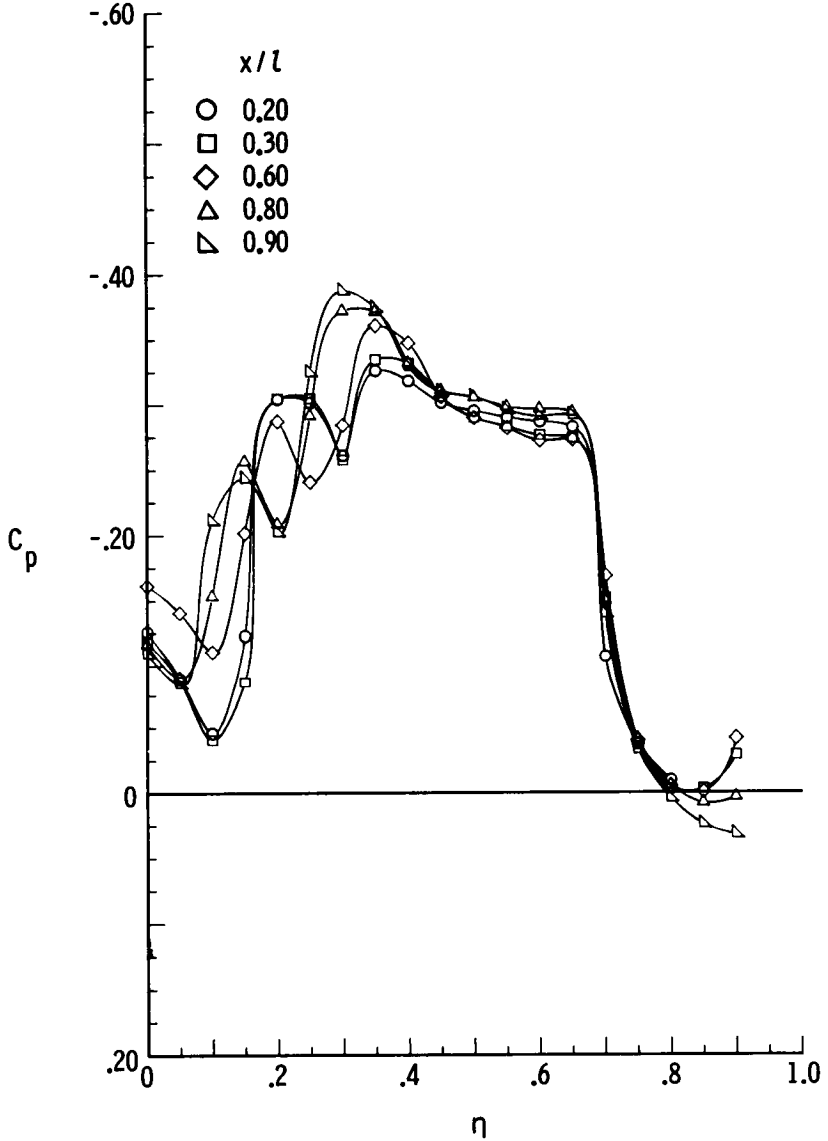

(f) M = 1.70; β = -8°.

Figure B29.- Continued.

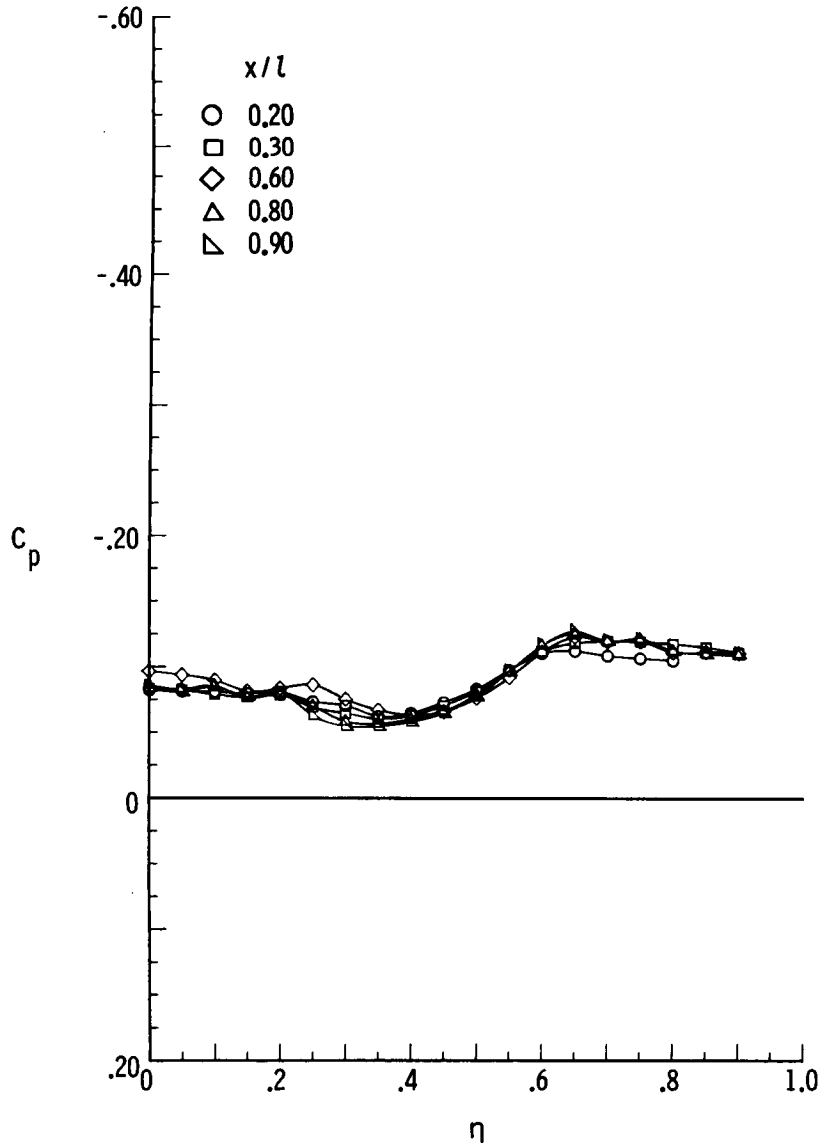

(g) M = 2.80; β = 8°.

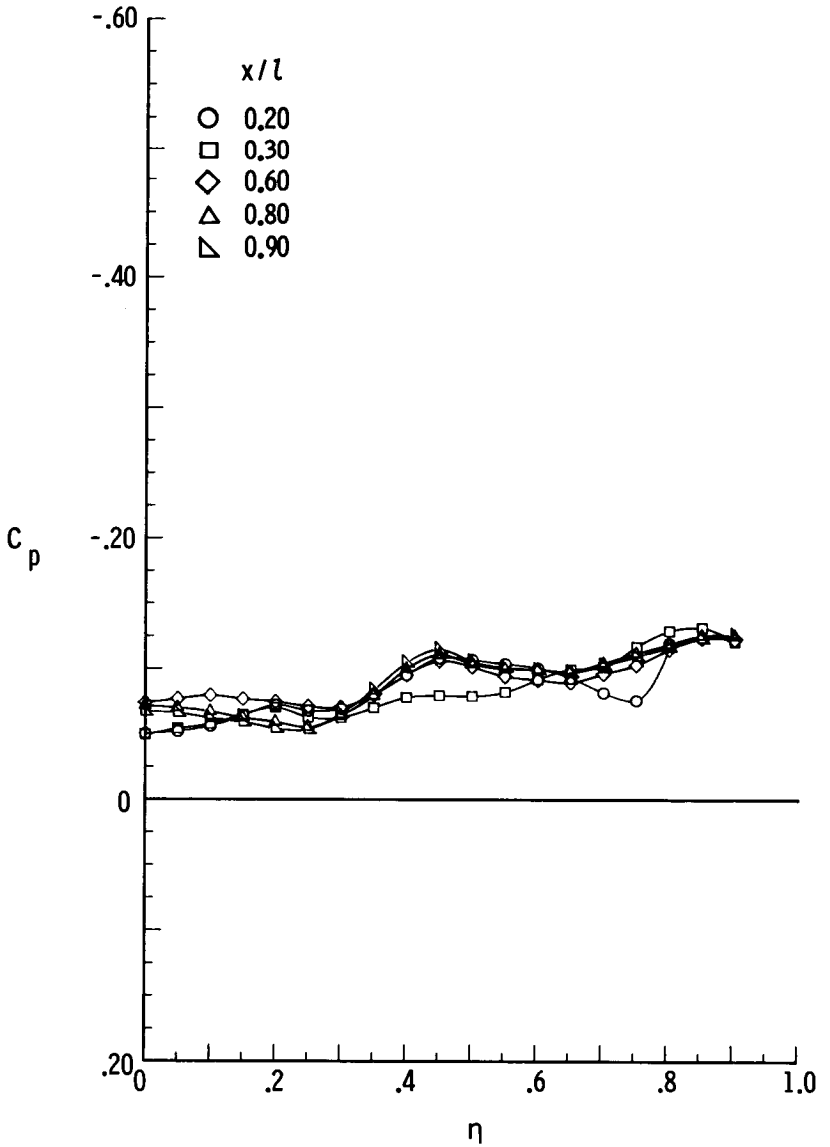

(h) M = 2.80; β = 4°.

Figure B29.- Continued.

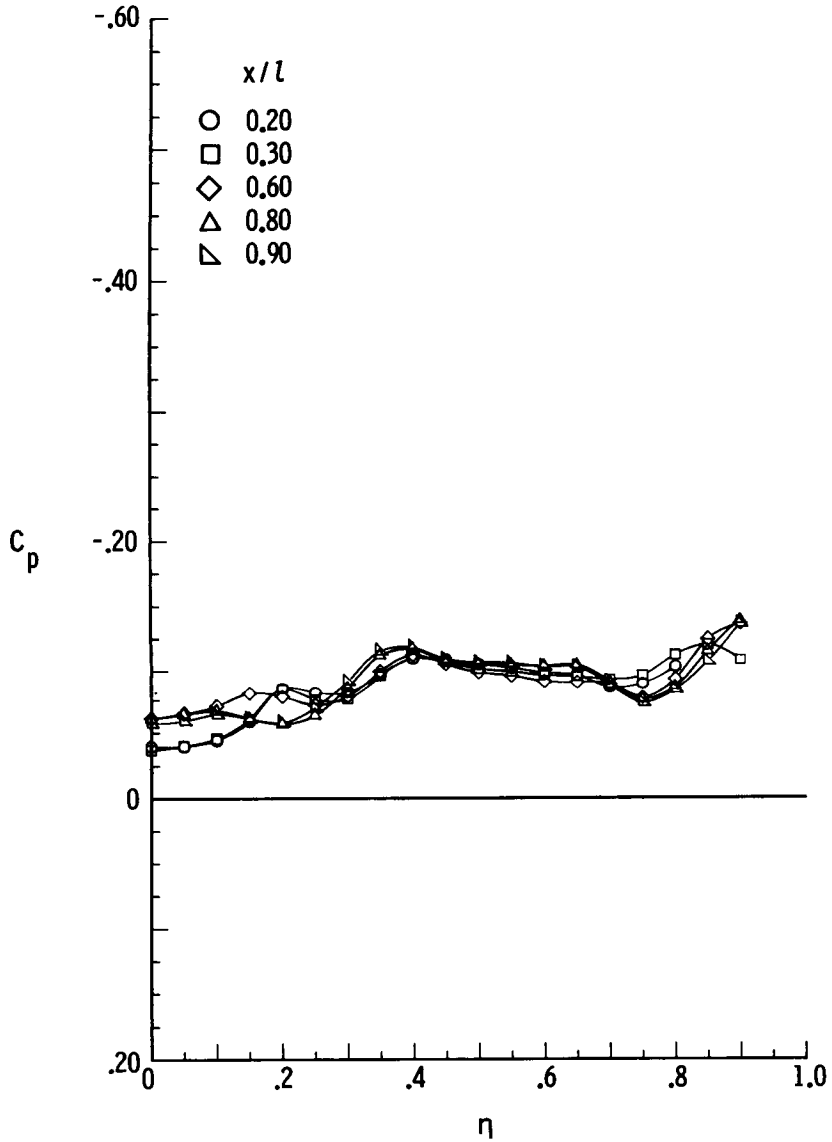

(i) M = 2.80; β = 2°.

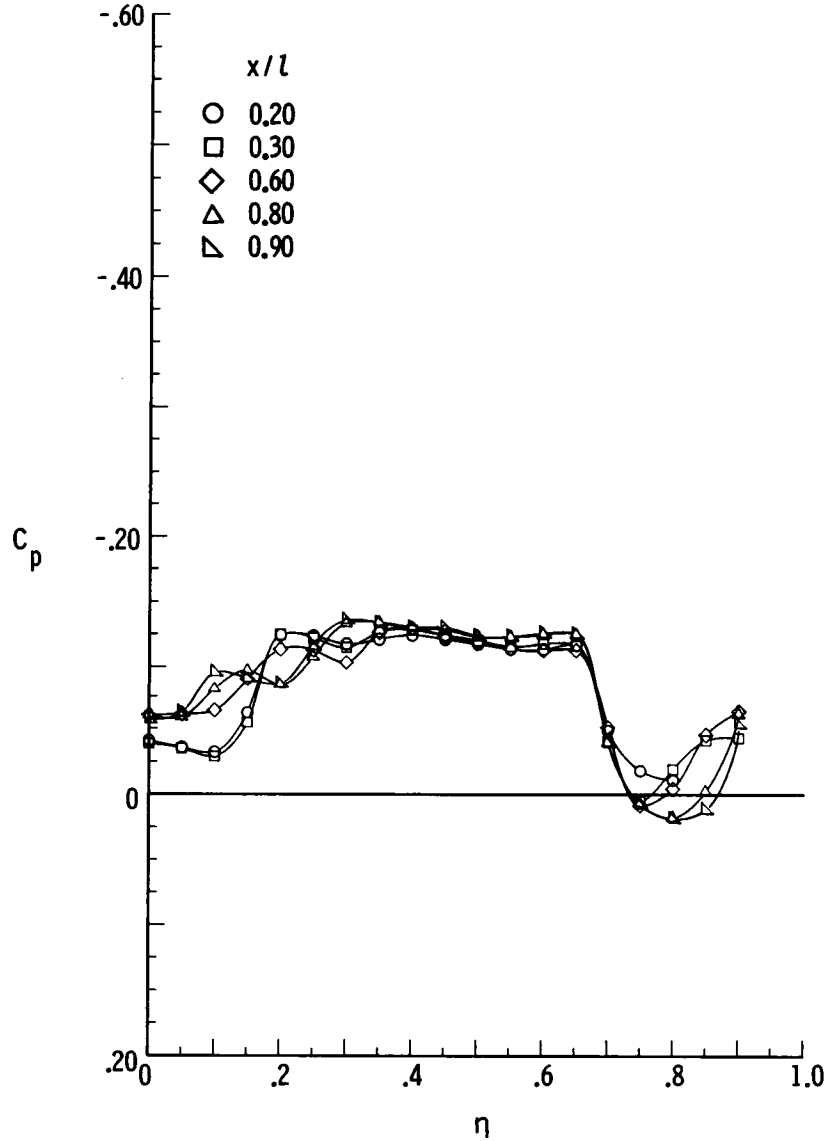

(j) M = 2.80; β = -2°.

Figure B29.- Continued.

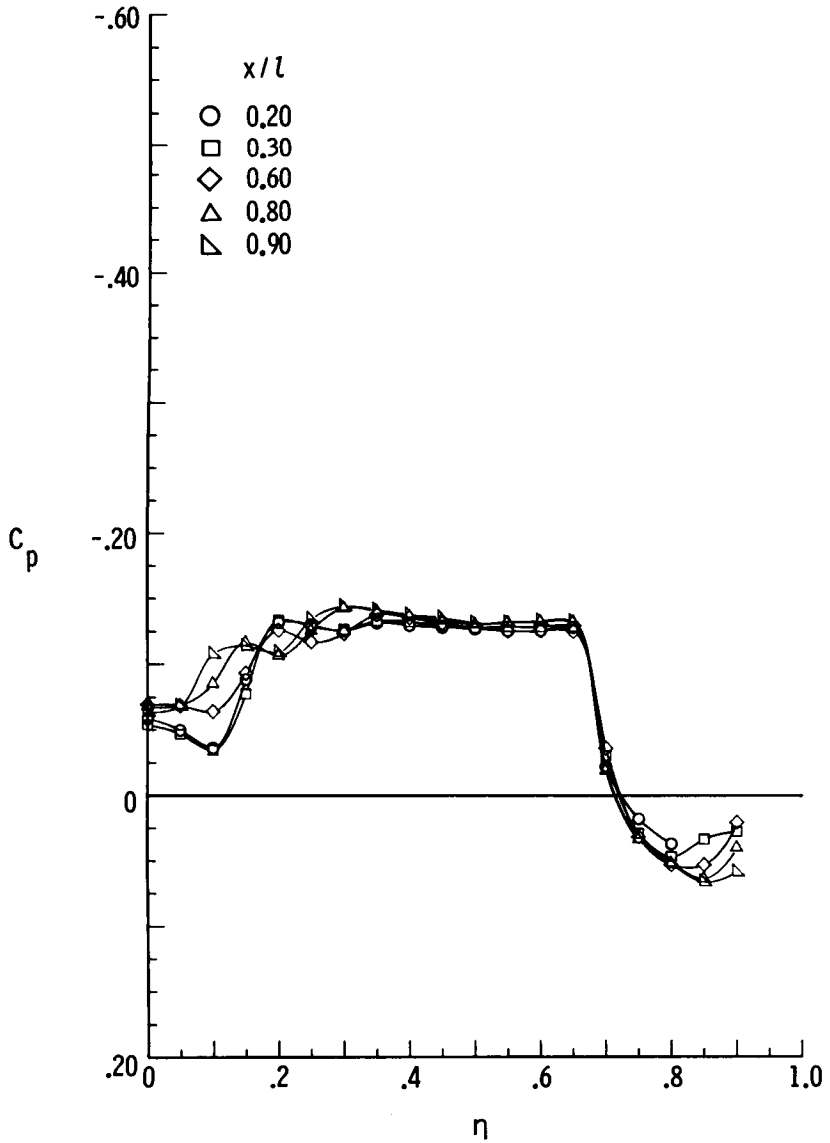

(k) M = 2.80; β = -4°.

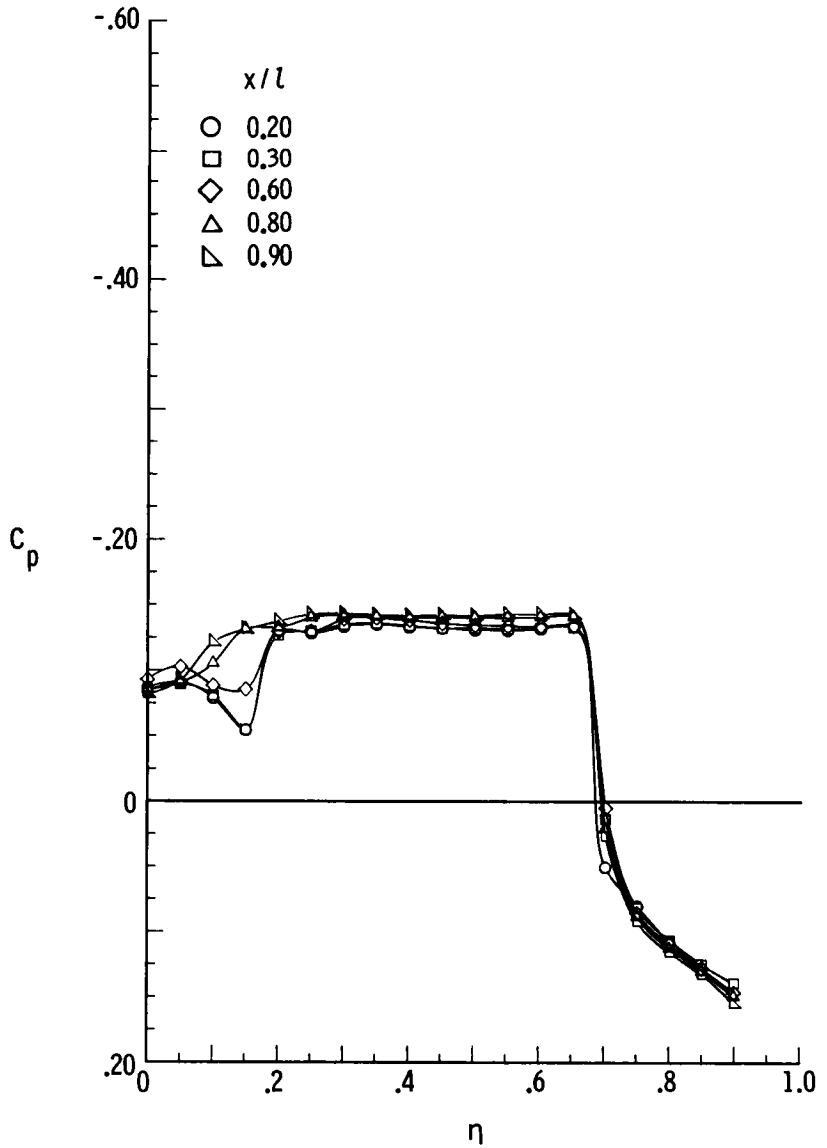

(l) M = 2.80; β = -8°.

Figure B29.- Concluded.

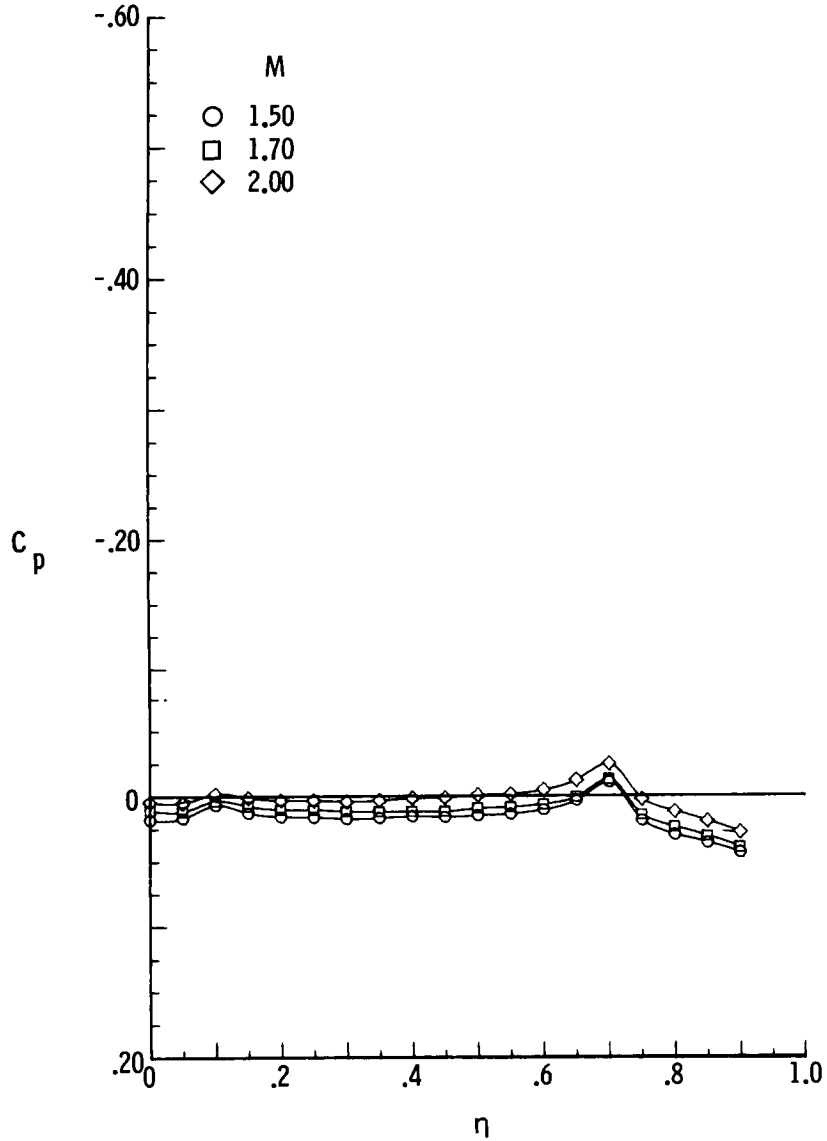

(a) $\alpha = 0°$.

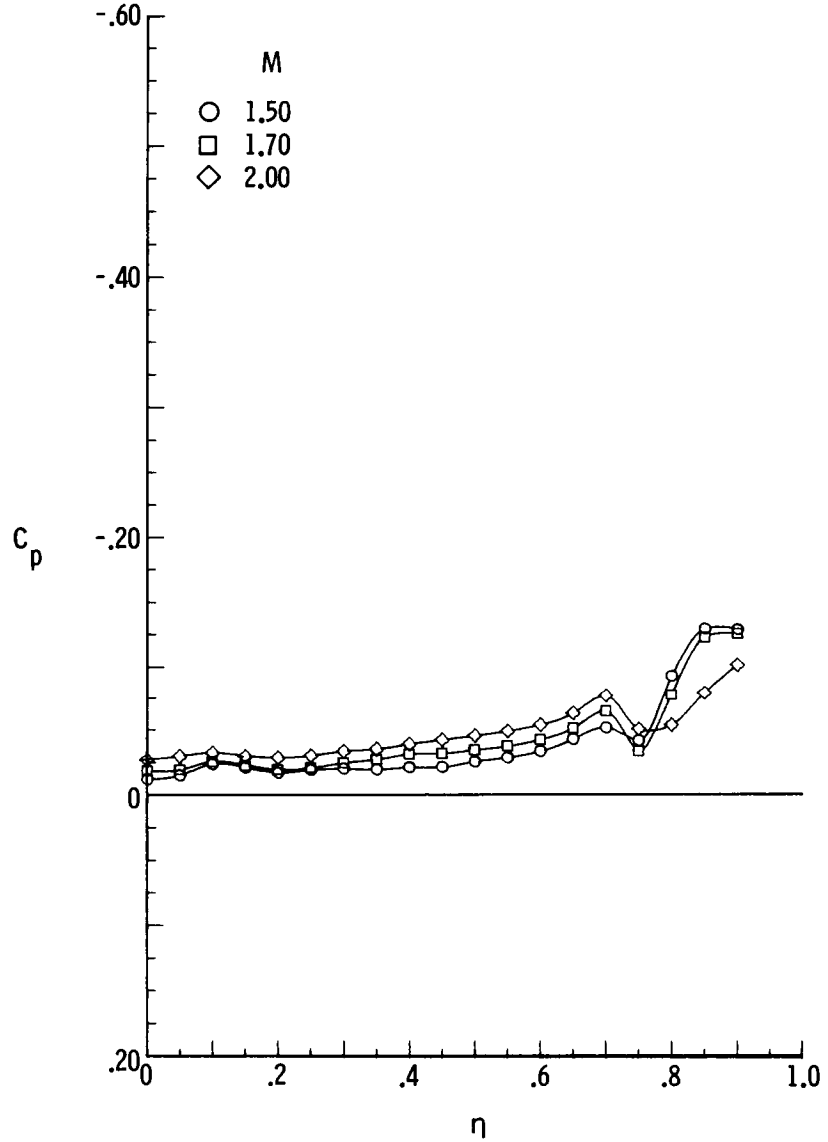

(b) $\alpha = 4°$.

Figure B30.- Pressure plots for 75° delta wing with $\delta_F = 5°$ with forebody for varying M, $R = 2 \times 10^6$, $\beta = 0°$, and $x/\ell = 0.90$.

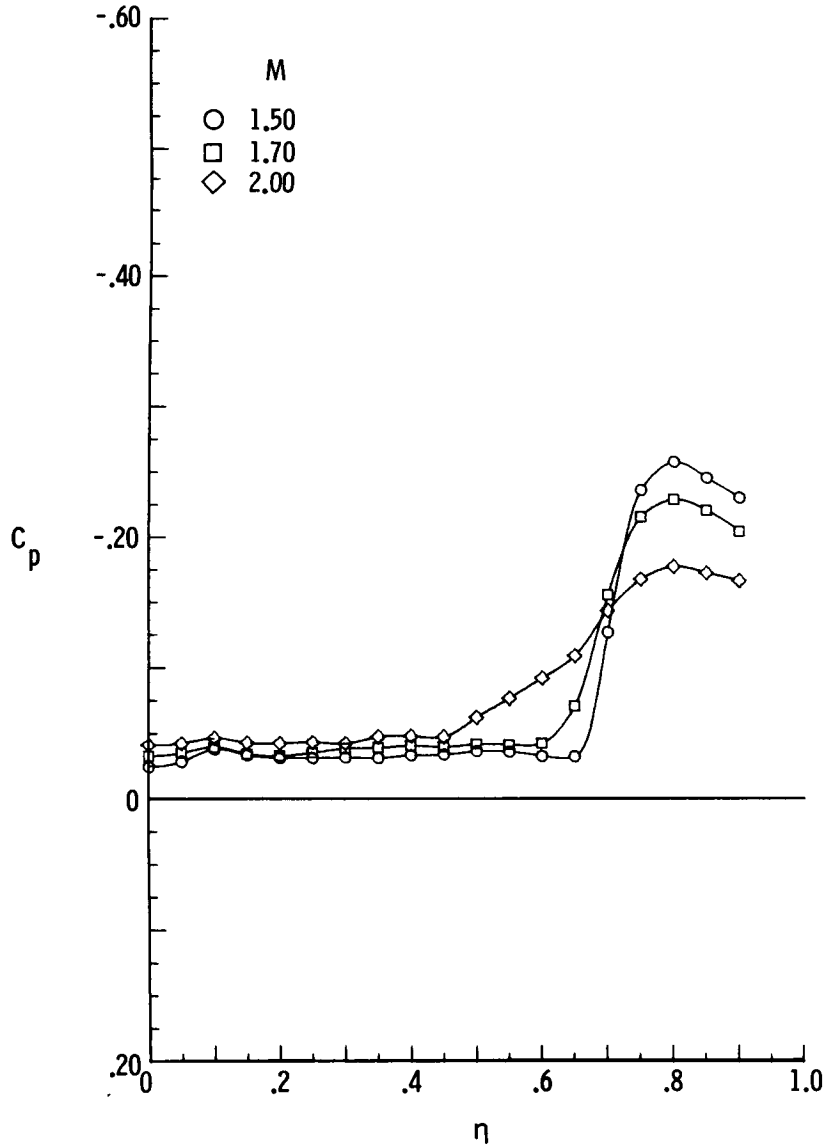

(c) $\alpha = 6°$.

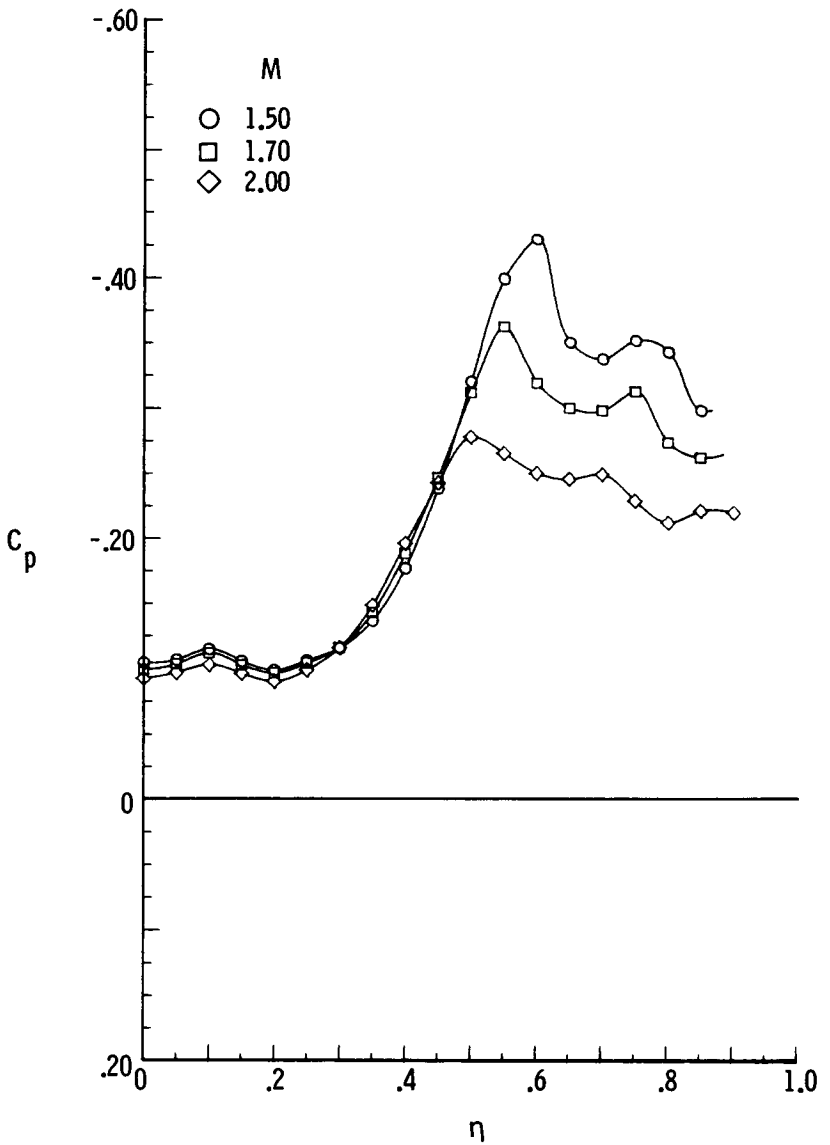

(d) $\alpha = 12°$.

Figure B30.- Concluded.

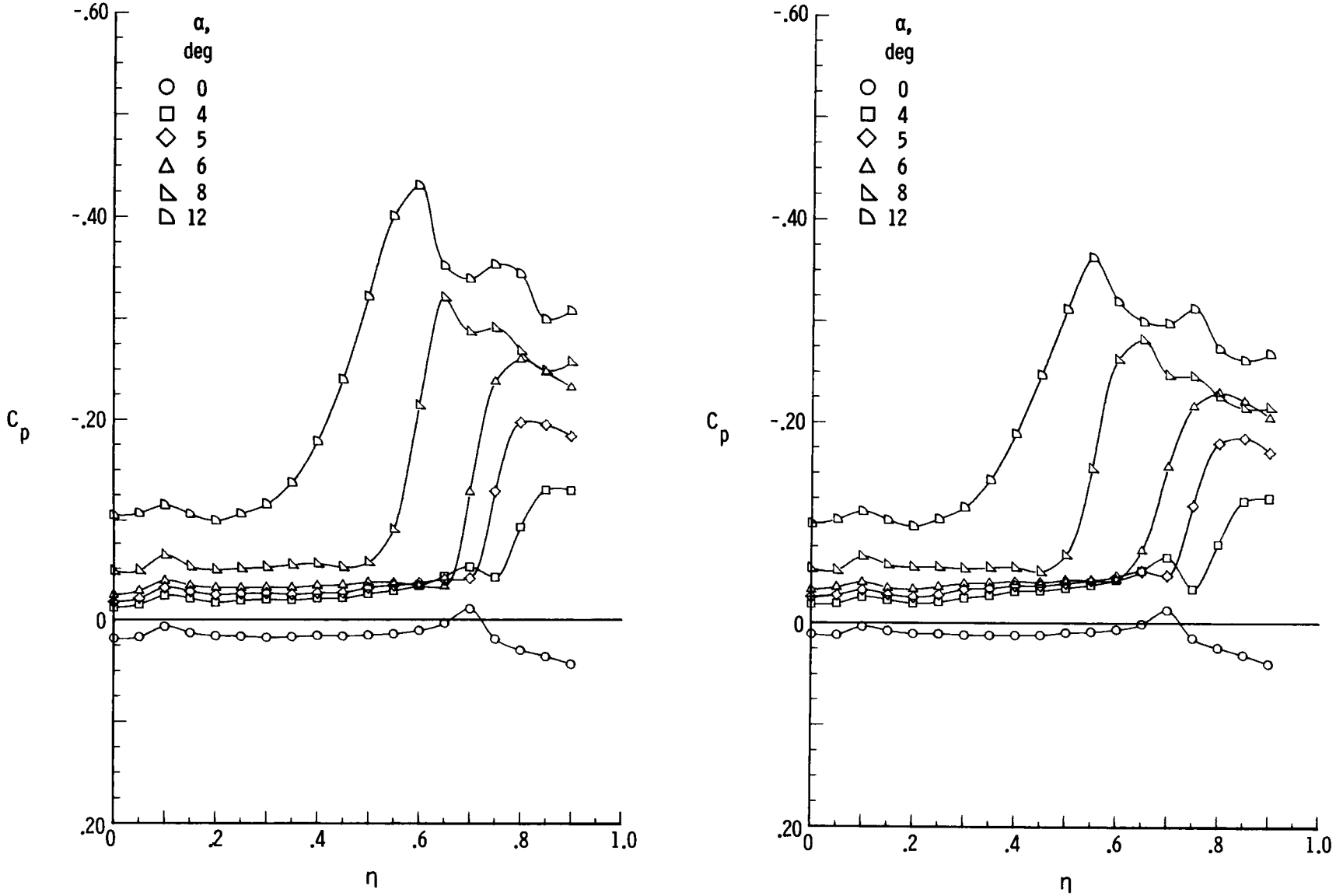

(a) M = 1.50.

(b) M = 1.70.

Figure B31.- Pressure plots of 75° delta wing with $\delta_F = 5°$ with forebody for varying α, $R = 2 \times 10^6$, $\beta = 0°$, and $x/\ell = 0.90$.

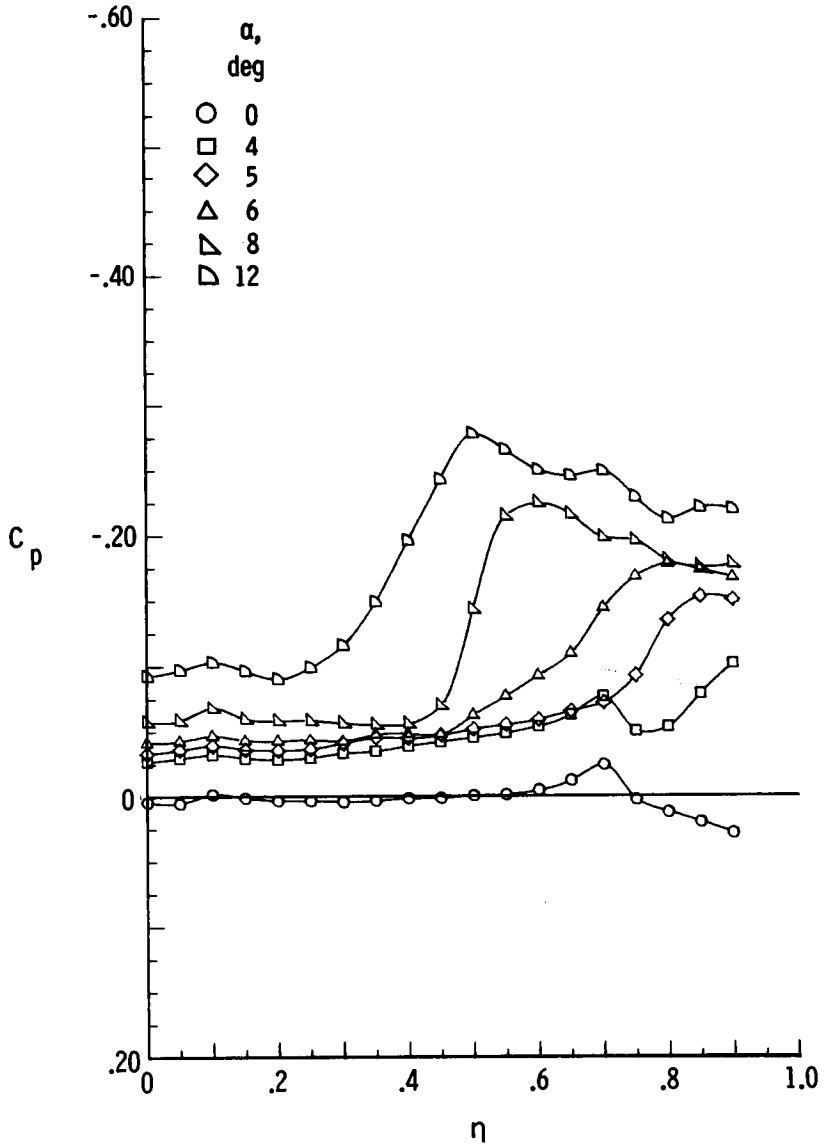

(c) M = 2.00.

Figure B31.- Concluded.

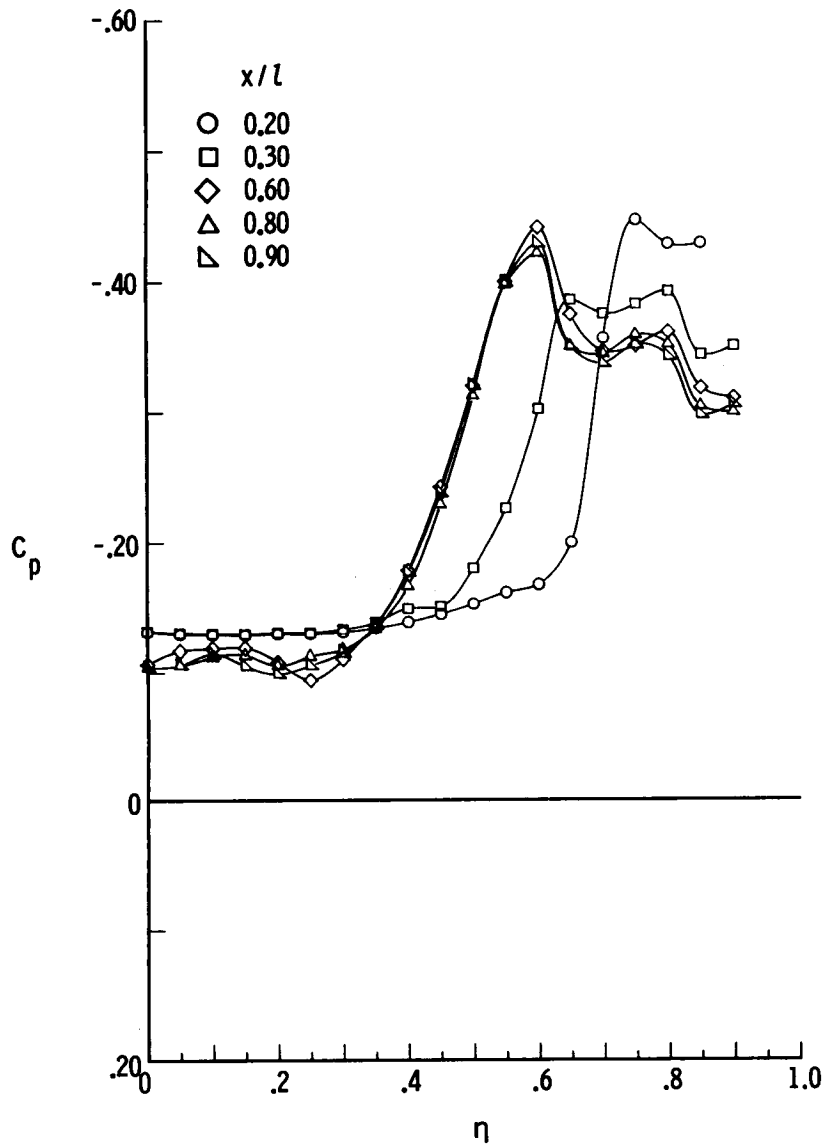

(a) M = 1.50.

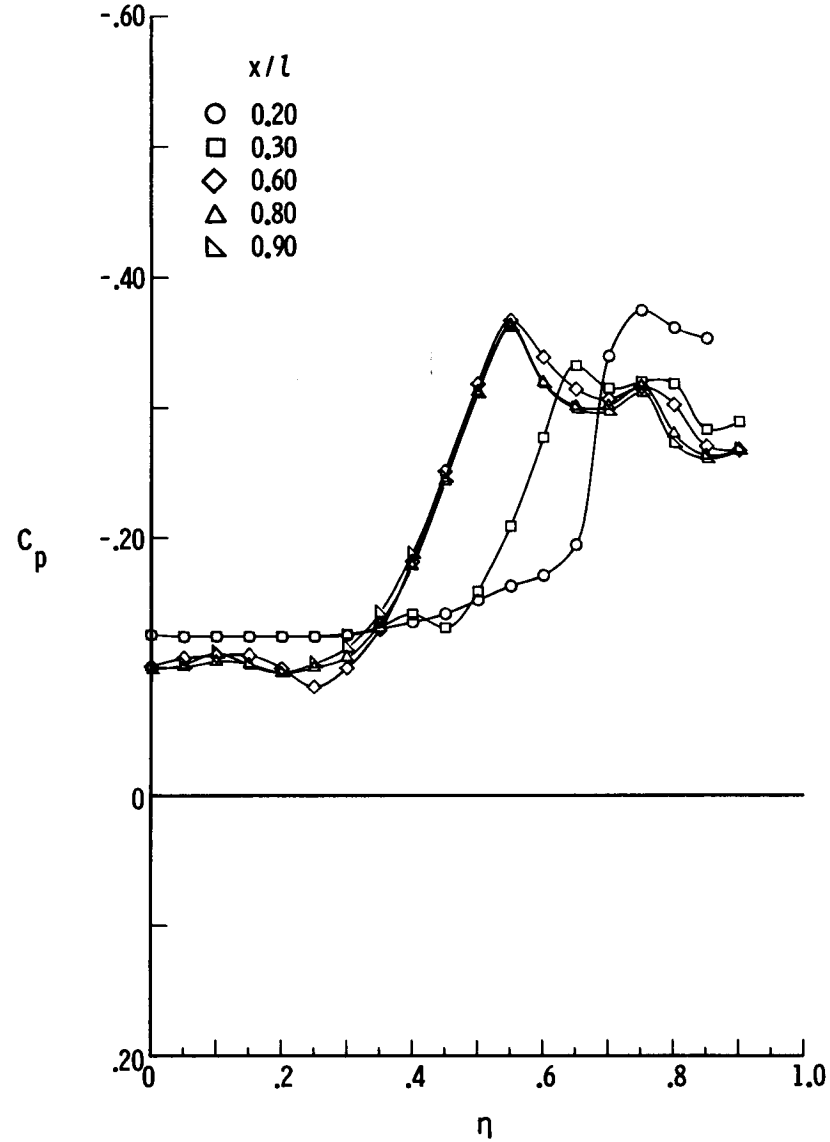

(b) M = 1.70.

Figure B32.- Pressure plots of 75° delta wing with $\delta_F = 5°$ with forebody for varying x/l, $R = 2 \times 10^6$, $\alpha = 12°$, and $\beta = 0°$.

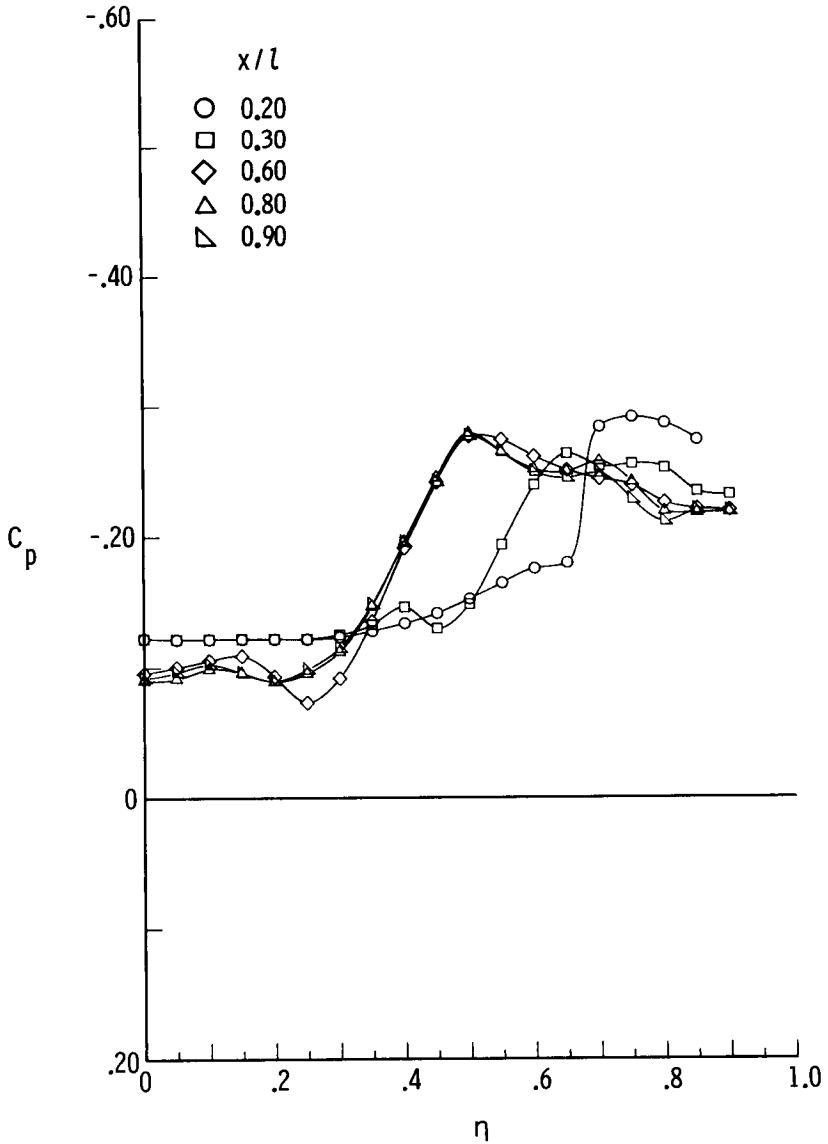

(c) M = 2.00.

Figure B32.- Concluded.

Standard Bibliographic Page

1. Report No.	2. Government Accession No.	3. Recipient's Catalog No.
NASA TP-2660, Part 1		

4. Title and Subtitle	5. Report Date
Study of Lee-Side Flows Over Conically Cambered Delta Wings at Supersonic Speeds	July 1987
	6. Performing Organization Code
7. Author(s)	8. Performing Organization Report No.
Richard M. Wood and Carolyn B. Watson	L-16192
9. Performing Organization Name and Address	10. Work Unit No.
NASA Langley Research Center Hampton, VA 23665-5225	505-62-81-07
	11. Contract or Grant No.
12. Sponsoring Agency Name and Address	13. Type of Report and Period Covered
National Aeronautics and Space Administration Washington, DC 20546-0001	Technical Paper
	14. Sponsoring Agency Code

15. Supplementary Notes

16. Abstract

An experimental investigation was performed in which surface pressure data, flow visualization data, and force and moment data were obtained on four conical delta wing models which differed in leading-edge camber only. Wing leading-edge camber was achieved through a deflection of the outboard 30 percent of the local wing semispan of a reference 75° swept flat delta wing. The four wing models have leading-edge deflection angles δ_F of 0°, 5°, 10°, and 15° measured streamwise. Data for the wings with δ_F = 10° and 15° showed that hinge-line separation dominated the lee-side wing loading and prohibited the development of leading-edge separation on the deflected portion of wing leading edge. However, data for the wing with δ_F = 5° showed that at an angle of attack of 5°, a vortex was positioned on the deflected leading edge with reattachment at the hinge line. Flow visualization results have been presented which detail the influence of Mach number, angle of attack, and camber on the lee-side flow characteristics of conically cambered delta wings. Analysis of photographic data identified the existence of 12 distinctive lee-side flow types. In general, the aerodynamic force and moment data correlated well with the pressure and flow visualization results.

17. Key Words (Suggested by Authors(s))	18. Distribution Statement
Supersonic aerodynamics Conicity Delta wings Flow visualization Surface pressures Forces and moments Reynolds number	Unclassified - Unlimited Subject Category 02

19. Security Classif.(of this report)	20. Security Classif.(of this page)	21. No. of Pages	22. Price
Unclassified	Unclassified	211	A10

For sale by the National Technical Information Service, Springfield, Virginia 22161